Detection and Identification of Electrons and Photons

Applications in the ATLAS Experiment, for the ATLAS ITk Detector and at the DESY II Test Beam

Dissertation
zur Erlangung des akademischen Grades
eines Doktor der Naturwissenschaften

vorgelegt von

Jan-Hendrik Arling
geboren in Ostercappeln





Technische Universität Dortmund
Lehrstuhl für Experimentelle Physik IV
Fakultät Physik
Dortmund

Deutsches Elektronen-Synchrotron
ATLAS Gruppe
Fachbereich Teilchenphysik
Hamburg

- Juli 2020 -

Der Fakultät Physik der TU Dortmund zur Erlangung des akademischen Grades eines Doktors der Naturwissenschaften vorgelegte Dissertation.

1. Gutachter : Prof. Dr. Kevin Kröninger (Technische Universität Dortmund)

2. Gutachter : Prof. Dr. Ingrid-Maria Gregor (Universität Bonn & DESY Hamburg)

Vorsitzender der Prüfungskommision : Prof. Dr. Markus Betz (TU Dortmund)

Vertretung der wiss. Mitarbeiter : Dr. Anton Savitzky (TU Dortmund)

Datum des Einreichens der Arbeit: 10. Juli 2020

Datum der mündlichen Prüfung: 14. September 2020

Abstract

In this thesis, the importance for the best possible exploitation of particle detectors to detect and identify electrons and photons is addressed by selecting three different examples for applications of precisely measuring electrons and photons at high-energy physics and test beam experiments.
In the first example, the optimization of the photon identification within the **A** **T**oroidal **L**HC **A**pparatu**S** (ATLAS) detector currently operated at the **L**arge **H**adron **C**ollider (LHC) is investigated. Appropriate selection criteria are needed in the photon identification to efficiently discriminate prompt photons, which stem directly from the hard-scattering process in the proton-proton collisions, from photons originating from hadronic jet decays. Discriminating variables are derived from the electromagnetic showering process of photons in the ATLAS calorimeter and can be used to identify prompt photons out of the more abundant non-prompt photon background. Based on the performance results in Run 2 employing rectangular cuts on the shower shape variables, systematic studies using a multivariate approach with a **B**oosted **D**ecision **T**ree (BDT) are conducted to optimize the photon identification performance. For this purpose, a dedicated software framework was developed allowing to tune the optimization and evaluate the performance results. First results for the BDT-based photon identification are promising, when comparing the signal and background efficiencies to the cut-based approach.
The second example addresses the planned upgrade of the ATLAS detector by building a new tracking detector with the **I**nner **T**rac**k**er (ITk) for the high-luminosity phase of the LHC. Apart from the selection of suitable sensor technologies, e.g. silicon sensors, to detect and measure particles, the corresponding support structures for the detector need to be considered. The petals are the building blocks for the ITk strip end-cap detector and consists of a light-weight core structure providing mechanical support and cooling for the loaded on silicon micro-strip sensor modules. The thermo-mechanical performance of the petal design is studied by testing prototypes in dedicated setups employing infrared thermography, dual-phase CO_2 cooling and geometrical metrology. The results of the thermo-mechanical characterization proves a well-performing design of the local support structure fulfilling most of the ITk detector specifications.
In the final example, the beam of multi-GeV electrons at the DESY II Test Beam Facility is used to investigate the potential of the **M**aterial **B**udget **I**maging (MBI) technique. This technique aims to reconstruct the material distribution of samples by measuring the deflection angles of traversing electrons with the high-resolution EUDET-type beam telescopes. Due to the underlying multiple Coulomb scattering, the reconstructed kink angle distribution depends directly on the material budget of the sample, such that its characteristic radiation length can be measured. With the spatial information of the reconstructed tracks, it is also possible to resolve a two-dimensional image of the material budget distribution. The results of several test beam measurements for a large variety of materials are studied, ranging from performance studies on the MBI technique with calibration materials up to the imaging of complex composite structures.

Zusammenfassung

In der vorliegenden Dissertation wird die Bedeutung für die bestmögliche Nutzung von Teilchendetektoren zum Nachweis und zur Identifizierung von Elektronen und Photonen anhand von drei verschiedenen Beispielen für hochpräzise Messungen von Elektronen und Photonen bei Hochenergiephysik- und Teststrahlexperimenten diskutiert.
Im ersten Beispiel wird die Optimierung der Photonenidentifikation beim **A** **T**oroidal **L**HC **A**pparatu**S** (ATLAS)-Detektor, der derzeit am **L**arge **H**adron **C**ollider (LHC) betrieben wird, untersucht. Geeignete Auswahlkriterien werden bei der Photonenidentifikation benötigt, um effizient prompte Photonen, die direkt aus dem harten Streuprozess der Kollisionen stammen, von Photonen aus dem Zerfall hadronischer Jets unterscheiden zu können. Für die Klassifikation von Signal und Untergrund werden Variablen aus dem elektromagnetischen Schauerprozess im ATLAS-Kalorimeter abgeleitet. Basierend auf den Ergebnissen von Run 2 mit der Verwendung von rechteckigen Schnitten auf die diskriminierenden Variablen werden hier systematische Studien für einen multivariaten Ansatz mit einem **B**oosted **D**ecision **T**ree (BDT) durchgeführt, um die Effizienz der Photonenidentifikation zu erhöhen. Mithilfe eines speziell entwickelten Software-Pakets ist es möglich, die Optimierung anzupassen und die Ergebnisse in Bezug auf die Effizienz zu bewerten. Erste Ergebnisse für die BDT-basierte Photonenidentifikation sind vielversprechend, wenn man die Effizienz für Signal und Untergrund mit dem schnittbasierten Ansatz vergleicht.
Das zweite Beispiel befasst sich mit dem geplanten Upgrade des ATLAS-Detektors durch den Bau eines neuen Spurdetektors, dem **I**nner **T**rac**k**er (ITk), für den Betrieb am High-Luminosity LHC. Neben der Auswahl geeigneter Sensortechnologien zur Teilchendetektion sind die entsprechenden Trägerstrukturen für den Detektor zu berücksichtigen. Die Petals sind die elementaren Bausteine für die Endkappe des ITk-Streifendetektors und bestehen aus einer Leichtbau-Struktur, welche die mechanische Stabilität und die Kühlung für die darauf befindlichen Module von Silizium-Mikrostreifensensoren gewährleistet. Die thermo-mechanischen Eigenschaften des Petaldesigns werden in speziell entwickelten Messaufbauten unter Verwendung von Infrarot-Thermografie, zweiphasiger CO_2-Kühlung und geometrischer Metrologie untersucht. Die Ergebnisse der thermo-mechanischen Charakterisierung zeigen ein gut funktionierendes Design der Haltestruktur, welches die meisten Spezifikationen des ITk-Detektors erfüllt.
Im letzten Beispiel wird der Elektronenstrahl der DESY II-Teststrahlanlage genutzt, um das Potenzial der **M**aterial **B**udget **I**maging (MBI)-Technik zu untersuchen. Ziel ist es, die Materialverteilung von Proben zu rekonstruieren, indem die Ablenkwinkel der gestreuten Elektronen mit hochauflösenden Strahlteleskopen gemessen werden. Die rekonstruierte Verteilung der Ablenkwinkel hängt hierbei aufgrund von mehrfacher Coulomb-Streuung direkt von der Materialverteilung der Probe ab, sodass ihre charakteristische Strahlungslänge gemessen werden kann. Mit den vollständig rekonstruierten Teilchenspuren ist es auch möglich, die zweidimensionale Materialverteilung zu messen. Die Ergebnisse von Teststrahlmessungen für eine Vielzahl von Materialien werden untersucht, die von Studien zu MBI mit Kalibrationsmaterialien bis zur Bildgebung für komplexe Strukturen reicht.

Preface

The conducted studies and presented measurements in this thesis were performed in collaborative work within the individual project groups. Therefore, several of the shown results were only possible to reach over the time frame of my PhD due to the help and support of these people, which should be expressed by this preface.
In the following, the specific contributions from my side to performed studies and submitted publications are described, structured according to the three main topics of my thesis.

Photon Identification in the ATLAS Experiment

The optimization of the photon identification for the ATLAS experiment, which will be addressed in Chapter 4, was performed as my qualifying ATLAS authorship task.
Here, the work was conducted in close collaboration with the ATLAS E/gamma combined performance group and especially the photon ID sub-group.
During my one-and-a-half year of nearly full time work on the photon identification, a new cut-based photon ID menu for the physics analyses in Run 2 was prepared. This process was supported from my side by auxiliary studies on the performance of the optimized menu by running performance tests based on Monte Carlo simulated data. Finally, the collaborative work cummulated in the publication of "Measurement of the photon identification efficiencies with the ATLAS detector using LHC Run 2 data collected in 2015 and 2016" [128], including the reoptimized photon identification with my supporting investigations.

Studies on the Petal for the ATLAS ITk Strip End-cap Detector

My work on the investigation and optimization of the petal core as the local support structure for the ATLAS ITk strip end-cap detector was focused on the thermo-mechanical characterization of the structure, as it will be discussed in Chapter 6 and 7.
The measurements on the petal prototypes were conducted within the ATLAS ITk group at DESY as well as in close contact to the worldwide ATLAS ITk collaboration. First of all, the achieved results on the thermal investigation of the petal were presented in the Preliminary Design Review (Oct. 2018) and the Final Design Review (Feb. 2020). Here, both ATLAS internal reviews were passed successfully regarding the performed thermo-mechanical characterization tests within the DESY ITk group.
Moreover, two summer student projects at DESY were supervised for developments regarding the ATLAS ITk detector: on the one hand, the thermal setup for testing petals was further improved in terms of the usable instrumentation ("Thermal imaging of silicon detector components" [170]); on the other hand, auxiliary measurements regarding the emissivity of silicon modules as well as the application of appropriate correction techniques to the thermo-mechanical petal prototype were conducted ("Thermal Performance of the Petal Prototype" [181]).

Test Beam, Beam Telescopes and Material Budget Imaging

During my PhD work, I was also involved in the user support, maintainence and future improvements at the DESY II Test Beam Facility with its EUDET-type beam telescopes, which offers the user the possibility to test detector prototypes with a multi-GeV particle beam as it will be described in Chapter 8.
On the one hand, I was actively participating in the telescope support and maintainence group, allowing a high reliability for the provided user instrumentation, as well as developing future upgrades of the telescopes [261] and the testbeam infrastructure [210] at DESY.
On the other hand, I contributed to the correspondingly offered software tools for data acquisition and data analysis. Here, I contributed to the development of the DAQ software framework EUDAQ1 by implementing the possibility to control the motor-driven linear stages for the beam telescopes, which resulted in the publication "EUDAQ - A Data Acquisition Software Framework for Common Beam Telescopes" [221]. Furthermore, I was an active developer for the test beam reconstruction framework EUTelescope, for which I took over the maintainence responsibility in the end of 2018. As such, I simplified the installation process, cleaned up the code repository and contributed to the new implementation of the General Broken Lines algorithm. For new test beam users, I provided educative examples and offered tutorials at the "Beam Telescope and Test Beam" workshops in 2019 and 2020. The new developments cummulated into the publication "EUTelescope: A modular reconstruction framework for beam telescope data" [224].
As part of the studies to the technique of material budget imaging at the DESY II Test Beam Facility, for which the results are presented in Chapter 9, two summer student projects were supervised: on the one hand, resolution studies for the 2D material budget images of complex structures were conducted ("Studies of X_0 measurements at the DESY II test beam facility" [254]); on the other hand, the calibration of material budget imaging for the purpose of medical applications was investigated ("Calibration with water for track-based multiple scattering tomography at the DESY II Test Beam Facility" [259]).

Unity is strength...
when there is teamwork and collaboration,
wonderful things can be achieved.

- Mattie Stepanek

Contents

Abstract i

Zusammenfassung iii

Preface v

List of Contents vii

Introduction 1

1 Particle Physics and the Standard Model 7
1.1 The Standard Model of Particle Physics . . . 7
1.1.1 Elementary Particles in the Standard Model . . . 9
1.1.2 Fundamental forces in the Standard Model . . . 9
1.1.3 The Higgs mechanism in the Standard Model . . . 11
1.2 High-Energy Physics at the Large Hadron Collider . . . 12
1.2.1 Center-of-mass energy, luminosity and pile-up . . . 13
1.2.2 Partons, hadronization and underlying event . . . 14
1.2.3 Schedule and performance of the LHC . . . 15
1.3 Testing the Standard Model: Precision Measurements . . . 17
1.3.1 W boson mass . . . 17
1.3.2 Higgs boson: mass & couplings . . . 18
1.3.3 Light-by-light scattering . . . 21
1.4 Open Questions: Physics beyond the Standard Model . . . 23
1.4.1 Problems in the Standard Model . . . 23
1.4.2 Beyond Standard Model theory . . . 25

2 Particle Detection and the ATLAS Detector 27
2.1 Interaction with Matter . . . 28
2.1.1 Energy loss of charged particles . . . 28
2.1.2 Multiple Coulomb scattering of charged particles . . . 31
2.1.3 Interactions of photons with matter . . . 32
2.1.4 Electromagnetic showers . . . 34
2.2 Silicon Detectors . . . 35
2.2.1 Semiconductors and doping . . . 35
2.2.2 *pn*-junction and reverse biasing . . . 36
2.2.3 Sensor segmentation and readout . . . 39
2.2.4 Signal formation and performance parameters . . . 39
2.2.5 Radiation damage and detector degradation . . . 41

2.3 The ATLAS Detector . . . 44
2.3.1 Coordinates and kinematics . . . 45
2.3.2 ATLAS Inner Detector . . . 46
2.3.3 ATLAS Calorimeter System . . . 47
2.3.4 ATLAS Muon Spectrometer . . . 49
2.3.5 ATLAS Trigger and Data Acquisition System . . . 49

3 Photons in ATLAS 51
3.1 Photons in Physics Analyses . . . 52
3.2 Reconstruction of Photons . . . 52
3.3 Isolation of Photons . . . 54
3.4 Identification of Photons . . . 55
3.4.1 Monte Carlo samples for photon identification optimization . . . 56
3.4.2 Shower shape variables . . . 57
3.4.3 *Loose* and *tight* identification . . . 62
3.5 Photon Efficiency Measurement . . . 65
3.5.1 Radiative Z decays . . . 65
3.5.2 Electron extrapolation . . . 66
3.5.3 Matrix method . . . 67
3.5.4 Combination . . . 68

4 Optimization of Photon Identification 71
4.1 Cuts, Multi-Variate Analysis and Machine Learning . . . 72
4.1.1 Rectangular cuts . . . 72
4.1.2 Boosted decision trees . . . 73
4.1.3 Neural networks . . . 73
4.1.4 Advantages and disadvantages . . . 74
4.2 The *PhotonIDOptimizer* Framework . . . 75
4.2.1 Design and functionality . . . 76
4.2.2 Operation principle . . . 76
4.2.3 Validation study . . . 78
4.3 Optimization using Rectangular Cuts . . . 79
4.3.1 Parameter tuning for cut-based optimization . . . 79
4.3.2 Dependence of cut values . . . 81
4.3.3 Study with radiative Z sample . . . 82
4.4 Optimization using Boosted Decision Trees . . . 83
4.4.1 Parameter tuning for BDT optimization . . . 83
4.4.2 BDT optimization and performance studies . . . 85
4.4.3 Study on a two-BDT approach . . . 88
4.4.4 Study of p_{T}-dependent BDT . . . 91
4.5 Conclusion . . . 93

5 High-Luminosity LHC and the ATLAS ITk Detector 95
5.1 The High-Luminosity Phase of the LHC . . . 96
5.1.1 Accelerator upgrades . . . 96
5.1.2 Physics motivation . . . 97
5.2 The ATLAS Inner Tracker . . . 97
5.2.1 ITk requirements & challenges . . . 98
5.2.2 ITk detector design . . . 100

5.3 The ATLAS ITk Strip End-cap Detector . . . 101
5.3.1 Silicon modules . . . 102
5.3.2 Local support core . . . 104
5.3.3 TDAQ & global support . . . 106
5.3.4 Production, testing & database . . . 107

6 Thermo-Mechanical Studies on Petals 109
6.1 Objectives and Specifications . . . 110
6.1.1 Specifications on thermo-mechanical properties . . . 111
6.1.2 Quality assurance & quality control . . . 113
6.2 Measurement Techniques & Equipment . . . 114
6.2.1 Geometrical metrology . . . 114
6.2.2 Infrared thermography . . . 115
6.2.3 CO_2 cooling & diagnostics . . . 117
6.2.4 Temperature & humidity logging . . . 122
6.2.5 Thermal & CO_2 simulations . . . 122
6.3 Prototypes: Petals & Cores . . . 125
6.3.1 Petal core prototypes . . . 125
6.3.2 Thermo-mechanical petal . . . 126
6.4 Emissivity and Correction Methods . . . 128
6.4.1 Emissivity and its dependencies . . . 128
6.4.2 Emissivity and its correction techniques . . . 130
6.4.3 Experimental studies on the emissivity . . . 132
6.4.4 Emissivity correction for petals . . . 137
6.5 Characterization of the Thermal Performance . . . 139
6.5.1 Setup for the thermal performance evaluation . . . 139
6.5.2 Thermal performance study on petal cores . . . 141
6.5.3 Thermal performance study on the TM petal . . . 153
6.6 Investigation on Thermal Deformations . . . 163
6.6.1 Setup and measurement principle . . . 163
6.6.2 Results and evaluation . . . 165
6.7 Thermal Cycling and Thermal Shock Test . . . 171
6.7.1 Setup for thermal cycling . . . 171
6.7.2 Performance after thermal cycling . . . 172
6.7.3 Thermal shock test on petal cores . . . 175
6.7.4 Thermal shock test on the TM petal . . . 176
6.8 Conclusion . . . 177

7 Investigations on Dual-Phase CO_2 Cooling 181
7.1 CO_2 Cooling System for the ITk Detector . . . 182
7.1.1 Design of the CO_2 cooling system . . . 182
7.1.2 Specifications of the CO_2 cooling system . . . 184
7.2 Influence of the CO_2 Flow Orientation . . . 184
7.2.1 Orientation study with petal cores . . . 185
7.2.2 Orientation study with the TM petal . . . 186
7.3 Investigations on the Pressure Drop . . . 188
7.3.1 Pressure drop analysis for petal cores . . . 188
7.3.2 Pressure drop analysis for the TM petal . . . 189
7.3.3 Dependence on the mass flow and orientation . . . 191
7.3.4 Simulations of the pressure drop . . . 192

7.4 Analysis of the CO_2 State . . . 194
7.4.1 CO_2 state over the full cooling cycle . . . 194
7.4.2 Estimation of the vapour quality . . . 195
7.4.3 Investigation of subcooling . . . 197
7.4.4 Estimation of the CO_2 state . . . 199
7.4.5 Simulations of the CO_2 state and the vapour quality . . . 201
7.5 Conclusion . . . 202

8 Test Beams & Beam Telescopes 205
8.1 DESY II Test Beam Facility . . . 206
8.1.1 Beam generation . . . 206
8.1.2 Infrastructure . . . 208
8.2 EUDET-Type Beam Telescopes . . . 209
8.2.1 Telescope sensors and mechanics . . . 210
8.2.2 Trigger and data acquisition system . . . 211
8.2.3 Integration of DUT . . . 212
8.3 Data Acquisition with EUDAQ . . . 213
8.3.1 Framework architecture . . . 213
8.3.2 Operation principle . . . 214
8.3.3 Implementation of automated DUT movement . . . 215
8.4 Data Analysis with EUTelescope . . . 216
8.4.1 Framework architecture . . . 217
8.4.2 Operation principle . . . 218
8.4.3 Reconstruction flow . . . 219
8.4.4 Track reconstruction with GBL . . . 224
8.5 Characteristics of Test Beam Experiments . . . 227
8.5.1 Testbeam parameters . . . 227
8.5.2 Telescope parameters . . . 230
8.5.3 Calibration of lead-glass counter . . . 232

9 Material Budget Imaging 235
9.1 Radiation Length & Multiple Scattering . . . 236
9.1.1 Radiation length and material budget . . . 237
9.1.2 Theory of multiple Coulomb scattering . . . 237
9.1.3 Radiation length of materials . . . 239
9.1.4 Basics of material budget imaging . . . 240
9.2 Test Beam Campaigns: Setups & Samples . . . 241
9.2.1 Test beam parameters . . . 241
9.2.2 Telescope setup & parameters . . . 242
9.2.3 Measurement routine & samples . . . 244
9.3 Reconstruction of Kink Angles . . . 251
9.3.1 Kink angle reconstruction with GBL . . . 251
9.3.2 Track reconstruction in EUTelescope . . . 252
9.3.3 Dependence of track quality parameters . . . 253
9.4 Analysis of Kink Angle Distributions . . . 255
9.4.1 Dependence of kink angle distributions . . . 256
9.4.2 Estimators for the scattering width . . . 258
9.4.3 Correlation of horizontal and vertical kinks . . . 262
9.4.4 Acceptance effects for kink angle distributions . . . 263
9.4.5 Influence of the horizontal beam momentum variation . . . 265

9.5 Calibration for Material Budget Imaging . . . 267
9.5.1 Correction of air scattering . . . 268
9.5.2 Calibration of material budget evaluation . . . 269
9.5.3 Dependencies of the calibration . . . 271
9.5.4 Water calibration for medical applications . . . 275
9.5.5 Material budget of composite structures . . . 277
9.6 Investigation of ATLAS ITk Materials & Structures . . . 279
9.6.1 Material budget calculation for ATLAS ITk materials . . . 280
9.6.2 Material budget imaging of ATLAS ITk structures . . . 284
9.7 Investigation on Energy Loss Effects . . . 297
9.7.1 Measurement of kink angle widths for high-Z material samples . . . 298
9.7.2 Calorimeter measurement of the energy loss . . . 299
9.7.3 Energy loss correction for the Highland model . . . 301
9.8 Conclusion . . . 303

Conclusion and Outlook **309**

List of Acronyms **I**

List of Figures **V**

List of Tables **XIII**

Bibliography **XV**

Acknowledgements **XXXI**

Appendix **i**
A Thermo-Mechanical Studies on Petals . . . i
A.1 Thermal performance of petal cores . . . i
A.2 Thermal performance of the TM petal . . . vii
A.3 Calculation of the local flatness . . . x
B Investigations on Dual-Phase CO_2 Cooling . . . xi
B.1 CO_2 orientation study . . . xi
B.2 CO_2 pressure drop study . . . xiii
B.3 Heat transfer by free convection . . . xiv
B.4 Estimation of the vapour quality by sightglass analysis . . . xvi
B.5 Calculations for the CO_2 state analysis of the TM petal . . . xviii
C Material Budget Imaging . . . xix
C.1 Analytical calculation of radiation length . . . xix
C.2 Determination of the fiducial area . . . xx
C.3 Estimator of the kink angle mean value . . . xxi
C.4 Energy dependence of MBI calibration . . . xxii
C.5 Resolution and contrast for material budget image . . . xxiv
C.6 Two-dimensional stitching of material budget images . . . xxvi

Introduction

The research in particle physics is directly connected to the wish to understand the nature of the elementary particles and their interactions via the fundamental forces. When describing the processes on the sub-atomic scale and understand the smallest constituents of our surrounding world, the findings can be extrapolated to larger scales to also receive a better understanding of the universe. Here, the scientists are eager to ask the question how the universe was created and how it evolved to the universe we can observe nowadays.

To achieve the level of understanding, we have reached up to now, decades of investigations on the theoretical and experimental particle physics have passed, being connected to generation of scientists developing the theoretical models to describe the interaction of particles inside the up-to-now successful theory of the **S**tandard **M**odel (SM) of particle physics or conducting experiments for the detection of new elementary particles to be added to the zoo of particles, we know of by now. In the beginning of the discipline of particle physics, many experiments were conducted as small scale laboratory measurements involving only a handful of ambitious particle physicists, describing the results of groundbreaking experiments in the fields of particle and nuclear physics.

But for the today's research in particle physics, much larger investments are required, for which the best example is most probably the **L**arge **H**adron **C**ollider (LHC) located at the center of the European Organization for Nuclear Research (CERN) with the **A** **T**oroidal **L**HC **A**pparatu**S** (ATLAS) experiment as one of the four big particle physics experiments. Here, the LHC is by far the most powerful tool of modern particle physics offering a particle accelerator installed in a nearly 27 km circular tunnel and accelerating two bunches of protons close to the speed of light. When the beams of highly energetic protons collide, the quarks as the constituents of protons interact with each other, producing new highly energetic particles, which are characteristic for the type of interaction happened in the collision. The particle physics experiments such as ATLAS provides large detector assemblies, which are located at the interaction point to detect and measure the newly created particles in the proton-proton collisions. By analysing millions of recorded collision events, conclusions about the interaction mechanisms and the involved particles can be inferred. Therefore, large accelerator complexes with experiments providing very precise particle detectors are required for the today's investigations in the area of experimental particle physics. Here, the number of people in terms of technical staff as well as scientists required to operate the accelerator and its experiments is huge. In the case of the ATLAS collaboration, thousands of people are involved working worldwide on the success of the experiment.

The aim of this thesis is to highlight the importance for the best possible exploitation of particle detectors to detect and identify particles as well as to measure their properties with the highest precision and accuracy. The focus will be on the detection and identification of electrons and photons, which are very often involved in the particle physics research.

Various mechanisms for the interaction of the particles with matter via the electromagnetic force exist, allowing to study properties of the material when traversed by these particles or vice versa to actually detect them as used in the case of designing a particle detector.

Three rather different applications are selected in this thesis to show the relevance for an advanced detection and identification of electrons and photons:

- For several physics analyses of the high-energy physics experiments at the LHC, it is important to efficiently reconstruct and identify photons in *pp* collisions. One important example is here certainly the observation of the Higgs boson by the ATLAS and CMS experiments in 2012 using the decay channel of the Higgs boson into two photons. Photon identification means in this case that prompt photons stemming directly from the hard-scattering interaction (as for the diphoton decay of the Higgs boson) are distinguished from background photons originating e.g. from the decay of hadronic jets in the collision event. Therefore, the goal of the employed identification algorithm should be to reach a high efficiency for the identification of prompt photons, while providing also a high suppression for background photons.
  The *optimization of the photon identification* is the first topic of this work.

- In the course of the planned upgrade of the ATLAS detector by 2026, a new tracking detector with the **I**nner **T**rac**k**er (ITk) will be built. As at the same time the LHC accelerator is upgraded to the **H**igh-**L**uminosity **LHC** (HL-LHC) aiming for unprecedented levels of luminosities in the proton-proton collisions, the particle detectors are facing very challenging conditions. The goal for the ITk detector is therefore to maintain the high precision of detecting and measuring charged particles such as electrons created in the collisions. But apart from the design of the silicon sensors as the preferred choice for the tracking detectors due to their high precision and efficiency to measure the spatial positions for the traversing particles, the support structures for the sensor modules have to be designed well.
  Here, it is important that a high mechanical stability is provided for the silicon sensors over the full life time of the detector, meaning ten to fifteen years. Moreover, a sufficient cooling of the sensor modules is required, which is especially the case after the exposure to higher particle fluence and the resulting effects of radiation damage in the silicon. But at the same time, a minimal amount of material should be used to not deteriorate the measurement of the particle trajectories and their energies. This set of requirements cummulated in the design of the petal as the building block of the ITk strip end-cap detector consisting of a core structure providing all required services for the mounted on silicon strip modules.
  The *thermal-mechanical characterization of petals* is therefore the second topic of this thesis, involving also investigations on the dual-phase CO_2 cooling for the petals.

- The DESY II Test Beam Facility provides multi-GeV electron beams to conduct beam tests of novel detector technologies. But for this work, another application is studied using the beam particles for an imaging technique, called **M**aterial **B**udget **I**maging (MBI). Here, the material budget of a sample can be measured in a position-resolved way exploiting the high resolution EUDET-type beam telescopes offered at DESY. This is possible as the deflection angles of scattered electrons depend on the amount and type of the material traversed by the electrons. Therefore, materials as well as complex composite structures can be investigated in terms of their respective material budget, allowing also to evaluate their characteristic radiation lengths.
  The application and potential of the *material budget imaging* technique is studied as the third topic of the dissertation.

In Chapter 1, a general introduction to the principles of particle physics is given. Here, the theoretical description of the elementary particles and the fundamental forces within the SM of particle physics is summarized, which is followed by introducing the LHC and several characteristics of the physics inside the collision of particles. Moreover, a selection of precision measurements performed with the ATLAS detector as one of the large high-energy physics experiments at the LHC is provided, testing the SM to highest accuracies. Nonetheless, there are open questions in particle physics not answered by the SM theory, which opens up the possibility of physics beyond the SM.

Chapter 2 introduces the concept of particle detection exploiting the different type of interactions of particles with matter, focusing here on mechanisms observed for electrons and photons. Furthermore, silicon detectors are a common choice for the application in tracking detectors and their material properties as a semiconductor and the ways to use it for particle detection are described. Here, also the effect of high particle fluences degrading the sensor performance due to radiation damages in the silicon material is shown. Finally, the ATLAS detector with its several sub-detector systems ranging from the innermost tracking detector over the calorimeter system up to the muon spectrometer is presented.

In Chapter 3, the creation of prompt photons in the proton-proton collisions at the LHC and their meaning in terms of the involved physics processes is highlighted. Here, the efficient reconstruction of photon candidates as well as the identification of prompt photons stemming directly from the hard scattering interaction instead of photons originating from hadronic jet decays plays a crucial role. For the discrimination, the characteristic signatures of photons showering in the electromagnetic calorimeter of the ATLAS detector can be exploited. The currently employed algorithms in the ATLAS experiment to reconstruct and identify photons are described, defining also appropriate photon isolation criteria. In the final part, measurements of the photon identification efficiency as a measure for the performance of the employed methods using the recorded Run-2 data are presented.

Chapter 4 addresses the performed work on the optimization of the photon identification to discriminate prompt photons from the much more abundant non-prompt photon background important for several physics analyses. Here, a multitude of tools for the optimization are available ranging from the currently employed rectangular cuts up to multi-variate methods and the use of machine learning techniques. The developed software framework in the course of this work is presented, which allows to study the photon identification optimization in a systematic way. Results of the optimization using rectangular cuts as well as using a boosted decision tree for the classification of prompt photons are discussed, comparing the corresponding performance by evaluating the photon identification efficiency for signal and background photon samples. Finally, the current status of the application of a boosted decision tree for the photon identification in the ATLAS experiment is discussed.

In Chapter 5, the prospective future of high-energy particle physics with the high-luminosity phase of the LHC is explained. Due to the far more challenging conditions of the upgraded LHC, which can be expressed e.g. by the much higher particle fluence or the number of pile-up events, the physics experiments at the LHC with their respective particle detectors have to be upgraded as well. Therefore, the plans for the new tracking detector for ATLAS with the ITk detector are described in terms of the requirements on the detector to achieve high precision measurements on the detected particles by an appropriate detector design.

Here, the focus is on the ITk strip end-cap detector describing the design of the petals as the building blocks of the detector and consisting of the silicon sensor modules mounted on the local support cores.

Chapter 6 describes the conducted studies in terms of the thermo-mechanical characterization of the petal design. Here, a number of objectives and specifications are defined for the petal as a high reliability over the full life time of the ITk strip end-cap detector is required. Therefore, detailed measurements on several prototype structures are performed using a multitude of techniques and equipment to assess the thermo-mechanical properties of the petal. Its thermal performance is evaluated using the technique of infrared thermography, for which the results are strongly dependent on the emissivity of the object investigated in a number of auxilliary studies. Apart from testing the thermal performance for the nominal conditions in the detector, further tests are performed for more extreme temperature scenarios probing effects of thermal deformations, the influence of thermal cycling on the petal performance or the resisitivity of the petal in thermal shock tests. Finally, the petal design is evaluated based on the characterization results and in respect to the defined specifications for the thermo-mechanical properties.

In Chapter 7, investigations on the dual-phase CO_2 cooling are presented, which is the selected choice for the cooling of the silicon sensors in the ATLAS ITk detector. Therefore, the design and specifications for the planned cooling system focusing on the ITk strip detector are described. This is followed by dedicated tests of the properties and characteristics of evaporative CO_2 for the application in the cooling of petals. Here, the influence of the flow orientation on the cooling performance, the characteristic pressure drop over the cooling loop of the petal as well as the actual CO_2 state inside the pipe are studied. The results are then concluded, evaluating the measurements in terms of the defined specifications for the dual-phase CO_2 cooling.

Chapter 8 introduces the DESY II Test Beam Facility offering a multi-GeV electron beam to perform beam tests of detector prototypes or for other applications such as material studies. The available infrastructure as well as the mechanism of the beam generation are explained. Here, a key component for beam tests are the EUDET-type beam telescopes allowing to reconstruct the particle trajectories with high resolution. The hardware components of the telescope as well as the provided software tools with EUDAQ for the data acquisition and EUTelescope for the data analysis in terms of track reconstruction are described. Finally, characteristic parameters influencing the performance of the beam test in terms of the selectable beam properties and the choice of the telescope setup and its settings are discussed.

In Chapter 9, the electron beam at the DESY II Test Beam Facility together with the beam telescopes is exploited to investigate the material budget of samples traversed by the beam particles. Here, the technique of material budget imaging allows to measure the two-dimensional distribution of material budgets in the sample using the high resolution telescopes in terms of the spatial and angular resolution. The theory of multiple Coulomb scattering as the underlying physics process as well as the connection to the characteristic radiation length of a material is described. This is followed by an overview about the conducted test beam measurements in terms of beam parameters, telescope settings and tested material samples. The reconstruction within the EUTelescope framework using the General Broken Lines algorithm leads to an unbiased measurement of kink angle distributions, for which various influences are experimentally investigated.

To infer the correct estimates of the sample's material budget from the kink angle distribution, the Highland model is used in the analysis and an appropriate calibration procedure is applied. The results for the mapping of material budgets for various materials as well as complex composite structure, with a focus on components used for the ATLAS ITk detector, are discussed. In the final part, the results are evaluated in terms of limits and capabilities of the MBI technique for further applications.

At the end of this thesis, the overall findings and results for the performed measurements and studies are summarized, covering the optimization of the photon identification for the ATLAS experiment, the thermo-mechanical characterization of petals for the new ATLAS ITk detector and the exploitation of the test beam for the MBI technique. Moreover, an outlook on the future developments and challenges in the respective topics is given.

Chapter 1

Particle Physics and the Standard Model

The topic of this chapter is to describe the basics of particle physics, ranging from an introduction to the theoretical description of particle physics up to the experimental methods employed to investigate the nature of matter and the fundamental forces.

In Section 1.1, the **S**tandard **M**odel (SM) of particle physics is introduced as the currently best employed theoretical model to describe the world of particle physics. Here, the SM covers the constituents of matter by introducing the elementary particles and the fundamental forces are described as the interactions between the particles.

To test the validity of theoretical models, experimental particle physics have to provide methods and tools to investigate the elementary particles and their interactions. Such investigations can be conducted by creating highly energetic particle collisions with powerful particle accelerators. The world largest particle accelerator, currently in operation for experiments of high-energy particle physics, is the **L**arge **H**adron **C**ollider (LHC), which is addressed in Section 1.2.

The physics programme of the accelerator-based experiments at the LHC are in general very broad and versatile, covering quite different areas of particle physics. Therefore, only a very small collection of recent results from the **A** **T**oroidal **L**HC **A**pparatu**S** (ATLAS) experiment, one of the four main experiments at the LHC, will be discussed in Section 1.3.

Finally, the theoretical challenges as well as problems within the SM description are the topic in Section 1.4. Possible solutions by extending the SM theory, called physics **B**eyond **S**tandard **M**odel (BSM), are described as well.

1.1 The Standard Model of Particle Physics

The **S**tandard **M**odel (SM) is the underlying theoretical model for the description of the building blocks of matter, the *elementary particles*, and their interactions via the *fundamental forces*. It is formulated as a quantum field theory, combining the theories of quantum mechanics and special relativity.
The history of the SM can be probably tracked back to the discovery of the *electron* by J. J. Thomson in 1897 [1] as well as the first investigations of the atomic model by E. Rutherford [2] in 1909.

The theory of quantum mechanics entered the particle physics theory in the late 1920s by the work of W. Heisenberg [3] and E. Schrödinger [4], and P. Dirac connected it in 1928 to the theory of special relativity [5].
In dedicated experiments, more elementary particles and their corresponding anti-particles were detected, e.g. the *positron* [6] in 1932 as well as the *muon* [7] in 1936 by C. D. Anderson or the existence of the *neutrino* [8] in 1956 by C. Cowan *et al.*
In parallel, the description of the fundamental forces were embedded into the SM with the theory of **Q**uantum **E**lectro **D**ynamics (QED) [9] and later the theory of **Q**uantum **C**hromo **D**ynamics (QCD) [10]. These theories were developed on the basis of experimental data from particle accelerators and their corresponding high-energy physics experiments. With the discovery of the Higgs boson in 2012 by the LHC experiments, a missing part in the successful theoretical description of the SM could be added.

This brief historical overview is far from complete, but further explanations to the SM and its history can be found in the literature [11, 12, 13]; nonetheless, it should be clear that generations of particle physicists have shaped and are still shaping the understanding of the nature of particle physics within the theoretical framework of the Standard Model.

In the following, the structure of the SM will be briefly discussed, starting with the elementary particles in Section 1.1.1, followed by the fundamental forces in Section 1.1.2 and finally concluding with the Higgs mechanism in Section 1.1.3. As a schematical overview, the ingredients of the Standard Model of particle physics are shown in Figure 1.1.

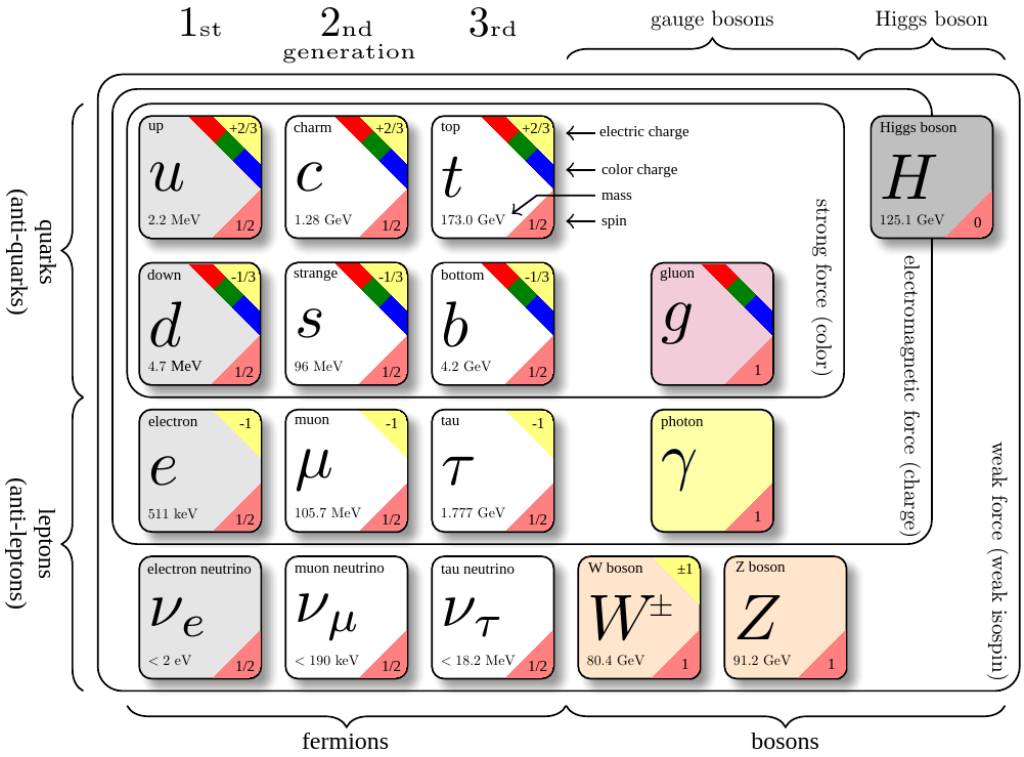

Figure 1.1: The Standard Model of particle physics describing the elementary particles, consisting of *leptons* and *quarks*, and their interactions via mediators, the *gauge bosons*. The elementary matter particles are complemented by their respective *anti-particles*. The physical quantities such as the mass, the charge (electric, color) and the spin are denoted [14]. Inspired by [15].

1.1.1 Elementary Particles in the Standard Model

Physical matter in the universe is composed of the elementary particles in the SM, which are fundamental spin-1/2 particles called *fermions*. From the underlying field theory, fermions are local excitations of the underlying matter fields.
The fermions can be categorized into *leptons* and *quarks*, where both contain three generations of particles according to their quantum numbers.

Leptons

The charged leptons carry an integer electrical charge of -1, whereas the associated neutrinos (ν) are neutral. The leptons can be organized in families along their flavor: the *electron* and *electron-neutrino* (e, ν_e), the *muon* and *muon-neutrino* (μ, ν_μ), and the *tau* and *tau-neutrino* (τ, ν_τ). The six leptons are complemented by their corresponding *anti-particles*, which are particles with equal mass, but opposite charge sign, such as the electron (e^-) and the *positron* (e^+).

Quarks

The quarks are organized into *up-type* quarks with a fractional electric charge of $+2/3$ and *down-type* quarks with charge $-1/3$. Moreover, due the underlying strong force, quarks are carrying a *color charge*, with three possible colors and their anti-colors.
Otherwise, the three-doublet structure is the same as for the lepton case: the *up* and *down* quark (u, d), the *charm* and *strange* quark (c, s), and the *top* and *bottom* quark (t, b).
Additionally, quarks cannot be observed in isolation due to the *confinement theorem* [16], but only as colorless bound states called *hadrons* in form of *baryons* or *mesons*.
Examples for baryons are the *proton* composed out of two u-quarks and one d-quark with $p = (uud)$ or the neutron as $n = (udd)$.
As the six quarks are also accompanied by their anti-quark partners, it is possible to build hadrons from anti-particles, like an antiproton $\bar{p} = (\bar{u}\bar{u}\bar{d})$, a baryon, or quark-antiquark bound state, a meson, like the charged pions $\pi^- = (\bar{u}d)$ and $\pi^+ = (u\bar{d})$.
In general, fermions (quarks and leptons) belonging to a higher generation are unstable, as it is energetically favorable for this higher mass particle to decay into the lighter particle. An example for a leptonic decay of a higher generation fermion is the muon decaying into an electron with a mean lifetime of $\sim 2.2\,\mu s$ [14].

1.1.2 Fundamental forces in the Standard Model

The fundamental forces of nature are introduced in the quantum field theory of the SM as gauge fields representing a certain symmetry group and describing the interactions (kinematics and dynamics) of the matter fields. The carriers of the forces are spin-1 particles called *gauge bosons*, which are the excitations of the corresponding gauge fields and mediate the force between the elementary particles represented by the fermions.
The interactions obey a certain symmetry and such represent the conservation of a physical quantity or quantum number, according to the Noether's theorem [17]. This symmetry is preserved in the quantum field theory by requiring the Lagrangian of the corresponding interaction to be invariant under local (space-time) transformation of the symmetry group.
Three fundamental forces are represented in the SM description: the *electromagnetic force* described by **Q**uantum **E**lectro **D**ynamics (QED) [9], the *weak force* described by the weak theory [18] and the *strong force* described by **Q**uantum **C**hromo **D**ynamics (QCD) [10].

The combined symmetry group representing the gauge group theory of the interactions in the SM are given as

$$G_{\mathrm{SM}} = SU(3)_C \times SU(2)_L \times U(1)_Y \tag{1.1}$$

with the $SU(3)_C$ group for the QCD with conserved color charge C and the $SU(2)_L \times U(1)_Y$ as the combined electroweak theory with weak isospin I and hypercharge Y as conserved quantum numbers. As such, the SM Lagrangian can be written as

$$\mathcal{L}_{\mathrm{SM}} = \mathcal{L}_{\mathrm{QCD}} + \mathcal{L}_{\mathrm{EW}}. \tag{1.2}$$

Electroweak interaction

The electroweak theory, introduced in 1979 by S. Glashow, A. Salam and S. Weinberg [19, 20, 21, 22], combines the electromagnetic force and the weak force and describes the invariance under the weak hypercharge $U(1)_Y$ and the weak isospin $SU(2)_L$ transformations.
As denoted by the L for the symmetry group, the weak interaction only couples to left-handed fermions with the weak isospin[1], whereas for the electromagnetic interaction the hypercharge[2] as quantum number is introduced.
The introduced gauge fields in the electroweak theory, W^μ and B^μ, are not the physical fields of the interaction observed in nature. Instead linear combinations of these fields are constructed for the gauge bosons of the electroweak interaction with the charged vector boson $W^\pm$, the neutral vector boson Z^0 and the photon γ.
From a theoretical point of view, these gauge bosons have to be massless so that $\mathcal{L}_{\mathrm{EW}}$ satisfies the local gauge symmetry under $SU(2)_L$ transformation. But as it was observed that the weak bosons $W^\pm$ [24, 25] and Z^0 [26, 27] are massive particles, the symmetry must be broken to include mass terms. This is known as the **E**lectro**W**eak **S**ymmetry **B**reaking (EWSB) mechanism, which is discussed in detail in Section 1.1.3.
In summary, the electromagnetic force is mediated by the massless photon coupling to all charged particles in the SM, whereas the weak force is mediated by the massive $W^\pm$ and Z^0 vector bosons coupling via the isospin to all fermions and to each other.

Strong interaction

The interaction via the strong force is described by QCD theory and is based on the symmetry group $SU(3)_C$ with the color charge C as the conserved quantum number.
The corresponding gauge fields are eight gluon fields mediating the strong force between quarks, carrying a non-vanishing color charge. Moreover, due to the non-abelian nature of the symmetry group, a self-interaction between gluons via the color charge is allowed.
The underlying QCD theory is characterized by two further phenomena: *color confinement* and *asymptotic freedom*.
As described earlier, particles in nature are only observed with a net color charge of zero, building composites of quarks called baryons (qqq or $\bar{q}\bar{q}\bar{q}$) and mesons ($q\bar{q}$) due to color confinement. The coupling constant of the strong force, α_s, shows a dependence on the energy scale: for high energies (corresponding to small distances) α_s decreases asymptotically such that the quark behaves like a bare quasi-free particle, called asymptotic freedom [28, 29]. Due to this energy scale dependence, QCD interactions can be calculated perturbatively, in orders of the strong coupling constant, for high energy transfer interactions.

[1] Weak isospin T: Generators of the corresponding $SU(2)$ group are the weak isospin operators $\hat{T} = \frac{\sigma_i}{2}$ with the three Pauli matrices σ_i.

[2] Hypercharge Y: The electric charge Q is associated with the hypercharge Y and the third component of the weak isospin T_3 via the Gell-Mann Nishijima formula: $\hat{Q} = \frac{\hat{Y}}{2} + \hat{T}_3$[23].

On the contrary, for low energy interactions (approximately below 200 MeV [16]), α_s becomes large enough to create quarks and gluons from the vacuum state and hadrons as bound states are constructed due to the concept of color confinement.
In summary, the strong force is mediated by the massless gluons coupling to all other color charged particles, which are the quarks and the gluons themselves.

1.1.3 The Higgs mechanism in the Standard Model

In the description of the electroweak interaction, the underlying symmetry gauge group does not allow for fermions and bosons to be massive in order to conserve the local symmetry. This paradigm strongly contradicts the experimental observation of fermion masses as well as massive vector bosons for the weak interaction.
With the concept of the EWSB mechanism, it is possible to restore the local gauge symmetry, when breaking the symmetry. In the same moment, the *Higgs mechanism* is introduced, which allows all other massive elementary particles to interact with the Higgs field and to acquire their observed masses.
Proposed in 1970 by R. Brout, F. Englert and P. Higgs [30, 31], the Higgs field is a self-interacting complex scalar field with a new scalar particle named the *Higgs boson*.
The Higgs boson was observed by the ATLAS and CMS experiment at the LHC in 2012 [32] and the Nobel prize in physics was awarded "for the theoretical discovery of a mechanism that contributes to our understanding of the origin of mass of subatomic particles" to F. Englert and P. Higgs in 2013.

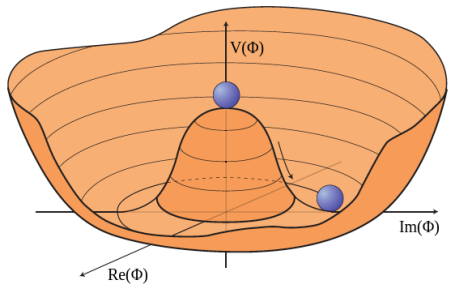

Figure 1.2: Representation of the Higgs potential $V(\Phi) = \mu^2|\Phi|^2+\lambda|\Phi|^4$ with spontaneous symmetry breaking into an arbitrary vacuum state with non-vanishing vacuum expectation value v [33].

The Higgs potential, $V(\Phi)$, as depicted in Figure 1.2, can be parameterized as

$$V(\Phi) = \mu^2|\Phi|^2 + \lambda|\Phi|^4,\ \mu^2 < 0,\ \lambda > 0 \tag{1.3}$$

and shows a non-vanishing vacuum expectation value $v = \sqrt{-\mu^2/\lambda}$ which spontaneously breaks the $SU(2)_L \times U(1)_Y$ symmetry.
The four degrees of freedom of the Higgs field Φ are absorbed by the masses of the W and Z bosons as well as a massive spin-0 Higgs boson as the excitation of the Higgs field itself. As such, the acquired masses by the Higgs mechanism are linked to the vacuum expectation value as

$$m_W = \frac{gv}{2},\ m_Z = \frac{v}{2}\sqrt{g^2 + g'^2},\ m_H = \sqrt{2\lambda v}, \tag{1.4}$$

with the electroweak coupling constants g, g' as well as the Higgs self-coupling λ.
Also, the fermion masses are introduced via the Yukawa interaction of the matter fields (leptons and quarks) with the Higgs field as

$$m_f = \frac{y_f v}{\sqrt{2}} \tag{1.5}$$

with the Yukawa coupling v_f for each fermion f.

1.2 High-Energy Physics at the Large Hadron Collider

The **L**arge **H**adron **C**ollider (LHC) [34], the largest particle accelerator in the world, pushes the frontiers of modern particle physics in terms of high energy and luminosity.
It is operated as a proton-proton collider with the option to collide also heavy ions in a synchrotron ring with a circumference of 26.7 km. The machine has been successfully operating since 2011 at the European Organization for Nuclear Research (CERN) in Geneva, Switzerland. Its design *center-of-mass energy* is $\sqrt{s}$ =14 TeV, colliding *bunches* of up to 10^{11} protons with a design *luminosity* of $10^{34}\,\mathrm{cm}^{-2}\,\mathrm{s}^{-1}$.

The proton bunches are accelerated up to energies of 7 TeV through a series of pre-accelerators (LINAC2, BOOSTER, PS and SPS), with the LHC accelerator as the final stage using superconducting RF cavities with frequencies of 400 MHz. The particle beams are guided on the ring through superconducting dipole magnets cooled down to 1.9 K and with magnet field strengths of up to 8.3 T.

The LHC provides proton-proton collisions at four **I**nteraction **P**oints (IPs), which host the four main particle physics detectors: The two largest experiments, **A** **T**oroidal **L**HC **A**pparatu**S** (ATLAS) [35] and **C**ompact **M**uon **S**olenoid (CMS) [36], are multi-purpose detectors which are designed to fulfill a broad spectrum of measurements to test the Standard Model of particle physics and to search for BSM physics phenomena.
The **A** **L**arge **I**on **C**ollider **E**xperiment (ALICE) [37] is focusing on heavy ion collisions, which are produced in dedicated run periods at the LHC, and studies the nature of the quark-gluon plasma. Finally, the **L**arge **H**adron **C**ollider **b**eauty (LHCb) experiment [38] is dedicated to studying B physics and investigating the phenomenon of CP violation.

An overview of CERN, with the LHC accelerator chain and additional accelerators at the CERN site as well as the LHC experiments, is schematically depicted in Figure 1.3.

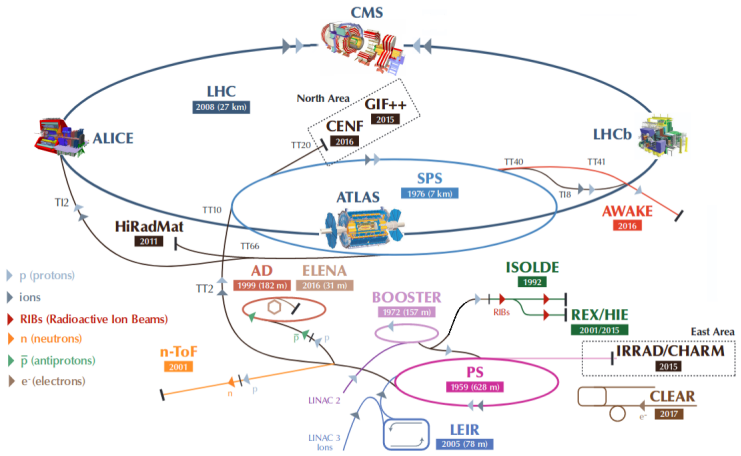

Figure 1.3: Layout of the accelerators at CERN. Visualized are the accelerator chain for the LHC as well as additional accelerators for diverse tasks on the CERN site. For the LHC, the four experiments, ATLAS, CMS, LHCb and ALICE, located at the IPs of the LHC ring, are indicated. Modified from [39].

In Section 1.2.1, important parameters of particle colliders and their dependence on the particle accelerator are described, providing the link between accelerator physics and experimental particle physics to study collision events.
This is followed by a link to particle physics theory in Section 1.2.2, providing a brief overview of the underlying processes in a typical proton-proton collision.
Finally, the schedule of the LHC as well as its delivered performance so far is discussed in Section 1.2.3.

1.2.1 Center-of-mass energy, luminosity and pile-up

For the collision of particles at a particle accelerator, such as the proton-proton collisions at the LHC, a number of parameters and quantities exist to describe the operation and performance of an accelerator as well as to calculate properties of particle interactions such as the interaction cross sections.
The *center-of-mass energy* $\sqrt{s}$ is the energy in a particle collision that is available to generate other particles of even higher mass than the colliding particles. This is possible due to the mass-energy equivalence with $E = mc^2$ introduced by A. Einstein [40]. For the particle collisions at the LHC with its proton beams of a kinetic energy up to 7 TeV each, the resulting center-of-mass energy at the IP is $\sqrt{s} = 14\,\text{TeV}$.
The generation of new particles via interactions in such a particle collision is a completely statistical process. But the probability of a certain particle to be produced in an interaction at a given center-of-mass energy is described by the *cross-section* σ of the process.

For a particle accelerator, the *instantaneous luminosity* $\mathcal{L}$ describes the number of possible interactions per unit time and per area, such that the event rate dN/dt is

$$\frac{dN}{dt} = \mathcal{L} \times \sigma. \tag{1.6}$$

The total number N of observed events in a particle physics experiment for a given cross-section σ is then

$$N = L \times \sigma \tag{1.7}$$

with the *integrated luminosity* L defined as

$$L = \int \mathcal{L} dt. \tag{1.8}$$

The instantaneous luminosity depends on a number of accelerator parameters as

$$\mathcal{L} = \frac{n_b N^2 f_{\text{rev}}}{4\pi\beta^* \epsilon_n} R \tag{1.9}$$

with the number of protons per bunch N, the number of bunches n_b, the revolution frequency f_{rev}, the beam beta function β^*, the transverse normalized emittance ϵ_n and a geometrical reduction factor R.
The LHC was designed for a nominal luminosity of $\mathcal{L} = 10^{34}\,\text{cm}^{-2}\,\text{s}^{-1}$, but the ultimate goal for particle physics experiments is to increase this number by optimizing the machine parameters to record even more collision data for precise measurements of the SM.

A particle collision in a collider experiment is not an interaction of a single proton from one beam with a proton from the opposite beam, but instead a collision of many more protons in each bunch crossing. Therefore, due to the so called *pile-up*, it is often difficult to investigate a single interaction of interest due to huge overlay of other interactions.
There are two different types of pile-up events occurring in particle collisions:
in-time pile-up describes the number μ of proton-proton collisions happening in the same bunch crossing, whereas *out-of-time pile-up* describes interactions from the previous or next bunch crossings overlaying with the current event. For the latter case, the experiment has to provide a fast detector and trigger response to separate each bunch crossing, which are only divided by 25 ns in time for the case of the *pp* collisions at the LHC.
In general, the effect of pile-up poses challenges to the detector performance due to the higher number of interactions and corresponding higher combinatorial background in the reconstruction. Therefore, pile-up mitigation in reconstruction and identification algorithms for the particle physics experiments is one of the topics in Chapter 4.

1.2.2 Partons, hadronization and underlying event

In hadron colliders, such as the LHC, the interactions occur between the *partons*, e.g. the quarks and gluons inside the colliding protons. Therefore, the available center-of-mass energy $\sqrt{s}$ is distributed among the partons according to the **P**arton **D**istribution **F**unction (PDF) for the hadron at a certain energy.
In pertubative QCD, the cross-section of a proton-proton interaction, $\sigma(P_1,P_2)$, can be factorized [41] into two parts: first, into a hard scattering process of the involved partons i,j and its corresponding cross-section $\hat{\sigma}_{ij}$; and the second part is the probability to find the partons with energy fraction $x_{i,j}$ of the center-of-mass energy, given by the PDFs $f_{i,j}$ [42]. The principle of the factorization theorem is schematically depicted in Figure 1.4.

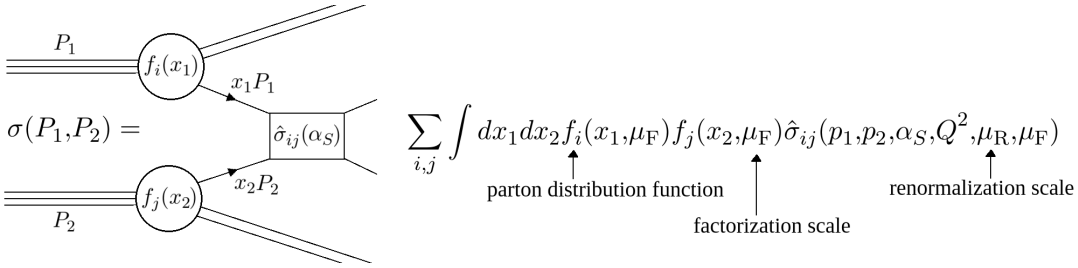

Figure 1.4: Factorization theorem for the pertubative calculation of cross-sections in a hadron collision. The cross-section is evaluated using the parton cross-section $\hat{\sigma}_{ij}$ and the corresponding PDFs $f_{i,j}$ for a defined energy scale, represented by a *factorization scale* μ_F as well as a*renormalization scale* μ_R.

In general, a typical pp collision event consists of a hard scattering process of partons, which is of interest for the physics analysis, but is accompanied at the same time by other interactions. Here, the *underlying event* describes another hard scattering interaction happening between the remaining partons. Furthermore, partons can be irradiated off the interaction, which is differentiated in the *initial* and *final state radiation*. The newly created partons in these interaction processes are showering in the detector, producing further partons called *parton showering*. Finally, the partons create color charge neutral hadrons as the final states, which is described by the *hadronization* process.
Figure 1.5 shows a schematically representation of the full event for a pp collision.

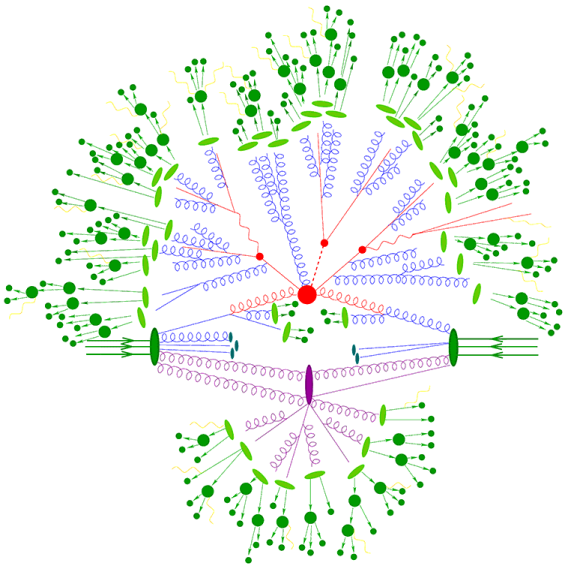

Figure 1.5: Schematic of a full event in a high-energy pp collision [43]. The initial state protons interact via a hard scattering process of interest on the parton level (red), which is accompanied by possible other hard scattering processes of other partons, the *underlying event* (magenta). For the *parton showering* (blue), the newly created partons are showering in the detector producing further partons or new partons are irradiated off the interactions by *initial* and *final state radiation*. The final states of the event are color charge neutral, hadrons due to *hadronization* (green).

Here, the particle detector records the hadronic final states on a particle level instead of the parton level. Moreover, for the simulation of collision events the hard scattering process can be calculated perturbatively by the factorization theorem. But the other processes occurring apart from the hard scattering event are modelled accordingly using different parton showering and hadronization algorithms.

1.2.3 Schedule and performance of the LHC

The successful operation of the LHC for over nine years by now is shown in the LHC schedule in Figure 1.6, highlighting the different stages of operation in terms of the achieved center-of-mass energy and the luminosity.

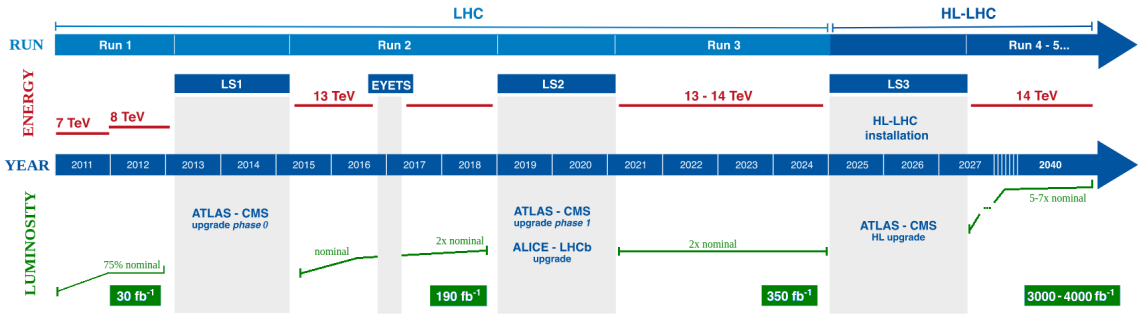

Figure 1.6: Schedule for the operation of the LHC and the future HL-LHC. Shown are the center-of-mass energy as well as the luminosity for each run interrupted with several long shutdowns (LS) for maintenance and upgrades of the machine as well as the detectors. Modified from [44].

In the beginning of operation in 2011, the LHC started with a center-of-mass energy of 7 TeV and well below its design luminosity of $10^{34}\,\mathrm{cm}^{-2}\,\mathrm{s}^{-1}$. In year 2012, the energy was increased to 8 TeV and reached 75% of the nominal luminosity. These two years are called LHC Run 1 and delivered a total integrated luminosity of $30\,\mathrm{fb}^{-1}$.
During Long Shutdown 1 (LS1), some of the detectors were upgraded for the so called Phase-0 upgrade programme, e.g. with the insertion of the IBL pixel layer in the ATLAS detector (cf. Sec. 2.3.2).

For Run 2, lasting from 2015 to 2018, the center-of-mass energy was raised to $\sqrt{s} = 13\,\mathrm{TeV}$ and two times the nominal luminosity was reached. In total, Run 2 collected an integrated luminosity of $190\,\mathrm{fb}^{-1}$. The LS2 is in progress as of this writing, again hand in hand with the detector Phase-1 upgrade programme for all four LHC experiments.
In 2021, the LHC will restart operation in Run 3 with the same energy as before or finally reaching its design center-of-mass energy of $\sqrt{s} = 14\,\mathrm{TeV}$. The goal for Run-3 data taking is to collect $350\,\mathrm{fb}^{-1}$ of total integrated luminosity by 2024.

With LS3, a new era of the LHC will take place by upgrading the machine to the **H**igh-**L**uminosity **LHC** (HL-LHC), aiming for a luminosity of five to seven times the original design luminosity. Details of the planning for the HL-LHC phase as well as the required detector upgrades foreseen for the following runs will be discussed in Chapter 5.

The measured luminosity collected for the ATLAS experiment for LHC Run 1 and Run 2 is summarized in Figure 1.7, showing the available amount of *pp* collision data for physics analyses of precise SM tests and searches for new physics.

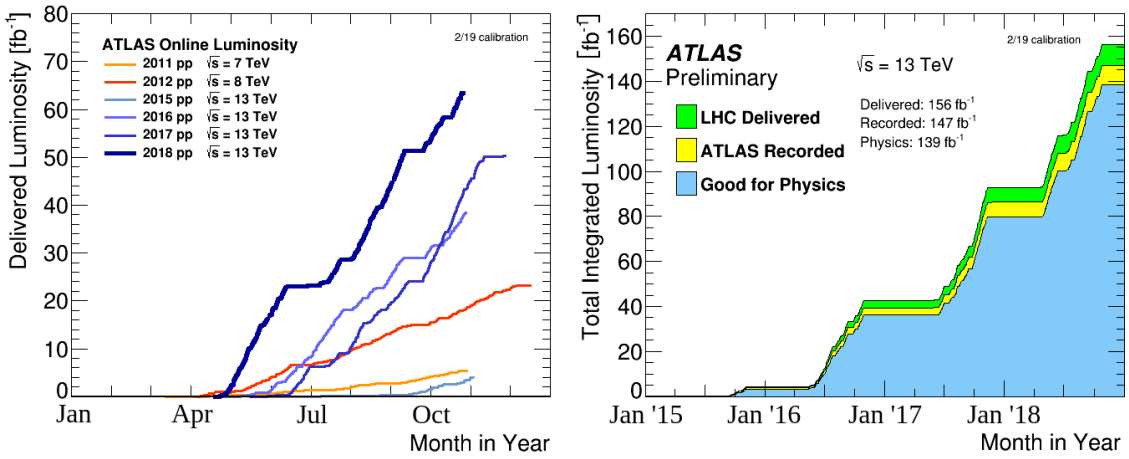

Figure 1.7: Measurement of the luminosity for the ATLAS experiment in LHC Run 1 and Run 2. Shown is the delivered luminosity for the ATLAS experiment per month for the years 2011 to 2018 (left) as well as the total integrated luminosity for Run-2 data taking categorized according to the amount delivered by the LHC, recorded by the ATLAS detector and usable for physics analyses after data cleaning (right). Modified from [45].

Moreover, the pile-up conditions for the ATLAS experiment in Run 2 for the different years of operation is shown in Figure 1.8. Here, the mean number of interactions per bunch crossing ranges from 10 to 70 and the averaged values over the individual run periods are between $< \mu >= 13$ and $< \mu >= 38$.

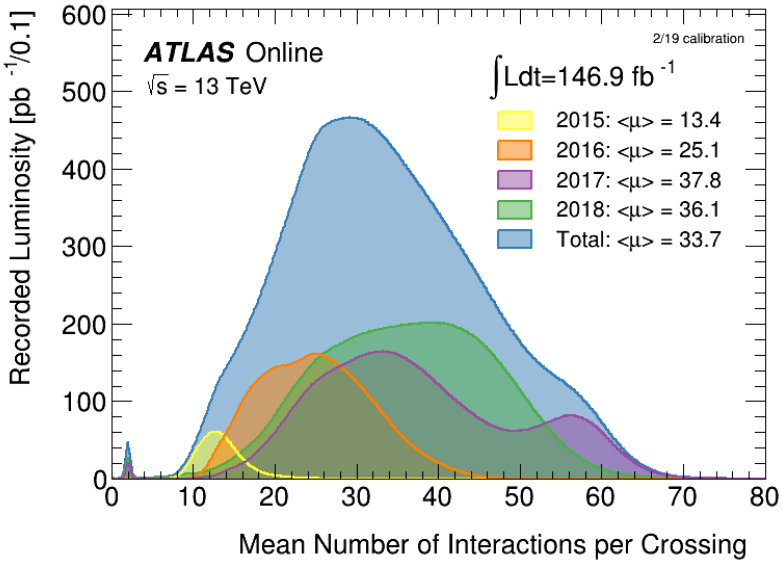

Figure 1.8: Pile-up conditions for the ATLAS experiment in LHC Run 2, split into years of data taking. Shown is the measurement of the mean number of interactions per bunch crossing according to the recorded luminosity in the run period. Modified from [45].

Especially the pile-up conditions in 2017 and 2018 with values above 50 are very challenging for the detector performance as well as the used reconstruction and identification algorithms.

1.3 Testing the Standard Model: Precision Measurements

The LHC physics programme with its four main experiments has provided over the years of successful operation and data taking a wealth of interesting results to test the Standard Model as well as its boundaries. To draw a complete picture of these results is nearly impossible, especially due the specialized physics programmes of LHCb and ALICE. Therefore, in the following the focus will be on some results of the ATLAS experiment, whereas detailed information and a more complete overview can be found e.g. in [46].
The selected examples are show cases for the precision measurements pursued to test the SM predictions with the highest accuracy. This is only possible due to the high performance of the detectors as well as the reconstruction and identification algorithms. Here, a special focus for the given examples is placed on the performance of the tracking detectors in the reconstruction of electrons as well as the identification of photons.

In Section 1.3.1, the most precise measurement of the W boson mass with the ATLAS detector presents an example for the importance of a well-understood reconstruction of electrons and muons to test the SM with highest accuracy.
In the Higgs sector, the mass as well as the couplings to fermions and bosons are precisely measured to verify the predicted Higgs boson characterics in the SM.
A comparison of the Run-1 and Run-2 results for the discovery of the Higgs boson in 2012 in the four-lepton and diphoton decay channel as well as the status of the coupling measurements are discussed in Section 1.3.2.
Finally, a more exotic measurement is presented in Section 1.3.3 with the observation of light-by-light scattering in Pb-Pb collisions by the ATLAS experiment that requires an optimized identification of photons to suppress backgrounds.

1.3.1 *W* boson mass

The precise determination of the mass of SM particles is a valuable input for understanding the nature of particle physics. The measurement of the mass of the W boson as a carrier for the electroweak force is therefore a perfect test of the SM in the precision regime. Moreover, it allows a comparison to the underlying theory concepts by performing electroweak fits of SM parameters to determine the W boson mass [47].

In the analysis [48], a dataset of proton–proton collision with an integrated luminosity of $4.6\,\text{fb}^{-1}$ collected in 2011 at $\sqrt{s} = 7\,\text{TeV}$ with the ATLAS detector is used. The Drell-Yan process, $W \to l\nu$, is evaluated for in total $7.8 \cdot 10^6$ candidates in the $W \to \mu\nu$ channel and $5.9 \cdot 10^6$ candidates in the $W \to e\nu$ channel. The mass of the W boson is extracted with template fits to the reconstructed distributions of the charged lepton transverse momentum, p_{T}^{l}, and of the W boson transverse mass[3], m_{T}, in the electron and muon decay channels. In Figure 1.9, the fitted distributions evaluated for the $W^- \to e^-\bar{\nu}$ decay channel are shown.

In the combination of the results from the individual evaluated decay channels, as it is shown in Figure 1.10a, the W boson mass is determined to be

$$m_W = 80370 \pm 7(\text{stat.}) \pm 11(\text{exp. syst.}) \pm 14(\text{mod. syst.})\,\text{MeV} = 80370 \pm 19\,\text{MeV}, \quad (1.10)$$

with the statistical, the experimental systematic and the physics-modelling systematic uncertainty, respectively.

[3] $m_{\text{T}} = \sqrt{2p_{\text{T}}^{l} p_{\text{T}}^{\text{miss}}(1 - \cos\Delta\phi)}$ with the missing transverse momentum $p_{\text{T}}^{\text{miss}}$ originating from the neutrino and the azimuthal opening angle $\Delta\phi$ between the decay particles.

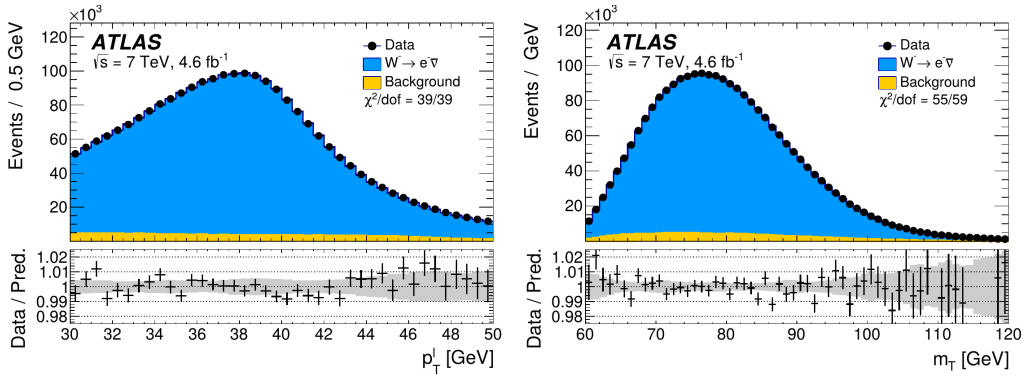

Figure 1.9: Distributions of the transverse momentum of the charged lepton, p_{T}^{l}, (left) and the transverse mass of the W boson, m_{T}, (right) evaluated for the $W^- \to e^- \bar{\nu}$ decay channel [48].

The precise measurement result for the mass in terms of the experimental systematic uncertainty is only possible due to a precisely measured electron and muon reconstruction efficiency. This can be seen when comparing the uncertainties for the full combination of all channels with a total uncertainty of 18.5 MeV to the electron uncertainty of 6.4 MeV and the muon uncertainty of 6.6 MeV. A comparison of the W boson mass determined from this measurement with previous measurements of LEP and Tevatron as well as to the electroweak fit is shown in Figure 1.10b.

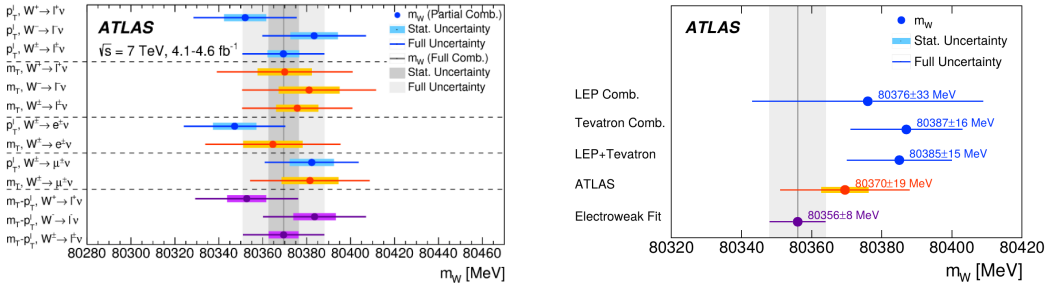

(a) W boson mass from each channel and combinations, including statistical and systematic uncertainties.

(b) Comparison of W boson mass with LEP and Tevatron measurements as well as the electroweak fit result.

Figure 1.10: Evaluation of the W boson mass per decay channel and comparison of the combined result to other measurements [48].

1.3.2 Higgs boson: mass & couplings

The discovery of the Higgs boson in 2012 by the ATLAS and CMS experiments is the major result for the LHC physics programme so far, solving one of the biggest remaining puzzles in the SM theory.
The Higgs decay channels used in the Run-1 analysis [49] leading to the discovery are the four lepton ($H \to ZZ^* \to 4l$) and the diphoton ($H \to \gamma\gamma$) decay channel. Even though these decay channels only have branching ratios of 2.6% and 0.2%, respectively, the clear signature with distinct creation of two pairs of opposite sign leptons ($4e$, 4μ, $2e2\mu/2\mu2e$) or two photons in the detector provides a major advantage over e.g. the $b\bar{b}$ decay mode with much more abundant background processes. The corresponding production and decay modes for the Higgs boson for proton-proton collisions at LHC are displayed in Figure 1.11.

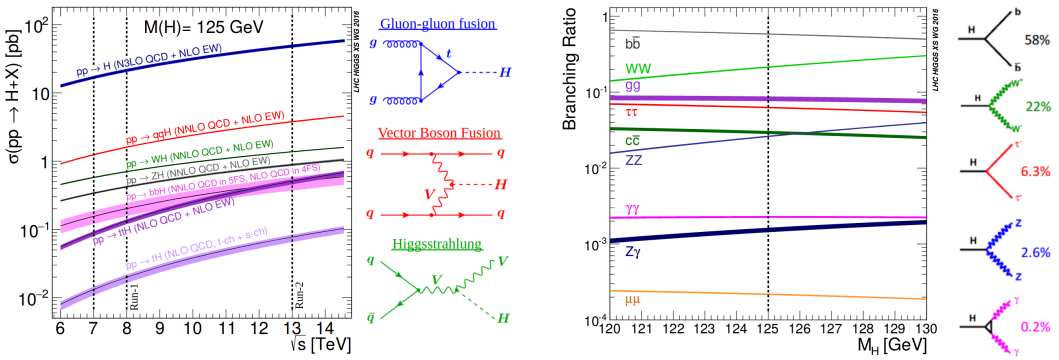

(a) Higgs boson production modes. **(b)** Higgs boson decay modes.

Figure 1.11: Higgs boson production and decay modes. In (a), the production cross-sections per mode as function of the center-of-mass energy is shown together with the Feynman graphs of the dominant modes (gg fusion, VBF, Higgsstrahlung). In (b), the branching ratios for the different decay modes as function of the Higgs boson mass are displayed. Modified from [50].

For the four-lepton channel, a well developed reconstruction of electrons and muons is necessary, accurately providing the transverse momentum of each lepton as well as its electric charge. In the invariant mass distribution m_{4l}, shown in Figure 1.12a for the Run-1 analysis, a second peak, next to the resonant Z boson mass peak at 91 GeV, at a mass of 125 GeV is visible, which is compatible with the signature of a Higgs boson.
The number of observed events in the signal window ($m_{\mathrm{H}} = 125 \pm 5$ GeV) is 6 for the 4μ, 5 for the $2e2\mu/2\mu2e$ and 2 for the $4e$ channel. Comparing now the distribution from Run 1 with an integrated luminosity of 4.8 fb^{-1} at $\sqrt{s} = 7$ TeV and 5.8 fb^{-1} at $\sqrt{s} = 8$ TeV with the result from the full Run-2 dataset with 139 fb^{-1} of data recorded at $\sqrt{s} = 13$ TeV, as displayed in Figure 1.12b, the Higgs mass peak is much more pronounced compared to the irreducible background processes (ZZ^*, tXX, VVV, Z+jets and $t\bar{t}$).
Here, the number of observed events in a broader signal window ($m_{\mathrm{H}} = 125 \pm 10$ GeV) are 118 for the 4μ, 98/57 for the $2e2\mu/2\mu2e$ and 43 for the $4e$ channel.

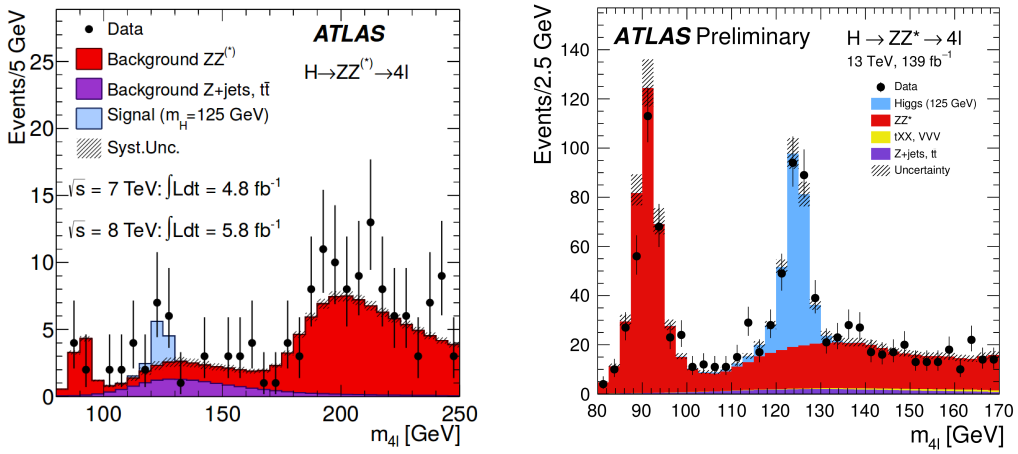

(a) ATLAS Run-1 result. **(b)** ATLAS Run-2 result.

Figure 1.12: Invariant mass distribution m_{4l} in the $H \to 4l$ analysis. In Run 1 with 4.8 fb^{-1} at $\sqrt{s} = 7$ TeV and 5.8 fb^{-1} at $\sqrt{s} = 7$ TeV [49], and Run 2 with 139 fb^{-1} at $\sqrt{s} = 13$ TeV [51].

The significance of the Higgs boson signature improves simply by the higher number of events in the Run-2 analysis compared to Run 1. But in addition, the systematic uncertainty from the lepton reconstruction and identification efficiency has decreased due to optimized reconstruction algorithms: in Run 1, e.g. the relative uncertainty on the signal acceptance due to the uncertainty on the electron reconstruction and identification efficiency was $\pm 8.0\%/\pm 2.3\%/\pm 7.6\%$ for the $4e/2e2\mu/2\mu 2e$ channel for $m_{4l} = 115\,\text{GeV}$, whereas for the Run-2 analysis uncertainties are below $1.0 - 2.0\%$ for electrons.

In the diphoton decay channel of the Higgs boson, a high photon reconstruction and identification efficiency is required to measure the invariant diphoton mass $m_{\gamma\gamma}$.
The analysis is divided into categories for *unconverted* and *converted* photons in different detector regions (η) and for different bins of transverse momenta (p_{T}).
In the resulting invariant mass spectrum of the two reconstructed photons, the background is inclusively fitted with a, depending on the chosen category, 4th order polynomial or exponential function. A signal fit using a convolution of a Crystal Ball function with a Gaussian function for the tails is performed to extract Higgs candidates at invariant diphoton masses around $m_{\text{H}} = 126.5\,\text{GeV}$.

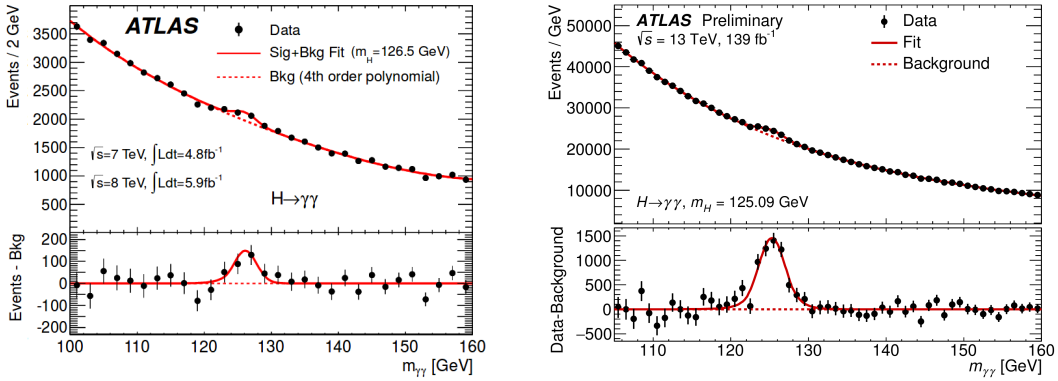

(a) ATLAS Run-1 result. **(b)** ATLAS Run-2 result.

Figure 1.13: Invariant mass distribution $m_{\gamma\gamma}$ in the $H \to \gamma\gamma$ analysis. In Run 1 with $4.8\,\text{fb}^{-1}$ at $\sqrt{s} = 7\,\text{TeV}$ and $5.9\,\text{fb}^{-1}$ at $\sqrt{s} = 7\,\text{TeV}$ [49], and Run 2 with $139\,\text{fb}^{-1}$ at $\sqrt{s} = 13\,\text{TeV}$ [52].

In Figure 1.13a, the summed $m_{\gamma\gamma}$ distribution for all analysis categories of the Run-1 analysis including the signal+background fit is shown, using a dataset with integrated luminosity of $4.8\,\text{fb}^{-1}$ at $\sqrt{s} = 7\,\text{TeV}$ and $5.9\,\text{fb}^{-1}$ at $\sqrt{s} = 8\,\text{TeV}$.
Comparing the signal peak in the mass spectrum subtracted from background with the result from the Run-2 analysis, as displayed in Figure 1.13b, the Higgs mass peak at $m_{\text{H}} = 125.09\,\text{GeV}$ is much more distinct with 6550 ± 530 extracted signal candidates. This is again caused by the higher statistics in the dataset with $139\,\text{fb}^{-1}$ at $\sqrt{s} = 13\,\text{TeV}$ compared to the Run-1 result. But at the same time an improvement in the systematic uncertainty of the photon reconstruction and identification efficiency was reached, resulting in an improved determination of the Higgs mass.
In Run 1, the dominant experimental uncertainty on the signal yield is due to the photon reconstruction and identification with $\pm 8\%$ and $\pm 11\%$ for the $\sqrt{s} = 7\,\text{TeV}$ and $\sqrt{s} = 8\,\text{TeV}$ dataset, respectively. For Run 2, using a changed categorization strategy to reflect different measurements of the Higgs boson such as differential cross-sections, the photon identification efficiency uncertainty could be decreased to 1%.

Finally, another important test of the compatibility of the observed Higgs boson with the SM prediction is to measure the Yukawa coupling to fermions and bosons, expressed as reduced coupling strength modifiers $\kappa_{\mathrm{F}}\frac{m_{\mathrm{F}}}{\nu}$ for fermions and $\sqrt{\kappa_{\mathrm{V}}}\frac{m_{\mathrm{V}}}{\nu}$ for weak gauge bosons with the vacuum expectation value ν of the Higgs field.

For the first Run-2 analysis [53], different datasets of up to $80\,\mathrm{fb}^{-1}$ at $\sqrt{s} = 13\,\mathrm{TeV}$ were used, combining the Higgs boson decay modes $H \to \gamma\gamma, ZZ^*, WW^*, \tau\tau, b\bar{b}, \mu\mu$, and the resulting coupling strength κ versus the particle mass is shown in Figure 1.14.

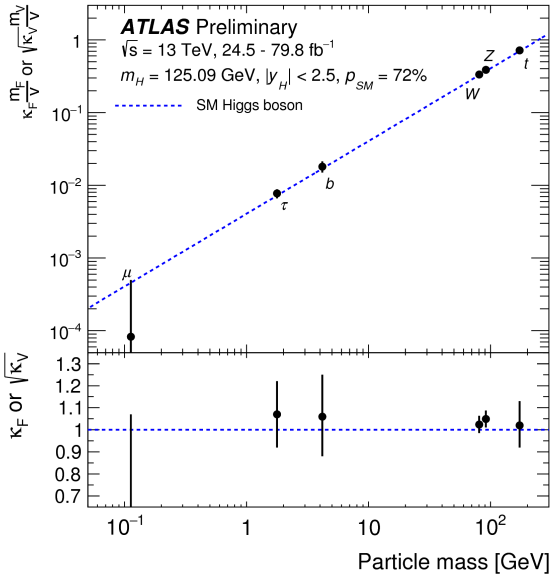

Figure 1.14: Higgs boson couplings to fermions and bosons from ATLAS Run-2 results expressed as reduced coupling strength modifiers κ_{F} and κ_{V}, respectively [53]. The measurement combines datasets of up to $80\,\mathrm{fb}^{-1}$ at $\sqrt{s} = 13\,\mathrm{TeV}$ for the Higgs boson decay modes $H \to \gamma\gamma, ZZ^*, WW^*, \tau\tau, b\bar{b}, \mu\mu$.

The very good agreement between the SM prediction and the experimental results for the Higgs boson couplings to the fermions and bosons suggests that the properties of the observed Higgs boson is compatible with the predicted SM Higgs boson. For further investigations, the coupling strengths to the lighter fermions need to be measured requiring higher integrated luminosities for the physics analyses as foreseen for the HL-LHC era.

1.3.3 Light-by-light scattering

The final example of ATLAS measurements at LHC is the observation of the light-by-light scattering process, $\gamma\gamma \to \gamma\gamma$, in heavy-ion collisions (Pb+Pb) at a center-of-mass energy of $\sqrt{s_{\mathrm{NN}}} = 5.02\,\mathrm{TeV}$, using a data sample of $1.73\,\mathrm{nb}^{-1}$ [54].
An event display of such a scattering interaction for the ATLAS detector as well as the corresponding Feynman graph are shown in Figure 1.15.

For the event selection, two photons are required to be produced exclusively in the event. Therefore, any further particle activity in the event is discarded by applying a veto on tracks in the event. Each photon is required to have a transverse energy of $E_{\mathrm{T}} > 3\,\mathrm{GeV}$ and the invariant diphoton mass should be at least 6 GeV. Moreover, the required back-to-back topology of the scattered photons results in criterion on a small diphoton transverse momentum as well as a small acoplanarity[4].

[4] The acoplanarity *Aco* in the scattering experiment measures the degree of deviation to coplanarity for the paths of the scattered photons with $Aco = 1 - |\Delta\phi_{\gamma\gamma}|/\pi$. With the requirement on a small acoplanarity the prompt-photon background from the central exclusive production via $gg \to \gamma\gamma$ reactions is reduced.

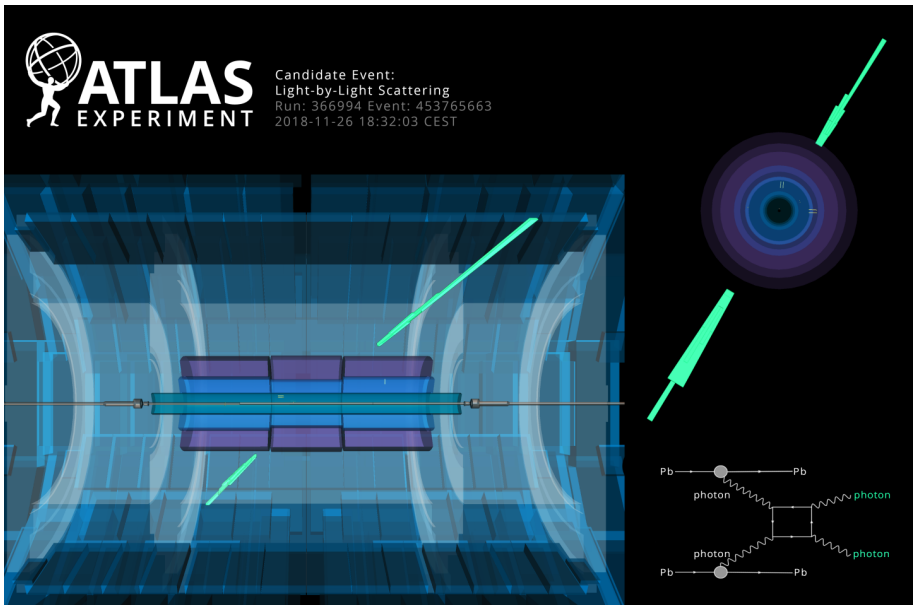

Figure 1.15: ATLAS event display of a light-by-light scattering candidate in Pb-Pb collisions and the corresponding Feynman diagram of the interaction [55].

The acoplanarity distribution as well as the invariant mass spectrum of the selected diphoton candidates in Pb-Pb collisions are depicted in Figure 1.16.

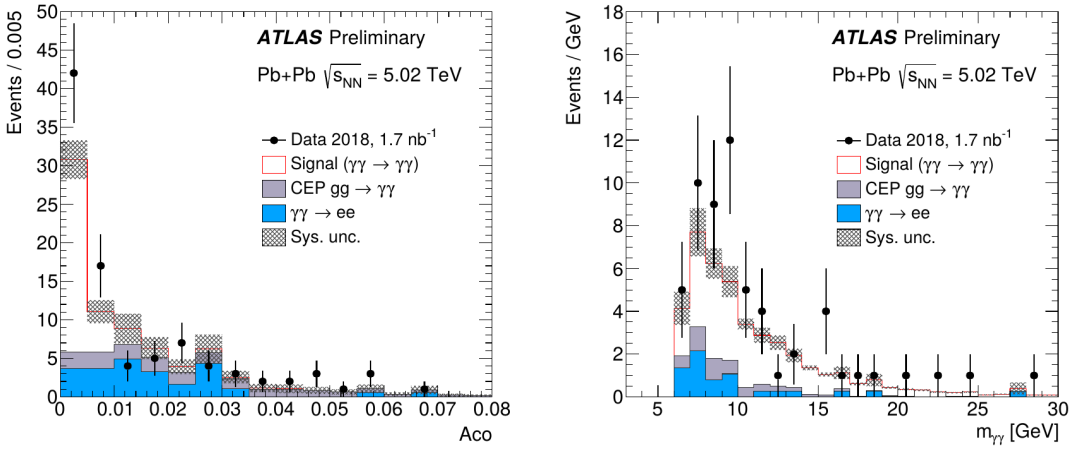

(a) Acoplanarity distribution.

(b) Invariant diphoton mass spectrum.

Figure 1.16: Acoplanarity distribution and invariant mass spectrum of light-by-light scattering candidates measured with the ATLAS detector in Pb-Pb collision data with $\sqrt{s_{\mathrm{NN}}} = 5.02\,\mathrm{TeV}$ and $1.7\,\mathrm{nb}^{-1}$ [54]. In (a), the acoplanarity distribution of the diphoton candidates shows a good background suppression when applying a selection cut with Aco<0.01. In (b), the invariant diphoton mass spectrum $m_{\gamma\gamma}$ is shown for the selected light-by-light scattering events.

In total, 59 candidate events are observed over a background expectation of 12 ± 3 events, such that a signal excess is observed with a significance of 8.2σ. The main background processes are central exclusive production of $gg \to \gamma\gamma$ as well as $\gamma\gamma \to ee$ with misidentified electrons. For this analysis, the photon reconstruction and identification are tuned at low-E_{T} to achieve such a good signal selection.

1.4 Open Questions: Physics beyond the Standard Model

The SM has proven to be a very successful theory to describe interactions of elementary particles via the strong and electroweak forces, as can be concluded from most of the experimental measurements, e.g. from the high-energy physics programme at LHC, so far. Nonetheless, the SM has shortcomings for describing certain aspects of nature and has unresolved issues within its theory, which are addressed by the search for physics **B**eyond **S**tandard **M**odel (BSM).
In Section 1.4.1, a selection of the unsolved problems in the SM theory are enumerated, followed by a small selection of theoretical BSM models tested within the LHC physics programme in Section 1.4.2.

1.4.1 Problems in the Standard Model

In the following an incomplete list of the problems and shortcomings within the theoretical description of the SM are discussed.

Gravity

The gauge bosons incorporated in the SM describe the strong and electroweak forces, which are only three of the four fundamental forces in nature. The missing force, gravity, could be included as a quantum field theory in the SM by introducing a new particle, the *graviton*. Due to the well-observed gravitational force, used frequently for explanations in the context of cosmology, the SM description cannot be the final theory, as it seems also not compatible with *general relativity* [40].

Hierarchy problem

A inherent property of the SM is the *hierarchy problem* concerning the Higgs field and the mass of the corresponding Higgs boson. The observed mass, $m_{\mathrm{H}} \approx 125\,\mathrm{GeV/c^2}$, is influenced by large quantum loop corrections from virtual particles, with

$$m_{\mathrm{H}}^2 \sim m_{\mathrm{H0}}^2 + \delta m_{\mathrm{H}}^2, \tag{1.11}$$

where m_{H0} is the bare Higgs mass and δm_{H} the radiative corrections, as schematically shown in Figure 1.17. Taking the corrections at the order of the Planck scale ($\Lambda_P \sim 10^{19}\,\mathrm{GeV}$), a *fine-tuning* of the bare Higgs mass is required to converge with the Higgs mass in the observed order of $10^2\,\mathrm{GeV}$, which appears *unnatural* from a theory point-of-view [56].

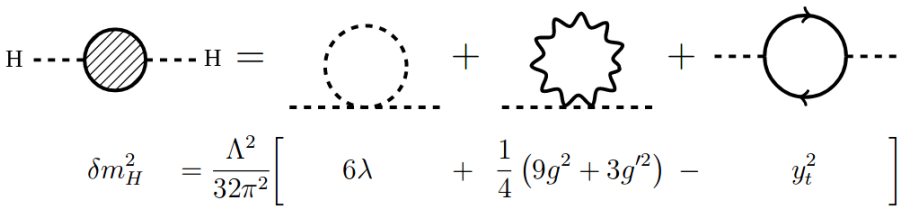

Figure 1.17: The quantum loop corrections to the Higgs boson mass by self-interaction, gauge and fermion loops with its couplings λ, g,g' and y calculated at a cut-off scale Λ.

A promising solution to the Hierarchy problem is offered by the concept of supersymmetry, which will be discussed in Section 1.4.2 as a possible extension of the SM theory.

Grand unification and renormalization

The ***G**rand **U**nifying **T**heory (GUT)* [57] predicts the unification of the strong and electroweak forces at an energy scale, called GUT scale. This is motivated by the fact that the SM theory is based on a *renormalizable theory*, meaning that all quantities predicted by the theory are well defined and have a finite value. These quantities will therefore depend on the energy scale at which they are measured, the renormalization scale.
One example is the coupling constants for the electromagnetic, weak and strong force which are changing with the energy scale, described as *running coupling constants*.
For the SM, the picture for the running coupling constants, depicted in Figure 1.18, does not show a crossing point for all three couplings as predicted by GUT.

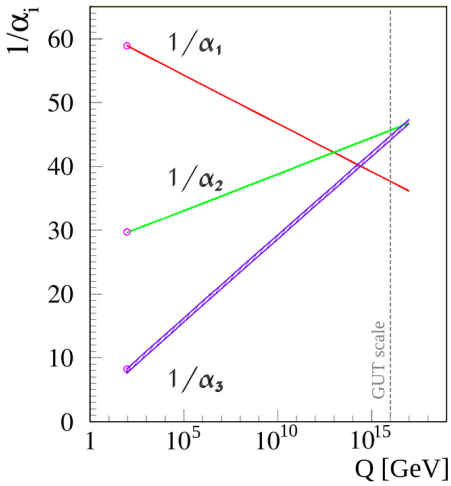

Figure 1.18: Running coupling constants of the three SM interactions with α_i (i = 1,2,3) for the $U(1)_Y$, $SU(2)_L$ and $SU(3)_C$ symmetry groups as a function of the energy scale Q. At the GUT scale with 10^{16} GeV, it is believed that the electromagnetic, the weak and the strong force become equal in strength and unify to one force.

Fermion masses

The fermion masses follow a hierarchical pattern within three generations, whereas the SM theory does not pose any prediction on the observed masses or the mass difference between generations. Moreover, neutrinos are massless particles in the SM, but with the experimental observation of neutrino oscillations between flavour eigenstates [58, 59] it is evident that neutrino masses must be included in the theory. A possible way to do so is via a Majorana mass term as an extension to the SM [60], which requires that the neutrino is its own antiparticle. The nature of the neutrinos as well as their absolute masses are therefore recent topics of experimental investigations.

CP-violation and matter-antimatter asymmetry

The violation of the charge and parity symmetry, called CP-violation, was observed for the SM only in the electroweak sector. The CP-violating phases are added in the CKM [61, 62] and the PMNS [63, 64] mixing matrices for quarks and neutrinos, respectively.
But no CP-violation is observed in the strong sector so far. This rather puzzling observation is called the *strong CP-problem* [65]. A possible solution is to introduce a new pseudoscalar particle, the *axion* [66], which has to be a very light and long-lived particle and could also offer a dark matter candidate.
Related to this topic is the question why nowadays no antimatter is present anymore, whereas the amount of matter and antimatter is assumed to be the same after the big bang. In the process of baryogenesis this baryonic asymmetry could be produced, but this phenomenon requires more CP-violation than experimentally observed [67].

Cosmology: dark matter & dark energy

In 1933, cosmological observations of the rotational velocity of galaxies [68, 69] showed a difference to the expected behaviour: the orbital speeds of visible stars or gas clouds in the observed galaxies are increasing with the radial distance from the galaxy's center, whereas the expected velocity curve derived by applying the theory of gravity to the matter observed in the galaxy shows a decreasing characteric.
This observation led to the postulation of *dark matter* by requiring a different form of matter apart from the luminous baryonic matter that is needed in a much larger fraction. With the discovery of an accelerating expansion rate of the universe, the theory of *dark energy* [70, 71] was also introduced into the cosmological considerations.
Current estimates, using various experimental results e.g. from the Cosmic Microwave Background [72], predict that the baryon matter density is $\sim 5\%$, whereas the rest of the universe is made up of $\sim 27\%$ dark matter and $\sim 69\%$ dark energy. But at the same time, the nature of dark matter as well as dark energy remains unknown.

1.4.2 Beyond Standard Model theory

The previously discussed shortcomings of the SM can be resolved with possible theoretical extensions to the SM theory. Out of several such models, three often discussed ones will be shortly explained in the following: *supersymmetry*, *extra dimensions* and *string theory*. Although, these models provide elegant solutions for several unresolved issues of the SM theory, so far neither of them have been experimentally observed.

Supersymmetry (SUSY)

For the supersymmetric extension of the SM, called SUSY [73, 74], every SM particle gets a supersymmetric partner with the same quantum numbers but with a $\pm 1/2$ different spin. In its simplest version, the **M**inimal **S**upersymmetric **S**tandard **M**odel (MSSM), introduces bosonic partners for fermions, called *squarks* and *sleptons*, and fermionic partners for bosons, called *gluinos* and *gauginos*. As superpartners have not been observed yet, the symmetry of the mass between particles and sparticles must be broken.
With this gauge theory, several aspects of the problems in the SM theory could be solved, e.g. the SUSY model provides a dark matter candidate with the lightest neutralino, neutral weakly-interacting sparticle. In addition, the hierarchy problem would be addressed by the cancelling contribution of the superpartners in the loop corrections of the Higgs boson.

Extra dimensions & string theory

In models with extra dimensions [74], the usual three spatial dimensions are extended by more space dimensions. For example, the SM would be confined to a 4-dimensional manifold while gravity could propagate through all the dimensions. Due to this behaviour, the weakness of the gravitational interaction in comparison to the other interactions in the SM theory is not fundamental, but a consequence of the existence of the extra dimensions. The detection of the extra dimensions would be only possible at very high energies and with the observation of the graviton.
In string theory [75], defining a collection of hypothetical models for the description of particle physics phenomena, particles are introduced as tiny vibrating strings instead of the point-like objects used for the elementary particles in quantum field theories.
Here, also models with up to seven undiscovered dimensions of space are considered, connecting string theory to the theory of extra dimensions.

Chapter 2

Particle Detection and the ATLAS Detector

A particle detector in high-energy physics application is an experimental apparatus used to detect, track, and identify different kinds of particles produced within a particle physics experiment, most prominently in a particle collision at an accelerator. The basic task of registering the presence of a particle is extended by the measurement of physical quantities of the particle, such as its energy, momentum, charge or type.
Here, the operation principle of a particle detector relies on the fact that particles interact with matter via the fundamental forces of nature. To allow for a detection and measurement of a particle, it is necessary to understand the interaction mechanisms happening within the detector volume. Section 2.1 addresses the interaction types of particles with matter.

A particle tracking detector is a special kind of detector optimized to allow for a position-resolved measurement of the incidence position of the particle and to reconstruct the particle trajectory through the detector volume. For this purpose, semiconductor detectors made out of silicon are most often used. Starting in the 1980s with the first application of silicon detectors [76, 77], the field of silicon detector development and its application in particle physics experiments has rapidly evolved. The trend of building tracking detector systems with even larger sensor areas as well as improved resolution for high accuracy track reconstruction is visualized in Figure 2.1 for a collection of past, running and planned particle tracking detectors.

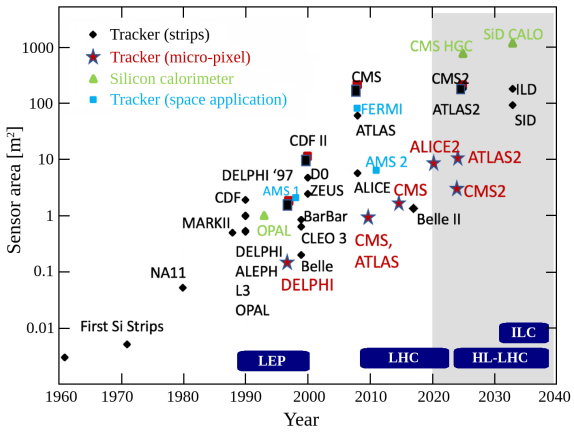

Figure 2.1: Graph of the silicon sensor area of detector systems versus years. Shown are applications for particle tracking with strip (black) or micro-pixel (red) segmentation, as calorimeter devices (green) or in space (cyan). Overlayed are major high-energy particle colliders with LEP, LHC and the planned HL-LHC and ILC. Inspired from [78].

The basics and operation principle of silicon detectors as well as their characteristic properties will be the topic of Section 2.2.

Finally, to fulfill the manifold requirements to detect and identify particles created in high-energy particle collisions such as at the LHC, a complex system of different types of detectors, each optimized for a special kind of measurement, are arranged together building up a complete particle physics experiment. As an example of such an experimental apparatus, the detector concept of the **A** **T**oroidal **L**HC **A**pparatu**S** (ATLAS) experiment at the LHC will be introduced in Section 2.3.

2.1 Interaction with Matter

When a particle traverses a block of material, it will interact with the atoms in the material in a defined way depending on the particle's properties such as electric charge, mass, spin, or kinetic energy. This interaction process is exploited when a particle in an experimental setup should be detected and measured. In general, the interaction type can be differentiated by the underlying force as e.g. described in the SM of particle physics.
So, charged particles like electrons and muons as well as photons interact with matter via the electromagnetic force, but also nuclear interactions described within QCD theory can be relevant for neutral and charged hadrons in a particle physics experiment. For this thesis, the focus will be on the electromagnetic interactions of particles with matter.

In Section 2.1.1, the energy loss of charged particles traversing a material and its dependence on the incident particle as well as the material properties will be addressed. Moreover, a charged particle will not only lose energy in the material, but also be deflected from its initial path due the effect of multiple Coulomb scattering, as introduced in Section 2.1.2. The interaction mechanisms of photons in matter are different from the ones of charged particles, which will be themed in Section 2.1.3. Finally, the concept of electromagnetic showers of electrons and photons in matter will be briefly discussed in Section 2.1.4.

2.1.1 Energy loss of charged particles

When a charged particle interacts with matter, it interacts with a nucleus of a close by atom or with an electron in the atomic shell of the material. Depending on the mass of the incident particle as well as the type of the material, the interaction cross sections vary a lot. The dominant processes for loosing energy in the material are due to ionization and excitation of atoms and by the emission of bremsstrahlung. For the former case, the incident particle transfers fractions of its energy onto an electron in the atomic shell via a scattering process, followed by either an excitation of this electron or by an ionization. In the case of bremsstrahlung, the incident particle is deaccelerated by the Coulomb field of the nuclei, emitting parts of its energy as bremsstrahlung photons.

The mean energy loss, expressed as the mass stopping power in units of $[\mathrm{MeV\,cm^2/g}]$, for an anti-muon by interacting with copper is shown in Figure 2.2. Here, depending on $\beta\gamma$ of the incident particle, with $\beta = v/c$ and the relativistic Lorentz factor $\gamma = 1/\sqrt{1-\beta^2}$, the statistical energy loss in the material is given. The description of the stopping power in a material can be divided into regions of $\beta\gamma$: the *low energy region*, the *Bethe region* at intermediate energies and the *radiative region* for higher energies.
The energy loss for electrons and positrons in a material follows the same processes of ionization and bremsstrahlung. But as the incident particle and the particles in the material are the same (electrons) with equal spin and charge, other scattering processes can occur additionally (e.g. Møller and Bhabha scattering), changing the interaction cross sections compared to the energy loss for heavy, charged particles.

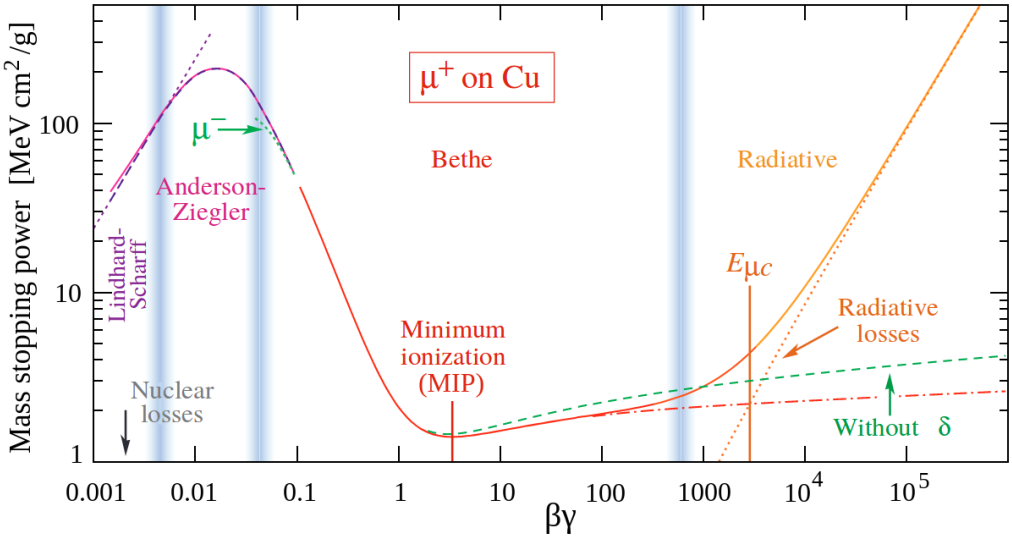

Figure 2.2: Mean energy loss of a positive muon (μ^+) in copper expressed as the mass stopping power $\langle -dE/dx \rangle$ as function of $\beta\gamma$. The central part for $\beta\gamma$ can be empirically described by the Bethe-Bloch formula followed by the radiative regime for higher values of $\beta\gamma$. Modified from [14].

Moreover, the energy loss due to radiative effects rises significantly faster for higher electron energies due to a lower mass for electron and positrons as incident particle. In Figure 2.3, the dominant processes for the different energy regimes of the incident electron or positron are shown exemplary for the energy loss in lead.

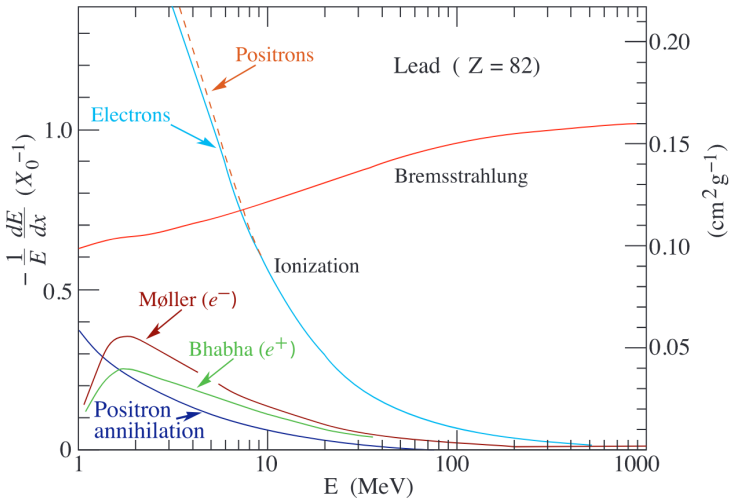

Figure 2.3: Energy loss for electrons and positrons in lead from the various processes depending on the incident particle energy [14].

Low energy region

For the low energy region, meaning $\beta\gamma$ smaller than 0.05, the energy loss is not described in a closed form due to the necessary inclusion of higher-order shell corrections. For particles slower than $\sim 0.01c$, so comparable to the velocity of the outer atomic shell electrons, the stopping power is described by Lindhard [79] to be proportional to β. For $0.01 < \beta\gamma < 0.05$, Anderson and Ziegler [80] developed a phenomenological description for the energy loss of protons. Moreover, negatively charged particles show a reduced stopping power compared to positively charged ones, described by Barkas [81].

Bethe region

The mean rate of energy loss by moderately relativistic charged heavy particles is empirically described by the Bethe formula [82], taking into account ionization and excitation processes by using a first-order Born cross section as approximation.
The Bethe formula yields good results within an accuracy of a few percent for a range of $0.1 \lesssim \beta\gamma \lesssim 1000$ and intermediate-Z materials.

The energy loss per path length in the material is determined by

$$\left\langle -\frac{dE}{dx} \right\rangle = Kz^2 \frac{Z}{A} \frac{1}{\beta^2} \left[\frac{1}{2} \ln \frac{2m_e c^2 \beta^2 \gamma^2 W_{\max}}{I^2} - \beta^2 - \frac{\delta(\beta\gamma)}{2} \right], \tag{2.1}$$

with the constant $K = 4\pi N_A r_e^2 m_e c^2$, the incident particle's charge number z, the atomic and mass numbers Z and A, the electron mass m_e, the mean excitation energy I, the maximum energy transfer $W_{\max}$ and the density-effect correction $\delta(\beta\gamma)$.

The mass stopping power is given in units of $[dE/dx] = \text{MeV}/(\text{g}/\text{cm}^2)$ relative to the surface density $dx = \rho \cdot dl$ with material density ρ and path length dl. Moreover, a distinct minimum for the energy loss at $\beta\gamma \approx 3$ characterizes the minimum ionization, such that a particle here is described as **M**inimum **I**onizing **P**article (MIP), creating the smallest possible signal in a detector. Depending slightly on the material's atomic number, a MIP experience roughly a stopping power of $1.5\,\text{MeV}\,\text{cm}^2/\text{g}$.

The Bethe formula only provides the mean energy loss of a particle traversal through a material, but not the exact energy loss distribution for a given particle energy. The energy loss for individual particles shows statistical fluctuations with pronounced tails to higher energy depositions due to rare high energy transfer interactions, such as so-called *delta electrons*. This is described by the Landau-Vavilov distribution [83, 84], featuring a most probable value for the energy deposition lower than the mean value.
For thin silicon sensors of typical sensor thicknesses in the order of $\mathcal{O}(100\,\mu\text{m})$, a better description of the energy loss distribution is reached with the Straggling functions [85], as exemplary shown in Figure 2.4 for energy loss of 500 MeV pions in silicon.

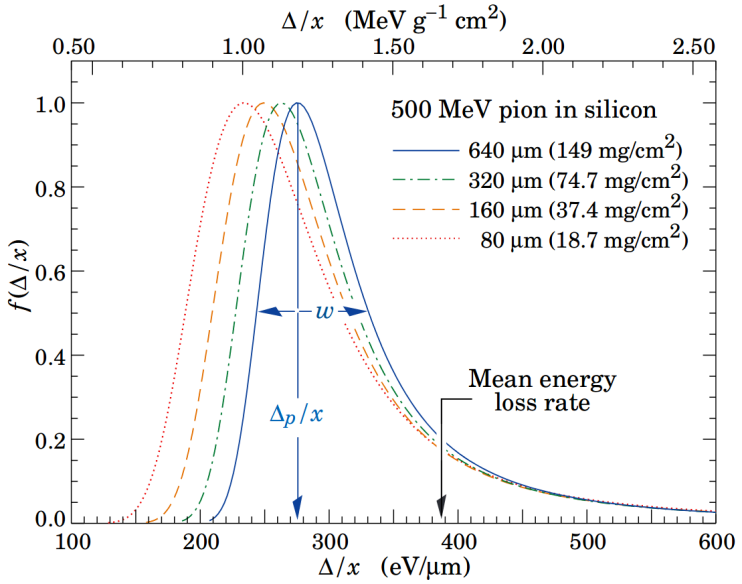

Figure 2.4: Straggling functions describing the energy loss in thin silicon detectors, shown for 500 MeV pions and different silicon thicknesses, normalized to unity at the most probable value $\Delta p/x$ [14].

Radiative region

For higher energies of the incident particle, the dominant energy loss occurs due to radiative effects by emitting bremsstrahlung photons. The mean energy loss via bremsstrahlung is determined by

$$\left\langle -\frac{dE}{dx} \right\rangle = 4\alpha N_A z^2 \frac{Z^2}{A} \left(\frac{1}{4\pi\epsilon_0} \frac{e^2}{mc^2} \right)^2 E \ln\left(\frac{183}{Z^{1/3}} \right), \tag{2.2}$$

with the fine-structure constant α, the Avogadro number N_A, the vacuum permittivity ϵ_0, the elementary charge e, the incident particle mass m and its energy E.
The energy loss via bremsstrahlung shows a linear dependence to the particle energy, whereas the ionization loss varies only logarithmically with the electron energy. The *critical energy* E_c describes the point where the contribution of both is equal, and can be parametrized for solid materials as:

$$E_c = \frac{610\,\text{MeV}}{Z + 1.24}. \tag{2.3}$$

Moreover, by introducing the *radiation length* X_0 as

$$\frac{1}{X_0} = 4\alpha N_A z^2 \frac{Z^2}{A} \left(\frac{1}{4\pi\epsilon_0} \frac{e^2}{mc^2} \right)^2 \ln\left(\frac{183}{Z^{1/3}} \right), \tag{2.4}$$

the mean energy loss simplifies to

$$\left\langle -\frac{dE}{dx} \right\rangle = \frac{E}{X_0}. \tag{2.5}$$

As such the radiation length depends on the material properties and the incident particle mass, but most commonly, the radiation length is used in the context of electrons being then a material constant.

2.1.2 Multiple Coulomb scattering of charged particles

When a charged particle traverses a material, it interacts with the electric field of the nuclei. As explained before, it can loose energy due to radiative effects, but also the incident particle is deflected by small angles when passing a nucleus in the material, called Coulomb scattering at a nuclei, which can be described by the Rutherford cross section. For a traversal of a material, many of these small-angle scatters sum up to an effective deflection and displacement of the primary particle, as it is visualized in Figure 2.5a. Depending on the material's density and the particle's path length in it, the probability for a larger deflection is higher. The core of the scattering distribution can be described with a Gaussian function via the central limit theorem, but due to less frequent hard scatters non-Gaussian tails for higher deflections are introduced as well. This behaviour is exemplary shown for a measurement of the scattering in air and aluminum in Figure 2.5b.

A theoretical description of multiple Coulomb scattering was done by Molière [86, 87], but an approximate parametrization of the probability density function uses the angular distribution projected onto a lateral plane described with

$$\theta_0 := \sigma_\theta^{\text{plane}} = \frac{1}{\sqrt{2}} \sigma_\theta^{\text{space}}. \tag{2.6}$$

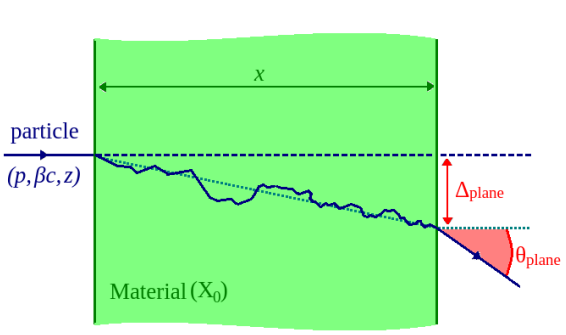

(a) Multiple Coulomb scattering of a particle with momentum p in a material with length x and radiation length X_0, leading to an effective scattering angle θ_{plane} and a displacement Δ_{plane}.

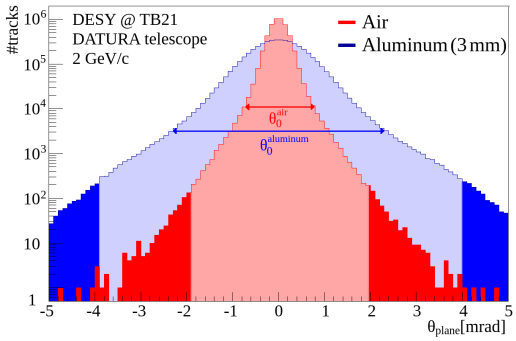

(b) Scattering angle distributions for 2 GeV/c electrons in air and aluminum, showing the central 98% and the scattering width θ_0 for both scatterers.

Figure 2.5: Multiple Coulomb scattering and the scattering angle distribution.

In the *Highland formula*, introduced by Highland [88] and revised by Lynch and Dahl [89], the width of the scattering distribution using the central 98% part is parametrized by

$$\theta_0 = \frac{13.6\,\text{MeV}}{\beta cp} z \sqrt{\frac{x}{X_0}} \left(1 + 0.038 \ln\left(\frac{x}{X_0}\right)\right), \tag{2.7}$$

with the momentum p, the velocity βc, the charge number of the incident particle z and the thickness x of the scattering medium relative to its radiation length X_0.

The dependence of the multiple scattering on the material path is often referred to as the *material budget* ϵ of the scatterer, defined as

$$\epsilon := \frac{x}{X_0}. \tag{2.8}$$

Besides the deflection, the lateral displacement of the incident particle in a lateral plane due to multiple Coulomb scattering can be calculated as

$$\sigma_{\text{displacement}} = \frac{x}{\sqrt{3}} \theta_0. \tag{2.9}$$

The effect of multiple Coulomb scattering is important for the design and development of particle detectors, especially for tracking detectors. Moreover, the dependence of the effective scattering angle θ_0 of a particle to its traversed material budget ϵ will be exploited in Chapter 9 for the technique of **M**aterial **B**udget **I**maging (MBI).

2.1.3 Interactions of photons with matter

The interaction of photons with matter is different from charged particles due to its lack of electric charge and mass. Three effects play an important role for the measurements of photons in a particle physics experiment: the *photoelectric effect*, the *Compton effect* and the *pair production*. The absorption of photons in matter follows an exponential behaviour with an absorption coefficient μ or the mean free path as $\lambda = 1/\mu$.
The total cross section of photons in a material with atomic number Z is a combination of the mentioned effects with changing contributions, depending on the photon energy, as summarized in Figure 2.6 for the total cross section in lead.

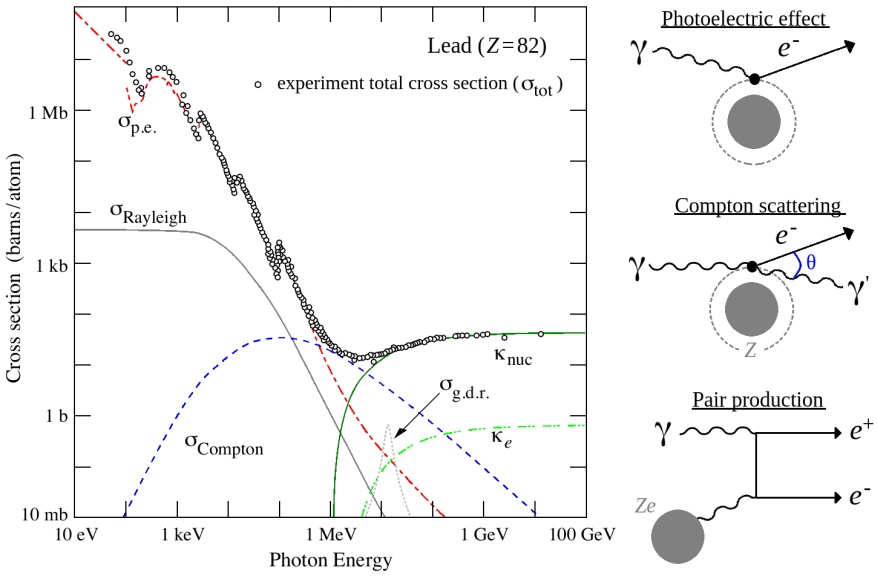

Figure 2.6: Total cross section of photons in lead ($Z = 82$) with its individual contributions from *photoelectric effect* ($\sigma_{\text{p.e.}}$), *Compton effect* (σ_{Compton}) and *pair production* (n_e, n_{nuc}), also shown as Feynman diagrams. Modified from [14].

Photoelectric effect

In the photoelectric effect, a photon is absorbed by an orbital electron which is emitted into the electron continuum. If the photon energy (E_γ) is larger than the binding energy (E_{B}), the exceeding energy is transferred as kinetic energy $T = E_\gamma - E_{\text{B}}$ to the emitted electron. The cross section, $\sigma_{\text{p.e.}}$, decreases for higher photon energies and increases strongly with higher Z of the material.

Compton effect

If the photon interacts with an orbital electron via an inelastic scattering process and looses part of its kinetic energy, the mechanism this called Compton effect. In this case, the remaining energy E'_γ of the scattered photon and its scattering angle θ between emitted electron and the photon are coupled by the interaction. The Compton effect is dominant for medium photon energies and its cross section follows a continuous distribution determined by the Klein-Nishina formula [90].

Pair production

The most important interaction mechanism for photons in high-energy particle physics experiments is the pair production. The photon interacts with the Coulomb field of a nucleus in the material and creates an electron-positron pair. The critical energy for this process is at least two times the rest mass of an electron and therefore this effect is the dominant contribution in the cross section for higher photon energies. Moreover, the pair production is closely linked to the effect of bremsstrahlung (called *Bethe-Heitler processes* [91]), discussed in Section 2.1.1. Therefore, the pair production cross section can be expressed as function of the radiation length X_0 as

$$\sigma_{\text{pair production}} \sim \frac{7}{9}\frac{1}{X_0}\frac{A}{N_A \rho}, \tag{2.10}$$

and the mean free path of photons due to pair production is $\lambda_\gamma = \frac{9}{7}X_0$.

2.1.4 Electromagnetic showers

The interaction of a multi-GeV electron or photon in a material can be described as an *electromagnetic shower* involving a cascade of creation of new electron-positron pairs during energy loss in the material, as displayed in Figure 2.7.

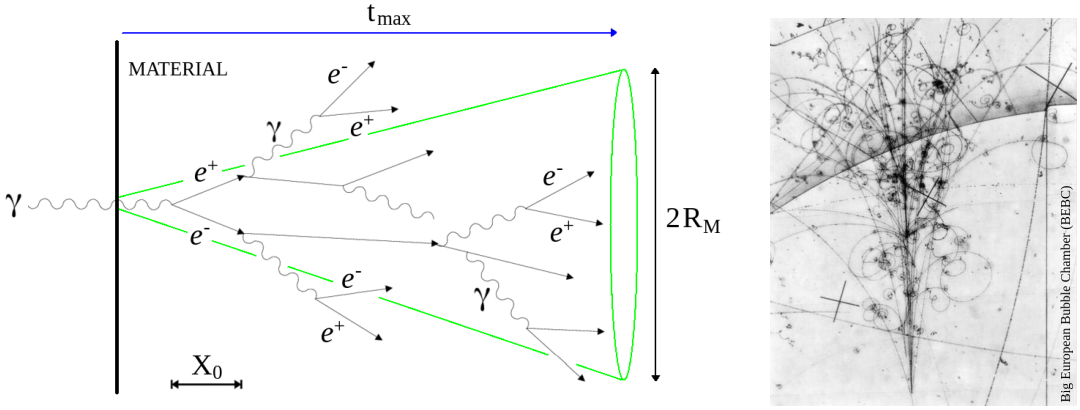

Figure 2.7: *Left:* Schematic of electromagnetic shower induced by high-energetic photon in a material with radiation length X_0. The characteristic development in longitudinal and lateral direction can be described by the *shower maximum* $t_{\max}$ and the *Molière radius* R_M, respectively.
Right: Electromagnetic shower from high energy neutrino interaction recorded with the Big European Bubble Chamber (BEBC) [92].

Starting with a highly energetic electron of energy E_0, it will loose energy by bremsstrahlung effects, such that a large number of photons are radiated. From these photons, a high fraction are very soft and thus will get absorbed by Compton scattering or the photo-electric effect, as explained before. Nonetheless, a number of photons have energies higher than two times the electron rest mass and can undergo the pair production process by creating new electron-positron pairs. These, in turn, radiate bremsstrahlung photons again and new branches are added to the electromagnetic cascade, involving a multiplication of the number of shower particles. Only when the average electron energy is around the critical energy E_c (cf. Eq. 2.3), the development of the electromagnetic shower stops, having created on average $N \approx E_0/E_c$ particles.

The longitudinal and lateral development of an electromagnetic shower can be parametrized by using the material specific radiation length X_0, so the *shower maximum* $t_{\max}$ [93] is parametrized as

$$t_{\max} = \frac{x_{\max}}{X_0} = \ln\left(\frac{E_0}{E_c}\right) + C, \tag{2.11}$$

with $C = -0.5$ for electron-induced and $C = 0.5$ for photon-induced showers.

The characteristics of the lateral shower development is described by the *Molière radius* R_M [93], containing 90% of the energy in a cylinder with a radius R_M, and scaling with the scale energy $X_s = 21.2\,\text{MeV}$ as

$$R_M = X_s \frac{X_0}{E_c}. \tag{2.12}$$

2.2 Silicon Detectors

For the purpose of tracking detectors in particle physics experiments, nowadays semiconductor devices are the most often used technology. In most cases, silicon is used in such detectors due to its characteristics in terms of moderate band gap and ionization energy while having a high signal-to-noise ratio at room temperature operation. Another benefit of silicon is the abundance of the material and the availability of industrial producers, offering high quality production processes with relatively low costs.

A silicon tracking detector allows to measure the position of a particle traversal with a spatial resolution of several microns due to small scale sensor segmentation, while providing a high detection efficiency as well as a low material budget along the path. Moreover, with readout times of several nanoseconds and the possibility to design radiation hard devices, silicon detectors are the preferred technology for the application in the field of high-energy collider experiments.

In the following, the concept of silicon tracking detectors is discussed, but comprehensive reviews on silicon detectors can be found in literature, e.g. [78, 94, 95]. In Section 2.2.1, the basic concept of semiconductors and doping of silicon is introduced, followed by the operation principle in Section 2.2.2. To allow for position measurements in one or two dimensions, sensors are segmented and read out by the front-end electronics as explained in Section 2.2.3. The signal formation and performance parameters of silicon devices are discussed in Section 2.2.4. Finally, Section 2.2.5 addresses the effects of radiation on silicon detectors and its influence on the detector performance.

2.2.1 Semiconductors and doping

In a crystalline material, atoms are bound in a lattice which implies that the discrete energy levels for electrons in an atom and the ones unbound atoms of it form energy bands. An energy band describes a wider range of possible energy levels for the electrons in the material with gaps of forbidden regions in between. The electrical properties of materials can be described by the model of energy bands and materials can be categorized due to their properties into *conductors*, *semiconductors* and *insulators*.

The probability density function to find electrons at an energy level E is described by the Fermi-Dirac statistics [96, 97] with a distribution as

$$f(E) = \frac{1}{e^{(E-E_F)/k_B T} + 1}, \tag{2.13}$$

with the Fermi level E_F[5], the Boltzmann constant k_B and the temperature T. The valence band is the energy band which is fully occupied with electrons at an absolute temperature of $T = 0\,\mathrm{K}$, whereas the conduction band is the energy band above of it. Electrons in the conduction band have the ability to move freely along the lattice and defining therefore the electrical conductivity of the material.
As depicted in Figure 2.8, depending on the position of the Fermi level, the conduction band and the valence band, the following categorization in insulator, semiconductor and conductor can be made.

[5] The Fermi level is defined as energy level with probability $f(E_F) = 0.5$ marking the highest occupied energy level at a temperature of $T = 0\,\mathrm{K}$.

- *insulator*: A large band gap separates the two energy bands with the Fermi level in between, implicating a low probability to thermally excite electrons.
- *semiconductor*: A smaller band gap between the bands implies an insulating material at $T = 0\,\mathrm{K}$ with the possibility to thermally excite electrons for higher temperatures.
- *conductor*: The bands are either overlapping or the Fermi level is inside the conduction band, resulting in electrons always occupying the conduction band.

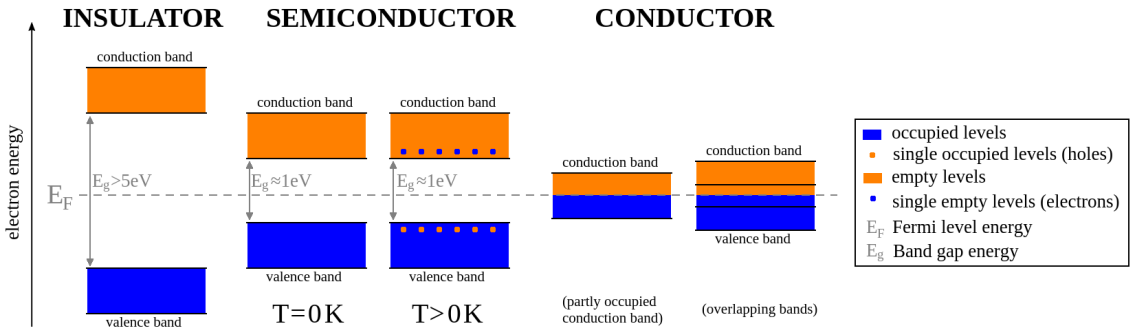

Figure 2.8: Energy band model for insulators, semiconductors and conductors.

Silicon belongs to the category of *semiconductors* with a band gap of $E_g = 1.12\,\mathrm{eV}$ at room temperature. Electrons cannot only be thermally excited into the conduction band, but also by an external excitation such as ionization energy which is used for the application in particle detection. Moreover, in this excitation process not only the electron is transferred to the conduction band but also a *hole*, being a silicon atom with a missing electron, is left behind in the valence band. To create charge carriers in form of an electron-hole pair in silicon, a mean energy deposit of $E_{eh} = 3.6\,\mathrm{eV}$ is required. This energy is higher than the band gap energy, as silicon has an indirect band gap, such that energy is not only translated into the excitation but also into lattice vibrations via phonon creation.

For the application as an active sensor material, silicon is rarely used in its pure crystalline structure, representing an *intrinsic* semiconductor. Instead, an *extrinsic* semiconductor is used by the method of semiconductor *doping*. In this process, impurities are implanted into the silicon bulk by replacing a small fraction of silicon atoms with atoms of other elements, changing the material properties of the doped silicon. For the n-doping, an atom of a group-V element such as phosphorus is substituting a silicon (group-IV) lattice atom, creating an unbound electron from the impurity. In terms of the band structure, an additional energy level close the conduction band, the *donor level*, is created enabling an easier creation of electrons as charge carriers. On the contrary, for p-doping a group-III element like boron is added, creating an energy level close to the valence band, the *acceptor level*, enabling an easier creation of holes in the valence band. The exact positions of the donor and acceptor levels depend on the implanted elements, but are exemplary visualized in Figure 2.9. As the technique of semiconductor doping is a well established process in industry, it is widely used for the design of active sensors with different doping concentrations and highly precise implant placement.

2.2.2 *pn*-junction and reverse biasing

For the application as a particle tracking detector, silicon with a thickness of $\mathcal{O}(100\,\mu\mathrm{m})$ is used to detect a traversing particle by the created charge carriers in the sensor material.

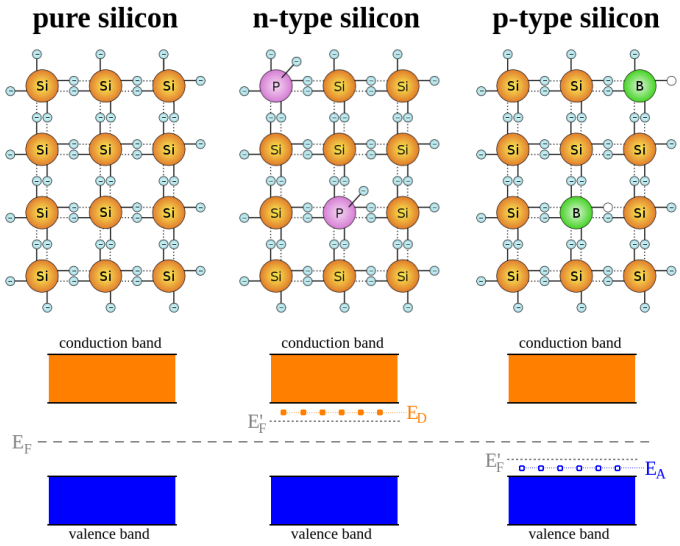

Figure 2.9: Energy bands and atomic lattices of pure, n- and p-type silicon with additional donor (E_D) and acceptor levels (E_A) and shifted Fermi levels (E'_F), respectively.

Typically, $\mathcal{O}(10^4)$ electron-hole pairs are created in the ionization process but this number have to be compared to the number of intrinsically free charge carriers in the doped silicon material being $\mathcal{O}(10^9)$. This low number of externally excited electrons would be not detectable, if the sensor is not depleted from free charge carriers.

This is achievable by forming a *pn*-junction inside the sensor: Bringing the n-type and p-type doped silicon regions together, implies that the excess of free electrons from the n-type region diffuse into the p-type region and vice versa for the holes. An equilibrium state is reached when the charge drift is opposed by the electric field of the charge carriers building up in parallel. Here, intrinsically a zone fully depleted of free charge carriers is created in the junction, called *depletion region*. The changed band structure in the *pn*-junction and the depletion region are depicted in Figure 2.10.

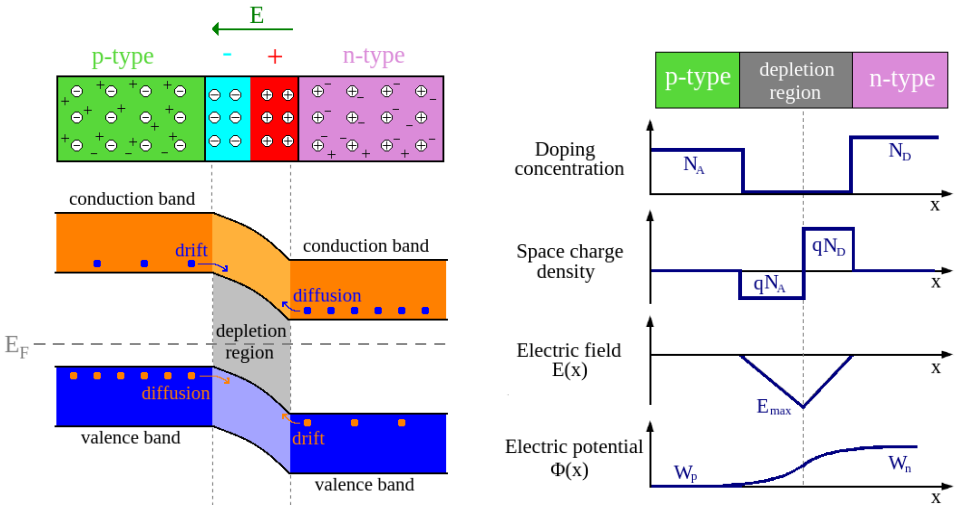

(a) *pn*-junction **(b)** *depletion region*

Figure 2.10: Energy bands for the *pn*-junction and properties in the created *depletion region*. Modified from [95].

For calculating the width of the intrinsic depletion region, the electrical potential within the *pn*-junction can be determined by solving the Poisson's equation.

With the homogeneous doping concentrations N_A and N_D of the p- and n-type silicon, the *built-in voltage* U_{bi} as the potential difference across the depleted zone is calculated as:

$$U_{\text{bi}} = \frac{k_B T}{e} \ln\left(\frac{N_A N_D}{n_i^2}\right) = \frac{e|N_D - N_A|}{2\epsilon_r \epsilon_0} d^2. \tag{2.14}$$

With typical doping concentrations and at room temperature, the built-in voltage is in the range of $U_{\text{bi}} \approx 0.6 - 0.9\text{V}$ resulting in a width of the depleted region of $\mathcal{O}(10\,\mu\text{m})$.

For the operation as particle detector, it is beneficial to reach a fully depleted sensor over its total thickness. An additional, external voltage can be applied to the pn-junction which changes the dimensions of the depleted zone: when a higher potential is connected to the n-doped silicon and the lower potential to the p-doped side, a *reverse bias* is applied resulting in an increase of the depletion region. In this case, the built-in voltage is comparably small and can be neglected. The *full depletion voltage* is the required voltage to fully deplete the sensor with thickness d_{sensor} from free charges and can be determined with Eq. 2.14 to be

$$U_{\text{dep}} = \frac{e|N_D - N_A|}{2\epsilon_r \epsilon_0} d_{\text{sensor}}^2, \tag{2.15}$$

or using the silicon bulk resisitivity ρ and the electron mobility μ_e, one gets

$$U_{\text{dep}} = \frac{1}{2\epsilon_r \epsilon_0} \frac{d_{\text{sensor}}^2}{\rho \cdot \mu_e}. \tag{2.16}$$

According to Eq. 2.16, a higher resisitivity of the silicon material results in a lower bias voltage needed for a full depletion of the sensor volume. With typical silicon resisitivities of $200\,\Omega\text{cm}$ to $1\,\text{k}\Omega\text{cm}$ and sensor thicknesses ranging between $100\,\mu\text{m}$ and $300\,\mu\text{m}$, the required depletion voltage is between $100\,\text{V}$ and $1\,000\,\text{V}$.
The electric field inside the depletion region created by the bias voltage increase linearly till it reach the pn-junction with its maximum and then decrease again forming a triangular shape, with the relative sign of the field amplitude depending on the doping (cf. Fig. 2.10b). In most applications for particle detection, the doping concentrations are highly asymmetrically, with a small, highly doped volume on top of a large, low doped volume. The electric field shows then the same asymmetry with a steep rise and a long falling edge.

Charge carriers, either created by an extrinsic deposition of energy (e.g. a traversing particle) or thermally excited, are drifting inside the depletion region and inducing a current in the sensor. Whereas the signal to measure stems from the particle ionization process, the thermally excited electrons lead also to a current in the sensor, referred to as *leakage current*. The leakage current can be divided into a surface and a bulk generation current, whereas the latter can be parametrized by the thermal excitation probability as

$$I_{\text{leak}}(T) \propto T^2 e^{-\frac{E_{\text{g}}}{2k_B T}}, \tag{2.17}$$

or relative to a reference temperature T_{ref} as

$$I_{\text{leak}}(T) = I_{\text{leak}}(T_{\text{ref}}) \left(\frac{T}{T_{\text{ref}}}\right)^2 \exp\left(-\frac{E_{\text{g}}}{2k_B T}\left[\frac{1}{T} - \frac{1}{T_{\text{ref}}}\right]\right), \tag{2.18}$$

with the band gap energy E_{g} [94]. As such, the leakage current in the sensor depends strongly on the operational temperature for the bulk generation current as well as on the purity of the silicon and the surface processing for the surface generation current. In general, the goal should be to keep the leakage current low (e.g. by cooling of the sensor), since the higher the leakage current, the higher the noise in the silicon sensor.

2.2.3 Sensor segmentation and readout

Silicon sensors in particle tracking applications are required to measure the spatial position of the traversing particle with high resolution. Therefore, silicon detectors are usually segmented, either in one dimension called *strip sensors* or two dimensions called *pixel sensors*. Due to this segmentation, the collected charge carriers drifting towards the sensor surface can be assigned to the volume of creation, allowing to determine the initial particle position.

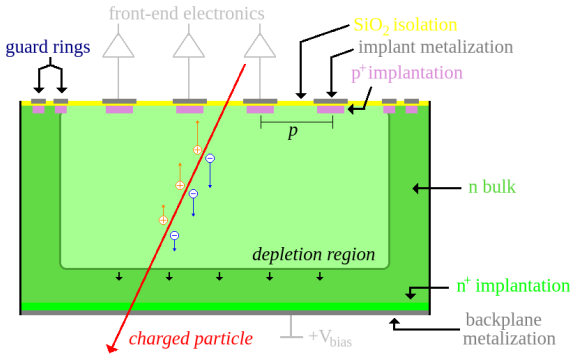

Figure 2.11: Design of a p-in-n silicon sensor with highly doped p^+ strip implants in n-type bulk material. Biasing of detector is done via metal implants and backplane metalization with additional guard ring structures at sensor edges. The front-end electronics is AC-coupled to the strips with a SiO_2 isolation layer. For the traversal of a charged particle, eh-pairs start to drift in the electric field.

In Figure 2.11, a typical silicon sensor produced in p-in-n technology is shown, which is currently used in the ATLAS SCT detector (cf. Sec. 2.3.2). On the sensor surface of a n-type silicon bulk, the front side features highly doped p^+-type implants whereas the back side is highly doped with n^+-type silicon. Due to the different doping concentration at the top and bottom surfaces, it is possible to fully deplete the lower doped n-type bulk region by a reverse bias voltage.
Within the fully depleted region of the pn-junction, holes as charge carriers drift to the implant side and are collected there, while electrons drift towards the backplane. For isolating the implants, featuring either strip or pixel shapes, a silicon dioxide (SiO_2) layer is applied between the implants. The readout of the collected charge inside the segmented implants is done via a metalization layer on top of it. The signal is either transferred via a direct electrical connection to the metal layer (*DC coupling*) or capacitively coupled to it with a SiO_2 layer as isolation (*AC coupling*).

For *hybrid* detectors, the readout electronics is separated from the silicon sensor itself allowing for a modular and decoupled design of sensor and readout. Nonetheless, the signal has to be routed towards the readout electronics as for strip detectors by wire bond connections or for pixel detectors by direct bump bonding of the readout chip on top of the silicon sensor. On the contrary, *monolithic* detectors have the readout electronics already integrated into the same silicon volume as the active sensor (e.g. **M**onolithic **A**ctive **P**ixel **S**ensors (MAPS), cf. Sec. 8.2).
In general, silicon sensors are specifically designed for each individual application in a particle detector, such that for the sensor the dopant type and concentration in implants, backplane and bulk can be different as well as the choice of the readout electronics.

2.2.4 Signal formation and performance parameters

When a highly energetic charged particle traverses the active volume of a silicon sensor, it interacts with the material and deposits parts of its energy in the sensor, as it was described in Section 2.1. The deposited energy can be used for ionization, creating electrons in the conduction band and holes in the valence band as charge carriers in the material.

With the required energy of $E_{eh} = 3.6\,\text{eV}$ to create an electron-hole pair in silicon, the number of created charge carriers is given by

$$N_{eh} \approx \frac{E_{\text{loss}}}{E_{eh}}. \tag{2.19}$$

Using the mean energy loss for a MIP in silicon of 3.8 MeV/cm, the mean number of charge carrier pairs per path length is $\sim 106/\mu\text{m}$. But as the energy loss in silicon follows a Landau distribution, the most probable value for the number of created electron-hole pairs is $\sim 76/\mu\text{m}$. Therefore, for typical sensor thicknesses of $\mathcal{O}(100\,\mu\text{m})$ one expects $\mathcal{O}(10^4)$ charge carriers per traversing particle.
The created electrons and holes start to drift in the electric field of the reversely biased silicon sensor to the implants or the backplane as electrodes, depending on the direction of the field and the charge sign. The drift velocity in the electric field depends strongly on the *charge carrier mobility* μ, which differs between electrons and holes by a factor of three. Hence, the collection time of electrons in silicon sensors takes several nanoseconds, whereas holes are significantly slower and are leading to a reduced current. Therefore, for tracking detectors with a high repetition rate of particles, such as in LHC conditions with a timing of 25 ns, the doping polarities for the bulk and implants of the sensor should be chosen to collect the faster electrons as charge signal.
However, not only the collected charges at the readout electrodes provide the recorded signal, as already the drift of the charge carriers in the bulk induces a current on the electrodes. In the Shockley-Ramo theorem [98, 99], the induced current on a chosen electrode can be determined by its weighting field[6] and the charge carrier's velocity as

$$i = q\vec{E_w} \cdot \vec{v}. \tag{2.20}$$

For a segmented sensor, such as a pixel or strip sensor, the position of the recorded charge signal gives information about the spatial position of the particle traversal. Therefore, for tracking detectors a good *spatial resolution* is a key quantity. In first order, the achievable spatial resolution depends on the fineness of the segmentation with the width between readout cells referred to as the *pitch* p. Assuming that a hit is only registered by one cell around its center with half-pitch distance, the particle distribution for this cell is then homogeneously one over the entire cell dimension. The sensor resolution in this case is the root mean square of the unity box function as

$$\sigma_{\text{spatial}} = \frac{p}{\sqrt{12}}. \tag{2.21}$$

In most cases, the created charge in a silicon sensor is collected in more than one readout cell, forming a charge cluster which allows an even better position estimation by calculating e.g. the center of gravity of cells. *Charge sharing* in silicon sensor can be invoked by either rotating the sensor being not perpendicular to the particle direction or by applying a magnetic field perpendicular to the drift direction. But charge sharing is also a natural effect of the charge drift itself due to *diffusion*: while drifting in the electric field towards the collection electrodes, the generated charges also undergo a diffusion process, consisting of random, often lateral movements along the drift path [100]. The enlargement of the charge cloud can be described by the diffusion length for a time interval t as

$$\sigma_{\text{diffusion}} = \sqrt{2Dt}. \tag{2.22}$$

[6] The weighting field is the corresponding electrical field for an electrode with unit potential, when all other electrodes have ground potential and any free charges are removed.

Here, the diffusion constant D depends on the charge carrier mobility and the silicon temperature. For typical drift times of $\mathcal{O}(10\,\text{ns})$ the resulting width of the charge cloud due to diffusion is then $\mathcal{O}(10\,\mu\text{m})$, leading to charge collection in more than one readout cell of the sensor and improving such the spatial resolution compared to the binary case.

Another performance factor for silicon sensors is the **C**harge **C**ollection **E**fficiency (CCE), measuring the amount of collected charges Q in the readout electrode relative to the total amount of created charges Q_i by the ionization process as

$$\text{CCE} = \frac{Q}{Q_i} = \frac{Q}{eN_{eh}}. \tag{2.23}$$

The reasons for an imperfect charge collection are effects such as charge trapping in silicon impurities, recombination of electrons and holes or trapping of charges due to electric field anomalies. In general, a low CCE deteriorates the spatial resolution as well as the detection efficiency of a silicon sensor.

2.2.5 Radiation damage and detector degradation

In particle physics experiments, silicon detectors are operating in a harsh radiation environment due to a large number of traversing highly energetic particles, causing damage in the sensors as well as the readout electronics. Therefore, in the development of silicon detectors at collider experiments, even more for hadron colliders than lepton colliders and more for the innermost than the outermost tracking detector layers from the beam pipe, radiation hardness of detectors is a crucial parameter. The radiation damage by energy and momentum transfer of the traversing particles to the silicon material can be categorized into two defect types: crystal defects by displacement of lattice atoms via non-ionizing radiation referred to as *bulk damage* and defects on the surface (and mostly in the SiO_2 layer) by ionizing radiation referred to as *surface damage*.

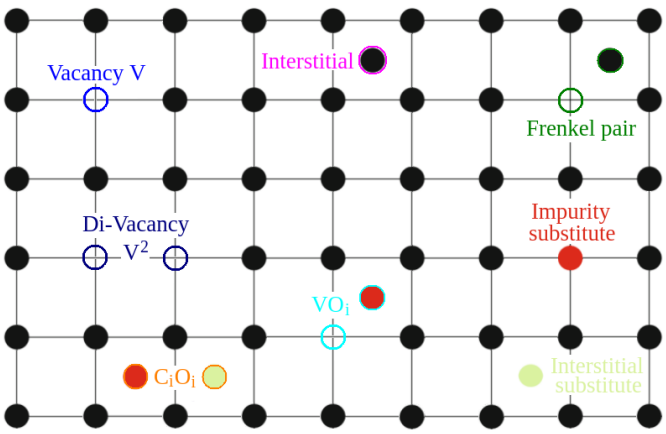

Figure 2.12: Overview of bulk damage in the silicon crystal lattice caused by radiation. Due to the momentum transfer on the PKA, the nucleus can be removed from the lattice (vacancy), placed between lattice atoms (interstitial) or forming a vacancy-interstitial pair (Frenkel pair). Moreover, additional impurities of other elements (e.g. C and O) can be inserted in the lattice. Modified from [78].

In the case of bulk damage, the incident radiation transfers a large fraction of its energy to a silicon atom by which it is displaced from the crystal lattice and leaves a *vacancy* (V). The displaced atom is called *primary knock-on atom* (PKA) and due to momentum transfer it can move through the lattice causing even more damage in the silicon bulk. Finally, the PKA will be trapped between lattice atoms forming an *interstitial* (I) or in the case of a nearby vacancy building a *Frenkel pair*. Defects can also occur in the connection with dopant atoms being dislocated and creating impurities in the crystal lattice, mostly by the naturally present carbon (C) or oxygen (O) atoms.

Moreover, depending on the type of radiation, e.g. neutrons or charged particles, it is more likely that the PKA causes either *cluster defects* or *point defects*, respectively [101]. A schematic of different radiation damage effects in the crystal lattice is shown in Figure 2.12.

To compare the effects on the detector performance of radiation damage caused by different primary particles and their energy, the particle fluences in the irradiation process can be normalized. The **N**on-**I**onizing **E**nergy **L**oss (NIEL) scaling hypothesis normalizes the fluence to the equivalent of 1 MeV neutrons inducing the same radiation damage [102]. The fluence spectrum $\phi_i(E)$ of an arbitrary particle type i can be normalized by the hardness factor κ_i defined as

$$\kappa_i = \frac{\int D_i(E)\,\phi_i(E)\,dE}{D_n(E = 1\,\mathrm{MeV})\int \phi_i(E)\,dE} \tag{2.24}$$

with the particle specific damage functions $D(E)$ being the displacement cross section as function of the particle energy [103]. As such it is possible to scale the total received particle fluence $\Phi_i(E)$ to the neutron equivalent fluence with

$$\Phi_{\mathrm{eq}}\left[\frac{n_{\mathrm{eq}}}{\mathrm{cm}^2}\right] = \kappa_i \cdot \Phi_i(E). \tag{2.25}$$

In the case of surface damage, defects from traversing particles are primarily caused by ionization of the SiO_2 isolation layer on top of the active sensor material. Contrary to the behaviour in the semiconducting bulk material where generated electron-hole pairs are collected by the electrodes, charge carriers in the oxide layer as insulator material are trapped in this region. This is especially the case for holes due to their lower mobility, which can result in an accumulation of holes at the oxide-silicon interface. In the oxide, a positive charge is building up and attracts electrons in the silicon bulk forming a negative space charge underneath the isolation layer.

The described radiation damage processes on a microscopic scale alter the properties of silicon detectors on a macroscopic scale, as explained in the following. Even though that due to the high hadron fluence at collider experiments the bulk damage is the main challenge for silicon detector applications, the impact of surface damage by ionization is not negligible. Depending on the sensor design, multiple effects mostly in terms of electrical properties can alter the detector performance e.g. by an increased noise level [104]. Moreover, the front-end electronics used for the sensor readout can be affected by radiation, e.g. by **S**ingle **E**vent **U**pset (SEU) causing a shift of internal thresholds resulting in an unexpected detector behaviour.
For the bulk damage, the energy band structure of the silicon detector is altered by additional impurities and the main effects arising from this are the following:

- Leakage current
  With the newly introduced energy levels by the defects, the probability for creating electron-hole pairs via thermal excitation is increased, resulting in an increased leakage current (cf. Eq. 2.17). Here, the problem is not a signal degradation as the additional current is still below the typical detection threshold of the sensor, but a strong increase of the power consumption as well as noise. A linear dependence of the leakage current with the experienced neutron equivalent fluence Φ_{eq} can be described as

  $$I_{\mathrm{leak}}(\Phi_{\mathrm{eq}}) = I_{\mathrm{leak},0} + \alpha V \Phi_{\mathrm{eq}} \tag{2.26}$$

  with the initial leakage current $I_{\mathrm{leak},0}$, the sensor volume V and the *current related damage rate* α. The fluence dependence of the leakage current for n- and p-type silicon sensors is depicted in Figure 2.13a.

Due to this dependence, the leakage current in irradiated sensors is not anymore negligible as for unirradiated sensors, as it reaches values of $\mathcal{O}(\mathrm{mA})$. With the applied bias voltage of $\mathcal{O}(500\,\mathrm{V})$, this results in a significant power dissipation in the sensor and, in return, in the generation of heat. As the leakage current is strongly dependent on the temperature, the additional dependence on the irradiation can cause a too high power dissipation and a positive feedback loop of these processes, known as *thermal runaway*. Therefore, a sufficient cooling for the irradiated silicon sensors is crucial at the particle physics experiments.

- Depletion voltage
  With displacements in the crystal lattice by radiation, the doping concentration for n- and p-type regions in the sensor are altered, changing the effective space charge concentration $|N_D - N_A|$ and as such the depletion voltage as defined in Eq. 2.15. Radiation defects creating donor states result therefore in an increase of the bias voltage for a full depletion of the sensor, which is the behaviour for a p-type bulk sensor. For n-type material, the contrary happens with an increase of acceptor states leading to a lower depletion voltage, until the radiation is as high that the material behaves more like p-type material, called *type inversion*, and the depletion voltage grows again linearly with fluence. This behaviour is shown in Figure 2.13b.

- Charge collection efficiency
  Drifting electrons and holes in the sensor can be trapped to an energy level inside the band gap and can remain there for times larger than the collection time of the readout cycle. In irradiated sensor, a higher trapping probability can be observed resulting in a reduced CCE and such a smaller total signal in the sensor. The effective trapping time constants $\tau_{e/h}$ depend on the experienced fluence Φ_{eq} as

$$\frac{1}{\tau_{e/h}} = \frac{1}{\tau_{0,e/h}} + \gamma_{e/h}\Phi_{\mathrm{eq}} \tag{2.27}$$

  with the initial trapping time $\tau_{0,e/h}$ and the linear factor $\gamma_{e/h}$.

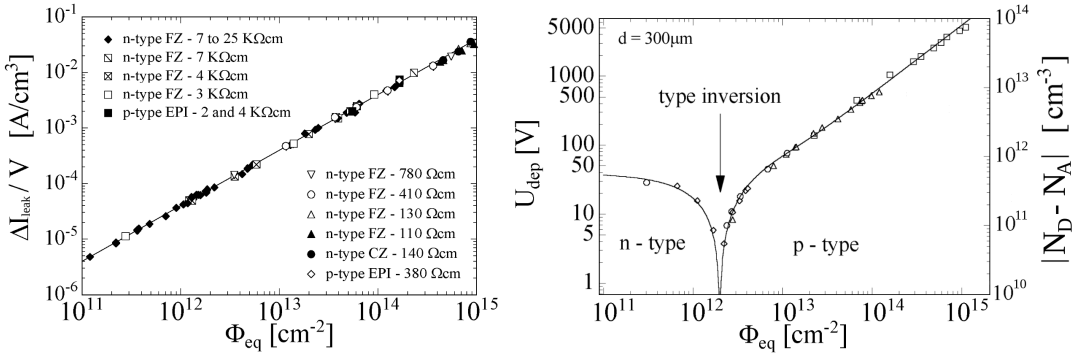

(a) Leakage current. **(b)** Depletion voltage.

Figure 2.13: Fluence dependence of the leakage current and the depletion voltage for silicon sensors. For the relative leakage current increase per volume, $\Delta I_{\mathrm{leak}}/V$, a linear behaviour with the *current related damage rate* α is observed. For the depletion voltage, U_{dep}, as dependent on the effective space charge concentration, $|N_D - N_A|$, an initial n-type material undergoes a *type inversion* to a p-type material. Modified from [105].

The induced defects by radiation damage are not static and can migrate through the crystal lattice via thermal movement. Therefore, it is possible that defects interact with others and even after irradiation the doping concentration is still changing, influencing the macroscopic detector properties. This process of evolution in time is called *annealing* and the speed of annealing effects depend on the temperature. Due to annealing, the current related damage rate describing the behaviour of the leakage current with fluence is changing with time, as shown in Figure 2.14a. Moreover, the annealing behaviour of the effective doping concentration $|N_D - N_A|$ and as such the depletion voltage of the sensor is empirically described by the *Hamburg model*. This model depends on the fluence, the time and the temperature and describes three components of annealing, *beneficial annealing*, *stable annealing* and *reverse annealing*, as visible in Figure 2.14b.

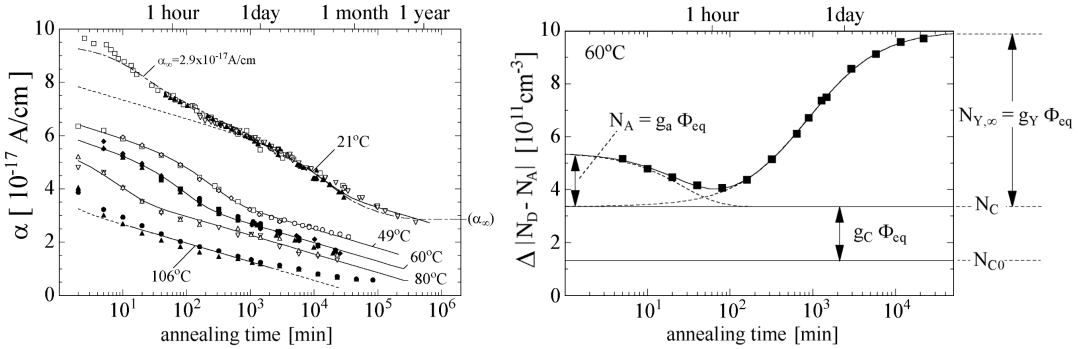

(a) Current related damage rate. **(b)** Effective space charge concentration.

Figure 2.14: Annealing behaviour for the current related damage rate, α, and the change in the effective space charge concentration, $\Delta|N_D - N_A|$, for silicon sensors. Modified from [105].

In general, annealing has a positive effect on the silicon detector performance after irradiation. Therefore, in the operation at high-energy particle physics experiments the detectors are warmed up for several days to allow for annealing of irradiated silicon sensors.

2.3 The ATLAS Detector

The ATLAS experiment [35] is a multi-purpose particle detector designed in an approximately forward-backward symmetric cylindrical way. It measures roughly 44 m in length and 25 m in diameter and provides nearly 4π coverage in the solid angle.
The different sub-detector parts are arranged in an onion-like order from the **I**nteraction **P**oint (IP) to the outside, each serving in a certain function for the particle reconstruction and for measuring the properties of the emerging particles in the collisions. Additionally, the detector subsystems are often separated in a central cylindrical part, called *barrel*, and two disk-shaped *end-caps* in the forward and backward direction, respectively. By this layered design covering nearly the full solid angle around the IP, the possibility to detect and identify the emerging particles is highly increased.

The different sub-detector systems are arranged in the following manner: around the beam pipe the inner detector tracking system is located, surrounded by a thin superconducting solenoid magnet producing a 2 T axial magnetic field; this is followed by the electromagnetic and hadronic calorimeters, and finally a muon spectrometer using three large toroid magnets. An overview of the ATLAS detector with its sub-systems is shown in Figure 2.15.

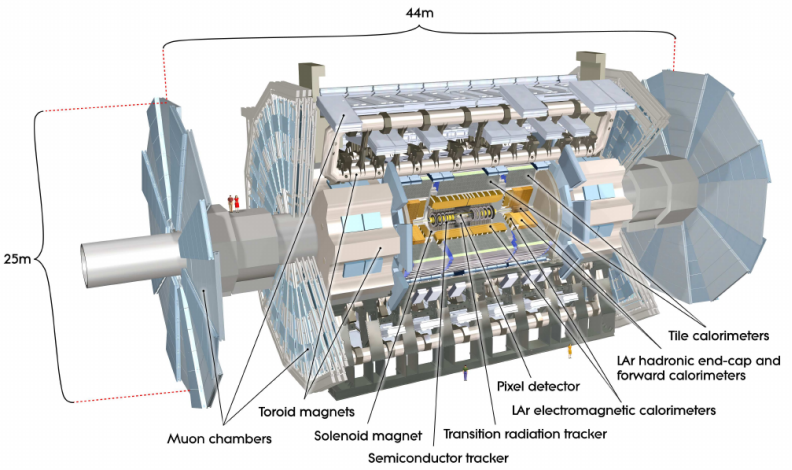

Figure 2.15: Cut-away view of the ATLAS detector [35]. The sub-detector systems are arranged in onion-like order, starting from the inner tracking detector surrounded by a solenoid magnet, followed by the bisected calorimeter system and enclosed by the muon system using a toroidal magnet system.

In the following sections, the subsystems are described in more detail: the coordinate system and kinematic variables in ATLAS are introduced in Section 2.3.1 followed by a description from the inner to the outer parts of the detector with the tracking system in Section 2.3.2, the calorimeter system in Section 2.3.3, the muon spectrometer in Section 2.3.4, and the trigger and data acquisition system in Section 2.3.5.

2.3.1 Coordinates and kinematics

In the ATLAS experiment a right-handed coordinate system with its origin at the nominal **I**nteraction **P**oint (IP) in the center of the detector and the z-axis along the beam pipe is used. The x-axis points from the IP to the center of the LHC ring, and the y-axis points upward. Cylindrical coordinates (r,ϕ) are used in the transverse plane, with ϕ being the azimuthal angle around the z-axis and r the distance from the beam pipe. The polar angle θ describes the angle from the positive z-axis.

A typical quantity in high-energy physics experiments is the particle's rapidity defined as

$$y = \frac{1}{2} \ln \left(\frac{E + p_z}{E - p_z} \right), \tag{2.28}$$

with the particle energy E and its longitudinal momentum p_z.
For the approximation of a relativistic particle ($pc \gg mc^2$), the pseudorapidity is defined only in terms of the polar angle θ as

$$\eta = -\ln \tan \left(\frac{\theta}{2} \right). \tag{2.29}$$

Due to the particle kinematics in a collider experiment, another important quantity is the transverse momentum of a particle measured in the x-y plane as follows:

$$p_{\mathrm{T}} = \sqrt{p_x^2 + p_y^2}. \tag{2.30}$$

Finally, the pseudorapidity can be used to describe the angular distance between particles in the η-ϕ space with

$$\Delta R = \sqrt{\Delta\eta^2 + \Delta\phi^2}. \tag{2.31}$$

2.3.2 ATLAS Inner Detector

The tracking system of ATLAS is built up of the **I**nner **D**etector (ID) [106, 107, 108] As the innermost part of the ATLAS detector, it is located closest to the interaction point and covers an hermetic area within the pseudorapidity range of $|\eta| < 2.5$. It provides precise reconstruction of charged particle tracks allowing excellent transverse momentum resolution as well as electrical charge determination. Moreover, primary as well as possible secondary vertices can be measured with high spatial resolution by extrapolation of reconstructed tracks to common points of origin. To identify charge and momentum of the traversing particles, a thin superconducting solenoid provides a 2 T axial magnetic field. The ID layout, as visualized in Figure 2.16, is optimized for these performance requirements and consists of three independent but complementary sub-detectors: the **Pixel** Detector (Pixel), the **S**emi**C**onductor **T**racker (SCT) and the **T**ransition **R**adiation **T**racker (TRT).

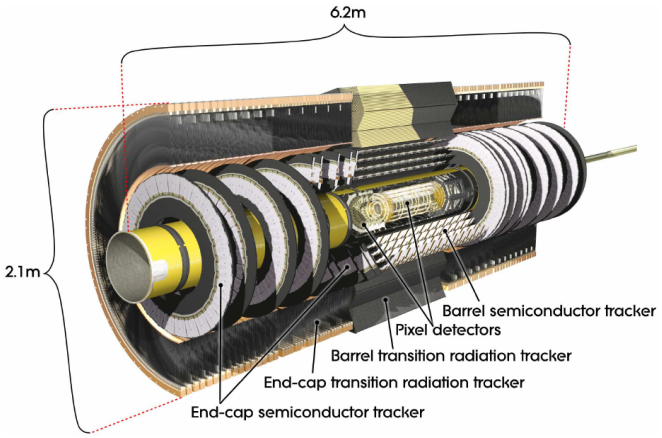

Figure 2.16: Cut-away view of the ATLAS Inner Detector [35]. The innermost region close to the IP is covered by the pixel detector, followed by the SCT detector and the outermost TRT detector. All tracking systems facilitate a barrel region around the IP and end-caps covering the forward regions. The later installed IBL detector is not shown.

Pixel Detector (Pixel)

For the inner radii next to the beam pipe, a high number of discrete space-points for high-resolution pattern recognition in track finding is required. Therefore, the innermost part is made of silicon pixel sensors arranged in three layers in the barrel ($r = 50.5$, 88.5 and 112.5 mm) and three disks for the end-cap regions ($z = \pm 495$, ± 580 and ± 650 mm). Typically, three measurement points for a traversing charged particle originating from the IP region can be recorded in the pixel detector. The silicon pixel modules consists of n^+-in-n silicon sensors with a thickness of 250 µm and minimal pixel sizes of $50 \times 400\,\mu m^2$. A total area of $1.7\,m^2$ is covered and readout is provided by 80 million readout channels. Before Run 2 of LHC operation in 2014, the pixel detector was upgraded by inserting a fourth layer of silicon sensors directly on top of the beam pipe ($r = 33$ mm), the **I**nsertable **B**-**L**ayer (IBL) [109]. It allows for significant improvement in vertexing, b-tagging and the discrimination between prompt tracks and photon conversions.

Semiconductor Tracker (SCT)

The SCT surrounds the pixel detector and consists of four barrel layers (299 mm $< r <$ 514 mm) and nine disks per end-cap region (854 mm $< |z| <$ 2 720 mm), covering a pseudorapidity region of $|\eta| < 2.5$. The silicon strip modules, made out of 285 µm thick p-in-n sensors with a strip pitch of 80 µm and assembled as two-sided modules with a stereo angle of 40 mrad, provide typically further eight hits per track at intermediate distances from the IP. The SCT with its 6.3 million readout channels covers a total area of $61\,m^2$.

Transition Radiation Tracker (TRT)

The outermost part of the tracking system is covered by the TRT with a pseudorapidity coverage of $|\eta| < 2.0$. It is assembled out of narrow straw drift tubes with a diameter of 4 mm and filled with a Xe gas mixture around the 30 µm thin gold-plated cathode wire for readout. Moreover, the space between the tubes is interleaved with transition radiators consisting out of a polypropylene/polyethylene mesh, allowing additional information on the particle type due to the emitted transition radiation. The barrel region, divided into three rings, is composed of 50000 straws interleaved with fibres (73 layers), while in the end-cap regions wheels of 250000 straws with interleaved foils (160 planes) are located. The TRT with its detection volume of 12 m^3 is readout out by 350000 channels and adds for typical charged particles on average further 35 hits to the reconstructed track.

In Figure 2.17, the different layers of the ATLAS ID and their radial positions in the barrel section are displayed.

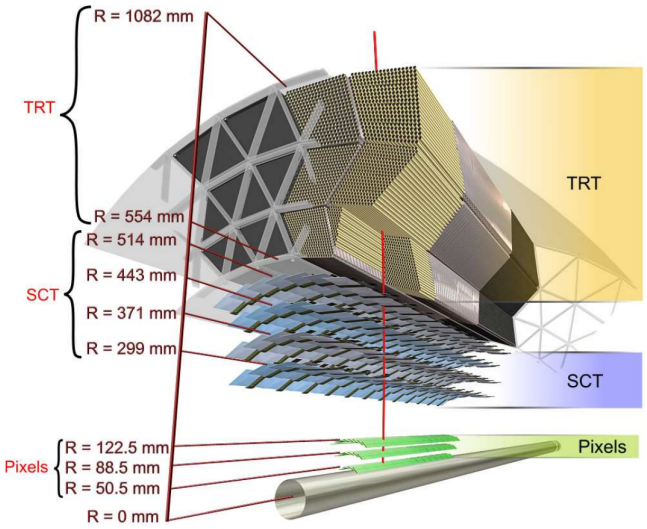

Figure 2.17: Cross-sectional view through the ATLAS Inner Detector [35]. Shown is the barrel region of the detector, with three pixel layers, followed by four double-sided SCT layers and the outermost TRT region. Not shown here is the later installed IBL on top of the beam pipe.

2.3.3 ATLAS Calorimeter System

The purpose of the ATLAS calorimeter system is to stop electrically charged as well as neutral particles and measure their deposited energies. The system is designed as a fully ϕ-symmetric detector and provides coverage around the beam pipe. It is divided in a barrel and two end-cap regions as well as the electromagnetic and the hadronic part. An overview about the calorimeter system in the ATLAS experiment is shown in Figure 2.18.

Electromagnetic calorimeter

The **E**lectro**M**agnetic (EM) calorimeter [110] is a high-granularity lead/**L**iquid **Ar**gon (LAr) sampling calorimeter assembled with accordion-shaped absorbers and electrodes. This special geometry allows the calorimeters to have several active layers in depth while ensuring full coverage in ϕ. The EM calorimeter measures the energy and the position of electromagnetic showers within $|\eta| < 3.2$, wherein the barrel section is covering the pseudorapidity region $|\eta| < 1.475$ and the two end-cap sections in the $1.375 < |\eta| < 3.2$ region. In the transition region between barrel and end-caps section ($1.37 < |\eta| < 1.52$), a large amount of material is in front of the first active calorimeter layer.

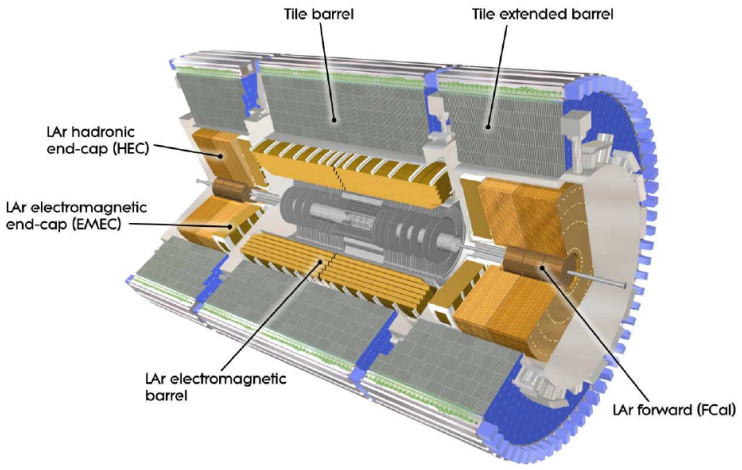

Figure 2.18: Cut-away view of the ATLAS calorimeter system [35]. The first stage is the high-granularity LAr sampling EM calorimeter, followed by the hadronic tile calorimeter as the second stage. The calorimeter systems are divided in a barrel section around the IP and end-caps covering the forward regions.

For the area $|\eta| < 2.5$, the EM calorimeter is composed of three sampling layers, arranged longitudinal in shower depth. The first layer has a thickness of about 4.4 X_0 and is also segmented into high-granularity strips (typical cell size: 0.003×0.0982 in $\Delta\eta \times \Delta\phi$) in the η-direction for $|\eta| < 1.4$ and $1.5 < |\eta| < 2.4$. The fine granularity in η of the strips allows an event-by-event discrimination between single or overlapping electromagnetic showers caused by different particles (e.g. single photons or π^0 mesons).
The second layer of the system provides a thickness of about 17 X_0 and a granularity of 0.025×0.0245 in $\Delta\eta \times \Delta\phi$. Here, most of the energy deposited by photon and electron showers can be collected.
The third layer has a granularity of 0.05×0.0245 in $\Delta\eta \times \Delta\phi$ and a depth of only 2 X_0. The gained information can be used to correct for leakage beyond the EM calorimeter of high-energy showers. Additionally for the pseudorapidity area $|\eta| < 1.8$, the presampler, a thin active LAr layer in front of the accordion calorimeter, provides a correction for upstream energy loss. A sketch of the described segmentation in longitudinal and lateral direction for the EM calorimeter is shown in Figure 2.19.

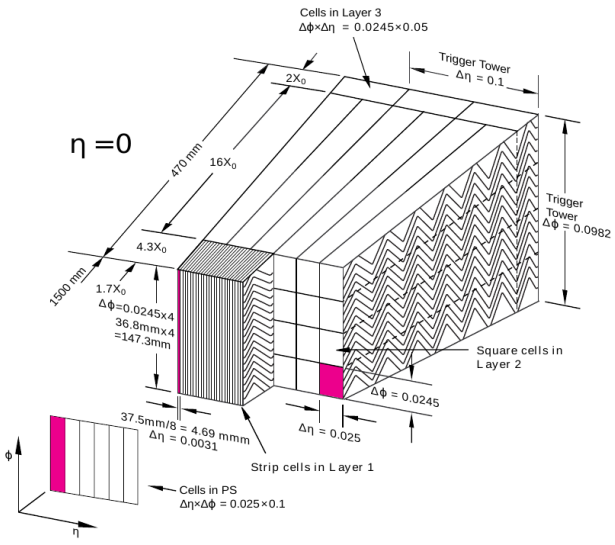

Figure 2.19: Sketch of the lateral and longitudinal segmentation of the ATLAS electromagnetic calorimeter (located at $\eta = 0$) [35]. The different longitudinal layers (one presampler (PS) and three layers in the accordion calorimeter) are depicted, including the granularity in η and ϕ of the cells of each layer and of the trigger towers.

Hadronic calorimeter

The hadronic tile calorimeter [111] consists of scintillator tiles with steel as absorber medium. It is composed of three parts, one central barrel and two extended barrels. A particle traversing through the absorber material induces a shower of secondary particles producing scintillation light, which can be readout via wavelength shifting fibres in attached photo-multipliers (PMT). The used technology is the optimal choice between a maximum in radial depth and a minimum in costs. In total, a pseudorapidity area of $0 < |\eta| < 1.7$ is covered by the tile calorimeter. To enlarge the pseudorapidity coverage into the forward direction, the system is extended for $1.5 < |\eta| < 3.2$ by a copper/LAr sampling calorimeter (HEC) and for $3.1 < |\eta| < 4.9$ by a copper-tungsten/LAr sampling calorimeter (FCal).

2.3.4 ATLAS Muon Spectrometer

The ATLAS Muon Spectrometer [112] is the outermost sub-detector designated to detect muons and measure their momentum, relying on the magnetic deflection of the muon tracks. The magnetic field with strengths between 0.5 and 1 T is provided by the toroid magnet system, consisting of eight superconducting coils in the barrel part ($|\eta| < 1.4$) and two smaller end-cap toroid magnets for a pseudorapidity range of $1.6 < |\eta| < 2.7$. For efficient tracking of muons, high precision tracking chambers are used with Monitored Drift Tubes (MDT) for $|\eta| < 2.7$ and Cathode Strip Chambers (CSC) for $|\eta| > 2.0$. Moreover, the ATLAS muon system serves for triggering and bunch crossing identification due to muon chambers with very fast response time (timing resolution $\sim 1.5 - 4$ ns): Resistive Plate Chambers (RPC) for $|\eta| < 1.05$ and Thin Gap Chambers (TGC) for $1.05 < |\eta| < 2.4$ in barrel and end-cap region, respectively.
A cross section of the overall layout of the ATLAS Muon Spectrometer and the arrangement of the four different types of gas ionization drift chambers in the toroid magnet system are depicted in Figure 2.20.

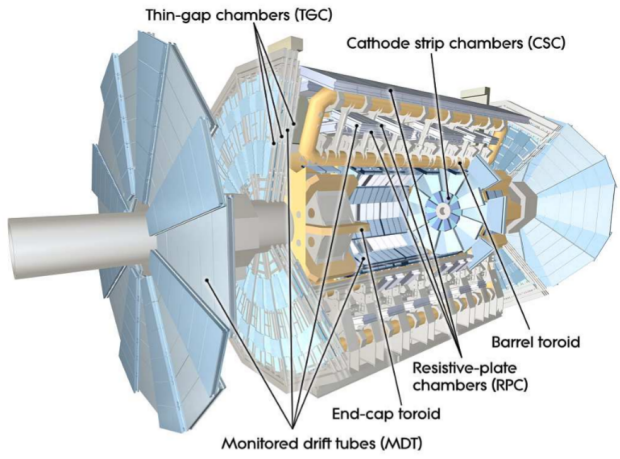

Figure 2.20: Cut-away view of the ATLAS Muon Spectrometer [35]. Four different types of muon chambers are arranged inside the toroid magnet system: for tracking of muons MDTs and CSCs are used, whereas RPCs and TGCs provide trigger information.

2.3.5 ATLAS Trigger and Data Acquisition System

The frequency of proton–proton collisions at the LHC of up to 40 MHz creates an enormous amount of detector events per bunch crossing, which cannot be stored directly. Therefore, the ATLAS trigger system [113] pre-selects events during online data taking following given rules on event signatures (*trigger menu*) as defined by the physics coordination of the ATLAS experiment. The final data recording rate is on average 1 kHz.

The ATLAS trigger system as used for Run-2 data taking comprises of a two-level concept of event selection with the hardware **L**evel-**1** trigger (L1) and the software-based **H**igh-**L**evel **T**rigger (HLT). An overview of the **T**rigger and **D**ata **A**c**Q**uisition (TDAQ) system of the ATLAS experiment is depicted in Figure 2.21.

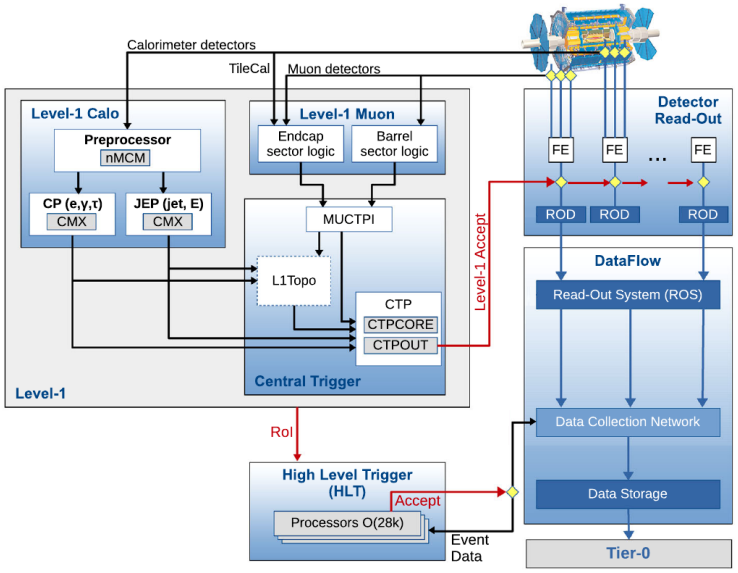

Figure 2.21: Overview of the ATLAS **T**rigger and **D**ata **A**c**Q**uisition (TDAQ) system for Run-2. A two-level trigger concept with the hardware **L**evel-**1** trigger (L1) and the software-based **H**igh-**L**evel **T**rigger (HLT) is used. Modified from [113].

The L1 stage uses detector information from the muon trigger chambers and the calorimeter system and can therefore be separated in the following parts: the L1 calorimeter trigger system (L1Calo), the L1 muon trigger system (L1Muon), the L1 topological trigger modules (L1Topo) and the Central Trigger Processors (CTP).

The rates of each trigger is controlled via prescale factors[7] depending on the instantaneous luminosity. Each of the defined trigger parts is sensitive to categories of collision events:

- The L1Calo trigger is sensitive to high transverse energy objects (electrons, photons, jets, taus) and events with large total transverse and missing energy.
- The L1Muon trigger accepts muon events with predefined thresholds in p_{T}.
- The L1Topo trigger combines information from L1Calo and/or L1Muon into topological variables based on geometric properties of the event.

The CTP receives the inputs from the different trigger parts and makes the final decision whether to accept the event or discard it in less than 2.5 µs. As such the L1 trigger reduces the event rate from the initial 40 MHz down to 100 kHz.

Moreover, Regions-of-Interest (ROIs) with detailed trigger information are determined for each accepted event in the L1 stage and passed as input to the HLT stage. The HLT runs on a computing cluster accessing data from the ROIs and applying offline-like reconstruction algorithms using the full-event information. The final output rate from the HLT is around 1 kHz. Thereafter, the accepted events are transferred to local storage and finally exported to the Tier-0 facility at CERN's computing center for offline reconstruction [114].

[7] The prescale factor is the fraction of events will be accepted by the trigger, e.g. a prescaling of 20 means 1 out of 20 events will be accepted.

Chapter 3

Photons in ATLAS

In proton-proton collisions at the LHC, a large variety of physics processes involve the production of prompt photons in the final state. Prompt photons are characterized as photons not originating from hadron decays, but directly associated to the hard scatter interaction of the pp collision. Examples of physics processes involving the production of photons are summarized in Section 3.1.

Before a photon can be used in physics analyses as an physics object, meaning to have a associated transverse momentum as well as other characteristic information (e.g. direction from the interaction vertex), the photon candidate has to be reconstructed from signals in the different subdetector systems traversed by the photon. The selection of photon candidates is handled by the *photon reconstruction* and the process for the ATLAS experiment is described in Section 3.2.

On the physics analysis level, it is also necessary to have criteria to decide if a photon is surrounded by additional particle activity, or if it is *isolated* from other particles. An important application of the isolation criterion in physics analyses is to differentiate between photon and jet activity, because many interesting physics processes involve isolated hard-scatter photons, instead of another particle produced collinear to the photon. As such, the definition of the *photon isolation* criteria in the ATLAS experiment is introduced in Section 3.3.

In the last step, the reconstructed photon candidate have to be identified as a real, prompt photon. Reasons to wrongly assign a detector signal to a physical photon can be due to the background of non-prompt photons created in subsequent hadronic decays, e.g. the decay of the neutral pion into two close-by photons ($\pi^0 \to \gamma\gamma$), or by misidentified objects like an electron or hadronic jets, but also a mismeasurement of the detector. This task is executed by the *photon identification* algorithm and the strategy currently used in the ATLAS experiment is explained in Section 3.4.

Finally, the performance of the reconstruction and identification algorithms must be evaluated, such that in physics analysis the best possible object reconstruction and identification can be used and the correct systematic uncertainties are assigned. The dedicated measurement procedures to evaluate the *photon identification efficiency* are described in Section 3.5.

3.1 Photons in Physics Analyses

Physics processes involving the production of prompt photons in pp collisions at the LHC can be splitted into three dominant categories: non-resonant production in the SM, electroweak interactions as well as BSM physics signatures with photons in the final state.

Non-resonant production

The first category with prompt photons in the final state is the non-resonant production in the SM. Here, the final state is accompanied by jet activity (qg,$q\bar{q} \to \gamma q$) or another photon (gg,$q\bar{q} \to \gamma\gamma$). By measuring the production cross sections of these hard scattering processes, it is possible to retrieve precise insights into the dynamics of the strong interaction and as such into perturbative QCD [115, 116, 117]. Furthermore, prompt photon production can probe the gluon PDF of the proton using the process $qg \to \gamma q$ [118].

Electroweak interaction

The second category involves the electroweak sector, e.g. the photon can directly couple to W bosons. Moreover, the Higgs boson belongs to the same category, as it can decay into a pair of photons ($H \to \gamma\gamma$) [119, 120], via intermediate loops of massive charged particles.

BSM physics

Finally, the third category is characterized by some expected signatures of BSM physics involving prompt photons in the final state. Examples are: the decay of additional resonances into a pair of photons (e.g. the graviton decay in models with extra dimensions) [121, 122]; the decay of a pair of supersymmetric particles in a final state with a pair of photons and large missing transverse momentum [123, 124]; or final states with highly energetic photons and jets due to the relaxation of excited quarks or other exotic phenomena [125, 126].

To identify the processes involving prompt photons in the final state, a well-advanced detection of photons in pp collisions at the LHC with $\sqrt{s} = 13\,\text{TeV}$ is needed for the ATLAS experiment. On the one hand, photons must be reconstructed as physics objects out of the signals recorded in the detector. On the other hand, the identification of prompt photons has to be fulfilled. As the majority of reconstructed photon objects stem from background photons, this task is particularly challenging. The background photons are mostly real, non-isolated photons originating from other large-cross-section processes or hadrons depositing energy in the detector consistent with the signature of a real photon.

3.2 Reconstruction of Photons

A photon can be reconstructed in the detector as an energy deposition in the electromagnetic calorimeter. Depending on the interactions happening before the EM calorimeter, one has to differentiate between two types of photons: An *unconverted photon* is a photon that enters the calorimeter as an actual photon, before depositing its energy and starting the shower process. A *converted photon* is a photon which has created an electron-positron pair via pair production in the material layers before the calorimeter and the energy in the EM calorimeter is therefore deposited by the electron and positron in the shower process. This differentiation is important as the characteristics of the electromagnetic showers for unconverted and converted photons will be different, e.g. the shower width in the ϕ direction of the calorimeter cells is systematically larger for converted photons.

Another physical object having a highly similar signature in the detector is an *electron* with a track associated to an energy deposition in the EM calorimeter. Otherwise, the interactions of photons and electrons in the EM calorimeter produce very similar electromagnetic showers, mostly depositing their energy in a restricted number of neighboring calorimeter cells. Therefore, the reconstruction procedure for photons and electrons proceed in parallel in the ATLAS experiment.
The specifics of the reconstruction of electron candidates (e.g. a dedicated, cluster-seeded track-finding algorithm to increase the efficiency for low-momentum electron tracks) can be found in [127]. In the following, the photon reconstruction is described as it is used for Run-2 data [128], which remained largely unchanged compared to the reconstruction procedure in Run 1 [129] with only minor adaptations.

Seed cluster finding

In the first reconstruction step, a preliminary set of seed clusters consisting of EM calorimeter cells is created. Here, a sliding-window algorithm [130] with a size of 3×5 in units of $\Delta\eta \times \Delta\phi = 0.025 \times 0.0245$ (corresponding to the EM middle layer granularity) is used to search for seed clusters as longitudinal towers in the calorimeter with a total transverse momentum above 2.5 GeV. A clustering algorithm [130] removes duplicated clusters of lower energy from nearby seed clusters. This initial cluster reconstruction has an efficiency higher than 99% for photons with $E_{\mathrm{T}} > 20\,\mathrm{GeV}$, as evaluated in MC simulations.

Track matching

In this step, tracks as reconstructed in the ATLAS Inner Detector are loosely matched to seed clusters, to allow for a reconstruction of electrons and photon conversions. For the track matching, on the one hand the angular distance between the cluster barycenter[8] and the extrapolated track position in the middle layer of the EM calorimeter can be determined. On the other hand, pattern recognition and fitting algorithms can be used to also account for energy loss processes in the intervening material layers.

Conversion vertex reconstruction

The inputs for the reconstruction of the conversion vertex of the photon candidates are the previously loosely-matched tracks, of which there are two types: tracks with hits in the silicon detector (*Si tracks*) and tracks only reconstructed in the TRT detector (*TRT tracks*). The reconstruction of two-track conversion vertices requires two particle tracks forming a vertex consistent with that of a massless particle. But the efficiency to reconstruct these conversions decreases strongly for conversions taking place at larger radii in the ID, as one of the two produced tracks is not reconstructed because it is either a very soft electron produced in an asymmetric conversion or very close to the other such that it is not possible to distinguish the two tracks. In these cases, single-track vertices are built from tracks without hits in the innermost sensitive layers of the ID. In general, tracks used for the conversion vertex reconstruction should have a high probability to be electron tracks as determined by the particle identification within the TRT detector.
In case of multiple conversion vertices matched to the same cluster, the following ordering is applied: double-track conversions are preferred over single-track conversions, and tracks with more silicon hits as well as a vertex with the smallest conversion radius are preferred.

[8] The barycenter of a cluster is defined as its energy-weighted center.

Arbitration

In the final step, the arbitration for a given electromagnetic cluster is performed to decide if an object is reconstructed as an unconverted or converted photon or an electron: unconverted photon candidates are all clusters without an assigned conversion vertex candidate or any matched tracks; EM clusters matched to a conversion vertex candidate are considered as converted photon candidate, but as the same cluster can be also marked as electron candidate, a decision for the classification as converted photon or electron is done based on a track parameter evaluation. Moreover, criteria on the matched tracks are applied to recover unconverted photons erroneously classified as electrons.
The efficiency for reconstructing prompt photons with $E_{\mathrm{T}} > 25\,\mathrm{GeV}$ as photon candidates can be estimated from MC simulations to be 96% with the rest being reconstructed erroneously as electrons.

Calibration

In the calibration, the photon energy measurement is performed using information from the calorimeter by constructing clusters with different sizes. The used cluster size depends on the photon conversion state, to compensate for the wider opening of the converted photon shower due to the magnetic field in the ATLAS solenoid.
Furthermore, the photon energy is calibrated to account for upstream energy loss in the material and longitudinal as well as lateral leakage in the calorimeter, similar to the approach for electrons. The assigned transverse momentum of a photon E_{T} is calculated as the calibrated cluster energy E relative to the pseudorapidity η_2 of the cluster's barycenter in the second EM calorimeter layer with $E_{\mathrm{T}} = E/\cosh(\eta_2)$.

3.3 Isolation of Photons

Comparing the showers of hadronic jets and photons in the electromagnetic calorimeter, one can state that jet showers are much broader than photon showers. In the hadronization process of jets, a lot more activity outside of the central shower region is created for the showering of a jet. This difference can be exploited by introducing an isolation variable.
The isolation is defined based on the transverse energy flow in a cone around the direction of the reconstructed photon candidate, within an angular distance

$$\Delta R = \sqrt{\Delta\eta^2 + \Delta\phi^2}. \tag{3.1}$$

The isolation requirement can be constructed based on calorimeter-based or track-based quantities, correspondingly on how the transverse energy flow is characterized.
The *calorimetric isolation*, $E_{\mathrm{T}}^{\mathrm{iso}}$, is defined as the sum of transverse energies of topological clusters [130] in the calorimeters, after the subtraction of the energy deposited by the photon candidate and correcting for the contribution from underlying event and pile-up activity. A more detailed description about the calculation of the calorimetric isolation variable can be found in [129].
The *track isolation*, $p_{\mathrm{T}}^{\mathrm{iso}}$, is defined as the sum of the transverse momenta of all the tracks not belonging to the photon candidate with transverse momentum above a threshold of 1 GeV, while having a distance parameter to the primary vertex of less than 3 mm. Additionally, all tracks associated to photon conversions are excluded.

For this work, mainly in connection with the study on the photon identification, the three isolation working points *FixedCutLoose*, *FixedCutTight* and *FixedCutTightCaloOnly* are of interest, which are defined in Table 3.1.

Working point	calorimetric-isolation $E_{\mathrm{T}}^{\mathrm{iso}}$	track-isolation $p_{\mathrm{T}}^{\mathrm{iso}}$
FixedCutLoose	$< 0.065 \cdot E_{\mathrm{T}}$, $\Delta R = 0.2$	$< 0.05 \cdot E_{\mathrm{T}}$, $\Delta R = 0.2$
FixedCutTight	$< 0.022 \cdot E_{\mathrm{T}} + 2.45\,\mathrm{GeV}$, $\Delta R = 0.4$	$< 0.05 \cdot E_{\mathrm{T}}$, $\Delta R = 0.2$
FixedCutTightCaloOnly	$< 0.022 \cdot E_{\mathrm{T}} + 2.45\,\mathrm{GeV}$, $\Delta R = 0.4$	-/-

Table 3.1: Overview of photon isolation working points, defining criteria on the calorimetric-isolation $E_{\mathrm{T}}^{\mathrm{iso}}$ and the track-isolation $p_{\mathrm{T}}^{\mathrm{iso}}$ inside a cone around the photon candidate with angular distance ΔR as defined in Eq. 3.1.

The such defined photon isolation and its working points are not independent from the photon identification described in the next section. Therefore, in the optimization of the photon identification, one has to account for the correlation effect to the isolation, which will be investigated in Chapter 4.

3.4 Identification of Photons

The reconstructed photon candidates have to be identified as prompt photons originating from the *pp* collisions to separate them from background events. This is particularly challenging since the majority of reconstructed photon candidates arise from non-prompt photons created in hadron decays in jets, with a smaller fraction from fake candidates associated to energy depositions of hadrons in the EM calorimeter mimicking the signature of real photons.
To study the differences of signal-like and background-like photons in a systematic way, one needs to have samples of signal and background candidates from **M**onte **C**arlo (MC) simulations, which are described briefly in Section 3.4.1.
For the purpose of discriminating the signatures of prompt and non-prompt photons and fake QCD jets, quantities describing the shape and properties of the associated electromagnetic showers in the EM calorimeter are introduced, referred to as *shower shape variables*. The shower shape variables, as currently employed in the ATLAS experiment, are introduced in Section 3.4.2, showing also several dependencies on the kinematics of the photon, its conversion state and the event topology.
In general, the discrimination power to separate signal from background photons can be observed when comparing the signatures of a prompt photon in the EM calorimeter with the signature of a neutral pion decaying into a pair of photons ($\pi^0 \to \gamma\gamma$), as visualized in Figure 3.1.

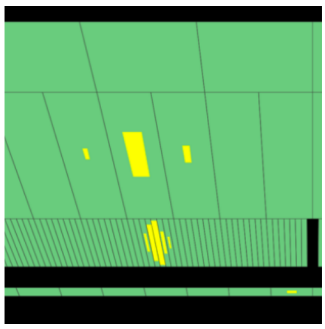

(a) Prompt photon signature.

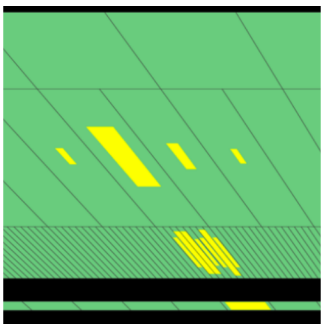

(b) Photon signature from $\pi^0 \to \gamma\gamma$ decay.

Figure 3.1: Signature in the EM calorimeter from prompt photon interaction and background photons originating from $\pi^0 \to \gamma\gamma$ decay.

Whereas photons originating from the hard scattering process typically produce a narrow energy deposition in the EM calorimeter cells with very small leakage into the hadronic calorimeter, background photons from jets produce a much wider electromagnetic shower and the shower is not completely contained into the EM region of the calorimeter, but a significant amount of energy is also deposited into the hadronic part. Additionally, for the case of photon candidates stemming from the neutral pion decay, the energy deposition often shows two separate local energy maxima in the finely segmented region of the first EM calorimeter layer.
The identification of photon candidates in ATLAS relies on defining rectangular cuts on the shower shape variables. In general, two reference sets of cuts, the *loose* and the *tight* identification, are defined for the application in physics analyses. The same set of discriminating variables was also used for the photon identification in Run 1 [129], but the cuts were retuned for the collision data collected at $\sqrt{s} = 13\,\text{TeV}$ in the years 2015 and 2016 in Run 2 [128], which is discussed in Section 3.4.3.
Reasons for this tuning of cuts are changing conditions, e.g. the harsher Run-2 conditions with a higher pile-up compared to Run 1, which required reducing the dependency of the identification efficiency on the pile-up.

3.4.1 Monte Carlo samples for photon identification optimization

Monte **C**arlo (MC) simulation is used for the photon identification to provide samples representing the signal- and background-like photon candidates to allow for an optimization of the photon identification method. In general, MC simulation is an important tool to model the physical processes in pp collisions as close as possible to the real physics events by using random sampling. As the direct calculation of the physical processes is theoretically very challenging, event generators are used to create particles from the collision event and the detector response is reproduced by a detector simulation based on GEANT4 [131]. This approach is possible due to the factorization theorem (cf. Sec. 1.2.2) which permits breaking down the problem into the calculation of the hard process cross-section via perturbative QCD and simulating the parton showering and hadronization process afterwards.
For the prompt-photon production MC sample, leading-order γ+jet events from the hard scattering of $qg \to q\gamma$ and $q\bar{q} \to g\gamma$ are generated with Pythia8 [132]. As background MC sample for photons originating from jets, all tree-level $2 \to 2$ QCD processes in di-jet events[9] generated with Pythia8 are used. The corresponding Feynman graphs for the simulated processes used for the photon identification are summarized in Figure 3.2.

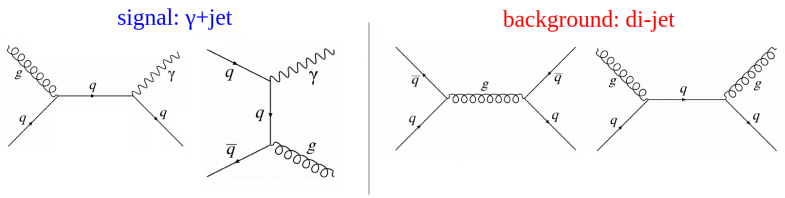

Figure 3.2: Feynman graphs of signal- and background-like processes in Monte Carlo simulation used for the photon identification.

The detector response for MC samples are produced using a full GEANT4 simulation of the ATLAS detector [133], and pile-up pp interactions from the same and nearby bunch crossings are included in the simulation. Here, the distributions of μ in MC were reweighted to the observed ones in Run-2 data for 2015 and 2016.

[9] γ+jet events originating from quark fragmentation in dijet events are removed and instead added as prompt-photons to the signal MC sample.

3.4.2 Shower shape variables

The shower shape variables introduced to allow a discrimination of prompt photons from background photons stemming from hadronic decays or jets characterize the lateral and longitudinal electromagnetic shower development in the EM calorimeter as well as the fraction of shower leakage into the hadronic calorimeter.
The definitions of the employed shower shape variables are listed in Table 3.2 and a schematic representation of them is shown in Figure 3.3.

Category	Variable	Description
Hadronic leakage	R_{had}	Ratio of E_{T} in the hadronic calorimeter to E_{T} of the EM cluster (used for $0.8 < \lvert\eta\rvert < 1.37$).
	R_{had_1}	Ratio of E_{T} in first sampling layer of hadronic calorimeter to E_{T} of the EM cluster.
EM middle layer (S_2)	R_η	Ratio of the energy in 3×7 $\eta\times\phi$ cells over the energy in 7×7 cells centered around the photon cluster position.
	R_ϕ	Ratio of the energy in 3×3 $\eta\times\phi$ cells over the energy in 3×7 cells centered around the photon cluster position.
	$w_{\eta 2}$	Lateral shower width calculated inside a window of 3×5 cells.
EM strip layer (S_1)	w_{s3}	Lateral shower width calculated for 3×2 $\eta\times\phi$ strips around the highest-energy strip.
	w_{stot}	Total lateral shower width calculated for 20×2 $\eta\times\phi$ strips around the highest-energy strip.
	f_{side}	Energy fraction outside the core of three central strips but within seven strips.
	ΔE_s	Energy difference between the second maximum in the strip layer with the minimum value found between the first and second maxima.
	E_{ratio}	Ratio of the energy difference between the first and second maximum of energy deposits to their energy sum.
	f_1	Ratio of the first layer energy to the total energy of the EM cluster.

Table 3.2: Definition of shower shape variables for photon identification.

In general, the such defined shower shape variables are correlated and dependent on the conversion state of the photon, the pseudorapidity η, the transverse energy E_{T} as well as the pile-up μ. In the following, these dependencies are shown for exemplary selected shower shape variables using simulated photons from signal MC. Moreover, systematic differences in the shower shape distributions are observed comparing data and simulation samples, for which the applied correction method is also explained.

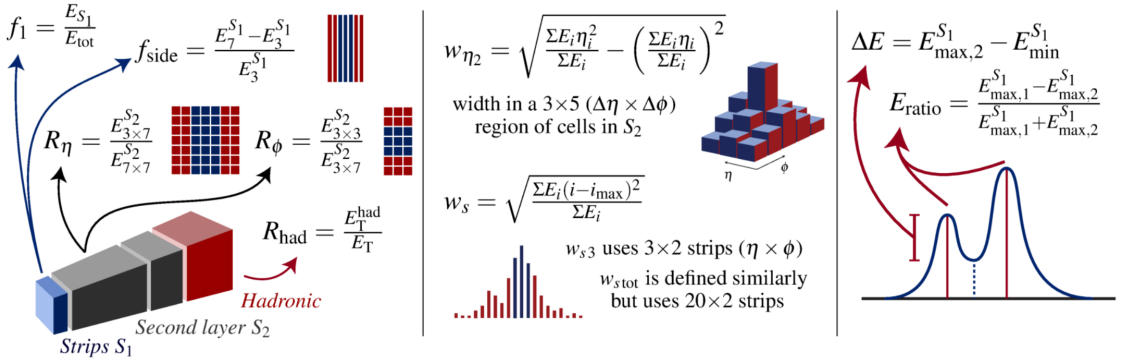

Figure 3.3: Overview about electromagnetic shower shape variables and their definition as used in the photon identification [128].

Dependence on the conversion state

Some of the shower shape variables show a dependence on the conversion state of the photon as for a converted photon a broader distribution in the lateral direction due to the showering process of the pair produced electron-positron pair is expected. For the variables like R_ϕ, $w_{\eta 2}$, w_{stot} and f_{side} major differences in the distributions are observed, whereas for R_{had}, ΔE_s and E_{ratio} the conversion state does not really matter. In Figure 3.4, the distribution for R_ϕ is exemplary shown for unconverted and converted photons.

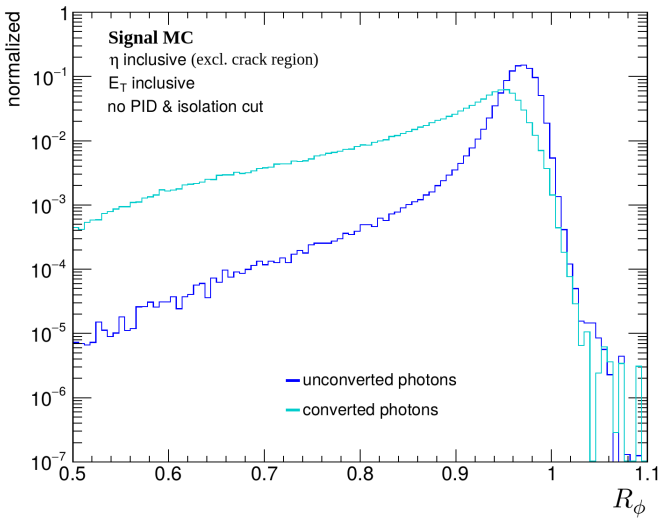

Figure 3.4: Shower shape dependence on the photon conversion state as shown for variable R_ϕ. A signal MC sample with a selection inclusive in η and E_T and without any identification or isolation cut applied is used.

Dependence on the pseudorapidity η

A dependence of the shower shape distributions with the pseudorapidity η can be explained by the fact that the amount of additional material in front of the EM calorimeter varies as function of η. Here, again mostly affected are variables like $w_{\eta 2}$, w_{s3}, w_{stot}, R_η and f_{side}, whereas R_{had}, R_ϕ and E_{ratio} are much less affected.
Moreover, the detector volume around the interaction point is not hermetically enclosed by the EM calorimeter, as can be seen in Figure 3.5. Most prominently, the so-called crack region can be identified, marking the transition from the barrel part of the EM calorimeter to the end-cap part at $1.37 < |\eta| < 1.52$. As here a lower granularity of the calorimeter cells exist, this region is typically excluded for the identification of photons in ATLAS.

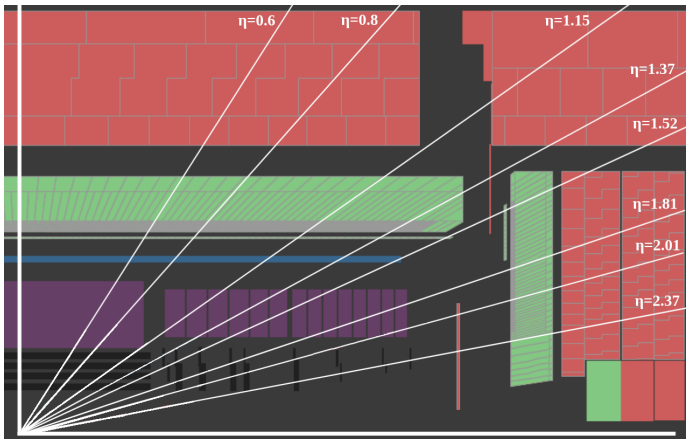

Figure 3.5: The ATLAS detector geometry shown as one quarter segment with the IP as origin and the subsystems as silicon tracking detectors (black), TRT detector (lila), solenoid magnet (grey), EM calorimeter (green) and hadronic calorimeter (red). The pseudorapidity regions as used for the photon identification are marked (white lines) with the "crack region" at $1.37 < |\eta| < 1.52$ typically excluded.

For the typically used binning in the pseudorapidity with the seven intervals $0.0 < |\eta| < 0.6$, $0.6 < |\eta| < 0.8$, $0.8 < |\eta| < 1.15$, $1.15 < |\eta| < 1.37$, $1.52 < |\eta| < 1.81$, $1.81 < |\eta| < 2.01$ and $2.01 < |\eta| < 2.37$, the shower shape distributions for w_{stot}, f_{side} and ΔE_s are shown in Figure 3.6. Due to the uneven material distribution upstream of the calorimeter, no obvious trend in the change of the distributions can be identified.

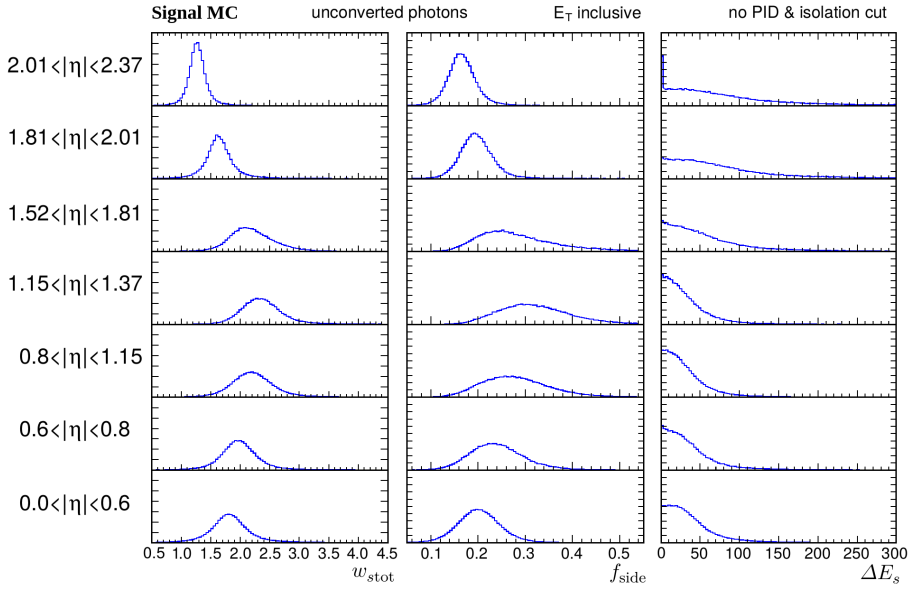

Figure 3.6: The shower shape dependence on the photon pseudorapidity η as shown for variables w_{stot}, f_{side} and ΔE_s. A signal MC sample with a selection on unconverted photons, inclusive in E_{T} and without any identification or isolation cut applied is used.

Dependence on the transverse energy E_{T}

Some of the shower shape variables also show a dependence on the transverse energy E_{T} of the photon, as a higher energy photon showers differently than a low energy photon. As shown in Figure 3.7 for the variables R_η, $w_{\eta 2}$ and w_{s3}, the shower width at higher transverse energies is smaller.

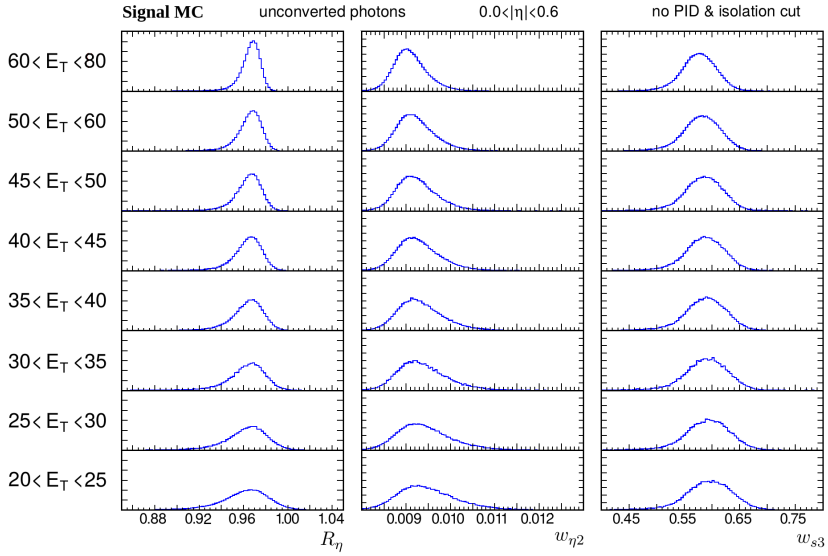

Figure 3.7: The shower shape dependence on the photon transverse energy E_{T} as shown for variables R_{η}, $w_{\eta 2}$ and w_{s3}. A signal MC sample with a selection on unconverted photons for $0.0 < |\eta| < 0.6$ and without any identification or isolation cut applied is used.

Dependence on the pile-up μ

Finally, the pile-up μ of the event has also a dependence on the shower shape distributions. The in-time pile-up with additional soft pp interactions accompanying the hard scattering process as well as the out-of-time pile-up with interactions from bunch crossings before or after the triggered event affect the shower shapes due to the presence of low-E_{T} activity in the calorimeter. Figure 3.8 shows the distributions of the strongest affected variables ΔE_s, E_{ratio} and R_{had} for different numbers of superimposed pp events.

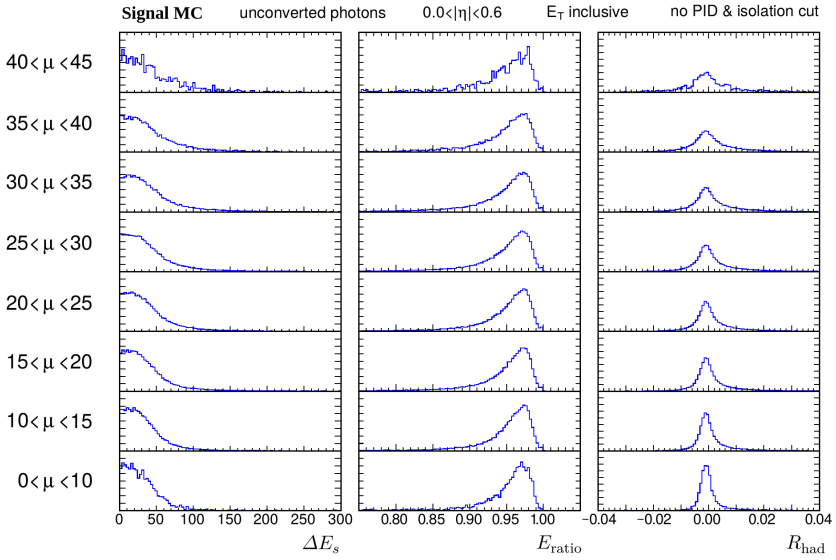

Figure 3.8: The shower shape dependence on the event pile-up μ as shown for variables ΔE_s, E_{ratio} and R_{had}. A signal MC sample with a selection on unconverted photons for $0.0 < |\eta| < 0.6$, inclusive in E_{T} and without any identification or isolation cut applied is used.

Shower shape correlations

The shower shape variables defined with information from the EM calorimeter information in terms of widths, ratios and shape differences are correlated. These correlations are shown in Figure 3.9 as matrix of the linear correlation coefficients for the case of unconverted photons in the $|\eta| < 0.6$ bin. When comparing the correlations of shower shapes for signal-like and background-like photon candidates, one observes differences between them which will be a complicating factor in the photon identification process, as explained later.

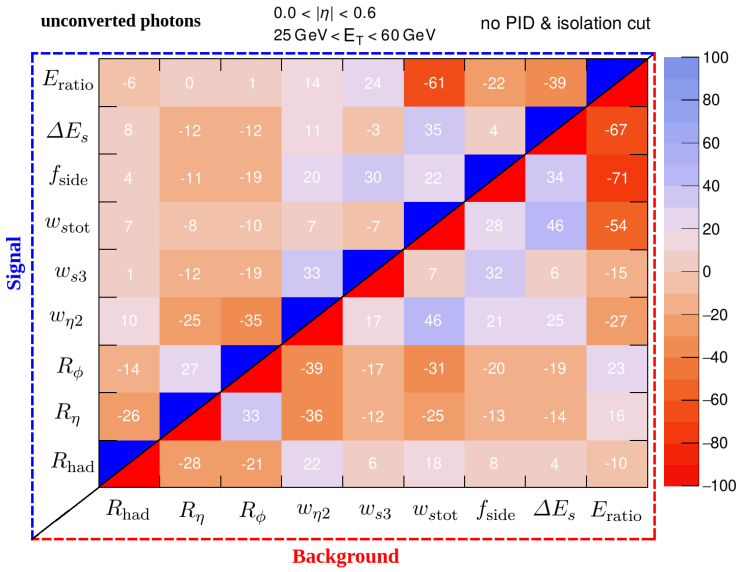

Figure 3.9: Linear correlation matrix of shower shape variables for unconverted photons in the $|\eta| < 0.6$ bin, without any photon identification or isolation cuts applied. Compared are simulated photon candidates from signal MC (left matrix half) and background MC (right matrix half).

Data-MC differences and fudge factors

When comparing the shower shape distributions measured in data with the MC simulated profiles, one can observe a good description in shape but small systematic differences in the average values. This is especially the case for the photon transverse shower shapes, pointing to a mismodelling in MC simulation of the lateral profile development of the shower while the longitudinal shower profiles are overall well described. This discrepancy between data and MC distributions can be corrected by applying simple shifts to the MC-simulated values to align them with the distributions observed in data, called *fudge factors*. As an example for this correction, Figure 3.10 shows the distribution for R_η inclusive in η (excluding the crack region) for unconverted photons as measured in data compared to the MC simulated case uncorrected as well as after the shifting.

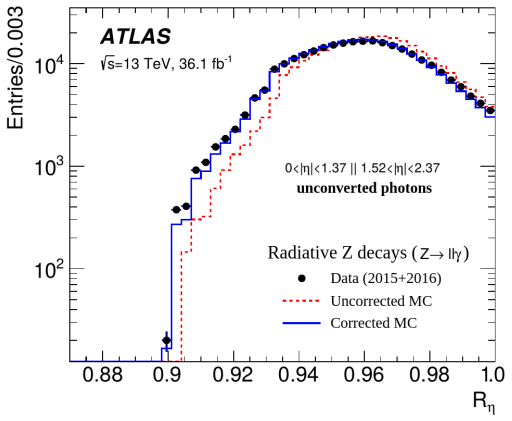

Figure 3.10: Correction of data-MC differences for the shower shape variable R_η for an inclusive η selection (excluding the crack region) and unconverted photons. Shown is the measured distribution in data from selected radiative Z decays ($Z \to ll\gamma$) (black dots) compared to the uncorrected MC simulation (dashed red line) and the corrected MC simulation after fudging (solid blue line).
Modified from [128].

3.4.3 *Loose* and *tight* identification

With the defined shower shapes, it is possible to discriminate prompt photons from background photons originating from hadronic decays due to distinct features and differences in these distributions. In Figure 3.11, the shower shape distributions are plotted for signal and background MC simulation for unconverted photon candidates in the $|\eta| < 0.6$ bin. The discrimination power of the individual variables are different, but by applying selection cuts on the ensemble a good selection of signal-like prompt photon candidates while excluding large fractions of background-like non-prompt photons and fakes can be reached.

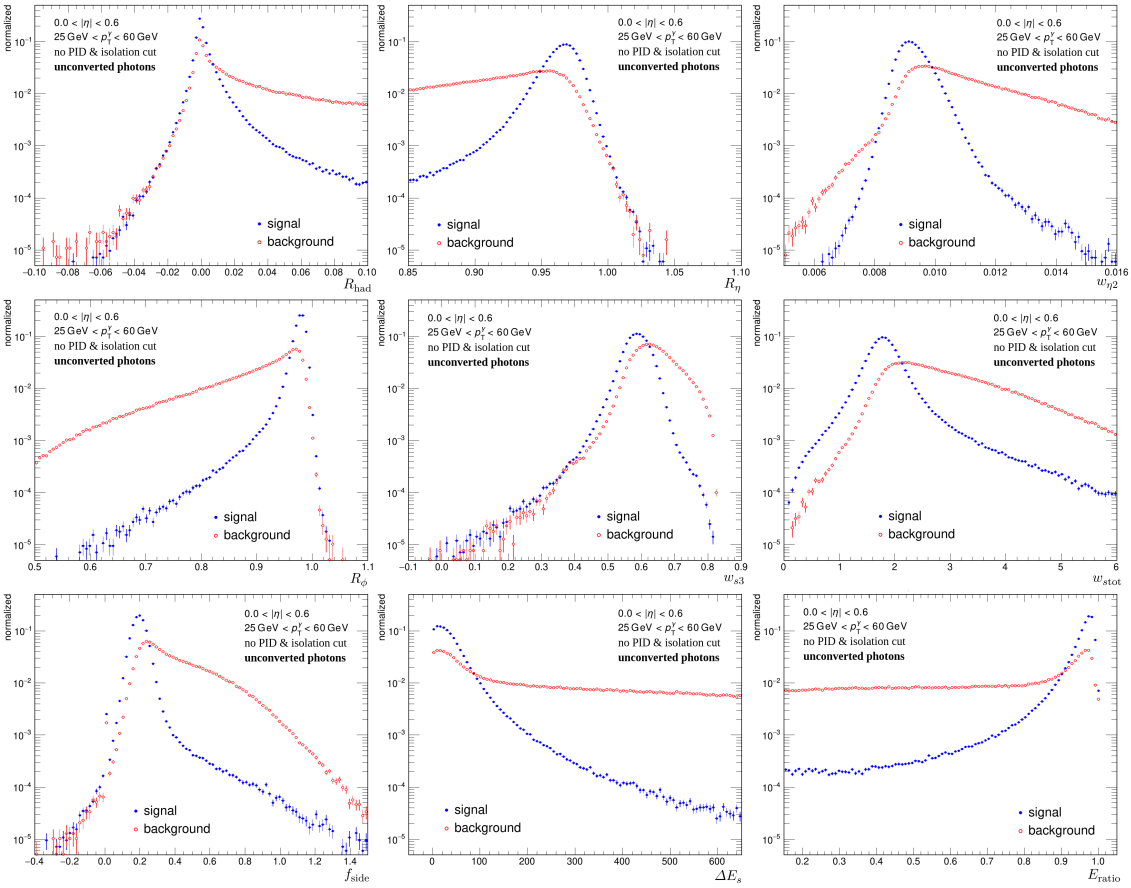

Figure 3.11: Discrimination power of the shape variables used for photon identification. Shown are the shower shape distributions for signal (blue) and background (red) for unconverted photons in the $|\eta| < 0.6$ bin, without any photon identification or isolation cuts applied.

Here, the identification in the ATLAS experiment for Run-2 is currently based on applying rectangular cuts on the shower shape variables, differentiating into two sets of cuts, the *loose* and the *tight* identification working point.

For the evaluation of the photon identification, the signal efficiency ϵ_{ID} is defined as

$$\epsilon_{\text{ID}} = \frac{N_\gamma^{\text{ID}}}{N_\gamma^{\text{truth}}} \tag{3.2}$$

with the number of reconstructed photon candidates passing the identification selection (N_γ^{ID}) and the number of true photons in the sample (N_γ^{truth}).

The background rejection R can be defined as

$$R = \frac{1}{\epsilon_{\text{bkg}}} \tag{3.3}$$

with the background identification efficiency ϵ_{bkg} for background photons in the sample.

The goal of the loose selection is to select photons with a high signal efficiency of $\sim 99\%$ while rejecting background by a factor of ~ 1000. It is used as selection of background control regions in physics analyses as well as for the photon trigger decision. For this, cuts on shower shapes in the second layer of the EM calorimeter and on the energy deposited in the hadronic calorimeter are used, namely on the variables R_η, $w_{\eta 2}$ and R_{had}.
On the contrary, the tight selection aims for a reduced signal efficiency of $85 - 95\%$, but with a highly improved background rejection factor of ~ 5000, yielding especially good rejection of hadronic jet background for selection of signal regions in physics analyses. Here, mainly information from the finely segmented strip layer of the calorimeter is added on top of the loose selection, using then all defined shower shape variables as listed in Table 3.2.

As the shower shape variables show the previously discussed dependencies, the identification cuts are optimized separately for unconverted and converted photons and are defined for seven intervals of the reconstructed photon pseudorapidity as $|\eta| \in (0.0 - 0.6, 0.6 - 0.8, 0.8 - 1.15, 1.15 - 1.37, 1.52 - 1.81, 1.81 - 2.01, 2.01 - 2.37)$. The dependencies on the transverse energy as well as the pile-up are not directly used in the optimization process but the identification efficiency is checked as function of E_{T} as well as μ.

The strategy of the cut-based optimization of the photon identification is summarized in Figure 3.12: a signal sample with single-photons and a background sample with jets from MC simulation is used as input for the optimization; to address data-MC differences in the photon shower shapes, fudge factors are applied as correction; the optimization of cuts is performed within ROOT's **T**oolkit for **M**ulti **V**ariate **A**nalysis (TMVA) [134] using the labelled datasets of signal and background photons; an additional fine-tuning of cuts is applied by hand; the training is checked and evaluated by data-driven measurements and can be repeated with different boundary conditions if needed.

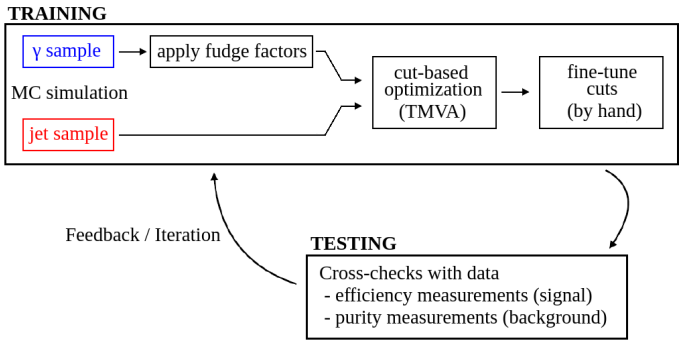

Figure 3.12: Strategy of the cut-based photon identification optimization in the ATLAS experiment using rectangular cuts on the discriminating shower shape variables.

In Figure 3.13, the tight identification efficiency after cut optimization[10] determined from MC simulation is shown as function of the transverse energy of the photon for the signal efficiency as well as the background efficiency for unconverted and converted photons in the $|\eta| < 0.6$ bin.

[10] Tuning of cut values for Run-2 data in 2015+2016 with MC simulation reweighted with 2015+2016 pile-up profile, as described in [128].

Here, a characteristic efficiency drop for smaller transverse energies can be observed as the identification of low-E_{T} photons is more difficult than for higher transverse energies. In the plateau region, the signal efficiency for unconverted photons is around 85% and for converted photons even 95%, with similar background efficiencies.

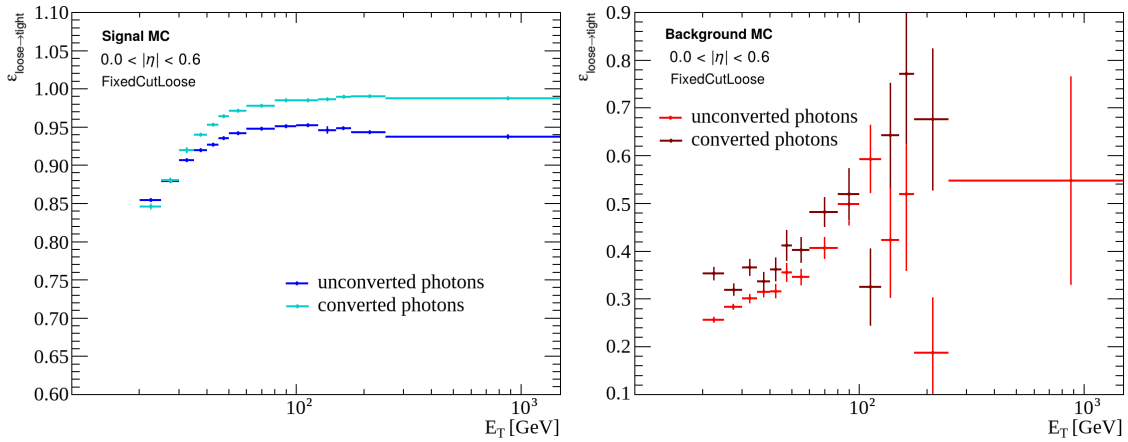

Figure 3.13: Photon identification efficiency for loose-to-tight ID, $\epsilon_{\mathrm{loose}\rightarrow\mathrm{tight}}$, versus the photon transverse energy, E_{T}. Shown are the signal efficiencies (left) and background efficiencies (right) for unconverted and converted photons in $|\eta| < 0.6$ with *FixedCutLoose* isolation applied.

Moreover, the tight identification efficiency as function of the event pile-up μ is shown in Figure 3.14 for unconverted and converted photons in the same pseudorapidity bin.
Here, a rather flat efficiency versus μ is observed showing that the tight identification is only minor pile-up dependent which is an important requirement for the application in physics analyses.

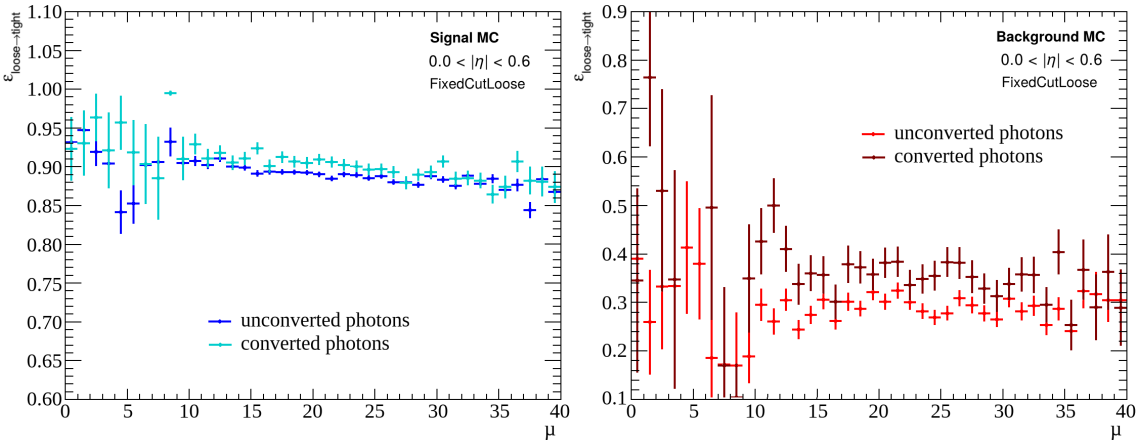

Figure 3.14: Photon identification efficiency for loose-to-tight ID, $\epsilon_{\mathrm{loose}\rightarrow\mathrm{tight}}$, versus the pile-up, μ. Shown are the signal efficiencies (left) and background efficiencies (right) for unconverted and converted photons in $|\eta| < 0.6$ with *FixedCutLoose* isolation applied.

3.5 Photon Efficiency Measurement

To evaluate how well photons can be identified with the ATLAS detector, one can measure the *photon identification efficiency* in recorded pp collision data. For photons, this is not trivial as for measurements of other particle identifications, such as electrons or muons, because for photons no physical process providing a clean signal of photons exists (e.g. for electrons one can use the $Z \to ee$ process).

For Run 1 and Run 2, three different data-driven methods for measuring the photon identification efficiency ϵ_{ID} of the *tight* photon identification working point are used in the ATLAS experiment and will be introduced in the following: the method of *radiative Z decays* in Section 3.5.1, the *electron extrapolation* method in Section 3.5.2 and the *matrix method* in Section 3.5.3. These methods are independent from each other and cover different transverse energy (E_{T}) regions, which are visualized in Figure 3.15.

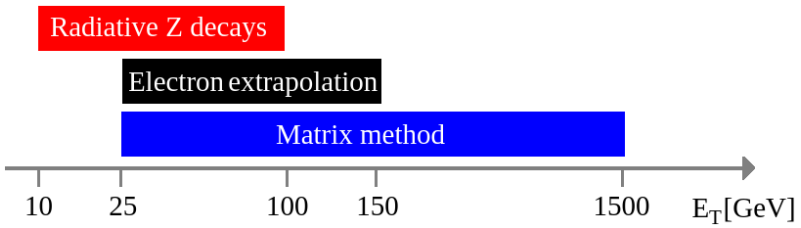

Figure 3.15: Overview about the data-driven methods for measuring the photon identification efficiency: the *radiative Z decays* method for low E_{T}, the *electron extrapolation* method for medium E_{T} and the *matrix method* for high E_{T}.

Moreover, converted and unconverted photons are evaluated separately and the efficiencies are measured in a two-dimensional interval grid in photon E_{T} and $|\eta|$ with boundaries at 10, 15, 20, 25, 30, 35, 40, 45, 50, 60, 80, 100, 125, 150, 175, 250 and 1 500 GeV and 0, 0.6, 1.37, 1.81 and 2.37, respectively. In the end, it is possible to combine the results of the three methods with overlapping E_{T} regions gaining a higher accuracy and to derive a data-driven efficiency for the photon identification, as it is discussed in Section 3.5.4. The latest results in terms of the photon identification efficiency for the ATLAS experiment are collected in [128], which are discussed as well in the following.

3.5.1 Radiative Z decays

In the radiative Z decay method, a clean sample of low-energy photons is obtained from radiative Z decays via the process $Z \to ll\gamma$ with $l = e,\mu$. For the selection, a photon candidate as well as an opposite-charged pair of electron or muon candidates is required. The photon candidate has to have a transverse momentum higher than 10 GeV, to fulfill the loose isolation criterion and to be in a pseudorapidity range of $|\eta| < 1.37$ or $1.52 < |\eta| < 2.37$, but no other selection criterion to avoid biasing the efficiency measurement. Muon and electron candidates are selected with a medium identification and satisfying a loose isolation criterion, respectively. The events of radiative decays are selected by a cut on the invariant mass of the dilepton system, $40 < m_{ll} < 83$ GeV, and the invariant mass of the two leptons and the photon, $80 < m_{ll\gamma} < 100$ GeV, to isolate from photons radiated off by **I**nitial **S**tate **R**adiation (ISR). The selection on the mass distributions is shown in a two-dimensional representation for the electron-channel in Figure 3.16.

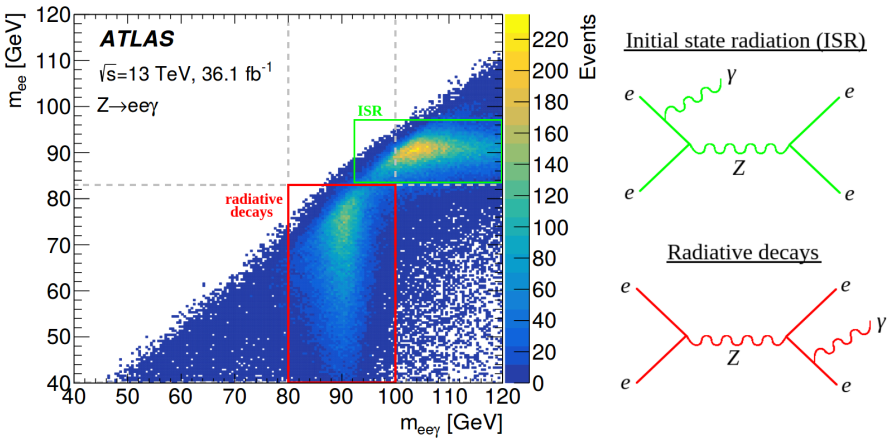

Figure 3.16: Invariant mass of the two electron system (m_{ee}) as function of the invariant mass of the two electrons and the photon ($m_{ee\gamma}$) for selected events in $Z \to ee\gamma$. The selection cuts on the masses to isolate radiative decays from photons stemming from ISR are shown together with the corresponding Feynman graphs. Modified from [128].

Finally, the photon identification efficiency is evaluated as

$$\epsilon_{\mathrm{ID}} = \frac{P^{\mathrm{pass}} N^{\mathrm{pass}}_{\mathrm{data}}}{P^{\mathrm{total}} N^{\mathrm{total}}_{\mathrm{data}}} \tag{3.4}$$

with the number of events N and the purities P in the full sample (total) compared to the subset of the sample passing the tight photon identification cut (pass). Systematic uncertainties assigned to the efficiency measurement are stemming from a closure test with known sample fractions, from the level of background contamination (misidentified jets accompanying the $Z \to ll$ process), the modelling of the detector geometry as well as the simulation uncertainty from the choice of the MC event generator.

3.5.2 Electron extrapolation

For the electron extrapolation method, a clean sample of electron candidates stemming from $Z \to ee$ decays is used. Via a Smirnov transformation [135], the shower shape distributions of electron candidates are modified to reproduce the distributions for photon candidates. In the first step, electrons are selected in a tag-and-probe framework, with most of the selections (e.g. tight identification) applied to one of the electrons (*tag*) and a loose selection to the other electron (*probe*). From the latter, required to fulfill the loose isolation criterion, the shower shape distributions are obtained. To account for differences in the distributions of photon and electron shower shapes, a set of probe electrons as well as single-photon samples are simulated with corresponding kinematics (E_{T}, $|\eta|$ and isolation) and a Smirnov transform S for each shower shape variable x_i is defined as

$$x_{\gamma,i} = S_i(x_{e,i}) := F^{-1}_{\gamma,i} F_{e,i}(x_{e,i}) \tag{3.5}$$

with the cumulative shower shape distributions $F_{\gamma,i}$ and $F_{e,i}$ for simulated photons and electrons, respectively.
With these transformations for each shower shape variable and for unconverted and converted photons separately, the distributions of the selected probe electron candidates can be transformed to mimic the distributions of photon candidates, as exemplary depicted for the variable R_ϕ in Figure 3.17.

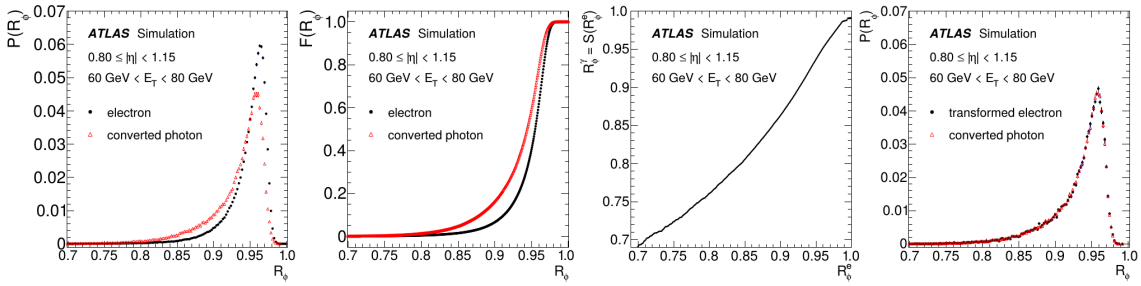

Figure 3.17: Electron extrapolation method exemplary shown for the shower shape variable R_ϕ for converted photons (from left to right): simulated shower shape distributions for electron and converted photon candidates; cumulative distributions; Smirnov transform as $R^\gamma_\phi = S(R^e_\phi)$; resulting shower shape distributions for transformed electron candidates compared to converted photon candidates. Modified from [128].

Finally, the photon identification can be applied to the transformed variables and the ratio of the number of transformed electron candidates passing the photon selections to the total number of electron candidates is used to estimate the photon identification efficiency ϵ_{ID}. Systematic uncertainties assigned to the electron extrapolation method are stemming from a closure test with pure MC samples, from the background subtraction in the $Z \to ee$ selection, from differences in the number of conversions in MC and from data-MC differences in the shower shapes not corrected by simple shifts (cf. *fudge factors*).

3.5.3 Matrix method

In the matrix method or *inclusive photon* method, an inclusive photon sample collected by single-photon triggers (trigger thresholds from 10 GeV to 140 GeV and loose photon identification) with the loose isolation requirement is used. Nonetheless, the overall fraction of true photon candidates in the sample is rather low. The identification efficiency can be estimated again with Eq. 3.4, for which the purities are estimated using a tight isolation criterion, requiring no track with $p_{\text{T}} > 1\,\text{GeV}$ within a distance of $0.1 < \Delta R < 0.4$ of the photon cluster. As such, the purities can be calculated by comparing the efficiency for the isolation selection in data before/after applying the tight photon identification, $\epsilon^{\text{total/pass}}$, with reference efficiency values estimating the true photon component, $\epsilon_\gamma^{\text{total/pass}}$, as well as the background component, $\epsilon_{\text{bkg}}^{\text{total/pass}}$, as

$$P^{\text{total/pass}} = \frac{\epsilon^{\text{total/pass}} - \epsilon_{\text{bkg}}^{\text{total/pass}}}{\epsilon_\gamma^{\text{total/pass}} - \epsilon_{\text{bkg}}^{\text{total/pass}}}. \tag{3.6}$$

Here, ϵ_γ is estimated from simulation, $\epsilon_{\text{bkg}}^{\text{total}}$ is measured in the sample subset failing the tight photon identification and $\epsilon_{\text{bkg}}^{\text{pass}}$ is evaluated by inverting tight identification cuts ($w_{s,3}$, f_{side}, ΔE_s and E_{ratio}) which are expected to be uncorrelated with the isolation criteria. In Figure 3.18, the track isolation efficiencies for prompt and fake photons as well as the signal purities for the inclusive sample and the tight identification sample as a function of transverse photon energy for unconverted photons in $|\eta| < 0.6$ are shown.
Systematic uncertainties in the matrix method are originating from a closure test of the background efficiencies $\epsilon_{\text{bkg}}^{\text{total/pass}}$, from the change of the cone size ΔR in the isolation requirement and from the modelling of the detector geometry.

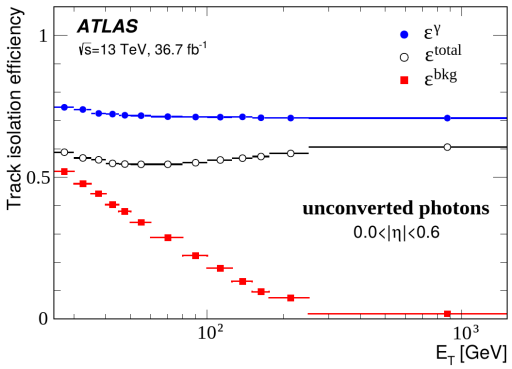

(a) Track isolation efficiency for prompt (blue), fake (red) and all (black) photons.

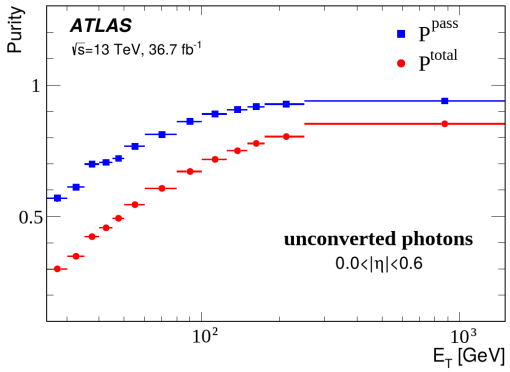

(b) Signal purity for inclusive sample (red) and for passing tight identification (blue).

Figure 3.18: Track isolation efficiency and signal purity distributions as function of photon E_{T} used for the matrix method with unconverted photons in $|\eta| < 0.6$. Modified from [128].

3.5.4 Combination

The resulting efficiencies for the tight identification ϵ_{ID} measured in data for each of the three methods are shown exemplary in Figure 3.19 for unconverted and converted photons in the $|\eta| < 0.6$ bin. The three methods show excellent agreement for the overlapping energy ranges and overall the tight ID efficiency ranges from $50 - 60\%$ at $E_{\mathrm{T}} = 10\,\mathrm{GeV}$ to $95 - 99\%$ (unconverted) and $88 - 96\%$ (converted) for photons with E_{T} above 250 GeV.

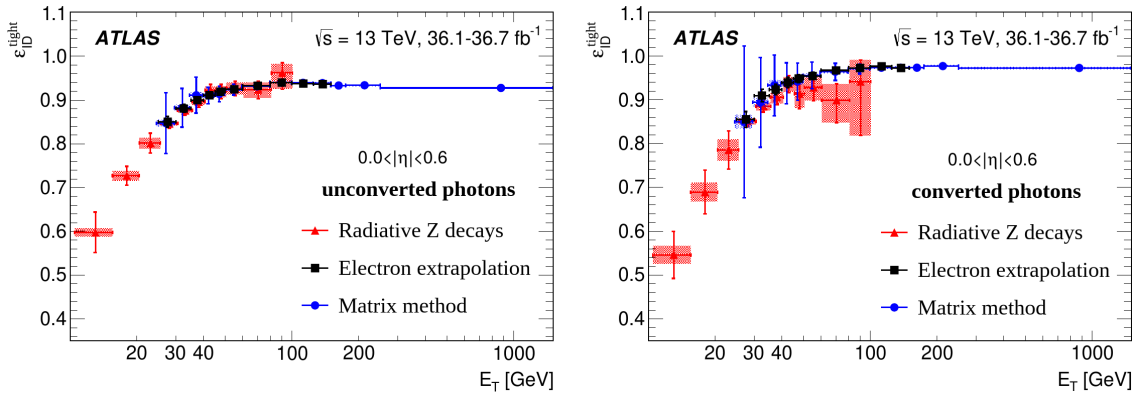

Figure 3.19: Efficiency of the tight photon identification as function of photon E_{T} combined for the three methods in the $|\eta| < 0.6$ bin for unconverted (left) and converted (right) photons. Modified from [128].

Moreover, efficiency **S**cale **F**actors (SFs) can be determined as ratios of the obtained data-driven values of ϵ_{ID} to the values from MC simulation. For the radiative Z decay method, a simulation with $Z \to ll\gamma$ samples is used, whereas for both other methods a simulated $\gamma + \mathrm{jet}$ sample is appropriate. A combination of the three measurements can be performed to further increase the measurement precision in the ranges where measurements from different methods are available. For this, the SF values are combined instead of the obtained efficiencies directly due to the differences in the photon sample composition. With the BLUE algorithm [136], the combined scale factor in each measurement bin is computed as a linear combination of the per-method scale factors.

The relative coefficients are derived from the statistical and systematic uncertainties as well as their correlations[11].
In Figure 3.20, the combined results in the $|\eta| < 0.6$ bin are shown for unconverted and converted photons. Overall, the central values of the SF are compatible within uncertainties being at the order of 1% or less and reaching values of up to 25% for low E_{T} due to limited photon statistics in some pseudorapidity bins.

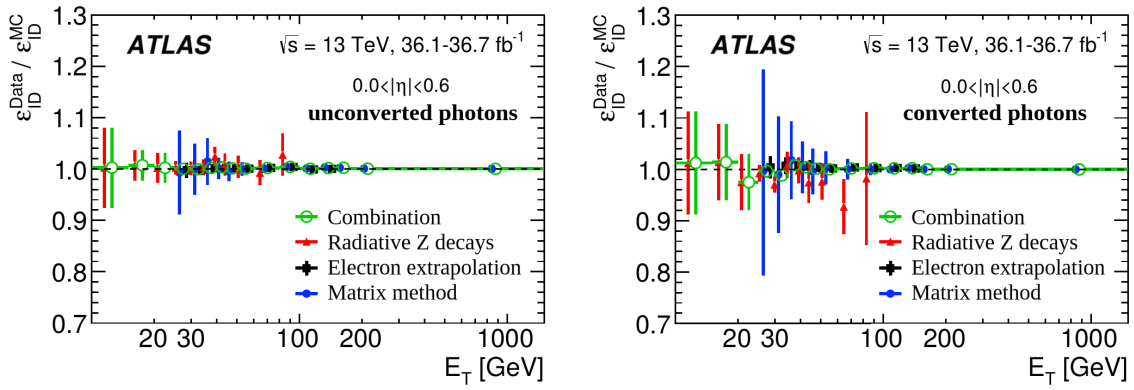

Figure 3.20: Scale factors for the photon identification efficiency for each method separately as well as the combination in the $|\eta| < 0.6$ bin for unconverted (left) and converted (right) photons. Modified from [128].

Finally, it is also important to check the dependence of the photon identification efficiency on the pile-up μ. For this, the simulation of radiative Z decays is reweighted to reproduce the pile-up distribution as observed in data. The evolution of ϵ_{ID} for these events, measured in data and MC simulation, as a function of μ for the $|\eta| < 0.6$ bin is shown in Figure 3.21 for unconverted and converted photons. In general, it can be observed that the efficiency significantly drops by about $10 - 15\%$ comparing pile-up conditions of $\mu \sim 5$ with $\mu \sim 40$.

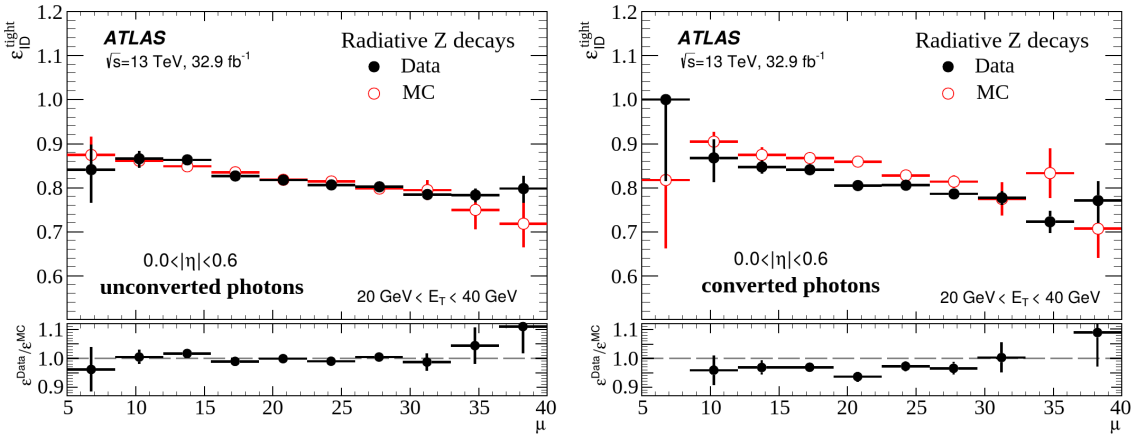

Figure 3.21: Pile-up dependence of the photon identification efficiency measured in radiative Z decays in data and MC simulation in the $|\eta| < 0.6$ bin for unconverted (left) and converted (right) photons. Modified from [128].

[11] In this case, all sources of statistical and systematic uncertainties are assumed to be uncorrelated.

Chapter 4

Optimization of Photon Identification

For the photon identification, selection criteria on the discriminating variables for the photon candidate objects have to be applied. Here, the simplest choice is to use rectangular cuts on the shower shape variables as it is currently employed in the ATLAS experiment. But the application of more involved classifiers for discrimination e.g. using **M**ulti **V**ariate **A**nalysis (MVA) techniques can result in a performance improvement of the identification. These sophisticated methods belonging to the field of **M**achine **L**earning (ML) applications have gained a high interest in high-energy particle physics, ranging from the application in object reconstruction such as b-tagging [137] or track reconstruction [138] to the classification of signal and background events in high-level physics analyses. A brief introduction to MVA methods and their basic principles is given in Section 4.1, discussing also the advantages and disadvantages for the application in the photon identification optimization.

To study different optimization approaches for the discrimination of prompt photons from background photons, a dedicated software framework has been developed in the course of this thesis. It allows a user-defined configuration of the input parameters such as data samples or boundary conditions and the choice of the optimization method. As such, different approaches can be trained and the results can be evaluated and validated to allow a fair comparison. Section 4.2 introduces the framework design and its functionalities.

In Section 4.3, the first deployment of the optimization framework is shown which aimed for a cross-check of the development of the tuned tight photon identification menu based on rectangular cuts to accommodate the changed running conditions of the LHC from Run-1 to Run-2 data taking. Here, studies to allow for the best possible tuning of cut values and to optimize the performance of the photon identification in terms of signal efficiency and background rejection while having a controlled behaviour of the identification working point e.g. in terms of pile-up dependence were conducted.

Moreover, the optimization framework was used to study the performance of the photon identification by deploying a **B**oosted **D**ecision **T**ree (BDT) approach as one possible MVA method. The tuning of the BDT as well as conducted performance studies and ideas for a possible integration into the standard photon identification process for the ATLAS experiment are explained in Section 4.4.

Finally, a conclusion of the work on the optimization of the photon identification for the ATLAS experiment is drawn in Section 4.5.

4.1 Cuts, Multi-Variate Analysis and Machine Learning

The problem of the classification of data into categories such as signal and background regions depending on the input of discriminating variables is a multidimensional optimization problem. In the case of the photon identification optimization with nine input variables in form of shower shape distributions, the underlying problem has nine dimensions. Moreover, non-trivial correlations between the different variable inputs exist. This problem becomes therefore unsuitable to be solved by manual calculation but rather by employing the calculation and processing power of computers. The spectrum of so-called **M**achine **L**earning (ML) applications is rather broad and describes in its basic sense the application of parallelizable processing power for solving classification and optimization problems by learning from input data sets to make predictions for new data sets.

In this work, the optimization was performed with ROOT's **T**oolkit for **M**ulti **V**ariate **A**nalysis (TMVA) [134], which automatically searches for selection criteria that allow to maximize the signal efficiency while keeping the background efficiency low, and gives the user nonetheless the possibility to configure the system with own restrictions. As such, TMVA offers the use of many methods for discriminating between the signal and background, each of them with advantages and disadvantages highly dependent on the kind of classification problem and the input data.

As a small selection of possible methods, the following three methods will be discussed here: in Section 4.1.1 the application of *rectangular cuts* is explained, followed by the use of a ***B**oosted **D**ecision **T**ree (BDT)* in Section 4.1.2, and employing a ***N**eural **N**etwork (NN)* in the classification in Section 4.1.3. Finally, the advantages and disadvantages of these methods for the optimization of the photon identification are summarized in Section 4.1.4.

4.1.1 Rectangular cuts

Rectangular cuts are probably the most basic kind of selection using simple cuts in a way that the signal region is selected to be between two cut values for each of the discriminating variables. This is exemplary shown in Figure 4.1 for the shower shape variable R_ϕ as used for the photon identification, where the cut was optimized to be ~ 0.95, meaning that all photon candidates with values higher than this cut value "pass" the selection or "fail" otherwise, so a binary decision is given. If the photon candidate passes also all other cuts defined for the other shower shape variables, then it will be identified as a photon.

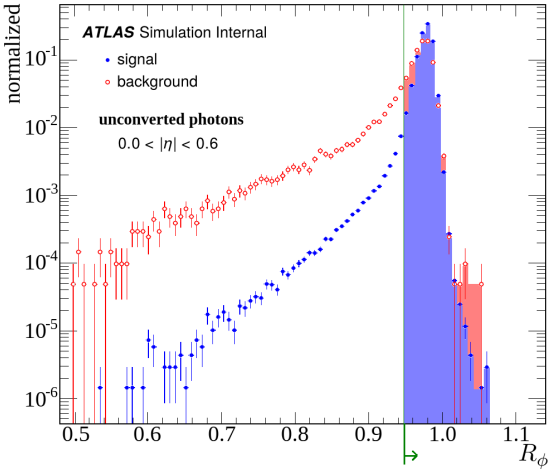

Figure 4.1: Shower shape variable R_ϕ for unconverted photons in the $|\eta| < 0.6$ bin with optimized cut value (green) for tight photon identification, selecting signal photon candidates (blue area) as well as background photons (red area).

4.1.2 Boosted decision trees

Decision trees are often used multivariate classifiers and can be interpreted as a binary tree structure with repeated left/right decisions at nodes for a single variable at a time, until reaching a stop criterion. Due to its structure, a straightforward interpretation is possible which can be visualized as shown in Figure 4.2. The phase space of discriminating variables is splitted by the consecutive node decisions into many regions classified as signal- or background-like depending on the majority of training events in the final node. Here, each path down the tree to each leaf node represents an individual cut sequence for a hypercube in the phase space.

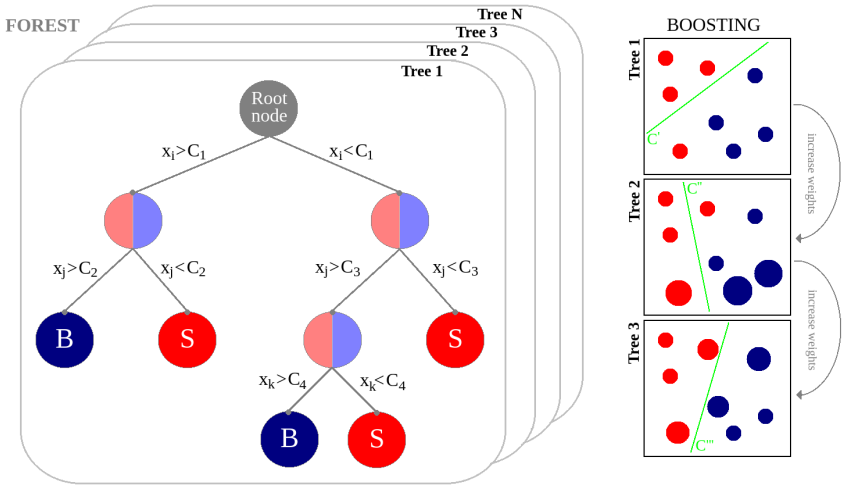

Figure 4.2: Visualization of a *boosted decision tree*. A *forest* is made up of single-decision trees with end nodes marking signal (S) or background (B) depending on applied cuts (C) at each node on discriminating variables (x). *Boosting* is applied by changing the event weights for each tree from the forest, gaining different classifications.

As a single decision tree is rather instable with respect to statistical fluctuations in the training sample, this problem is solved by constructing a *forest* of decision trees. The event classification is done then on a majority vote from each tree in the forest. Even though that each tree is derived from the same training sample, the weights of the events in the sample are modified in the so-called *boosting*. This allows for an increased statistical stability as well as an improved performance but eliminates also the straightforward interpretation. Moreover, the boosting seems to perform better on trees with a smaller depth and having individually a smaller classification power (*weak classifiers*). A limited growing during training eliminates also the need of *pruning*, meaning to remove statistically insignificant nodes after training, and as such BDTs do not show the tendency of *overtraining*.

4.1.3 Neural networks

A *neural network* is a multivariate classifier using a simulated collection of interconnected neurons, where each neuron produces a certain response depending on the input signal. It can be interpreted as a non-linear mapping of input information from a multi-dimensional input space $x_1,...,x_n$ onto a one-dimensional $y_{\text{classification}}$ or a multi-dimensional output space $y_1,...,y_m$. The layout of the neural network follows often a design with neurons organized in layers and only direct connections between neighboring layers allowed, which is called ***M**ulti **L**ayer **P**erceptron (MLP)*.

As shown in Figure 4.3, the first layer is the input layer for the discriminating variables, followed by a *hidden layer* connecting the input layer to the final layer, representing the output layer.

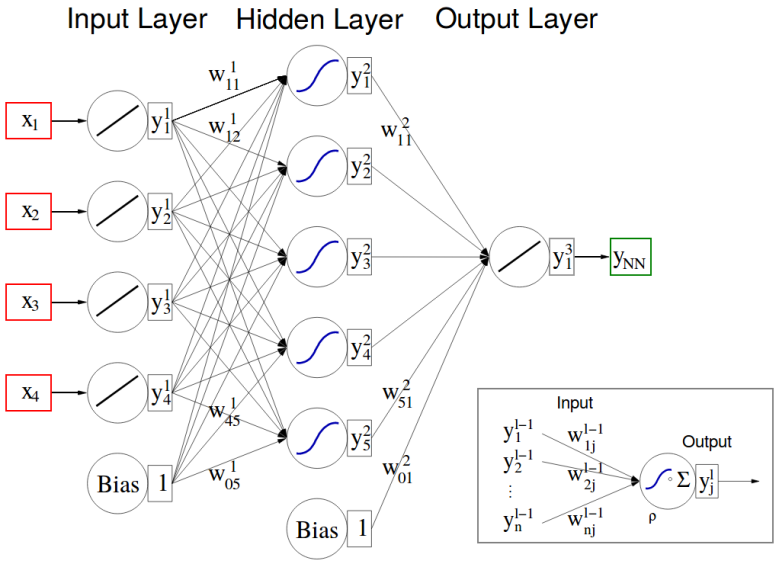

Figure 4.3: Visualization of a *neural network* as a MLP with four inputs (x_i) into the input layer, one hidden layer and one neuron in the output layer (y_{NN}). The response functions (ρ) for each neuron are selected and the weights (w) of the neural connections will be optimized. Modified from [134].

A *weight* (w) is associated to each neural connection and at each neuron, the input signal is transformed by a selectable, often non-linear *response function* (ρ). In the optimization step, the weights of the neural network are adjusted to allow for an optimal classification performance by using the so-called *back propagation*. When adding several hidden layers to the NN, it is called *deep neural network* for which recent ML developments have shown the capability to learn complex, non-linear relations when trained on a sufficiently large amount of training data.

4.1.4 Advantages and disadvantages

After introducing three possible methods for classification problems, the advantages and disadvantages of these in respect to the application in the photon identification optimization shall be discussed in the following and are also summarized in Table 4.1.
Starting with the use of rectangular cuts, a clear advantage here is the ease of tuning the cuts for different detector configurations (e.g. higher pile-up as for Run 2) and also the possibility to fine-tune cuts by hand due to the straightforward interpretation. The latter point of transparency is contradicted by the presence of non-trivial correlations between the shower shape variables. Also, the application of cuts is known to underperform with strong non-linear correlations and/or with several weakly discriminating variables, so that here sophisticated MVA methods will be rewarding.
So in the case of a BDT, the phase space can be splitted into a large number of hypercubes each identified as either signal-like or background-like, whereas a cut-based analysis selects only a single hypercube in the variable phase space. An even higher performance can in principle be expected by the application of a NN approach, as it can learn non-linear relations represented in the underlying input data. Here, the problem is more in the interpretation of results and the possibility to tune the NN performance with a huge phase space of hyperparameters, compared to the easier tuning of a BDT approach.
Both MVA techniques have a disadvantage compared to the currently used cut-based approach, as here the definition of control regions for photons in physics analyses by simply inverting cuts on a subset of discriminating variables is not possible.

One such problem to use a MVA-based photon identification is in the efficiency measurement using the matrix method, as here a photon selection uncorrelated to the isolation criteria is required, which will be addressed in Section 4.4 for a BDT approach .

Rectangular Cuts	Boosted Decision Tree	Neural Network
+ simple & easy updateable	+ multi-variate optimization	+ multi-variate optimization
+ individual fine-tuning possible	+ exploit correlations in optimization	+ learning of non-linear relations
+ small correlation of ID with isolation	o correlation of ID with isolation possible	- large phase space of hyperparameters
+ control regions by cut inversion	- definition of control regions	- correlation of ID with isolation
- univariate optimization		- definition of control regions
- underperforming with strong variable correlations		

Table 4.1: Advantages and disadvantages of classification methods, namely *rectangular cuts*, *boosted decision tree* and *neural network*, for the optimization of the photon identification in the ATLAS experiment.

4.2 The *PhotonIDOptimizer* Framework

The *PhotonIDOptimizer* framework was developed to allow for an easy tuning of the photon identification with the possibility to study and tune different optimization methods.
On the one hand, the currently used cut-based optimization should be implemented in the framework as it can be used for the validation of the new framework by comparing the results to the tuning tool for the cut-based menu in the ATLAS experiment. On the other hand, in principle all methods for classification implemented in TMVA are available for selection, as TMVA is used as the underlying optimization framework. But in the first step, an optimization using BDTs for the exploration of MVA methods was integrated into the framework.

The optimization of the photon identification using MVA methods was previously studied in Run 1 by employing a neural network [139]. Here, the trained NN showed an improvement in the efficiency, but the comparison was made to the existing tight photon identification menu without retuning. Moreover, it was recognized that using the NN approach led to an increase of the systematic uncertainties for the data-driven efficiency measurements (cf. Sec. 3.5). In the end, the cut-based method remained the baseline for the photon identification showing comparable performance after retuning the cuts and no issues with the efficiency measurements in data.

Therefore, for the study of MVA methods in Run 2 the prerequisites from the efficiency measurements which led to the systematic uncertainty increase in Run 1 are taken into account from the beginning. On the one hand, the matrix method relies on the fact that only a small correlation between the photon identification and isolation exists. On the other hand, the electron extrapolation method is only possible when in the photon identification the correlations between the shower shape variables are not extensively exploited.

This is due to the fact that the correlations in the transformed shower shapes from the selected electron candidates will be most probably different as for photon candidates.
The *PhotonIDOptimizer* framework provides a well suited environment to optimize and test MVA-based photon identification by comparing the performance results to the cut-based baseline while checking the compatibility with the data-driven efficiency measurements.

In the following, the design of the *PhotonIDOptimizer* framework and its functionalities are shown in Section 4.2.1. In Section 4.2.2, the typical operation principle for the photon identification optimization with the framework is explained. Finally, the results of a validation study, by comparing to the currently employed cut-based tuning tool in the ATLAS experiment, are briefly discussed in Section 4.2.3.

4.2.1 Design and functionality

The *PhotonIDOptimizer* framework is a standalone software package written in C++ and executed by Python start-up scripts with user-controllable configuration files. It is based on the ATLAS AnalysisBase software environment and can be accessed within the ATLAS collaboration via CERN's GitLab [140]. For the optimization and classification, ROOT's TMVA package [134] is used. By the configuration files, the user can choose the optimization method and its parameters and select the input datasets for the training and if needed to apply data preparation. Moreover, it is possible to choose a sub-sampling of the optimization phase space due to the observed dependencies of the shower shape variables (cf. Sec. 3.4.2): by the photon conversion type, by the isolation working point and by the photon kinematics such as a range in E_{T} and the binning in η.
The computational intensive optimization can be parallelized by using batch processing via HTCondor [141]. To evaluate the optimization output, an additional plotting tool is part of the framework allowing to validate the identification performance relative to the currently employed identification working points. Most importantly, the signal efficiency as well as the background efficiency can be evaluated as function of transverse energy or pile-up. Furthermore, the shower shape variables and their linear correlations as inputs to the discrimination are plotted[12].
As input for the optimization, Monte Carlo samples representing the signal- and background-like photon candidates are needed. As signal MC a γ+jet sample produced with Pythia8 is used, whereas the background MC sample is simulated as di-jet events with Pythia8 (cf. Sec. 3.4.1). Moreover, to validate the identification performance by comparing simulated events with data, data and MC samples of radiative Z decays are used[13].

4.2.2 Operation principle

In the following, the general setup for the photon identification optimization with the *PhotonIDOptimizer* framework is described. In the configuration file, the MC samples for signal and background are specified and signal photon candidates are selected by requiring a MC truth matching, whereas for background fakes this is inverted. Moreover, only candidates fulfilling the loose ID requirement are passed, as photons passing the tight ID should be also fulfilling the more basic loose ID selection. As another preselection, regional cuts on the discriminating shower shapes can be applied, e.g. to exclude unphysical regions originating from the MC simulation.

[12] Most of the plots of shower shape distributions and their dependencies shown in Section 3.4 were produced with the *PhotonIDOptimizer* framework.
[13] The simulated samples of $Z \to ll\gamma$ events were generated with SHERPA [142].

In principle, also a photon isolation requirement (cf. Sec. 3.3) could be applied at this stage, but as one of the prerequisites from the efficiency measurements is that the identification and isolation working points should be rather independent, no isolation is applied for the optimization. Finally, the discriminating variables as the set of defined shower shape variables are specified, with the additional possibility to constrain the phase space in the optimization by lower and upper boundaries.
After defining the inputs for signal and background, the optimization method can be selected. In the current implementation of the framework, the cut-based and BDT optimization was validated and will be used in the following. Moreover, the optimization parameters for the selected method as given by the TMVA implementation can be defined. Due to the shower shape dependence on the photon type and the photon kinematics, the optimization should be performed parallelized in sub-categories as specified by the user. In the following, the typical slicing in the two photon conversion types and seven bins of $|\eta|$ is used, resulting in 14 optimization categories. As the identification efficiency for low-E_{T} photons is in general worse than for higher transverse energies, the training can be performed especially on these candidates. Therefore, sometimes only candidates within a transverse momentum of $25\,\mathrm{GeV} < p_{\mathrm{T}} < 60\,\mathrm{GeV}$ are used in the optimization.
The final part of the configuration is to define a selection for the analysis and validation of the results after the training. Here, typically an inclusive selection in E_{T} is used with the additional application of a photon isolation working point[14].

After the training, the output of the optimization can be compared for different methods or parameter settings, by using the provided plotting tools in the framework, evaluating the performance of the discriminator by

- plotting the background rejection $(1 - \epsilon_{\mathrm{bkg}})$ as function of the signal efficiency $(\epsilon_{\mathrm{sig}})$, resulting in the so-called **R**eceiver **O**perating **C**haracteristic (ROC) curve;
- plotting the significance $(\epsilon_{\mathrm{sig}}/\sqrt{\epsilon_{\mathrm{sig}} + \epsilon_{\mathrm{bkg}}})$ as function of the signal efficiency $(\epsilon_{\mathrm{sig}})$.

Examples for a ROC and a significance curve for a cut-based optimization are shown in Figure 4.4. Here, for each given signal efficiency a set of discriminating cuts was tuned reaching the corresponding background rejection.

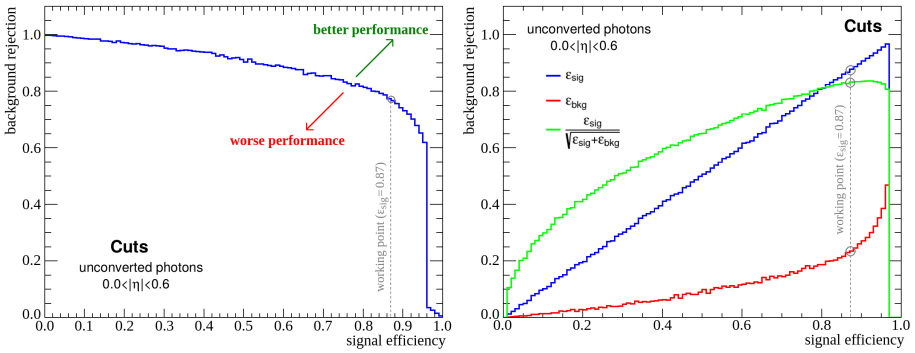

Figure 4.4: Performance plots of the *PhotonIDOptimizer* framework for an exemplary cut-based optimization. The ROC curve (left) evaluates for a given signal efficiency the corresponding background rejection with the optimal performance in the upper right corner. The significance curve (right) features a maximum and can be evaluated for a selected working point (e.g. at $\epsilon_{\mathrm{sig}} = 0.87$).

[14] For the studies in this thesis, the *FixedCutLoose* photon isolation working point (cf. Tab. 3.1) is used.

In the next step, a signal efficiency point can be selected representing the aimed for identification efficiency, which is in the case of the tight photon identification at $\epsilon_{\text{sig}} = 0.87$. With this optimization point, the plotting tool evaluates the photon identification efficiency in detail, which was extensively used for the following studies.

4.2.3 Validation study

For the validation of the framework, the result of a cut-based identification optimization was compared with the standard ATLAS tuning tool for Run 2, using the same configuration as input. In Figure 4.5, the results in terms of the ROC curves are compared. Here, only minor differences between the standard tool and the newly developed *PhotonIDOptimizer* framework are observed. These differences can be accounted for by the numerical process of the optimization based on a randomized process with different seed values.

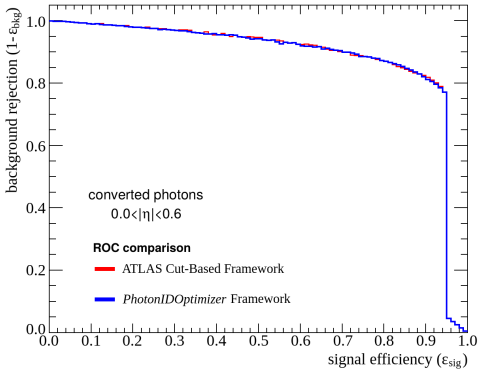

Figure 4.5: ROC curves for the cut-based photon identification optimization. Shown is the comparison for the standard ATLAS cut-based tuning framework for Run 2 (red) and the *PhotonIDOptimizer* framework (blue) for converted photons in $|\eta| < 0.6$.

The loose-to-tight photon identification efficiency for signal and background photons as function of the transverse energy is shown in Figure 4.6. Here, the tight ID cuts for both tools were evaluated for a working point of $\epsilon_{\text{sig}} = 0.87$ and are compared in terms of the resulting signal and background efficiency. Again, only small differences for both optimizations can be observed. Moreover, comparing the efficiencies of the re-optimized tight ID menu with the one used for Run 1, a slight improvement in the signal efficiency and a bigger improvement in the background rejection can be observed.

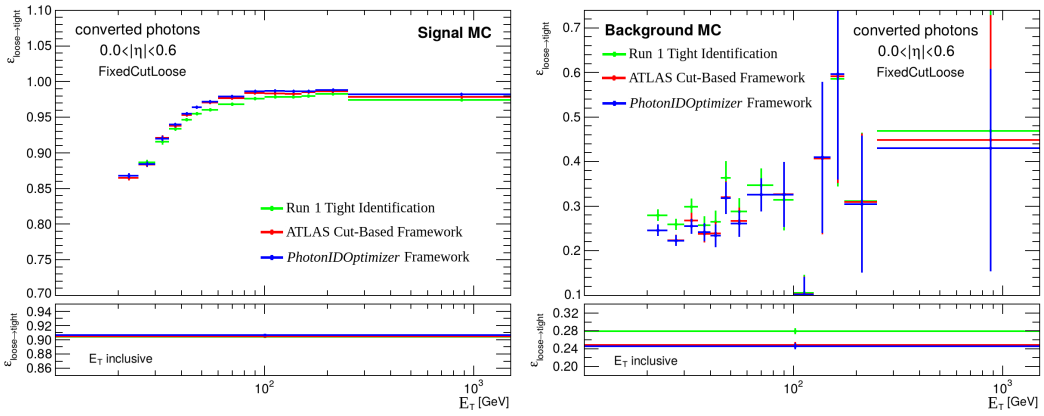

Figure 4.6: Loose-to-tight photon ID efficiency versus E_{T}. Compared are the ATLAS Run 1 tight ID working point (green), the standard ATLAS cut-based tuning framework for Run 2 (red) and the *PhotonIDOptimizer* framework (blue). Shown are the signal efficiencies (left) and background efficiencies (right) for converted photons in $|\eta| < 0.6$ with *FixedCutLoose* isolation applied.

4.3 Optimization using Rectangular Cuts

The *PhotonIDOptimizer* framework was used to cross-check and to provide auxilliary studies for the tuning of the rectangular cuts for the tight photon identification in Run 2. As discussed before, the framework was successfully validated against the standard ATLAS cut-based tuning framework and can therefore provide additional insights in the optimization process. In the following, a selection of conducted studies with rectangular cuts for the photon identification optimization is discussed.

In Section 4.3.1, the parameter tuning of the cut-based optimization and the final choice of settings for the rectangular cuts is shown. The output of cut values on the discriminating shower shape variables can be tested in terms of their dependence on the optimization region, e.g. the pseudorapidity, which is explained in Section 4.3.2. Finally, a study with photons from a radiative Z sample, both in data and MC, is introduced in Section 4.3.3, providing valuable input on the data-MC differences in terms of chosen cut values.

4.3.1 Parameter tuning for cut-based optimization

In the first step, a study of the optimal parameter settings for the cut-based photon identification optimization was conducted. The *PhotonIDOptimizer* framework allows to sweep through a number of parameter settings while running on the same input configuration otherwise. Therefore, some optimization settings as specified within TMVA were systematically tested.
Firstly, the general fitting algorithm to optimize the cut value can be tested:

- *Monte Carlo sampling*: The fit parameters are randomly sampled and the optimal set of parameters is used for the discrimination. This is a simple and straightforward, albeit inefficient fitting method.
- ***G**enetic **A**lgorithm (GA)*: The optimization problem is modelled by a group (*population*) of abstract representations (*genomes*) of possible solutions (*individuals*). By applying an evolution process, the individuals of the population should evolve towards an optimal solution of the problem. For the evaluation of the goodness of an individual, a problem-dependent *fitness* function is defined. The general process is then to initialize a starting population, evaluating each individual by the fitness function and select only a fraction of best performing individuals. The surviving individuals are copied, mutated and crossed-over to reproduce the initial population size and the procedure can be repeated for several cycles. Finally, the best evaluated individual represents the optimal solution for the problem.
- *Simulated annealing*: The algorithm achieves a slow, but correct convergence of an optimization problem with multiple solutions and is inspired by the process of *annealing* in condensed matter physics. Here, it can be observed that for infinitesimal annealing activity the system will always converge in its global energy minimum, representing the optimal solution for a discriminator.

In the following, the impact of the optimization parameters is discussed for an exemplary optimization with unconverted photons in $|\eta| < 0.6$ with a selection of $25\,\text{GeV} < E_\text{T} < 60\,\text{GeV}$ and no isolation requirement applied.
In Figure 4.7a, the ROC curves for the three different fitting algorithms with default parameters from TMVA are shown. It can be observed that the MC sampling is performing the worst, whereas the simulated annealing approach shows a comparable performance as the GA approach. In the following, only the GA approach is further investigated.

The most important parameter to enhance the quality of the optimization is the population size (*PopSize*). In Figure 4.7b the ROC curves for population sizes from 300 (default) to 700 are displayed. The parameter *Steps* in the algorithm describes the termination of the reproduction step, as the process terminates within the number of steps or when the fitness function is evaluated less than the convergence criterion. The ROC curves for sweeping the number of steps from 20 to 60 (with 40 as default) are shown in Figure 4.7c. Finally, the parameter *Cycles* represents the number of iterations of the whole process with storing the best solution for each cycle and combining them in the last iteration to reach an optimal solution. In Figure 4.7d the ROC curves for 3 (default) to 7 cycles are displayed.

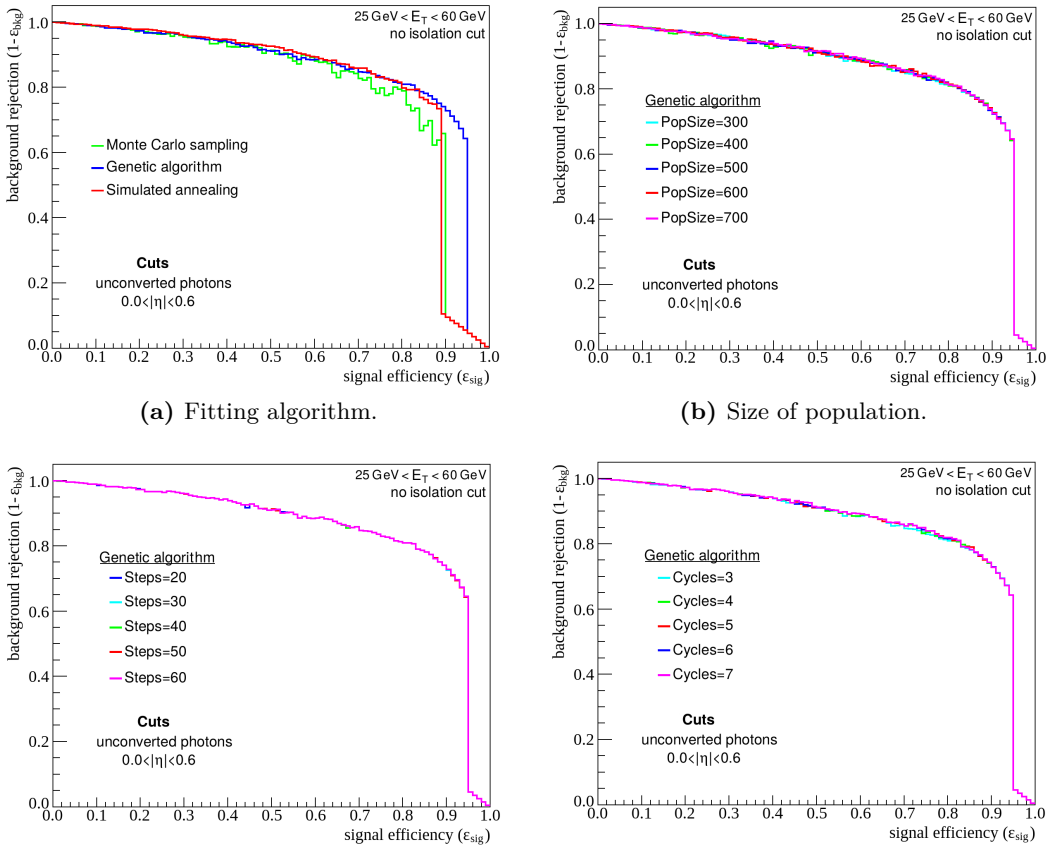

(a) Fitting algorithm.

(b) Size of population.

(c) Number of steps.

(d) Number of cycles.

Figure 4.7: Sweep of optimization parameters for *rectangular cuts* optimization.

In general, the performance for all three parameter sweeps in terms of the ROC curve is comparable with only minor differences. To evaluate these differences, the integral of the ROC curve can be calculated, called **A**rea **U**nder **C**urve (AUC), and then compared for the different cases. The results of the calculated AUC for the full region as well as for a **R**egion **O**f **I**nterest (ROI) defined as $0.8 < \epsilon_{\text{sig}} < 0.9$ are shown in Table 4.2.
In general, a slight improvement for higher numbers of the parameters *PopSize*, *Steps* and *Cycles* can be observed. But the performance gain is only reachable with more computational power, meaning an increased calculation time which at least increases for all three parameters with $O(size)$. For the reoptimization of the tight ID for Run 2, the cut-based optimization used the GA approach with a population size of 500, a step size of 20 and with 6 cycles (marked in blue in Figure 4.7), yielding an AUC of 85.73 and 8.54 for the full region and the ROI, respectively.

PopSize	AUC		*Steps*	AUC		*Cycles*	AUC	
	full	ROI		full	ROI		full	ROI
300	85.51	8.53	20	85.50	8.53	3	85.51	8.53
400	85.58	8.54	30	85.50	8.53	4	85.66	8.56
500	85.56	8.53	40	85.51	8.53	5	85.71	8.56
600	85.64	8.54	50	85.51	8.53	6	85.73	8.56
700	85.64	8.54	60	85.52	8.53	7	85.79	8.57

Table 4.2: AUC performance of parameter sweep for GA cut optimization.

4.3.2 Dependence of cut values

The *PhotonIDOptimizer* plotting tools allow to evaluate the reoptimized photon identification efficiency for signal and background photons as function of the transverse energy as well as the event pile-up, as it was shown before. Moreover, for the cut-based optimization the dependence of the cut values can be checked over the different optimization regions. In Figure 4.8a the dependence of the cut values on the pseudorapidity bin and separated for unconverted and converted photons is shown. Here, due to the dependence of the shower shape variables on η and the conversion state (cf. Sec. 3.4.2) one expects changing cut values for different optimization regions. So, the cut value on R_ϕ for unconverted and converted photons is quite different as also the shape distributions are different. For the dependence on η, the shower shape variables w_{stot} and f_{side} are good examples, showing a dependence on η for their shape distributions which is then also reflected in the applied cut value. Apart from these expected variations, very large fluctuations between neighboring categories could point to an unphysical behaviour of the cut menu.
A similar argument holds for the cut value as function of the tuned signal efficiency, as it is shown in Figure 4.8b. Here, for some of the discriminating variables larger fluctuations can be observed indicating most probably a lower discrimination power for this variable.

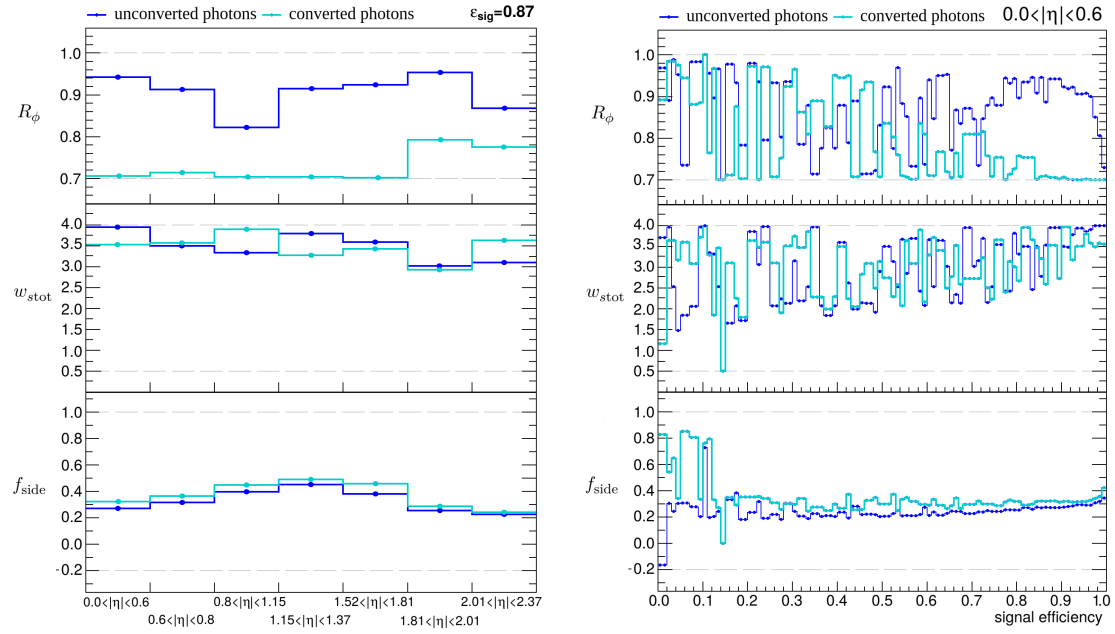

(a) Dependence on the pseudorapidity η for unconverted and converted photons at $\epsilon_{\text{sig}} = 0.87$.

(b) Dependence on the signal efficiency ϵ_{sig} for unconverted and converted photons in $|\eta| < 0.6$.

Figure 4.8: Dependence of cut values for the shower shape variables R_ϕ, w_{stot} and f_{side}.

4.3.3 Study with radiative Z sample

The *PhotonIDOptimizer* framework provides also a special plotting tool which uses photon candidates from the radiative Z process. Here, a $Z \to ee\gamma$ data and MC sample is used to study data-MC differences and their influence on the photon identification performance. For variables with larger differences between data and MC, a cut value which was optimized using only the MC sample can be too tight for the variable in data.
The shower shape variable f_{side} is known to be mismodelled in MC simulation and was therefore the focus of an auxilliary study. The proposed new tight ID menu for Run 2 involved a tightening of the f_{side} cut value to improve the performance. But at the same time, in checks with the data-driven efficiency measurements, the electron extrapolation method (cf. Sec. 3.5.2) showed larger uncertainties for the two last bins in η for unconverted photons. In the following, the results of the investigation of the behaviour of the variable f_{side} due to the tightening of the cut are explained.
In Figure 4.9, the data and MC distributions for the variable f_{side} are shown for unconverted photons in the first as well as the two problematic last η bins. Overlayed are also the cut values for the tight ID menu in Run 1 as well as the reoptimized proposal for Run 2.

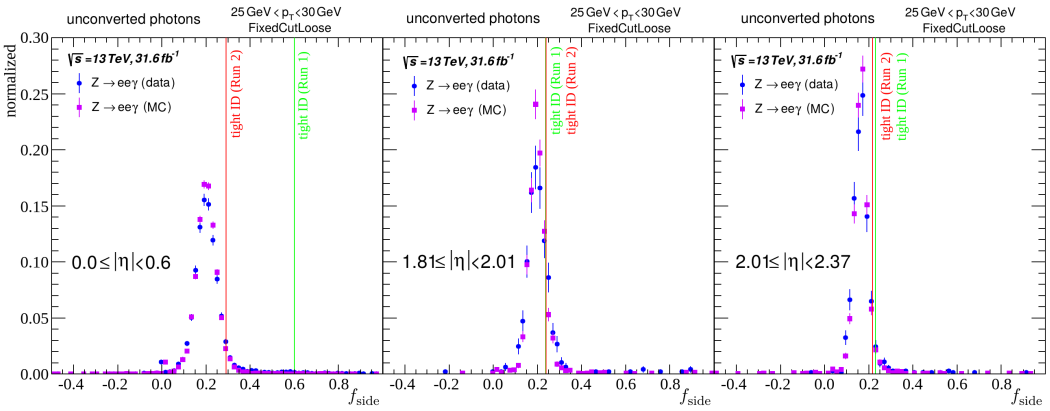

Figure 4.9: Data-MC differences of the shower shape variable f_{side} for $|\eta| < 0.6$, $1.81 < |\eta| < 2.01$ and $2.01 < |\eta| < 2.37$. Shown are unconverted photons from $Z \to ee\gamma$ data and MC samples selected with $25\,\text{GeV} < E_{\text{T}} < 30\,\text{GeV}$ and *FixedCutLoose* isolation. The cut values from the tight ID menu in Run 1 (green) and the proposed menu for Run 2 (red) are overlayed.

For the first η bin, a tightening of the cut value compared to the one in Run 1 is rather safe. But for the two last η bins, the distributions are cutted rather strongly into their right tails. Any mismodelling of the shower shape would directly influence the photon identification efficiency. This was also the observed effect in the electron extrapolation method, as here the photon distributions are inferred from transformed electron shower shapes fully relying on MC simulation.
Therefore, in the reoptimized tight ID menu for Run 2, the cut values for f_{side} for the case of unconverted photons in $1.81 < |\eta| < 2.01$ and $2.01 < |\eta| < 2.37$ were fixed to 0.275 and 0.230, respectively. The cut-based optimization was then repeated for the two optimization regions with the fixed f_{side} cut value. Table 4.3 shows the resulting tight photon identification efficiencies in the two respective η bins for data and MC in $Z \to ee\gamma$ samples, for a selection of unconverted photons with $25\,\text{GeV} < E_{\text{T}} < 30\,\text{GeV}$ and *FixedCutLoose* isolation applied. Compared are the case of the tight ID menu in Run 1, the proposed Run-2 menu before, the proposed Run-2 menu with the fixed f_{side} cut values and the proposed Run-2 menu after retuning with the fixed f_{side} cut values.

	$1.81 < \|\eta\| < 2.01$		$2.01 < \|\eta\| < 2.37$	
tight ID menu	data efficiency	MC efficiency	data efficiency	MC efficiency
Run 1	0.75 ± 0.05	0.79 ± 0.03	0.87 ± 0.05	0.87 ± 0.03
Run 2 (proposed)	0.76 ± 0.05	0.82 ± 0.03	0.86 ± 0.05	0.87 ± 0.03
Run 2 (fixed f_{side})	0.87 ± 0.05	0.88 ± 0.03	0.88 ± 0.05	0.89 ± 0.03
Run 2 (retuned)	0.82 ± 0.06	0.83 ± 0.03	0.87 ± 0.05	0.87 ± 0.03

Table 4.3: Tight photon ID efficiencies for data and MC in $Z \to ee\gamma$ samples evaluated with four different tight ID cut menus, shown for unconverted photons in $1.81 < |\eta| < 2.01$ and $2.01 < |\eta| < 2.37$. Photons are selected with $25\,\text{GeV} < E_{\text{T}} < 30\,\text{GeV}$ and the *FixedCutLoose* isolation working point.

With the retuned Run-2 menu for the fixed f_{side} cut values, a good performance in terms of the photon identification efficiency is reached, showing also a good agreement between data and MC. Moreover, by this measure the uncertainties in the electron extrapolation method for the two problematic η bins reduced again and the menu was selected as the new tight ID menu for the analysis of data from 2015 and 2016.

4.4 Optimization using Boosted Decision Trees

The main goal of the *PhotonIDOptimizer* framework is to provide an optimization tool to study MVA techniques in the photon identification. For this work, several studies with a **B**oosted **D**ecision **T**ree (BDT) approach were conducted and the performance was evaluated against the reoptimized cut-based menu for Run 2, using the same input configuration as for the cut-based tuning.

In Section 4.4.1, the results of a parameter tuning for a BDT approach are discussed, followed by the optimization results for the BDT and further detailed studies of the performance in Section 4.4.2. To account for the prerequisites of the matrix method in terms of the correlation to the photon isolation, a new approach with the training of two separate BDTs was studied in Section 4.4.3. Finally, the test results of a p_{T}-dependent BDT training for the photon identification are shown in Section 4.4.4, as in parallel a p_{T}-dependent cut-based optimization was conducted in the collaboration.

4.4.1 Parameter tuning for BDT optimization

For the photon identification optimization with a BDT, a study of the optimal parameter settings was conducted similar to the study for the cut-based optimization. In general, the method of *adaptive boosting* and for the separation criterion at the nodes the *Gini index* were selected for the BDT approach.
The *AdaBoost* algorithm is reweighting the event weights of misclassified events for the next iteration of decision trees by multiplication with a *boost weight*, α. Here, α is derived from the misclassification rate, err, of the previous decision tree as $\alpha = (1 - err)/err$ and then renormalized by the total sum of event weights.
To assess the performance of a cut on a variable at a node of the decision tree, a separation criterion have to be applied, in this case the *Gini index*. It is defined as $p(1-p)$ with the purity p and is similar to other criteria symmetric in p with a maximum at $p = 0.5$. The reason for this is that for the classification problem a node decision selecting dominantly background events is as valuable as a decision for signal events.

In the following, the impact of four optimization parameters in the BDT approach is discussed again for an exemplary optimization with unconverted photons in $|\eta| < 0.6$ with a selection of $25\,\text{GeV} < E_\text{T} < 60\,\text{GeV}$ and no isolation applied. In Figure 4.10a, the number of used decision trees in the forest (*NTrees*) is sweeped between 400 and 1200 (with 800 as default). The parameter *MaxDepth* describes the maximum of allowed node layers of the decision trees and Figure 4.10b shows the ROC curves for a depth of 1 to 5 (with 3 as default). In Figure 4.10c, the parameter *MinNodeSize* is changed between 2% and 8% (with 5% as default) and is the requirement on the minimum percentage of training events in each leaf node to allow for the classification decision. Finally, the parameter *nCuts* represents the granularity for the search of the optimal cut value on a single variable at a node. The ROC curves for a step size of 10 to 50 (with 20 as default) for the cut decision are displayed in Figure 4.10d, showing also the special case of $nCuts = -1$ for which an algorithm tests all possible cuts on the sample and selects the best one.

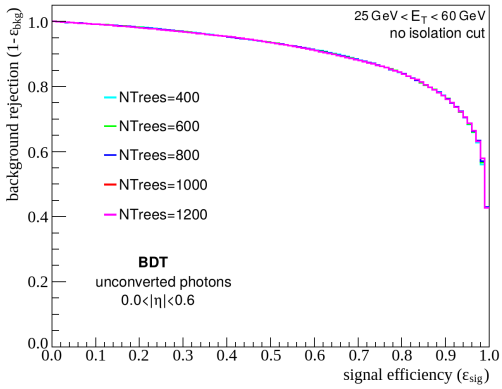

(a) Number of trees.

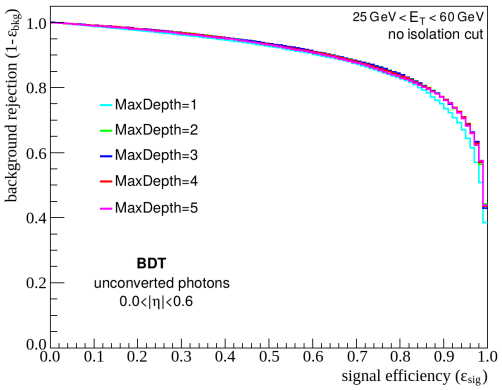

(b) Depth of decision tree.

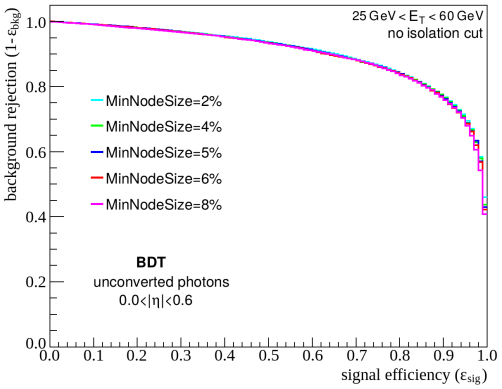

(c) Minimum node size.

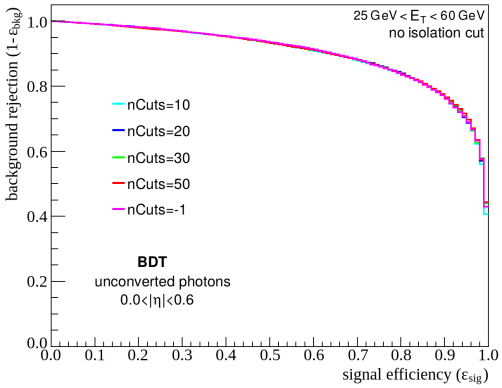

(d) Number of cuts.

Figure 4.10: Sweep of optimization parameters for *BDT* optimization.

The performance for each parameter sweep in terms of the ROC curve is rather comparable with only minor differences. In Table 4.4 the differences are evaluated by calculating the AUC for the full region and the ROI for the four parameter sweeps. Here, one can observe a performance gain for a smaller number of trees and for a reasonable depth of nodes (two or three layers) to fully explore the features of *weak classifiers* via boosting. Moreover, it seems sufficient to have a low percentage of training events in the leaf nodes and to use 20 cuts in terms of granularity, as the performance gain for the special case of $nCuts = -1$ is only minor, also compared to the higher computational investment.

NTrees	AUC		*Max*	AUC		*MinNode*	AUC		*nCuts*	AUC	
	full	ROI	*Depth*	full	ROI	*Size*	full	ROI		full	ROI
400	90.24	8.84	1	89.12	8.66	2%	90.45	8.87	10	90.06	8.83
600	90.23	8.84	2	90.22	8.84	4%	90.25	8.86	20	90.22	8.84
800	90.22	8.84	3	90.22	8.84	5%	90.22	8.84	30	90.20	8.82
1000	90.20	8.84	4	90.09	8.82	6%	90.09	8.82	50	90.21	8.85
1200	90.19	8.84	5	89.88	8.79	8%	89.98	8.81	-1	90.23	8.82

Table 4.4: AUC performance of parameter sweep for BDT optimization.

For the following BDT studies, the optimal set of parameters were selected as *NTrees*= 400, *MaxDepth*= 3, *MinNodeSize*= 2% and *nCuts*= 20, yielding an AUC of 90.75 and 8.95 for the full region and the ROI, respectively.

4.4.2 BDT optimization and performance studies

A BDT with the previously determined optimal settings was trained on the same input configuration as for the cut-based optimization[15].
The output of the BDT optimization is a *classifier score* with −1 meaning background-like and +1 meaning signal-like. To apply a classification on the sample, a cut on the distribution of the classifier score has to be applied. The corresponding signal efficiency of this cut value on the classifier score can be calculated as the integral of the signal training sample with a score higher than the cut value divided by all signal MC events. On the contrary, the background efficiency is the fraction of background events with a classifier score lower than the cut value over all background events. Therefore, it is possible to plot the signal and background efficiency as well as the significance as function of the classifier score. To make then a fair comparison with the cut-based optimization, the cut value on the classifier score is determined by requiring the same signal efficiency, meaning a working point of $\epsilon_{\text{sig}} = 0.87$ in this case. In the next step, the such determined cut on the classifier score can be used to classify tight ID photons in the given signal and background sample.

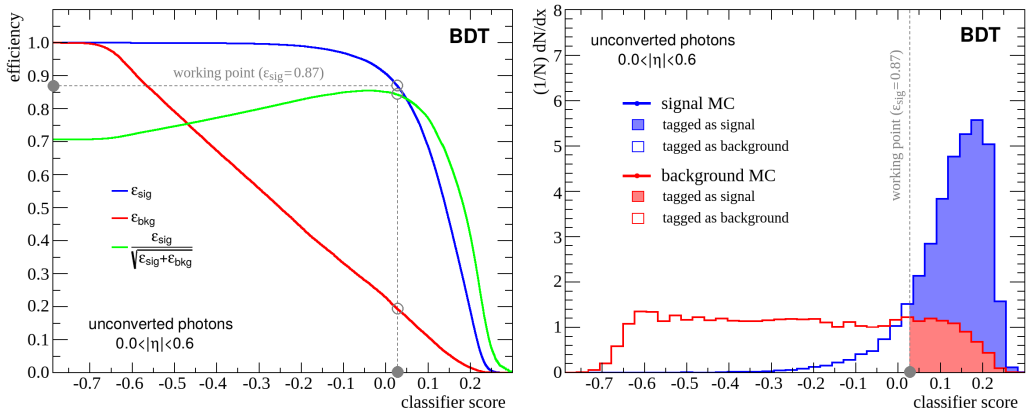

Figure 4.11: BDT performance plots as function of the *classifier score*. The signal and background efficiency as well as the significance are shown as function of the classifier score and the cut value is selected with $\epsilon_{\text{sig}} = 0.87$ (left). Moreover, the classifier distributions for the signal and background training sample are shown with the determined cut value on the classifier score (right).

[15] Training with signal and background MC samples, separated by conversion type and in η bins, with a selection on low E_{T} photons with $25\,\text{GeV} < E_{\text{T}} < 60\,\text{GeV}$ and applying loose ID cut, but no isolation.

The corresponding performance plots of the BDT output as classifier score are shown exemplary for unconverted photons in $|\eta| < 0.6$ in Figure 4.11. With the working point of $\epsilon_{\text{sig}} = 0.87$, the cut value on the classifier score was evaluated to be 0.028.
For the evaluation of the optimized BDT classification, the loose-to-tight photon identification efficiency for signal and background photons as function of the transverse energy can be used. In Figure 4.12, the tight photon identification for the BDT approach is compared to the reoptimized tight ID menu for Run 2 performed with rectangular cuts. Here, unconverted photons in $|\eta| < 0.6$ and with the *FixedCutLoose* isolation working point are selected as example.

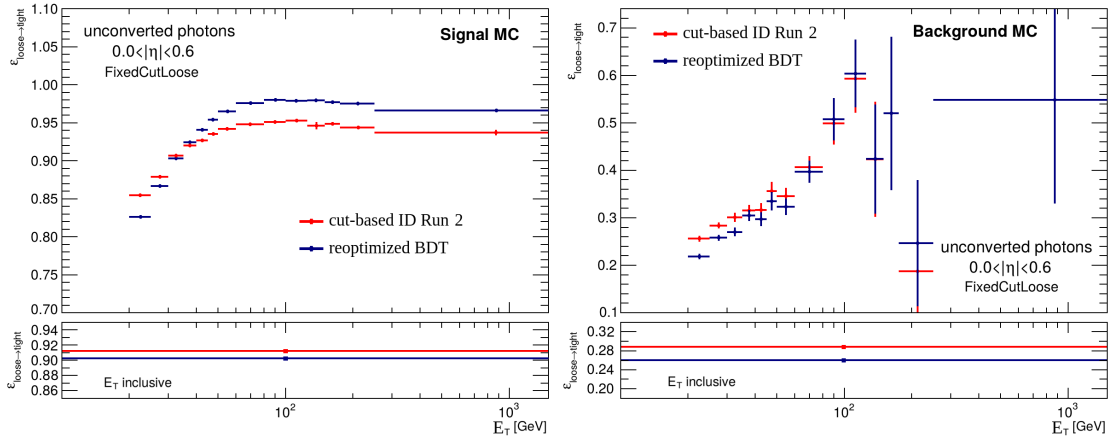

Figure 4.12: Loose-to-tight photon ID efficiency versus transverse energy E_{T}.
Compared are the reoptimized, cut-based tight ID for Run 2 (red) with the BDT optimization (blue) evaluated at a working point of $\epsilon_{\text{sig}} = 0.87$.
The signal (left) and background (right) efficiencies for unconverted photons in $|\eta| < 0.6$ with *FixedCutLoose* isolation applied are shown.

For the signal efficiency, the BDT performance for low-E_{T} photons is worse than the cut-based optimization and vice versa for higher transverse energies. At the same time, the background efficiency is lower for the BDT optimization in the low-E_{T} region, indicating a better rejection of non-prompt photons but by loosing efficiency for prompt photons.
Also a comparable behaviour for the pile-up dependence of the tight photon identification between the cut-based and the BDT optimization can be observed, as shown in Figure 4.13.

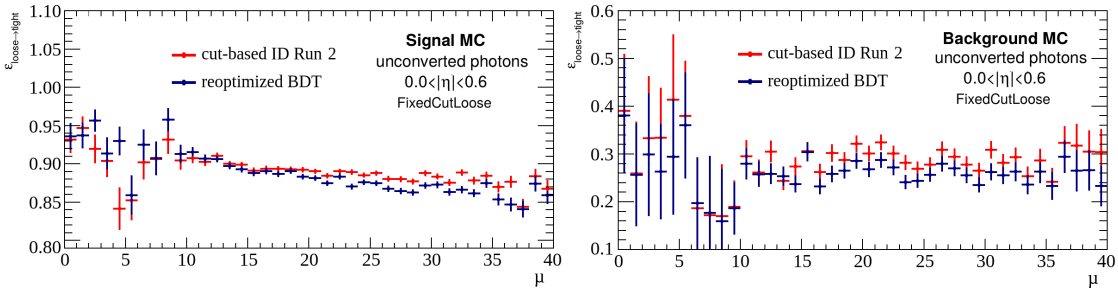

Figure 4.13: Loose-to-tight photon ID efficiency versus pile-up μ.
Compared are the reoptimized, cut-based tight ID for Run 2 (red) with the BDT optimization (blue) evaluated at a working point of $\epsilon_{\text{sig}} = 0.87$.
The signal (left) and background (right) efficiencies for unconverted photons in $|\eta| < 0.6$ with *FixedCutLoose* isolation applied are shown.

In general, the performance of the tight ID optimized with the BDT approach is better or at least equal to the cut-based optimization. Moreover, the working point of $\epsilon_{\text{sig}} = 0.87$ was selected to allow for a comparison with the cut-based tight ID, but is not the optimal cut value in terms of maximizing the significance (cf. Fig. 4.11).
To analyse the BDT performance in more detail, a study on the discrimination power of the individual shower shape variables in the BDT was conducted with the so-called *N-1 test*. Here, the BDT training is repeated systematically with excluding in every iteration one of the discriminating input variables and the performance of these different cases is then compared. In Figure 4.14, the individual ROC curves in the N-1 study for unconverted photons in $|\eta| < 0.6$ are overlayed and compared to the performance of the BDT training with the full variable input set. When excluding a variable with a good discrimination power, the ROC curve is expected to be lower than the case of using all variables and vice versa for the case of variables with less discrimination power.

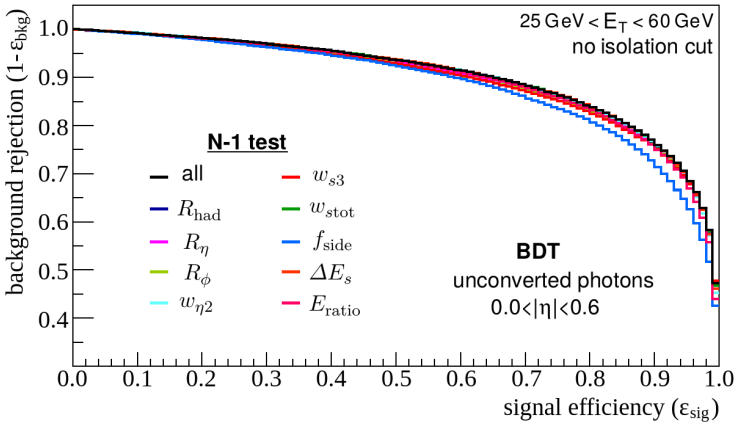

Figure 4.14: Comparison of ROC curves for the N-1 study. Single variables (as stated in the legend) are excluded systematically from the BDT training and the performances are compared to the "all variable case" (black). The results are shown exemplary for unconverted photons in $|\eta| < 0.6$.

To assess the quality of the individual shower shape variables by the N-1 test in a more quantitative way, Table 4.5 shows the calculated AUC for the full region as well as the ROI for the cases of unconverted and converted photons in $|\eta| < 0.6$ and $0.6 \leq |\eta| < 0.8$.

	unconverted				converted			
N-1	$0.0 \leq \lvert\eta\rvert < 0.6$		$0.6 \leq \lvert\eta\rvert < 0.8$		$0.0 \leq \lvert\eta\rvert < 0.6$		$0.6 \leq \lvert\eta\rvert < 0.8$	
variable	full	ROI	full	ROI	full	ROI	full	ROI
R_{had}	90.00	8.75	88.67	8.44	89.12	8.62	87.69	8.39
R_η	89.93	8.75	88.40	8.41	89.68	8.77	87.74	8.40
R_ϕ	89.75	8.72	88.32	8.36	*89.99*	*8.81*	*88.36*	*8.52*
$w_{\eta 2}$	90.25	8.80	*89.00*	*8.47*	89.84	8.79	88.28	8.48
w_{s3}	89.63	8.69	88.43	8.37	89.40	8.67	87.88	8.39
w_{stot}	*90.32*	*8.83*	*88.98*	*8.48*	*89.97*	*8.82*	88.31	8.48
f_{side}	**88.53**	**8.42**	**87.33**	**8.11**	**88.16**	**8.40**	**86.78**	**8.14**
ΔE_s	*90.35*	*8.83*	*88.92*	*8.47*	*90.01*	*8.82*	*88.41*	*8.50*
E_{ratio}	89.95	8.73	88.52	8.34	89.52	8.73	88.03	8.38
all	90.37	8.83	89.03	8.50	89.97	8.81	88.43	8.50

Table 4.5: Comparison of AUC performance for the N-1 study in the full region as well as the ROI for the cases of excluding single variables from the BDT training. The **best performing** and the *worst performing* variables in the N-1 test are marked, respectively. The AUC values are shown exemplary for unconverted and converted photons in $|\eta| < 0.6$ and $0.6 \leq |\eta| < 0.8$.

In all four optimization regions, the best performing variable with the highest reduction of the AUC performance is the shower shape f_{side}. On the contrary, a smaller discrimination power can be assigned to the variables $w_{\eta 2}$, w_{stot} and ΔE_s.
The performance in terms of the resulting loose-to-tight photon ID efficiency for the cases of excluding f_{side} as best performing and ΔE_s as one of the worse performing variables compared to the all variable case is shown in Figure 4.15 for unconverted photons in $|\eta| < 0.6$. Here, the rejection of non-prompt photons is significantly reduced when excluding the discriminating f_{side} variable from the BDT training, whereas the signal efficiency for higher transverse energies is reduced when excluding the ΔE_s variable.

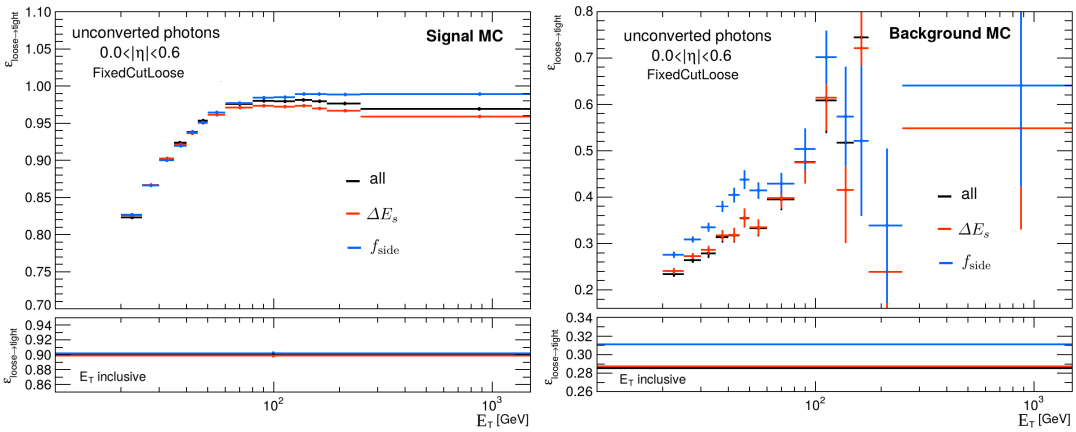

Figure 4.15: Loose-to-tight photon ID efficiency versus transverse energy E_{T}. Compared are the BDT training results with all variables (black), without ΔE_s (orange) and without f_{side} (lightblue). The signal (left) and background (right) efficiencies for unconverted photons in $|\eta| < 0.6$ with *FixedCutLoose* isolation applied are shown.

The result of the N-1 test is that clearly the f_{side} variable has an important role for a good discrimination of prompt photons, but the conclusion to exclude the worse performing variables from the training is not necessarily the best option, as a BDT with a small depth gains performance from weak classifiers due to the boosting step.

4.4.3 Study on a two-BDT approach

In the previous section, the tight photon identification based on a BDT approach showed already a good performance compared to the cut-based optimization as baseline.
To implement a MVA-based ID, the initially discussed prerequisites from the data-driven efficiency measurements have to be fulfilled to allow for an application in physics analyses. One of the prerequisites from the matrix method (cf. Sec. 3.5.3) is that the photon identification criterion is not strongly correlated with the photon isolation. This is due to the fact that the background efficiency of photons passing the tight ID is estimated by the inversion of individual cut values on the shower shape variables which are expected to be uncorrelated to the isolation criterion as used for the inclusive photon selection.

As this approach is not possible for a tight ID based on a BDT, a different strategy was developed: The idea is to train two independent BDTs using sub-selections of the nine shower shape variables as inputs and acquiring two output BDT classifiers which can be combined in a second optimization step for the tight photon identification.

But also one of the two classifiers should be least correlated to the photon isolation, so that the criterion on this classifier can be inverted for the selection in the matrix method, similar to the current usage with the cut-based ID menu.
For the selection of shower shape variables into the two categories, with one set least correlated to the isolation working points, the linear correlation coefficients of the shower shapes to the three used isolation requirements, namely *FixedCutLoose*, *FixedCutTight* and *FixedCutTightCaloOnly*, were used, as shown in Figure 4.16 for the exemplary case of converted photons in $|\eta| < 0.6$ and with the used training selection.

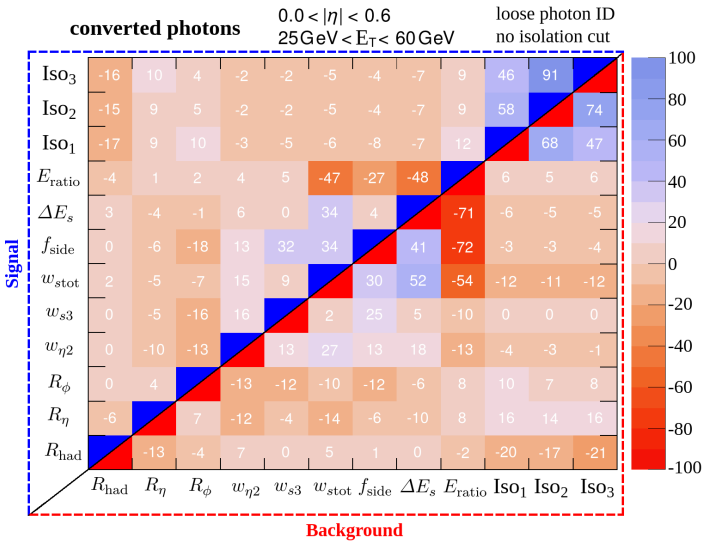

Figure 4.16: Linear correlation matrix of shower shape variables and isolation working points (Iso_1 = *FixedCutLoose*, Iso_2 = *FixedCutTight*, Iso_3 = *FixedCutTightCaloOnly*) for converted photons in the $|\eta| < 0.6$ bin with loose ID applied. Compared are photon candidates from signal MC (left matrix half) and background MC (right matrix half).

Into the category of variables with least correlation to the isolation, the shower shape variables w_{s3}, f_{side}, ΔE_s and E_{ratio} are assorted, called in the following *narrow-strip* variables due to their derivation from quantities in the first, fine granularity layer of the EM calorimeter. The shower shapes R_{had}, R_η, R_ϕ, $w_{\eta 2}$ and w_{stot} are accordingly assorted in the other category, called *relaxed-tight* variables.

In the next step, two BDTs with the same configuration but with the two different input variable sets were trained. The performance of the two-BDT approach can be compared to the trained BDT with all variables in terms of the ROC curve, as shown in Figure 4.17 for unconverted photons in $|\eta| < 0.6$. Here, as expected the two individual trained BDTs are not as well performing as the BDT trained on the full variable set. The narrow-strip variables performing also better in the discrimination than the relaxed-tight variables.

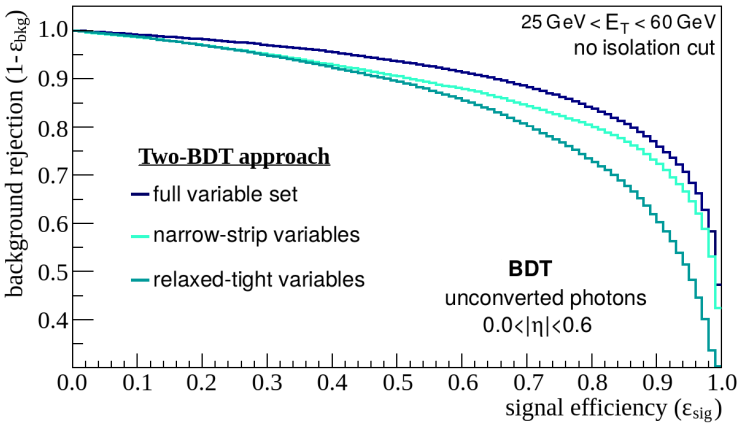

Figure 4.17: Comparison of ROC curves for the two-BDT approach. The performance of the BDTs trained with all variables (blue), with the *narrow-strip* variables (cyan) and with the *relaxed-tight* variables (petrol) are compared, as shown exemplary for unconverted photons in $|\eta| < 0.6$.

After the training, the two newly derived BDT classifier scores, called $\mathrm{BDT}_{\text{relaxed-tight}}$ and $\mathrm{BDT}_{\text{narrow-strip}}$, can be added to the signal and background photon sample on an event-by-event basis and a detailed analysis of the classifier properties can be conducted with the *PhotonIDOptimizer* framework using the new data samples as input.
On the one hand, the linear correlation coefficients of the BDT classifiers to the isolation working points can be checked, which is shown in Figure 4.18. The classifier score from the BDT trained on the narrow-strip variables shows indeed lower correlation coefficients to the isolation working points for the signal as well as the background photon sample than the classifier from the BDT trained with the relaxed-tight variables. Moreover, large positive correlations can be found between the classifiers itself and to the cut-based tight ID, which is expected as all provide discrimination for the classification problem.

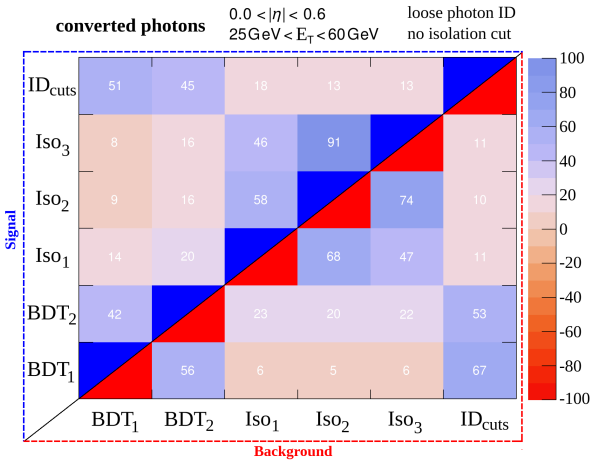

Figure 4.18: Linear correlation matrix of BDT classifiers (BDT_1 = *narrow-strip*, BDT_2 = *relaxed-tight*) and isolation working points (Iso_1 = *FixedCutLoose*, Iso_2 = *FixedCutTight*, Iso_3 = *FixedCutTightCaloOnly*) as well as the cut-based tight ID ($\mathrm{ID}_{\text{cuts}}$) for converted photons in the $|\eta| < 0.6$ bin with loose ID applied. Compared are photon candidates from signal MC (left matrix half) and background MC (right matrix half).

On the other hand, the two-dimensional phase space of the two derived BDT classifiers can be analysed for the signal and background photon sample, as done in Figure 4.19. Here, a partly rectangular shape in the distributions can be observed, allowing to determine the tight photon identification as the combination of the two BDTs by a cut-based optimization with the classifier scores as input.

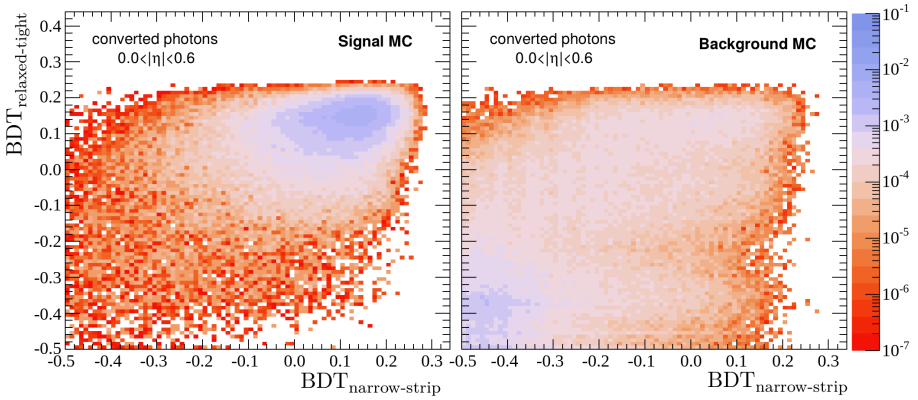

Figure 4.19: Distribution of classifiers $\mathrm{BDT}_{\text{relaxed-tight}}$ and $\mathrm{BDT}_{\text{narrow-strip}}$ for signal and background MC sample, exemplary shown for converted photons in $|\eta| < 0.6$.

Therefore, the *PhotonIDOptimizer* framework was used for a second optimization with the cut-based approach, using the same parameter settings as before[16].

[16] Due to the input set of only two variables, another iteration of optimizing the parameter settings for this case could improve the performance.

The performance of the two-BDT approach is evaluated with the loose-to-tight photon identification efficiency for signal and background photons as function of the transverse energy, as shown in Figure 4.20 for converted photons in $|\eta| < 0.6$ fulfilling the *FixedCutLoose* isolation. Here, the efficiencies for the two-BDT approach are compared to the BDT training with all variables as input and to the cut-based tight ID menu for Run 2.

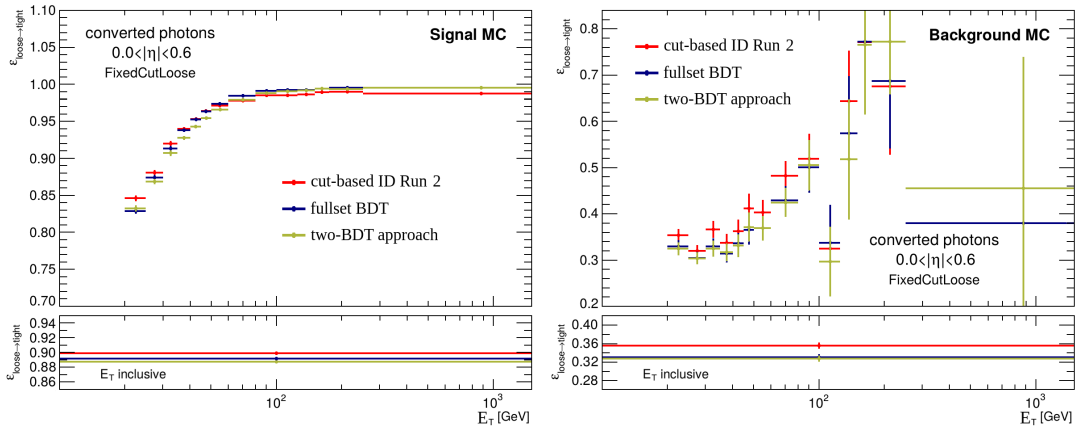

Figure 4.20: Loose-to-tight photon ID efficiency versus transverse energy E_{T}. Compared are the two-BDT approach (lightgreen) with the fullset BDT (blue) and the cut-based tight ID for Run 2 (red), evaluated at $\epsilon_{\mathrm{sig}} = 0.87$. The signal (left) and background (right) efficiencies for converted photons in $|\eta| < 0.6$ with *FixedCutLoose* isolation applied are shown.

Similar efficiencies for signal and background are observed for the two-BDT approach compared to the BDT trained with all variables. Therefore, as the next stage for this study, the performance in the matrix method should be tested to verify that the strategy with two separately trained BDTs allows for an application of a MVA-based tight photon identification in the ATLAS experiment.

4.4.4 Study of p_{T}-dependent BDT

In a final study of the application of a BDT for the tight photon identification optimization, a p_{T}-dependent training was studied. As at the same time, the tight photon ID was again reoptimized using a p_{T}-dependent cut-based optimization, the same approach should be tested for the BDT training. In general, some of the shower shape variables show a strong dependence on the transverse momentum of the photon candidate (cf. Sec. 3.4.2), motivating the p_{T}-dependent training approach.
For the BDT training, four different configurations are defined: an inclusive training selection in p_{T} (*PtInclusive*) and selections for low, medium and high p_{T} photons with $25\,\mathrm{GeV} < p_{\mathrm{T}} < 35\,\mathrm{GeV}$ (*PtLow*), $35\,\mathrm{GeV} < p_{\mathrm{T}} < 60\,\mathrm{GeV}$ (*PtMedium*) and $60\,\mathrm{GeV} < p_{\mathrm{T}} < 100\,\mathrm{GeV}$ (*PtHigh*), respectively.
The results are evaluated globally across the training selection by reconstructing the ROC curves for the full data sample and not only using the ROC curve performance in the individual selections. The performance of the four BDTs can then be evaluated in four equally defined evaluation regions as used for the training, to study systematically the effect of the p_{T}-dependent training. Moreover, the influence of the isolation is tested, by comparing ROC curves evaluated on all photons with photons fulfilling the *FixedCutLoose* requirement. The cut-based tight ID working point[17] is marked for both cases.

[17] The cut-based tight ID is derived from a p_{T}-inclusive training and not yet from a p_{T}-dependent training.

In Figure 4.21, the BDT performances are compared in the described way for the four evaluation regions, *PtInclusive*, *PtLow*, *PtMedium* and *PtHigh*.

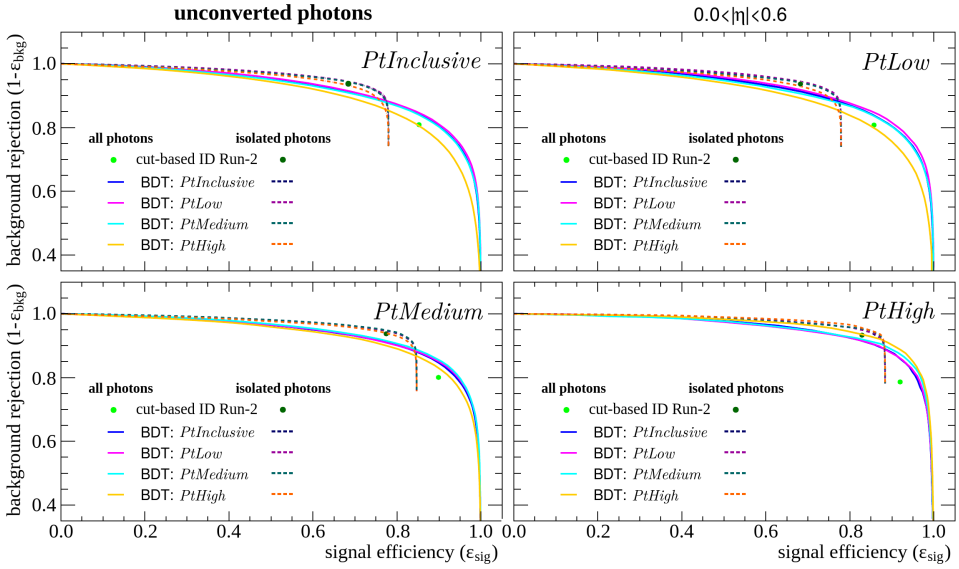

Figure 4.21: Comparison of ROC curves for p_{T}-dependent BDTs, trained as well as evaluated in the four defined p_{T} regions *PtInclusive*, *PtLow*, *PtMedium* and *PtHigh*. Unconverted photons in $|\eta| < 0.6$ are selected and used either as full sample or with *FixedCutLoose* isolation applied.

To assess the effect of the p_{T}-dependent training in the different evaluation regions quantitatively, the factor of signal enhancement, $\mathrm{f_S}$, and the factor of background rejection increase, $\mathrm{f_R}$, is introduced as

$$\mathrm{f_S} = \frac{\epsilon_{\mathrm{sig}}^{\mathrm{BDT}}}{\epsilon_{\mathrm{sig}}^{\mathrm{cuts}}} \quad \text{and} \quad \mathrm{f_R} = \frac{R^{\mathrm{BDT}}}{R^{\mathrm{cuts}}} = \frac{\epsilon_{\mathrm{bkg}}^{\mathrm{cuts}}}{\epsilon_{\mathrm{bkg}}^{\mathrm{BDT}}}. \tag{4.1}$$

As such, the relative performance gain between the cut-based tight ID working point and the different BDT outputs can be calculated and the best performing combination of defined p_{T} training region and the evaluation region can be found. This is shown in Table 4.6 for an example of unconverted photons in $|\eta| < 0.6$.

evaluation region		$\mathrm{f_S}$				$\mathrm{f_R}$			
		PtInclusive	*PtLow*	*PtMedium*	*PtHigh*	*PtInclusive*	*PtLow*	*PtMedium*	*PtHigh*
all photons	*PtInclusive*	1.0486	**1.0569**	1.0470	0.9949	1.0404	**1.0460**	1.0381	0.9954
	PtLow	1.0444	**1.0586**	1.0427	0.9865	1.0368	**1.0490**	1.0348	0.9883
	PtMedium	1.0465	1.0516	**1.0551**	1.0306	1.0579	1.0628	**1.0690**	1.0368
	PtHigh	1.0468	1.0511	1.0572	**1.0613**	1.0929	1.0943	1.1107	**1.1292**
isolated photons	*PtInclusive*	1.0279	**1.0347**	1.0257	0.9723	1.0064	**1.0072**	1.0057	0.9940
	PtLow	1.0279	**1.0433**	1.0270	0.9687	1.0062	**1.0091**	1.0056	0.9933
	PtMedium	1.0355	1.0389	**1.0433**	1.0074	1.0098	1.0099	**1.0119**	1.0021
	PtHigh	1.0383	1.0431	1.0506	**1.0547**	1.0195	1.0174	1.0211	**1.0245**

Table 4.6: Comparison of $\mathrm{f_S}$ and $\mathrm{f_R}$ values for the four defined training and evaluation regions in p_{T} for photons with and without isolation applied. Values are shown exemplary for unconverted photons in $|\eta| < 0.6$ with the value for the best performing training in each evaluation region highlighted.

The conclusion from this study on the p_{T}-dependent training of a BDT is that a training performed in the *PtLow*, *PtMedium* and *PtHigh* region gives the best optimization result in terms of the factors $\mathrm{f_S}$ and $\mathrm{f_R}$ in the respective evaluation region. Therefore, this result indicates a better performance for a p_{T}-dependent training instead of a p_{T}-independent training. In case of the selection of only one training region, the *PtLow* region should be selected as it shows good performance results in all evaluation regions.
When comparing the values for the case of all photons with the case of applying *FixedCutLoose* isolation, the performance gain in all scenarios is reduced. Especially the gain in the background rejection is nearly neutralized for the evaluation with isolated photons. This observation can be interpreted that the determined tight ID from the BDT overlaps with the definition of the photon isolation requirements, reducing the number of background photons in the sample already by the isolation cuts.

4.5 Conclusion

The optimization of the tight photon identification working point requires to apply a set of selection criteria on the discriminating shower shape variables. Here, the different features of signal-like prompt photons and background-like non-prompt photons from hadronic jets or fakes when showering in the EM calorimeter of the ATLAS detector are exploited. The currently employed optimization using rectangular cuts on the discriminating variables shows good results in terms of signal efficiency and background rejection. Moreover, the cut-based approach is the easiest solution to the classification problem and allows for a straightforward implementation and an easy interpretation. Nonetheless, with this univariate method not all features of the optimization phase space are exploited as it is possible with a photon identification based on a multivariate technique.

The goal in this work was to path the way for a MVA-based photon identification in the ATLAS experiment by conducting dedicated studies to explore the potential of MVA techniques on the problem of optimizing the performance of the tight photon identification. For this purpose a versatile optimization tool with the *PhotonIDOptimizer* framework was developed and in the first step validated with the currently employed tool for the cut-based optimization. The developed framework offers not only the possibility to train different optimization approaches such as a BDT, but allows also for a detailed analysis of the performance of the optimization output, e.g. by evaluating the identification efficiency for signal and background samples as function of the photon energy E_{T} or the pile-up μ.

With the *PhotonIDOptimizer* framework, it was possible to perform dedicated studies in the ongoing process of reoptimizing the tight photon identification for the data analysis in Run 2 with the ATLAS experiment, as it was needed due to the changed operation conditions. The optimization parameters of the cut-based approach were systematically studied and the dependencies of the resulting cut values for a tuned tight ID menu were explored. Moreover, the investigations of the cut value on the f_{side} variable and its impact for data-MC differences as studied with photon samples from radiative Z decays had a direct implication for the reoptimized tight ID menu as used for physics analyses with 2015 and 2016 data.

The original idea of studying a MVA-based photon identification was performed using a BDT approach as chosen optimization method in the *PhotonIDOptimizer* framework. Starting again with investigations on the optimal parameter settings for the BDT approach, the performance of the BDT in the tight photon identification was tested and compared to the cut-based ID, showing very comparable results.

Furthermore, a detailed study of the discrimination power of the individual shower shape variables in the BDT approach was conducted, for which the N-1 test allowed for a deeper insight in the BDT performance.

One of the problems of a MVA-based photon identification is the implementation in the data-driven photon efficiency measurements, such as in the matrix method. Here, the tight photon ID should be least correlated to the photon isolation to acquire an inclusive photon sample for the efficiency measurement. In the cut-based approach, this is easy doable by inverting a number of tight ID cuts on the shower shape variables, but for a BDT approach another strategy had to be developed. Therefore, two separate BDTs are trained on two sets of shower shape variables with two classifier outputs. It was proven that one of the classifiers is least correlated to the isolation requirement and could be used in the matrix method similar as for the cut-based ID. With the combination of both classifiers based on rectangular cuts, the tight photon ID is determined in the two-BDT approach. Here, good performance results are observed when comparing to the full BDT approach as well as to the cut-based tight ID for Run 2. In the next step, the two-BDT approach have to be tested in the matrix method to evaluate the performance also in the data-driven efficiency measurements and to check the application strategy.

For the next iteration of reoptimizing the cut-based tight ID, it was decided to use a p_{T}-dependent optimization approach to exploit also the shower shape dependence on the transverse photon energy in the optimization. In parallel, the impact of a p_{T}-dependent training for a BDT was investigated with the *PhotonIDOptimizer* framework. It shows that also for the BDT case a p_{T}-dependent training results in a performance gain. But it was also observed that the application of a photon isolation requirement together with the tight photon ID requirement has a big influence on the performance gain of the method, which should be studied in more detail.

Chapter 5

High-Luminosity LHC and the ATLAS ITk Detector

The LHC physics programme will be extended with an upgrade of the accelerator in 2024 to reach the highest levels of luminosity and to deliver even more pp collisions to the experiments from 2026 onwards. This running phase is the so-called **H**igh-**L**uminosity **LHC** (HL-LHC) and its technical challenges as well as the physics motivation for the HL-LHC programme will be briefly discussed in Section 5.1.

With an upgraded accelerator, the beam conditions for the experiments will also change dramatically posing new challenges to the detectors. As an example, an average pile-up of $\langle\mu\rangle = 200$ as well as unprecedented levels of radiation are expected for the HL-LHC operation, requiring upgraded detector systems to withstand these harsh conditions as well as to maintain the high measurement precision. For the ATLAS experiment, the so-called ATLAS Phase-2 Upgrade programme was developed. In this programme the different subdetectors will be upgraded, including the inner tracking detector, the calorimeter system, the muon spectrometer and the **T**rigger and **D**ata **A**c**Q**uisition (TDAQ) system, as schematically shown in Figure 5.1. The technical details of the developed upgrade plans for each subsystem are published in **T**echnical **D**esign **R**eports (TDRs).

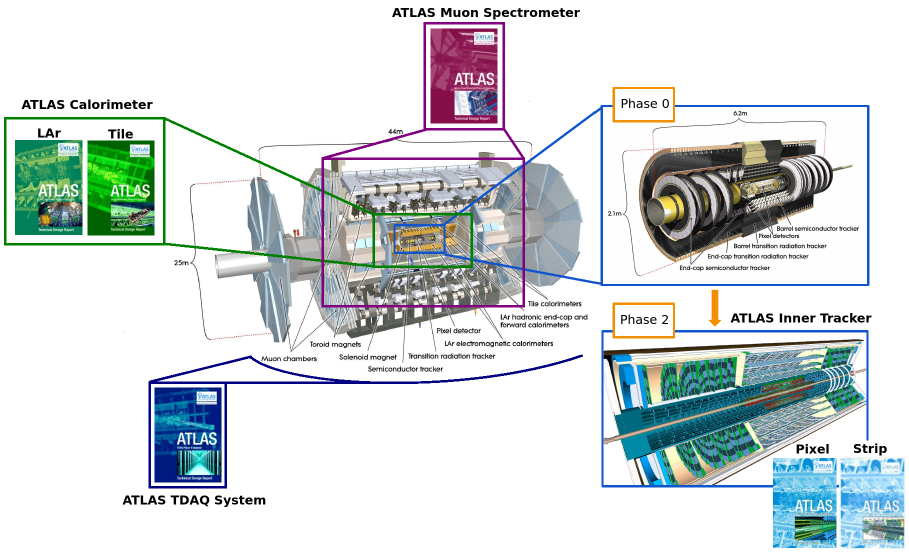

Figure 5.1: Programme for the ATLAS Phase-2 upgrade for the HL-LHC phase.

The range of the involved upgrade activities spans from replacements of readout electronic boards in the calorimeters, over the installation of faster signal transmissions and upgraded logic processors for the TDAQ system to a full replacement of the current tracking detector by a new system, the ATLAS **I**nner **T**rac**k**er (ITk). An overview about the planned ITk detector with its design choices to fulfill the physics requirements and to cope with the challenging environment of the HL-LHC is given in Section 5.2.

For this thesis, a subpart of the ATLAS ITk detector was the topic of study: the ITk strip end-cap detector. In Section 5.3 the full concept of the detector subsystem is introduced, starting with the sensor and its readout electronics, followed by the design of the local support structures and ending with the integration into the global system structure. Moreover, aspects like production planning and tracking and plans for **Q**uality **A**ssurance (QA) and **Q**uality **C**ontrol (QC) testing during production will be addressed.

5.1 The High-Luminosity Phase of the LHC

The LHC operation in its current mode at a center-of-mass energy of 13 TeV (with the possibility to be increased to 14 TeV) and an instantaneous luminosity of $2 \cdot 10^{34}\,\mathrm{cm}^{-2}\,\mathrm{s}^{-1}$ will proceed for Run-3 scheduled for 2021 to 2024 (cf. Sec. 1.2.3).
In Long Shutdown 3 (LS3) the machine will be upgraded for the **H**igh-**L**uminosity **LHC** (HL-LHC) phase aiming for levelled luminosities of $(5-7) \times 10^{34}\,\mathrm{cm}^{-2}\,\mathrm{s}^{-1}$ with the goal to deliver an integrated luminosity of up to $4\,000\,\mathrm{fb}^{-1}$ to the experiments by 2040.
The technical challenges of the accelerator upgrades are discussed in Section 5.1.1 and the motivation in terms of the physics programme conducted at the HL-LHC is given in Section 5.1.2.

5.1.1 Accelerator upgrades

The upgrades on the accelerator required to reach this luminosity increase, which depends on several input parameters for the instantaneous luminosity (cf. Eq. 1.9), will provide the following features:

- **Number of protons N**: The number of protons per bunch will be nearly doubled, resulting in a beam current of over 1 A exceeding the ultimate beam conditions which were anticipated when building the LHC and posing challenges to the systems (e.g. RF cavities and cryogenic systems).
- **Beam beta function β^***: By using stronger and larger aperture quadrupole magnets for focusing the beam at the interaction points, β^* can be reduced from 0.55 to 0.2.
- **Geometrical reduction factor R**: As a result of the stronger beam focusing, the beams crossing angle is increased reducing the geometrical reduction factor R. To mitigate this effect, crab cavities will be used to turn the proton bunches at the interaction points to allow a better overlap.
- **Transverse normalized emittance ϵ_n**: For a higher brightness of the beam, the emittance have to be reduced. As the emittance cannot be lowered along the accelerator chain, a smaller emittance must be achieved at the start of the chain. Therefore, the injector system will be renewed by replacing the current LINAC2 with LINAC4 providing a doubled beam brightness.

Further details about the machine parameters and the upgrade programme itself can be found in [143].

5.1.2 Physics motivation

Current physics analyses and their interpretations are often constrained by their statistical uncertainty instead of systematic uncertainties from the measurement itself. Therefore, from a physics point-of-view, the HL-LHC will help to test the SM with even higher precision. The collection of more collision data allows to perform precision measurements with a higher accuracy, but also to search for new phenomena linked with BSM theories (cf. Sec. 1.4.2) such as supersymmetry or the search for Dark Matter at high-energy colliders. A comprehensive report about the wide-ranging physics potential of the HL-LHC programme can be found in [144].
Here, as one example the HL-LHC projections for measurements in the Higgs sector (cf. Sec. 1.3.2) are briefly themed. More collision data allows to test the Higgs boson decays with high accuracy and opens up the possibility to precisely measure also the differential cross sections[18] enabling to test differential properties of the SM Higgs boson. Also, the precise measurement of the coupling strengths of the Higgs boson to the SM fermion and gauge bosons is an important test. With $3\,000\,\text{fb}^{-1}$ of data, most of the coupling strengths κ could be measured with a total uncertainty of below 4% as shown in Figure 5.2.

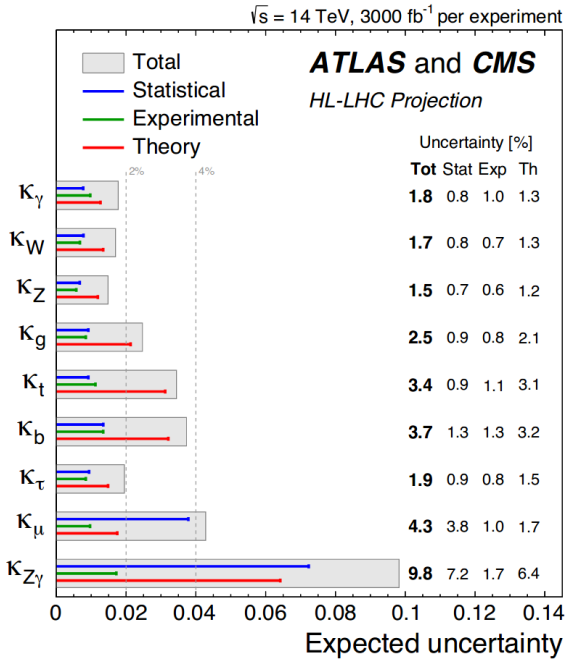

Figure 5.2: HL-LHC projection of expected uncertainties for Higgs couplings [144]. Shown are the statistical, experimental and theoretical uncertainties for the coupling strengths κ of SM fermion and gauge bosons to the Higgs boson expected for $3\,000\,\text{fb}^{-1}$ of data.

5.2 The ATLAS Inner Tracker

For the HL-LHC phase, the current tracking detector of the ATLAS experiment, the ATLAS **I**nner **D**etector (ID) (cf. Sec. 2.3.2), will be completely replaced by the ATLAS **I**nner **T**rac**k**er (ITk). The ATLAS ID with its subsystems IBL, Pixel, SCT and TRT was designed for LHC running conditions, meaning 10 years of operation at the nominal instantaneous luminosity of $10^{34}\,\text{cm}^{-2}\,\text{s}^{-1}$, a center-of-mass energy of 14 TeV, a 25 ns bunch spacing and an average pile-up of 23 pp interactions per bunch crossing. As some of these specifications are even surpassed in the current running conditions for Run 2, the detector performance would significantly degrade at HL-LHC conditions if not even fail completely.

[18] In the observation channels, $H \to 4l, \gamma\gamma$, first results of differential cross sections with Run-2 data were already published [51, 52].

Therefore, in LS3 a full-replacement of the tracking detector is planned using the same inner detector volume within the 2 T solenoid magnet. The main goal of the design of the ITk, featuring only silicon detectors, is to deliver equal or better tracking performance compared to the current ID, although the operating conditions are much more challenging. In Section 5.2.1 the tracking detector requirements and challenges posed by the HL-LHC conditions are discussed, which led to the planned detector design as introduced in Section 5.2.2.

5.2.1 ITk requirements & challenges

The main challenges arising with the expected HL-LHC conditions and the requirements on the ITk detector performance can be categorized in the following way:

Occupancy and track rate

With the expected number of pp interactions per bunch crossing, ranging on average between $\langle\mu\rangle = 140$ to 200, the tracking detector has to cope with a very high track rate. This environment is depicted in Figure 5.3, showing the occupancy of the tracking detector volume comparing LHC Run-2 conditions with $\langle\mu\rangle = 60$ to HL-LHC operation with the expected pile-up of $\langle\mu\rangle = 200$.

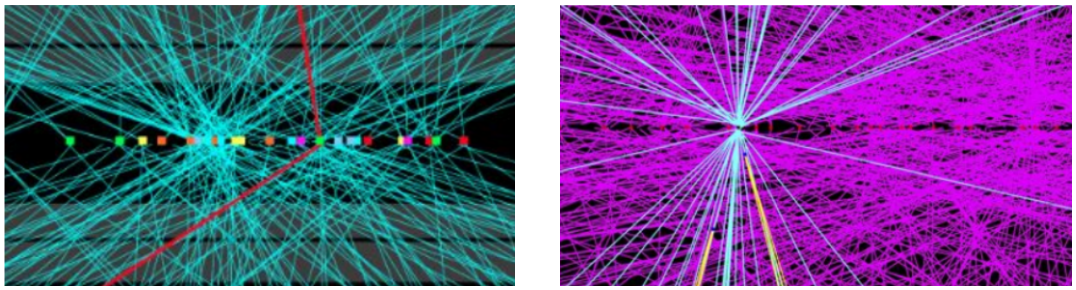

(a) LHC Run 2 with $\langle\mu\rangle = 60$. **(b)** HL-LHC with $\langle\mu\rangle = 200$.

Figure 5.3: Simulation of track occupancy close to the IP shown for pile-up conditions of LHC Run 2 and HL-LHC in $t\bar{t}$ event.

In order to maintain the tracking performance required for a precise object reconstruction for charged particles, meaning to separate multiple nearby tracks and to reconstruct vertex positions, the granularity of the detector must be increased accordingly.

Radiation damage

Due to the large number of produced particles in pp collisions, a high particle fluence with high radiation levels is expected. The sensors, the readout electronics and the structural elements of the detector have to withstand these radiation levels, requiring them to be radiation hard up to unprecedented levels.
The simulated fluence and radiation dose for an integrated luminosity of $4\,000\,\text{fb}^{-1}$ are shown in Figure 5.4 for a quarter segment of the detector. Comparing the expected radiation levels for the HL-LHC operation to the current radiation levels experienced by the ATLAS ID, an increase by a factor of ten is observed. Here, the radiation levels decrease from the inner detector layers to the outer layers due to the distance from the IP, but also the forward region of the detector will be exposed to higher fluences.

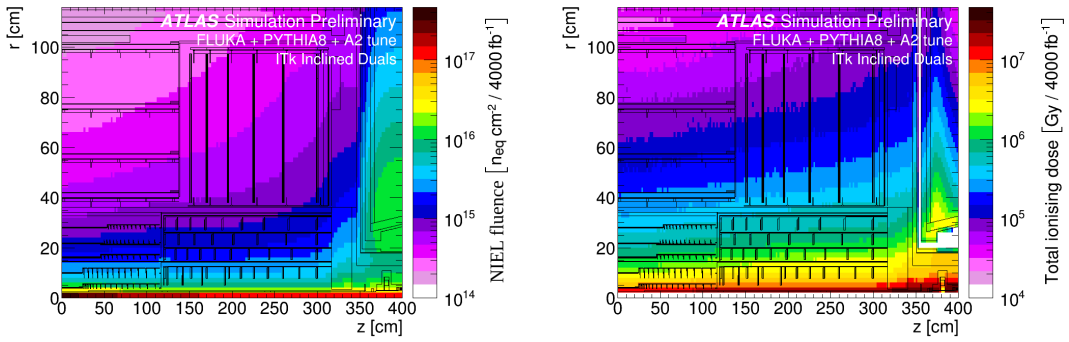

(a) 1 MeV neutron equivalent fluence. **(b)** Total ionizing dose.

Figure 5.4: Simulated radiation environment for the ATLAS ITk detector for an integrated luminosity of $4\,000\,\mathrm{fb}^{-1}$. Shown is one quarter segment of the detector with the IP at zero, the beam line aligned along the horizontal axis and the radius as the vertical axis. Figures taken from [145].

Data rate and triggering

With more particle activity in the tracking detector from one bunch crossing but also due to the overlay from previous or following bunch crossings, the factor of fast readout of the sensors is essential. At the same time, due to the increased granularity to provide the required efficiency in the tracking and as such more readout channels, a higher data bandwidth of the readout is necessary. Therefore, fast optical links for data transmission and the ability of event buffering have to be implemented in the tracking detector design to cope with the HL-LHC conditions.
Moreover, the performance of the trigger system is a main challenge for the ATLAS experiment. Currently, the ATLAS ID does not provide any information to the hardware-based **L**evel-**1** trigger (L1) (cf. Sec. 2.3.5). But by adding tracking information to the trigger decision, lower trigger thresholds are possible having a direct benefit for the physics performance. Therefore, the ATLAS ITk detector will provide track information to the trigger system operating at a trigger rate of 1 MHz.

Coverage and material budget

The coverage of the tracking detector in pseudorapidity from currently $|\eta| = 2.7$ for the ID will be extended to $|\eta| = 4$ for the ITk. This is motivated by the requirement of a wide range of physics analyses foreseen for the HL-LHC to allow track reconstruction in the far forward direction by having a larger angular coverage. Examples are an improved identification of hard-scatter vertices relevant for studies of **V**ector **B**oson **F**usion (VBF), a better rejection of pile-up jets, an improved b-jet identification or to reconstruct leptons also in the forward direction, which is especially relevant for BSM analyses.

Another requirement for the design of a tracking detector is to minimize its material budget, as any additional material deteriorates the tracking performance due to multiple scattering and create photon conversions and energy loss of particles before the calorimeters. In Figure 5.5, the material distribution in units of radiation length (X_0) versus the pseudorapidity is shown, comparing the current ATLAS ID to the expected material budget distribution of the ITk detector. As it can be observed, the material budget can be reduced in the planned ITk detector by around 30% for $|\eta| < 4$ and even more for higher $|\eta|$ regions.

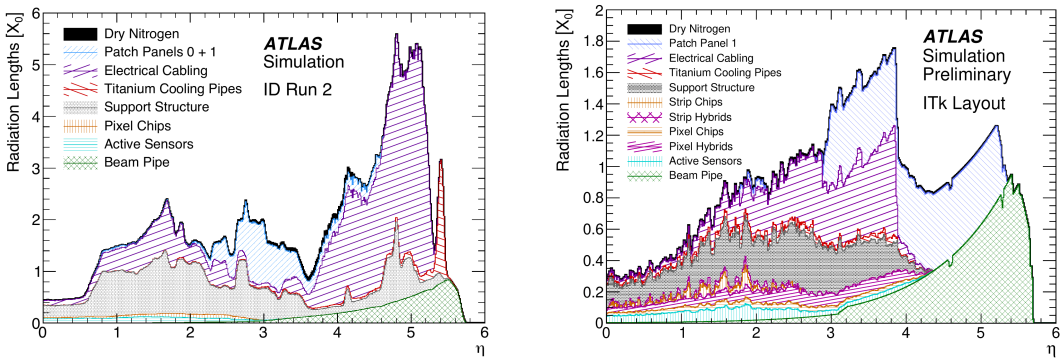

(a) ATLAS Inner Detector. **(b)** ATLAS ITk detector.

Figure 5.5: Material budget distribution along η in units of radiation length X_0 separated by material categories, comparing the current ATLAS Inner Detector with the planned ATLAS ITk detector. Figures taken from [146] and [147].

5.2.2 ITk detector design

The ATLAS ITk detector design addresses the demanding requirements and challenges coming from the HL-LHC running conditions as explained before. The ITk detector as replacement of the current ATLAS ID will be an all-silicon tracking detector to reach the required tracking resolution due to the expected pile-up levels.
Moreover, it consists of a silicon pixel detector subsystem (*ITk Pixel detector*) in the region closest to the beam pipe and a silicon microstrip detector subsystem (*ITk Strip detector*) at higher radii from the beam pipe. With this separation, the granularity of the detector is optimized to resolve nearby tracks while minimizing against the number of readout channels and cost of the system. Each detector subsystem is divided into a *barrel* region, located centrally around the IP, and two *end-caps* covering the forward regions of the detector. An overview of the ITk detector layout is depicted in Figure 5.6.

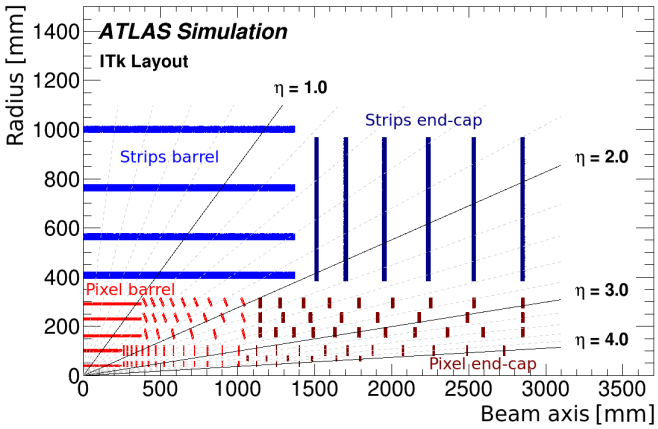

Figure 5.6: Layout for the ATLAS ITk detector separated in the *barrel* and *end-cap* region and the *pixel* subsystem (red) and the *strip* subsystem (blue). Shown is one quarter of the detector with the IP at zero, the beam line aligned along the horizontal axis and the radius as the vertical axis.
Modified from [147].

ITk Pixel detector

The ITk Pixel detector [148] uses silicon pixel modules with pixel sizes down to $50 \times 50\,\mu m^2$ allowing a very fine sensor granularity. The sensor technology (planar and 3D silicon sensors) is taken over from the experience of the Pixel and IBL detector from the ATLAS ID and a new front-end chip (RD-53) is being developed in 65 nm CMOS technology.

The barrel region of the ITk Pixel detector will consist of five layers populated with sensor modules, whereas in the forward region inclined modules are used. This is completed by the pixel end-cap system consisting of four individually located ring layers with modules. Due to the severe radiation damage (up to $2 \times 10^{16}\, n_{\mathrm{eq}}/\mathrm{cm}^2$) accumulating especially in the innermost pixel layers, the design of the detector allows for a potential replacement of the two innermost barrel layers as well as the innermost end-cap ring layer.
Overall, the ITk Pixel detector provides hermetic tracking coverage up to $|\eta| = 4$, covers roughly $14\,\mathrm{m}^2$ of silicon and features 580 million readout channels. The data transmission, powering and cooling of the individual modules is a big challenge in the design.

ITk Strip detector

The ITk Strip detector [146] uses silicon microstrip modules with different strip lengths and pitch sizes depending on the location in barrel or end-cap. The implementation of a stereo angle allows to measure the second track coordinate and the basic strip concept can be compared to the ATLAS SCT detector.
The barrel section consists of four layers with the two inner layers equipped with strips of 24.1 mm length (short strip/SS) and the two outer with 48.2 mm length (long strip/LS). The strip pitch is 75.5 µm and a stereo angle of ±26 mrad is implemented for each side of the layer by rotating the relative sensor position. The end-cap section is built up of six disks along the beam axis with strip modules radially distributed and the strips pointing to the center of the beam axis. The strip length is changing as function of radius to allow for a constant occupancy level. The same is the case for the strip pitch for the different wedge shaped sensor segments. A stereo angle of ±20 mrad for each side of the disk is implemented by rotating the sensing strips relative to the radial orientation of each disk. Overall, the ITk Strip detector extends to hermetic coverage of up to $|\eta| = 2.7$ and provides 60 million readout channels for a total silicon area of roughly $165\,\mathrm{m}^2$.

5.3 The ATLAS ITk Strip End-cap Detector

The focus in this work is on the end-cap region of the ATLAS ITk Strip detector, but the concept for the barrel and end-cap region is quite similar and follows the same idea: a highly modular approach to allow for parallelization of building components and assembling structures in a distributed production over many worldwide located ITk institutes.

The end-cap structure consists of six disks aligned along the beam axis, and disks are made out of *petals*, which are the main building blocks of the detector. A petal consists of a wedge-shaped support structure called *core* and a number of *silicon modules* glued on both sides of it. A core is the light-weight support structure for the silicon modules, providing data transmission, powering and cooling capabilities. A module is the main sensing element consisting of a wedge-shaped *silicon microstrip sensor* with the readout, control and power electronics directly glued on top. The gateway to the off-detector electronics is provided by the ***E**nd **o**f **S**ubstructure (EoS)* card enabling connections for readout, power and control of the modules via the *bus tapes* at the top and bottom surface of the core.
The basic anatomy of a petal is depicted in Figure 5.7.

In the following the different assembly steps for the end-cap detector will be explained. Starting with the smallest assembly, a silicon module, in Section 5.3.1, which is mounted onto a petal core as local support structure as introduced in Section 5.3.2 and finally integrated into the TDAQ system and the global end-cap structure as shown in Section 5.3.3.

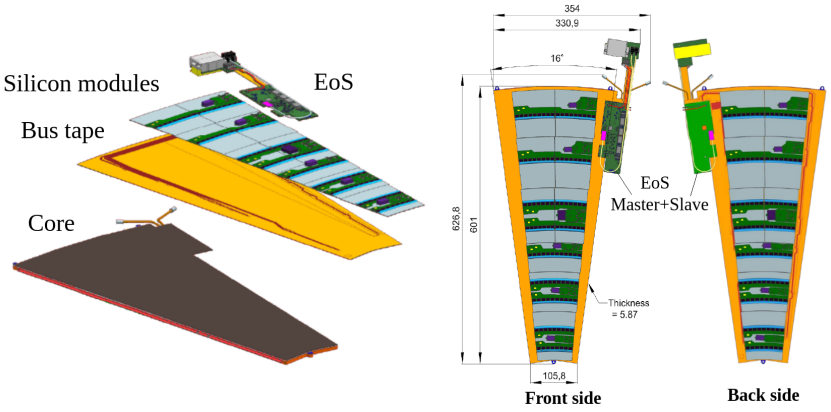

Figure 5.7: Anatomy of the ITk strip end-cap petal: *Silicon modules* are directly glued on top of the *bus tape* as part of the *core* as support structure. Additionally, the ***E**nd **o**f **S**ubstructure (EoS)* gateway is mounted on the petal "ear". The petal core is maximally 627 mm long, 354 mm wide and 5.87 mm thick.

With final remarks on the production planning, the testing procedures for **Q**uality **A**ssurance (QA) and **Q**uality **C**ontrol (QC) as well as the documentation within the ITk **P**roduction **D**atabase (PD) the introduction to the detector concept will be concluded in Section 5.3.4. More details for the barrel and end-cap design of the ITk strip detector can be found in the corresponding TDR [146].

5.3.1 Silicon modules

The module is the most basic unit as the sensing element and consists of a silicon microstrip sensor, one or two circuit boards for sensor readout (*hybrid*) and a circuit board for module powering and control (*powerboard*). Due to the wedge-shaped structure of a petal in the end-cap, in total nine different modules are on each side of a petal with six different sensor geometries to allow for hermetic coverage of the petal surface. Each sensor has a similar surface area of around $(10 \times 10)\,\mathrm{cm}^2$, determined by the available 6-inch wafer technology. In Figure 5.8, the different modules for a petal and their naming convention are introduced, with the latter guided by rings starting from the inner radius with R0 to the outer radius with R5. The three outermost modules are split modules consisting of two silicon sensors named S0 and S1, respectively.

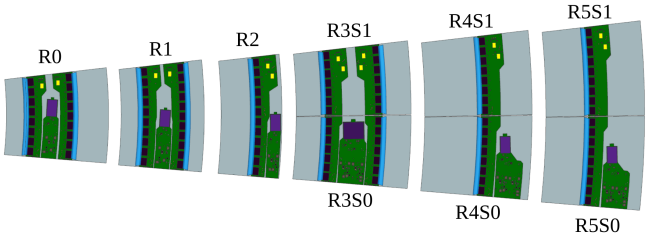

Figure 5.8: Naming scheme for ITk strip end-cap modules from the innermost to the outermost ring with R0 to R5. Shown are also the number of components per module in terms of readout and power electronics.

MODULE	R0	R1	R2	R3S0	R3S1	R4S0	R4S1	R5S0	R5S1
Hybrid H0									
ABCStar	8	10	12	7	7	8	8	9	9
HCCStar	1	1	2	0	2	0	2	0	2
Hybrid H1									
ABCStar	9	11		7	7				
HCCStar	1	1		0	2				
Powerboard									
DCDC	1	1	1	2		1		1	

Due to the large number of required modules, in total 3456 modules per end-cap, the module design was developed with a mass production scheme and low cost in mind. Dedicated production tooling for the module assembly is developed and single units of assemblies can be produced and tested independently at different module production sites. To minimize the material budget of the assembled modules, the kapton flex circuit boards (hybrids and powerboard) are directly glued on top of the silicon sensor without any additional connectors or bridges. A schematic view of a ITk strip module as well as a R0 prototype module are shown in Figure 5.9.

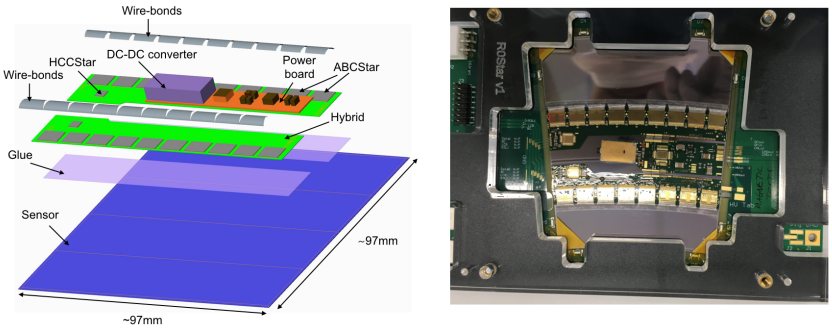

Figure 5.9: Design of the ITk strip end-cap module. An exploded schematic view (left) shows the constituents of a module: a *silicon sensor* (blue) with microstrips connected via wire-bonds to the front-end electronics (grey) hosted on hybrids (green) and powered via a powerboard (orange). A picture (right) of a real assembly is shown for the case of a prototype R0 module.

Microstrip sensor

The silicon microstrip sensors are produced in a n^+-in-p technology on Float Zone substrate [149] with p-stop implants for inter-strip isolation, as depicted in Figure 5.10. The sensors are 300-320 µm thick and made on 6-inch wafers in single-sided production.

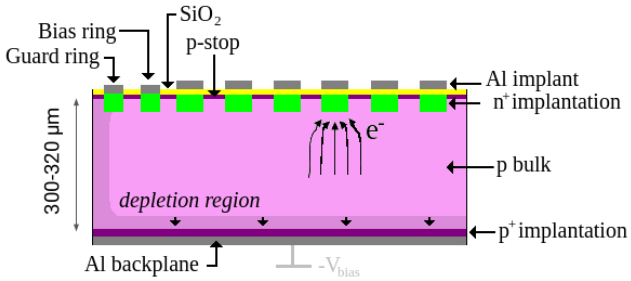

Figure 5.10: Design of the ITk microstrip silicon sensor. A schematic cross-section of the n^+-in-p sensor with p-stop for inter-strip isolation is shown.

The change from the currently used p-in-n technology in the ATLAS SCT detector is motivated by the properties of doped silicon for high hadron fluences (cf. Sec. 2.2.5). For the ITk Strip detector fluences of up to $1.6 \times 10^{15}\,n_{eq}/cm^2$, including a safety factor of 1.5, are expected, which varies with the exact location inside the detector volume.
On the one hand, n-in-p sensors do not suffer from the radiation-induced type inversion as observed for p-in-n silicon detectors. On the other hand, using electrons as charge carriers allows for a faster charge collection, a stronger signal as well as less charge trapping. In order to allow r-ϕ-coverage with radial strips pointing to the beam axis as foreseen for the end-cap part, six different annular sensor shapes are used. The strip length in the different sensors is varying from 15.1 to 60.2 mm and the average strip pitch ranges from 60.9 to 80.7 µm to accommodate the expected track density and the resulting occupancy.

For three-dimensional spacepoint reconstruction, a stereo rotation between the strips of back-to-back sensors mounted on both sides is applied. Here, the strip implants in the sensor themselves are skewed to point slightly off-center with a stereo angle of ±20 mrad.

Readout and power electronics

For the front-end, power and control electronics a number of **A**pplication **S**pecific **I**ntegrated **C**ircuits (ASICs) are required. They are produced in 130 nm CMOS technology for the ITk strip modules and their types and functionality are explained in the following. To cope with the high radiation doses and to reduce the impact of SEUs (cf. Sec. 2.2.5), a triplication logic is implemented in the chip design.
The measured charge deposited by the incoming particles in the microstrip sensor is converted to a binary hit/no-hit information by means of a programmable threshold and comparator in the front-end readout chip, called **A**TLAS **B**inary **C**hip (ABCStar). The ASIC provides an analogue preamplifier and shaper circuit and processes the signals from 256 strips connected via wire-bonds. The ABCStar chips required to read out two complete strip segments of the sensor are grouped together on a hybrid [150], consisting of a light-weight polyamide-based **P**rinted **C**ircuit **B**oard (PCB) directly glued on top of the silicon sensor. The **H**ybrid **C**ontroller **C**hip (HCCStar) processes the collected hit information from maximally eleven connected ABCStar chips on one hybrid and transfers it to the service bus of the petal. For the nine different module types (R0-R5) in total thirteen hybrids with varying numbers of readout ASICs have to be designed.
The powering and control of the front-end electronics is organized by the powerboard as additional PCB glued onto the silicon sensor. Here, the radiation-hard bPOL12V DC-DC converter [151] allows to reduce the input voltage of 11 V to the required low voltage of 1.5 V for the ASICs. By the use of a DC-DC converter, ohmic losses in the power cables can be reduced, while minimizing the material budget, as one single power cable pair serves every module on a petal side.
In addition, the powerboard contains a high-voltage bias filter and switch as well as the **A**utonomous **M**onitor & **C**ontrol **C**hip (AMAC), which is responsible for power control and operation monitoring.

5.3.2 Local support core

The petal core is the local support structure for the ITk strip end-cap detector and provides the mechanical support as well as all required services for a completely autonomous multi-module system. As such, the general requirements concern the geometric stability, the supply of electrical connections to and from the sensor modules and the cooling performance.

The mechanical requirements are targeted by employing high-stiffness **C**arbon **F**iber (CF) materials in a sandwich geometry with embedded cooling structures surrounded by high thermal conductivity carbon-based foam to provide the required cooling performance for the generated heat in the modules. For the interface of the local supports to the global support structure, three position locators are attached to the core defining the position of each local support.

The electrical services in terms of power, data and control signals are transferred to the modules from the EoS card via a thin, polyamide-based bus tape embedded in the core surfaces. Overall, the local support design follows the approach to minimize the material budget by employing light-weight structures such as CF-based materials.

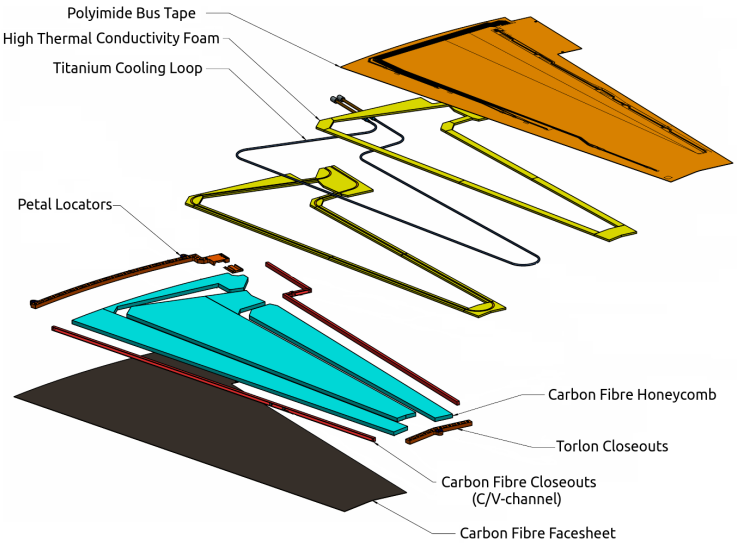

Figure 5.11: Design of the local support structure for the ITk strip end-cap detector. The exploded view of a petal core shows the sandwich structure with different materials.

The design of a petal core [152] is shown in Figure 5.11 and explained in the following. The core consists of a sandwich structure with CF face-sheets on top and bottom surface. A face-sheet consists of three layers of high-modulus uni-directional CF prepreg in 0-90-0 orientation, which are cocured together with the bus tape in an autoclave process under high temperature and pressure (120°C, 7 bar). The bus tape provides the electrical services in terms of low and high voltage and data transmission for the modules and is a thin polyamide-based tape with embedded copper traces. The inner sandwich structure is filled with low-density CF honeycomb glued on the face sheets providing the mechanical rigidity. The sides of the core are sealed with close-outs, where at the lateral sides, C/V-channels made out of pultruded CF are used. The top and bottom close-outs are made out of thermoplastic material (Torlon) and integrate the three, highly precise machined **P**etal **L**ocators (PLs) providing the mounting points for the kinematic mounting of the core in the global structure locking points. Inside the sandwich structure, a titanium cooling loop with a pipe diameter of only 2.28 mm is embedded to provide cooling of the petal using evaporative CO_2 cooling at a design temperature of $-35°C$. The cooling loop is surrounded by a carbon-based foam ($K \approx 30\,\mathrm{W/mK}$), providing a high thermal conductivity path to the face-sheet surface, with glue joints made by a carbon-loaded adhesive to improve the thermal and electrical conductance. Moreover, the core is electrically isolated from the external cooling services in the global support structure via two ceramic insulating electrical break assemblies, which are orbitally welded to the cooling loop.

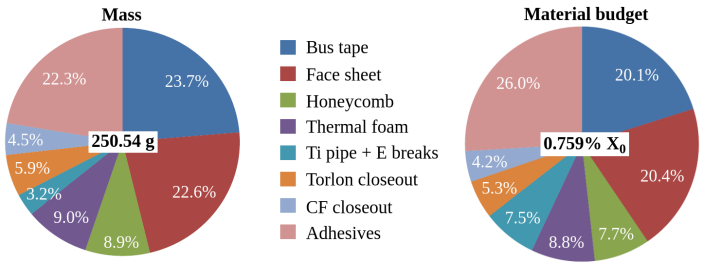

Figure 5.12: Mass and material budget estimate of the petal core categorized by materials.

The final core assembly is a light-weight mechanical structure and provides electrical connections and cooling to the directly glued on silicon modules. As shown in Figure 5.12, the total mass of a core is $\mathcal{O}(250\,\mathrm{g})$, representing roughly $0.76\%\,\mathrm{X}_0$ which can be compared to an estimated material budget of $1.4\%\,\mathrm{X}_0$ for the modules.

In Figure 5.13, a selection of involved steps in the multi-stage process of core assembly is depicted. Several prototypes of different design iterations have been created by now, as will be introduced together with corresponding test results in Chapter 6.

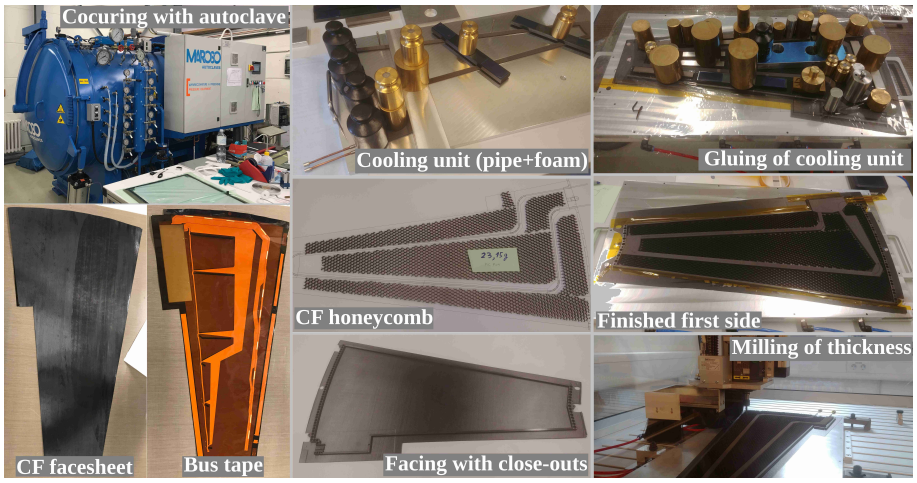

Figure 5.13: Impressions from the multi-step assembly process for a petal core.

5.3.3 TDAQ & global support

The trigger and data acquisition system planned for the ITk strip detector as depicted in Figure 5.14 can be summarized as following: The binary hit information created in the ABCStar chip is transferred to the HCCStar chip on the same hybrid, which connects to the data lines on the bus tape. In the other direction, **T**rigger, **C**lock and **C**ontrol (TTC) signals received by the HCCStar ASIC are distributed to the individually connected front-end ASICs. For the powering, a low-voltage power converter and a high-voltage switching circuit are combined in the powerboard controlled by the AMAC chip and connected to power lines on the bus tape.

Figure 5.14: DAQ and powering scheme for the ITk strip end-cap detector. The EoS card provides the gateway to the off-detector electronics for input of power and TTC signals and output of data and feedback to the **D**etector **C**ontrol **S**ystem (DCS). Power and data lines in the bus tape are used for the electrical connection to the modules.

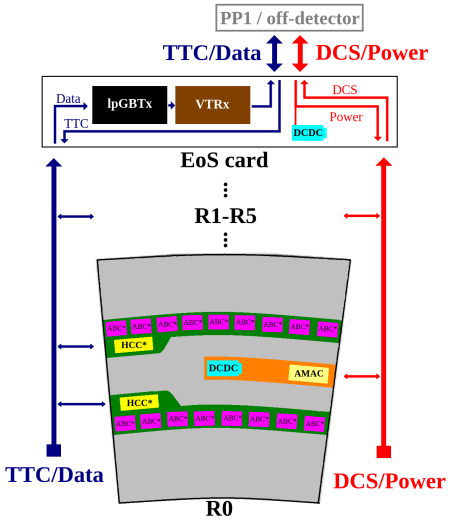

The gateway between the on-detector electronics on the petal and the off-detector system is provided by the **E**nd **o**f **S**ubstructure (EoS). The EoS distributes power to the module's powerboard and sends TTC signals (e.g. 40 MHz system clock and L0/L1 trigger commands) to each HCCStar via the TTC bus on the bus tape.

The receiving data from the modules are sent optically to the off-detector system using the low-power GigaBit Transceiver (lpGBTx) and the Versatile link (VTRx+) fibre optic driver on the EoS. To cope with the operation at the L1 trigger rate of 1 MHz, the data rate from the module to the EoS is 640 MBit/s. The EoS card is operated in a master/slave mode, attached on both sides of the petal core and powered via hosted DCDC converters.

The fully assembled petal, consisting of a core loaded in both sides with nine silicon modules and one EoS card with electrical connections via wire-bonds to the bus tape, can be integrated in the end-cap structure and connected to the electrical services and cooling lines. In total, 192 petals are integrated into one end-cap consisting of six disks D0-D5 positioned between 1 512 mm $< z <$ 3 000 mm, as depicted in Figure 5.15.

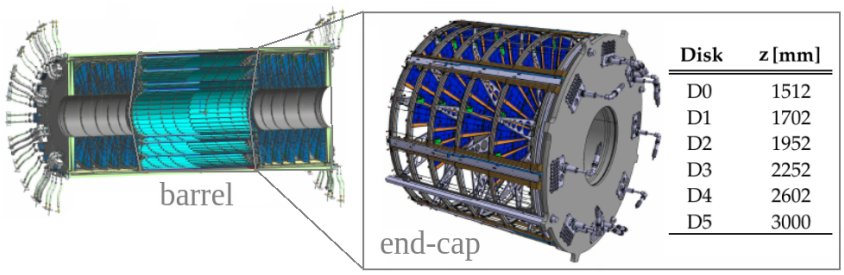

Figure 5.15: Design of the global support structure for the ITk strip detector, highlighting the end-cap structure populated with petals.

Each disk consists of a wheel support structure and 32 petals are inserted from both sides of the disk. The global support structure is also made out of CF materials and all services are connected at the end of the structures via service trays on the global structure. By this design, the overall material budget can be reduced as any additional material of cables or cooling lines inside the tracking detector volume is avoided.

5.3.4 Production, testing & database

The production of the ITk strip detector involves the assembly of a high quantity of components ranging from silicon modules to loaded support structures up to the final integration in the global supports. Therefore, the design of sub-assemblies such as modules or fully loaded petals follow the strategy to form independent and functional sub-systems which can be fully tested before being installed in the end-cap structure. Moreover, the production involving the building, assembly and testing of items is distributed over many different institutes worldwide with a time frame of 3.5 years. The distributed production model for the two ITk strip end-caps is depicted in Figure 5.16.

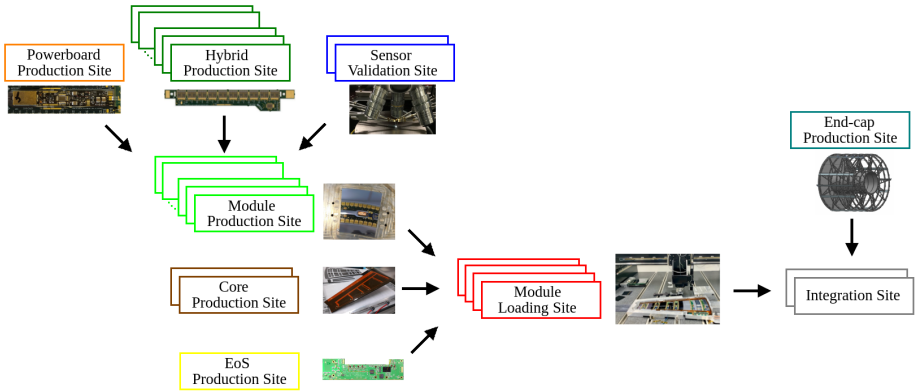

Figure 5.16: Production flow for the ITk strip end-cap detector.

An essential part for the project is also to ensure a high reliability of all on-detector components, as these are expected to operate reliably over the full ten to fifteen years lifetime of the detector with only minor maintenance possibilities. Therefore, dedicated test procedures for each component in terms of **Q**uality **A**ssurance (QA) and **Q**uality **C**ontrol (QC) are being developed and will be carried out in the production phase.
Here, QC tests are performed on every production item, validating their performance in conformance with the specifications, such as assessing the thermal performance of a petal or determine the surface flatness of an assembled local support core.
On the contrary, QA tests are statistical studies of the component quality during R&D and on a batch basis in production, aiming for an improvement in reliability as well as validating the component design. This involves also destructive testing, meaning to allow more extreme conditions than expected for regular detector operation, such as elevated or reduced operation temperatures as well as rapid temperature changes. A change in the device performance after the test compared to before can indicate possible failures in the design. A series of developed QA and QC tests assessing the thermo-mechanical performance of petals will be introduced in detail in Chapter 6.

Finally, the coordination and tracking of the distributed production of the detector components, the continuous recording of test results of them as well as the possibility to back trace potential problems during operation is an important requirement for the project.
For this purpose, a central database for the entire ITk detector involving the pixel and strip sub-detectors as well as all common electronics and mechanics items is developed.
The ITk **P**roduction **D**atabase (PD) will store information about most of the components and assemblies (e.g. petals, cores, modules) in the detector and can track their integration into new assemblies by a parent-child relationship. Moreover, test results can be uploaded to update the status of a component and allow to enter the next stage in the production flow, and the tracking of shipments between production sites is implemented.
A portion of the work devoted to this thesis included the implementation of a petal core assembly in the PD including stages and tests, as schematically shown in Figure 5.17.

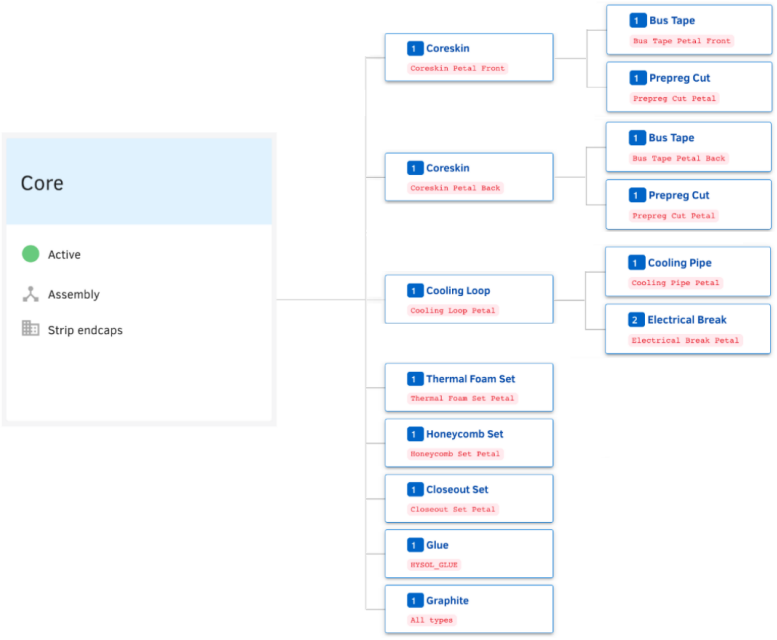

Figure 5.17: Implementation of the petal core assembly in the ITk production database. Shown are the different components of the assembly, connected in a parent-childhood relationship to back trace any occurring problems with the assembly.

Chapter 6

Thermo-Mechanical Studies on Petals

The petals consisting of the core as local support structure and the glued on silicon strip modules are the building blocks in the planned ATLAS ITk strip end-cap detector. In the course of this thesis, the petal core structure was thoroughly tested in terms of its mechanical, thermal and thermo-mechanical performance. On the one hand, the performed studies allow to verify the local support design under the specified conditions expected for the detector operation of ATLAS at the HL-LHC. On the other hand, the developed test setups will be used evaluate the performance of each individual core during the production phase in terms of **Q**uality **A**ssurance (QA) and **Q**uality **C**ontrol (QC) tests. This approach of intensive tests on the core structure ensures a high quality and the possibility to detect any defect as early as possible in the production chain for the full ITk detector.

For the evaluation of the mechanical, thermal and thermo-mechanical tests, the objectives for the petal core have to be clearly identified and the corresponding technical specifications need to be defined. The relevant characteristics for the design verification as well as the QA and QC tests are addressed in Section 6.1.

For the testing of petal cores, different measurement techniques are applied and dedicated equipment is used. This ranges from metrology measurements of the core's geometry, over the thermal performance assessment of the cooled core using infrared thermography and CO_2 cooling, to the comparison of the experimental results with dedicated simulations of the core's characteristics. Section 6.2 introduces the characteristics of the applied methods and the properties of the used tools to measure the mechanical, thermal and thermo-mechanical performance values.

The performance tests in this work were conducted on a number of prototypes of petal cores as well as the thermo-mechanical petal, which were built in the last five years during the R&D phase at DESY. The different features in terms of used materials in the assembly as well as the design iterations are explained in Section 6.3.

For the method of infrared thermography the material specific *emissivity* of the object under test is important. Here, the emissivity depends on a number of parameters of the test object and describes basically how well the recorded temperature with the infrared camera reflects the real object's temperature. For objects with low emissivity, special correction techniques have to be applied to assess the temperature by the method of infrared thermography correctly.

A number of experimental studies concerning the emissivity of the tested objects in this work, namely petal cores and the thermo-mechanical petal, as well as the applied correction methods are discussed in Section 6.4.

One of the main objectives of the petal core as local support structure in the detector is to provide a sufficient cooling to the glued on silicon sensor modules. The produced power in the silicon sensors as well as the front-end readout and power electronics needs to be dissipated in the cooling loop of the core using evaporative CO_2 cooling. To avoid the effect of thermal runaway, the cooling performance of the full detector has to be sufficient over the full lifetime of the detector, as the emitted power depends also on the received radiation fluence. Therefore, the *thermal performance* of the petal core is critical for a successful detector operation. The thermal performance is measured for a number of prototypes to validate the structure's design and will be also a key parameter for the QC testing of cores in the production.
Section 6.5 introduces the developed test setup for the thermal performance assessment using infrared thermography and shows the results of a number of performed studies on different petal core prototypes as well as the thermo-mechanical petal under varying operation conditions.

Another objective of the local support structure is to provide a mechanical rigid structure for the silicon sensor modules, which includes the typical occurring temperature shifts during detector operation. Therefore, the petal core design is investigated on mechanical deformations caused by temperature differences to verify its design.
Section 6.6 explains the developed test setup and evaluates the *thermal deformation* results for the performed test on a petal core prototype.

Furthermore, the petal core has to provide also a good mechanical integrity for two other temperature scenarios. On the one hand, a number of regular temperature cycles, meaning cool-down and warm-up phases of the full ITk detector within the normal operation temperatures, are expected over its full life cycle. The influence of this *thermal cycling* on the core is evaluated in terms of the relevant mechanical and thermal performance specifications. On the other hand, extreme temperature scenarios can occur in case of failure in the cooling system or during detector commissioning. The resistance of the developed local support structure is evaluated in dedicated *thermal shock* tests.
The conducted studies and their results for the thermal cycling and the thermal shock tests on a petal core prototype are discussed in Section 6.7.

Finally, a conclusion on the performed tests on the petal cores and their thermo-mechanical characterization is drawn in Section 6.8. Here, also the local support design is evaluated with respect to the defined mechanical, thermal and thermo-mechanical specifications for the ATLAS ITk strip end-cap detector.

6.1 Objectives and Specifications

The petal core as the local support structure for the silicon strip modules in the ITk end-cap is an integral part of the detector design. Any failure during operation in the tracking detector would directly influence its performance and should therefore be avoided by requiring a high reliability of its components.

On the one hand, a number of mechanical requirements have to be fulfilled: the core has to provide a high stability and rigidity during operation to have a good alignment of the silicon sensors for the track reconstruction; a flat surface of the core is important due to the mounting of silicon modules directly on top and the placing of these has to be accurate in the spatial dimensions; furthermore, the core is mounted into the global end-cap structure via a kinematic mounting using highly accurate locator holes for positioning into the end-cap locking points.
On the other hand, also a number of thermal requirements are defined: the core has to provide sufficient cooling performance for the silicon modules, which is especially important after high radiation doses at the end-of-life of the detector to avoid the effect of thermal runaway (cf. Sec. 2.2.5); the core structure has to withstand several temperature cycles due to changing cooling requirements or due to the normal detector operation with dedicated warm-up phases for the whole detector; in case of failure of the CO_2 cooling system extreme temperatures below the design temperature can occur, but the core should also in these cases maintain its mechanical as well as electrical properties.
Moreover, apart from the mechanical and thermal requirements the petal core design should minimize the material budget in the tracking detector as much as possible, but has to provide also all the required electrical connections for powering, control and data transmission of the silicon modules.

From these defined requirements in terms of the thermo-mechanical properties of a petal core, a list of specifications can be derived explaining the design requirements and specifying also the allowed tolerances on the properties. To evaluate the design, dedicated tests are performed on petal core prototypes and the specifications are checked with these measurements. For the design validation in the R&D phase, the range of measurements is larger than for controlling the quality during the production of petals. Moreover, measurements under extreme conditions are performed on the prototypes in the R&D phase, involving also destructive testing of cores. These two types of tests are differentiated in QA and QC testing, as it was introduced in Section 5.3.4.

In the following, the specifications for the characterization of petals in terms of their thermo-mechanical properties are summarized in Section 6.1.1, highlighting the important specifications as investigated in this work. Section 6.1.2 introduces the corresponding QA and QC test procedures planned to check the specifications on prototype petals in the R&D phase as well as during the petal production for the ATLAS ITk end-cap detector.

6.1.1 Specifications on thermo-mechanical properties

The specifications on petals [153] in terms of their thermo-mechanical behaviour can be categorized as following: *mechanical* requirements in terms of accuracy in dimensions, *thermal* properties in terms of required cooling performance and *thermo-mechanical* requirements in terms of mechanical properties for different operation temperature scenarios. For each case, a number of specifications for the petal design are defined as shown in the following.

Mechanical specifications

In the first category, specifications on the mechanical integrity of the core are defined, as it is the main task as the local support structure for the strip modules.
The *local flatness* of a petal core is defined as the maximal deviation from a planar fit over the module areas and has to be less than 50 µm to allow for module mounting.

The difference of flatness between the core surface and the module planarity is then balanced by the thickness of the applied glue layer.
For the accuracy of the ***P**etal **L**ocator (PL)* a maximal deviation of the center holes of 25 µm in any direction is tolerated to allow for mounting in the global support structure. Moreover, the diameters of the PL holes are specified as $4.000\,\text{mm} + 0.012\,\text{mm}$ (H7 tolerance) for the bottom PL and the top slot locator and $5.00\,\text{mm} \pm 0.05\,\text{mm}$ for the oversized top hole for kinematic mounting. To allow for a high accuracy in the module-on-core procedure, the deviation between the *fiducial holes*[19] in the PL with the locator holes should be within 25 µm. The geometrical dimensions as well as the specifications on the PLs can be found in the technical drawing of the petal core [154] as shown in Figure 6.1.

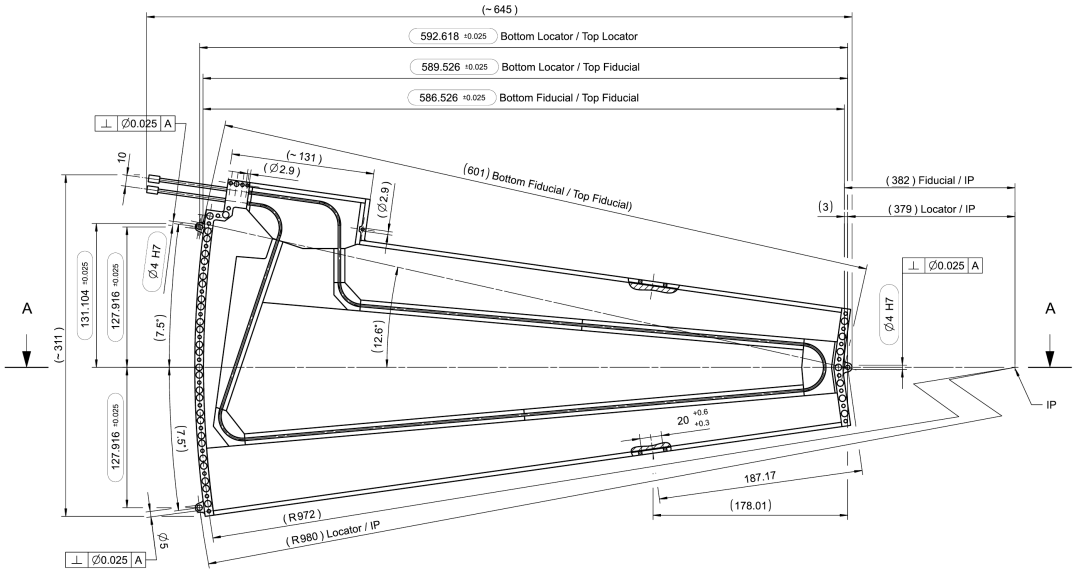

Figure 6.1: Technical drawing of the petal core with specified tolerances [154].

Thermal specifications

In the next category, the thermal specifications on petal cores are described as a core provides the heat sink for the power created in the strip modules and their associated on-detector electronics.
The core has to provide sufficient *thermal contact* to the glued on modules via its core surface, as for a broken interface, e.g. due to surface delamination or because of insufficient glue coverage, a complete silicon module has to be switched off and is lost for the particle tracking. The required *thermal impedance* of the core is defined by its thermal path: cooling will be provided by evaporative CO_2 in the titanium cooling loop, embedded in the high thermal conductivity carbon foam and therefore transmitted to the CF surface. From here, the cooling is conducting via the glue interface to the module and transmitted horizontally over the module area by the thermal conductance of the silicon sensors. Accordingly, for the positions of modules a high agreement to the design thermal impedance of 20% is required for regions with a direct foam interface and 30% otherwise.
The minimal *operating temperature* for a petal is at a design coolant temperature of -38° C. In general, the specified temperature range is between -56° C and $+70^\circ$ C accommodating failure scenarios of the cooling system as well as the phase of detector commissioning.

[19] The fiducial holes with a diameter of 300 µm are used for laser alignment of the robotic gantry system for the module-on-core placement with the coordinate system of the core.

Thermo-mechanical specifications

In the last category, the mechanical and thermal properties are evaluated for the normal operating temperature ranges as well as under extreme conditions.
Over the life cycle of the ITk detector a number of temperature cycles are expected during normal operation. A loss of mechanical support or thermal contact for these changing conditions is a risk for individual modules or a complete petal. Therefore, the mechanical and thermal properties of the core have to be evaluated after 100 temperature cycles between a specified temperature of -40° C to $+40^{\circ}$ C. Also the influence of mechanical deformations on the core due to normal temperature gradients during operation are specified to be less than 100 µm in terms of the local flatness.
Finally, also the mechanical and thermal properties after extreme temperature conditions, most significantly at low temperatures, should be evaluated to validate the resistance of the core design against these harsh conditions.

6.1.2 Quality assurance & quality control

The defined specifications on the mechanical, thermal and thermo-mechanical properties of a petal core can be tested by dedicated measurements of prototype petal cores in the R&D phase as well as on a regular basis during the production of the required 384 petals for the ATLAS ITk strip end-cap detector. Here, tests can be categorized in QA and QC tests depending on their defined objective.

A number of required components and materials for the core assembly are manufactured directly by industry partners, so that the appropriate specifications on the raw materials are assigned to the respective material orders. As an example, the high thermal conductivity carbon foam is delivered in batches consisting of material blocks with measured values of density and thermal conductance by the manufacturer. In the assembly process, these measurements are repeated on a fraction of blocks and compared to the manufacturer's values, but otherwise the material is used for the next production step.
For each needed core component from industry, a dedicated QC and QA test program has been developed to check the manufacturer's data and ensure a high reliability and traceability of the material quality. Moreover, produced components by the assembly site itself such as manufactured parts like cutted foam pieces are tested as well.

The focus in this work will be not on testing the performance and specifications of the individual core components but to assess the quality of the fully assembled petal core. By measuring the mechanical, thermal and thermo-mechanical properties of assembled cores and comparing the measured values to the specifications, possible errors in the manufacturing process can be detected early in the production cycle. For example, a missing glue interface between the foam and the CF surface would degrade the thermal conductance of the core, resulting in the worst case in a dead module in the final detector. Therefore, an intensive QA and QC measurement program is a key part for the success of the detector to detect such failure modes as early as possible in the production chain.

In the following sections, the developed test procedures for petal cores to assess and check their mechanical, thermal and thermo-mechanical specifications will be discussed, but here a short overview about the planned QA and QC tests [155] is provided.

For the QC of mechanical properties like local flatness and PL dimensions, *geometrical metrology* measurements with an optical 3D microscope were developed, allowing to check the specifications in an automated measurement procedure after the core manufacturing. The QC measurement for the thermal performance of a core uses the concept of *infrared thermography* performed in a dedicated test setup involving cooling of the petal core to the lowest temperature set point under defined ambient conditions.
The QA tests are defined for testing the thermo-mechanical properties of cores for changing or extreme operation conditions in terms of temperatures, which are *thermal deformation*, *thermal cycling* and *thermal shock* measurements. For the thermal deformation measurement, the optical 3D microscope from the geometrical metrology tests is combined with the cooling infrastructure of the thermal performance test. Furthermore, to compare the performance results before and after thermal cycling and shock, the defined QC measurements are executed accordingly.
The defined QC tests, namely the geometrical metrology and thermal performance measurements, were executed on all manufactured prototypes in the R&D phase and will also be conducted on each petal core in the production phase. On the contrary, the thermo-mechanical QA tests were executed on selected prototypes in the R&D phase to validate the design and the tests of thermal cycling and shock will be only repeated on 1% of manufactured cores in the pre-production phase.

6.2 Measurement Techniques & Equipment

For the performance evaluation of petal cores in terms of their mechanical, thermal and thermo-mechanical properties, dedicated QA and QC setups were developed using a number of different measurement techniques and equipment.
In the following, the characteristics of the used methods and the properties of the tools to measure the respective performance values are discussed. In Section 6.2.1, the equipment for geometrical metrology measurements using an optical 3D microscope is introduced. The concept of infrared thermography as used for the thermal QC tests of petal cores is explained in Section 6.2.2. This is followed by an introduction to evaporative CO_2 cooling using the TRACI system and additional equipment for CO_2 diagnostics in Section 6.2.3. Section 6.2.4 addresses the measurement techniques used for temperature and humidity logging of the environmental conditions during the tests as well as direct probe measurements of temperatures on the test object itself. Finally, the used tools for thermal simulations of the petal as well as the CO_2 coolant properties are introduced in Section 6.2.5.

6.2.1 Geometrical metrology

The SmartScope® CNC 670 system [156], called in the following *SmartScope*, as an optical 3D microscope is used for the geometrical metrology measurements . Due to its large XYZ measuring range with 650 mm × 660 mm × 200 mm, a petal can be easily fitted on the optical granite table with moving in Y via a granite bridge and moving the instrument head precisely in X and Z. Additionally to the high precision in the X and Y position, the measurement of the height is performed by bringing the camera image into focus and using the focus length for different selectable magnifications to determine the distance in Z.
As a transparent surface like the petal core surface with the transparent bus tape has no surface structure to bring into focus, the built-in grid projector can be used. By this method, an LED source projects an easily focused grid pattern onto the surface of the part, which is in focus when the projected grid pattern is in focus.

The SmartScope can be programmed via the metrology software MeasureMind® 3D.
At first, the coordinate system of the petal is defined in two steps by using distinct features of the petal, e.g. the PL holes: in the rough alignment, the object contour is identified on the optical table and in the fine alignment, the accuracy is improved by using the selected magnification for the measurement. Secondly, a number of measurement points are defined, ranging from measurements of the surface height up to the measurement of certain features like holes and their respective diameters; finally, the such defined routine can be executed automatically and repeated for different petal core prototypes with high repeatability.
In Figure 6.2, the system with a petal core as test object is shown together with the alignment procedure and the grid projection technique for transparent surfaces.

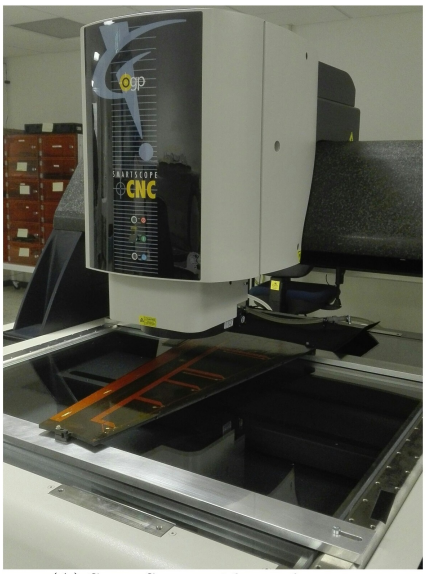

(A) SmartScope with petal core.

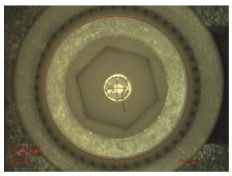
(B) Rough alignment.

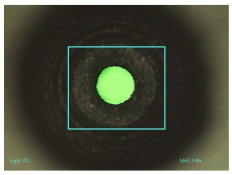
(C) Fine alignment.

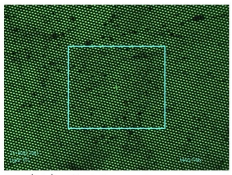
(D) Grid projection.

Figure 6.2: Geometrical metrology with the SmartScope. The petal core is placed on the optical table of the SmartScope (A). The coordinate system for the measurement is defined in two steps: the rough alignment detects features, e.g. the PL screw head (B), to define the object's contour, which is improved by the fine alignment with high magnification, e.g. using then the PL fiducial hole (C). Moreover, the grid projection technique (D) is used due to the transparent bus tape surface on the petal core.

6.2.2 Infrared thermography

The technique of *infrared thermography* [157], also called *infrared thermal imaging*, is used for the assessment of the petal's thermal performance. Here, an **I**nfra**R**ed (IR) camera detects the emitted radiation from an object in the IR range of the electromagnetic spectrum, typically between 9 and 14 µm, and produces spatially-resolved images of the detected radiation. As the emitted radiation of the object depends on its temperature, the detected radiation can be converted into temperature values to create an image of the temperature distribution of the object, called *thermogram*.

The advantages of IR thermography for temperature measurements are the following: the distribution of the object's surface temperature can be compared over a wide range depending on the **F**ield **O**f **V**iew (FOV) of the IR camera; the temperature can be assessed without direct interference to the object like a direct probe measurement and causes therefore no confusion on the object's temperature; the measurement is performed in real time and as such the temperature distribution can be observed for changing operation conditions; finally, it is a non-destructive measurement and therefore well suited for QC testing. The main disadvantage of IR thermal imaging is that all the incident radiation is detected by the IR camera and therefore the displayed temperature is usually not the real temperature of the object. The reason is that the detected radiant power is the sum of multiple sources, namely the emitted, transmitted and reflected radiant power.

Here, the theory of the blackbody radiation is used for the explanation, as described in the following: every object at any given absolute temperature above the absolute lowest temperature of $T = 0\,\mathrm{K}$ emits thermal radiation; for the case of a *blackbody*, the maximal emitted radiant power depends only its temperature; a blackbody is the ideal case of a perfect emitter, meaning that its surfaces are ideal to absorb every incident radiation and no other surface can emit more energy.
The total radiant power emitted into the hemisphere for a wavelength interval $(\lambda,\lambda + d\lambda)$ by a blackbody is described with Planck's law as

$$M_\lambda(T)d\lambda = \frac{2\pi hc^2}{\lambda^5}\frac{1}{\exp\left(\frac{hc}{\lambda kT}\right) - 1}d\lambda. \tag{6.1}$$

Here, h is Planck's constant and T the absolute temperature of the blackbody.
Moreover, the radiated power of the blackbody over all wavelengths per unit area can be calculated from its temperature T by the Stefan-Boltzmann law as

$$M(T) = \int_0^\infty M_\lambda(T)d\lambda = \sigma T^4, \tag{6.2}$$

with the Stefan-Boltzmann constant σ.
For the emitted thermal radiation of real objects, the blackbody radiation has to be corrected by the *emissivity* ε as the ratio of the amount of radiation actually emitted from the surface to that emitted by a blackbody at the same temperature. The emissivity $\varepsilon(\lambda,T)$ of an object is in the range of $0 \leq \epsilon \leq 1$ and depends in general on the wavelength, but for most materials ε is independent of λ (*gray body*).
Due to the conservation of energy, any incident radiation (Φ_0) on an object is either reflected (Φ_R) on the object's surface, transmitted (Φ_T) through the object or absorbed (Φ_A) within the object, fulfilling

$$\Phi_0 = \Phi_\mathrm{R} + \Phi_\mathrm{T} + \Phi_\mathrm{A}. \tag{6.3}$$

By normalization with the incident radiation and introducing the reflexivity ρ, the transmissivity τ and the absorptivity α, the formula becomes

$$1 = \rho + \tau + \alpha = \rho + \tau + \varepsilon, \tag{6.4}$$

where for the last equivalence, Kirchhoff's law was used saying that the amount of absorbed radiation is equal to the emitted one.
This behaviour is depicted for the application in IR thermography in Figure 6.3, where the real object temperature is represented by the emitted radiation, but confused by the transmissive and reflective part recorded as well by the IR camera.

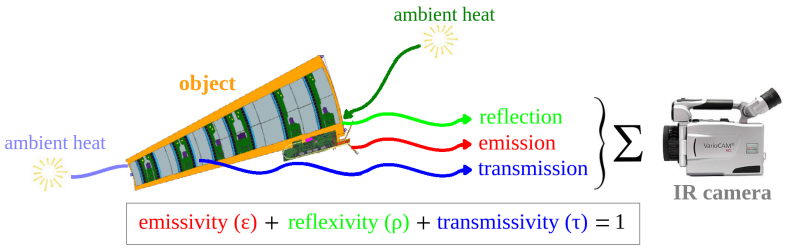

Figure 6.3: IR camera receives radiation from object emission, reflection of ambient heat and transmission of ambient heat with $\varepsilon + \rho + \tau = 1$.

As the most solid materials are opaque in the IR spectrum, the transmissivity can be neglected and the emissivity is directly accessible from the total reflexivity via $\varepsilon = 1 - r$. For example, a metal surface with high reflexivities of above 90% has an emissivity of below 0.1 or even less in the case of a highly polished surface.

On the contrary, when the metal surface is painted, its emissivity can be well above 90%. For the application of IR thermography, it is therefore important to assess the object's emissivity and to apply an appropriate emissivity correction to the recorded thermograms. In Section 6.4 the emissivity of the objects tested with thermal imaging in this work are studied in detail and also the applied correction methods are discussed.
The IR camera VarioCAM® HD research 875 [158] is used in the thermal performance QC test setup. The camera offers a detector format of 1024×768 pixels with 30 Hz full-frame rate and a measurement accuracy of $\pm 1\,\mathrm{K}$ over a temperature range of $(-40 \ldots 2000)\,^{\circ}\mathrm{C}$. The detector is an uncooled microbolometer[20] arranged in a focal plane array (FPA)[21] with a sensitivity in the spectral range of $(7.5 \ldots 14)\,\mu\mathrm{m}$.
The horizontal and vertical FOV of the camera depend on the focal length f of the camera lens and the horizontal (b_H) and vertical (b_V) FPA dimensions. With the FOV, the object dimensions to be imaged in a distance D to the camera are calculated as

$$x_\mathrm{H,V} = 2D \tan\left(\frac{\mathrm{FOV_{H,V}}}{2}\right) \quad \text{with} \quad \mathrm{FOV_{H,V}} = 2 \arctan\left(\frac{b_\mathrm{H,V}}{2f}\right). \tag{6.5}$$

For the data recording and analysis of thermograms, the proprietary IRBIS® 3 professional software is used, offering several additional functionalities such as an emissivity correction tool or the definition of measurement markers in the thermogram.

6.2.3 CO_2 cooling & diagnostics

For the cooling of the ATLAS ITk detector, dual-phase CO_2 cooling will be used. In the following, the basics of dual-phase CO_2 cooling and its advantages for the application in a particle physics detector are discussed. For testing of petals in the R&D phase, the TRACI cooling system is used and its operational principle will be explained. Moreover, an overview of additional equipment for CO_2 diagnostics is given.

Evaporative CO_2 cooling

A sufficient cooling system for the ATLAS ITk detector is required to remove the generated heat in the silicon sensors and the front-end electronics from the detector, avoiding a thermal runaway in the silicon sensors. The required cooling power for the complete system is estimated to be roughly 245 kW with a design temperature of $-38\,^{\circ}\mathrm{C}$.
The use of dual-phase CO_2 cooling is advantageous due to several reasons:

- a large latent heat transfer is possible due to the phase change energy for the transition of liquid to gaseous CO_2 and allows for low mass flows of the coolant;
- a low mass flow as well as a low liquid viscosity results in a low pressure drop along the cooling pipe in the detector;
- a low pressure drop allows to use small pipe diameters reducing the material budget of the cooling services in the detector;
- a high heat transfer capability is possible despite small pipe diameters due to **H**eat **T**ransfer **C**oefficient (HTC) values of typically $8\,000\,\mathrm{W/(K \cdot m^2)}$;
- a high thermal stability is reached due to the high pressure in the system;

[20] In the microbolometer detector, the incident radiation creates heat in the detector material, changing its electrical resistance which can be measured and processed to temperature values.
[21] Microbolometer cells are arranged in a matrix pattern with a pixel pitch of 17 µm in the focal plane.

- a practical temperature range of $-40\,^{\circ}\mathrm{C}$ to $25\,^{\circ}\mathrm{C}$ for detector application is accessible;
- CO_2 is a natural, non-toxic and non-flammable gas and well suited for high-energy physics application as it is mostly radiation resistant and non-magnetic.

A possible disadvantage is the high pressure of the evaporative CO_2 with $10 - 100\,\mathrm{bar}$. Due to the high amount of stored energy in the cooling system as the pressure times the volume, special technical precautions are needed. Also, a more sophisticated system design than for a mono-phase coolant is needed as the detector is used as evaporator.

For the analysis of the thermodynamical processes happening in the evaporative CO_2 cooling, the CO_2 phase diagram as function of the pressure p and the enthalpy[22] h is used. The so-called log(p)-h diagram for CO_2 is shown in Figure 6.4.

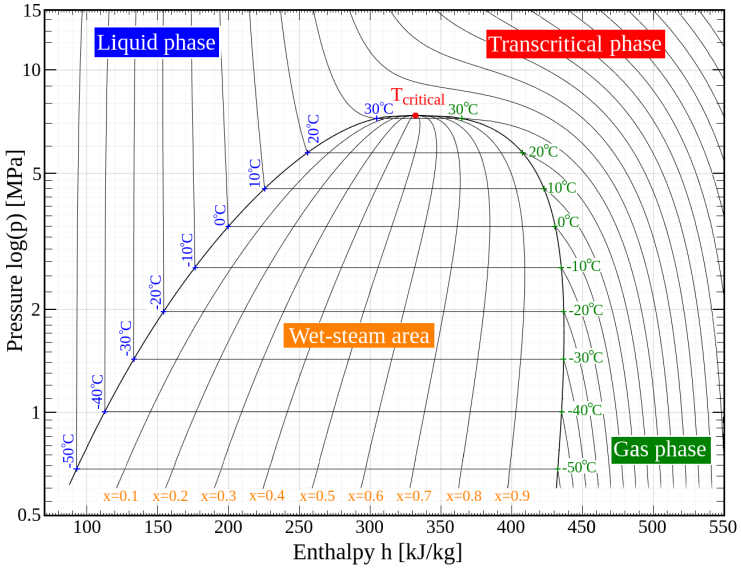

Figure 6.4: Phase diagram of CO_2 as log(p)-h diagram. The evaporation line for the *liquid phase* and the condensation line for the *gaseous phase* defines the dual-phase region, called *wet-steam area*. On the isothermal lines of constant temperature and pressure, the *vapour quality* x is changing with the enthalpy. In the *transcritical phase* above its critical point, the fluid behaves like a liquid and gas at the same time.

Here, the phase diagram is divided by the evaporation and condensation line into four different areas: the *liquid phase*, the *gas phase*, the *wet-steam area* and the *transcritical phase*. In the transcritical phase above the critical point at $T_{\mathrm{crit}} = 31\,^{\circ}\mathrm{C}$ and $p_{\mathrm{crit}} = 73.8\,\mathrm{bar}$, the CO_2 fluid behaves like a liquid and gas at the same time with rather unstable properties. On the contrary, in the wet-steam area the CO_2 behaviour is well described with the temperature on an isothermal line corresponding to an associated pressure. For a higher enthalpy, the ratio of liquid to gas, called the *vapour quality* x, is changing due an increase of the system energy. Therefore, the energy of an enthalpy increase in the wet-steam area is absorbed by the evaporation with $\Delta h = f(p_1,x_1,p_2,x_2)$, whereas in the liquid or gas phase the fluid temperature changes as $\Delta h = f(p_1,T_1,p_2,T_2)$. Moreover, *subcooling* is the temperature difference of the liquid CO_2 to the evaporation temperature at the same pressure, and *superheating* the corresponding effect for gaseous CO_2.

The flow pattern of dual-phase CO_2 in the wet-steam area depends strongly on the vapour quality x, as depicted in Figure 6.5. The reason is that the phase change of evaporation takes energy (latent heat transfer) as well as movement and space from the fluid, changing the flow pattern inside the cooling pipe. Additionally, for high vapour qualities with lower liquid availability, a situation might arise in which an area of the tube wall is not covered by liquid again due to the changed fluid flow after evaporation.

[22] In a thermodynamical system, the enthalpy H is equal to the sum of the system's internal energy and the product of its pressure and volume: $H = U + pV$.

In this *dry out*, the local HTC value decreases significantly from latent heat transfer to convectional heat transfer, which can create hot spots on the sensors and should be avoided for the detector cooling. Therefore, it is important to well design the cooling capacity, $\dot{Q} = \Delta h \cdot \dot{m}$, of the system, meaning also an operation with vapour qualities up to only 0.5.

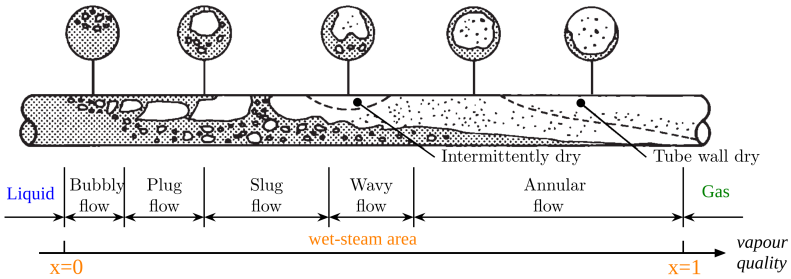

Figure 6.5: Flow pattern of dual-phase CO_2 in a horizontal tube as function of the vapour quality x.
Modified from [159].

TRACI cooling system

In the thermal tests performed with the petal prototypes, evaporative CO_2 cooling is used to emulate the conditions for the real detector operation. For this purpose, the **T**ransportable **R**efrigeration **A**pparatus for **C**O_2 **I**nvestigation (TRACI) cooling system (version 2) [160] is used in the tests, which was developed at CERN and provides a nominal cooling power of 100 W. As the estimated power consumption of a petal is in the same order, the system should provide sufficient cooling power. But as it is observed in the later tests, the minimal CO_2 temperature reached is only about $-25\,^{\circ}$C due to different reasons. The portable TRACI system offers stable CO_2 temperatures and an easy, stand-alone operation using the **I**ntegrated **2**-**P**hase **A**ccumulator **C**ontrolled **L**oop (I-2PACL) concept. For this concept, a pumped dual-phase loop of CO_2 is used and the saturation temperature is controlled via an *accumulator* filled with liquid and vapour. By cooling or heating the liquid-vapour mixture in the accumulator, the CO_2 pressure can be controlled. As the pressure of dual-phase CO_2 corresponds directly to the fluid temperature (cf. Fig. 6.4), the system allows an easy control for different temperature set points. The circulating fluid in the closed experiment loop is condensed and sub-cooled before the pump in a *heat exchanger*, which is connected to a *primary chiller* with R404A as coolant. Due to an heat exchange of the liquid CO_2 in the accumulator, the saturation temperature is aligned to the selectable pressure set point in the accumulator. Finally, the connection of the system to the experiment's cooling loop is realized via a *concentric cooling line*[23]. The advantage of the integrated 2PACL concept is that the heat exchanger for reaching the saturation temperature is integrated in the accumulator itself instead of an internal heat exchanger in the concentric transfer line for the standard 2PACL concept. This allows for an easier system control and minimizes the required piping.
The operation cycle in the I-2PACL cooling concept with the thermodynamical processes in the log(p)-h diagram is depicted in Figure 6.6 and can be divided in the following steps:

- 0: The CO_2 saturation temperature is set by the CO_2 pressure in the accumulator via cooling or heating the liquid-vapour mixture inside.
- $1 \rightarrow 2$: Liquid CO_2 in the sub-cooled state is compressed by the pump and the pressure and temperature increases.
- $2 \rightarrow 3$: Liquid CO_2 flows through a spiral inside the accumulator allowing for an heat exchange with the saturated liquid inside and aligning the saturation temperatures.

[23] The concentric line is vacuum insulated and the inner tube is used for the outflowing CO_2 in the liquid phase, whereas the outer tube is filled with the backflowing dual-phase CO_2 from the experiment.

- 3 → 4: The pressure of the fluid is decreased to the pressure in the accumulator through the concentric transfer line and a capillary valve before the experiment.
- 4 → 5: The liquid CO_2 is evaporated in the experiment's cooling loop due to the generated heat in the detector.
- 5 → 6: In the return flow of dual-phase CO_2, heat is exchanged in the concentric transfer line with the liquid CO_2 flowing to the experiment.
- 6 → 1: Dual-phase CO_2 is fully condensated via heat exchange with the primary chiller to reach subcooling for liquid CO_2 and to enable pump operation without cavitations.

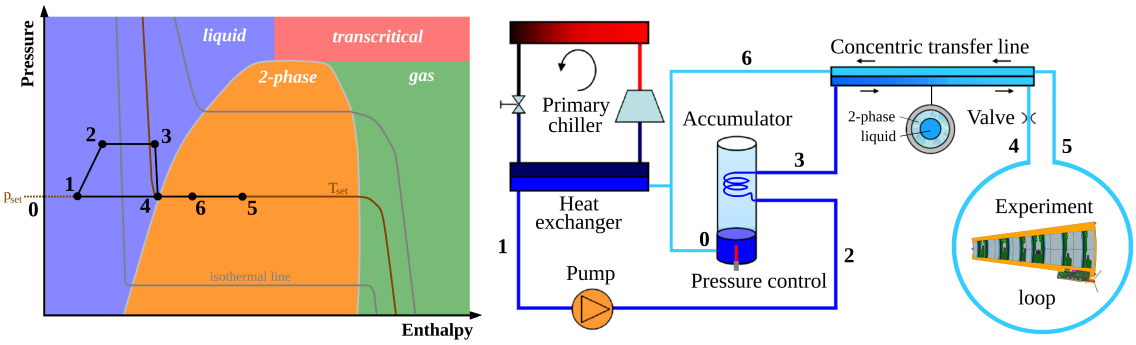

Figure 6.6: Operation cycle for the I-2PACL concept and thermodynamical processes of CO_2 in the log(p)-h diagram.

At the end of the three meter long concentric and flexible transfer line, the so-called *local box* is connected. Here, the in- and outlet piping of the experiment is connected and the desired detector *mass flow* can be controlled in two ways: either by the *experiment flow control valve* for the control of the direct flow of CO_2 through the experiment's cooling loop or by the *bypass flow control valve*, for which it is also possible to operate TRACI without a connected experiment. The operational range in the mass flow is between 1 and 4 g/s. Moreover, the local box is used for *venting* of the experiment, *refilling* CO_2 to the system and *vacuuming* the experiment after connecting the experiment's cooling loop. With the additional *safety relief valve* the experiment is protected against over-pressure due to trapped CO_2 in the loop.
The layout of the complete TRACI cooling system with the primary air-cooled R404A chiller, the CO_2 loop using the I-2PACL concept and the local box for connection to the experiment is shown in Figure 6.7.

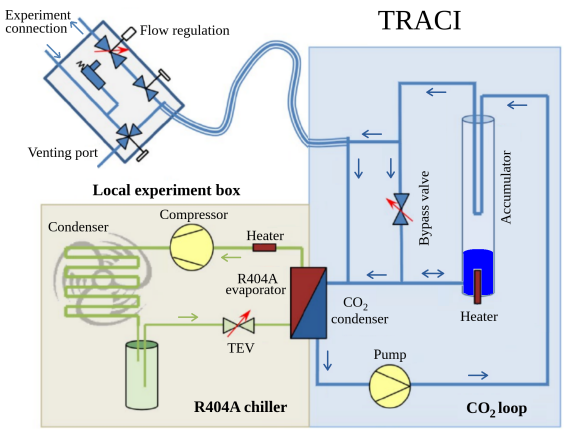

Figure 6.7: Layout of TRACI with the primary R404A chiller, the CO_2 loop controlled via the accumulator within the I-2PACL concept and the local box for connection to the experiment's cooling loop.

CO_2 diagnostics

The TRACI cooling system allows to measure a number of internal system parameters in terms of temperature and pressure values at different parts of the system. For the readout, a NI cDAQ-9174 system [161] is used and connected via an USB connection to a readout PC. The automated data logging is controlled by a LabView programme on the PC. The temperature and pressure sensors measuring the ouflowing liquid CO_2 and the backflowing dual-phase CO_2 as well as the flow meter to measure the adjustable mass flow through the experiment are important for the analysis of the CO_2 state.
Additional equipment for the CO_2 diagnostics is used to allow a deeper insight in the thermodynamical processes happening during evaporative cooling in the experiment's loop. For this purpose, additional temperature and pressure sensors were integrated after the local box and before the experiment's cooling loop for the in- and outlet. The CO_2 pressure is measured with a UNIK 5000 pressure transmitter [162], providing an accuracy of ± 0.1 bar in the measurement range of $0 - 100$ bar and for operational temperatures between -40 and $80\,^{\circ}$C. The CO_2 temperature is measured with a thermocouple[24] of type T [164] providing an accuracy of ± 0.5 K over the measurement range between -40 and $125\,^{\circ}$C. Here, the tip of the thermocouple is inserted directly into the fluid.
For the readout, a Keithley 2701 multimeter and DAQ system [165] is used for recording the current signals from the pressure transmitters and the voltage signals from the thermocouples. The multimeter is connected via an USB-to-RS232 adapter to a PC and the readout is controlled via a Python script, which allows to convert the raw sensor signals into pressure and temperature values by applying the provided calibration functions. The detailed layout of the p-T probe with photographs of the assembly is shown in Figure 6.8.

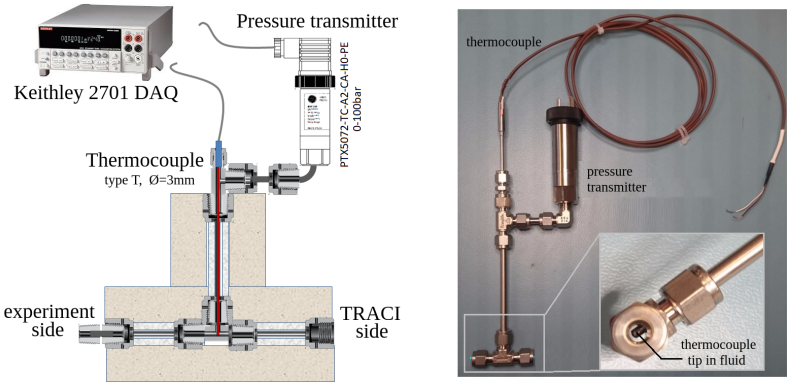

Figure 6.8: Layout and photographs of the p-T probe for CO_2 diagnostics close to the in- and outlet of the experiment's cooling loop. Shown are the pressure transmitter and the thermocouple sensor in the assembly.

Moreover, a high-density NiCr cartridge heater [166] as heating element with a power of up to 200 W is integrated in the piping from the local box to the experiment's inlet. The temperature at the heating element is measured by a thermocouple type J and recorded with the DAQ system as well. By applying different heat loads additionally to the experiment's heat load, the state of the dual-phase CO_2 in terms of the vapour quality can be influenced. For the tests of the thermal performance of petal prototypes, the heating element was not used, but only in dedicated tests to assess the evaporative CO_2 properties.
The last part of additional equipment is the integration of sightglasses [167] into the piping at the local box offering a glass window of $\varnothing = 35$ mm. By this tool, a visual control of the CO_2 phase for the outgoing and returning fluid is possible, allowing to estimate the vapour quality from the observed flow pattern.

[24] A thermocouple consists of an electrical junction of two dissimilar electrical conductors (e.g. copper and constantan for type T). Due to the Seebeck effect [163], a temperature-dependent voltage is produced at the electrical junction which can be used to measure the temperature at the contact point.

Figure 6.9 shows the additional CO_2 diagnostics integrated at the local box with the heating element and the sightglasses to and from the experiment's cooling loop.

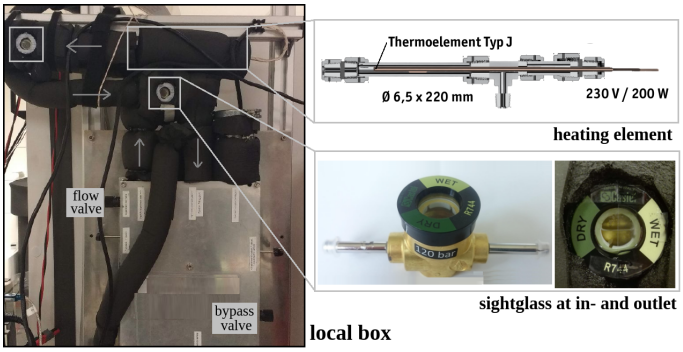

Figure 6.9: Integration of a heating element and two sightglasses for CO_2 diagnostics at the local box of TRACI.

6.2.4 Temperature & humidity logging

The environmental conditions in a test setup are of special interest when performing thermal studies. On the one hand, the cooling tests have to performed in a dry atmosphere to avoid condensation and ice on the cooled down test object. Therefore, the test object is enclosed and the volume is flushed with dry air or nitrogen to reduce the **R**elative **H**umidity (RH). The RH value should be measured and logged for the full test to control the dry atmosphere. On the other hand, the air temperature in the test setup is of interest, e.g. to infer the transferred heat by convection or to calculate the dew point using the measured RH value.
The SHT21 sensor [168] allows to measure the temperature in an operating range of $(-40 \ldots 120)\,^{\circ}\mathrm{C}$ with an accuracy of $\pm(0.3 \ldots 1.3)\,^{\circ}\mathrm{C}$ and the relative humidity between $(0 \ldots 100)\%$ with an accuracy of $\pm(2 \ldots 5)\%$. A Raspberry Pi system [169] is used to readout three SHT21 sensors sequentially via I^2C/GPIO and is programmed via a Python script with a repetition rate of 10 s.
Moreover, to allow direct probe measurements of a test object's temperature, Pt100 sensors[25] are used. For the readout, a Keithley 2701 DAQ system with plug-in multiplexer cards is used, allowing to acquire sequential temperature readings of ten Pt100 sensors via 4-wire sensing[26] per multiplexer. Again, a dedicated Python script allows automated data taking with the multimeter via a connected readout PC.
The automated readout and data logging of temperature and humidity values is applied in different test setups in the following and were developed in the course of a summer student project [170] to ease the QC measurements during production.

6.2.5 Thermal & CO_2 simulations

The comparison of experimental results to simulations allows to gain a deeper understanding of the investigated object and the impact of the performed test. On the one hand, results of mechanical and thermal testing of the petal can be compared to simulation results using the method of FEA. By comparing the simulation with experimental data, the simulation model can be validated and used in the following for design studies and its optimization. This is important for the R&D phase of the detector development, as not for each design iteration of the petal a new prototype object can be built and tested.

[25] The Pt100 sensor is a resistance thermometer made out of platin with a nominal resistance of 100 Ω at 0 °C and a defined resistance characteristic to measure the corresponding temperature.
[26] The 4-point probe method allows to correct for the resistance of the cable connection and avoids possible measurement errors due to different cable lengths.

On the other hand, properties of the evaporative CO_2 cooling can be predicted with CoBra simulations. Here, the modelling of the CO_2 temperature along the cooling loop as well as the HTC are of special interest, which are used as input for the thermal FEA.

FEA simulation

The method of **F**inite **E**lement **A**nalysis (FEA) [171, 172] is the preferred tool to solve problems of engineering and mathematical models, in areas such as structural analysis, heat transfer or fluid dynamics. The goal of FEA is to find a numerical solution for the partial differential equations describing the physical process of the problem, which are formulated either in two or three space variables with defined boundary conditions. To find a solution, the large system of the problem is divided into smaller and simpler parts, called the *finite elements*.
For the purpose of discretisation in the space dimensions, a mesh for the modelled object is created. Here, each mesh element defines the numerical domain for the solution using a finite number of points. The problem simplifies to a boundary value problem for each element and can be formulated as a system of algebraic equations. In the final step, the simple equations for each finite element are assembled together to the entire model and the solution is estimated by variational methods with minimizing an associated error function. The FEA for the petal is performed with the ANSYS Workbench 2020 R1 [173]. The focus is on the simulation of the thermal performance of the petal with a steady-state analysis for different temperature scenarios. On the one hand, the temperature distribution of the petal core can be simulated and compared to the experimental results. On the other hand, a FEA for a fully loaded petal with all silicon sensors and electronics is performed. By using the power inputs of the active parts, like the power consumption in the silicon sensors due to leakage currents and the produced heat in the front-end electronics, the cooling performance of the petal can be evaluated in simulation.
In Figure 6.10a the mesh for the petal core FEA is shown, which is composed out of roughly 570000 finite elements for the thermal simulation. The model definition for the petal FEA is depicted in Figure 6.10b, including the definition of modules with silicon sensors, hybrids, powerboards and ASICs.

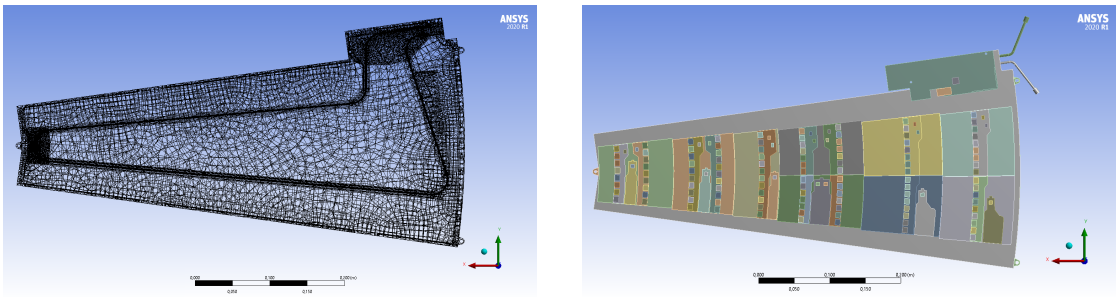

(a) Mesh for the petal core FEA. **(b)** FEA model of the petal.

Figure 6.10: FEA simulation of petal core and petal with ANSYS Workbench 2020 R1.

The petal FEA results are also used as an input to the thermo-electrical model of the petal [174]. This model enables to study the headroom in terms of cooling power to the case of thermal runaway for different cooling scenarios as well as power inputs. Especially interesting in this case is the expected performance at the detector's end-of-life as the power consumption increases with the acquired radiation dose.

For the definition of the simulation model, the geometrical CAD model of the petal with all its components can be imported. To simplify the model and to avoid small volume definitions requiring a large number of mesh elements, the glue layers are modelled only by defining the interface between the attached components with an appropriate thermal conductance. Furthermore, the physical properties of the materials in the individual components have to be defined, such as the thermal conductivity values for a thermal FEA. In principle, it is interesting to perform also a mechanical FEA of the petal, but the problem here is that a number of parameters important for the structural analysis are not directly accessible, such as the Young's modulus which is extracted from test measurements. Further information on the FEA model and its parameters can be found in [175].

CoBra simulation

For the thermal analysis, a good knowledge about the properties of the coolant is required, such as the coolant temperature and the HTC to the cooling pipe. When using dual-phase CO_2 as coolant, the behaviour is not easy predictable, as the temperature and HTC depends on the pressure drop in the cooling pipe as well as the transferred heat from the object. The available prediction models for CO_2 are based on the experimental observations of flow patterns in cooling pipes for different scenarios. With the empirical Thome models [176, 177], the flow conditions and the related heat transfer and pressure drop in a modelled cooling pipe can be predicted reasonably well.
For the analysis of a full detector cooling branch, the **Co_2 Bra**nch Calculator (CoBra) [178] is used. Here, the cooling loop is modelled as simple tube geometry with appropriate pipe diameters and any heat transfer or internal heat exchange between elements can be implemented. Finally, the CO_2 properties from the model are retrieved by an iterative method along the cooling pipe, providing predictions for the flow regime and changes in the fluid properties like temperature and pressure differences.
The predicted values along the petal cooling pipe for different scenarios like generated heat and CO_2 set point temperatures can be used as input for the thermal FEA. Moreover, the experimental data for detailed CO_2 measurements with the petal will be compared with the predicted CoBra values in Chapter 7. The CoBra GUI with an exemplary simulation of the CO_2 properties in the petal core is shown in Figure 6.11.

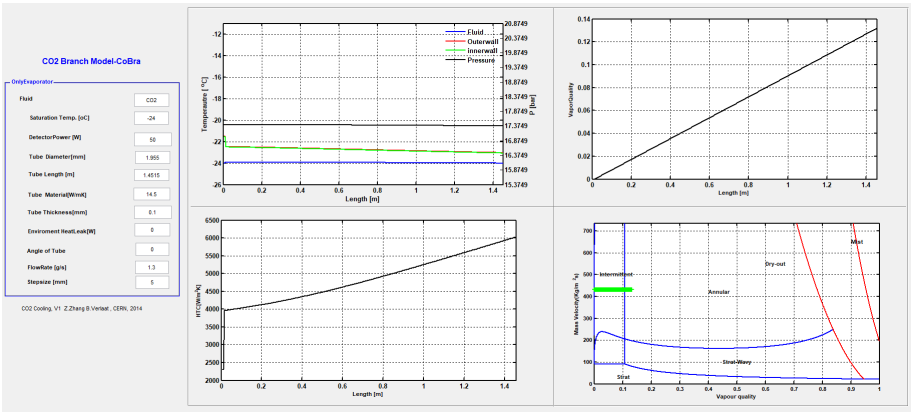

Figure 6.11: Overview of the CoBra GUI showing an exemplary CO_2 simulation for the petal core as simulated evaporator. The following quantities are predicted along the cooling loop: the CO_2 pressure and the CO_2 and tube wall temperatures (upper left), the vapour quality (upper right) and the HTC (lower left). Moreover, the CO_2 flow regime is predicted (lower right).

6.3 Prototypes: Petals & Cores

During this work, several petal prototypes were investigated and measured in terms of their mechanical, thermal and thermo-mechanical properties. As the petal design is still under development, each prototype represents another design iteration with minor and major differences between them. In general, two kinds of prototype classes are differentiated in the following: the measured prototypes of petal cores as bare local support structures are compared in Section 6.3.1 and the thermo-mechanical petal prototype loaded with thermo-mechanical silicon modules is introduced in Section 6.3.2.

6.3.1 Petal core prototypes

In total, nine petal core prototypes of different design stages were built at the DESY assembly site, which are summarized in Table 6.1 and discussed in the following.

Name	Fabrication	Design features	Use case
Core 00	07/2015	paper honeycomb (core 00); no petal locators;	
Core 01	12/2015	PEEK closeouts; early version of bus tape;	*thermo-mechanical petal*
Core 02	04/2017	commercial woven CF facesheet; no bus tapes;	
Core 03	08/2017	larger honeycomb cells (core 03);	
Core 04	09/2018	in-house cocured CF facesheets; insertable PLs (core 04);	
Core 05	09/2018	rejected bus tape (core 05);	
Core 06	04/2019	semielectrical bus tape;	*semielectrical petals*
Core 07	04/2019	non final-design CF prepreg;	
Core 08	11/2019	electrical breaks (core 08) ;	*FDR petal*

Table 6.1: Overview of petal core prototypes of different design stages arranged in appropriate categories of similar properties.

The petal cores 00 and 01 are the very early designs (e.g. no petal locators are integrated) and are assembled partly with different materials than the planned design: paper honeycomb instead of CF honeycomb is used in core 00; the top and bottom closeouts are PEEK instead of Torlon; the lateral closeouts are PEEK instead of pultruded CF. Nonetheless, a very early version of the bus tape is cocured to the CF facesheets.
The common feature of the cores 02 and 03 is that both have no bus tape, but the facesheet is made of commercial woven CF layers. The designs have slight differences in terms of the close-out and the EoS region and in core 03 a larger CF honeycomb cell size was tested.
The designs of core 04 and 05 are identical with the exception that the PLs are insertable for core 04. Moreover, these prototypes uses the first in-house cocured CF facesheets, but only core 05 features a bus tape, which is marked as rejected due to its electrical properties.
Finally, the cores 06, 07 and 08 belong to the same group, as the same assembly design as well as bus tape design was used. The materials are as in the final design, but only a different CF prepreg was used in the cocuring process. Furthermore, the cooling pipe of core 08 features for the first time the electrical break assemblies for electrical isolation of the core from the global structure.
Figure 6.12 shows a collection of pictures of the different petal core prototypes during or after the assembly, highlighting the different design stages of the cores.

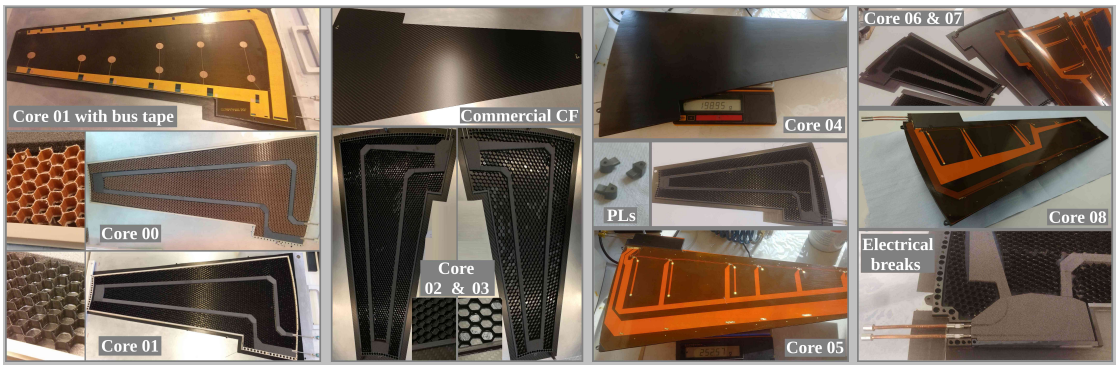

Figure 6.12: Petal core prototypes built at DESY with different design stages.

Some of the core prototypes serve also for special use cases:

- The core 01 is used as the local support structure for the *thermo-mechanical petal* prototype as discussed in the next section.
- The use of the cores 06 and 07 is dedicated to the *semielectrical petal* prototypes, which allows to test the module-on-core procedure with semielectrical silicon modules.
- The core 08 is used for the final design verification for the petal core design and the test results of the *FDR petal* served as input to the ATLAS **F**inal **D**esign **R**eview (FDR) for the local support structure of the ITk strip detector in February 2020.

Furthermore, the mechanical, thermal and thermo-mechanical tests were performed with different petal core prototypes. The cores 00, 02 and 03 were used for mechanical tests to assess the Young's modulus of the sandwich structure in a three-point bending test setup and to analyse the vibrational modes in a vibration-resonance setup. The test setups and the results of the design validation are discussed in [179] with a comparison to FEA simulation in [175]. The mechanical characterization of the cores in terms of geometrical metrology is standardly performed after the core assembly, whereas the applied test procedure has evolved over the different prototype stages.
The thermal deformation tests, as it will be discussed in Section 6.6, were performed only with core 05. The thermal performance assessment was conducted for almost all cores (despite the cores 00 and 06 due to time reasons) and is the topic of Section 6.5. The most intensively tested petal core is core 08 as the FDR petal. This involves also the thermo-mechanical QA tests under extreme temperature scenarios, meaning thermal cycling and thermal shock, as addressed in Section 6.7.

6.3.2 Thermo-mechanical petal

The thermo-mechanical petal prototype, in short *TM petal*, is a test object to study the performance of a petal core loaded with dummy silicon modules in terms of its thermo-mechanical characteristics. In Figure 6.13, an overview of the different components of the TM petal is shown and explained in the following.
As local support structure, the core 01 is used which features a bus tape of an early design stage. The copper traces in the bus tape are fully functional and can be used for powering, whereas only dummy data lines are implemented in the design. On both sides of the petal core, dummy silicon modules were manually glued on the bus tape.
A dummy module consists of a blank, wedge-shaped silicon crystals with a thickness of 320 µm mimicking the silicon strip sensor. Moreover, dummy hybrid PCBs are glued on the silicon crystals as in a real silicon strip module, but are populated with glass ASICs featuring internal pattern heaters to emulate the heat load.

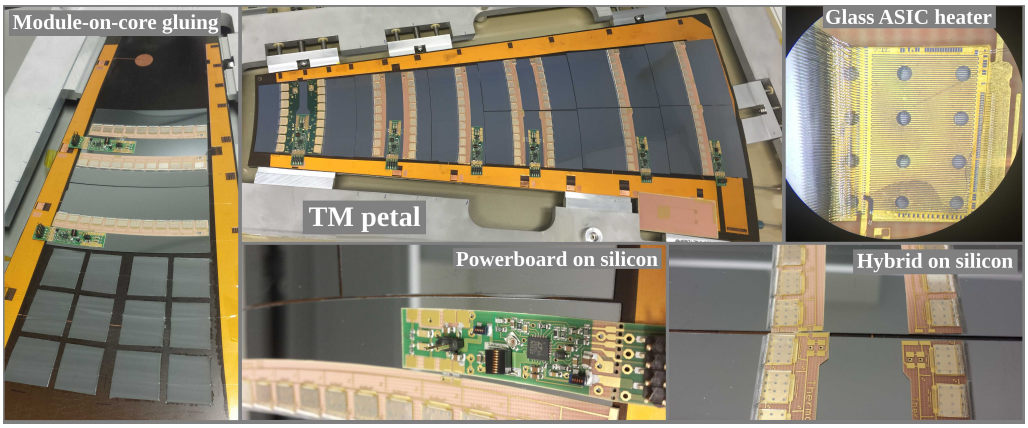

Figure 6.13: Overview of the thermo-mechanical petal prototype at DESY.

For the powering of the glass ASICs, a dummy powerboard PCB is glued on the silicon, featuring a DC-DC converter. The output voltage can be regulated by a potentiometer to emulate the expected heat load for each module as the power consumption in the front-end electronics and the DC-DC converter itself. Finally, the EoS board is emulated with a PCB featuring a resistive heater of the appropriate heat load.
In Table 6.2, the measured power consumption of the individual components per module and petal side for an input voltage of 10.5 V are shown.

Module		$I_{\text{in}}^{\text{DCDC}}$ [A]	$U_{\text{out}}^{\text{DCDC}}$ [V]	$I_{\text{out}}^{\text{DCDC}}$ [A]	P_{ASICs} [W]	P_{DCDC} [W]	P_{total} [W]
	R0	0.308	4.993	0.431	2.152	1.082	3.234
	R1	0.432	6.023	0.550	3.313	1.223	4.536
	R2	0.312	5.958	0.350	2.085	1.191	3.276
front	R3	0.516	6.035	0.696	4.200	1.218	5.418
	R4	0.345	5.918	0.450	2.663	0.959	3.623
	R5	0.381	6.019	0.510	3.070	0.931	4.001
	$\sum$				**17.483**	**6.604**	**24.087**
	R0	0.364	5.813	0.476	2.767	1.055	3.822
	R1	0.430	5.749	0.559	3.214	1.301	4.515
	R2	0.273	6.032	0.365	2.202	0.665	2.867
back	R3	0.517	5.764	0.724	4.173	1.255	5.429
	R4	0.313	5.738	0.431	2.473	0.813	3.287
	R5	0.403	5.956	0.542	3.228	1.003	4.232
	$\sum$				**18.057**	**6.093**	**24.150**

Table 6.2: Power consumption in ASICs and DC-DC converters for the TM petal per module and side, calculated from the measured voltages and currents at the input and output of each DC-DC converter.

The total emulated heat load of the TM petal is 54 W, with a load per petal side of 24 W in the modules and 3 W in the EoS. For the thermal tests, different powering scenarios of the TM petal can be studied as it is possible to control the individual modules and EoS by a switching matrix for the power supply.
The TM petal served on the one hand as test object for the module-on-core procedure by training the module handling with wire bonds as well as the gluing process. On the other hand, an intensive test programme to assess the thermal performance of the TM petal under various conditions has been conducted in the course of this work.

6.4 Emissivity and Correction Methods

For the thermal tests using the technique of IR thermography, the assessment of the emissivity of the investigated petal cores and the TM petal are important. In general, the emissivity of an object depends on a number of material properties. These emissivity dependencies and further influences in the IR thermography, like the so-called *Narcissus effect*, are explained in Section 6.4.1. Afterwards, methods to measure the emissivity of an object and to correct the temperatures in the IR thermography are introduced in Section 6.4.2. For the study of a material's emissivity and on the influences in the IR measurement, dedicated tests were conducted, as described in Section 6.4.3. Here, the focus is on the assessment of the emissivity of petal related material surfaces and the validation of possible correction methods for these surfaces. Finally, the applied correction methods for the emissivity of the petal core prototypes and the TM petal are discussed in Section 6.4.4.

6.4.1 Emissivity and its dependencies

The emissivity of a test object in the IR thermography is a material property and depends intrinsically on the following object properties:

- *Material*: The material type is the dominant parameter of the emissivity. Typically, the emissivity of materials can be classified in non-metals and metals. Here, most non-metallic materials like glass, plastic, paper, paints and also human skin are gray emitters with fairly high emissivities above 0.8. On the contrary, metals show low emissivities of below 0.2 and are therefore problematic for IR thermography.
- *Surface structure*: For a given material, the emissivity varies significantly with the material's surface structure. In the case of metals, a polished surface can reach emissivity values as low as 0.02, whereas for a roughened surface of the same material values of 0.8 are reachable.
- *Geometry*: If the object has well-defined features in the surface, like grooves or holes, the emissivity for these geometries is different from a flat surface. The reason is that a groove and even more a hole act like a cavity for the emitted radiation, meaning that the amount of emitted radiation is enhanced due to internal reflections on the inner surfaces.

The type of the object's material surface and its structure and geometry are the major dependencies for the object's emissivity, but variations in the object's emissivity can also occur due to the following parameters in the IR thermography:

- *Viewing angle*: The emitted radiation is a directional quantity and can be defined relative to the solid angle element $d\Omega$ with two characteristic angles δ and ϕ. Whereas a blackbody behaves like a perfect isotropically diffuse emitter and the emitted radiation is independent from $d\Omega$, the emitted radiation of a real material surface varies with the direction of emission. This means that the emissivity depends in general on the angle of observation with respect to the surface normal.
- *Wavelength*: Typically, material properties depend also on the wavelength, which can be especially observed for the reflexivity. Due to the direct link of reflexivity and emissivity, the material's emissivity shows also a variation with the wavelength.
- *Temperature*: The emissivity varies for some materials strongly with the material's temperature, typically over larger temperature ranges of $\mathcal{O}(100 - 1000\,\mathrm{K})$.

For the used IR camera with a small wavelength interval of $7.5 - 14\,\mu$m, the emissivity variation over the used wavelength interval can be neglected. The same applies for the temperature dependence, as the object's temperature changes only in a small interval between 25 and $-40\,^{\circ}$C and the emissivity can be considered as constant herein.
For the angular dependence, measurements on typically used materials in IR thermography have demonstrated that the material's emissivity is nearly constant from the normal direction at 0° to viewing angles of at least 45° [157]. This was also confirmed by a dedicated measurement in the IR thermography test setup, which is discussed in Section 6.4.3.

When studying a low emissive object with an IR camera, another effect depending on the angle between camera and object is observed. In the *Narcissus effect*, a reflection of the camera itself is detected in the thermogram if the camera observes a high reflective material in the normal direction. This is shown in Figure 6.14 for the Narcissus effect on an aluminium plate and a silicon wafer. In the thermograms, recorded with emissivity of 1.0, the warm camera contour and especially the camera lens with the uncooled bolometer sensor behind are clearly visible as hot spots. The easiest way to avoid the Narcissus effect in the IR thermography setup is to tilt the camera relative to the object. By this change in the viewing angle away from the normal incident direction, no incident reflected radiation from the camera detector area reaches the camera objective anymore.

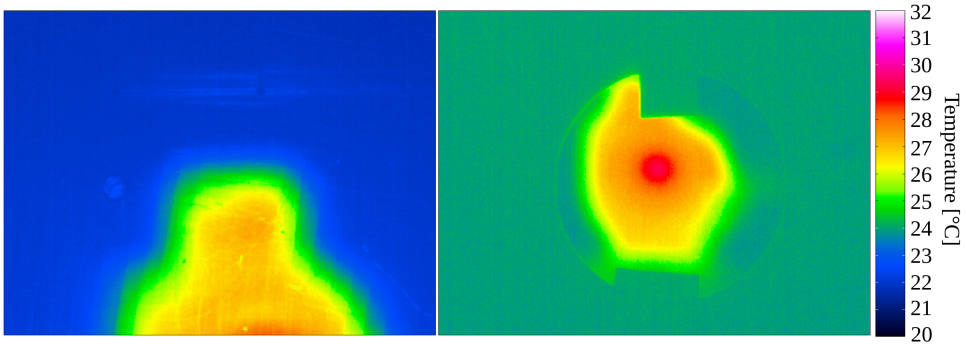

Figure 6.14: The *Narcissus effect* detected on an aluminium plate (left) and a silicon wafer (right) at room temperature. Shown are the corresponding thermograms recorded with $\epsilon = 1.0$ with clear indications of the reflection of the camera and its lens as warm contours.

Finally, another possible influence on the IR thermography can be caused by conducting the measurements in an air atmosphere. The developed test setup in this work is flushed with dry air to reduce the RH and to avoid condensation and ice building on the object's surface. But in general, the transmission of thermal radiation through a medium can cause an attenuation. E.g. for the transmission in air, energy in the IR wavelengths is mainly absorbed by contained H_2O and CO_2 molecules.
To evaluate the impact of the transmission through air on the measurement, three major contributions play a role: the distance between object and IR camera within the air volume; the air composition in terms of fractions of molecules e.g. its water content due to humidity; and the sensitive wavelength interval of the IR camera.
Figure 6.15 shows the transmission spectrum for a ten meter long air path with a RH of 50%. In the wavelength interval of $8 - 14\,\mu$m, covering a large fraction of the IR camera's sensitivity interval, a nearly constant transmission of one is observed. For the lower wavelengths of $7.5 - 8\,\mu$m, the reduced transmission originates dominantly from the H_2O absorption bands, which is therefore strongly dependent on the RH value.

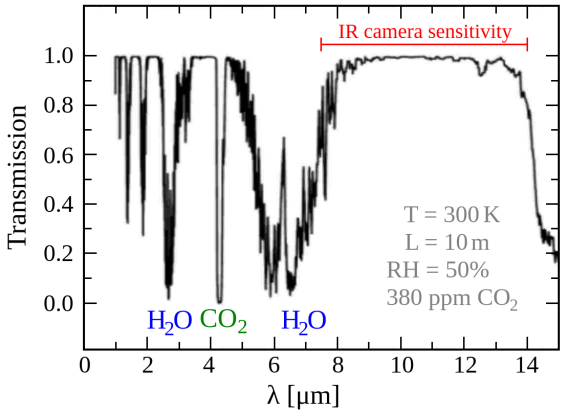

Figure 6.15: Transmission spectrum of air for a path length of L= 10 m at T= 300 K and RH= 50%. Marked are the dominant absorption bands of H_2O and CO_2 molecules and the wavelength interval of the IR camera with $7.5-14\,\mu$m is overlayed. Modified from [157].

The conclusion for the developed measurement setup for the thermal performance performance assessment of petals is that the effect of attenuation due to transmission in air is negligible, as the camera operates in the $7.5-14\,\mu$m wavelength interval, the RH is typically $\mathcal{O}(1\%)$ due to dry air flushing and the distance between camera and object is only $\mathcal{O}(1.1\,\text{m})$.

Therefore, the main factor for the IR thermography of petal core prototypes and the TM petal is the emissivity dependence on the material type and the surface structure. This is demonstrated by dedicated studies on the test objects' surfaces and their emissivity characteristics in Section 6.4.3.

6.4.2 Emissivity and its correction techniques

For the measurement of the emissivity, meaning here the directional near normal emissivity integrated over the wavelength interval of the IR camera, several methods exist. Some of the practical methods for adjusting the emissivity in IR thermography are the following:

- *Tape*: By placing pieces of tape on the test object, the surface temperature on the tape areas can be assessed if the tape's emissivity is known. Providing a good thermal contact and waiting until a state of thermal equilibrium is established, adjacent surface temperatures of the object are assumed to be equal. Therefore, the object's emissivity can be found by varying ϵ for the uncovered areas using the camera software, until their temperatures are equal to the known tape surface temperature. The advantages of the tape method are a non-destructive measurement of ϵ with the possibility to remove the tape pieces afterwards.

- *Paint*: By spraying the object's surface with paint, the emissivity is equal to the paint's emissivity. With a known emissivity for the paint, the same approach as in the tape method can be applied to infer the object's emissivity. The paint method has advantages on rough surfaces compared to the tape method due to the better thermal contact, but has the drawback of removing the paint after testing.

- *Thermocouple*: By placing a contact thermometer, e.g. a Pt100 temperature sensor, directly on the object, the measured surface temperature can be used to calibrate the IR image and infer the object's emissivity. For this method, the requirements are to achieve a good thermal contact, to establish a thermal equilibrium on the object and, most critical, to not change the object temperature by the conduction of heat with the attached thermocouple. This method is in principle non-destructive and reversable, but to achieve a good thermal contact, the temperature sensor can be fixed on the object's surface by thermal-conducting glue.

- *Hole cavity*: A destructive method is the creation of a cavity by drilling a hole in the object. Due to the cavity effect, the emitted radiation of the hole behaves like a blackbody emitter with a very high emissivity value. The emissivity of adjacent regions to the hole can then be inferred in the same manner as the tape method. The clear advantage is that the method is independent of the object's surface structure, but is destructive and therefore for many test objects not usable.

The accuracy on the measured emissivity values depends on the applied method: for the tape and paint method, the accuracy on the known emissivity is the influencing factor; for the thermocouple method, the accuracy of the temperature measurement is the dominant factor; and for the hole cavity, the perfection of the hole is the relevant parameter.

For the detailed emissivity studies in the next section, a tape with known emissivity, a high-emissive black paint spray and direct probe Pt100 sensors are used. Nonetheless, examples of the application for all four correction methods are shown here qualitatively.
In Figure 6.16a, the measurement of a cooled aluminium plate with tape, paint and attached temperature sensors is shown. Assuming a global emissivity of 1.0, the reflective, uncovered aluminium area records a temperature of $17.2 \pm 0.2\,^{\circ}\mathrm{C}$ dominated by the ambient temperature of the setup. The values for the taped area with $-14.3 \pm 0.3\,^{\circ}\mathrm{C}$ and the painted area with $-15.3 \pm 0.3\,^{\circ}\mathrm{C}$ reflect better the cold object temperature.
Figure 6.16b shows the measurement of a cooled aluminium block covered partly with tape, attached temperature sensors and with four drilled holes, having two different diameters ($d_1 < d_2$) and two depths ($l_1 < l_2$). The measured temperature on the aluminium is $19.5 \pm 0.7\,^{\circ}\mathrm{C}$ compared to the taped region with $-14.0 \pm 0.3\,^{\circ}\mathrm{C}$. For the different holes, the following temperatures are assessed: $5.5 \pm 1.1\,^{\circ}\mathrm{C}$ (hole 1, d_1, l_1), $-0.4 \pm 0.6\,^{\circ}\mathrm{C}$ (hole 2, d_1, l_2), $9.5 \pm 1.6\,^{\circ}\mathrm{C}$ (hole 3, d_2, l_1) and $-4.7 \pm 1.0\,^{\circ}\mathrm{C}$ (hole 4, d_2, l_2). This shows that for the cavity effect, the ratio of hole diameter and depth is a critical parameter. In a final comparison, the temperatures from the Pt100 sensors can be compared for both cases.

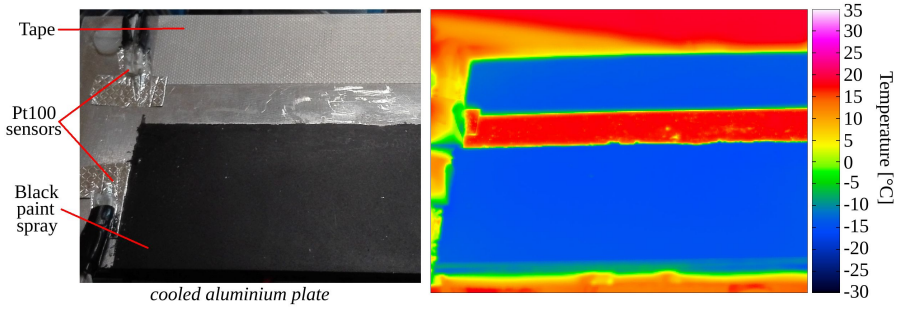

(a) Cooled aluminium plate with tape, black paint and thermocouples.

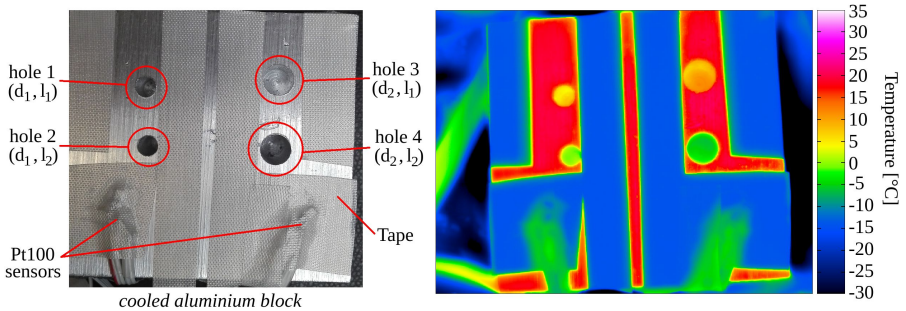

(b) Cooled aluminium block with tape, thermocouples and hole cavities.

Figure 6.16: Examples for the application of emissivity correction methods.

6.4.3 Experimental studies on the emissivity

In the following, several studies on the emissivity and the influencing parameters for the thermal measurement of petal cores and the TM petal are discussed.

Study on the viewing angle dependence

A possible dependence of the test object's emissivity on the viewing angle between object and IR camera was studied by a dedicated test using the developed setup for thermal testing (cf. Section 6.5.1). Here, a hollow aluminium rod was filled with hot water and covered with tape for the emissivity correction. The object was horizontally mounted in the test setup and the thermogram was recorded with the IR camera for an emissivity value matching the tape area. For a temperature cross-check, a Pt100 sensor was placed on the aluminium rod to assess the temperature by a direct probe measurement.
By defining markers in the IRBIS software, the temperature values in these measurement areas are recorded along the rod. For each of the defined markers, the corresponding viewing angle is then calculated from the setup's geometry.
Figure 6.17 shows the measured temperature values from the IR camera along the rod. The comparison to the measured temperature with the Pt100 sensor shows a good agreement with the IR results. The IR temperatures along the rod show a variation with the viewing angle in the order of 0.3 °C. Moreover, a trend to slightly lower temperatures for higher viewing angles can be observed, but all values are well within the assumed uncertainty of the IR camera with ±1.5%. Therefore, it can be concluded that the angular emissivity dependence is a negligible effect for IR measurements performed in the setup.

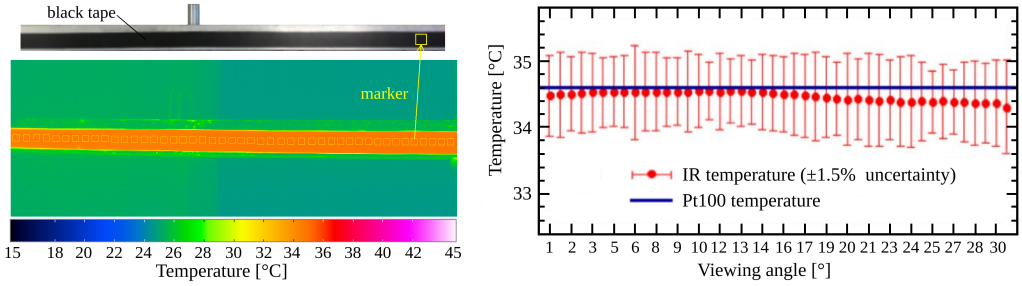

Figure 6.17: Measurement of the angular emissivity dependence in the IR thermography setup. The temperatures along an aluminium rod, filled with hot water and covered by black tape, are measured with an IR camera and compared to a Pt100 sensor. The recorded thermogram with defined markers (left) is used to analyse the temperature variation for different viewing angles (right).

Study on petal core surfaces

For the study of the emissivity of material surfaces occurring on the petal core prototypes, a simple test setup was used: an aluminium vacuum plate, normally employed for the petal core assembly, was directly cooled by dry ice[27] on the backside. To avoid condensation, the setup is surrounded by dry air flushing. In the next step, different objects can be placed on the cold plate using vacuum for fixation. The temperature distribution on the object is measured with the IR camera[28] mounted on a movable stage in a distance of approximately 30 cm and with a slight angle. The test setup is depicted in Figure 6.18a.

[27] Dry ice as the solid form of carbon dioxide is a perfect coolant in test setups. When sublimating at a temperature of −78.5 °C, no residues of the coolant like water are left behind.
[28] The emissivity value in the IRBIS software is set to $\epsilon = 1.0$ for the following thermograms.

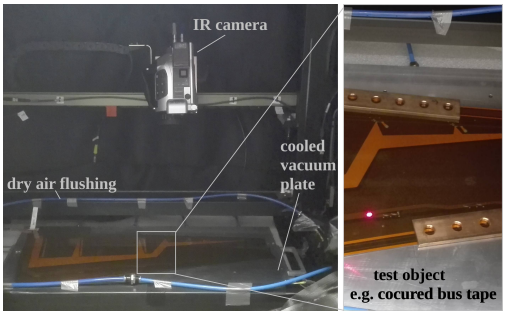

(a) Setup with IR camera and dry air flushing.

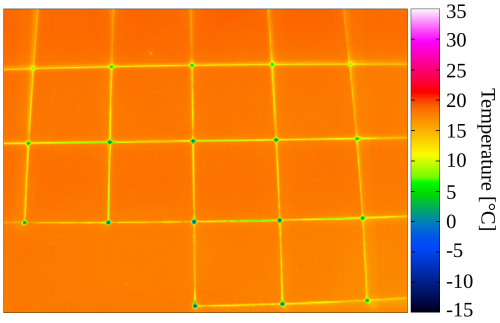

(b) Aluminium vacuum plate.

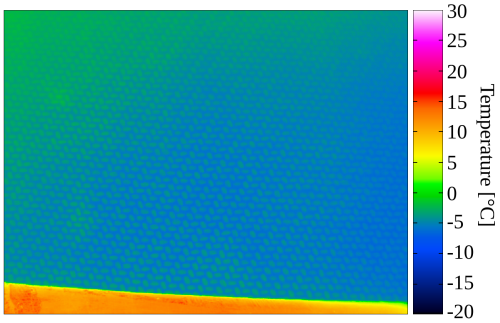

(c) Commercial woven CF facesheet.

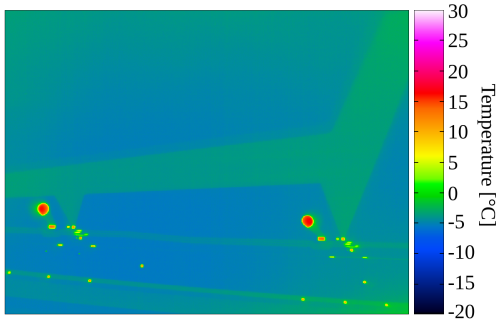

(d) Cocured bus tape.

Figure 6.18: Investigation on the emissivity of the petal core surfaces in a dedicated test setup with an IR camera, dry air flushing and cooled vacuum plate by dry ice. Shown are the setup and thermograms of the aluminium vacuum plate as well as two placed test objects, a CF facesheet and a cocured bus tape.

In Figure 6.18b, the thermogram of the cooled down aluminium vacuum plate is shown. Here, the poor emissivity of aluminium is visible as the measured temperature of approximately 18 °C is not the real object's temperature but mostly showing the reflected ambient temperature. Moreover, the dependence of the emissivity on the surface geometry can be observed, as the temperature values at the vacuum lines representing a groove structure are lower than on the flat areas of the plate. This means that the emissivity in the grooves is higher and shows therefore temperature values closer to the real object's temperature.
As test objects, two different kinds of surfaces are relevant for testing petal core prototypes: either a blank CF facesheet or a cocured bus tape. Figure 6.18c shows the recorded thermogram when a commercial woven CF facesheet is placed on the vacuum plate. Here, the inner material structure of the woven CF is visible as regular temperature distribution of areas with lower and higher temperatures. This difference can be explained in two ways: On the one hand, a different thermal conductivity in the vertical direction of the facesheet could be the reason. Due to the woven structure, the thermal conductance is not isotropic and could therefore result in the observed pattern along the individual fibers. On the other hand, the observed pattern could be explained by different emissivity values with a relative difference of roughly 5% for the apparently warmer areas.
Finally, the thermogram for the cocured bus tape as test object is shown in Figure 6.18d. Here, the temperature distribution is in most cases quite regular with two exceptions. On the one hand, the gold pads as openings in the polyamide top layer of the bus tape show a much higher temperature. This is due to the low emissivity of metals and the temperature reflects again the ambient temperature instead of the object's temperature.

On the other hand, the copper traces below the polyamide layer are visible with slightly higher temperatures. This observation can be explained again by the two same arguments as before: either the copper areas, which are horizontally distributed below the polyamide surface, result in a different thermal conductance in the vertical direction through the tape; or the emissivity of areas with copper traces is lower by roughly 4%.

Study on the transmissivity of silicon

For the TM petal as well as any other petal loaded with silicon modules, the surface is mostly covered by silicon, which is only partly overlayed by the populated PCBs of hybrids and powerboards. Silicon is a low emissive material, but contrary to low emissive metals, it has also a non-negligible transmissive part. As shown in Figure 6.19, the transmissivity of silicon in the IR camera sensitivity range of $7.5 - 14\,\mu$m is varying between 0.05 and 0.5.

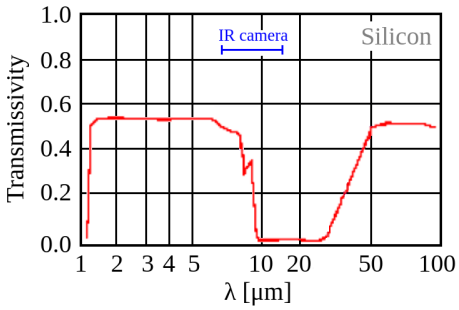

Figure 6.19: Transmissivity spectrum of silicon with the overlayed IR camera sensitivity range of $7.5 - 14\,\mu$m. Modified from [180].

In an experimental setup with the IR camera on a tripod, different silicon components relevant for the IR thermography of petals are tested. Here, the test objects are hold in front of a hot plate of varying temperatures, but without direct thermal contact to avoid conductive heat transfer. By measuring the temperature on the object's surface with the IR camera, the influence of transmissivity can be easily observed: if the object is transmissive, fractions of the emitted heat from the hot plate will be detected, whereas for an IR opaque object with low emissivity, the temperature will reflect the ambient temperature. In Figure 6.20, the thermograms for three different silicon components are shown, with the hot plate heated to a temperature of 80 °C.

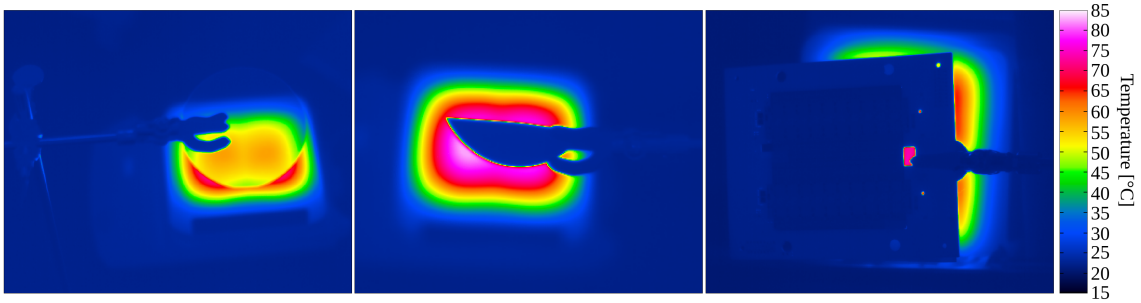

Figure 6.20: Measurement of the transmissivity of silicon using an IR camera and a hot plate. Shown are the thermograms recorded with $\epsilon = 1.0$ for three objects: a blank silicon wafer (left), a fabricated silicon wafer with backplane metalization (middle) and a silicon strip barrel module on a testframe (right).

Firstly, the transmission of a blank silicon wafer as used for the TM petal is demonstrated as higher temperatures are measured on the parts of the round wafer above the hot plate. Comparing the temperature on the wafer edge with the temperature directly on the hot plate, roughly 80% of the hot plate's temperature are measured on the wafer surface.

Secondly, a half-moon of a fabricated silicon wafer with backplane metalization shows no indication of transmitted heat radiation as its contour is clearly visible in the thermogram at ambient temperature. Finally, the same is observed for a silicon strip barrel module mounted on a test frame. The reason for the negligible transmission for the fabricated silicon components is most probably the aluminium layer on the backside.
Nonetheless, for the case of IR thermography of the TM petal with blank silicon an appropriate correction has to be applied to assess its real surface temperature, which is discussed in the next section.

Study on the black paint emissivity

For the correction of the low emissivity of silicon on the TM petal, the tape and paint methods are applied using a high emissive tape with a specified emissivity of $\epsilon = 0.95$ and a black paint spray with an unknown emissivity specification. In the course of a summer student project, a dedicated test setup was developed which allowed to measure the paint emissivity and further details of the measurement can be found in [181].

In the setup, as shown in Figure 6.21, an aluminium plate cooled with the cold side of two *Peltier elements*[29] is used. The surface is coated with black paint of unknown emissivity as well as covered by the tape with known emissivity. As a further reference, four Pt100 temperature sensors are clamped on the surface. The such prepared object is enclosed by a simple cardboard box with a hole for the camera lens to shield the measurement from reflections caused by outside heat radiation. Moreover, the warm side of the Peltier elements is cooled by a water chiller and with a constant dry air flushing the RH, logged with the Raspberry Pi system, is reduced in the setup. For different selected Peltier currents corresponding to different temperature set points, thermograms are recorded with the IR camera, the temperature of the clamped Pt100 sensors is recorded and the RH and ambient temperature is logged per measurement set point.

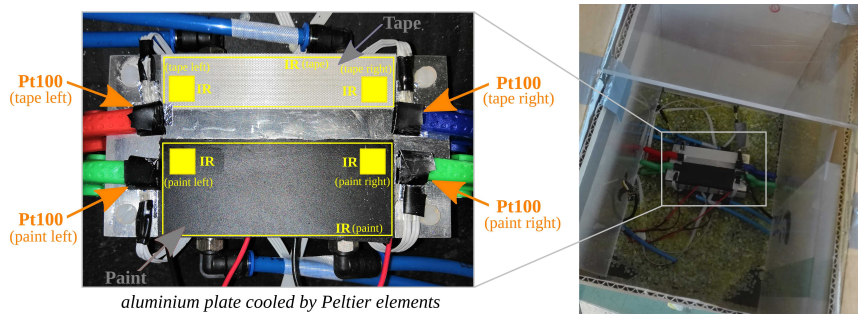

Figure 6.21: Setup of the paint emissivity study using an aluminium plate cooled with Peltier elements in a dry air flushed cardboard box. The aluminium surface has regions covered with black paint and with tape of known emissivity. Additionally, four Pt100 sensors are clamped on the surface for a contact measurement. IR marker areas (yellow) are defined for the tape and paint regions and can be compared to the nearby Pt100 sensors (orange).

[29] A Peltier element, also *thermoelectric cooler*, is a solid-state active heat pump and operates with the Peltier effect [182]. When a DC electric current is applied to the device, heat is transferred from one side, the *cold side*, to the other, the *warm side*, and changes therefore the temperature of both sides. In normal application, the warm side is attached to a heat sink to remain at a defined temperature, such that the cold side reaches a temperature below room temperature depending on the applied current and the device specification in terms of the reachable temperature difference.

Figure 6.22 shows one measurement cycle as function of the applied Peltier current with the recorded temperatures for each set point. For the IR measurement, the defined markers for the full area of tape and paint region are used with an emissivity value of 1.0. Moreover, the temperature measurement in an IR marker area is represented by the mean and its standard deviation for the contained pixels as well as the minimum and maximum value.

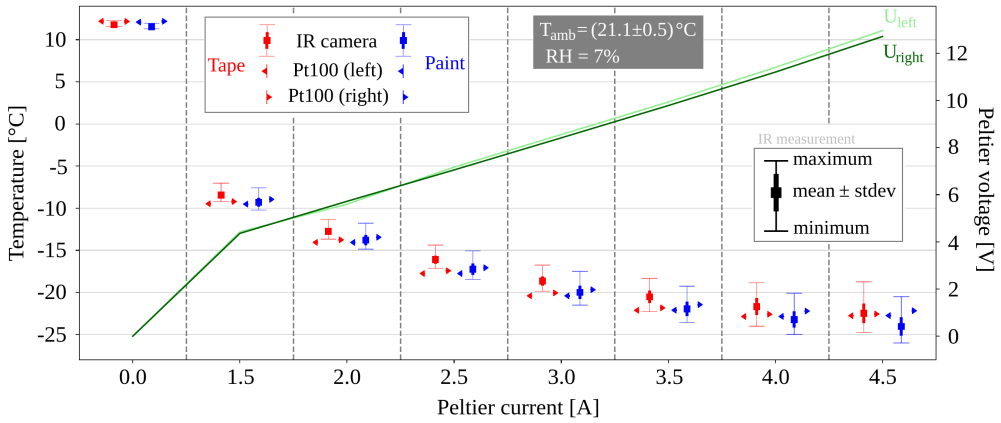

Figure 6.22: Typical measurement cycle with the Peltier setup for emissivity studies. For higher applied currents, the temperature on the cold side of the Peltier elements is lowered and allows to test different temperature set points. Shown are the measured temperatures of the IR camera in the tape and paint marker region and the corresponding Pt100 sensor readings.

A slight asymmetry of the temperature values is observed when comparing the two Pt100 sensors on the left side with the two on the right side. Therefore, four IR marker regions close to the Pt100 sensors are selected for the emissivity evaluation, assuming a thermal equilibrium over these surface areas. For the areas of tape, the thermogram is corrected by applying the known emissivity of $\epsilon = 0.95$ and using the measured ambient temperature to account for the reflective part of heat radiation, while any transmissive effect is neglected. For the areas of paint, the emissivity is systematically varied with the IR software to find the best value for matching temperature values to the taped regions.

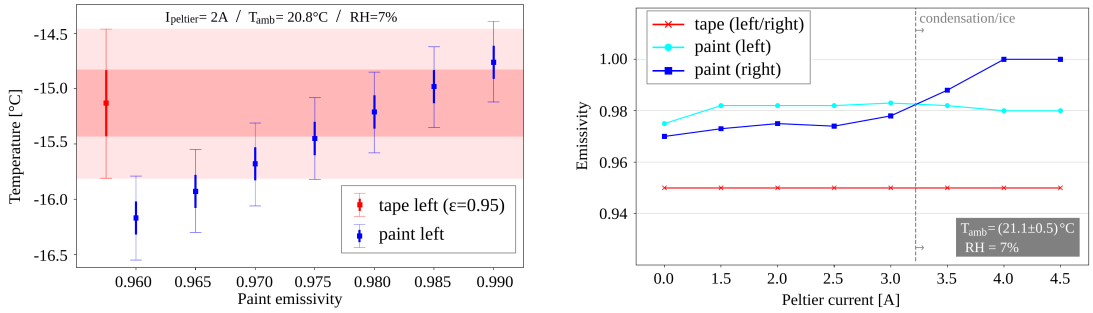

(a) Systematic variation of emissivity per set point. **(b)** Best matching emissivity per set point.

Figure 6.23: Determination of the emissivity value of black paint spray. The paint emissivity is systematically varied for each set point and marker area to match the temperature of the tape region.

Figure 6.23a shows the variation procedure for one selected Peltier set point and for the marker area *paint left*. Applying this method to all set points and both paint areas, the best matching emissivity value for the paint can be extracted, as depicted in Figure 6.23b.

For both paint regions, the determined emissivity value is relatively stable for different set points, with slightly higher values for the left marker area. The steep increase in the emissivity of the *paint right* area for higher set points can be explained due to ice building on the aluminium plate and therefore changing emissivites on the surface. On the one hand, the calculated dew point in the setup is about $-16\,^{\circ}\mathrm{C}$ such that condensation can appear. On the other hand, the ice formation can be also observed in the recorded thermograms. The emissivity of the used black paint is then calculated as the mean of both marker areas, excluding the higher set points, and has a value of 0.977 ± 0.004.
In general, this study showed a large dependence on the measurement conditions like humidity, ambient temperature and the Peltier cooling performance. Nonetheless, the black paint spray was proven to be a good candidate for the application on the TM petal to correct the low emissivity of silicon, as shown in the next section.

6.4.4 Emissivity correction for petals

The applied emissivity correction methods are different for the thermal testing of petal cores and the TM petal, as different effects are observed in the emissivity studies.

Correction for petal cores

For the different surfaces of core prototypes, either CF facesheets or cocured bus tapes, the overall emissivity of the surface is relatively equal and shows rather high emissivity values. The observed variations in the thermograms coincide with the geometrical surface features observable in the visual spectrum like the woven CF structure and the copper traces in the bus tape. To verify the reasons for the temperature variations, either caused by a difference in emissivity or a difference in thermal conductivity, two auxiliary experiments are conducted applying the tape method partly on the surface. If the same temperature variation is observed for the regions covered with tape, meaning an emissivity correction is applied, the reason is a different thermal conductivity, but if not it is an emissivity effect.

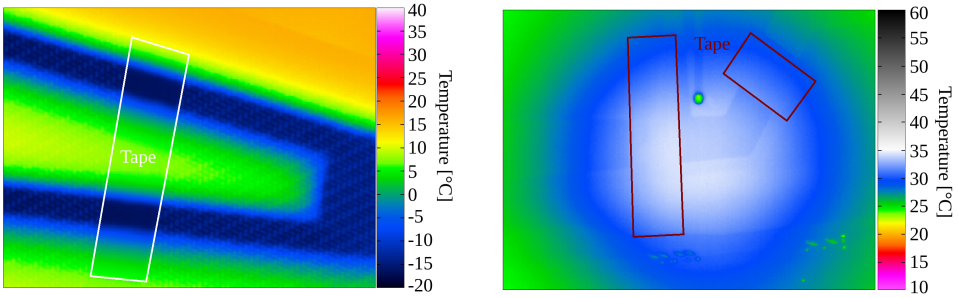

(a) Core with commercial woven CF surface. **(b)** Core with bus tape surface.

Figure 6.24: Study on the observed temperature variation for different core surfaces.

For core 03 as a prototype with the commercial woven CF facesheet as surface, the object was cooled using evaporative CO_2 and a thermogram is recorded in a region where the surface over the width of the core is partly covered by tape. As shown in Figure 6.24a, comparing the temperature distribution in the taped region with the neighboring untaped regions a temperature variation according to the woven CF structure is not observed. This indicates clearly a changing emissivity according to the woven geometry.
For core 08 as a prototype with a bus tape surface, a region of the core is heated from the back side by a circular pattern heater (evaporative CO_2 cooling was not available at that time) and two stripes of tape are applied on the copper traces in the bus tape.

Figure 6.24b shows the recorded thermogram with a uniform temperature distribution for the taped region and no indication of the covered copper traces. As the surface material of the bus tape is uniformly polayamide, the copper traces are most probably visible in the thermogram due to a transmissivity effect through the polyamide top layer.
For the thermal testing of petal cores in this work, no emissivity correction method is applied, because the IR thermography is planned as QC measurements for cores during production. As the temperature variation follows the pattern of the bus tape structure, this effect is easily correctable when comparing different cores with the same surface.

Correction for the TM petal

For the TM petal, it is necessary to correct the low emissivity of the silicon as sensor areas. In a first iteration, the tape method was implemented on both sides of the TM petal by covering the surface with stripes of tape as it is shown in Figure 6.25a.

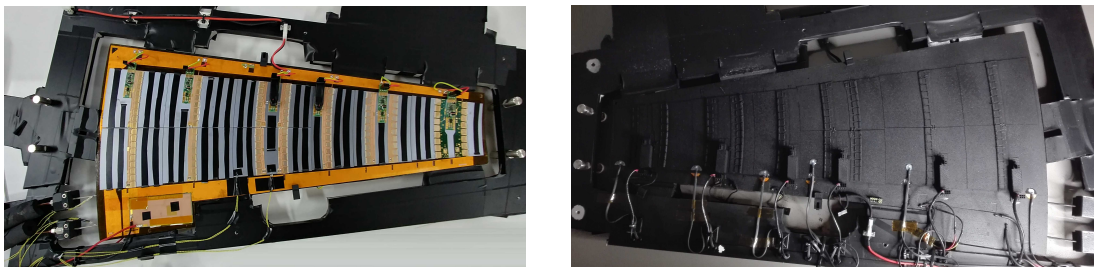

(a) TM petal with tape method. **(b)** TM petal with paint method.

Figure 6.25: Two iterations of emissivity corrections applied on the TM petal.

By this approach, it is in principle possible to measure the emissivity of silicon using the nearby tape regions with known emissivity. But the application of the tape correction method depends on two assumptions: establishing a thermal equilibrium state and neglecting the transmissivity. On the one hand, local temperature changes are observed in the TM petal due to the different thermal conductivity of areas, e.g. foam areas with good thermal contact compared to honeycomb areas. On the other hand, it was shown that the blank silicon wafers used for the TM petal are transmissive. Therefore, in a second iteration, the paint method was applied to the front side, which is shown in Figure 6.25b.

Figure 6.26 shows two additional measures for the IR measurement of the TM petal. Firstly, the dummy powerboards hosting the DC-DC converter are covered by 3D-printed black plastic caps. In IR measurements without the shielding covers, the generated heat in the converters caused hot air bubbles which influenced the measured temperature on the silicon. Secondly, the thermocouple method is implemented as cross check and Pt100 sensors are glued on each silicon module providing an independent, local temperature measurement.

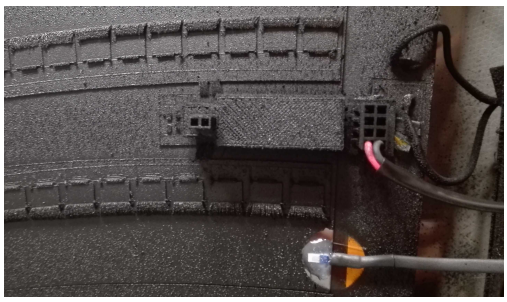

Figure 6.26: Painted TM petal with black plastic caps shielding the generated heat in the dummy powerboards and with Pt100 sensors glued on each silicon module for a direct temperature probe on the silicon surface.

6.5 Characterization of the Thermal Performance

The thermal performance of the petal core is a critical parameter as it serves in its functionality as the heat sink for the dissipated power in the silicon sensor modules. For the assessment of the thermal performance, the measurement technique of IR thermography is well suited and for cooling, dual-phase CO_2 is used to have the realistic conditions in the tests. On the one hand, a number of petal core prototypes were measured in the developed setup and allowed to verify the design of the local support structure. At the same time, quality parameters on the thermal performance assessment were investigated to apply for the regular QC tests on cores during production. On the other hand, the thermal performance of the TM petal mimicking the heat load of a fully loaded petal was studied for different powering scenarios. In both cases, the experimental results are compared to FEA simulation, which allowed to validate the FEA model used for further design optimization as well as for predictions of the operation over the full life cycle of the ITk detector.

The developed setup for the thermal performance assessment using IR thermography and evaporative CO_2 cooling is described in Section 6.5.1. The performed studies on the thermal performance of different prototypes of petal cores are discussed in Section 6.5.2 and the results on the tests with the TM petal are presented in Section 6.5.3.

6.5.1 Setup for the thermal performance evaluation

For the thermal test setup, a custom-made chamber, called **P**etal **T**hermal **M**easurement chamber (PTM) in the following, with dimensions of 160 cm×140 cm×80 cm offers a light-tight test environment. Due to the attached thermal isolation layers, the PTM shields thermal radiation from the laboratory to not influence the sensitive IR thermography.
The IR camera is mounted on one side of the box in a gantry system allowing for automatic x-y movements and the z position can be manually adjusted by a rail system. On the other side of the PTM, the petal under study is inserted using an anodized holder frame and is connected to the cooling lines. With a typical distance of 110 cm and a focal length of 30 mm for the used IR camera lens, the FOV according to Equation 6.5 is 64 cm × 48 cm allowing a full view on the petal. Moreover, the IR camera is slightly rotated to avoid the Narcissus effect and internal reflections in the PTM are blocked by a high-absorbing fabric. To avoid condensation when cooling the petal, a regulated dry air flushing is possible and the temperature and RH is logged by three SHT21 sensors distributed in the chamber and read out by a Raspberry Pi. Figure 6.27 shows the design and pictures of the PTM.

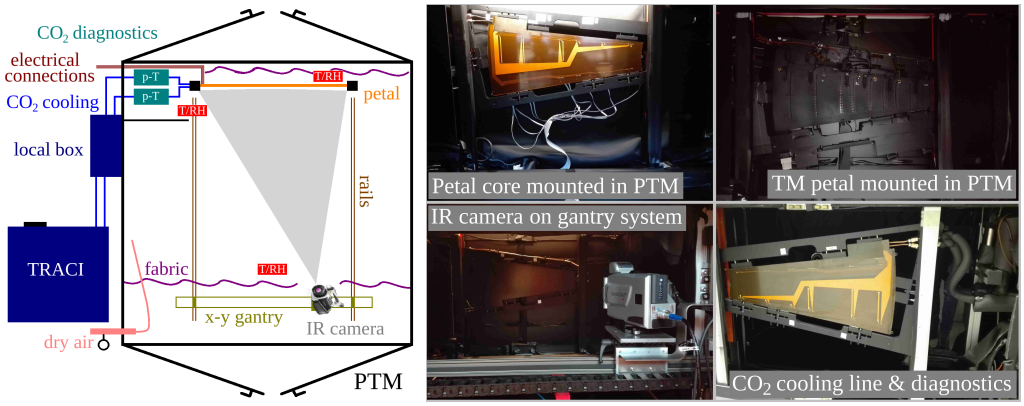

Figure 6.27: Design and impressions of the **P**etal **T**hermal **M**easurement chamber (PTM) for thermal testing of petal cores and the TM petal.

For the cooling of the petal, the TRACI CO_2 system is connected to the petal under study with its local experiment box mounted on the chamber side to allow for an easy access to the control valves. The additional CO_2 diagnostics systems (cf. Sec. 6.2.3) with the p-T probe read out by a Keithley multimeter and the sightglasses for visual control are also installed in the test setup.
For the thermal tests with the TM petal, the required power for the active electronics on the silicon dummy modules is provided by two power supplies with the electrical connection by a feed-through plate at the chamber wall. Moreover, the additionally used Pt100 temperature sensors, placed on the petal under test for a direct temperature probe, are connected to the Keithley readout system.
A Windows PC is used for the readout and control of the IR camera via the IRBIS software as well as for the data taking with TRACI via the LabView interface. The data taking of all the other instrumentation is controlled via Python scripts by a Linux PC.
Figure 6.28 shows the complete thermal test setup with PTM, TRACI CO_2 system, power supplies, Keithley multimeters and the two readout PCs.

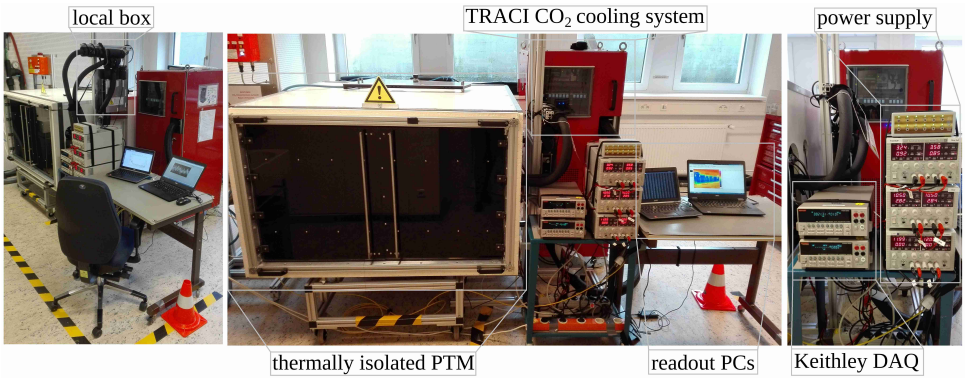

Figure 6.28: Thermal test setup for petals highlighting the different components.

The typical test procedure can be summarized as following:

- prepare the petal under test and place it with the holder in the PTM; connect the cooling lines to the in- and outlet of the petal's cooling loop; establish the electrical connections, e.g. power supply for the TM petal or additional Pt100 sensors, from the petal to the measurement and power supply devices via the wall feed-through;
- mount the IR camera on the gantry system and tilt it to avoid the Narcissus effect; align the camera, either with a large distance in z for a full field-of-view on the petal or with smaller distance for close-up investigations; place the photographic fabric around the camera to reduce reflections from heat sources (e.g. the camera itself or the active motors of the gantry);
- close the chamber and place the additional thermal isolation for the front and back side; start the ambient temperature and RH logging with the Raspberry Pi and open the valve for the dry air flushing to avoid condensation during testing[30];
- connect the vacuum pump to the venting port of the experimental local box and start vacuuming the experiment's cooling loop; start the DAQ system of TRACI via the LabView interface; operate TRACI via the by-pass flow and adjust to a set point at room temperature (e.g. 57 bar);

[30] Typically, after flushing the PTM for 30 minutes with 2 bar, a RH value of below 4% is reached, sufficient to avoid condensation. Afterwards, the flushing is reduced to avoid air turbulences in the setup.

- close the experiment's valve and disconnect the vacuum pump[31]; start the CO_2 diagnostics DAQ as well as the Keithley system for readout of the additional Pt100 sensors; open the flow valve to the experiment while closing the by-pass flow valve to start CO_2 cooling in the petal; adjust the mass flow and the system's pressure drop over the full cooling line to the designated values;
- control the IR camera remotely and adjust the focus manually to reach a clear thermogram; after stabilizing of the CO_2 pressure at the selected set point, the corresponding IR thermogram can be recorded[32]; in case of the TM petal, the power on the modules can be switched on to study different power scenarios;
- select the next set point via TRACI's control unit, wait for reaching a stabilized state and record the thermogram; repeat this procedure for any selected set point[33];
- after finalizing the data taking, TRACI is operated via by-pass at the lowest set point to retrieve CO_2 from the experiment's cooling loop and to store liquid CO_2 in the accumulator; when the draining is sufficient, the valves are closed and the TRACI system as well as all DAQ systems can be switched off; the petal can be disconnected.

The developed setup for thermal testing allows for a wide range of test scenarios for petal cores and fully loaded petals, like the TM petal prototype, in the R&D phase. Moreover, the thermal QC of petal cores during production will be performed with this setup using IR thermography and evaporative CO_2 cooling.

6.5.2 Thermal performance study on petal cores

The performed thermal studies on petal core prototypes are discussed in three categories according to the different surface types: cores with commercial woven CF facesheets, cores with cocured CF facesheets and the cores with cocured bus tapes. The presented results in the following covers only a fraction of the acquired data focusing on the main results in terms of the thermal performance evaluation for cores. Further results and details to the measurements are given in Appendix A.1.

Cores with commercial CF facesheet

The thermal performance of core 02 as a prototype featuring the commercial woven CF facesheet is intensively studied in the following. The front and back side of the core is investigated for CO_2 set points at 56, 51, 45, 40, 35, 31, 26, 23 and 20 bar corresponding to temperature steps of 5 °C and the CO_2 mass flow is regulated in this case to 2.5 g/s.
The typical measurement cycle is shown in Figure 6.29 by plotting the recorded data for the TRACI readout, the CO_2 diagnostics system and the ambient conditions in the PTM as function of the measurement time.
At each selected set point in terms of controlled CO_2 pressure of the TRACI system, an IR thermogram is recorded and the next set point is selected. The measured CO_2 temperature and pressure in the TRACI system as well as at the in- and outlet of the core's cooling loop shows the regulation to the new set point. After some oscillations around the designated set point, the temperature and pressure stabilize and the next IR thermogram is recorded.

[31] The vacuuming of the experiment can be stopped when reaching a value of approximately $5 \cdot 10^{-2}$ mbar.
[32] A sequence of 100 IR thermograms with a recording frequency of 5 Hz is stored and afterwards averaged to account for short time scale fluctuations in the measurement.
[33] The TRACI system allows to select pressure set points between 60 bar and 13 bar, whereas the lowest set point is often not reachable in the tests and the limit is around 17 bar.

At the same time, the corresponding CO_2 mass flow in the TRACI system is not directly regulated, but can be adjusted manually by turning the experiment flow valve. In the test of core 02, the flow should be adjusted to 2.5 g/s, but as shown in the plot the flow is not constant over the measurement time. The full pressure drop between the in- and outlet of the TRACI system is another tunable parameter which should be around 10 bar for a stable operation. It is controlled by the flow valves for the experiment as well as the by-pass and is therefore interconnected to the adjusted mass flow. As shown in the recorded data, for each change in the set point the pressure drop changes quite strongly as the system conditions are changing and stabilizes afterwards again. Finally, the ambient conditions in terms of temperature and relative humidity in the PTM are logged over the measurement cycle. The measured temperature and RH values are quite stable and condensation on the core during the measurement is avoided due to the low RH in the PTM.

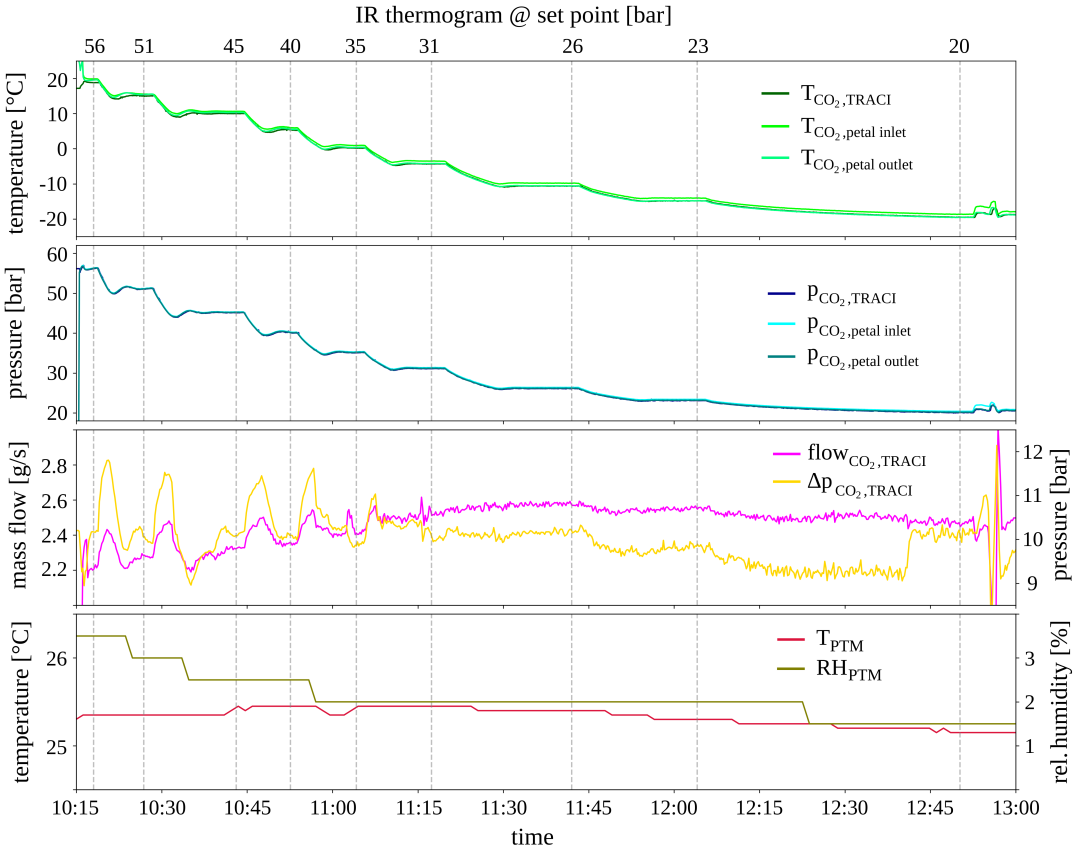

Figure 6.29: Typical measurement cycle for the thermal analysis of petal cores, here for the measurement of the back side of core 02. Shown are the recorded data by the TRACI system, the CO_2 diagnostics system and the monitored ambient conditions in the PTM as function of the measurement time.

With the constant logging of the conditions of the thermal test, the results of different test campaigns for petal cores can be compared. Moreover, a systematic study on individual system's parameters is possible, e.g. to evaluate the dependency of the thermal performance on the CO_2 conditions like the mass flow.

For the thermal performance analysis, the recorded thermograms of the petal core at different set points are used. Figure 6.30 shows the thermograms of the front and back side of core 02 at the set point of 20 bar corresponding to a CO_2 temperature of $-19.5\,^{\circ}C$.

In the thermograms, one can clearly identify the cooling loop surrounded by the carbon foam due to its high thermal conductivity, whereas the surface temperature above the areas with honeycomb or at the edges with the closeouts is comparably higher. This centered cooling approach with the focus on the cooling loop is sufficient for the petal design, as the silicon sensor modules glued on top of the core's surface act as a distributor of the cooling power over the full area. This strategy in terms of cooling can be also explained from another perspective: the generated heat produced in the active sensor and its readout and power electronics is transferred through the silicon to the dual-phase CO_2 in the cooling pipe via the high thermal conductivity foam interface to the core's surface. Therefore, the interface between the titanium cooling pipe, the surrounding foam and the top and bottom facesheet is the critical parameter for the thermal performance of the petal core design.

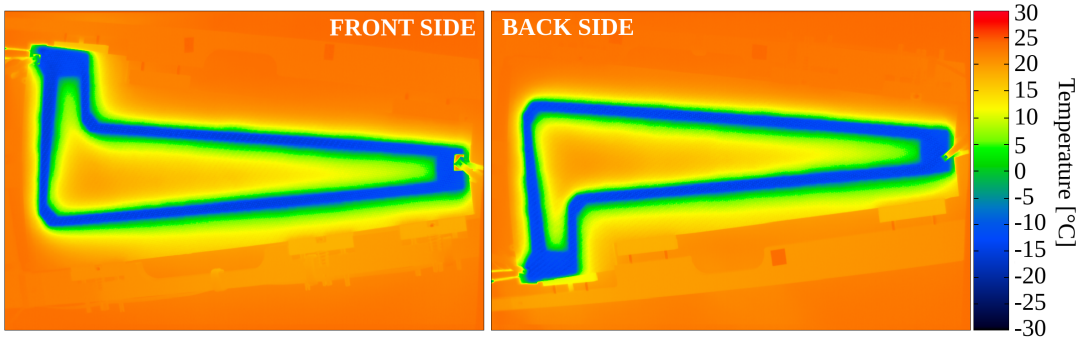

Figure 6.30: IR thermograms of the front and back side of core 02 for a CO_2 pressure set point of 20 bar. The cooling loop surrounded by the high thermal conductivity carbon foam is clearly visible due to the colder temperature contour as well as the surface structure of the woven CF facesheet.

On the one hand, it is possible to use the recorded thermograms in a qualitative way, e.g. to detect defects as visible temperature variations along the cooling loop indicating a delamination of the high thermal conductivity foam from the facesheet. On the other hand, a quantitative analysis can be performed by using the IR camera software IRBIS to define markers as a collection of recorded IR pixels of different shapes in the thermogram. For these markers, the average temperature and its standard deviation as well as the minimum and maximum temperature values are determined and allow a detailed analysis of the measured temperature distribution over the surface. As the interface between the surface and the cooling loop is the critical parameter for the thermal performance of petal cores, line markers of the same length are defined along the cooling loop in a regular distance. This approach is shown in Figure 6.31 for the back side of core 02 by defining 86 markers with a length of 40 pixels equally spaced with a distance of 25 pixels along the cooling loop.

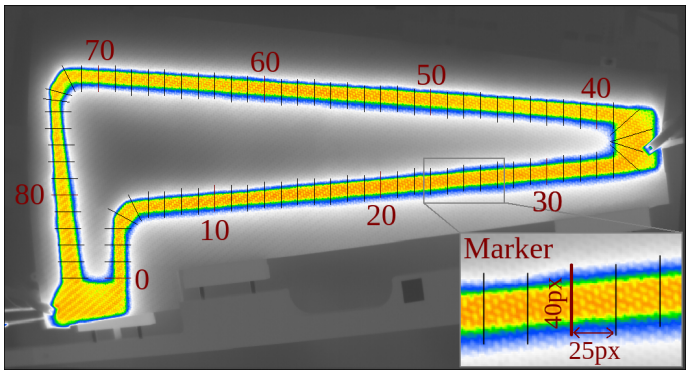

Figure 6.31: Definition of line markers along the cooling loop for the back side of core 02. Shown is an IR thermogram with 86 defined line markers of 40 pixel in length and equally spaced with a distance of 25 pixels along the cooling loop of the core.

Figure 6.32 shows the quantitative comparison along the cooling loop between the front and back side of core 02, evaluated at the CO_2 pressure set point of 20 bar according to the recorded thermograms of Figure 6.30 and using the defined line markers for both sides.

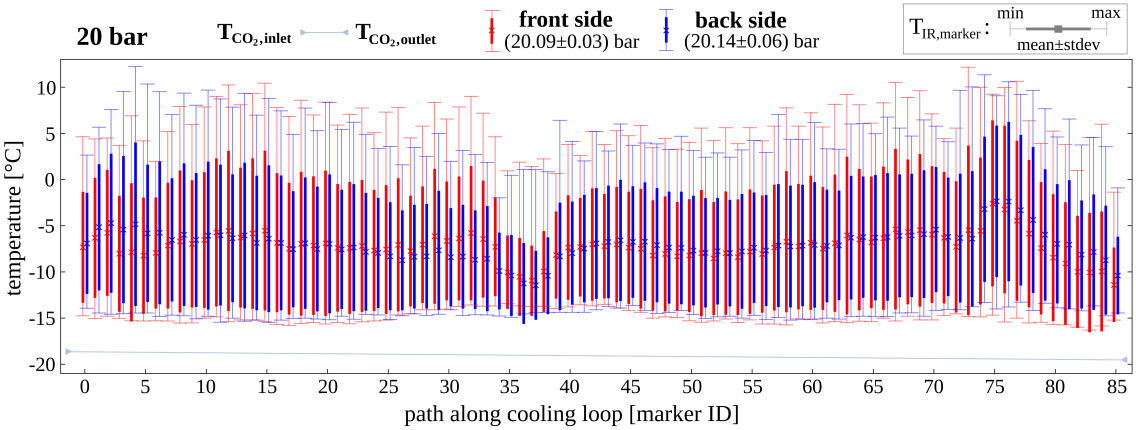

Figure 6.32: Comparison of the temperatures measured along the cooling loop for the front and back side of core 02 at the CO_2 pressure set point of 20 bar. The IR temperatures from the line markers are evaluated as the mean and its standard deviation over the selected IR pixels as well as the minimum and maximum value. Moreover, the measured CO_2 coolant temperature at the core's in- and outlet is shown for reference.

Firstly, a rather stable temperature distribution for the markers along the cooling loop are observed, indicating no obvious defect in the cooling interface. Also the comparison of the temperature distributions for the front and back side shows a very similar behaviour with only minor differences. These differences can be explained by slightly different testing conditions in terms of the cooling performance of TRACI with slightly different mass flows and pressure values at the individual adjusted set points.
Secondly, the temperature distributions shows a rather broad span of values between the minimum and maximum value, as they reflect all IR pixels defined in the line marker. In the marker definition, the center of the line is placed above the cooling loop but to evaluate the full width of the interface region it spans also to its edges, evaluating therefore also the neighboring area of lower thermal conductivity. These covered edge regions show a much warmer temperature and result in the observed distributions with a broad span between the coldest and warmest pixel value.
Finally, the measured temperatures on the core's surface are considerably higher than the CO_2 coolant temperature measured at the in- and outlet of the cooling loop. On the one hand, this observation can be explained by the thermal path in the petal core design and the thermal conductivities for the different interfaces from the coolant to the surface. Here, the thermal interfaces are the following: from the dual-phase CO_2 fluid to the titanium cooling pipe wall with a high thermal conductance due to the high HTC of the CO_2 coolant; from the titanium pipe to the surrounding high thermal conductivity foam via a glue interface; from the carbon foam to the CF facesheet via another glue interface. On the other hand, the IR thermograms are evaluated with an emissivity of 1.0 and even though the core's surface with the woven CF facesheet has a high emissivity, the measured temperatures have to be corrected accordingly for an absolute comparison.

The temperature distributions are analysed in detail in Figure 6.33 by comparing different CO_2 pressure set points of 56, 45, 35, 26 and 20 bar for the back side of core 02.

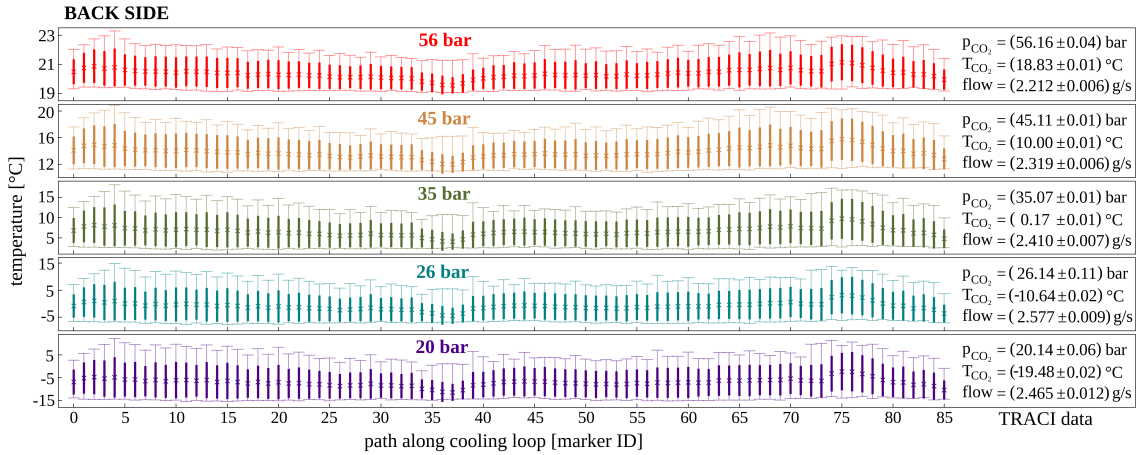

Figure 6.33: Temperature distributions for the IR line markers defined along the cooling loop, evaluated for the back side of core 02 and at the CO_2 pressure set points of 56, 45, 35, 26 and 20 bar.

The same behaviour for the temperature distributions along the cooling loop are observed for all the evaluated set points. Only the span between the minimum and maximum value on the line marker is changing with the set point, as for colder CO_2 coolant temperatures the difference between the measured temperatures above the foam regions with high thermal conductivity and the neighboring honeycomb areas of lower thermal conductivity is higher.

Figure 6.34 compares the measured CO_2 coolant temperature with the minimum temperature of the line markers along the cooling loop for the back side of core 02 and all the selected CO_2 pressure set points between 56 and 20 bar for the measurement campaign.

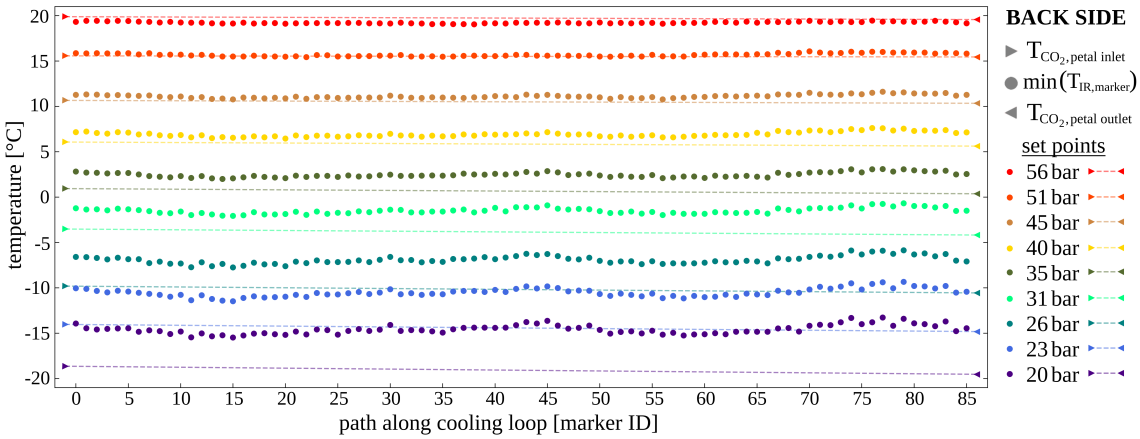

Figure 6.34: Comparison of the minimum temperatures measured along the cooling loop and the measured CO_2 coolant temperature at the core's in- and outlet for the back side of core 02 at different CO_2 pressure set points.

The absolute difference between the CO_2 coolant temperature and the temperature on the core's surface above the cooling loop is changing in magnitude with the selected set point. Here, the temperature is observed to be up to 6 °C higher at the surface point with the best thermal path than in the CO_2 coolant for the lowest tested temperature set point. As mentioned before, one reason for the observed temperature differences is the not adjusted emissivity value for the core's surface. In Figure 6.35 the resulting temperature differences are evaluated for varying emissivity values of $\epsilon = 1.0, 0.95, 0.93$ and 0.91.

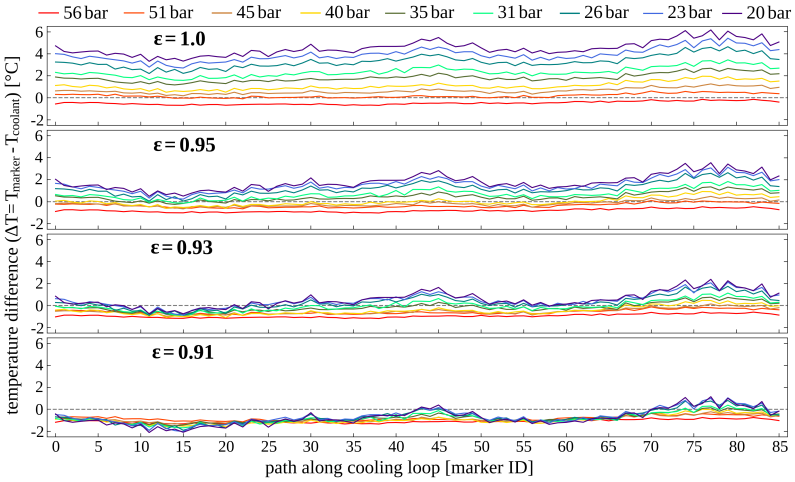

Figure 6.35: Difference between the minimum temperature along the cooling loop and the CO_2 coolant temperature for varying emissivity values of $\epsilon = 1.0, 0.95, 0.93$ and 0.91. Evaluated are the different CO_2 pressure set points measured for the back side of core 02.

Here, for decreasing emissivity values the temperature differences decreases as well, but for too low emissivities, like $\epsilon = 0.91$, the surface temperature is measured to be cooler than the CO_2 coolant for all set points, which is unphysical. From the discussed temperature variation study for the core 03 with the application of the tape method for emissivity correction, the estimated value of $\mathcal{O}(0.94)$ matches quite well with the observations in the temperature differences. The remaining temperature difference can be explained by losses along the thermal path and the interfaces with different thermal conductivities.

Cores with cocured CF facesheet

For the category of petal core prototypes with a cocured CF facesheet as surface, the thermal performance of core 04 is characterized for CO_2 pressure set points between 57 and 18.2 bar, which was the lowest reachable pressure with the TRACI system. For the measurement, the CO_2 mass flow is adjusted to 1.3 g/s and the overall pressure drop over the system is stabilized at 10 bar. Figure 6.36a shows the measurement cycle for the tested back side of core 04 and the recorded IR thermograms at the 35 bar set point as well as at the lowest set point of 18.2 bar are depicted in Figure 6.36b.

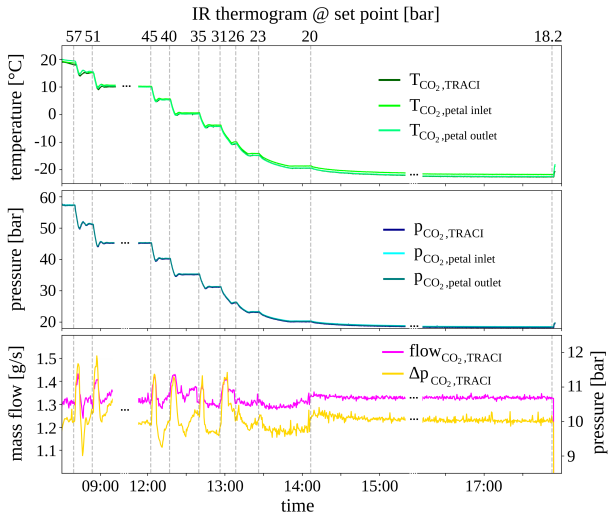

(a) Measurement cycle with selected set points.

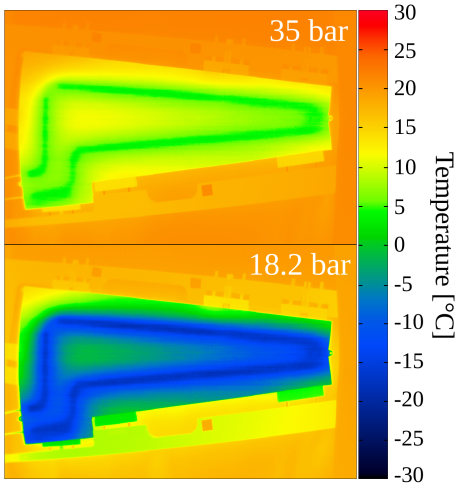

(b) IR thermogram at 35 and 18.2 bar.

Figure 6.36: Measurement of the thermal performance for the back side of core 04.

When comparing the thermogram of core 04 with the shown thermograms of core 02, the cooling loop can be identified in both cases and one can also clearly distinct the different surfaces of commercial woven CF and the cocured CF facesheet. For the cocured facesheet, the temperatures in the thermogram appear smeared along the horizontal direction which is caused by the regular fiber direction of the top layer of the cocured CF facesheet. Moreover, the cooling loop routing has changed between the two design stages.
For the quantitative analysis, line markers along the cooling loop (79 lines with 50 pixel in length and a distance of 25 pixels) are defined and evaluated for the different CO_2 pressure set points, as it is shown in Figure 6.37.

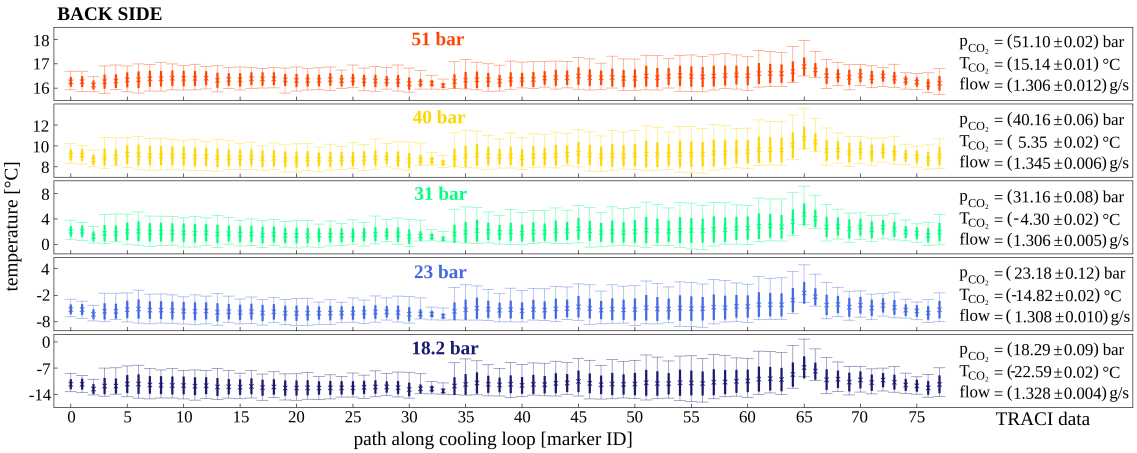

Figure 6.37: Temperature distributions for the IR line markers defined along the cooling loop, evaluated for the back side of core 04 and at the CO_2 pressure set points of 51, 40, 31, 23 and 18.2 bar.

For the different set points, similar temperature distributions along the cooling loop are observed as in the case of core 02, but the span between the minimum and maximum value over the line marker is smaller. This can be explained by a better thermal conductivity for the unidirectional fibers compared to the woven structure and the resulting broader contour of the cooling loop as observed in the thermogram. Moreover, regions with a smaller temperature spread compared to the neighboring regions, but with the same minimum temperature can be identified, e.g. between the marker IDs 30 to 35. This effect can be explained by the shape of the foam covering a wider region below the surface, e.g. at the region of the U-turn in the cooling pipe, and showing therefore a more uniform temperature over the marker pixels.
But the temperature distribution shows also another effect at marker IDs around 65, where considerably warmer temperatures are measured all over the marker consistently for all tested set points. Figure 6.38a shows a zoomed IR thermogram of the identified region at the top left turn of the cooling pipe using a higher contrast temperature scale. Here, a defect in the thermal interface, most probably due to a delamination of the surface from the foam, can be clearly observed, resulting in a reduced thermal conductivity and therefore higher temperatures on the surface.
In Figure 6.38b the minimum temperature for the defined markers in this region are analysed in detail and the defect can be localized to three IR markers with considerably higher minimal temperature values. Linear fits using the neighboring markers, while excluding the markers in the defect area, are performed for each set point to evaluate the absolute temperature difference for the influenced area. Here, the maximum difference is determined to be 4.5 °C absolute or 33% relative for the lowest CO_2 pressure set point.

Therefore, in the thermal QC test during production, the core would fail the thermal performance specification due to the identified delamination area above the cooling loop.

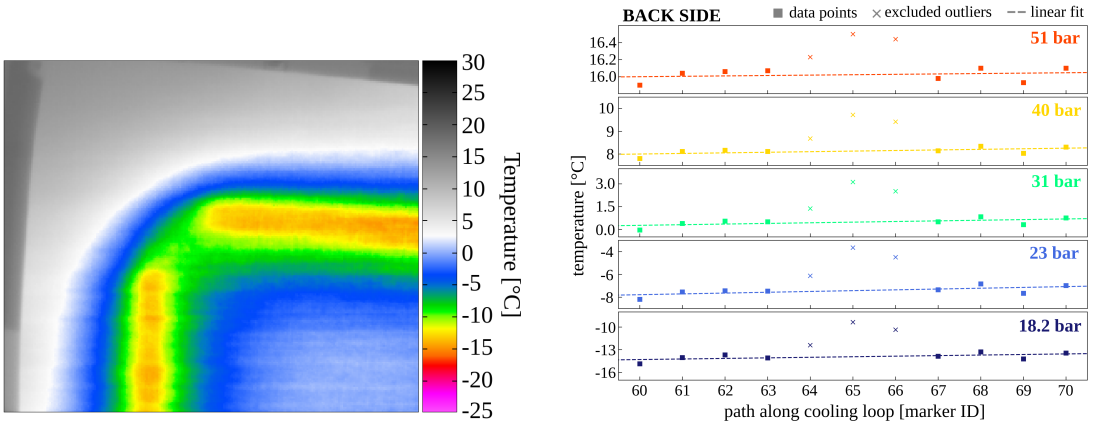

(a) Thermogram of the detected delamination in the upper left turn of the cooling loop at the 18.2 bar set point.

(b) Minimum temperature measured for the line markers in the defect region for several CO_2 pressure set points.

Figure 6.38: Investigation on the detected delamination for the back side of core 04.

Cores with cocured bus tapes

The thermal performance for petal core prototypes with a cocured bus tape are studied with the cores 07 and 08 for several CO_2 pressure set points, an adjusted mass flow of 1.3 g/s and an overall pressure drop over the system stabilized around 10 bar.
For core 07, the measurement cycle for CO_2 pressure set points between 57 bar and the lowest reachable set point is shown in Figure 6.39a for the logged TRACI and CO_2 diagnostics data investigating the front side. Apart from the standard programme, two additional thermal cycles are performed between 57 and 20 bar without intermediate steps and after reaching the lowest set point. This thermal cycling allows on the one hand to evaluate the repeatability of the measurement for these set points and investigate possible hysteresis effects. On the other hand, the measurement of the core's performance after several thermal cycles is designated as input to the design validation, as discussed in Section 6.7. Here, only two cycles between coolant temperatures of $+20\,^{\circ}C$ and $-20\,^{\circ}C$ using evaporative CO_2 were performed instead of the specified 100 thermal cycles of a core between $\pm 40\,^{\circ}C$. The reasons are the constrained cooling power of the TRACI system and the required time and active operation to perform such cycles with evaporative CO_2 cooling.
Furthermore, Figure 6.39b shows the recorded thermograms at the lowest reached set point of 18.1 bar and 18.8 bar for the front and back side, respectively. Here, the bus tape features, e.g. copper traces and open bond pads, are clearly visible as warmer contours due to a lower emissivity of these areas than the rest of the core's surface, as investigated before.

For the quantitative analysis of the thermal performance for cores with bus tapes, two approaches are chosen. On the one hand, line markers along the cooling loop (78 lines with 40 pixel in length and a distance of 25 pixels) are defined similar as before. On the other hand, polygonal area markers are defined according to the designated positions of the silicon sensor modules as well as the EoS region to evaluate the temperature distributions for these areas of interest. Both marker definitions are depicted in Figure 6.40.

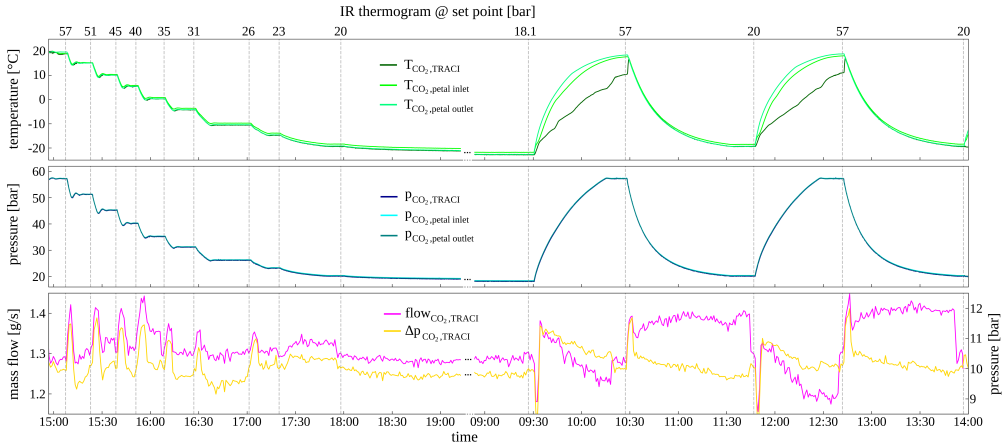

(a) Measurement cycle with selected set points for the front side of core 07. After reaching the lowest set point, two additional thermal cycles between 57 bar and 20 bar are performed.

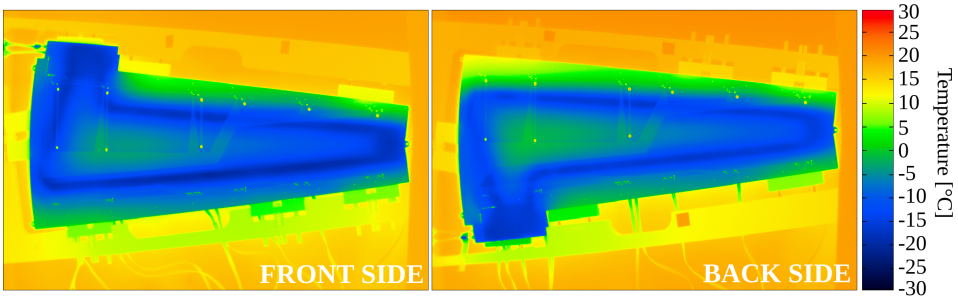

(b) IR thermograms for the front and back side of core 07 at the lowest reached set points of 18.1 bar and 18.8 bar, respectively.

Figure 6.39: Measurement of the thermal performance for core 07.

For the cores with bus tapes, no emissivity correction is applied and the measured temperature distributions will be therefore influenced by the warmer appearing bus tape features. As an example, the area between the line marker IDs 15 and 25 for the front side will show warmer temperatures as one of the wide copper traces overlays the cooling loop in this location, which will deteriorate the absolute thermal performance evaluation. But for the thermal QC of cores during production, the relative differences for each tested core can be evaluated and compared against a standard performing core, the "golden image", showing the same features in the IR thermography such that the emissivity effects will cancel.

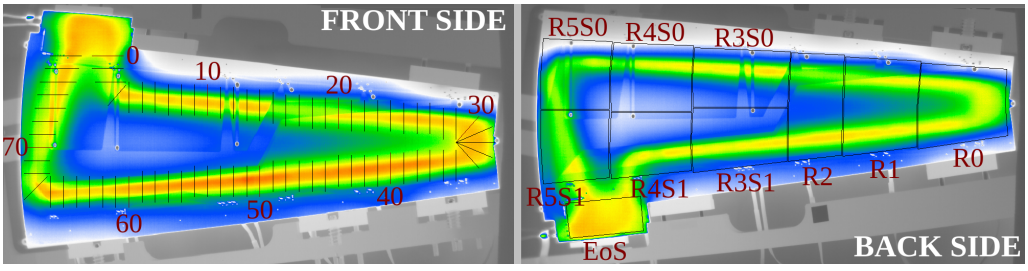

Figure 6.40: Definition of IR markers for the cores with cocured bus tapes using line markers along the cooling loop and polygonal area markers for the silicon module areas and the EoS region. Shown are exemplary the thermograms of core 07 with the 78 line markers (40 pixel in length, distance of 25 pixels) defined along the cooling loop on the front side (left) and the ten area markers covering the interesting core regions on the back side (right).

Figure 6.41 compares the measured temperature distribution along the cooling loop of the front side of core 07 for the three iterations of the adjusted set point to 20 bar by the described thermal cycling. Here, the results are very comparable with only minor difference which can be explained again by slightly different conditions, e.g. the ambient temperature and the TRACI cooling performance. Therefore, no hysteresis effect for the thermal performance is observed and a similar surface temperature is reached for all three iterations. Moreover, the effect of a deteriorated surface temperature due to the lower emissivity regions in the bus tape is visible for the temperature distribution along the cooling loop (e.g. the steep temperature change between the line markers 14 and 15).

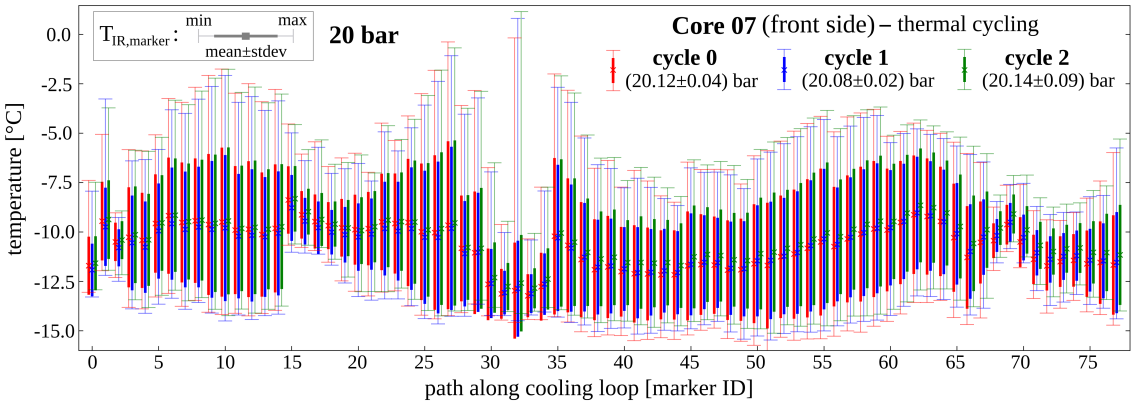

Figure 6.41: Comparison of the measured temperature distributions along the cooling loop after two temperature cycles for the set point at 20 bar. Shown are the results for the front side of core 07.

For core 08, the thermal performance for both sides was measured for the CO_2 pressure set points at 57, 35, 26, 20 and 17.5 bar, as the lowest reached set point. During the assembly of the core, a delamination defect was introduced in the EoS region of the back side.
In Figure 6.42, the thermograms for the EoS region at 17.5 bar in the front and back side of core 08 are compared. With the magnified view and the high contrast temperature scale, the affected thermal interface due to the delamination in the back side is clearly visible.
For a quantitative interpretation, the measured temperature distributions for the defined EoS marker area are compared for both sides: for the front side, the average EoS temperature is $(-17.61 \pm 1.89)^{\circ}$C with a minimum temperature of $-19.48\,^{\circ}$C, whereas the average temperature for the back side is $(-15.48 \pm 1.12)^{\circ}$C with a minimum temperature of $-17.59\,^{\circ}$C indicating the broken thermal path in this region.

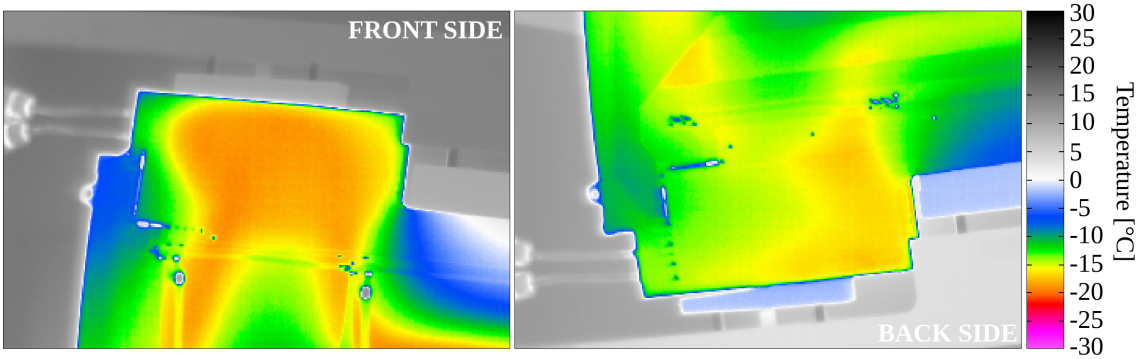

Figure 6.42: IR thermograms of the EoS region for the front and back side of core 08 at the CO_2 pressure set point of 17.5 bar.

Finally, the thermal performances of both tested cores with a cocured bus tape can be compared with each other. Figure 6.43 shows the measured temperature distributions along the cooling loop for a CO_2 pressure set point of 20 bar.

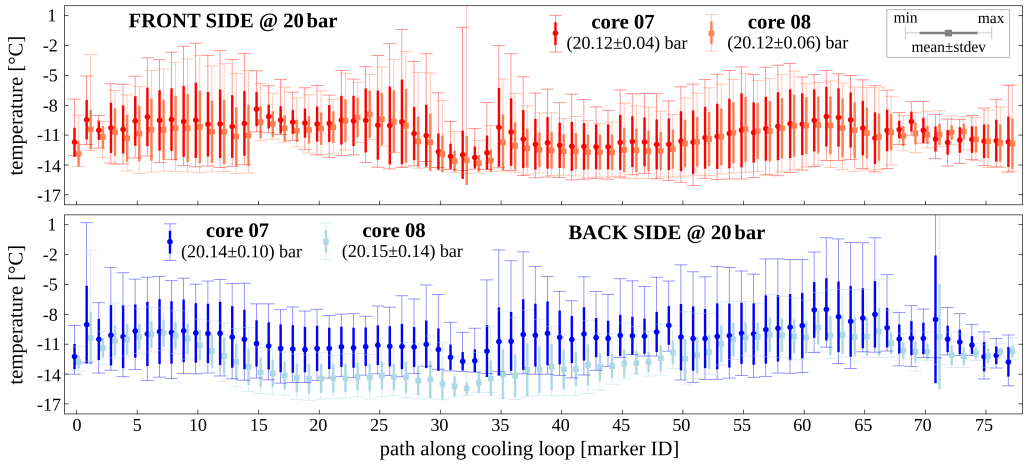

Figure 6.43: Comparison of the temperature distribution along the cooling loop for the front and back side of core 07 and 08 at a CO_2 pressure set point of 20 bar.

Here, the results for the front side are rather similar with the tendency to slightly lower average temperatures for core 08, but lower minimum and higher maximum temperatures for core 07. This observation can be explained by comparing the logged ambient temperatures in the PTM for the individual measurements: for the front side of core 07, the average air temperature is $(22.1 \pm 1.4)^{\circ}$C, whereas the corresponding measurement of the front side of core 08 is conducted at an ambient temperature of $(20.2 \pm 1.8)^{\circ}$C. Due to the core's emissivity different from a perfect emitter with $\epsilon = 1.0$, the measured IR temperatures are directly dependent on the ambient temperature, which results in the observed variations. For the comparison of the back side results, major discrepancies for the individual markers between core 07 and core 08 are observed, showing overall much colder temperatures and also a reduced span between the minimum and maximum measured temperature for core 08. The ambient temperatures for the two compared tests are $(22.4 \pm 1.8)^{\circ}$C for core 07 and only $(15.5 \pm 1.7)^{\circ}$C for core 08. The low temperature for the latter case is caused by inverting the standard measurement cycle: starting with the lowest set point, the ambient temperature in the PTM is cooled by the cold core for an overnight measurement and the higher set points are tested on the next day, but the ambient air is not heated up that fast. Therefore, the apparently observed difference in the thermal performance for the cores is caused by the influence of very different testing conditions.
The analysis of the temperature distributions on the defined areas representing the sensor and EoS regions is shown in Figure 6.44 for the same set point of 20 bar. Here, the comparison between the front side of core 07 and core 08 shows again rather similar results with maximal temperature differences of $\Delta T \sim \pm 2\,^{\circ}$C. On the contrary, the results for the back side show larger discrepancies between core 07 and core 08, which are caused by the different testing conditions. But also a clear indication for the delamination in the EoS region for the back side of core 08 can be identified in the data.
Moreover, two further observations can be made: on the one hand, the measured temperature distributions for the front and back side of core 07 are found to be very comparable; on the other hand, the measured maximum temperatures in the marker areas corresponding to the sensor regions are caused by the enclosed bond pads and reflect to a large fraction the ambient temperature due to the low emissivity of the gold pads.

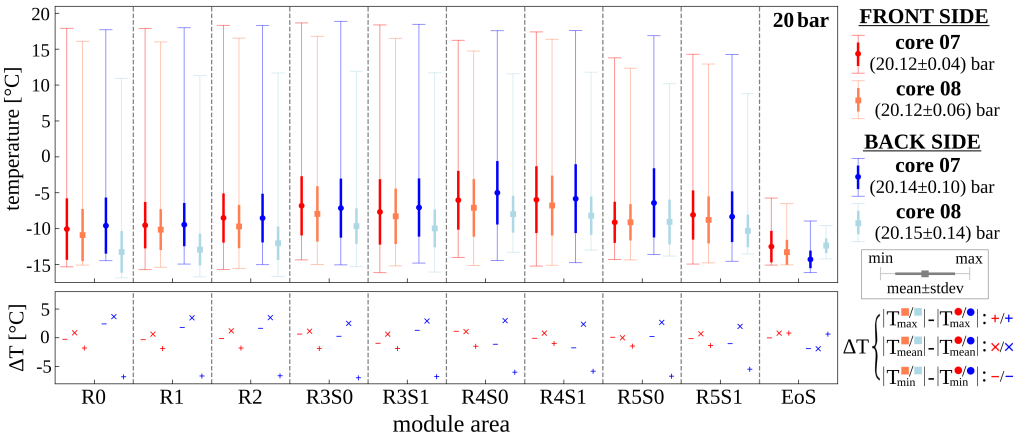

Figure 6.44: Comparison of the temperature distribution on the module areas for the front and back side of core 07 and 08 at a CO_2 pressure set point of 20 bar.

In general, the comparison showed overall a good thermal performance for both cores with cocured bus tapes. Here, the core 08 with the detected delamination in the EoS region on the back side have to be excluded, as it would not pass the thermal specifications for the QC testing during production. Moreover, the performed tests showed the influence of the testing conditions in terms of the ambient temperature and the cooling performance on the thermal results for cores without emissivity correction. For the thermal QC procedure, the tests have to be performed under stable conditions enabling a high repeatability to compare the individual cores and to characterize their thermal performances.

Finally, the experimental results of the measured IR temperatures for the core prototypes with a cocured bus tape can be compared to the thermal FEA results of a bare petal core. Here, the FEA uses the same design stage of the petal and assumes heat exchange by convection with air using an HTC of $5\,\mathrm{W/(K \cdot m^2)}$ on the surface. The CO_2 coolant properties are modelled according to the measured conditions with the TRACI system and the CO_2 diagnostics system in terms of pressure, temperature and flow rate. For the HTC of the evaporative CO_2, dedicated CoBra simulations are conducted corresponding to the experimental conditions. Figure 6.45 shows exemplary the simulated temperature distribution for nominal operating conditions with a CO_2 saturation temperature of $-35\,^{\circ}\mathrm{C}$.

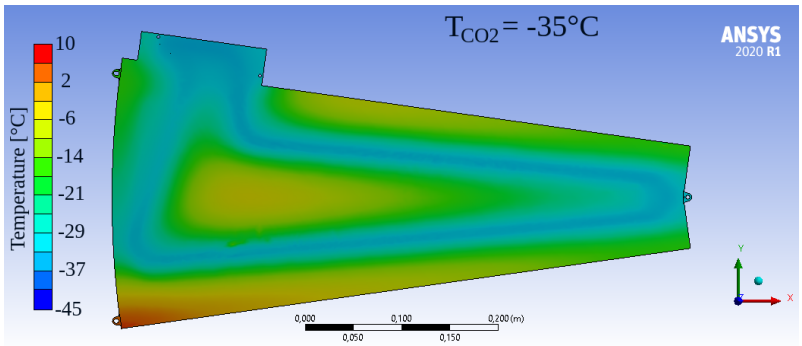

Figure 6.45: Simulated surface temperature on the semielectrical petal core using thermal FEA. Shown is the result for the back side at a CO_2 saturation temperature of $-35\,^{\circ}\mathrm{C}$.

In a qualitative comparison to the experimental data of IR thermograms, a very similar temperature distribution is observed for the FEA: the cooling loop is clearly visible due to the good thermal contact by the carbon foam; on the contrary, regions further away from this thermal interface, e.g. close to the edges of the core, are considerably warmer. The only difference is caused by the visible structure of copper traces in the bus tape, as it is observed for the IR data, but the FEA result does not show it as it is an emissivity effect.

6.5.3 Thermal performance study on the TM petal

After assessment of the thermal performance of a bare petal core, the thermo-mechanical petal prototype with its glued on dummy silicon modules allows to test and evaluate the thermal performance of an expected fully loaded petal. With the acquired thermal performance results for different testing conditions, e.g. simulating various heat load scenarios, it is possible to validate the cooling strategy of the petal design or to optimize the design in case of a detected problem.
In the course of this work, the TM petal was thoroughly tested for various scenarios in several test campaigns using the developed setup with the realistic cooling conditions using evaporative CO_2 cooling. In the following, a selection of the main results acquired with the TM petal is discussed, focusing on the studies in the painted state of the TM petal to apply an appropriate emissivity correction for the silicon areas. Therefore, all measurement results acquired with IR thermography are corrected for the emissivity of the paint, using its measured emissivity value of $\epsilon = 0.977$ (cf. Sec. 6.4.3), if not stated otherwise.
Further results and details to the performed tests are collected in Appendix A.2.

Performance evaluation for nominal conditions

For the first study, the thermal performance of the TM petal is evaluated for the nominal conditions[34], meaning an adjusted CO_2 mass flow of 1.3 g/s and comparing the unpowered state with the case of fully powering the petal with a heat load of 54 W.
Figure 6.46 shows one of the performed measurement cycles for CO_2 pressure set points between 51 bar and the lowest set point of 18.1 bar for all the logged instrumentation data.

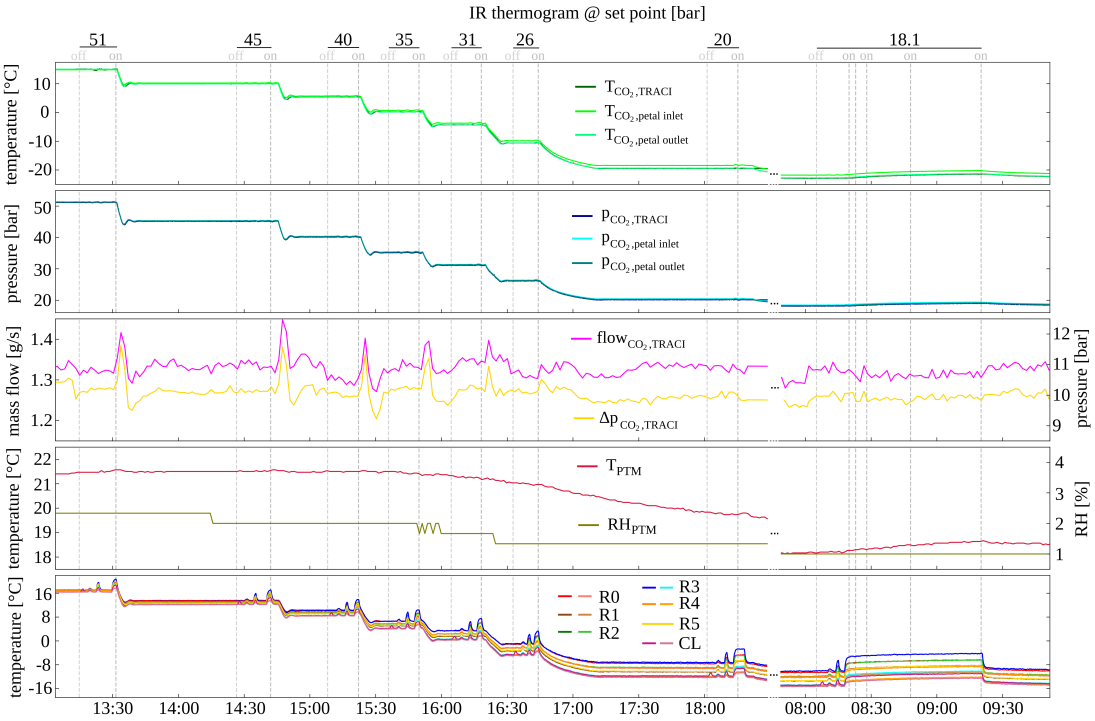

Figure 6.46: Measurement cycle for the TM petal under nominal conditions. Shown are the logged instrumentation data for the different set points.

[34] During the optimization of the petal design and the further development of the silicon sensor modules with more final designs of the readout and power electronics, the nominal conditions for the petal have changed to slightly different heat loads in the modules and an accordingly adjusted CO_2 mass flow.

For each set point, an IR thermogram is recorded for the unpowered as well as the powered state of the TM petal. Here, it is possible to study several powering scenarios, which will be discussed later. For this study, the "on" state means powering with the full heat load of 54 W and waiting several minutes for a stabilized condition. The response on the powering is also logged by the additionally attached Pt100 sensors located on the individual dummy silicon sensors and allows therefore a direct comparison with the measured IR temperatures. Furthermore, the measurement was conducted over night to stabilize at the lowest reachable set point. At the same time, the ambient temperature in the PTM drops from starting at room temperature of around 21 °C down to around 18 °C due to the convective heat exchange between the petal surface and the ambient air.

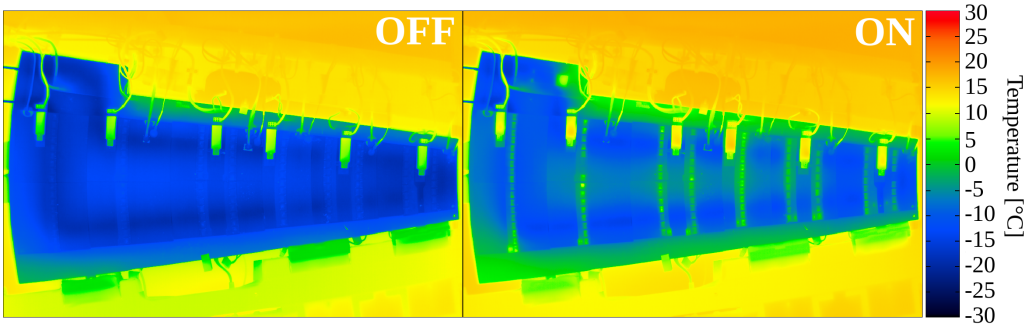

Figure 6.47: IR thermograms of the TM petal in the unpowered and powered state at the lowest CO_2 pressure set point of 18.1 bar.

Figure 6.47 compares the IR thermograms at the lowest set point of 18.1 bar for the unpowered and fully powered state of the TM petal. Similar as for the thermograms of cores, the cooling loop can still be identified due to the good thermal contact of the surrounding foam with the petal's surface. But with the good thermal conductivity of the silicon, the cooling power is distributed over the sensor plane resulting in a rather uniform temperature distribution on the silicon areas for the unpowered case. This is exactly the expected behaviour for the petal's cooling strategy.
Moreover, the hybrids and powerboards of the dummy silicon modules are only faintly visible for the unpowered case[35], but become clearly visible when switching on the module power. From a qualitative comparison of the thermograms, one can observe the increased surface temperature due to the generated heat in the powered electronics. Here, the areas above the cooling loop remain colder than the rest of the silicon area.

For the analysis of the thermal performance of the TM petal, the temperature distribution on the silicon areas is the most interesting result, as the electronics boards and their components are not the real components, e.g. the ASICs are dummy heating elements simulating only the expected heat load. Therefore, polygonal area markers are defined with the IR software selecting only the silicon areas which are not covered by any electronics. Figure 6.48 shows the applied marker definition for the TM petal and the naming convention for the areas. For the following quantitative analysis, the measured IR temperatures in these marker areas are either used directly or processed further by merging[36] the temperature distributions acquired from the marker areas belonging to the same silicon sensor area.

[35] The plastic covers for the DCDC converters are clearly visible as warmer contours, as here the thermal contact to the cooled powerboard PCB is bad such that the temperature is close to the ambient.

[36] The temperatures are calculated for the mean $T^{\text{sensor}}_{\text{mean}} = \frac{1}{n}\sum_i^n T^{\text{marker},i}_{\text{mean}}$ with $\sigma_T^{\text{sensor}} = \sqrt{\sum_i \left(\sigma_T^{\text{marker},i}\right)^2}$ and the minimum, $T^{\text{sensor}}_{\text{min}} = \min_i \left(T^{\text{marker},i}_{\text{min}}\right)$, and maximum, $T^{\text{sensor}}_{\text{max}} = \max_i \left(T^{\text{marker},i}_{\text{max}}\right)$, value.

Therefore, the temperatures for the individual sensor areas, namely R0, R1, R2, R3S0, R3S1, R4S0, R4S1, R5S0 and R5S1, can be compared in the thermal analysis.

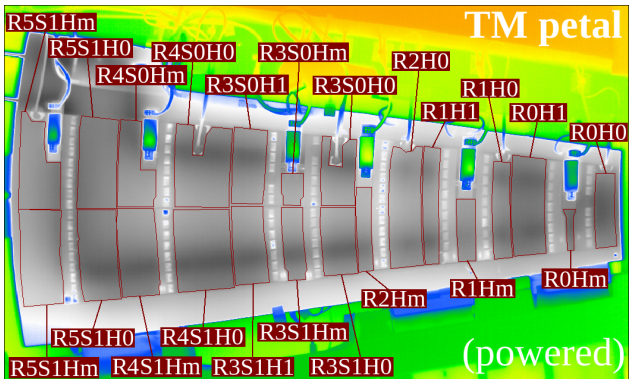

Figure 6.48: Definition of the area markers on the silicon areas for the TM petal. Shown is an IR thermogram of the powered TM petal with 22 defined area markers covering the splitted silicon areas, which are named according to the corresponding sensor (R0, R1, R2, R3S0, R3S1, R4S0, R4S1, R5S0 and R5S1) and its part according to the relative position to the hybrid (H0, Hm and H1).

In Figure 6.49, the temperature distributions measured in the defined marker areas for CO_2 pressure set points of 51, 40, 31 and 20 bar are compared for the case of the unpowered TM petal. Overall, a uniform temperature distribution for nearly all the individual silicon areas can be observed with only minor variations over the tested set points. The exception here is the marker area R5S1Hm with a higher temperature compared to the other areas as well as to the area R5S1H0 on the same silicon sensor. To mitigate a too hot temperature on the R5S1 sensor, the cooling loop geometry was changed in the petal core design following the thermal analysis of the TM petal to allow a better thermal path in this region.

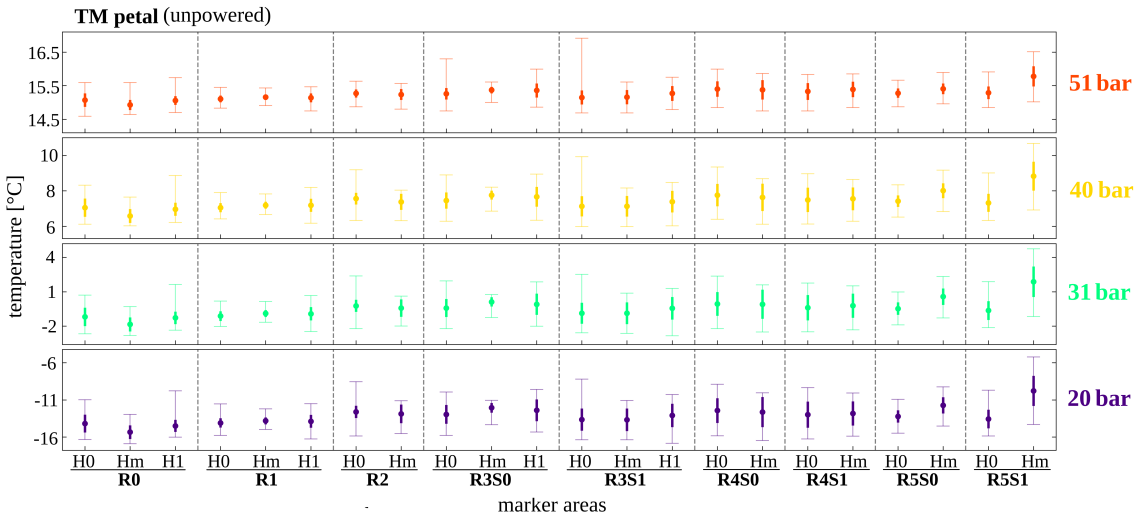

Figure 6.49: Temperature distributions for the individual marker areas on the unpowered TM petal and evaluated for CO_2 pressure set points of 51, 40, 31 and 20 bar.

Furthermore, the temperature difference of the silicon sensor areas between the unpowered and the powered state of the TM petal can be compared to investigate the thermal performance of the petal under the expected heat load generated by the active electronics. Figure 6.50a shows exemplary the comparison for the CO_2 pressure set point of 20 bar and the consistent increase of the silicon temperature for the individual sensor areas in the powered state of the TM petal. The difference in temperature for the two states, $\Delta T = T^{\mathrm{ON}} - T^{\mathrm{OFF}}$, evaluated for the mean, minimum and maximum value of the measured IR temperature distributions is plotted in Figure 6.50b for all the tested set points.

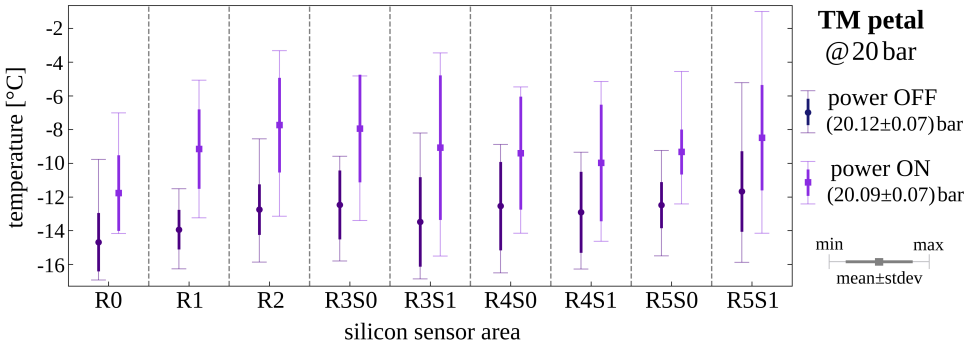

(a) Temperature distributions for the unpowered and powered state at 20 bar.

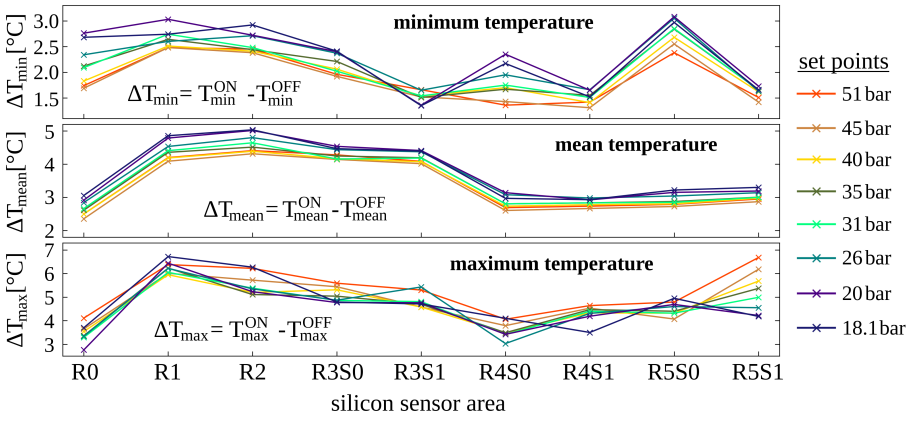

(b) Temperature difference $\Delta T = T^{\mathrm{ON}} - T^{\mathrm{OFF}}$ for the mean, minimum and maximum temperature, evaluated for all the tested set points.

Figure 6.50: Comparison of the silicon temperature on the sensor areas for the unpowered and powered state of the TM petal.

Firstly, the mean, minimum and maximum values of the measured IR temperature distributions increase for all the silicon sensor areas, as it is expected when switching on the active electronics. The amount of the temperature increase is rather uniform for all the tested set points, showing only minor variations for some of the silicon areas and mostly for the minimum and maximum value.
For the mean temperature, the silicon sensor areas can be grouped into two categories: the first group, consisting of R0, R4S0, R4S1, R5S0 and R5S1, shows on average over all set points a lower temperature increase of $(2.9 \pm 0.4)^{\circ}$C, than the second group, consisting of R1, R2, R3S0 and R3S1, with $(4.4 \pm 0.4)^{\circ}$C. This can be explained by the amount of hybrids and correspondingly of dummy front-end ASICs on the sensors, generating the heat causing the temperature increase. Here, all sensors from the second group, excluding R2, are equipped with two hybrids and 12 to 21 ABCs, explaining the higher mean temperature. For R2, the observation can be explained by the influence of the hotter neighboring sensors. On the contrary, R0 has two hybrids and 17 ABC chips, but shows the most moderate increase in the mean temperature compared to the other sensor areas. Here, the effect of a good thermal path and a resulting improved cooling of the sensor can be observed, which is caused by the location of the R0 module on top of the cooling loop's U-turn.
For the minimum temperature, another observation can be made: here, the temperature difference of the sensor areas S0 of the split modules R3, R4 and R5 is higher than for the S1 part. This effect is caused by the powerboard PCB located always on the S0 sensor for the split modules and the generated heat in the DCDC converters resulting in a higher increase of the minimum temperature.

Overall, the performed thermal performance study under nominal conditions shows no indication for a problem in the cooling strategy of the petal, when testing the TM petal in the unpowered and fully powered state.

Comparison of different CO_2 mass flows

In the following study, the effect of different CO_2 mass flows on the thermal performance of the TM petal is investigated. The results for the nominal flow conditions of 1.3 g/s are compared to a higher mass flow of 2.5 g/s, as it was used for some of the measurement campaigns in the beginning. Figure 6.51 shows exemplary the flow comparison for the unpowered and powered state of the TM petal at the CO_2 pressure set point of 26 bar.

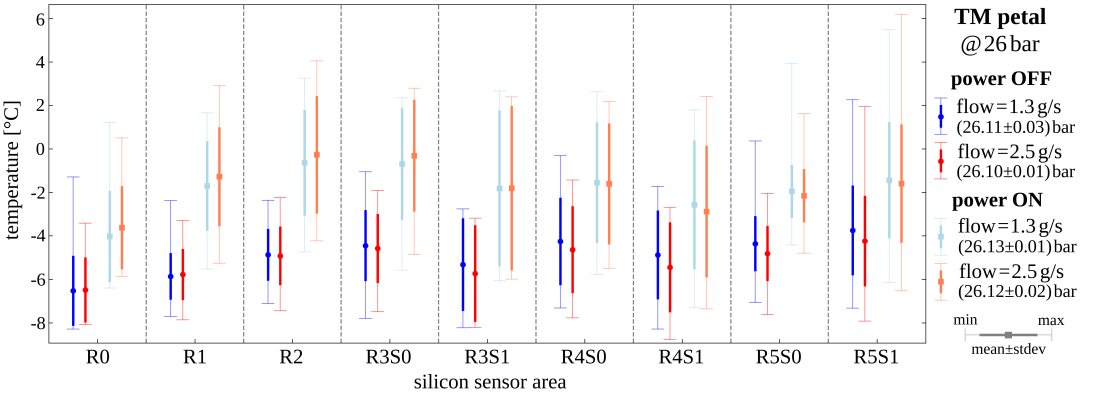

Figure 6.51: Temperature distributions on the silicon sensor areas comparing the effect of two different CO_2 mass flows of 1.3 and 2.5 g/s. Shown are the results for the unpowered and powered state of the TM petal at 26 bar.

Within small variations, consistent temperature distributions are measured on the silicon sensor areas for both tested mass flows and independent of the powering state of the TM petal. In general, a higher CO_2 mass flow allows for a more efficient cooling of the experiment as a larger amount of heat can be transferred per time. Moreover, the CO_2 vapour quality at the end of the petal's cooling loop is lower for a higher mass flow, which allows in principle a safer operation further away from a dry-out scenario. But at the same time, the mass flow is restricted by the available pressure drop in the detector's cooling loop as well as the achievable minimum operation temperature, which are defined by the specifications for the CO_2 cooling system. Therefore, the mass flow through the individual objects, such as petals for the strip end-cap detector, should be adjusted to allow a sufficient cooling with the minimal requirements on the system. The TM petal showed a rather equal thermal performance for both investigated mass flows, indicating that the selected nominal conditions with a mass flow of 1.3 g/s allows for a sufficient cooling, at least for the tested CO_2 pressure range of 56 to 18 bar using the TRACI system.

Investigations on powering scenarios

In the performed thermal tests of the TM petal, a detailed investigation on the powered state of the petal for different powering scenarios of the dummy electronics were conducted. First of all, the stability of the fully powered TM petal is analysed in terms of the measured silicon sensor temperatures using the IR data as well as the recorded temperature data from the additionally attached Pt100 sensors on the different modules. Figure 6.52a shows the selection of a measurement cycle logged for the TM petal at the lowest reached set point of 18.1 bar using the nominal CO_2 mass flow of 1.3 g/s.

Here, stable temperatures are recorded at the beginning for the unpowered state of the TM petal in terms of the CO_2 coolant as well as on the silicon modules measured by the Pt100 sensors. But after switching on the power in the electronics to simulate the full heat load of the petal, the measurement of the silicon temperatures shows a steep increase at the time of powering before gradually increasing further over time. For this longer time period of powering, the CO_2 coolant temperature rises as well gradually, which means that the initial CO_2 pressure set point of 18.1 bar is not stable in the powered state. Nonetheless, after approximately five to six hours a stable state of the system is reached as stable temperature values for the evaporative CO_2 cooling as well as for the Pt100 sensors on the silicon modules are logged. Afterwards, the power is switched off and the temperature on the silicon drops again steeply before lowering gradually over time. For the CO_2 coolant, the temperature decreases gradually without the heat load of the electronics and the TRACI system tries to reach the lower pressure set point again. To evaluate the silicon temperature for the different power states using IR thermography, thermograms are recorded in the unpowered state at the beginning, in the powered state for three different time intervals (after ten minutes, five and six hours) and after switching off the power.

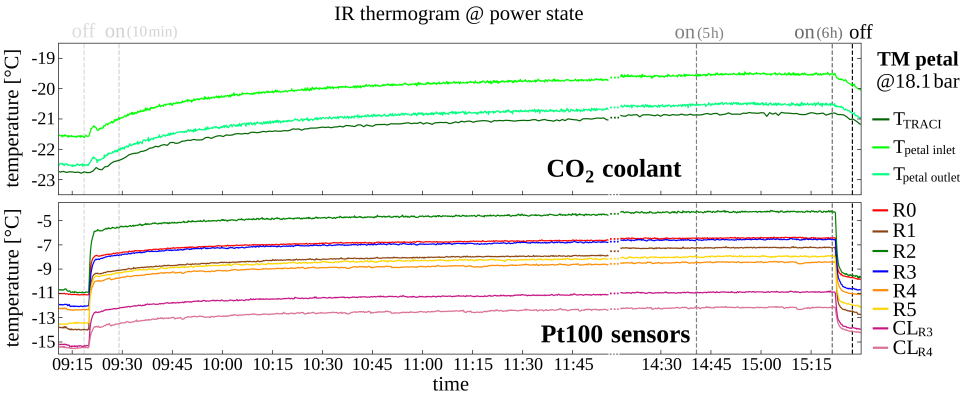

(a) CO_2 coolant temperature and Pt100 sensor temperatures for different power states.

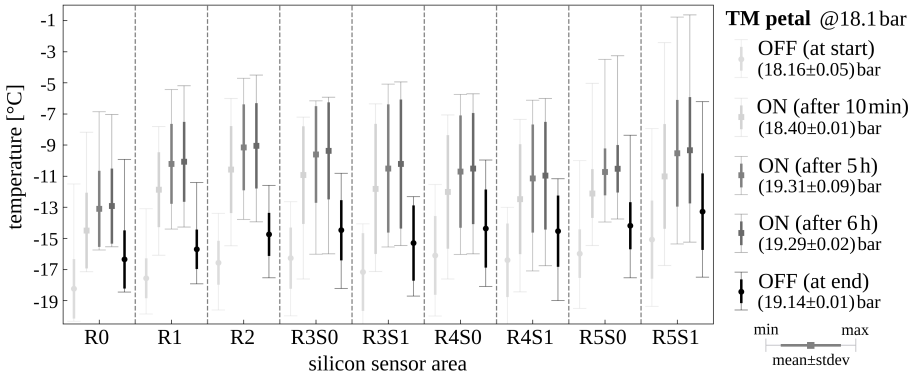

(b) IR temperatures on the silicon sensor areas for different power states.

Figure 6.52: Investigation on the temperature stability of the TM petal in the fully powered state for the lowest set point of 18.1 bar. Evaluated are the temperatures on the silicon sensor areas measured by the attached Pt100 sensors and by the IR camera for different times and power states.

Figure 6.52b compares the temperature distributions on the silicon sensor areas measured for the different power states. Here, the steep increase of the temperature on the silicon between the unpowered and powered state of the TM petal is visible as well as the gradual increase for longer times of powering, reaching a stable state after roughly six hours.

When comparing the temperatures for the unpowered state measured before and after the powering over the longer time period, the temperatures after powering are still higher than before, meaning that the system needs time to recover from the powering, as also the current CO_2 pressure is roughly 1 bar higher than the initial set point.

After investigating the stability of the TM petal in the fully powered state, the resulting temperatures for other power scenarios with the TM petal were tested, using the ability of the developed test setup to power individual modules on the TM petal.
Here, the following test cycle of different power states is investigated for the CO_2 pressure set point of 26 bar: after stabilizing at the set point, an IR thermogram in the unpowered state is recorded ("off"); then only the R0 module on the front side is powered for two minutes and an IR thermogram is recorded ("R0 on"); after waiting two minutes in the unpowered state, only the R3 module on the front side is powered and the IR temperatures are measured ("R3 on"); after two minutes without powering, an IR thermogram is recorded after three minutes of powering all the modules and the EoS of the back side ("backside on"); this procedure is repeated for powering the complete front side with a waiting time of three minutes in between ("frontside on"); after waiting again three minutes to recover, the TM petal is fully powered for 15 minutes and an IR thermogram of this state is recorded ("all on"); finally, the unpowered state of the TM petal is measured again after the powering with a waiting time of five minutes ("off").
The IR thermograms recorded for the different powering scenarios and consecutively tested in the measurement cycle as described before, are compared in Figure 6.53.

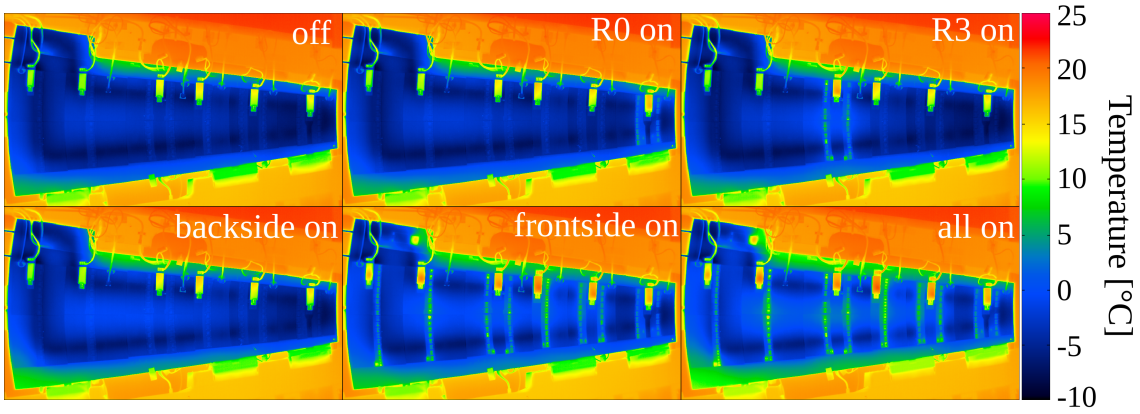

Figure 6.53: Comparison of the IR thermograms of the TM petal for the different powering scenarios tested consecutively at the 26 bar set point.

The temperatures on the silicon modules measured by the attached Pt100 sensors for this powering cycle are shown in Figure 6.54a and the IR temperatures on the silicon sensor areas are evaluated in Figure 6.54b for the corresponding power states.
When powering the R0 module, the typical steep increase with the following gradual saturation in the measured temperature for the Pt100 sensor on the R0 module is observed. Moreover, a small increase in the other silicon sensor temperatures is observed for the Pt100 sensors as well as the IR temperatures, indicating an influence of the powered R0 module on the CO_2 coolant as reaction of the changing conditions compared to the stable state before. Especially the neighboring R1 module seems to be influenced by the powered R0 module, as the R1 temperature shows a bit higher fluctuation compared to the further away modules. After switching off the power, the temperatures stabilize again around the initial conditions over the waiting time of two minutes.

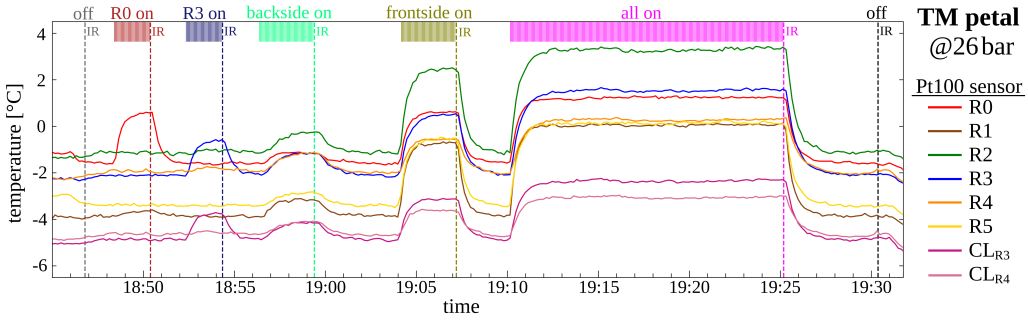

(a) Temperatures on the silicon modules measured by the Pt100 sensors.

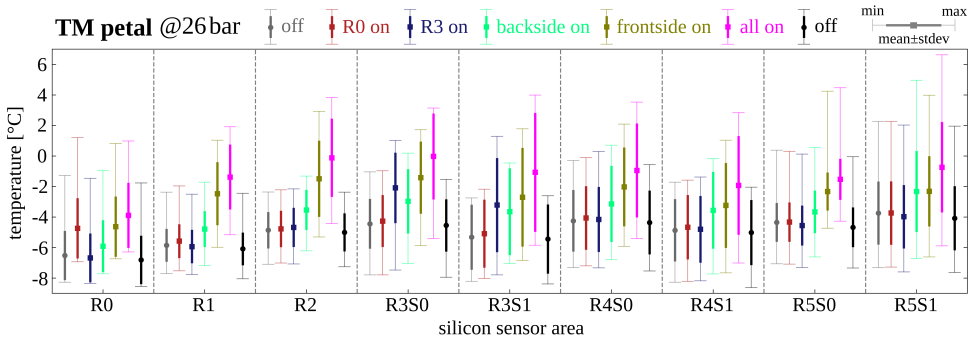

(b) Temperatures on the silicon sensor areas measured by the IR camera.

Figure 6.54: Investigation on the temperatures for the powering cycle of the TM petal at the 26 bar set point. Compared are the consecutively tested power states “off”, “R0 on”, “R3 on”, “backside on”, “frontside on”, “all on” and “off”.

When powering the R3 module, the same behaviour as before is observed: the two Pt100 sensors, one on the edge and one directly above the cooling loop of the R3S0 silicon sensor, shows a steep temperature increase with only smaller fluctuations in the other, unpowered modules, which is also seen in the evaluated IR temperatures.
In the next powering step, the powered modules and EoS of the back side of the TM petal are causing also an increase on the measured temperatures of the front side. This can be explained by the short thermal path between both sides of the petal as well as the changing conditions for the CO_2 coolant influenced by the heat load of the back side. But in comparison to the powered front side, as the next investigated power state, the temperature increase is much smaller. Here, an immediate reaction on all modules is observed whereas the absolute change in temperature compared to the unpowered state is varying between the different sensors, as discussed before.
When comparing the temperatures for the R0 sensor between the states of only powering R0 and powering the complete front side, a very similar temperature is measured by the Pt100 sensor as well as in the IR thermograms. But when performing the same comparison for the R3 module between the states of only powering R3 and powering the front side, the temperature for the latter state is higher. This is most probably caused by the heat load of the surrounding modules influencing the R3 module’s temperature, whereas the R0 module does not show this effect as it has only one neighbour and is also the best cooled module due to its location on the cooling loop’s U-turn.
For the case of the full heat load, the resulting temperature increase can be well constructed as the sum of the temperature increases caused by powering the front and back side individually. Finally, the unpowered state measured after the different powering scenarios shows very comparable temperatures as the state before the cycle, indicating a full recovery of the cooled TM petal to a stable operation point again.

Therefore, also the analysis of the thermal performance of the TM petal under different powering scenarios showed no indication of a problem in the petal's cooling concept.

Experimental validation of the petal FEA model

The experimental results from the thermal tests of the TM petal is also used to validate the FEA model of the thermal petal simulation. For this purpose, the petal FEA model of the appropriate design stage is adapted for the specialities of the TM petal, e.g. adapting the heat loads of the electronics. Moreover, the logged data with TRACI and the CO_2 diagnostics from the experiment are used to model the appropriate CO_2 conditions in terms of the coolant temperature and the HTC[37] in the FEA. Additionally, the heat exchange between the petal surface and the ambient air in the PTM is anticipated by assuming an HTC of $5\,\mathrm{W/(K \cdot m^2)}$ on the surface and using the measured air temperature of the experiment. For the experimental data, a measurement cycle of the TM petal with a CO_2 mass flow of 2.5 g/s is used for the comparison to the simulation results.

Figure 6.55 shows the resulting temperature distribution from the FEA simulation as well as the recorded IR thermogram with a corrected emissivity value of $\epsilon = 0.977$ for the case of the fully powered TM petal at the lowest reached CO_2 pressure set point of 18.6 bar, corresponding to a coolant temperature of $-21.7\,^{\circ}\mathrm{C}$. To allow for a direct comparison, the temperature scale of the FEA result is extracted and applied to the IR thermogram.

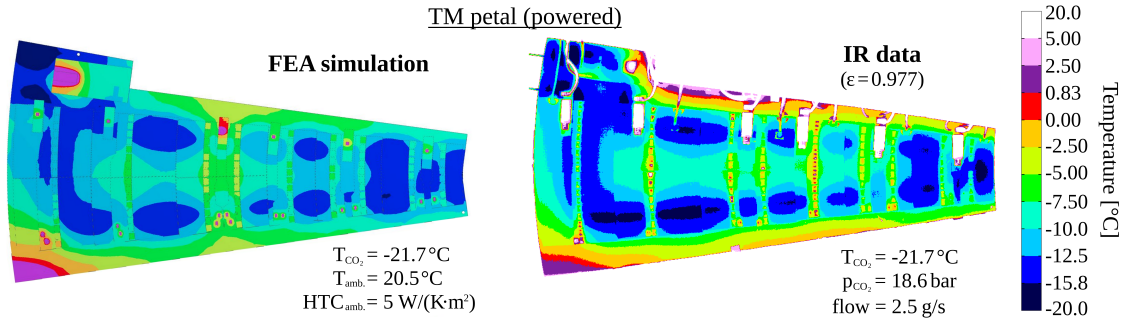

Figure 6.55: Comparison of the temperature distributions on the TM petal surface between the FEA simulation result and the experimental IR data. Shown are the results for the TM petal in the fully powered state at the lowest reached set point of 18.6 bar in the experiment. The measured instrumentation data in terms of the CO_2 coolant temperature of $-21.7\,^{\circ}\mathrm{C}$ and the ambient temperature of $20.5\,^{\circ}\mathrm{C}$ are used as input for the FEA.

Qualitatively, the simulated temperature distribution matches quite well with the measured IR temperatures. So when comparing the temperature pattern along the cooling loop, a similar behaviour is observed in both cases and also the too hot temperature on the R5S1 sensor is visible in the experimental as well as the simulated data. Nonetheless, some differences can be also observed: in the FEA, the plastic covers used in the experiment are not modelled, which allows e.g. to see the high temperature of the DCDC converter for the R3 module, whereas no information can be extracted from the IR data; the heat load emulated in the EoS board is not modelled correctly in the FEA due to a positional shift; the influence of the petal holder on the edges of the TM petal as well as the mounted Pt100 sensors are clearly visible for the experimental data as warmer temperature influence;

[37] The HTC value for the FEA is extracted from a corresponding CoBra simulation using the nominal heat load, the adjusted mass flow and the saturation temperature at each set point.

on the contrary, the petal in the FEA is modelled ideally without any contact to the surrounding other than the assumed convection with the ambient air volume.
For a quantitative comparison, the resulting temperature distributions on the silicon sensor areas for the same conditions as before are shown in Figure 6.56 for the experimental and simulated data. The measured IR temperatures are evaluated for the uncorrected case with an ideal emissivity of $\epsilon = 1.0$ as well as using the measured emissivity value of the painted TM petal with $\epsilon = 0.977$.

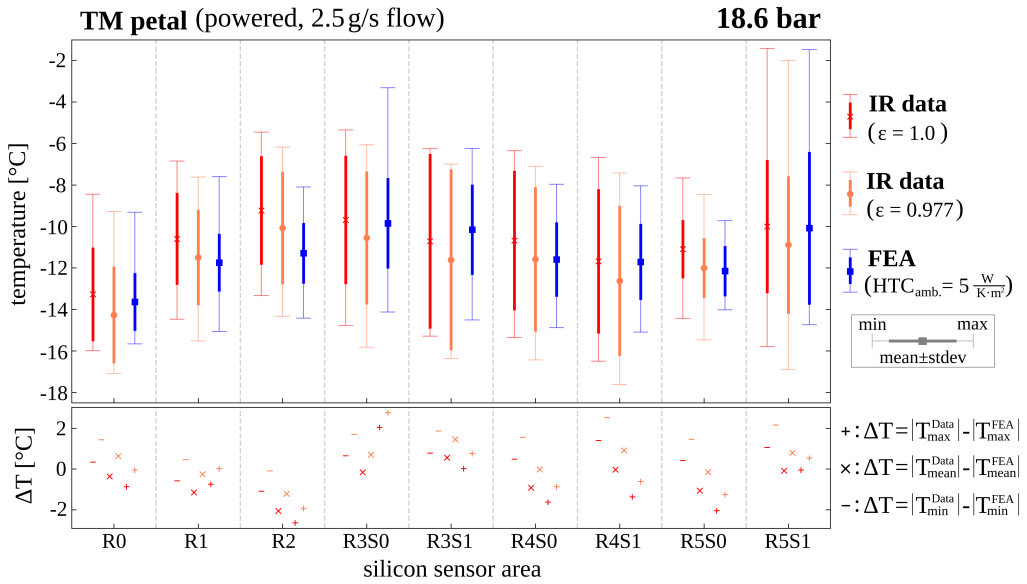

Figure 6.56: Comparison of the temperature distributions on the silicon sensor areas between the experimental data and the FEA simulation results. Shown are the results for the TM petal in the fully powered state at the lowest reached set point of 18.6 bar in the experiment. The IR data are evaluated for an ideal emissivity of $\epsilon = 1.0$ as well as the measured paint emissivity of $\epsilon = 0.977$. Moreover, the temperature differences between the experimental data and the FEA result are calculated for the mean, minimum and maximum value.

Here, the mean temperatures on the silicon extracted from the experimental and FEA data are matching within the assigned standard deviations, but for the individual silicon areas the results are fluctuating quite a lot, also when comparing the minimum and maximum temperature values. Moreover, it is also difficult to say if the emissivity corrected data matches better the simulation than the uncorrected case, as the results are not conclusive. Nonetheless, the temperature difference in terms of the mean, minimum and maximum values of the distributions between IR and FEA data is within $\pm 2.5\,^{\circ}\mathrm{C}$ for all cases. Due to the assumptions made in the FEA model, like the CO_2 coolant properties or the convection with the ambient air, and the experimental uncertainties, like the measurement uncertainty of the IR camera of ± 1,K, the emissivity value or the cooling performance of TRACI, the overall results of experiment and FEA are matching well and no major temperature differences on the petal surface are identified.
Therefore, it can be concluded that the experimental data of the TM petal allows for a validation of the corresponding petal FEA model. With the validated FEA, the petal design was further optimized, e.g. by adapting the cooling loop geometry to reach a lower temperature on the R5S1 sensor or by changing the position of the DCDC converters directly above the cooling loop to allow the best possible thermal path to one of the most critical heat producers on the petal.

6.6 Investigation on Thermal Deformations

The petal core design is investigated in terms of its thermo-mechanical behaviour by measuring the *thermal deformations* of the structure over the typical temperature ranges occurring in detector operation. With this thermo-mechanical analysis based on all the foreseeable load scenarios expected during the life cycle of the detector, it is possible to understand the effects of the thermal and static loads on the structural integrity of the petals and verify therefore its local support design.
Mechanical deformations in a solid material due to a change in temperature are caused by its *thermal expansion*. Here, the thermal expansion is the typical property of a material to increase in volume with heat and to decrease in volume with cold[38]. In the case of expansion, tensile forces are created in the solid, whereas compressive forces act in the material in the case of contraction. The amount of thermal expansion depends on the material's **C**oefficient of **T**hermal **E**xpansion (CTE), which describes how the size of an object changes with a change in temperature and can be expressed in terms of the change in length, area or volume. The linear expansion of a material is estimated as

$$\frac{\Delta L}{L} = \alpha_L \Delta T, \tag{6.6}$$

with ΔL as change in length due to expansion or contraction, L as the initial length, α_L as the linear CTE of the material and ΔT as the temperature difference.

The local support design of petals is symmetric so that in theory no thermal deformations should appear but small differences could cause deformations. Therefore, the thermal deformation study described in this work is conducted on the petal core 05 to measure and evaluate the occurring deformations. The developed setup to measure the thermal deformations of the structure and the measurement principle are explained in Section 6.6.1. The results for the core and the evaluation in terms of the thermo-mechanical specifications are presented in Section 6.6.2.

6.6.1 Setup and measurement principle

The core under study is placed on the SmartScope (cf. Sec. 6.2.1) to measure the surface geometry of the structure. It is important to apply the real petal fixation conditions in the setup, as the thermal expansion is different if the structure is free to expand or is constrained causing internal stress. Therefore, the core is mounted into the foreseen locking points of the global structure via the petal locator pins allowing the kinematic mounting. Figure 6.57 shows the mounting of core 05 on the SmartScope using the locking points.

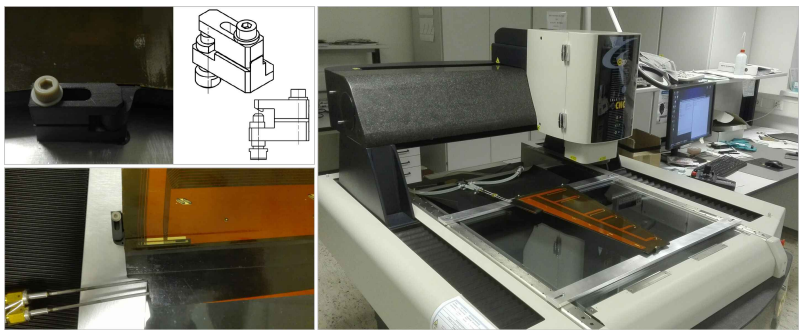

Figure 6.57: Mounting of core 05 on the SmartScope using the locking points for kinematic mounting. Shown is the petal fixation into the thermoplastic locator pins.

[38] Some materials, e.g. carbon or kevlar fibers, show contraction on heating within certain temperature ranges along the fiber direction, called negative thermal expansion.

As defined in Eq. 6.6, the thermal deformation depends on the absolute value of ΔT. The relative sign between the compared temperatures determines only the direction of deformation, either expansion or contraction of the structure. The evaluation of the deformations should be therefore independent, if the core is heated or cooled in the measurement. Nonetheless, both ways are tested in the study allowing to cross check the results.

For the *warm test*, a Huber mini-chiller filled with distilled water is used for a temperature range between $+20\,^{\circ}\mathrm{C}$ to $+80\,^{\circ}\mathrm{C}$. The water temperature is measured with additional thermocouples at the in- and outlet of the petal cooling loop.
For the *cold test*, evaporative CO_2 cooling with the TRACI system is used for coolant temperatures between $+20\,^{\circ}\mathrm{C}$ to $-20\,^{\circ}\mathrm{C}$. An additional temperature measurement is provided by Pt100 sensors glued on the titanium cooling pipe close to the in- and outlet. The advantage of the warm test is to reach a higher temperature difference of $\Delta T = +60\,^{\circ}\mathrm{C}$ compared to CO_2 cooling with $\Delta T = -40\,^{\circ}\mathrm{C}$. The disadvantage of the warm test is the changing water temperature along the loop, as it is observed with the IR camera in Figure 6.58a, whereas evaporative CO_2 cooling has a nearly constant coolant temperature and is also the real fluid used in the detector. On the contrary, the cold test conditions require a more sophisticated setup with dry air flushing to avoid condensation on the core surface. Therefore, the complete SmartScope machine is enclosed in a clean room tent for active humidity control, as shown in Figure 6.58b.

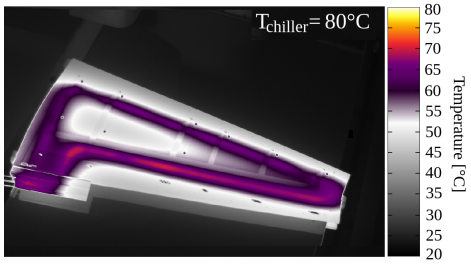

(a) *Warm test*: Thermogram of changing water temperature along loop.

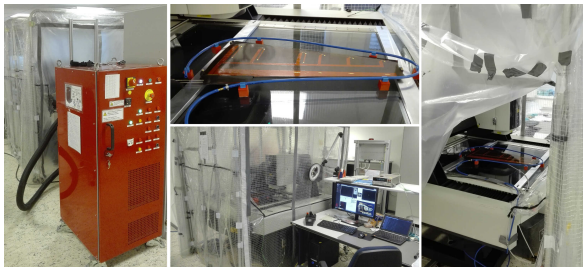

(b) *Cold test*: Setup with SmartScope housing with dry air flushing for humidity control.

Figure 6.58: Specialities in the thermal deformation setup for warm testing with distilled water and cold testing with evaporative CO_2.

For both tests, the first measurement point is at $20\,^{\circ}\mathrm{C}$ corresponding to room temperature and the temperature is then increased or decreased in steps of $10\,^{\circ}\mathrm{C}$. After waiting at each defined temperature set point for 30 minutes to establish a thermal equilibrium state, the programmed SmartScope routine is executed.
In the first step, the core's coordinate system is defined by the rough and fine alignment using the locking point screws and the fiducial holes in the PL. Afterwards, nearly 1100 measurement points are defined on the surface[39] in a $10\,\mathrm{mm} \times 10\,\mathrm{mm}$ pattern using the grid projection feature and a high magnification. As a result, a position-resolved height profile over the core's surface is created for each temperature set point.
Figure 6.59 shows the defined point pattern over the surface and the resulting height profile at room temperature. Here, the height z is relative to the height of the PL used as the origin of the coordinate system for the measurement. For the regions between the measurement points, linear grid interpolation is applied.

[39] The EoS region, uncovered by the bus tape and featuring therefore a step, is excluded and the focus is on the module area with a measurement time of one hour for the defined pattern.

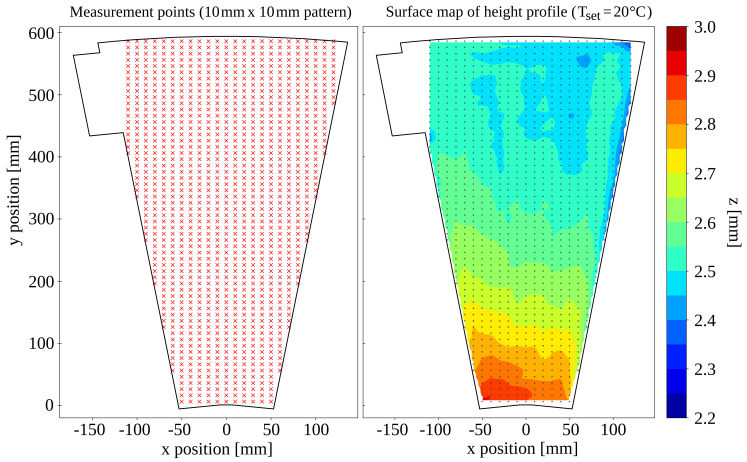

Figure 6.59: Measurement of the height profile over the core surface. Shown are the defined 10 mm×10 mm pattern of measurement points and the resulting height profile map at room temperature ($T_{\mathrm{set}} = 20\,^{\circ}\mathrm{C}$), using linear grid interpolation.

In a separate routine, the fiducial pads on the bus tape are detected as circular openings by the SmartScope feature finder and their relative positions are measured. By comparing the measured x- and y-positions of different temperature set points, a possible expansion or contraction in the respective direction can be analysed, as depicted in Figure 6.60.

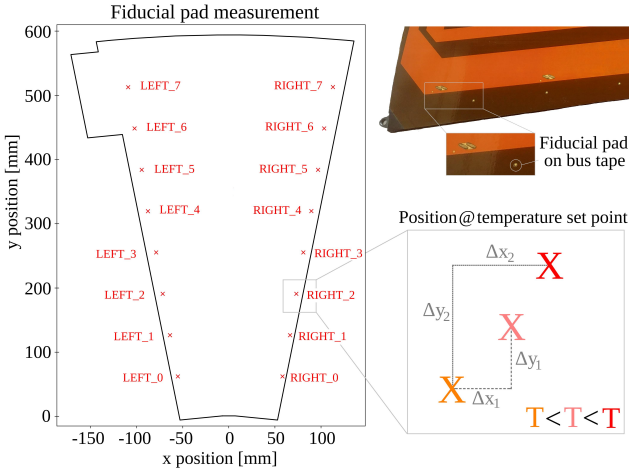

Figure 6.60: Position measurement of the sixteen fiducial pads on the bus tape for each temperature set point. Shown are the naming scheme as used in the following and a photograph of the bus tape. Moreover, the determination of relative position shifts Δx and Δy for different temperature set points is exemplary depicted.

For the warm test, the chiller set point is adjusted to reach the aimed for temperature set point at the inlet thermocouple due to the heat loss in the connection pipe. For the cold test, the temperature set points are adjusted by the CO_2 pressure with values of 57 bar, 45 bar, 35 bar, 26 bar and 20 bar and the mass flow is adjusted to 1.3 g/s.

6.6.2 Results and evaluation

The results of the thermal deformation study are analysed in three categories for each temperature set point: by evaluating *deformation maps* for the core's surface, by calculating the *local flatness* of the surface and by determining the position shifts of the *fiducial pads* on the bus tape surface. Each analysis category is evaluated in terms of the thermal deformation specifications of the petal core design (cf. Sec. 6.1.1).

Deformation maps

For the evaluation of the thermal deformations on the core's surface, the relative height difference Δz for the temperature difference ΔT at each measurement point in x and y direction is determined as

$$\Delta z = \Delta z(x_i, y_i, \Delta T) = z(x_i, y_i, T_{\mathrm{set}}) - z(x_i, y_i, T = 20\,^{\circ}\mathrm{C}). \tag{6.7}$$

Here, the height $z(T_{\text{set}})$ at the temperature set point T_{set} is corrected by the measured height $z(T = 20\,^{\circ}\text{C})$ at room temperature to account for the deformation caused by the temperature difference $\Delta T = T_{\text{set}} - 20\,^{\circ}\text{C}$.

The resulting *deformation map* for the largest temperature difference of $\Delta T = +60\,\text{K}$ for a water temperature of $T_{\text{set}} = +80\,^{\circ}\text{C}$ is shown in Figure 6.61. Here, negative values are observed for the core's right edge meaning a deformation downwards and vice versa for the left edge with positive values corresponding in a deformation upwards.

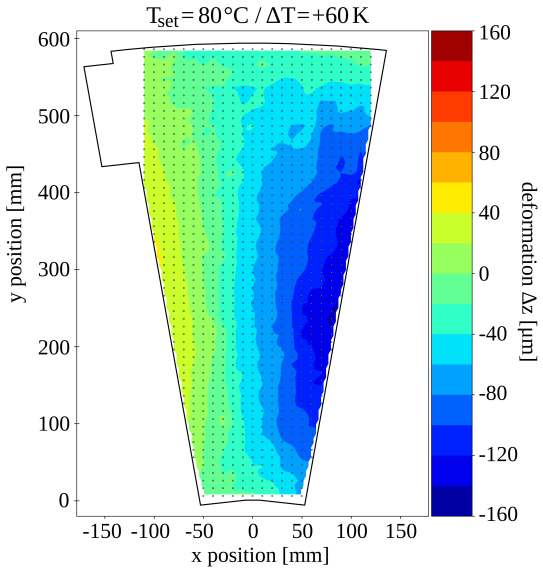

Figure 6.61: Map of the thermal deformation Δz for a temperature difference of $\Delta T = +60\,\text{K}$, corresponding to a temperature set point of $T_{\text{set}} = +80\,^{\circ}\text{C}$ for the warm test.

Figure 6.62a shows the deformation maps for the warm test with temperature differences of $\Delta T = +10$, $+20$, $+30$ and $+40\,\text{K}$ and the cold test results with temperature differences of $\Delta T = -10$, -20, -30 and $-40\,\text{K}$ are shown accordingly in Figure 6.62b.
Here, for higher temperature differences ΔT, an increase in the thermal deformation Δz is observed for the warm and cold test, respectively. But the direction of the thermal deformation depends on the relative sign of ΔT as described in Eq. 6.6: the right edge deforms downwards in the warm test and upwards in the cold test and vice versa for the left edge of the petal core surface.
Table 6.3 summarizes the thermal deformation results over the tested temperature differences in terms of the mean, minimum and maximum value.

	Thermal deformation		
ΔT	mean$\pm\sigma$ [µm]	minimum [µm]	maximum [µm]
$-40\,\text{K}$	8.3 ± 18.9	-29.7	73.5
$-30\,\text{K}$	5.9 ± 14.1	-22.2	39.7
$-20\,\text{K}$	5.9 ± 9.3	-13.2	27.6
$-10\,\text{K}$	-2.1 ± 5.9	-16.3	8.1
$+10\,\text{K}$	-15.6 ± 8.1	-36.1	-1.8
$+20\,\text{K}$	-13.4 ± 13.2	-51.7	12.4
$+30\,\text{K}$	-32.5 ± 24.6	-91.4	11.9
$+40\,\text{K}$	-21.2 ± 29.6	-93.4	34.3
$+60\,\text{K}$	-41.9 ± 44.0	-149.4	43.4

Table 6.3: Results of the measured thermal deformations over the tested ΔT range in terms of the mean, minimum and maximum value.

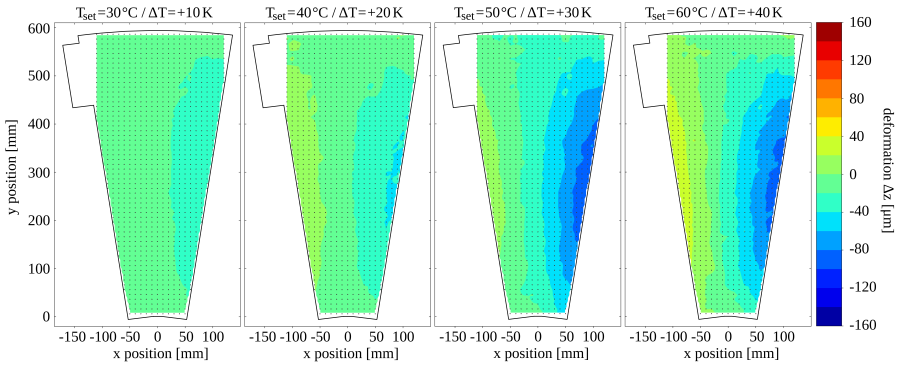

(a) Deformation maps for the *warm test* with water.

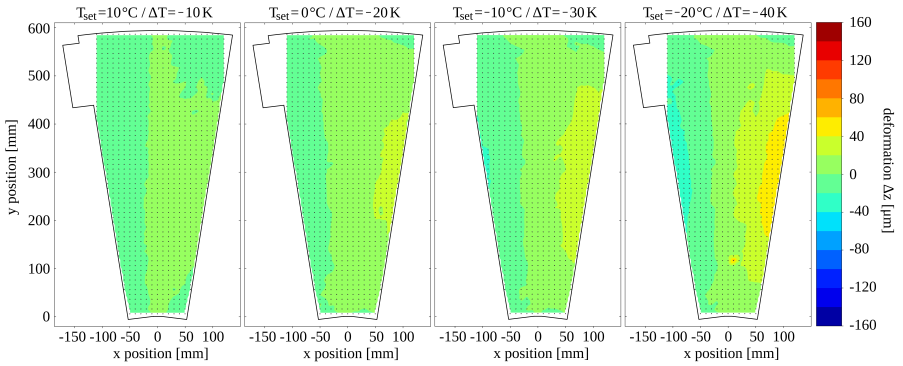

(b) Deformation maps for the *cold test* with CO_2.

Figure 6.62: Deformation maps for $\Delta T = \pm 10$, ± 20, ± 30 and $\pm 40\,\mathrm{K}$.

Moreover, the expected linearity for the thermal deformations over the measured ΔT range is tested in Figure 6.63. Here, the projection of measurement points along the x-axis, shown exemplary for the position $x = 0\,\mathrm{mm}$, can be analysed for the measured temperature differences. The dependence of $\Delta z \propto \Delta T$ can be clearly observed with consistent results for the warm and cold test. Furthermore, the warm test results show higher fluctuations between the individual measurement points, which can be explained by the changing water temperature along the core's cooling loop causing a non-uniformity over the petal geometry.

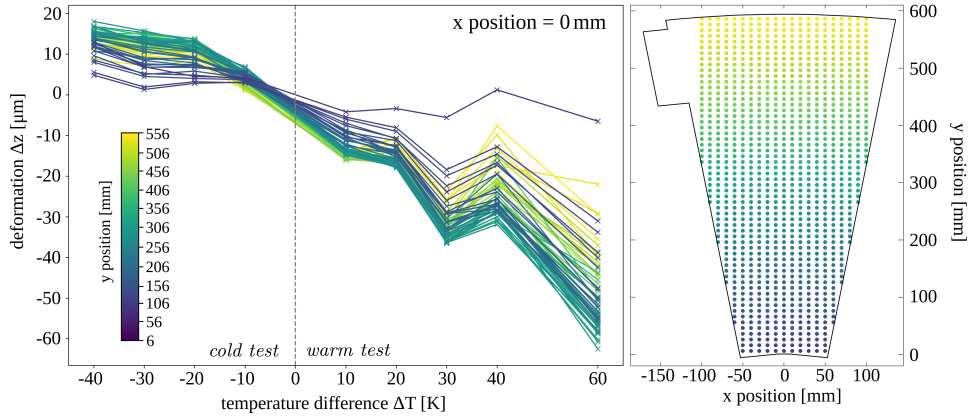

Figure 6.63: Linearity of the thermal deformations for positive and negative ΔT. Shown are exemplary the projected results for the position $x = 0\,\mathrm{mm}$.

In general, the observed thermal deformations on the surface are in the order of $\mathcal{O}(\pm 100\,\mu\mathrm{m})$ for the measured temperature differences between $\Delta T = -40\,\mathrm{K}$ and $\Delta T = +60\,\mathrm{K}$.

Therefore, these results indicate an appropriate and mechanically stable design of the local support structure for the expected operational temperature gradients in the detector.

Local flatness variation

The thermal deformation of the petal core is also evaluated in terms of the local flatness variation. The local flatness, determined over each module area, is specified to be less than 50 µm after core assembly and less than 100 µm for operational temperature shifts. The latter specification can be checked with the results of the thermal deformation study.
The flatness is a property of a plane, which characterizes its surface, and the terms and concepts related to flatness are defined in the ISO 12781-1 standard [183]. Here, the *local flatness deviation* is defined as the perpendicular distance of a single point on the object's surface from a constructed reference plane. The *reference plane* is the associated plane fitting the flatness surface according to specified conventions and any deviations from the flatness surface are calculated relative to this plane. Two procedures exist to determine the reference plane: on the one hand, the *minimum zone reference plane* is constructed by two parallel planes enclosing the flatness surface with the least separation; on the other hand, the *least squares reference plane* (LSPL) minimizes the sum of the squares of the local flatness deviations. For this work, the LSPL method was chosen to evaluate the local flatness of the petal core. Figure 6.64 depicts the definition of the local flatness deviation and the construction of the LSPL, for which the procedure is described in Appendix A.3.

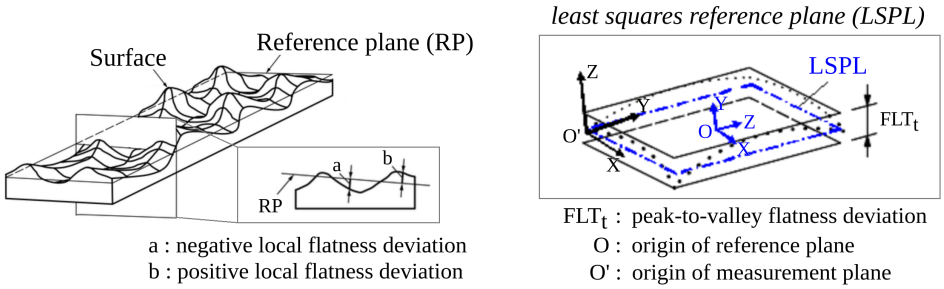

Figure 6.64: Definition of the local flatness of an object according to the ISO 12781-1 standard (left) and construction of the *least squares reference plane* (right). Modified from [183, 184].

The same measurement points as used for the evaluation of deformation maps are used for the local flatness calculation, but only points within the respective module area are selected. This assignment of the defined 10 mm×10 mm point pattern to the module areas R0 to R5 is illustrated in Figure 6.65.

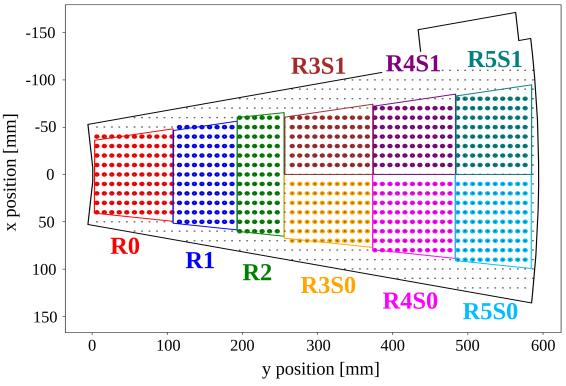

Figure 6.65: Definition of the module areas, R0 to R5, for the local flatness calculation. Here, only the measurement points of the defined 10 mm×10 mm pattern within the respective module area are selected for the local flatness evaluation.

The measured local flatness values for each temperature set point in the warm and cold test and for each module area are plotted in Figure 6.66. Moreover, both specification values on the local flatness are overlayed to allow for an evaluation of the local flatness variation in the thermal deformation study.

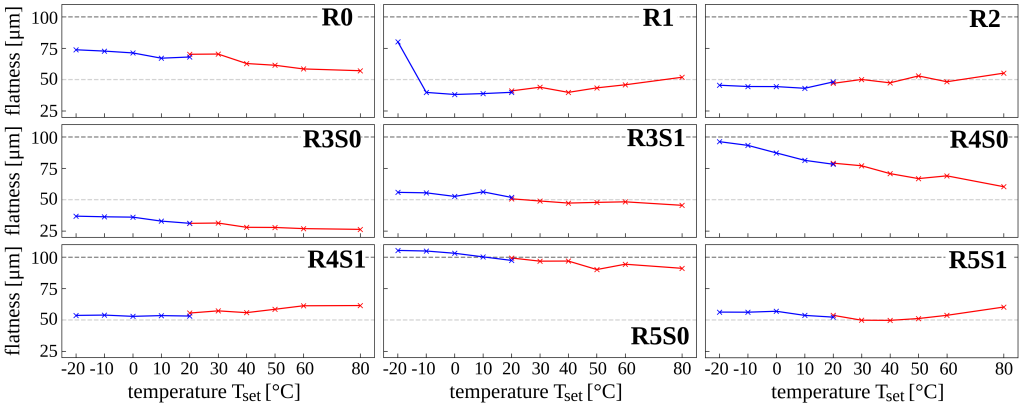

Figure 6.66: Measurement of the local flatness for temperature set points T_{set} between $-20\,^{\circ}\text{C}$ and $80\,^{\circ}\text{C}$ for each module area. Shown are the results of the warm (red) and cold test (blue) and overlayed with the specification values of $50\,\mu\text{m}$ after assembly and $100\,\mu\text{m}$ over operational temperature gradients.

First of all, it can be observed that the specification on the local flatness after assembly, as measured for the room temperature case, is not fulfilled in most of the module areas. This can be explained by a known feature in the assembly process[40] resulting in the observed local flatness deviations. Nonetheless, the measured variations in the local flatness for the different temperature set points can be used to evaluate the local flatness specification over operational temperature gradients.
Here, the maximal positive and negative variation over the tested temperature range between $-20\,^{\circ}\text{C}$ and $80\,^{\circ}\text{C}$ relative to the local flatness at room temperature is determined to be $\pm 10\,\mu\text{m}$ for all module areas, with two exceptions: the module area R4S0 shows a higher variation of $\pm 20\,\mu\text{m}$ and for the module area R1 an outlier for $T_{\text{set}} = -20\,^{\circ}\text{C}$ is observed, which is caused probably by a measurement error.
When comparing the flatness values of the warm and cold test, no general statement can be made as for five areas a negative slope to higher temperatures is observed, whereas the other four show rather a positive slope.
From the local flatness results in the thermal deformation study of core 05, it can be concluded that a petal core fulfilling the local flatness specification of $50\,\mu\text{m}$ after assembly will also fulfill the specification of $100\,\mu\text{m}$ over operational temperature gradients.

Fiducial pad positions

For the evaluation of expansion or contraction effects of the core, the dedicated measurement of the fiducial pad positions on the bus tape surface is used.
The position shifts Δx and Δy for each fiducial pad are calculated as

$$\Delta x = \Delta x(\Delta T) = x(T_{\text{set}}) - x(20\,^{\circ}\text{C}) \quad \text{and} \quad \Delta y = \Delta y(\Delta T) = y(T_{\text{set}}) - y(20\,^{\circ}\text{C}). \tag{6.8}$$

[40] When measuring the surface flatness of the vacuum plate used for the core assembly, local flatness variations in the same order of magnitude are observed. Therefore, for future core prototypes a reworked vacuum plate within specifications is used.

The difference in position for each temperature set point to the position at room temperature is calculated to evaluate the relative shift caused by the temperature difference ΔT. Figure 6.67 shows the measured shifts for temperature differences of $\Delta T = \pm 10$, ± 20, -30, ± 40 and $+60\,\mathrm{K}$ in the x- and y-direction, respectively[41].

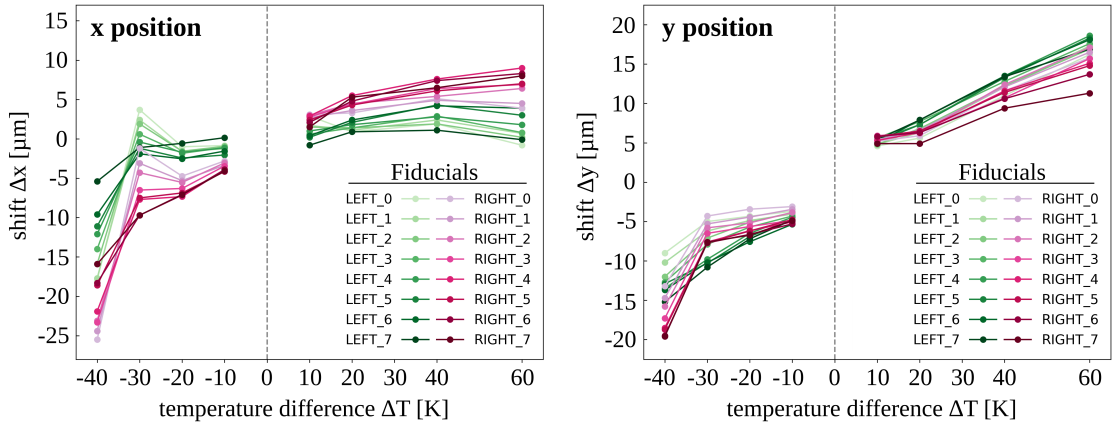

Figure 6.67: Measurement of the position shifts in x (left) and y (right) for the fiducial pads caused by the measured temperature differences ΔT.

Here, the shifts in x for positive ΔT are rather low, indicating a negligible expansion effect in the x-direction, but for negative ΔT, the contraction effect is much more pronounced. Moreover, the fiducials for the left and right side are clearly grouped together with a difference between each other. So far, no good interpretation of the shifts in x is found. For the Δy shifts, a clear trend for the measured temperature differences can be observed, showing an expansion for positive ΔT and a contraction for negative ΔT with a rather uniform behaviour for the left- and right-side fiducials.

For a detailed analysis of the effect in the y-direction, a linear fit is performed for the fiducials of the left and right side separately, using the mean value over the eight fiducials per side. The results for an unbiased and biased linear fit are shown in Figure 6.68 and give an estimated value of $\sim 0.31\ \frac{\mu\mathrm{m}}{\mathrm{K}}$ for the linear CTE in the y-direction.

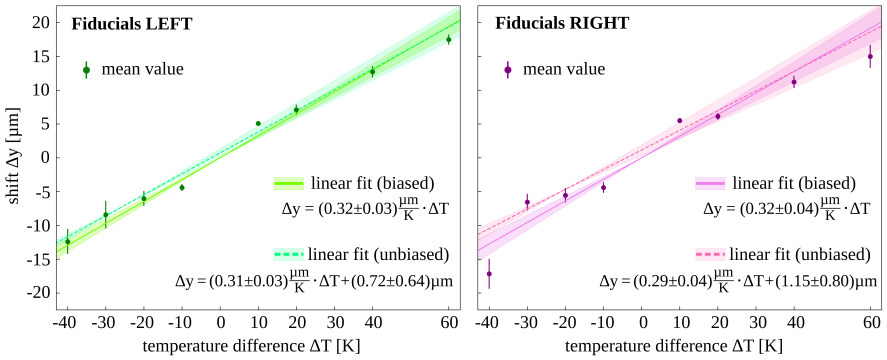

Figure 6.68: Fitting of the fiducial shifts Δy with linear functions (unbiased and biased), separately for the left and right fiducials.

In general, the observed shifts in the x- and y-direction due to thermal expansion and contraction over the operational temperature gradients are rather small with maximally $\pm 25\,\mu\mathrm{m}$. These shifts, translated into movements of the silicon sensor modules, can be corrected by track-based alignment procedures during detector operation.

[41] The measurement for $\Delta T = +30\,\mathrm{K}$ is not shown as a data recording problem occurred.

6.7 Thermal Cycling and Thermal Shock Test

The thermo-mechanical behaviour of the petal core design is also studied for two other temperature scenarios during detector operation.
On the one hand, a possible degradation in the performance for the core after a number of temperature cycles is investigated. In the *thermal cycling* study, the core is thermally cycled between a specified temperature of -40° C to $+40^{\circ}$ C for 100 iterations, mimicking the expected temperature cycles for the ITk detector operation over its lifetime. The mechanical and thermal performance parameters of the core are compared before and after thermal cycling to detect possible degradations. By this study, the petal core design can be verified to withstand the normal temperature cycles during detector operation.
On the other hand, the performance of the petal core should be verified for the extreme temperature conditions. In the *thermal shock* test, the core is exposed to very low temperatures to check the integrity of the structure. The core's mechanical and thermal performance is compared before and after the thermal shock test to validate the resistance of the design against the extreme temperature conditions.

The setup for the thermal cycling of the core is described in Section 6.7.1 and the performance results after thermal cycling are evaluated in Section 6.7.2. For the thermal shock test, the setup and the performed tests on the core are explained in Section 6.7.3. For the investigations in terms of thermal cycling and thermal shock, the petal core 08 is used to verify the latest design of the local support structure. Additionally, Section 6.7.4 shows the results of the thermal shock test on the TM petal to verify the stability of the glued on silicon dummy modules.

6.7.1 Setup for thermal cycling

For the thermal cycling, the core under study is placed in a climate chamber. The used climate chamber of model CTS T-40/200 [185] has a temperature range of -40° C to $+180^{\circ}$ C with a ramping speed of 4 K/min and allows with its volume of 200 l to fit a petal core inside, as shown in Figure 6.69. To avoid damages on the core surface by condensation, the sensitive bond pad openings in the bus tape are sealed by tape, external dry air flushing is enabled and hygroscopic silica gel is used. The temperature and humidity in the climate chamber is logged with three SHT21 sensors using the Raspberry Pi readout.



Figure 6.69: Setup for the thermal cycling of a petal core using a climate chamber. Core 08 is placed in the climate chamber, after protecting its bond pads with tape, and the temperature and humidity is logged with three SHT21 sensors.

In a series of pre-tests, the parameters and settings of the climate chamber were adjusted for temperature cycles between -40° C to $+40^{\circ}$ C. Figure 6.70 shows the measured temperatures of the SHT21 sensors for a typical programmed temperature cycle.

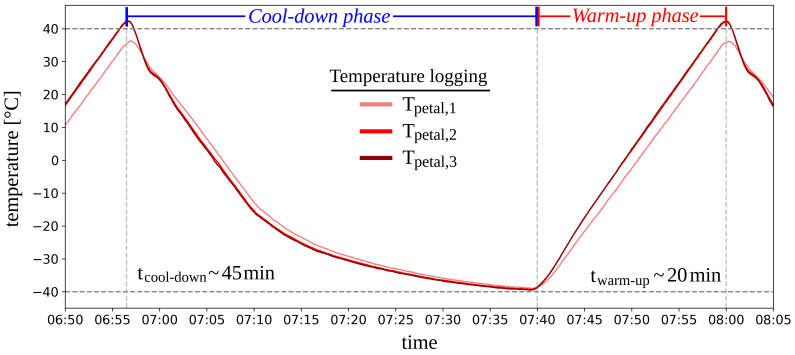

Figure 6.70: Measurement of a typical, programmed temperature cycle between -40° C to $+40^{\circ}$ C. Marked are the *cool-down* and *warm-up* phase and the required time is determined.

The required time for the warm-up phase from -40° C to $+40^{\circ}$ C is ~ 20 min, matching the specified ramping speed of 4 K/min. For the cool-down phase from $+40^{\circ}$ C to -40° C, the observed temperature trend shows in the beginning a linear dependence changing to an exponential behaviour saturating at the set point temperature[42] with a required time of ~ 45 min. Therefore, the complete thermal cycling for the core under study for 100 iterations takes about five days.

6.7.2 Performance after thermal cycling

The performed thermal cycling of core 08 with 100 temperature cycles between -40° C and $+40^{\circ}$ C is shown in Figure 6.71 with the average temperature in the climate chamber.

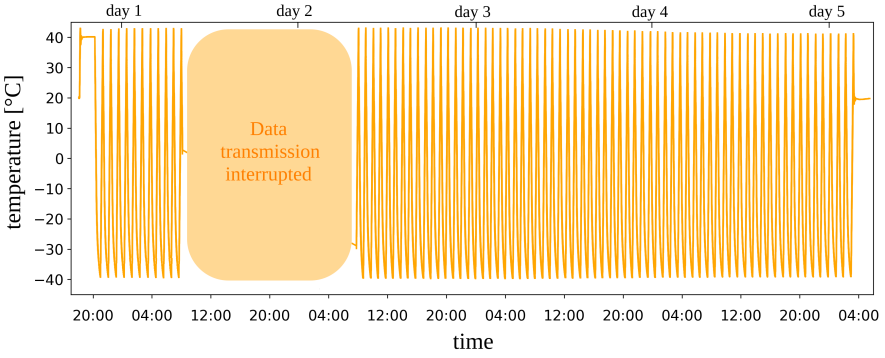

Figure 6.71: Average temperature in the climate chamber for 100 temperature cycles between -40° C to $+40^{\circ}$ C of core 08.

As a first check, a *visual inspection* of the core surface, e.g. to find regions of delaminations, showed no differences compared to the state before thermal cycling. Secondly, the *electrical performance* of the core's bus tape was compared before and after thermal cycling[43]. Here, an automated test setup for measuring the resistances along the copper traces, the so-called bus tape robot, is used, which is developed for the regular QA and QC tests of the bus tape. The preliminary results of the electrical tests showed no indication for a degradation. Moreover, the performance is evaluated for *geometrical metrology* and *thermal performance* tests, for which the results are discussed in the following.

Geometrical metrology results

The developed QC measurements in terms of the geometrical metrology were conducted before and after thermal cycling to allow for a performance comparison. The results for the accuracy on the petal locators in terms of hole diameters and geometrical distances are summarized in Table 6.4 for the measurement of the front side of core 08.

[42] The tolerance for the set point temperature of -40° C is specified with $\pm 0.5\,^{\circ}$C.
[43] The measurements were performed by colleagues at the Jožef Stefan Institute, Ljubljana/Slovenia.

Firstly, it can be observed that the specifications on the PLs are mostly fulfilled for core 08. The two exceptions are the oversized PL locator hole at the top closeout and both PL slots, but these deviations will be resolved by the use of new tools in the assembly. Secondly, the comparison of the results before and after thermal cycling shows variations in the order of $\mathcal{O}(\pm 10\,\mu\text{m})$, which is inside the measurement uncertainty and can be neglected.

Diameters [mm]		nominal	tolerance	measurement *before TC*	measurement *after TC*
petal locator hole	bottom	4.000	±0.012	4.008	4.005
	top	5.000	±0.050	4.886	4.884
petal locator slot	bottom	4.000	+0.012	3.977	3.986
	top	4.000	+0.012	3.933	3.897
fiducial hole	bottom	0.300	-/-	0.304	0.306
	top	0.300	-/-	0.303	0.306
Distances [mm]					
bottom PL→ top PL	x	592.618	±0.025	592.627	592.610
	y	127.916	±0.025	127.923	127.925
bottom PL→ top fiducial	x	589.526	±0.025	589.532	589.516
	y	131.104	±0.025	131.097	131.103
bottom fiducial→ top fiducial	x	586.526	±0.025	586.547	586.528

Table 6.4: Metrology measurements of the PL accuracy before and after thermal cycling for the front side of core 08. Shown are the diameters and distances for the PLs and fiducials with their nominal values and specified tolerance as well as the measurement before and after thermal cycling.

Moreover, the distances of the fiducial pads on the bus tape are measured and evaluated by the shifts relative to the nominal values from the Gerber design file. Figure 6.72 shows the results for the front and back side comparing shifts before and after thermal cycling using the fiducials on the left and right edge of the bus tape. Here, fluctuations in the determined nominal shifts of $-20\,\mu\text{m}$ to $10\,\mu\text{m}$ and $\pm 20\,\mu\text{m}$ are observed for the individual fiducial pad distances on the front and back side, respectively. But for the comparison of the shifts before and after thermal cycling, only marginal differences are observed.

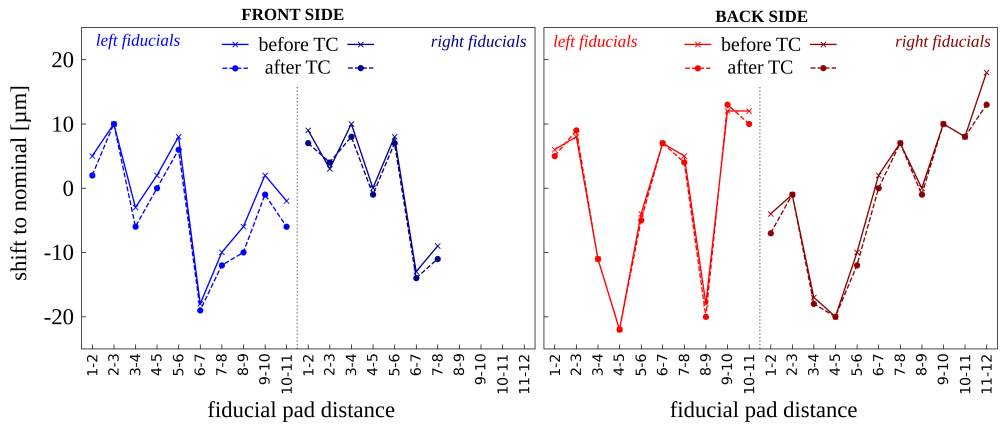

Figure 6.72: Shifts in the nominal distance of fiducial pads before and after thermal cycling for the front and back side of core 08.

Therefore, no degradation of the mechanical performance of the core after thermal cycling can be observed in the performed tests of geometrical metrology.

Thermal performance results

The thermal performance of the core before and after thermal cycling is compared using the developed thermal QC setup with IR thermography and CO_2 cooling. Here, thermograms for both sides of the core are recorded at different temperature set points and analysed. Figure 6.73a shows the performance comparison before and after thermal cycling for the front side with the temperature distribution along the cooling loop as well as the recorded thermograms for the lowest CO_2 pressure set point. The corresponding comparison for the back side of the core is shown in Figure 6.73b with the temperature distribution in the module areas as well as the recorded thermograms at the lowest set point.

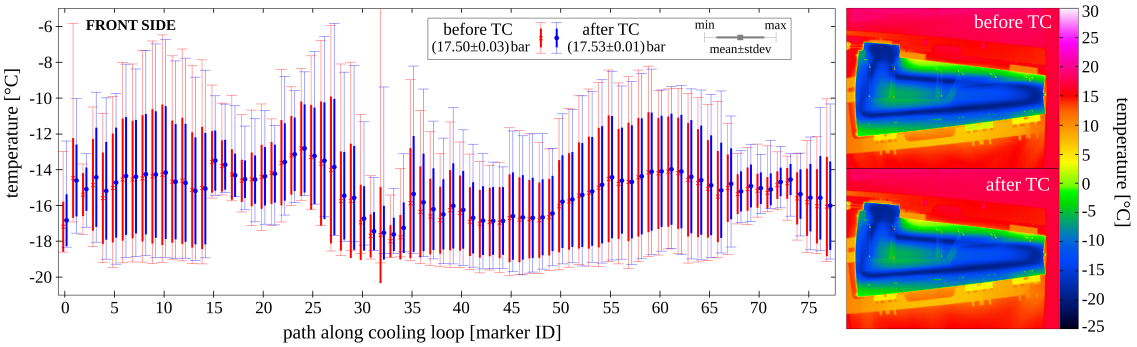

(a) Thermal performance comparison along the cooling loop for the front side of the core.

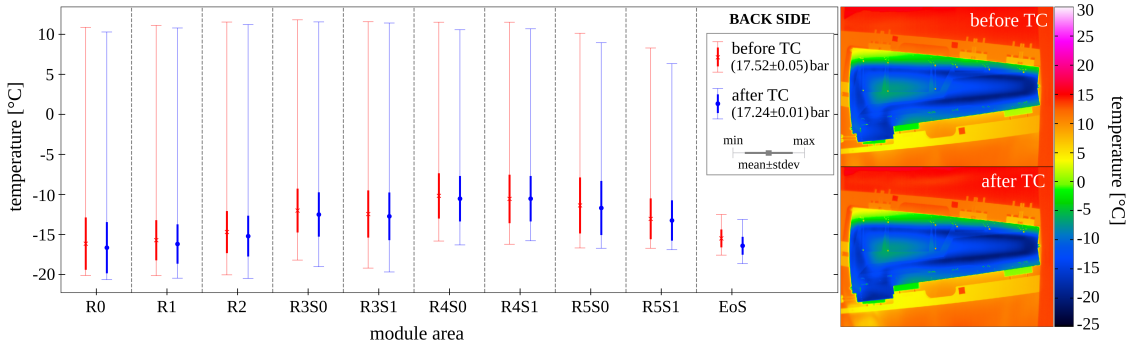

(b) Thermal performance comparison in the module areas for the back side of the core.

Figure 6.73: Comparison of the thermal performance before and after thermal cycling of the core. Shown are the temperature distributions along the cooling loop and in the module areas as well as the recorded thermograms for the front and back side of the core at the lowest CO_2 pressure set point.

For the front side, only minor differences for the measured temperatures along the cooling loop before and after thermal cycling can be found. As the conditions for both measurements can vary, e.g. sligthly different CO_2 pressure and mass flow values or a different ambient temperature, these differences are expected and do not indicate any degradation of the thermal performance after thermal cycling of the core. Also for the back side, the temperature distributions in the module areas show a good agreement for the measurement before and after thermal cycling. Minor differences are expected, as the thermograms were recorded for slightly different pressure set points in the comparison.

As conclusion, the performed thermal QC measurements do not show any degradation of the thermal performance of the core after thermal cycling.

6.7.3 Thermal shock test on petal cores

For the thermal shock test, the core under study is placed in an insulated box filled with dry ice pellets. In this setup, the core can be cooled down to extreme low temperatures up to the dry ice temperature of −78.5 °C to test the structure's integrity. The core is enclosed in a plastic bag to protect its surface from freezer burns and the temperature in the box is logged by two external temperature sensors[44]. Figure 6.74 shows impressions from the thermal shock test of the core with the different stages of the experiment.

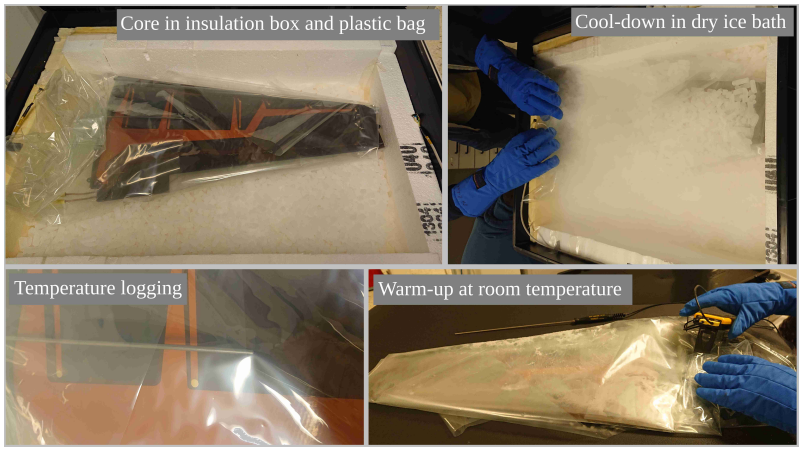

Figure 6.74: Impressions from the thermal shock test with core 08. Shown are the setup with an insulated box filled with dry ice pellets for cool-down and the warm-up phase at room temperature. The core's surface is protected by a plastic bag to avoid freezer burns.

For the thermal shock test, the core is placed in the box, the temperature probes are inserted and the box is sealed. After a waiting time of ten minutes, a thermal equilibrium state between the core and the dry ice bath is reached, which is indicated by the temperature values of the sensor close to the core compared to the measured temperature of the dry ice. Here, the core is cooled for further ten minutes at the coldest temperature of approximately −77 °C, retrieved from the box afterwards and warmed up at room temperature.
The logged temperatures for the thermal shock test of core 08 are plotted in Figure 6.75 together with annotations of the measurement procedure.

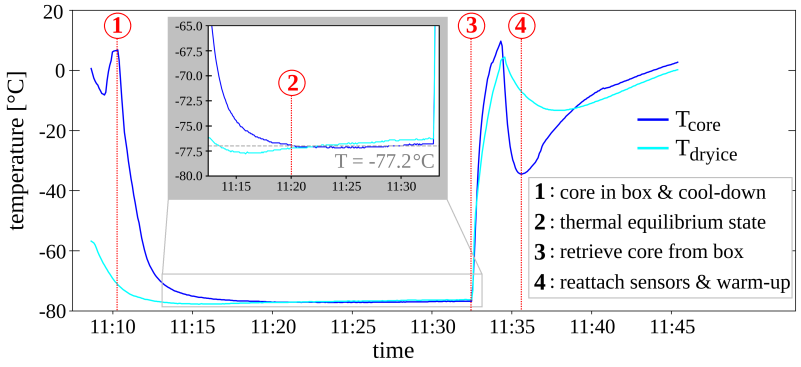

Figure 6.75: Logged temperature values during the thermal shock test with core 08. Additional annotations describe the test procedure of cool-down and warm-up phase.

After the thermal shock test, the core is visually inspected to detect any damage caused by the extreme temperature conditions. No delaminations in the cocured bus tape surface or broken glue joints in the structure are observed. Moreover, the thermal performance was evaluated again with the IR thermography setup for the front and back side of the core. Here, comparing the results between before and after thermal shock, no degradation in the thermal performance of the core is detected.

[44] *Greisinger GTF 1200* [186]: Immersion temperature probe with sheathed thermocouple of type K allowing to measure between −200 and +1 150 °C and read out with handheld data logger.

Therefore, the integrity of the core structure was proven for the low temperature case of $-77\,^{\circ}\mathrm{C}$, which is lower than the specified temperature of $-56\,^{\circ}\mathrm{C}$ in case of failures in the CO_2 cooling system. With no detected degradation in terms of mechanical and thermal performance, the resistance of the core design is validated for the low temperature case.

6.7.4 Thermal shock test on the TM petal

The thermal shock test is also conducted on the TM petal using the same setup with dry ice as for the core testing. But to protect the silicon dummy modules, especially the wire bonds, from mechanical damage, the TM petal is placed in an aluminium frame surrounded by dry ice pellets and the convective cooling effect of the cold air is used. An asymptotic behaviour of the temperature of the TM petal to the logged dry ice temperature is observed, reaching after approximately 45 minutes the lowest temperature with $-71.6\,^{\circ}\mathrm{C}$. Afterwards, the TM petal is retrieved from the box for the warm-up phase at room temperature.
The setup of the thermal shock test with the TM petal as well as the logged temperatures are shown in Figure 6.76.

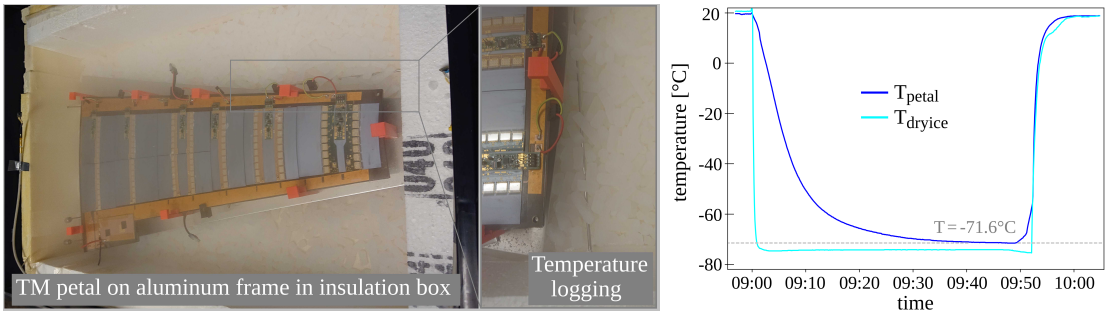

Figure 6.76: Impressions from the thermal shock test with the TM petal.
Shown is the TM petal in the insulated box placed on an aluminium frame in the dry ice bath before closing with an aluminium plate and a dry ice layer from the top (left). Moreover, the logged temperatures are plotted as function of time, showing the effect of convective air cooling with an asymptotic behaviour for the petal temperature (right).

By visual inspection, the TM petal after thermal shock is entirely intact and undamaged, like all glue joints between the core surface and the silicon dummy modules appear to be fully functional. Some impressions of the TM petal after thermal shock by visual inspection of the modules and IR thermograms of the cooled object are shown in Figure 6.77.

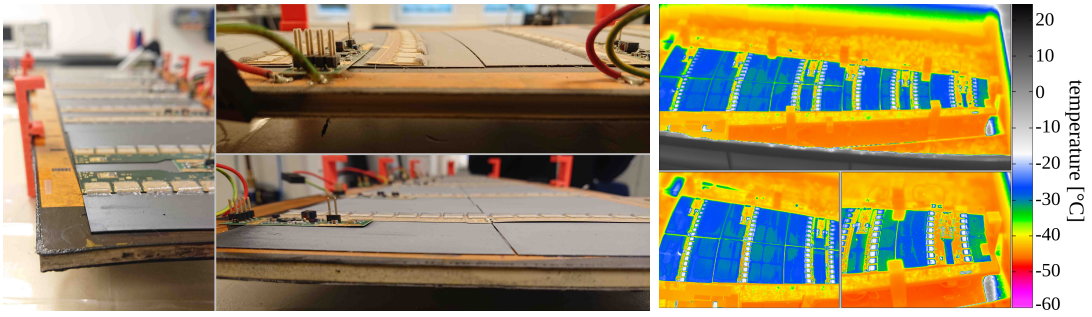

Figure 6.77: Visual and IR inspection of the TM petal after thermal shock test.

In general, the thermal shock test of the TM petal was successful, as no mechanical failure in the interfaces of the local support structure and the silicon sensor modules were detected.

6.8 Conclusion

The petal is the central component for the planned ATLAS ITk strip end-cap detector and will consist of the petal core as the local support structure and the glued on silicon sensor modules. For the success of the detector development and its production, the key is to thoroughly validate the detector design in the R&D phase and to achieve a high reliability of the components in the production phase. This will be established by an intensive test programme in terms of QA and QC test procedures.
In this chapter, the performed tests and acquired results for the mechanical, thermal and thermo-mechanical characterization of the petal core design as well as a first prototype of a fully populated petal with the so-called *thermo-mechanical petal* were presented.

With the defined specifications for the local support design in terms of its mechanical, thermal and thermo-mechanical properties, dedicated test setups were developed to test the key quantities such as the mechanical accuracy in terms of dimensions of the petal core or the thermal performance of the structure with the ability to cool the glued on silicon modules. For these test procedures, a wide range of measurement techniques together with the required tools and equipment is employed:

- geometrical metrology measurements are performed with an optical microscope, the SmartScope, to measure the dimensions of the petal geometry or to check the surface flatness to fulfill the specifications for the module-on-core loading procedure;
- infrared thermography with a high-resolution IR camera is used to measure the spatially-resolved temperature distribution on the petal surface for different cooling scenarios, which allows to measure the temperature in a non-destructive way;
- the application of evaporative CO_2 cooling to test the local support structure with the real coolant fluid in the later ITk detector and to understand the CO_2 properties inside the petal as the evaporator for the dual-phase cooling system;
- the control and monitoring of the ambient conditions in terms of air temperature and relative humidity for the different developed test setups, which allows to analyse the influence of these parameters on the measurements;
- but also simulation tools to predict the thermal behaviour of the petal by FEA simulation or to analyse the expected properties of the CO_2 fluid for different operation scenarios using CoBra simulations.

The such developed test setups allow to test and verify the different design iterations of the petal core and to find the best suited final design for the local support structure in the end-cap detector. Moreover, the developed procedures will be used for the QA and QC testing of the assembled components during the production of the petals, with a total number of 384 required petals assembled in the collaboration for both ITk end-caps.

In the course of this thesis, the so far assembled petal core prototypes in the R&D phase at DESY, featuring different design stages with several optimizations of the design influenced and guided by the test results, were tested thoroughly in terms of their mechanical, thermal and thermo-mechanical properties. Furthermore, the TM petal, as a test object with a petal core fully loaded with dummy modules consisting of real silicon crystals and dummy electronic boards with the option to actively power these components, allows to even characterize the petal design with the emulated heat load as it is expected for the final ITk detector over its full lifetime and for the operation in the challenging HL-LHC conditions.

The acquired and evaluated results for the tested core prototypes as well as the TM petal were used as a valuable input to successfully pass several ATLAS review processes for the local support structures of the ITk strip detector, such as the Preliminary Design Review in October 2018 [187, 188] and the Final Design Review in February 2020 [189].

For the IR thermography, the emissivity of the object's surface is the key parameter to measure the object's temperature with the IR camera correctly. Here, the various dependencies of the emissivity were studied in the context of the thermal performance assessment of petal cores and the TM petal.
The emissivity is dominantly influenced by the material type as well as the surface structure and geometry of the test object. On the one hand, the different surfaces of the core prototypes with commercial and cocured CF facesheets as well as the cocured bus tapes were tested in terms of their emissivity values, showing rather high emissivities.
On the other hand, the emissivity of the blank silicon crystals on the TM petal poses a challenge for IR thermography due to the observed rather low emissivity values.
In dedicated test measurements, it was also shown that the used silicon pieces for the dummy modules have a non-negligible transmissivity. For some further possible variations of the emissivity like the viewing angle or the transmission through air, it was shown that these dependencies are negligible for the developed thermal QC setup.
To correct for a low object's emissivity, e.g. the silicon crystals, the most common correction methods with the tape, paint and thermocouple method were discussed and were also applied for the conducted thermal testing of cores and the TM petal. As such, the temperature distribution on the TM petal is extracted after applying a black paint spray to the surface, for which the emissivity was determined in an auxiliary measurement to be 0.977 ± 0.004. This correction method can be easily applied to a prototype object like the TM petal, but for a regular QC test of fully loaded petals with silicon sensor modules, a non-destructive testing method have to be used. Therefore, a detailed study of the emissivity of silicon modules should be conducted using the introduced techniques of the emissivity measurement and correction, such as it was used for the determination of the black paint's emissivity with the developed Peltier test setup. This is also the reason, why for the thermal performance tests of petal cores, no emissivity correction, e.g. for the detected variation of the emissivity with the surface structure of the copper lines, is applied, as this measurement will be part of the regular QC procedures for petal cores during production. Instead, the idea here is to compare petal cores with the same design, such that these specialities in terms of emissivity variations consistent with the object's structure, e.g. in the bus tape, can be easily subtracted using a "golden image" approach.

The thermal performance of petal core prototypes and the TM petal were thoroughly studied using a newly developed test setup for the thermal QC procedure. The setup consists of the light-tight and thermally isolated PTM chamber, the IR camera for measuring the surface temperature on the inserted petal under test, the TRACI cooling system for evaporative CO_2 cooling of the connected cooling loop inside the petal under test as well as additional diagnostics and monitoring systems for the CO_2 properties and the ambient conditions like air temperature and relative humidity inside the PTM.
On the one hand, several petal core prototypes with the different surfaces were tested: core 02 with a commercial CF facesheet, core 04 with a cocured CF facesheet and the cores 07 and 08 with cocured bus tapes. Here, the temperature distributions along the cooling loop, clearly visible in the IR thermograms due to the good thermal conductivity of the carbon foam surrounding the titanium cooling pipe, were evaluated. For the cores with bus tapes, the temperature distributions on the foreseen module areas were also investigated.

The thermal performance for the different tested CO_2 pressure set points show overall very consistent results for all core prototypes. But with the thermal QC measurements, also two defects in the assembled core structures could be detected: for core 04, a delamination of the thermal interface for a section of the cooling loop was observed due to a higher temperature distribution for these IR markers; for core 08, a known delamination in the EoS region for the facesheet-to-foam interface was found as well. These examples show the ability to detect failures introduced during the assembly of the core by the thermal QC procedure: a defect, e.g. by a delamination in the thermal interface, can be detected by a degradation of the measurable thermal performance of the local support structure.
But in the performed test, also the influence of slightly different measurement conditions in terms of the cooling performance of the TRACI system or the ambient conditions in the PTM on the measured temperature distribution for the petal cores was clearly observed. For the final QC procedure during production, the test routine should therefore be further refined to allow direct comparisons between the different tested petal core objects in the thermal analysis under well controlled measurement conditions.
On the other hand, the thermal performance of the TM petal was investigated for various operation conditions. Here, the temperature distributions on the silicon areas, corrected with the determined emissivity value of the used black paint spray, were evaluated for the different tested CO_2 pressure set points.
One observation in the thermal measurement using the nominal conditions in terms of the design CO_2 mass flow of 1.3 g/s was that the temperature on the silicon area of the R5S1 sensor is considerably higher than the other silicon sensor areas. To avoid this imbalance of the resulting surface temperature for the silicon sensors, the routing of the cooling pipe in this part of the core was changed for the next design iteration.
Moreover, the difference between the unpowered and powered state of the TM petal was studied, showing the expected increase of the silicon surface temperature for the full heat load of 54 W. But at the same time, a thermally stable state of the powered TM petal was reached after a waiting time of around six hours, proving that the cooling concept of the petal design works as a stable system state is reached again.
In a further comparison of the thermal performance of the TM petal for two different CO_2 mass flows with 1.3 and 2.5 g/s, only marginal differences in the resulting temperature distributions on the silicon sensor areas were observed, indicating that the nominal CO_2 mass flow is sufficient for the dual-phase cooling of the petal with the full heat load.
Further investigations on different powering scenarios, exploiting the possibility to switch on individual modules, allowed to analyse the thermal behaviour of the TM petal in even more detail. Here, the influence of the powered module on its neighbours or the influence from the other side of the petal on the resulting temperature distribution could be observed, but again no problem in the cooling strategy was detected.
Finally, the experimental results acquired with the TM petal were used to compare the measured temperature distribution on the petal surface with the simulated result from thermal FEA simulations. Here, a very good agreement between the experimental and simulated data within the measurement uncertainties as well as the model assumptions was reached, allowing to validate the FEA model of the petal. Therefore, it was possible to further optimize the petal design using FEA simulations which resulted now in the nearly final design of the local support structure.

The petal core design was also studied in terms of its thermo-mechanical properties by investigating the thermal deformations, so the mechanical deformations caused by the expected temperature changes over the operation. For the measurement, a setup with the SmartScope to measure the deformation on the surface of the petal core 05 was used.

On the one hand, the core was heated up by using distilled water allowing to test temperature differences up to $\Delta T = +60\,\mathrm{K}$ relative to the room temperature. On the other hand, evaporative CO_2 with the TRACI system was used to reach temperature differences down to $\Delta T = -40\,\mathrm{K}$. With this test, it was possible to show that the magnitude of the deformation Δz of the surface caused by the temperature difference ΔT depends only on the absolute temperature difference. The relative sign of ΔT determines in this case only the direction of the deformation. Overall, the performed study showed thermal deformations on the surface of the tested petal in the order of $\mathcal{O}(\pm 100\,\mu\mathrm{m})$ for the measured temperature differences between $\Delta T = -40\,\mathrm{K}$ for the cold test and $\Delta T = +60\,\mathrm{K}$ for the warm test. This result indicates a mechanically stable petal core structure appropriate for the use as the local support structure for the silicon sensor modules in the ITk strip end-cap detector.
The thermal deformation results were also evaluated in terms of the specified local flatness requirement of the core. Here, the local flatness over the individual module areas was calculated for the different tested temperature differences. A moderate and consistent change of the local flatness values for the different temperature differences were observed, indicating that the specification value on the local flatness requirement over operational temperature gradients will be fulfilled for the tested petal core design.
Moreover, it was possible to study the expansion or contraction of the petal core by evaluating the x- and y-positions of the fiducial pads on the bus tape for the different temperature differences. For the x-direction, a negligible expansion effect for the positive ΔT values was found, whereas for negative ΔT the contraction is much more pronounced. A conclusive interpretation for this observation was not found so far.
For the measured shifts in the y-direction, a consistent trend to contract for negative ΔT and to expand for positive ΔT was observed. Therefore, it was possible to estimate the linear CTE in the y-direction to be around $\sim 0.31\,\mu\mathrm{m/K}$. In general, the measured shifts over the operational temperature gradients are in the order of $\mathcal{O}(25\,\mu\mathrm{m})$, which allows to correct the translated shifts of the silicon sensor modules by track-based alignment procedures in the ITk detector.

For the test of the thermo-mechanical behaviour of the petal core design for more extreme temperature scenarios, two further studies were conducted with petal core prototype 08. Firstly, the petal core was thermally cycled between $-40\,^{\circ}\mathrm{C}$ and $+40\,^{\circ}\mathrm{C}$ for 100 iterations, as it is typically expected for the normal detector operation over the full life cycle.
Here, the thermal cycling was performed with a climate chamber and the mechanical and thermal performance of the core was evaluated before and after thermal cycling. The performed tests of visual inspection, electrical testing of the bus tape, the geometrical metrology measurements as well as the evaluated thermal performance showed no indication for a degradation of the specified properties of the petal core after thermal cycling.
Secondly, the petal core was exposed to extreme cold temperatures by performing a thermal shock test using dry ice with a temperature down to $-78.5\,^{\circ}\mathrm{C}$. The mechanical and thermal performance of the core, measured again before and after the thermal shock test, showed no degradation, indicating the resistance of the petal core design for extreme low temperatures. At the same time, the thermal shock test was conducted with the TM petal populated with the dummy silicon modules. Also here, no defect such as a broken glue interface to a module could be detected.

Therefore, the thermo-mechanical studies conducted on several petal core prototypes as well as the TM petal showed a valid and appropriate design of the local support structure. It was proven by dedicated measurements that most of the defined specifications in terms of the mechanical, thermal and thermo-mechanical properties of the petal design are fulfilled.

Chapter 7

Investigations on Dual-Phase CO_2 Cooling

For a successful operation of the ATLAS ITk detector, the cooling of the silicon sensors and their readout and power electronics is a critical factor, especially due to the harsh running conditions for the HL-LHC. Evaporative CO_2 cooling is the selected choice for the ITk detector, but for CO_2 as a dual-phase coolant, the properties and their dependencies need to be studied in detail to allow for a good system operation. Therefore, a sophisticated system design for the dual-phase cooling is developed to fulfill the cooling specifications defined by the individual sub-detectors in the ITk.

The planned system design for the ITk detector and its requirements for the cooling system in terms of the CO_2 coolant temperature, the total pressure drop over the cooling loops as well as other parameters like the nominal mass flow rate through the individual cooling loops or the maximal vapour quality inside the loop are explained briefly in Section 7.1.

Apart from the overall system design, the individual local support structures of the ITk detector, e.g. the petal core for the strip end-cap detector, have to be tested and qualified for the CO_2 cooling to achieve the foreseen performance. Therefore, dedicated tests were conducted in the course of this work to study and analyse the various CO_2 coolant properties in the application of cooling the petal.

The petals will be arranged in the global structure of the end-cap in different orientations around ϕ, resulting in different CO_2 flow orientations. A possible influence of the flow orientation on the thermal performance of the petal is investigated in Section 7.2, using a petal core prototype as well as the TM petal.

The pressure drop over the petal's cooling loop is an important parameter, as it defines the CO_2 coolant temperature inside the local support structure and has influence on the overall cooling system. Section 7.3 shows measurements of the pressure drop for different petal core prototypes and the TM petal and the influence of the applied heat load, the mass flow and the flow orientation is investigated. The experimental results on the pressure and temperature drop for the petal are also compared to dedicated CoBra simulations of the CO_2 properties corresponding to the measurement conditions.

In Section 7.4, the CO_2 state in the petal's cooling loop is analysed in detail. On the one hand, the different state points along the operation cycle of the TRACI CO_2 cooling system following the I-2PACL concept can be analysed.

On the other hand, the results obtained from the visual inspection of the sightglasses at the in- and outlet of the petal's cooling loop are used to estimate the vapour quality of the dual-phase CO_2. Therefore, it is possible to analyse the CO_2 state inside the cooling loop and compare the estimation with theoretical calculations based on the measured CO_2 pressure and the applied heat load. Here, also CoBra simulations are performed for the analysis of the CO_2 state and the vapour quality.

Finally, a conclusion and outlook on the investigation of the dual-phase CO_2 cooling for the petal are given in Section 7.5.

7.1 CO_2 Cooling System for the ITk Detector

The CO_2 cooling system for the ATLAS ITk detector will provide a total cooling power of 245 kW distributed over 1142 individual cooling lines in the sub-detectors. For the strip end-cap part, cooling is provided for 384 cooling loops corresponding to the total number of petals and the expected heat load is nearly 39 kW.

In the following, the planned design of the dual-phase CO_2 cooling system for the ITk detector is shown in Section 7.1.1, with the focus on the needs for the ITk strip end-cap detector. Moreover, the system specifications for the CO_2 cooling of the detector are discussed in Section 7.1.2.

7.1.1 Design of the CO_2 cooling system

The overall system design planned for the dual-phase cooling infrastructure of the ATLAS ITk detector is depicted in Figure 7.1.

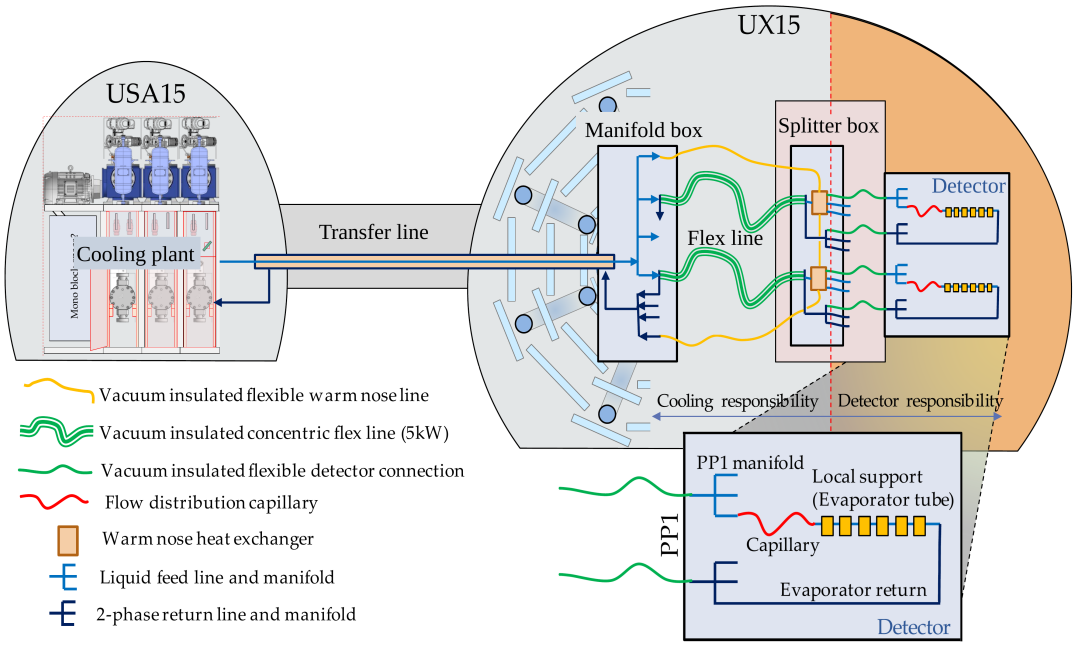

Figure 7.1: Design of the planned CO_2 cooling system for the ATLAS ITk detector. Liquid CO_2 is pumped from the cooling plant via the transfer and flex lines to the detector's cooling loop to provide dual-phase cooling in the local support structures. Modified from [190].

Starting at the central *cooling plants* located in the underground service hall USA15, CO_2 is subcooled to temperatures close to its freezing point of $-56\,^{\circ}C$. From here, the liquid CO_2 is pumped through long *transfer lines* to the on-detector distribution at the *manifold boxes* in the detector cavern UX15. Moreover, the concentric setup of the transfer lines causes a heat exchange with the warmer dual-phase CO_2 from the return line.
The distribution from the manifold boxes to the splitter boxes in the sub-detector systems is done by vacuum insulated, concentric *flex lines* specified for an individual cooling power of 5 kW. For the strip end-cap, one cooling line from the splitter box is dedicated to cool one half disk corresponding to 16 petals and each petal cooling loop is connected via a *capillary*. Due to the heat load of the petal, the local support serves as an evaporator for the dual-phase CO_2 which is guided back to the cooling plant via the return pipes in the flex and transfer lines.

The CO_2 state and its temperature, influenced by the individual parts in the cooling circuit, is shown in Figure 7.2 along the complete cooling line.

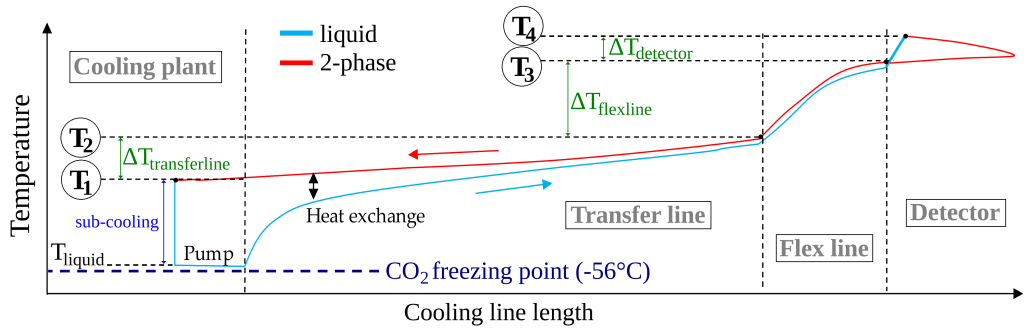

Figure 7.2: State and temperature of CO_2 for the complete cooling circuit. Shown are the individual stages for the pumped liquid CO_2 from the *cooling plant* via the concentric *transfer* and *flex lines* to the *detector* with its cooling loop as evaporator and the return flow of dual-phase CO_2. The CO_2 temperature after the transfer line (T_1), after the flex line (T_2) and at the outlet (T_3) and inlet (T_4) of the detector's cooling loop is influenced by the temperature drops ΔT along these lines. Modified from [190].

The CO_2 coolant temperature in the detector is controlled by the saturation pressure of the dual-phase CO_2 of the return flow at the cooling plant. Here, each cooling line along the CO_2 flow direction causes a pressure drop Δp on the CO_2 influenced by the cooling line parameters, e.g. the diameter or the surface roughness.
A pressure drop is translated to a corresponding temperature drop ΔT, whereas the dependency is not linear but the temperature loss increases for lower CO_2 pressures meaning lower cooling temperatures. Therefore, the complete cooling circuit can be analysed according to the budget of temperature gradients resulting in the actual CO_2 temperatures for the different stages.

For the minimum operation temperature of the system, determined by the temperature of the subcooled and liquid CO_2 at the pump of the cooling plant, which is close to the CO_2 freezing point, the situation is as following:

- the temperature of the returning dual-phase CO_2 at the cooling plant is $T_1 = -45\,^{\circ}C$;
- the temperature at the inlet of the transfer line is $T_2 = -43\,^{\circ}C$ caused by the temperature drop over the transfer line ($\Delta T_{transferline}$);

- the temperature at the inlet to the flex line and correspondingly at the outlet of the detector's cooling loop is $T_3 = -38\,^{\circ}C$[45] caused by the temperature drop over the flex line ($\Delta T_{flexline}$);
- the temperature at the inlet of the detector depends on the temperature drop over its cooling loop ($\Delta T_{detector}$) and has a target temperature of $T_4 = -35\,^{\circ}C$.

7.1.2 Specifications of the CO_2 cooling system

The specifications for the CO_2 cooling system for the ITk strip detector are defined relative to the detector's cooling loop as evaporator in the following way:

- The *evaporation temperature* at the detector's outlet is between $-38\,^{\circ}C$ and $15\,^{\circ}C$.
- The *mass flow* per evaporator is adjusted to the design rule of 1 g/s per 100 W.
- The *vapour quality* at the start of the evaporator is $0 < x < 0.03$ and the maximum value at the evaporator outlet is $x = 0.35$.
- The design *pressure drop* over the on-detector cooling lines is $\Delta p = 10\,bar$.
- The pressure drop in the capillary is adjusted to $8\,bar < \Delta p_{cap} < 10\,bar$.
- The pressure drop in the evaporator and its return line is $\Delta p_{evap} < 1.2\,bar$ corresponding to a temperature drop of $\Delta T_{evap} < 3\,^{\circ}C$.

The CO_2 cooling system will deliver the outlet pressure at the detector's cooling loop defining the CO_2 saturation temperature between $-38\,^{\circ}C$ and $15\,^{\circ}C$ as well as as the overall pressure difference of 10 bar over the on-detector cooling lines.
But the CO_2 temperature at the inlet of the detector's cooling loop as well as the mass flow through it will depend on the pressure drop of the local support design and is therefore a critical parameter, which is experimentally tested in Section 7.3 for the case of the petal.

Further details about the CO_2 cooling system for the ATLAS ITk detector and its specifications can be found in [190, 191].

7.2 Influence of the CO_2 Flow Orientation

In the first study, a possible influence of the petal orientation on its thermal performance caused by the horizontal and vertical flow is investigated.
In the end-cap structure, the petals are arranged in the disk for different angles in ϕ and therefore also the flow orientation of the CO_2 is different for each petal. Here, only the most extreme orientations are compared: the *vertical +90°* orientation (meaning the pipe connections at the bottom), the *vertical -90°* orientation (meaning the pipe connections at the top) and the *horizontal* orientation (meaning the standard test configuration).

For this test, the PTM in the thermal test setup is rotated to the different orientations, as exemplary shown in Figure 7.3 for the vertical $+90^{\circ}$ orientation. The relative position of the IR camera to the petal under test remains unchanged. The CO_2 coolant changes its flow orientation inside the petal's cooling loop to investigate the influence of gravity on the dual-phase flow.

[45] This is the case for the strip detector system. For the pixel detector, the temperature after the detector's cooling loop will be $-40\,^{\circ}C$ allowing for a larger temperature drop over the local support structure.



Figure 7.3: Test setup for the thermal performance of petals in different orientations. Shown is the petal core 02 mounted in the rotated PTM for the *vertical +90°* orientation and the otherwise unchanged equipment for the thermal testing of petals using IR thermography.

7.2.1 Orientation study with petal cores

The orientation study for petal core prototypes is performed with core 02 using a CO_2 mass flow of 2.5 g/s and assessing the thermal performance for its front side using the thermal QC setup with IR thermography.
The comparison of the temperature distributions along the cooling loop for the horizontal and the vertical +90° orientation is shown in Figure 7.4 for the lowest reached CO_2 pressure set point of 18.6 and 18.5 bar, respectively.

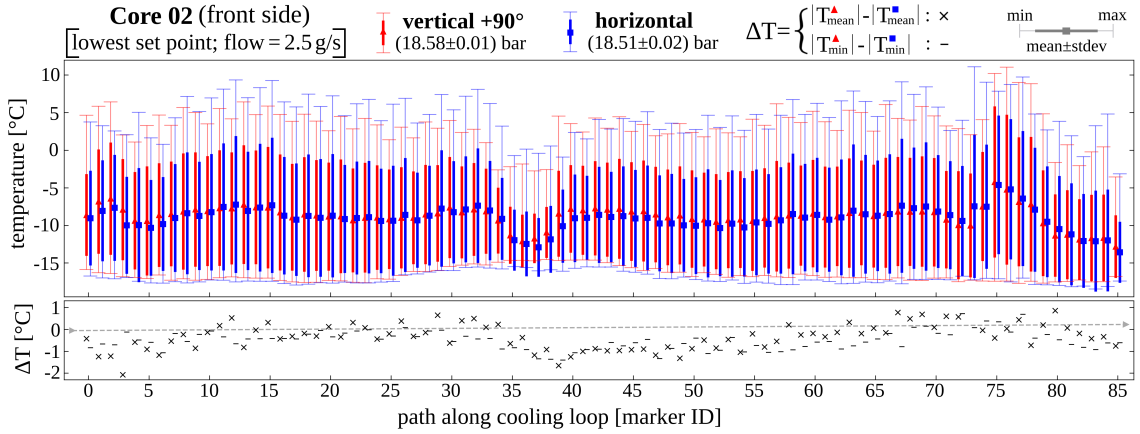

Figure 7.4: Comparison of the temperature distributions along the cooling loop for the *horizontal* and *vertical +90°* orientation of core 02, evaluated for its front side, with a mass flow of 2.5 g/s and at the lowest CO_2 pressure set points of 18.5 bar and 18.6 bar, respectively. The temperature differences ΔT based on the mean and minimum are calculated between both orientations.

Here, overall a good agreement between both measurements is observed showing the same pattern for the temperature distributions along the cooling loop. The maximal temperature difference, calculated based on the mean and the minimum temperature, is between +1 °C and −2 °C and well within the normal measurement uncertainty.
Therefore, no indications for different CO_2 coolant properties caused by the two tested CO_2 flow orientations in the core's cooling loop are observed, when testing core 02.

7.2.2 Orientation study with the TM petal

The TM petal in the unpowered and powered state is tested for all three selected orientations (*horizontal*, *vertical +90°* and *vertical -90°*) using a CO_2 mass of 2.5 g/s.
For a qualitative comparison, the recorded IR thermograms of the TM petal for the three orientations in the powered state are shown in Figure 7.5 and the corresponding thermograms for the unpowered state are shown in Appendix B.1.

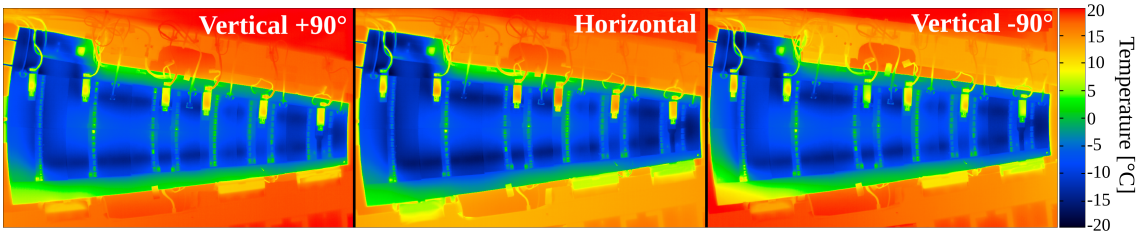

Figure 7.5: Thermograms of the TM petal in the powered state for the *horizontal*, *vertical +90°* and *vertical -90°* orientation and evaluated at the individually reached lowest CO_2 pressure set point.

Here, no significant difference in the temperature distribution for most of the modules are observed for all three tested orientations. The exceptions are the R0 and R5 module, where larger discrepancies, especially for the silicon sensor area R5S1, can be identified.

For the quantitative evaluation, Figure 7.6 shows the comparison of the temperature distributions on the silicon sensor areas at the lowest reached CO_2 pressure set points for the unpowered and powered state of the TM petal. The comparison evaluating the other tested CO_2 pressure set points is shown also in Appendix B.1.

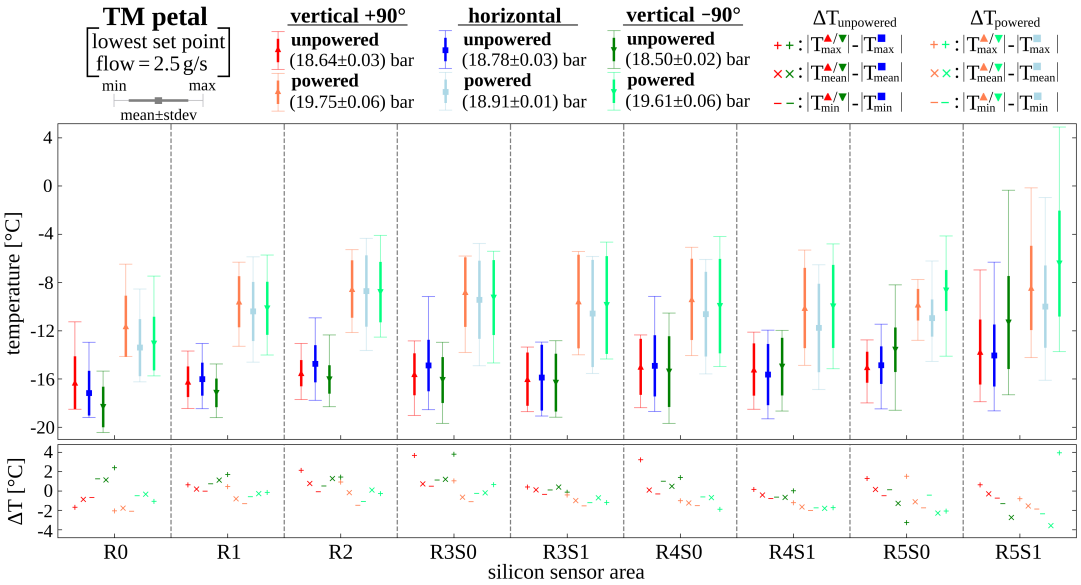

Figure 7.6: Comparison of the temperature distributions on the silicon sensor areas for the *horizontal*, *vertical +90°* and *vertical -90°* orientation of the TM petal, measured with a mass flow of 2.5 g/s at the lowest CO_2 pressure set points and for the unpowered and powered state, respectively. The temperature differences ΔT based on the mean, maximum and minimum temperature are calculated for both vertical orientations relative to the horizontal position.

For the unpowered case, the temperature distributions in the individual silicon sensor areas for the three different orientations show some variations for the mean, minimum and maximum value, but are matching otherwise quite well, when excluding the results for the R0 and R5 module. The variations are caused by the different reached lowest CO_2 pressure set points for the three different measurements. This results in slightly fluctuating coolant temperatures with the lowest temperature expected for the vertical -90° orientation, followed by the vertical +90° orientation and the relative highest set point for the horizontal orientation. For the measured silicon temperature of the R0 module, a clear ordering for the three orientations is observed: the vertical +90° orientation with the R0 module on the top shows the highest temperature, followed by the horizontal orientation and the lowest temperature is measured for the vertical -90° orientation with the R0 module at the bottom. Due to the U-turn of the cooling loop located under the R0 sensor, a possible effect in this region could be caused by gravity on the CO_2 fluid: for the bottom location of the U-turn, the CO_2 fluid may be "trapped" in this cooling loop segment by gravity and the relatively more coolant causes a lower temperature on the R0 sensor; vice versa for the top location, with relatively less CO_2 in the U-turn resulting in a higher temperature of the R0 silicon sensor area.
A similar effect could be the reason for the observed ordering in the R5 module, as here also a straight pipe section could be influenced by the possible effect of gravity in the vertical orientations. Due to the lower set point in the measurement with the vertical -90° orientation, lower temperatures are expected for this orientation but observed are consistently higher temperatures in the R5 module compared to the other orientations.

For the powered state, the resulting temperature distributions show overall a comparable or even better agreement between the three tested orientations, but at the same time the relative set point differences are different than before. Here, the previously clearly observed ordering for the silicon temperature of the R0 module is not so distinct anymore in the powered state, but the temperatures in the R5 module show still the biggest discrepancies between the different orientations.
Therefore, a conclusive interpretation of the performed orientation study with the TM petal in the unpowered and powered state is difficult due to the different testing conditions in terms of the CO_2 pressure set point.
A possible effect in the cooling loop's sections with rectangular or U-turns observed for both vertical orientations could be explained by gravitational effects on the flow of the CO_2 fluid, but for a definite interpretation further studies are required.
Apart from the special cases, the flow orientation seems to have no severe effect on the thermal performance of the TM petal, as the temperature differences for the individual cases relative to the normal, horizontal orientation are below $\pm 4\,\mathrm{K}$ for the mean, minimum and maximum temperature values.

The experimental results of the orientation study cannot be compared to CO_2 simulations using CoBra, as the underlying description of flow patterns in the Thome models is based on empirical results in horizontal tubes. Here, additional models for the empirical description of the CO_2 in vertical tubes as well as for arbitrary turns in the tube need to be developed.

Therefore, it is important to test possible gravitational effects on the CO_2 flow due to different orientations experimentally. Similar to the performed tests with the petals, a rotatable test setup for a complete cooling loop of a half disk of the end-cap with dummy heat loads for the 16 petals as evaporators is currently planned in the collaboration to verify the strip end-cap cooling loop design and to test different orientations.

7.3 Investigations on the Pressure Drop

The pressure drop Δp over the petal's cooling loop is an important parameter for the CO_2 cooling system of the detector. Here, from the cooling specifications of the system the CO_2 pressure and its corresponding temperature is defined for the outlet of the cooling loop, but the CO_2 temperature at the inlet as well as the design mass flow depends on the pressure drop in the evaporator.
For the strip detector system, the pressure drop for the cooling loop in the local support structure as well as the evaporator return line to the manifold distribution is specified with $\Delta p_{evap} < 1.2\,\text{bar}$, causing a temperature drop of $\Delta T_{evap} < 3\,^{\circ}\text{C}$.
For the verification of the local support design to match the cooling specifications, the pressure drop Δp and the resulting temperature drop ΔT over the petal's cooling loop is measured for various petal core prototypes and the TM petal under different conditions. Here, the logged data from the measurements of the thermal performance evaluation is reanalysed to calculate Δp and ΔT as

$$\Delta p = p_{petal,inlet} - p_{petal,outlet} \quad \text{and} \quad \Delta T = T_{petal,inlet} - T_{petal,outlet}, \tag{7.1}$$

using the recorded data from the CO_2 diagnostics system with the temperature and pressure sensors close to the in- and outlet of the petal.

7.3.1 Pressure drop analysis for petal cores

The analysis of Δp and ΔT for the measurement cycle of the front side of core 07 is shown in Figure 7.7. Here, different CO_2 pressure set points between 51 and 18.1 bar are tested with a CO_2 mass flow of 1.3 g/s. Moreover, the pressure drop over the complete cooling line between experiment and TRACI is stabilized at 10 bar, similar to the foreseen overall pressure drop for the ITk cooling system.

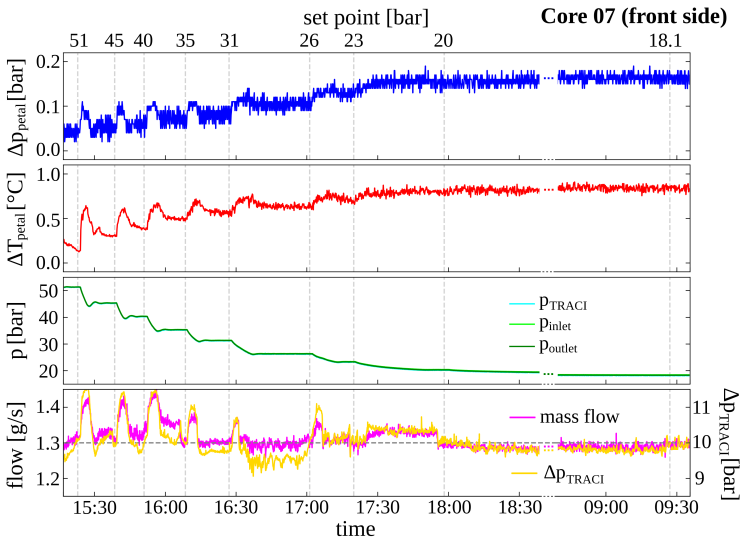

Figure 7.7: Analysis of the pressure and temperature drop for the measurement cycle between CO_2 pressure set points of 51 and 18.1 bar for the front side of core 07. Shown are the calculated values for Δp and ΔT over the core's cooling loop as well as the logged CO_2 pressure, the mass flow and the overall pressure drop for the complete system.

Firstly, it is observed that for lower CO_2 pressure set points, meaning lower coolant temperatures, the pressure drop is increasing from values of approximately 0.05 bar up to 0.17 bar for the lowest reached set point. At the same time, the temperature drop is increasing correspondingly to the pressure drop as expected.
Secondly, when the set point in the TRACI system is changed, larger fluctuations are observed in Δp and ΔT. These fluctuations, also observed for the logged mass flow and the overall pressure drop, are caused by the unstable system state during the change.

In the following, the pressure and temperature drop is therefore evaluated as the average over a short time period around each stabilized set point, marked accordingly in the measurement cycle. A comparison of the pressure and temperature drops measured for different petal core prototypes, namely the cores 04, 07 and 08 with their front and back sides, is shown in Figure 7.8 for the different tested CO_2 pressure set points.
Moreover, the measured mass flow and the overall pressure drop are compared for the evaluated times, showing rather comparable cooling conditions in the different measurements.

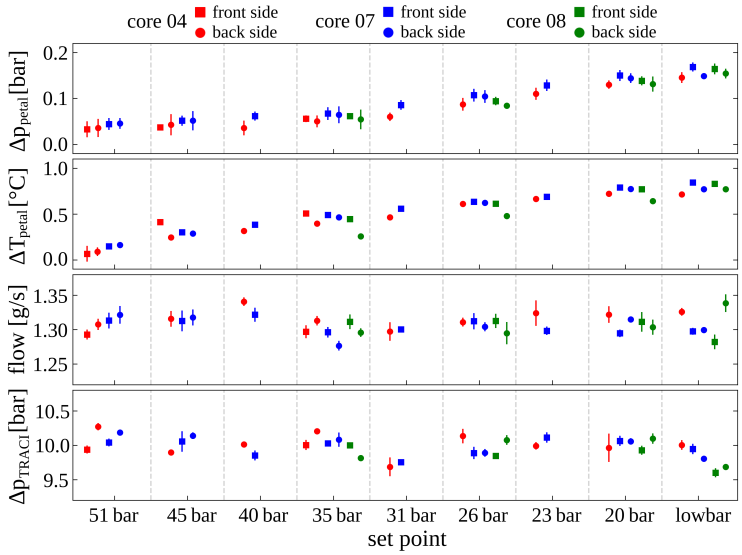

Figure 7.8: Comparison of the measured pressure and temperature drop for various petal core prototypes. Evaluated are the front and back side of the cores 04, 07 and 08 for the different tested CO_2 pressure set points between 51 bar and the individually reached lowest set points. Compared are the values of Δp and ΔT as well as the adjusted mass flow and the overall pressure drop.

Overall, the results for the pressure and temperature drop extracted from the six measurements of the three core prototypes are very consistent. When comparing the results for the two sides of the individual cores, only small variations at the different tested set points are observed, which can be explained by the slightly varying cooling conditions. This is expected, as the investigated side of the core should not influence the behaviour of the CO_2 fluid inside the cooling loop. The cores 07 and 08 are from the same design stage, whereas core 04 has a different cooling loop routing. But for the calculated Δp and ΔT no distinct discrepancy can be observed between the two design stages. The maximum value for the pressure drop of (0.156 ± 0.009) bar as the average over all measurements at the lowest set point of around 18 bar and the corresponding temperature drop of $(0.79 \pm 0.05)\,^{\circ}C$ are considerably lower than the specified maximal values for the evaporator with $\Delta p_{evap} < 1.2$ bar and $\Delta T_{evap} < 3\,^{\circ}C$. But a direct comparison to the specification values is difficult as the conditions are different: on the one hand, the specified pressure drop is based on the minimum operating temperature of $-38\,^{\circ}C$ at the evaporator outlet, whereas the CO_2 temperature range tested in the measurement is between $+15$ and $-24\,^{\circ}C$ due to the constrained cooling power of the TRACI system; on the other hand, the heat load of the fully loaded petal is used for the specification, whereas the heat load on the bare petal core is only caused by the convection with the ambient air in the test setup.

7.3.2 Pressure drop analysis for the TM petal

With the evaluation of the pressure and temperature drop measured for the tests with the TM petal, it is possible to investigate the effect on Δp and ΔT for the powered state of the TM petal with the emulated heat load in the dummy silicon modules and to compare it to the unpowered state, similar as tested before. Figure 7.9 shows the section of the measurement cycle at the lowest set point of 18.1 bar with the comparison of the unpowered and powered TM petal tested with the nominal CO_2 mass flow of 1.3 g/s.

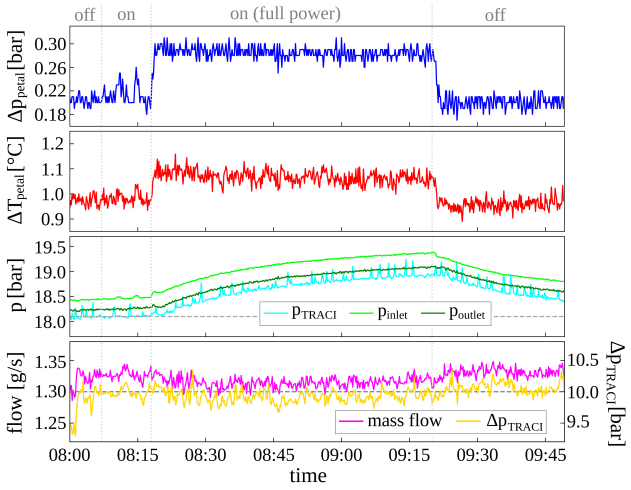

Figure 7.9: Comparison of the unpowered and powered state of the TM petal for the pressure and temperature drop at the lowest set point of 18.1 bar. Shown are the calculated values for Δp and ΔT over the core's cooling loop as well as the logged CO_2 pressure, the mass flow and the overall pressure drop for the complete system.

In the stabilized condition at the set point, the pressure drop over the cooling loop of the TM petal in the unpowered state is constantly at (0.20 ± 0.01) bar with a corresponding temperature drop of $(0.97 \pm 0.02)\,^{\circ}$C. When switching on the power for individual modules over short times, the pressure drop show an increase in the form of peaks to higher values, but returns to constant values after the powering. With the full heat load in the case of powering all modules on the TM petal, the pressure drop increases quite strongly and stabilizes at a rather constant value of (0.28 ± 0.01) bar for a constant powering. The corresponding temperature drop stabilizes in the same way at a value of $(1.08 \pm 0.02)\,^{\circ}$C. At the same time, the CO_2 pressure is changing as the TRACI system cannot maintain the lowest reached set point of the unpowered case, but this increase has no observable effect on the pressure drop. After switching off the power, the pressure and temperature drop returns quickly to the previous values of the unpowered state.
In Figure 7.10, Δp and ΔT is analysed for all tested CO_2 pressure set points comparing the unpowered and powered state of the TM petal.

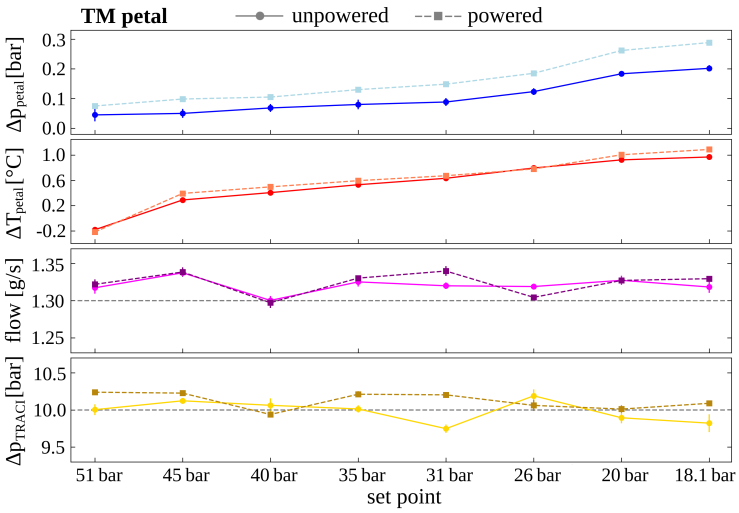

Figure 7.10: Analysis of the pressure and temperature drop for the TM petal in the unpowered and powered state, evaluated at the different tested CO_2 pressure set points between 51 and 18.1 bar. Compared are the values of Δp and ΔT as well as the adjusted mass flow and the overall pressure drop.

The pressure drop is significantly higher for the powered state than the unpowered state at all tested CO_2 pressure set points with a relative increase of $(60 \pm 17)\%$, whereas the temperature drop is only moderately higher by a relative factor of about $(14 \pm 10)\%$.
At the same time, the cooling conditions, as shown by the logged mass flow and the overall pressure drop of the system, are very comparable and allows therefore to interpret the observed increase in the pressure drop directly to the applied heat load.

Here, the latent heat transfer from the powered modules to the CO_2 coolant results in a change of the vapour quality of the dual-phase CO_2. The observed increase in the pressure drop over the (otherwise unchanged) cooling loop is caused by different fluid properties of the CO_2, such as its viscosity, influenced by the CO_2 vapour quality.

7.3.3 Dependence on the mass flow and orientation

The experimental investigations on the petal core prototypes and the TM petal can be also used to study possible dependencies of the pressure drop on other CO_2 properties.
On the one hand, the dependence of Δp and ΔT on the CO_2 mass flow is analysed. Figure 7.11 shows the comparison between measurements with a mass flow rate of 1.3 and 2.5 g/s for the TM petal in the unpowered state and over all tested set points.

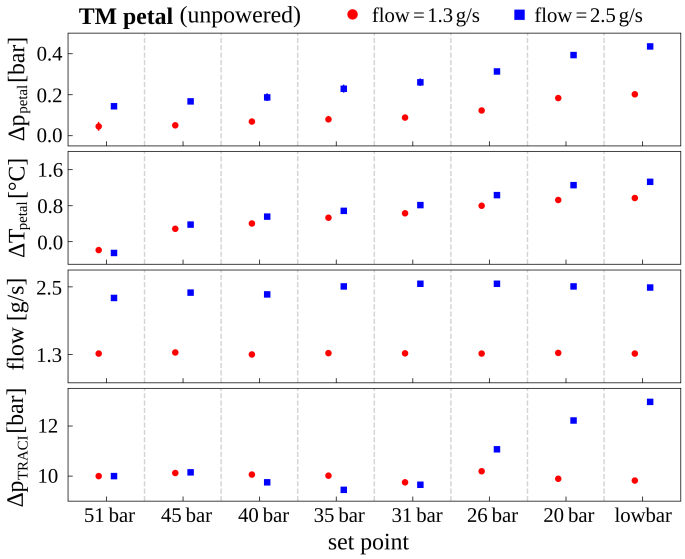

Figure 7.11: Analysis of the dependence of the pressure and temperature drop on the CO_2 mass flow. Compared are the results for mass flows of 1.3 and 2.5 g/s evaluated at the different tested CO_2 pressure set points for the TM petal in the unpowered state. The corresponding results for the powered state are shown in Appendix B.2.

Here, the observed Δp for the measurement with a mass flow of 2.5 g/s is considerably higher than the nominal case with a mass flow of 1.3 g/s. The relative factor of the pressure drop increase is on average 2.7 ± 0.4 for a nearly doubled mass flow through the cooling loop, whereas the difference in the temperature drop is not so distinct with a relative factor of 1.33 ± 0.03. Assuming similar fluid properties of the CO_2 coolant for both measurements, the higher mass flow rate results in a larger flow resistance in the cooling loop, which is observed by the increased pressure and temperature drop.

On the other hand, the performed measurements in different orientations of the TM petal can be used to investigate the influence of the flow orientation on the pressure and temperature drop. Figure 7.12 compares the calculated values of Δp and ΔT for the three tested orientations (*vertical +90°*, *horizontal* and *vertical -90°*) for the TM petal in the unpowered state and over all tested set points.
Overall, the measured pressure drops for the three orientations are consistent within smaller variations[46], which are caused most probably by slightly different cooling conditions.
For the temperature drop, the horizontal orientation shows in all cases the highest value for ΔT compared to the other two orientations, which could be caused by the different ambient conditions. But in general the pressure drop over the petal's cooling loop is rather independent on the flow orientation of the CO_2 coolant, as no significant differences are observed in the experimental investigation.

[46] Here, the two outliers for *vertical -90°* orientation at the set points of 35 and 31 bar are excluded.

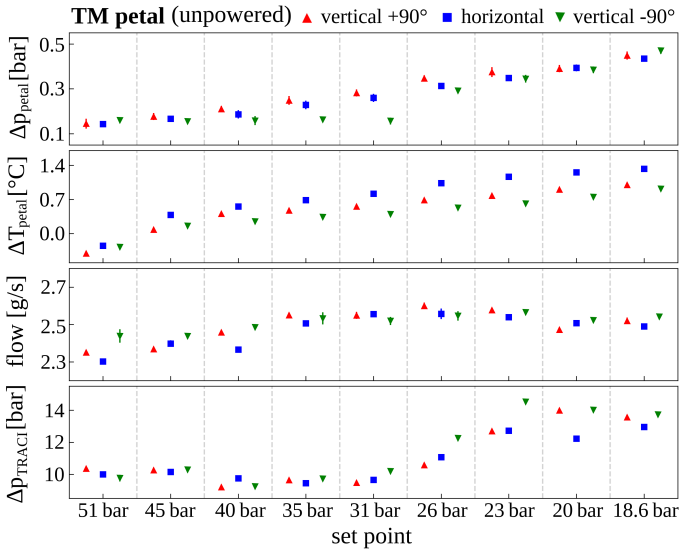

Figure 7.12: Analysis of the dependence of the pressure and temperature drop on the flow orientation. Compared are the results for the *vertical +90°*, *horizontal* and *vertical -90°* orientation evaluated at the different tested CO_2 pressure set points for the TM petal in the unpowered state with a mass flow of 2.5 g/s. The corresponding results for the powered state are shown in Appendix B.2.

7.3.4 Simulations of the pressure drop

Several input parameters need to be defined for the CO_2 simulation of the pressure drop in the petal's cooling loop when using the CoBra software.
On the one hand, the geometry of the cooling loop must be modelled in the simulation. Here, the cooling loop of the petal is a titanium pipe ($k_{Ti} = 14.5\,W/(m \cdot K)$) with a total length of 1 417 mm, an inner pipe diameter of 1.955 mm and a wall thickness of 160 µm.
On the other hand, the conditions for the CO_2 coolant must be specified. Here, the input parameters are the saturation temperature and the mass flow rate of the CO_2 fluid as well as the applied heat load of the experiment. To mimic the experimental conditions of the measurements, the logged data of the TRACI and the CO_2 diagnostics system is used for the temperature and mass flow input. But for the applied heat load, two cases need to be differentiated: firstly, for bare petal cores and the TM petal in the unpowered state, the transferred heat load originates only from the convection on the petal surface with the ambient air; secondly, the heat load applied by active powering of the dummy modules on the TM petal needs to be considered additionally to the convective heat flow.
The convective heat load on the petal is estimated by free convection according to [192] using the measured temperature on the petal surface as well as the ambient temperature in the setup. Figure 7.13 shows the estimated convective heat flow for the typical temperature ranges in the performed measurements. Details to the calculation are given in Appendix B.3.

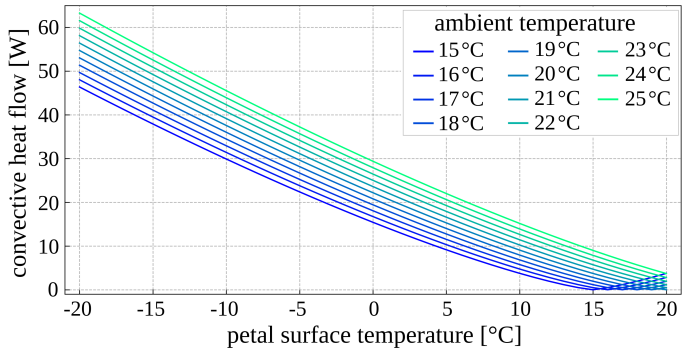

Figure 7.13: Calculation of the convective heat flow as function of the surface temperature on the petal and the ambient temperature in the setup, evaluated for the typical temperature ranges in the thermal measurements.

With the available version of the CoBra software, a detailed extraction of the pressure and temperature drop values for different experimental conditions was unfortunately not possible, but is planned when a newer version is provided by the developers.

To prepare for a direct comparison with the simulation, the measured pressure drop as function of the CO_2 pressure as well as the temperature drop as function of the CO_2 temperature are shown in Figure 7.14 for the case of all tested petal cores.

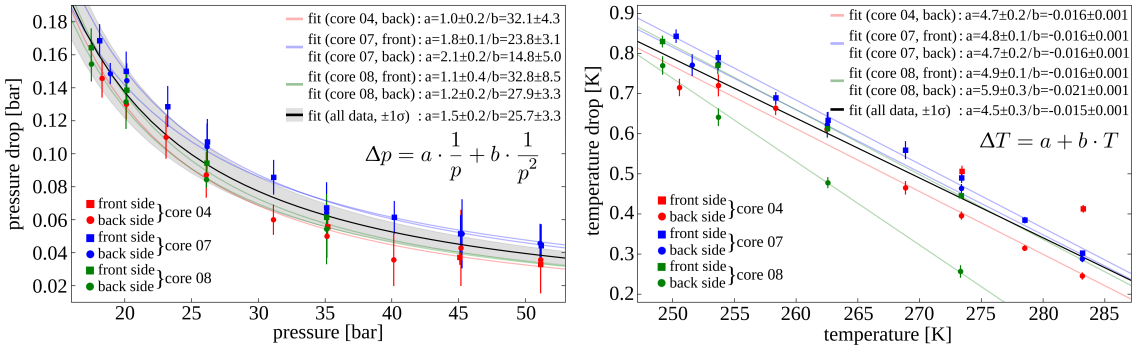

Figure 7.14: Evaluation of the measured pressure and temperature drop as function of the CO_2 pressure and temperature for cores 04, 07 and 08. The experimental data are fitted by empirical functions (cf. Eq. 7.2).

For the description of the functional dependence of Δp and ΔT, appropriate fit functions are evaluated empirically, which can be parametrized as

$$\Delta p = a \cdot \frac{1}{p} + b \cdot \frac{1}{p^2} \quad \text{and} \quad \Delta T = a + b \cdot T. \tag{7.2}$$

The pressure drop dependence for the individual measurements of cores is well described by the derived fit functions. Moreover, a fit to the merged data set for all tested cores provides a good description of the experimental data.
For the temperature drop, a linear function describes the data well, whereas for lower saturation temperatures a change of the behaviour of ΔT is observed. The spread between the individual measured cores is much larger, which is most probably caused by changing measurement conditions in the setup.

The pressure and temperature drop measured for the TM petal in the unpowered and powered state as well as for CO_2 mass flows of 1.3 and 2.5 g/s are shown in Figure 7.15.

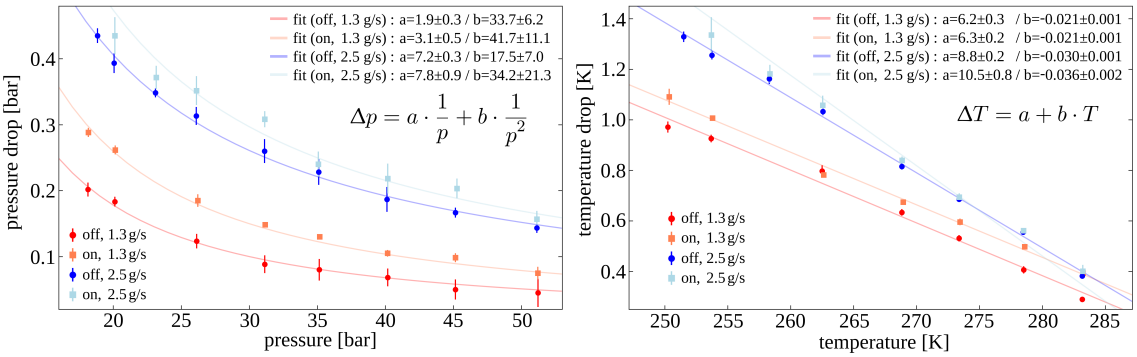

Figure 7.15: Evaluation of the measured pressure and temperature drop as function of the CO_2 pressure and temperature for the TM petal, comparing the unpowered and powered state as well as the mass flows of 1.3 and 2.5 g/s.

Again, the empirically found functions are fitted with the experimental data, providing overall a good description of the data. Moreover, the previously observed dependencies of Δp and ΔT on the powering state of the TM petal and on the mass flow rate are confirmed.

7.4 Analysis of the CO_2 State

The logged temperature and pressure values by the TRACI system as well as the CO_2 diagnostics at the petal in- and outlet are used to investigate the CO_2 state inside the petal's cooling loop to acquire a deeper insight in the cooling properties of the CO_2 fluid. Moreover, the additionally installed sightglasses allow to visually inspect the CO_2 state in terms of being in the liquid or gaseous phase for the incoming and outgoing flow.
In the following, various aspects for the CO_2 state in the TM petal during the performed thermal testing with changing CO_2 pressure set points are investigated.
On the one hand, the experimental observations are interpreted to follow the CO_2 state over the full cooling cycle between TRACI and the experiment's cooling loop as well as to estimate qualitatively the vapour quality before and after the cooling loop by observing the fill levels and flow patterns in the sightglasses. On the other hand, the experimental observations are compared to theoretical calculations based on the CO_2 properties[47] as well as to CoBra simulations reproducing the experimental conditions, e.g. to evaluate the expected behaviour for different heat loads of the petal.

7.4.1 CO_2 state over the full cooling cycle

For the performed measurements, the CO_2 state over the full cooling cycle can be analysed using the logged temperature and pressure values at the various points in the TRACI system as well as close to the petal's cooling loop. The goal is to investigate the operation cycle for the CO_2 fluid in the measurement according to the I-2PACL concept with the previously depicted operation stages in Figure 6.6.
The CO_2 state is analysed in the subcooled state before the pump (1), before the heat exchange with the accumulator (2), before entrance in the concentric transfer line (3), at the inlet (4) and outlet (5) of the petal's cooling loop, and the returning CO_2 state in the accumulator (6). At each operation stage, the enthalpy is calculated using the recorded temperature and pressure values at that point[48].
Figure 7.16 shows the measured operation cycle in the log(p)-h diagram for the full cooling cycle and at various CO_2 pressure set points between 51 and 18.6 bar.
The typical operation cycle of the I-2PACL concept for evaporative CO_2 cooling is observed: in state (1), the CO_2 is in the liquid phase at a sub-cooled temperature; state (2) with a higher pressure and enthalpy is reached by the compression in the pump; state (3) at a constant pressure but higher enthalpy results from the heat exchange with the saturated CO_2 in the accumulator for the adjusted pressure set point; state (4) characterizes the CO_2 state before entering the experiment's cooling loop and is reached by the heat exchange in the concentric transfer line and the pressure drop in the capillary; state (5) is influenced by the transferred heat and the pressure drop in the petal's cooling loop; and state (6) corresponds to the state of the returning dual-phase CO_2 in the accumulator.
The characteristic pressure drop along the cooling loop of the TM petal is clearly visible in the analysed operation cycle as the CO_2 state at the outlet (state point 5) shows a lower pressure value than at the inlet (state point 4). But due to the missing information of the vapour quality of the dual-phase CO_2, the measured state points from the pressure and temperature readings of the operation stages (4), (5) and (6) are all in the liquid phase close to the evaporation line.

[47] For the theoretical calculations, the thermodynamic and transport properties of the CO_2 fluid for the various conditions, e.g. in terms of pressure, temperature or enthalpy, are extracted from the REFPROP database [193, 194]. Moreover, the open source implementation CoolProp [195, 196] is used.
[48] In the TRACI system, the CO_2 pressure is not measured in all cases at the point of the temperature measurement. Therefore, the pressure value of the closest sensor in the same cooling branch is used then.

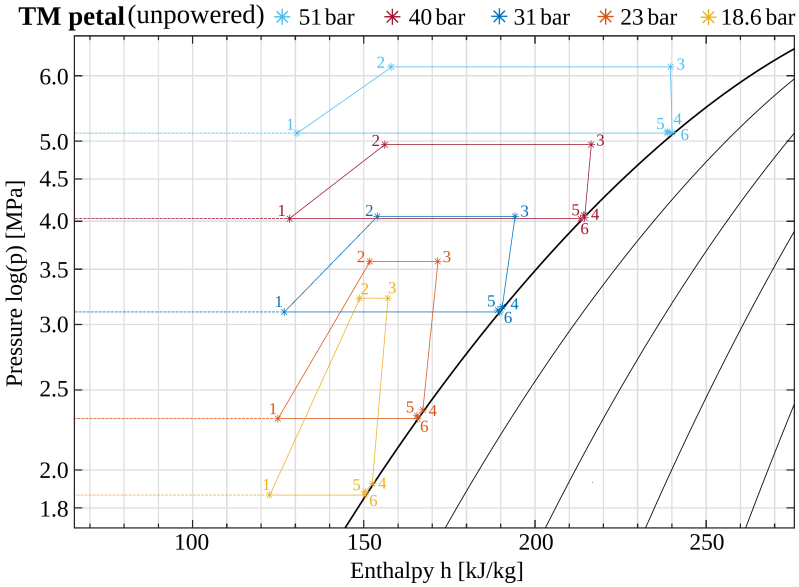

Figure 7.16: Analysis of the CO_2 state over the full cooling cycle between TRACI and the petal's cooling loop in the log(p)-h diagram. Shown are the results for a measurement with the TM petal in the unpowered state at the different operation stages from (1) to (6) and for the selected CO_2 pressure set points of 51, 40, 31, 23 and 18.6 bar.

Here, it is expected that at least the state points (5) and (6) are inside the wet-steam region along the isothermal lines, which is caused by the transferred heat from the TM petal and the resulting higher vapour quality.
Therefore, the vapour quality is a required input for a detailed analysis of the CO_2 state inside the cooling loop and is estimated in the following using the installed sightglasses at the in- and outlet of the petal's cooling loop.

7.4.2 Estimation of the vapour quality

The installed sightglasses at the in- and outlet of the petal's cooling loop are used to visually inspect the state of the CO_2 fluid before and after the experiment. The interesting quantity in this case is the vapour quality as the fraction of the gaseous phase to the liquid phase for the evaporative CO_2. From the specifications, the vapour quality at the entrance of the petal should be around $0 < x_{\text{in}} < 0.03$, meaning just in the dual-phase region. Due to the latent heat transfer from the generated heat in the petal, x increases along the cooling loop, but should be not higher than the specified value of $x_{\text{out}} = 0.35$ at the outlet of the evaporator to have enough headroom to the dry-out case.
The vapour quality cannot be measured directly in the experiment, but to acquire nonetheless an insight to the CO_2 state before and after the experiment's cooling loop, the sightglasses for visual inspection are a possible tool. Moreover, the performed study to estimate the vapour quality at the in- and outlet by the logged fill levels of the sightglasses is discussed in the following.

Figure 7.17 shows a selection of recorded photographs of the sightglasses at the in- and outlet for three different conditions in terms of the CO_2 pressure set point and the powering state for a performed measurement with the TM petal.
For the case of higher CO_2 pressure set points (cf. Fig. 7.17a), the inlet sightglass is fully filled with CO_2 in the liquid phase, whereas the outlet sightglass shows also a gaseous fraction by a reduced fill level. This could indicate that the CO_2 fluid enters the petal in the subcooled, liquid state, but changes to the dual-phase state in the cooling loop by the heat transfer from the petal. In this case, the dummy modules on the TM petal are not actively powered and therefore the heat load is caused only by the convective heat transfer from the ambient air in the test setup.

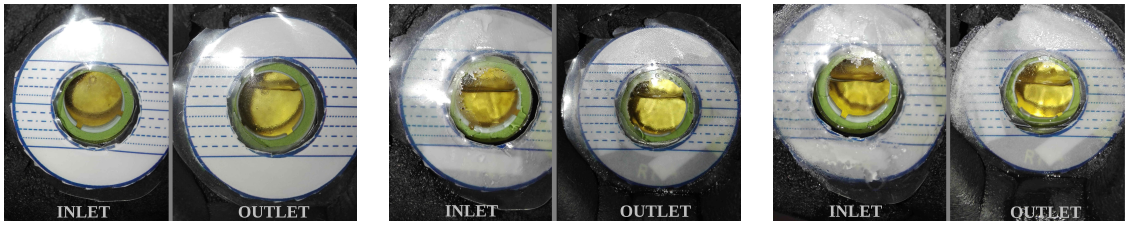

(a) 51 bar, unpowered. **(b)** 26 bar, unpowered. **(c)** 18.6 bar, powered.

Figure 7.17: Visual inspection of sightglasses at in- and outlet for different CO_2 pressure set points for a measurement with the TM petal.

For lower CO_2 pressures (cf. Fig. 7.17b), the observed fill level of the liquid phase in the inlet is reduced as well, indicating that the dual-phase state is already reached at the entrance of the petal due to the observed mixture of gaseous and liquid phase. This is a valuable observation for the purpose of thermal testing, because here the thermal performance of the petal is investigated for the case of dual-phase cooling and with the visual inspection of the sightglasses the dual-phase state is verified.
For even lower CO_2 pressures (cf. Fig. 7.17c), the cold fluid temperatures cause ice building on the sightglasses. Therefore, it is important to thermally insulate the sightglass windows when no visual inspection is required, as also the CO_2 state is influenced by the transferred heat via the sightglasses from the ambient surrounding. For the case of the powered state of the TM petal, corresponding to a higher heat load from the dummy silicon modules, it is expected to change the vapour quality to higher x, meaning a higher fraction of the gaseous phase. This is unfortunately not observed when comparing the fill levels in the sightglasses at the in- and outlet, as here rather equal levels at both locations are observed. But another observation, not visible in the photographs recording only one fixed condition in time, is that a turbulent flow of gas bubbles is observed at the outlet sightglass contrary to the flow at the inlet. This indicates that the vapour quality has changed along the cooling loop, as the flow pattern of the dual-phase CO_2 changes with x (cf. Fig. 6.5).
A video sequence showing the observed flow pattern at the outlet can be found in [197].

For a systematic investigation of the results from the visual inspection of the sightglasses, the fill levels at the inlet and outlet are logged manually in percentage for each CO_2 pressure set point and powering state of the TM petal for the complete measurement cycle. In the first step, the volumetric fractions of the gaseous to liquid phase, x_{vol}, are calculated from the recorded fill levels using the geometry of the sightglass volume.
But the vapour quality x is conventionally calculated as the mass fractions of the gaseous and liquid phase. Therefore, the fraction of the gaseous to liquid phase relative to the mass, x_{mass}, is calculated using the corresponding densities of the liquid and gaseous CO_2. The details of the calculations of x_{vol} and x_{mass} are shown in Appendix B.4.

Figure 7.18 shows the observed fill levels at the in- and outlet of the cooling loop as well as the calculated fractions relative to the volume and to the mass for the different tested CO_2 pressure set points and powering states of the TM petal.
For CO_2 pressure set points up to 41 bar, the fill levels of the inlet sightglass are 100%, corresponding to an estimated vapour quality of $x = 0$, so fully liquid CO_2. But for lower set points, the fill levels for the sightglasses at the in- and outlet are nearly equal with slightly higher levels at the inlet and are gently decreasing to the lowest measured set point. The volumetric fractions are therefore slightly higher at the outlet than the inlet and are increasing correspondingly to lower CO_2 saturation temperatures.

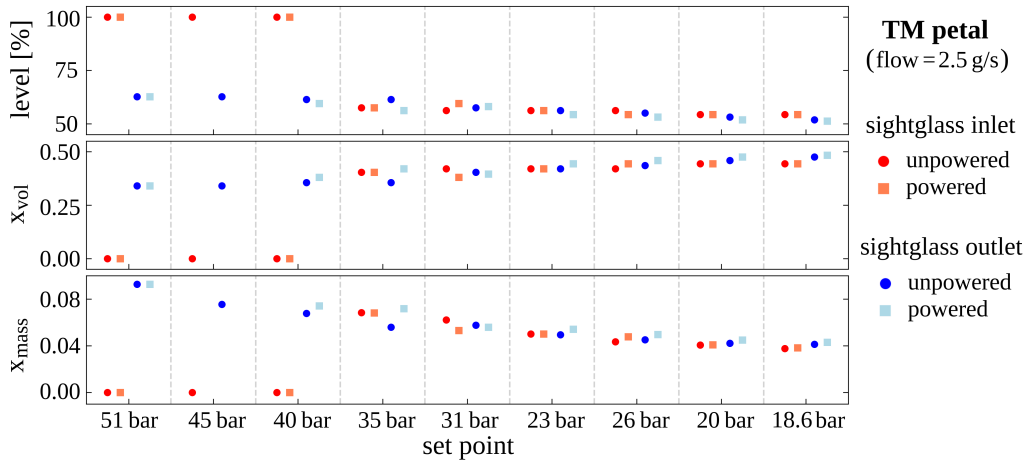

Figure 7.18: Estimation of the vapour quality from the sightglass inspection for the tested CO_2 pressure set points. From the observed fill levels in the sightglasses at the in- and outlet, the fraction of the gaseous to liquid phase of the dual-phase CO_2 is calculated relative to the volume, x_{vol}, and relative to the mass, x_{mass}. Shown are the recorded data for a measurement with the TM petal in the unpowered and powered state.

For the vapour quality based on the mass fractions the contrary behaviour with decreasing values for lower temperatures is observed. This is explained by the changing densities of the CO_2 fluid: the density of the liquid phase is increasing with lower pressure and temperature values, whereas the density of the gaseous phase is decreasing. Therefore, the estimated vapour quality is lower for lower set points which follows the expectation as the width of the wet-steam region in the log(p)-h diagram (cf. Fig. 6.4) is higher for lower saturation temperatures and with the same enthalpy a lower value of x is reached at a lower set point. The difference between the estimated vapour quality at the in- and outlet is very small or even negative in some cases, whereas here a higher difference is expected due to the transferred heat along the cooling loop. The same is expected for the comparison of the vapour qualities at the outlet for the unpowered and powered state, as here the difference in the heat load with 54 W by the dummy modules is significant.
These arguments indicate that at least the vapour quality of the dual-phase CO_2 after the cooling loop is not fully reflected by the fill levels in the sightglass.
For a better estimation, the observed difference in the flow pattern with a turbulent flow of gas bubbles at the outlet needs to be considered quantitatively[49].

7.4.3 Investigation of subcooling

Subcooling of a CO_2 fluid describes the temperature difference of the measured CO_2 temperature in the liquid phase to the saturation temperature on the evaporation line evaluated at the same CO_2 pressure. With the recorded temperature and pressure values at the in- and outlet of the petal's cooling loop, ΔT_{sub} is calculated as

$$\Delta T^i_{\text{sub}} = T^i_{\text{meas}} - T^i_{\text{sat}}\left(p^i_{\text{meas}}\right) \quad i = \text{inlet, outlet.} \tag{7.3}$$

Figure 7.19 shows the subcooling for the in- and outlet evaluated for a measurement with the TM petal for different CO_2 pressure set points in the unpowered and powered state.

[49] A first study to quantitatively assess the amount of gas bubbles in the flow using ultrasound measurements was conducted in this work, but the technique was proven to not provide the required accuracy.

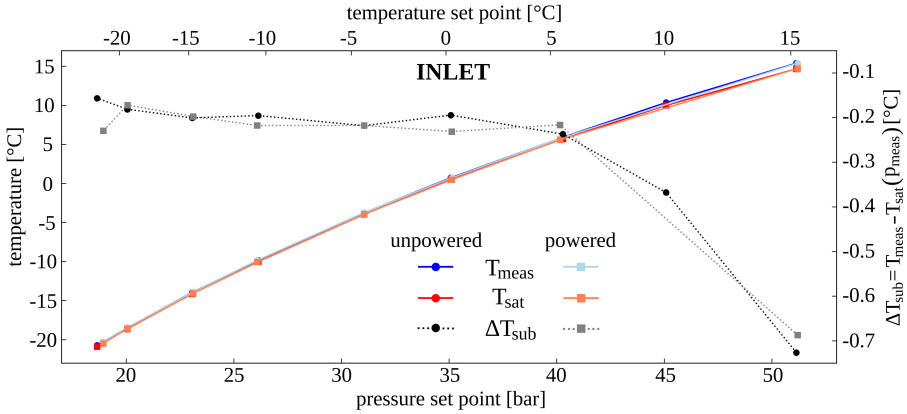

(a) Subcooling at the inlet of the petal's cooling loop.

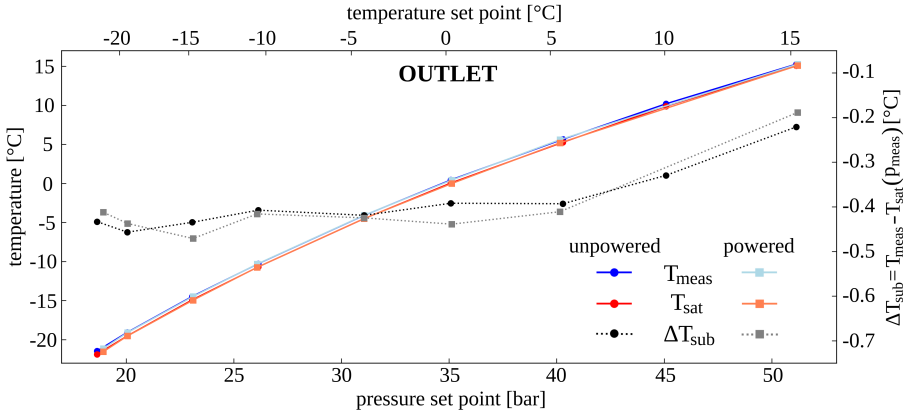

(b) Subcooling at the outlet of the petal's cooling loop.

Figure 7.19: Subcooling ΔT_{sub} calculated from the measured CO_2 temperature (T_{meas}) and the saturation temperature (T_{sat}) corresponding to the measured CO_2 pressure (p_{meas}). Evaluated are different CO_2 pressure set points for the unpowered and powered state of the TM petal.

For the subcooling at the inlet (cf. Fig. 7.19a), rather constant values of $\Delta T_{sub} \approx -0.2\,^{\circ}C$ are observed for lower CO_2 pressure set points. This can be explained by the influence from the warmer ambient on the not perfectly insulated temperature sensor causing a temperature offset to the saturation temperature as a systematic measurement error. But for the pressure set points of 51, 45 and also 40 bar, a larger subcooling is observed indicating a state of subcooled, liquid CO_2 before entering the petal's cooling loop.
This measured subcooling agrees very well with the observed fully filled sightglass at the inlet for the highest tested set points (cf. Fig. 7.18) and the estimated vapour quality of zero before the experiment. The reason for the subcooling at higher set points could be either caused by a too low heat transfer for the outflowing CO_2 in the accumulator or by too less expansion before the experiment's inlet.
For the subcooling at the outlet (cf. Fig. 7.19b), rather constant values of $\Delta T_{sub} \approx -0.4\,^{\circ}C$ for set points below 40 bar are observed, reflecting again the systematic offset of the temperature measurement. Due to the observed subcooling at the inlet for the highest set points, ΔT_{sub} at the outlet is lower for these set points, whereas the sightglass analysis indicates no difference in the behaviour compared to the other set points.
As a general observation, the measured subcooling at the in- and outlet seems to be independent of the powering state of the TM petal, which is expected for the case of the inlet, but not necessarily for the outlet.

7.4.4 Estimation of the CO_2 state

With the estimated vapour quality from the sightglass investigation at the in- and outlet, the CO_2 state inside the petal's cooling loop can be analysed in the log(p)-h diagram for the different tested CO_2 pressure set points.
The enthalpy values of the corresponding situations are calculated as

$$h^i_{\text{evap}} = h\left(T^i_{\text{meas}}, p^i_{\text{meas}}\right), \quad h^i_{\text{x}} = h\left(p^i_{\text{meas}}, x^i_{\text{mass}}\right), \quad i = \text{inlet, outlet} \tag{7.4}$$

for the case of not using and using the estimated vapour quality x_{mass} (cf. Fig. 7.18). Moreover, the such determined CO_2 states from the estimated vapour quality are compared to theoretical calculations of the enthalpy, when using the applied heat load in the experiment. For the unpowered case of the TM petal, the heat load stems only from the convective heat exchange with the ambient air, whereas for the powered case the additionally applied heat load of the active components on the dummy modules is taken into account. In Figure 7.20, the transferred heat load, $\dot{Q}$, as well as the resulting increase in the enthalpy, h_{load}, are calculated for the different set points evaluating the case of convection and active powering. Details to the calculation are given in Appendix B.5.

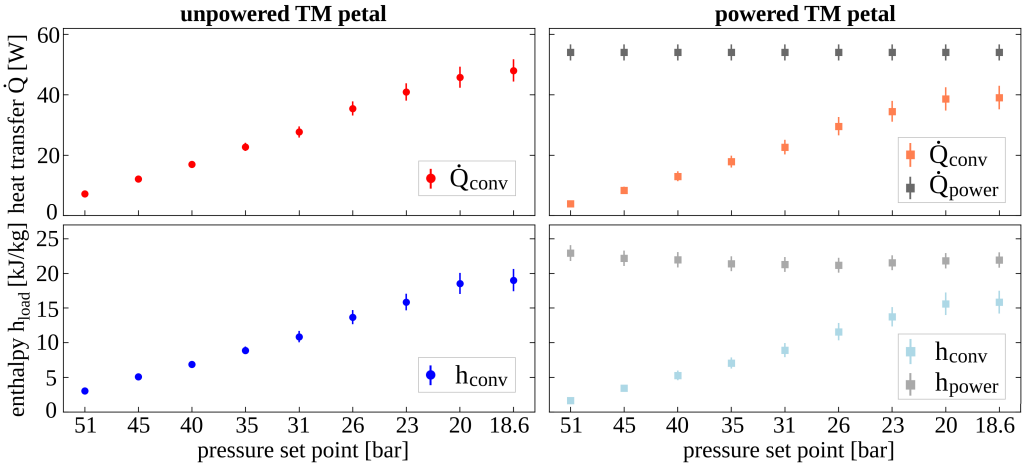

Figure 7.20: Transferred heat load, $\dot{Q}$, and increase of enthalpy, h_{load}, caused by convection with the ambient air as well as for active powering of the TM petal. Evaluated are the different tested CO_2 pressure set points for the unpowered (left) and powered (right) state of the TM petal.

On the one hand, the theoretical enthalpy increase along the cooling loop is evaluated relative to the CO_2 state on the evaporation line, and on the other hand using the estimated CO_2 state from the inlet sightglass, determined as:

$$h^{\text{outlet}}_{\text{theo}} = h^{\text{inlet}}_{\text{evap}} + h_{\text{load}}, \quad h^{\text{outlet}}_{\text{theo,x}} = h^{\text{inlet}}_{\text{x}} + h_{\text{load}}, \quad h_{\text{load}} = h_{\text{conv}} + h_{\text{power}}. \tag{7.5}$$

The resulting log(p)-h diagram with the estimated CO_2 states inside the petal's cooling loop for the different tested CO_2 pressure set points is shown in Figure 7.21a and Figure 7.21b for the unpowered and powered state of the TM petal, respectively.
The CO_2 state points using the estimated vapour quality values from the sightglass analysis show in nearly all cases lower values of x than the theoretically calculated state points. Only for the higher CO_2 pressure set points with the observed subcooling at the inlet and for the unpowered case of the TM petal, the vapour quality estimated from the sightglass at the outlet is higher than the calculated values.

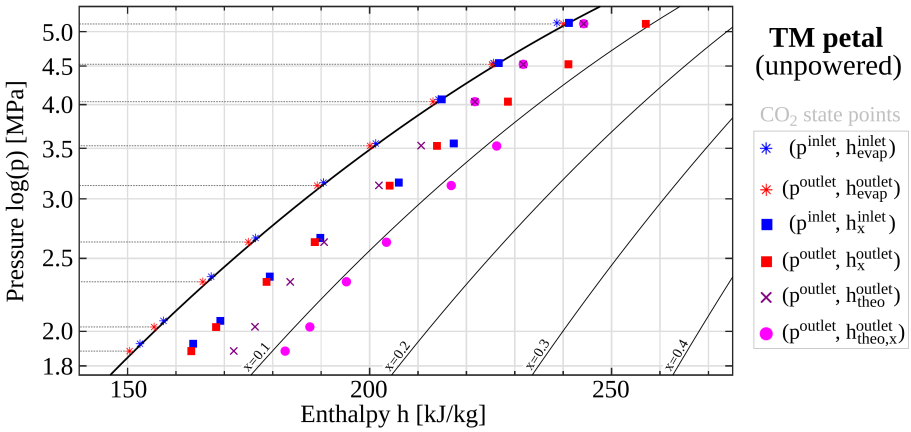

(a) Log(p)-h diagram with the estimated CO_2 states for the unpowered TM petal.

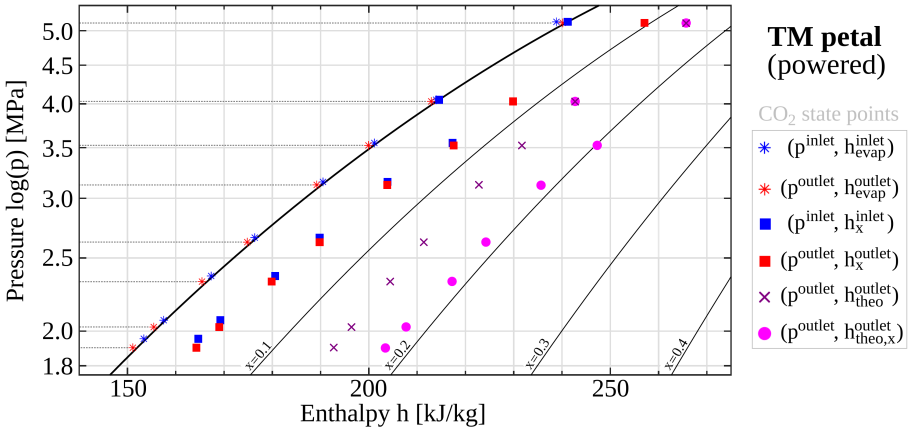

(b) Log(p)-h diagram with the estimated CO_2 states for the powered TM petal.

Figure 7.21: Estimation of the CO_2 state at the in- and outlet of the cooling loop for a measurement with the TM petal. The CO_2 states using the estimated vapour quality from the sightglass analysis (cf. Eq. 7.4) are compared to expected state points from theoretical calculations (cf. Eq. 7.5).

These observations indicate again that the fill levels in the sightglasses alone are not sufficient to estimate the vapour quality of the evaporative CO_2 correctly and further investigations on the observed flow pattern should be performed.
The following observations can be made for the theoretically calculated state points of the evaporative CO_2, focusing here on CO_2 pressures below 35 bar as the more interesting case for the ITk detector cooling: for the unpowered TM petal corresponding to a heat load caused by convection only, vapour qualities between $0.04 < x < 0.07$ or around $x = 0.11$ are observed, depending on the evaluated case relative to the evaporation line or relative to the estimated state point at the inlet; for the powered scenario with the additional heat load from the dummy modules on the TM petal, vapour qualities between $0.13 < x < 0.14$ or between $0.18 < x < 0.20$ are observed, respectively. The vapour quality at the outlet is for all cases of calculated state points well below the maximum value of $x = 0.35$ in the specifications. But in this investigation, only the nominal heat load of 54 W[50] is emulated with the TM petal. On the contrary, the CO_2 cooling system for the petals in the ITk strip end-cap must be designed for the maximum expected heat load of around 100 W on the petal, which is caused by radiation effects in the sensor modules.

[50] The current estimate for the nominal heat load on the petal is around 65 W.

These different load scenarios are studied in detail by the thermo-electrical model [174] and will be briefly discussed in the next part using CoBra simulations for the analysis of the CO_2 state inside the petal's cooling loop.

7.4.5 Simulations of the CO_2 state and the vapour quality

CoBra simulations can be performed to analyse the state of the CO_2 along its flow through the cooling loop of the petal. Important parameters to extract in this case are the vapour quality of the dual-phase CO_2, the flow pattern for the CO_2 coolant and the coolant's HTC to allow for an efficient heat transfer. Here, the vapour quality is changing linearly as function of the cooling loop length due to the applied heat load from the experiment, influencing accordingly the flow pattern as well as the HTC.
In Figure 7.22, the situation for the fully powered petal under nominal conditions, with a saturation temperature of $-38\,^{\circ}\mathrm{C}$ after the cooling loop, a CO_2 mass flow of $1.3\,\mathrm{g/s}$ and an expected heat load of $100\,\mathrm{W}$, is simulated.

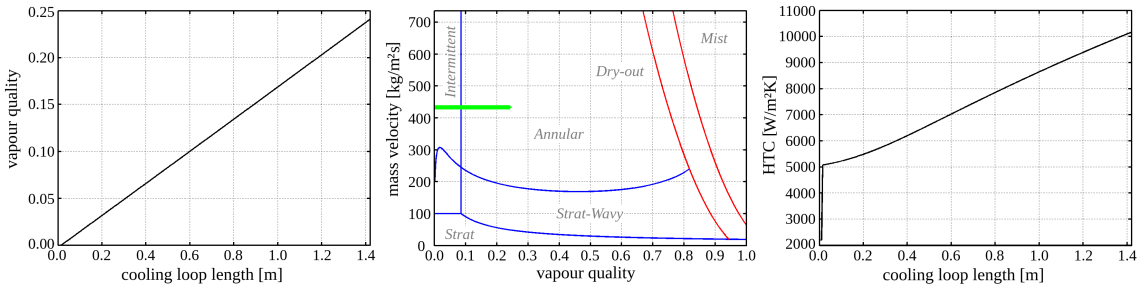

Figure 7.22: CoBra simulation for the nominal conditions of the fully powered petal ($T_{\mathrm{sat}} = -38\,^{\circ}\mathrm{C}$, $\dot{m} = 1.3\,\mathrm{g/s}$, $\dot{Q} = 100\,\mathrm{W}$). Shown is the vapour quality as function of cooling loop length, the corresponding flow pattern and the coolant's HTC.

For the comparison of the previous experimental results (cf. Fig. 7.21), the vapour quality is simulated for the according experimental conditions in terms of the saturation temperature and the flow at the set point as well as the applied heat load from convection and active powering of the TM petal, which is shown in Figure 7.23.

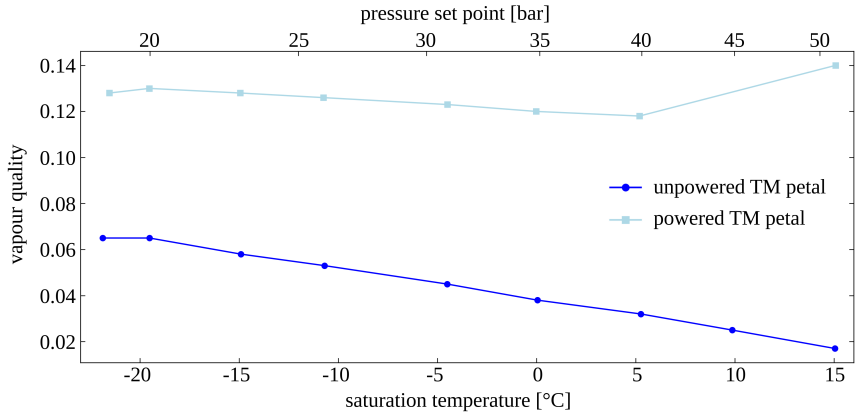

Figure 7.23: CoBra simulation of the vapour quality for the different tested set points of the TM petal in the unpowered and powered state. The experimental conditions in terms of the saturation temperature, the mass flow and the applied heat load are used as input for the simulation.

7.5 Conclusion

The properties of the dual-phase CO_2 cooling for the petal in the ATLAS ITk detector was analysed in several experimental studies. This is especially interesting, as the thermal performance of the petal core prototypes as well as the TM petal, which was investigated in Chapter 6, is directly connected to the cooling performance and its dependencies analysed in this chapter.

In a first study, the influence of the CO_2 flow orientation on the cooling performance was tested by rotating the PTM of the thermal QC test setup to measure the thermal performance with a core and the TM petal in different orientations. Here, the normal, horizontal orientation was compared with the two most extreme situations occurring in the end-cap with the vertical $+90^\circ$ and the vertical -90° orientation.
In the case of testing the core 02 and evaluating the temperature distributions along the cooling loop for two different orientations, no indication of a dependence of the thermal performance on the flow orientation was observed.
In the case of the TM petal, overall comparable temperatures were measured for the three orientations, with the exception of the temperatures on the silicon sensor areas of the R0 and the R5 module. Here, a tendency to an ordering of the temperatures according to the evaluated orientations could indicate an effect of gravity on the CO_2 fluid.
As these modules feature specialities in the cooling loop routing - the U-turn under module R0 and a straight section with perpendicular turns for the R5 module - the CO_2 coolant could be "trapped" in these regions for the vertical -90° orientation resulting in the observed lower temperatures on the corresponding silicon sensor areas. But for a definite interpretation of these results, further investigations with different CO_2 flow orientations should be conducted with the petal.

Another important quantity for the design of the dual-phase CO_2 cooling system for the ITk detector is the pressure drop in the cooling loop of the evaporator, in the case of the ITk strip end-cap the pressure drop over the petal's cooling loop.
The pressure drop Δp is important as it determines the saturation temperature of the CO_2 coolant at the inlet of the petal due to the according temperature drop ΔT.
Moreover, the parameters of the complete cooling system, e.g. the available CO_2 mass flow through the single cooling loops, are influence by the total budget of pressure and temperature drops along the various cooling lines of the full system.
With the recorded data of the CO_2 diagnostics system in terms of the pressure and temperature at the in- and outlet of the connected petal's cooling loop, it was possible to calculate Δp and ΔT for the performed measurements with cores and the TM petal under the different conditions regarding CO_2 pressure set points and applied heat loads.
For the tested petal core prototypes, the pressure and temperature drop is increasing for lower set points and the results for the different core designs are rather comparable.
For the TM petal, the resulting pressure drop for the unpowered and powered state was compared and showed that the pressure drop is higher for the powered state. This observation can be explained by the changing CO_2 fluid properties with the vapour quality, which is influenced by the applied heat load in the experiment.
Furthermore, the dependence of the pressure drop on the CO_2 mass flow as well as the CO_2 flow orientation was studied with the TM petal. Here, for a higher CO_2 mass flow also a higher pressure and temperature drop was observed, whereas no significant differences in Δp and ΔT were observed for the different tested orientations.

The experimental results of the pressure and temperature drop analysis should be also compared to simulated results. Here, CoBra simulations with the experimental conditions as input, e.g. the calculated convective heat flow from the ambient in the test setup or the actual measured CO_2 pressure and mass flow, are the preferred choice. Unfortunately, the available CoBra version during this work was not suited to perform this type of simulations, which will be done therefore in the future.
Nonetheless, the experimental data was fitted with empirical functions and a good description of the pressure and temperature drop as function of the CO_2 pressure and temperature was reached with the determined fit functions.

Finally, the CO_2 state inside the petal's cooling loop was analysed using the recorded data of the TRACI system as well as the CO_2 diagnostics system with the sightglasses at the in- and outlet. Here, the most interesting quantity of the dual-phase coolant is the vapour quality, as it determines the state of the CO_2 and its properties, e.g. the HTC.
On the one hand, it was possible to analyse the CO_2 state for the full cooling cycle for the different CO_2 pressure set points in a measurement by determining the state points in the log(p)-h diagram, showing the expected operation cycle for the I-2PACL system.
On the other hand, the vapour quality at the in- and outlet of the petal was estimated by using the recorded data from the visual inspection of the fill levels in the sightglasses. For the highest CO_2 pressure set points, a subcooling of the CO_2 fluid at the inlet was detected using the measured pressure and temperature values, which matches also well with the observation of only liquid CO_2 at the inlet sightglass for these set points.
Moreover, the CO_2 state inside the cooling loop was analysed with the estimated vapour qualities from the sightglass analysis and compared to theoretical calculations using the applied heat load to determine the CO_2 state points in the log(p)-h diagram.
Here, large differences between the estimated and the theoretically calculated state points are observed, which is most probably caused by the estimated vapour quality from the sightglasses. The fill levels in the sightglasses are not sufficient to determine the vapour quality of the CO_2 fluid correctly. To improve the estimation, the observed turbulent flow pattern at the outlet sightglass should be taken into account as well, as this indicates a higher vapour quality.
Furthermore, CoBra simulations for the CO_2 state and the vapour quality were conducted. Here, the vapour quality was simulated according to the experimental conditions.

Overall, the properties of the dual-phase CO_2 cooling for the petal were measured in several dedicated studies. Nonetheless, further investigations are needed in the future to confirm the observed results also for the specified CO_2 cooling temperature of $-38\,^{\circ}\mathrm{C}$ for the ATLAS ITk strip detector.

Chapter 8

Test Beams & Beam Telescopes

A full system test under realistic operation conditions is a key tool for the successful development of new particle detectors. Although novel sensor technologies and their properties can be studied and characterized in lab measurements, e.g. via electrical characterization or radioactive source measurements, it is necessary to perform measurements with realistic particle sources for the qualification of the detector, its read-out scheme and the integration in the **D**ata **A**c**Q**uisition (DAQ) system. Test beam facilities offer the users a beam of relativistic particles for their scientific studies, mostly related to the field of particle detector development, but covering also other disciplines and applications.
Test beam experiments require the full spectrum of experimental physics skills: from planning and commissioning of the experiment up to the data taking and analysis of the experimental data. Therefore, test beams offer also a great opportunity for educational purposes for students [198], teachers [199] and high school students [200].
Worldwide, several facilities exists providing external users with beam time for their studies. Here, a wide range of possibilities exists in terms of the type of particle (e.g. electrons, muons, pions), the type of beam (e.g. bunch spacing and beam size), the available momentum range (e.g. ranging from hundreds of MeV to hundreds of GeV) and the rate of particles. Some examples of available test beam facilities are PS/SPS at CERN [201], FTBF at Fermilab [202], ESTB at SLAC [203] and ELSA at Bonn [204]. For the studies conducted in this thesis, the DESY II Test Beam Facility at Deutsches Elektronen-Synchrotron (DESY) was used and its characteristics are presented in Section 8.1.

A reference system is needed for the characterization of new particle tracking detectors to quantify the resolution in space and/or time. A beam telescope consisting of several fine-pitch pixel or strip detectors can be used to obtain the particle trajectories in the test beam experiment and by interpolation to the **D**etector **U**nder **T**est (DUT) between the telescope sensors, a high position resolution is achieved. Several beam telescopes have been built with different design requirements such as high spatial or temporal resolution, coping with high beam rates or usable at low energy beam lines minimizing the amount of material. Examples are the MuPix telescope [205], the Timepix telescope [206], or the FE-I4 telescope [207]. The measurements of this thesis were conducted with the EUDET-type beam telescopes at DESY and their design and characteristics are discussed in Section 8.2.

For a successful test beam measurement not only hardware is required, but also dedicated software for DAQ and data reconstruction. To implement the detectors of the beam telescope as reference and the DUTs of the users into a common DAQ system, the EUDAQ software framework provides the required features in a consistent and user-friendly way. The concept and working principle of EUDAQ will be described in Section 8.3.

With the raw data, coming from the telescope, the DUT or other devices, the particle tracks have to be reconstructed. The reconstruction in this work is performed using the EUTelescope reconstruction framework, a versatile tool perfectly suited for the EUDET-type beam telescope analysis. The reconstruction steps from raw sensor data to final particle tracks and the operation of EUTelescope are introduced in Section 8.4.

Finally, the success of the test beam experiment is dependent on the right choice of parameters of the setup. This starts from adjustable beam parameters such as momentum and size of beam, continues with the settings and setup of the beam telescope, and ends with execution of the correct data reconstruction and analysis. For understanding the choices made later in the presented test beam measurements, a selection of parameters and their influence on the test beam measurement is discussed in Section 8.5.

8.1 DESY II Test Beam Facility

The DESY II Test Beam Facility provides testbeam users with beams of relativistic electrons or positrons within a selectable momentum spectrum of up to 6 GeV/c at three different beam lines, called TB21, TB22 and TB24 [208, 209]. These three beam lines are completely independent from each other, so that it is possible to operate and conduct three independent experiments simultaneously by different user groups. The use cases of the DESY II Test Beam Facility cover a rather broad spectrum, starting with the typical experiments of characterization of novel particle detectors, e.g. tracking detectors or calorimeters, up to investigations of the interaction of high momentum particles with matter or testing new ideas for medical applications. In general, a high demand on test beam time can be seen in the recent years and is also anticipated for the future of the test beam facility [210].
In the following, the steps of generating the particle beams at the DESY II Test Beam Facility are introduced in Section 8.1.1 and in Section 8.1.2 an overview about some additional available infrastructure is given.

8.1.1 Beam generation

The starting point for the beam generation for test beams is the DESY II synchrotron. It is a 292.8 m long ring accelerator operated at a frequency of 12.5 Hz corresponding to a 80 ms magnet cycle. In standard operation, a bunch of electrons ($\sim 10^{10}$) is stored for two magnet cycles, whereas it is injected with an energy of $E_{\text{min}} = 0.45\,\text{GeV}$ from the linear accelerator LINAC II and then accelerated to typically $E_{\text{max}} = 6.3\,\text{GeV}$. The typical DESY II operation cycle is depicted in Figure 8.1.

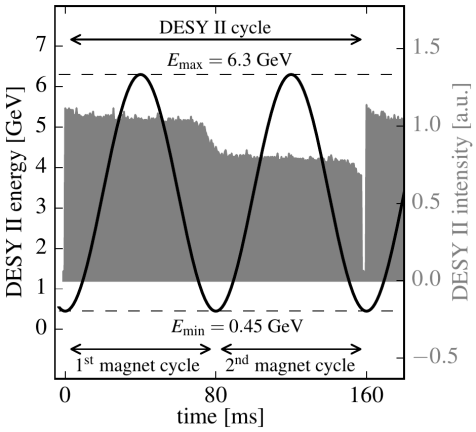

Figure 8.1: Illustration of DESY II operation cycle without beam extraction: The sinusoidal DESY II beam energy and the corresponding beam intensity is shown for a 160 ms DESY II cycle. The cycle starts with the bunch injection which is stored for two 80 ms magnet cycles before being dumped. Due to beam losses, the beam intensity of the second magnet cycle is smaller than the first one. Modified from [208].

The main purpose of DESY II is the injection of electrons into the PETRA III storage ring in the so-called "top-up" mode, but in parallel it is used for generating particle beams for the DESY II Test Beam Facility. For this, a double conversion process is used to create electron and positron beams for the test beam, where the same approach is used for all three test beam lines individually. The complete process of beam generation is schematically depicted in Figure 8.2 and explained in the following.

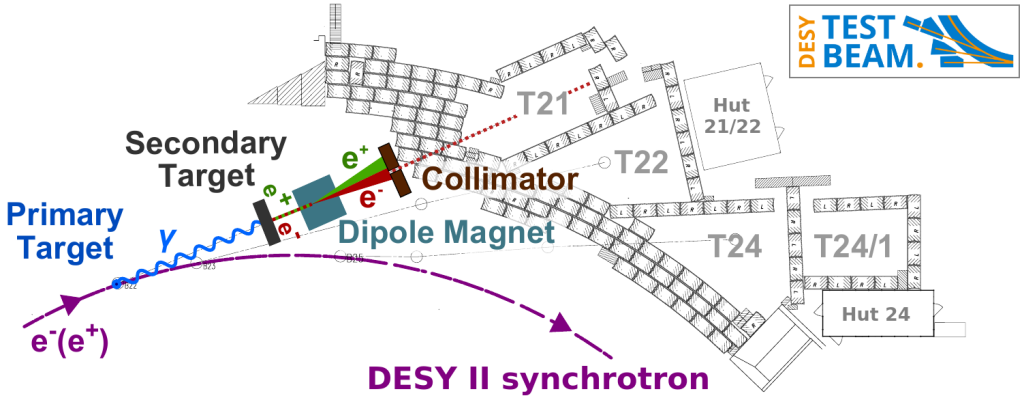

Figure 8.2: Schematical view of the beam generation at the DESY II Test Beam Facility, exemplified by the depicted steps for beam line TB21. By inserting a fiber target as primary target into the beam trajectory of the DESY II synchrotron, bremsstrahlung photons are created and travel tangentially off. At the secondary target, the photons are converted into electron-positron pairs and their momentum (up to 6 GeV/c) and charge can be selected by the dipole magnet behind. The final collimation of the particle beam happens before and in the test beam areas by steerable lead collimators. Modified from [208].

In the first conversion step, a carbon fiber with a diameter of only 7 µm as primary target can be moved into the particle trajectory of the DESY II synchrotron (cf. Fig. 8.3a). A small fraction of electrons are stopped at the inserted target and bremsstrahlung is emitted. The energy spectrum of the bremsstrahlung photons ranges up to 6.3 GeV as the maximum DESY II beam energy. Due to the movable system of fiber targets, it is possible to allow synchrotron operation with and without bremsstrahlung emission as well as to optimize the fiber position within the beam orbit for maximizing the conversion rate.
The emitted photons are extracted tangentially from the beam pipe through a 500 µm thin aluminum window. After travelling several meters through air in the extraction tunnel, they hit the secondary target consisting of copper or aluminum plates with different thicknesses (cf. Fig. 8.3b). Here, the second conversion step happens, as a large fraction of bremsstrahlung photons are converted by pair production into electron-positron pairs. The particles' momenta are ranging again up to the initial electron beam momentum.
After the secondary target, the electrons and positrons are in a high vacuum beam line and pass through a dipole magnet (cf. Figure 8.3b). The magnetic field allows the selection of the particle flavor and momentum depending on the polarity and strength of the field, as only particles within the selection range can pass into the extraction pipe.
For collimation of the particle beam, a primary collimator consisting of movable tungsten jaws allows to constrain the beam size in the horizontal and vertical plane independently and further limit the momentum acceptance (cf. Fig. 8.3c). The beam enters the experimental area through the beam shutter system and can be also shaped by an exchangeable secondary collimator consisting of lead blocks with fixed-size openings (cf. Fig. 8.3d).

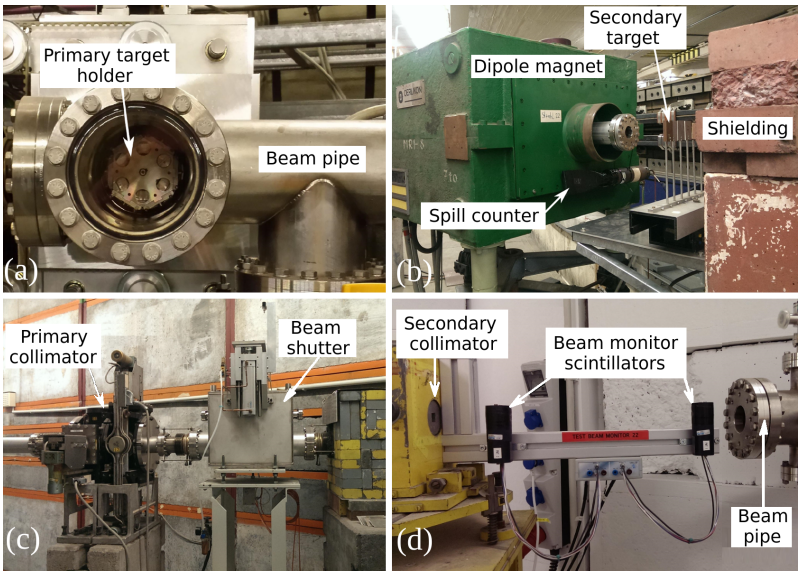

Figure 8.3: The components of the DESY II test beam generation. Thin carbon fibers as primary target are inserted into the beam pipe by a movable revolver to create bremsstrahlung photons (a). Photons are hitting then selectable metal plates as secondary target and pair-produced electrons/positrons pass the dipole magnet for selection on charge and momentum, while measuring the photon background rate by spill counters (b). First collimation of the beam by movable primary collimator system and passing of beam shutter system before entrance to test beam area (c). Finally, scintillators are measuring the particle rate and a secondary collimator with lead inserts is passed (d). Modified from [208].

For beam monitoring purposes, a measurement of the background radiation accompanying the photon beam after production and after the conversion at the secondary target is conducted by spill counters. Furthermore, a beam monitor consisting of two scintillators read out by PMTs inside the test beam area is employed.
The test beam users can control some of the parameters of the beam generation process, which leads to an influence on the beam properties such as particle rate, beam shape, particle momentum and momentum spread which is discussed in detail in Section 8.5.

8.1.2 Infrastructure

The users of the DESY II Test Beam Facility have access to further equipment and infrastructure for conducting their experiments. A complete overview of the available infrastructure is given in [208], but the used equipment for the measurements in this work is summarized in the following.
The operation of the test beam experiment during activated beam happens remotely from the test beam huts, which offer all user controls for the corresponding beam line and provide network connectivity. Moreover, each area has several sets of patch panels providing electrical connectivity usable for transmission of low voltage, high voltage and signals. For placing additional devices or test objects in the beam area, remote-controllable stages can be installed. Finally, a laser alignment system is employed using two line lasers allowing to align the users' devices with the beam axis in the horizontal and vertical plane.

This common infrastructure for all test beam areas is expanded by unique infrastructure for the individual beam lines, like gas systems, slow control units, test magnets and pixel beam telescopes. The beam lines TB21 and TB22 are permanently equipped with the EUDET-type pixel telescopes DATURA and DURANTA, offering very precise tracking systems for the test beam experiments. A detailed explanation of the telescopes as well as their performance will be presented in Section 8.2.
Furthermore, the beam line TB21 houses a normal conducting dipole magnet (called BRM) with a maximum magnetic field of 1.335 T and TB24/1 is equipped with a superconducting solenoid magnet (called PCMAG) with fields up to 1.25 T.
A lead-glass counter as calorimeter is also available to be installed after the experimental setup. Here, the energy of the beam particles can be measured within the constrained time and energy resolution of the calorimeter, as discussed in Section 8.5.3.

8.2 EUDET-Type Beam Telescopes

The EUDET-type beam telescopes are pixel telescopes originally developed and constructed within the Integrated Infrastructure Initiative by the EU in the EUDET project [211] with the goal to provide a high-resolution pixel beam telescope for test beam studies. Driven by the user community and the successive EU-funded projects AIDA and AIDA2020 [212], the development is still progressing and has resulted in a whole family of EUDET-type beam telescopes at different test beam facilities worldwide, as summarized in Table 8.1.

Name	Constructed	Operation Site
AIDA	2009/10	H6B/SPS, CERN
ANEMOME	2011	ELSA, Bonn
ACONITE	2012	H6A/SPS, CERN
DATURA	2012	TB21, DESY
CALADIUM	2013	ESA, SLAC
DURANTA	2015	TB22, DESY
AZALEA	2016	TB24, DESY

Table 8.1: Overview of EUDET-type beam telescopes operated in worldwide located test beam facilities, taken from [213].

Each of the EUDET-type beam telescopes consists of the following components:

- a set of six pixelated tracking detector planes equipped with 18.4 µm fine-pitch MIMOSA26 silicon sensors,
- the mechanics to position the detector planes and one or more **D**etector **U**nder **T**est (DUT) planes precisely in the particle beam,
- a scintillator trigger system and a common **T**rigger **L**ogic **U**nit (TLU),
- additional hardware for data acquisition.

Due to their high pointing resolution of $\sim 2\,\mu m$) and with capable event rate of $\sim 2\,kHz$ at the DESY II Test Beam Facility, the telescopes are used as tracking devices, mostly as a reference system for a DUT. The detector planes of the telescopes are arranged in an up- and downstream telescope arm with the DUT placed in between. In this case, the telescope provides precise spatial information on the incidence positions of the particles at the DUT.

For this work, measurements with the telescopes DATURA and DURANTA at the beam lines TB21 and TB22, respectively, were performed. The DATURA telescope is shown in Figure 8.4. In the following, the different components of the EUDET-type telescopes are introduced. More details about the hard- and software as well as the telescope performance can be found in [213, 214] with some of the performance results to be discussed in Section 8.5.

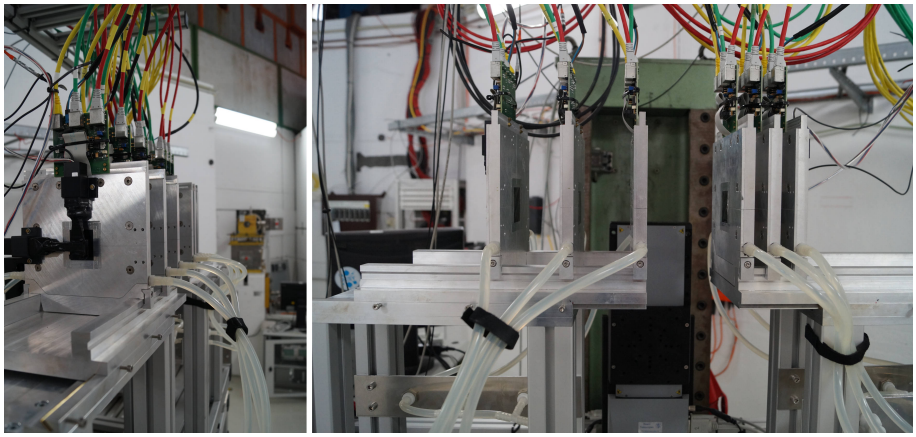

Figure 8.4: The EUDET-type beam telescope DURANTA in beam line TB22 at the DESY II Test Beam Facility. Six MIMOSA26 pixel sensor planes are mounted in water-cooled aluminium jigs with their readout electronic boards attached on the top and placed on the two movable holder arms, the upstream and downstream telescope arm. Two trigger systems each consisting of two crossed scintillators are mounted in front and behind the telescope planes.

In the following, the sensors and mechanical support structure for the EUDET-type beam telescopes is introduced in Section 8.2.1, followed by the description of the trigger and DAQ system in Section 8.2.2 and concluded in Section 8.2.3 with the integration of the user's DUT into the telescope setup.

8.2.1 Telescope sensors and mechanics

The sensor planes for the EUDET-type beam telescopes are the MIMOSA26 monolithic active pixel sensors [215, 216]. They are produced in the AMS 350 nm CMOS technology and are populated by an 1152×576 array of quadratic pixels with a pitch of 18.4 µm. The active area covered is 21.2 mm × 10.6 mm while the thickness is only 50 µm. The charge collection of free charge carriers created in the 20 µm high resistivity epitaxial layer is dominated by diffusion processes, as the sensor is mostly undepleted. The binary resolution of 5.3 µm is enhanced due to charge sharing effects, resulting in intrinsic sensor resolutions of down to $\sigma_{x,y} = 3.24\,\mu m$ [214]. The readout of the MIMOSA26 sensor is realized in a continuous rolling-shutter mode with a zero suppression on-chip. At the given clock frequency of 80 MHz, the integration time is about 115 µs. The sensor threshold can be programmed per plane as integer multiples of ξ_n of the RMS noise of that plane[51].
The MIMOSA26 sensor, as pictured in Figure 8.5, is mounted onto electronic boards for readout and power supply and then placed into an aluminium jig. Inside the jig, a water cooling loop provides stable temperatures during operation. The active area of the sensor is accessible by a beam window covered with light-tight Kapton foils of 25 µm thickness.

[51] The readout chip has actually four independent regions with thresholds and the average noise occupancy per pixel and readout frame for a threshold of $\xi_n = 6$ is about $6 \cdot 10^{-5}$, when measured at room temperature [216].

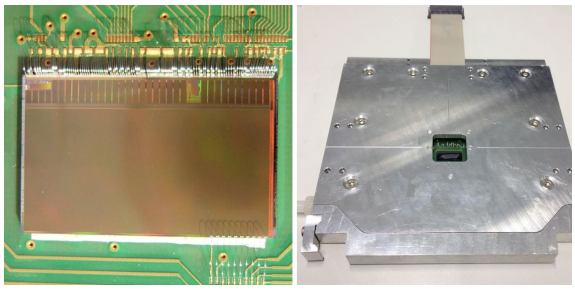

Figure 8.5: The MIMOSA26 monolithic active pixel sensor as used for a detector plane in the EUDET-type beam telescopes, with the silicon sensor wire-bonded on a readout PCB (left) and then mounted into a water cooled aluminum jig (right). Taken from [213].

Three such sensor planes are normally mounted together on a rail system as one upstream and one downstream arm of the telescope. The position of each plane can be changed along the beam direction, but is rather fixed in the lateral direction. The sensor planes itself were optimized for the moderate beam energies at the DESY II Test Beam Facility, thus the amount of material is minimized to reduce the influence of multiple scattering on the particle trajectory. With the silicon sensor covered by the two layers of Kapton, the resulting material budget is only $\epsilon_{\text{M26}} = 7.1 \cdot 10^{-4}$ per telescope plane[52].

A general telescope setup for the EUDET-type beam telescopes can be described in terms of plane numbering (i), plane positions (z_i) and materials (ϵ_i) as shown in Figure 8.6. The minimal distance between planes is an equidistant distance of $dz = 20\,\text{mm}$ due to the jig thickness, whereas the maximal distance is constrained to $dz = 150\,\text{mm}$ by the rail system.

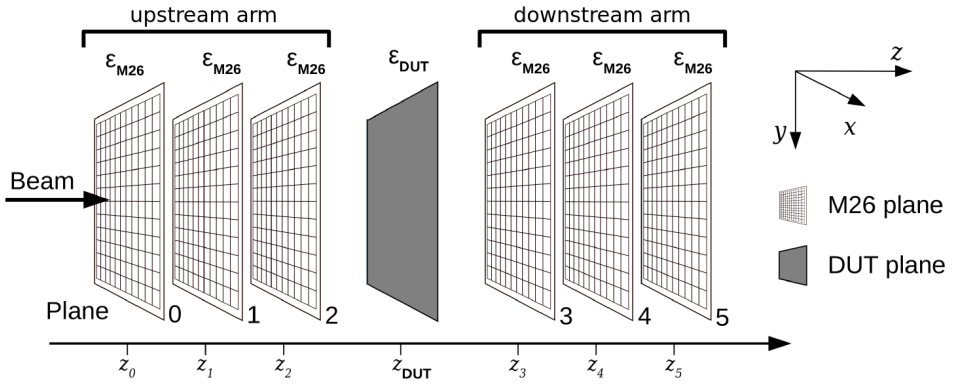

Figure 8.6: Sketch of the standard setup of the EUDET-type beam telescope. The MIMOSA26 sensor planes are numbered from 0-5 at positions z_0-z_5 with a material budget of ϵ_{M26} and arranged as up- and downstream telescope arm, surrounding the DUT at z_{DUT} with ϵ_{DUT}. Modified from [214].

8.2.2 Trigger and data acquisition system

A key component of the EUDET-type beam telescope is the **T**rigger **L**ogic **U**nit (TLU) [217, 218]. The TLU is the hardware interface integrating different devices for the synchronized readout in the common DAQ system such as the MIMOSA26 sensor planes of the telescope and the users' DUT. As communication channel, a RJ45 connector with four LVDS pairs transmitting the trigger clock, a busy and reset signal, and the trigger signal to the connected devices is used. As no common and stable clock cycle from the test beam generation is available, the telescope is triggered by a scintillator system.

[52] With values of $X_0^{\text{Silicon}} = 93.65\,\text{mm}$ and $X_0^{\text{Kapton}} = 285.6\,\text{mm}$ and the corresponding thicknesses of 50 µm.

In total four trigger units, each consisting of a scintillator with lightguide connected to a **P**hoto **M**ultiplier **T**ube (PMT), are used for particle triggering. They are mounted as doublets forming a cross with an overlapping area of about $20 \times 10\,\mathrm{mm}^2$, corresponding to the MIMOSA26 active sensor area, and are placed in front of the upstream telescope arm and behind the last sensor plane of the downstream arm. The PMTs for the scintillators are powered with low-voltage via the TLU and the output signals are processed internally with a discriminator and coincidence unit. A coincidence signal, defined by the user as bit mask of the four individual scintillator signals, is used as the particle trigger signal in the data taking and distributed to the connected devices. Moreover, the TLU accepts busy signals from the DAQs of connected devices which results in a veto for subsequent triggers as long as the busy signal persists. Different handshake modes exist to allow the user a defined triggering scheme and a synchronized readout of the telescope and the users' DUT.

The DAQ system is controlled via two DAQ PCs, the National Instruments *NI PC* and the Linux-based *RunControl PC*. On the one hand, the NI PC is used for the DAQ of the MIMOSA26 sensors: the sensors can be configured via JTAG files, the data taking can be started via a LabView program and finally the data is transmitted using NI-standards. On the other hand, on the RunControl PC the DAQ software, for this work the EUDAQ software (cf. Sec. 8.3), is running and can be controlled and configured by the user.

8.2.3 Integration of DUT

The purpose of a test beam measurement in most cases is the characterization of a users' device, called **D**etector **U**nder **T**est (DUT). Depending on the character of the DUT, different integration steps have to be fulfilled. If the DUT is a passive sample, a **S**catterer **U**nder **T**est (SUT), it has to be only mounted mechanically inside the telescope for characterization. But if the DUT is an active device producing signals, such as another silicon sensor, it should also be integrated in the DAQ system.

For the mechanical integration, high-precision 2D translation stages for a remote movement in x- and y-direction of the DUT between the telescope arms as well as a rotation stage can be used[53]. The stages can be steered via a standalone program on the NI PC or automatically by an implementation into the DAQ software (cf. Sec. 8.3.3).

Furthermore, the flexible rail system of the EUDET-type beam telescopes allows to change the distance between the up- and downstream arm of the telescope to insert larger DUTs. The MIMOSA26 sensors themselves can be also moved which allows to optimize the geometry in terms of plane distances and hence the resolution of the telescope track as a reference.
The figure of merit in this context is the pointing resolution, defining the resulting uncertainty on the interpolated position of incidence at the DUT position reconstructed from the particle hits in the MIMOSA26 sensor planes. This quantity can be influenced by changing the spacing in the z-direction of the telescope planes. In general, the optimal configuration of the telescope depends strongly on the material budget of the inserted DUT, previously denoted ϵ_{DUT}, and the distance between DUT and the telescope arms. The user can study the performance of the planned setup beforehand, by using the GBL Track Resolution Calculator [219], which calculates the theoretically expected performance parameters for a given telescope geometry, as will be discussed in Section 8.5.

[53] The available $xy\phi$-stages from Physik Instrumente (PI) provide 0.1 µm precision along 102 mm (type M-511.DD1) and 204 mm (type M-521.DD1) translation and 50 µrad for 2π rotations (type M-060.DG) [213].

8.3 Data Acquisition with EUDAQ

The data acquisition software EUDAQ is used for the DAQ of the EUDET-type beam telescopes and was developed together with the hardware, the telescope and the TLU, to provide appropriate software for the data acquisition at test beam environments. Due to its generic design, EUDAQ can be also used for the DAQ of completely different setups, whereas the focus here will be on the application for the EUDET-type beam telescopes. By now, two different versions of EUDAQ [220] are available:

- EUDAQ1 [221] as DAQ software for the operation in the so-called EUDET-mode, meaning one trigger creates one event corresponding to one sub-detector frame;
- EUDAQ2 [222] for running the data acquisition additionally in the so-called AIDA-mode, meaning the possibility to have multiple triggers in one sub-detector frame, requiring the upgraded AIDA-TLU [223].

The newer EUDAQ2 enables asynchronous data taking and offline event building by trigger IDs for synchronization, allowing therefore higher trigger rates compared to EUDAQ1. This is possible due to the circumvention of the limiting factor of the rather slow integration time of the MIMOSA26 sensors. For the conducted testbeam campaigns in this work, the telescope was operated with both versions having only minor implications for data taking.

In the following, the framework architecture with its main components is described in Section 8.3.1 and the operation principle of EUDAQ1 is presented in Section 8.3.2. Moreover, Section 8.3.3 introduces the implementation of an automatized DUT movement with the translation and rotation stages in EUDAQ.

8.3.1 Framework architecture

EUDAQ is a generic DAQ software framework with the goal to simplify the process of integration of devices in the common DAQ system. As such, it is written in C++, supports the most common platforms (i.e. Linux and Windows) and is designed in a modular fashion to provide a high level of interoperability.

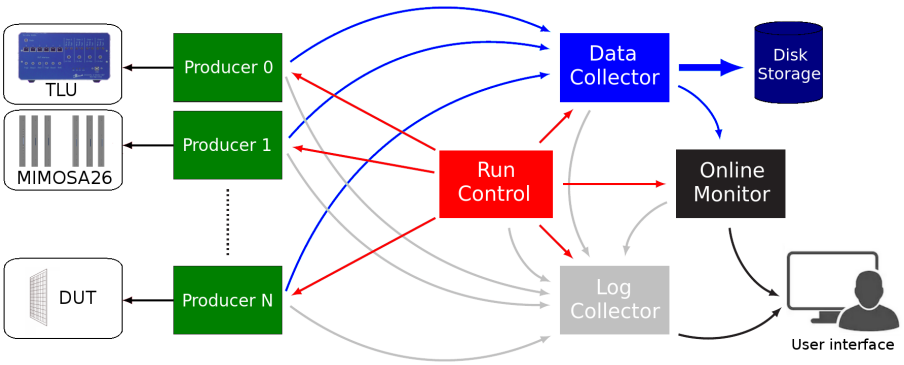

Figure 8.7: A general overview of the EUDAQ framework depicting its core components and the data flow. The individual communication channels are the *control* (red), the *data* (blue) and the *log* (grey) channel. The *producers* (green) are often the interface to the connected devices in the DAQ system, here exemplary as TLU, MIMOSA26 sensors and a DUT. For the user interface, the *Online Monitor* (darkgrey) can be used. Modified from [221].

The EUDAQ framework is divided into different processes, which usually run on several different computers connected via LAN and communicating using TCP/IP. The communication to the individual processes, corresponding often to the connected devices, is established via three separate channels: the command, the data and the log channel. Moreover, an online monitoring tool is also part of the software framework. A general overview of the EUDAQ framework is depicted in Figure 8.7.

The main user interface of EUDAQ is the central *Run Control*. It initializes and configures the connected components, sends commands for start and stop a run, and finally monitors the state of all other processes. Here, a run is a continuous period of data taking, typically with durations of a few minutes to several hours. The run is made of single events, representing the data collected from all included devices after a trigger signal.

A process inside the DAQ system producing data is represented in EUDAQ by a *producer*. A producer is implemented as a standardized interface for receiving commands and sending data and log messages. Furthermore, for every trigger a producer should send one event consisting of a standard header (run number, trigger number and status information) and the unprocessed raw data from the connected device, e.g. raw hit information of a tracking plane. To register the start and end of a run, special beginning-of-run (BORE) and end-of-run (EORE) events are attached. Due to the strong synchronization of events enabled by the trigger hardware design, a high degree of data integrity is ensured.

The data-generating processes represented by the producers transmit their data to the central *Data Collector*, where each data package per producer per trigger is collected and organized to built synchronized and ordered events. The merged data corresponding to a single trigger decision is then stored to disk. By default, the data are just the serialized event objects, consisting of a common header and the raw binary data provided by the connected devices, without any data interpretation or type formating.
The *Log Collector* stores all the incoming log and status messages of the connected producers and allows the user to monitor all distributed processes for any unexpected warnings or errors in a central location.

Finally, the *Online Monitor* as an optional tool in the EUDAQ framework reads the output data file and automatically generates a set of data quality plots to be monitored by the user. For example, hit maps per connected sensor plane or correlations between different telescope planes are a helpful input to verify if the system operates properly.
To allow for the later offline analysis, an interpretation of data as usually written to disk in the device's native format is needed. The *DataConverterPlugin* within EUDAQ was developed for this purpose, so that for a specific device a corresponding converter plugin can be used to convert the native raw data into a format which can be parsed externally.

8.3.2 Operation principle

The EUDAQ software already contains a number of often used producers, such as the EUDET-type beam telescope with its MIMOSA26 sensors and a TLU is integrated as producers into EUDAQ. Here, the *NIProducer* provides the interface to the MIMOSA26 DAQ and the *TLUProducer* connects via USB to the TLU hardware. Moreover, appropriate data converter plugins are provided for data interpretation.

For the operation of a DUT, the architecture of EUDAQ allows for a quick integration of the DUT's specific DAQ systems into EUDAQ. Each connected device is represented by a producer for receiving commands from the Run Control and to send the acquired data to the Data Collector. The user can implement the DUT by deriving from a C++ producer base class and following the documentation with several examples.

EUDAQ is started via the provided start-up scripts, opening the Run Control GUI and the core components of Data and Log Collector. Additionally, a selection of specific producers can be connected by TCP/IP connections to the Run Control as well as the Online Monitor. The user can now initialize and configure the connected components with loadable initialization and configuration files. After the successful configuration, the data taking can be started and events per trigger are built. Finally, the data taking for the specific run ca be stopped via the Run Control GUI.
The appearance of a started EUDAQ session for data taking with a EUDET-type beam telescope is shown in Figure 8.8, where the Run Control GUI for interaction with the DAQ system, the Log Collector for listing all messages reported within the system, and the Online Monitor for data quality monitoring are displayed in separate windows.

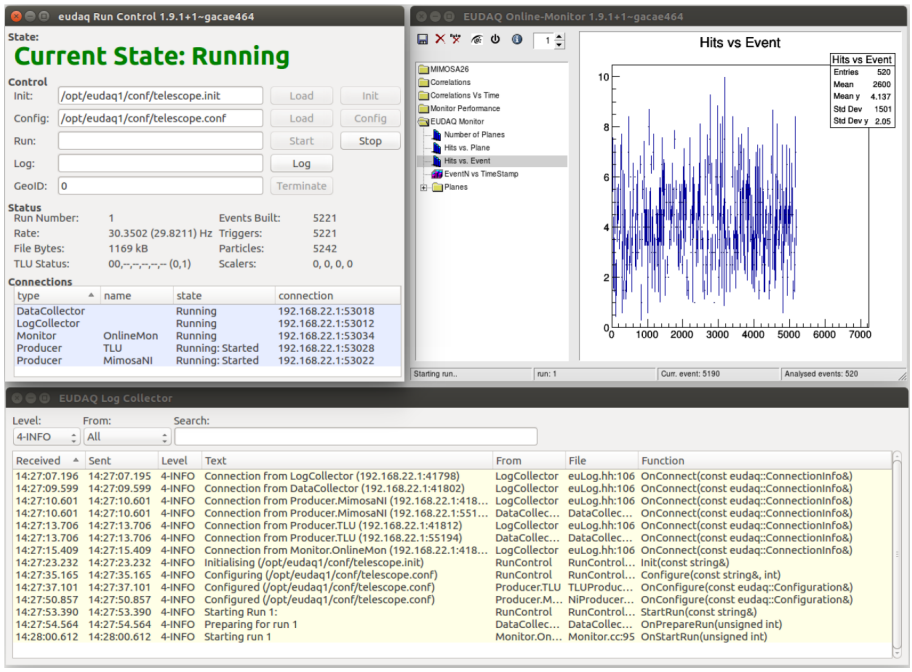

Figure 8.8: Operation of EUDAQ after a standard start-up for running the EUDET-type telescopes with five connected EUDAQ components. The windows of *Run Control* (upper left), *Online Monitor* (upper right) and *Log Collector* (lower) are displayed. Taken from [221].

8.3.3 Implementation of automated DUT movement

For test beam campaigns, a reliable and stable DAQ system with minimal intervention by the operators is highly desirable. In case of an active DUT, this is often not possible when a novel sensor is characterized which itself has unstable operation conditions or suffers from randomly occurring readout problems. On the contrary, in the case of a passive object like a SUT, often long data taking runs are required to get a sufficient amount of data.

Here, a reliable DAQ system such as it was proven to be EUDAQ as well as an automated data taking can ease the test beam operation. Within this thesis, the automated movement of the translation and rotation stages for the DUT integration was implemented in EUDAQ1. The controller of the motor stages was integrated as a *Slow Producer* in the EUDAQ framework. A Slow Producer is an alternative base class of a Producer, which can be used to integrate devices that generate data much less frequently or even triggerless. In this case, the Data Collector is not waiting for a data stream of the Slow Producer in contrast to a Producer. Other examples apart from the motor stages are all kinds of environment monitors, e.g. temperature logging.

The *PIController* is the implemented EUDAQ slow producer, using a wrapper class for the communication with the hardware controller. In the initialization step, the controller host as well as up to four connected linear or rotational stages have be to specified. During the configuration step, the commands for a movement of the stages is sent to the hardware and the resulting position is sent back to the Log Collector. During normal data taking for the other devices, the *PIController* is not sending any data.

Movements of the motor stages can be automatized by the user in two different ways: on the one hand, the user can specify one-dimensional movements by defining the start position, the increment per step as well as the number of steps in the configuration file; on the other hand, arbitrary movements, also in more than one direction, can be programmed by multiple configuration files for the respective coordinates. This is possible by exploiting the EUDAQ option *NextConfigFileOnFileLimit* which loads the subsequent configuration file automatically after completion of a run.

This feature allows the user a fully automated data taking as well as the possibility to record data of the SUT of even larger areas than the active area of the MIMOSA26 sensors, which were key ingredients for the results presented in Chapter 9.

8.4 Data Analysis with EUTelescope

For the reconstruction and analysis of test beam data recorded with the EUDET-type Beam Telescopes, the EUTelescope framework [224, 225] can be used. This software framework provides dedicated tools and processing steps for the reconstruction of raw event data from detector planes (e.g. taken with EUDAQ) to the final, reconstructed particle tracks. It was originally developed to allow data analysis for the constructed EUDET-type beam telescopes, but it also allows the integration of data analysis from any position-sensitive detector in a wide range of geometric arrangements. Other available custom reconstruction frameworks, such as Judith [226], Proteus [227] or TBSW [228], are serving the same purposes, but are often designed for specific use cases in terms of geometry, sensor choice and analysis flow. In contrast, the design of EUTelescope (and also Corryvreckan [229]) follows a modular, flexible and generic approach covering a broader range of use cases.

Firstly, the framework architecture and its dependency to external software packages is explained in Section 8.4.1, followed by the introduction of the operation principle of EUTelescope in Section 8.4.2. Thereafter, the different steps of the typical reconstruction flow from raw data events to reconstructed particle tracks are shown in Section 8.4.3. Finally, in Section 8.4.4 the implementation of the **G**eneral **B**roken **L**ines (GBL) algorithm for track reconstruction is discussed. For this work, the newest version (v2.0) of EUTelescope is used, whose features are described in more detail in [224].

8.4.1 Framework architecture

EUTelescope is designed as a modular, comprehensive and versatile framework and is composed of independent processors as well as core functionality written in C++.
The framework uses parts of the ILCSoft package [230], a software collection provided by the Linear Collider community, and is linked to a set of external software packages, as described in the following.

Marlin

Marlin [231] offers a modular application framework and is used for the coordination of EUTelescope processors applied consecutively in the data analysis. As back-end component, Marlin provides the entry point for the execution of EUTelescope processors and is responsible for the interface to the data and geometry description. For the configuration of the execution order of processors as well as the passing of parameters an XML-based steering file is used. Each processor implements a set of callback functions to allow for initialization, processing of data via an event-loop and finalization.

LCIO

The LCIO framework [232, 233] serves as underlying persistence framework and event data model in EUTelescope and is used for storing data objects for intermediate analysis results. Because of various implementations and interfaces of LCIO (C++, Java, Fortran and Python), a translation of data into the LCIO format and backwards for external analysis is available. The inherent data format is event-based and each event consists of LCIO collections storing various objects, e.g. raw pixel indices, clustered pixels or derived hit positions in the case of a beam telescope analysis. Moreover, objects can be linked to other objects within the same event (e.g. a hit can be linked to its pixel hits), whereas links between different events are not allowed. The conversion of raw data into the LCIO format can be done either inside the EUTelescope framework for EUDAQ1 data with a dedicated plug-in or by an external converter as for EUDAQ2 data.

GEAR

The GEAR toolkit [234] describes the geometry in EUTelescope by providing an abstract interface for the geometry description, e.g. to describe the beam telescope setup in terms of materials, thicknesses, read-out pitch sizes, and channel numbers. The initial conditions of the geometrical setup (e.g. plane positions and alignment constants) are parsed via an XML-file. This GEAR file can be updated by the execution of processors in the analysis, e.g. performing a telescope alignment resulting in an aligned GEAR file with updated alignment constants. Moreover, any material, either an active sensor plane or passive materials (such as shielding or cooling equipment), can be described in the GEAR file, so that it is taken into account in the reconstruction.

ILCINSTALL

The ILCINSTALL package [235] is used for the installation of EUTelescope and establishes the required dependencies to other software packages. During this work, the installation of EUTelescope [236] onto different machines (namely, on a local machine, the DESY NAF computing cluster [237] and the CERN LXPLUS computing cluster [238]) was simplified and the dependencies to external packages were reviewed. Moreover, for tutorials to new EUTelescope users, the functionality of Docker images [239] was exploited.

External packages

The functionality of EUTelescope is extended by interfaces to external packages, especially for detector alignment, track modelling, and data analysis and presentation, as follows:

- The Eigen3 library [240] is used for linear algebra calculations in the alignment.
- The ROOT package [241] enhances the functionality and usability of geometry description on top of GEAR by its own geometry package, and also provides plotting and data visualization tools.
- The MillepedeII package [242, 243] is used for the detector alignment by performing a least-squares fit with global and local parameters, describing the setup for the track-based alignment procedure.
- The GBL track model [244, 245, 246] is used for re-fitting the track, taking into account the effect of multiple scattering on the particles.

The general integration scheme of the EUTelescope framework into the ILCSoft package as described before is summarized in Figure 8.9.

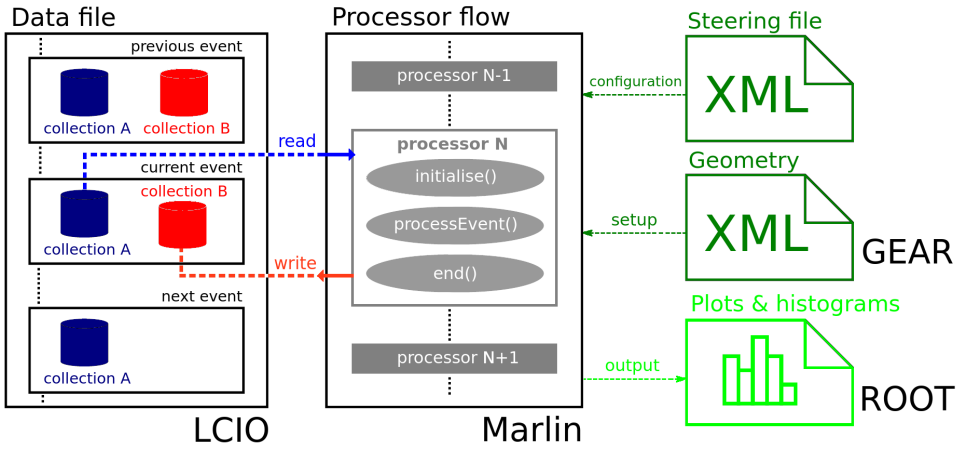

Figure 8.9: Integration scheme of the EUTelescope framework into the ILCSoft package. Marlin executes a series of processors, configured by an XML-style steering file and with a specified GEAR geometry file, handles the read- and write-operations on LCIO data and produces ROOT outputs.

8.4.2 Operation principle

The operation principle of EUTelescope is based on the consecutive application of processors, where a set of processors is typically clustered to perform a certain step in the reconstruction chain. Due to the factorization of tasks into single processors, code duplication is efficiently avoided and a high flexibility in terms of the application order is gained in EUTelescope.

A processor acts via the underlying Marlin interface on an input dataset with detector data provided in the LCIO format, reads its configuration and parameter settings from the corresponding steering file, and interacts with the geometry provided by a GEAR file. After processing the data, a processor can write new data collections or configuration databases into LCIO files and can update the geometry file in the GEAR format.

For monitoring the function of a processor, graphs and histograms with key figures of the processor's task can be written in ROOT files and log files are created. The interactions of a EUTelescope processor are summarized in Figure 8.10.

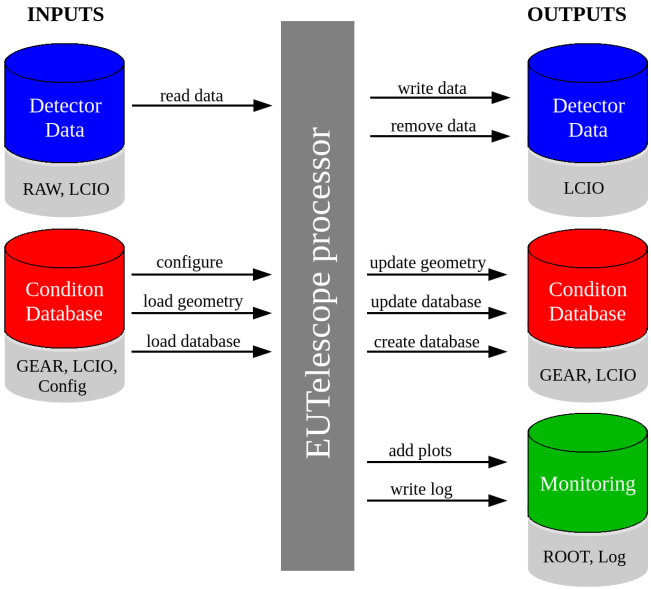

Figure 8.10: The operational principle of a EUTelescope processor with inputs and outputs. Detector data in format of RAW and LCIO is processed depending on inputs by condition databases as configuration files, GEAR geometry and databases. As output, data can be written or removed, databases can be created or updated, the geometry can be updated and also monitoring plots and log files are created.

With the used LCIO format in EUTelescope, the detector data is stored in events, where an event is defined by the subset of data belonging to a physical particle passage that triggered the DAQ system and is stored per detector in a numbered container. Typically, a number of consecutive events are clustered into runs characterized by a run number and represent a physical data-taking period with unchanged configurations in terms of beam and telescope settings.

A set of processors clustered to a specific reconstruction task can be applied to the data of a run by using the *jobsub* tool. The *jobsub* command automatically fills the configuration parameters specified by the user into the steering file, which specifies the type and order of processors to be applied. Then, it executes the task by calling the Marlin interface with the corresponding input data as specified by the given run number. Moreover, a number of options can be given to the *jobsub* tool. One example is the execution of the EUTelescope job on a batch cluster. For this work, the job submission to a batch cluster operated with HTCondor [141], e.g. on the DESY NAF computing cluster, was implemented.

8.4.3 Reconstruction flow

The typical reconstruction flow for the analysis of test beam data taken with the EUDET-type beam telescopes is illustrated in Figure 8.11. The individual reconstruction steps are explained in the following and accompanied by examples of ROOT output plots for processor monitoring taken from the analysis of a bare telescope setup with the DURANTA beam telescope at a beam momentum of 4 GeV/c.

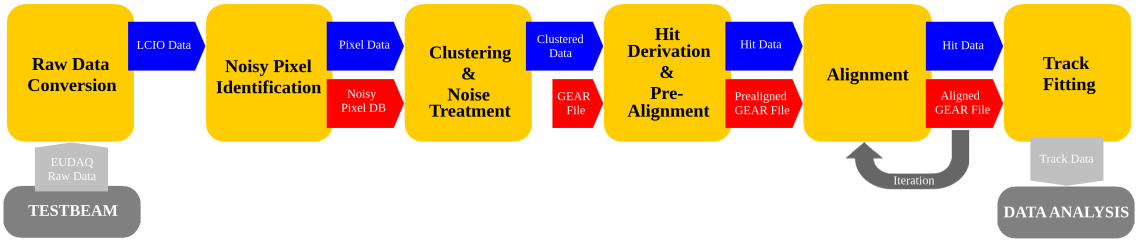

Figure 8.11: The reconstruction flow in EUTelescope for a typical test beam reconstruction with the EUDET-type beam telescope.

Raw data conversion

The initial step of the reconstruction flow is the conversion of the test beam data from the native format of the DAQ system to the corresponding LCIO format. For data acquired with the EUDAQ1 framework, the EUTelescope processor, *EUTelNativeReader*, is used. Contrary, the conversion of data acquired with the EUDAQ2 framework is performed externally with the *euCliConverter* plug-in prior to the data analysis in EUTelescope.

Noisy pixel identification

The next step is dedicated to identifying and marking noisy pixels in a conditions database usable for any subsequent noise treatment. Noisy or hot pixels are detector pixels, which are not induced by physical hits of particles and are firing rather constantly. Therefore, by counting the firing rate of all pixels and applying a threshold hot pixels can be identified. This threshold depends on beam properties like rate, intensity and shape and can be tuned by the user. The *EUTelNoisyPixelFinder* creates occupancy maps of the various sensor planes and noisy pixels defined by a criterion on the hit frequency are written to the noisy pixel database as a LCIO file.
For monitoring the noise behaviour, histograms showing the frequency distribution of firing pixels as well as maps for the spatial distribution of the noisy pixels on each sensor are created. In Figure 8.12a, the firing frequency of all pixels and for each of the six planes is shown. The occupancy cut to select noisy pixels is typically 0.1% and the resulting noisy pixel map showing the spatial distribution along x and y pixel indices for one selected plane is displayed in Figure 8.12b. Here, a strip of noisy pixels around a pixel index y of 300 can be observed, which should be masked or removed for the further reconstruction.

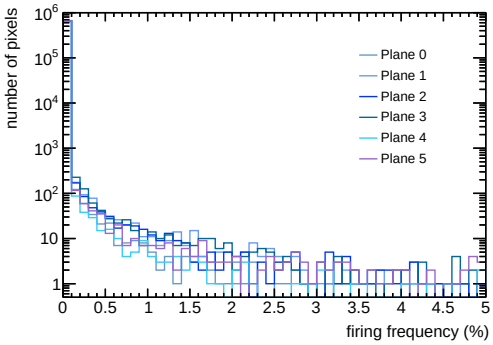

(a) Firing frequency distribution.

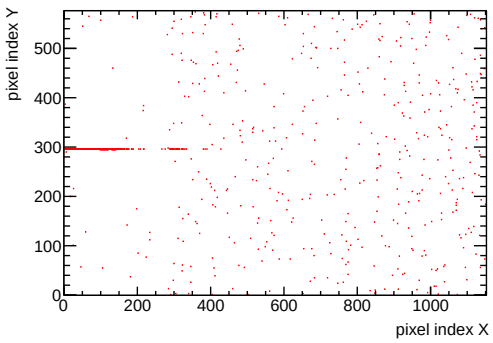

(b) Noisy pixel map.

Figure 8.12: Monitoring plots for the noisy pixel identification. Shown are the occupancy distributions for each plane in % for all pixels (a) and the spatial distribution of identified noisy pixels for one selected plane (b).

Clustering and noise treatment

In the clustering step, adjacent pixel hits are grouped into clusters, because a particle traversing a sensor plane usually causes a signal in more than one pixel due to the effect of charge sharing. Different clustering algorithms to deal with binary and non-binary read-out as well as equidistant and non-equidistant geometries are implemented.
The *EUTelSparseClustering* processor is designed for zero-suppressed hits in an equidistant pattern and based on the calculation of a distance parameter by the pixel indices[54]. Depending on the configurable distance parameter, pixels touching at least at an edge, at a corner (default case) or even further away are grouped together. After cluster building, clusters containing pixels listed in the noisy pixel database are masked by the *EUTelNoisyClusterMasker* processor and finally removed from the output LCIO collection using the *EUTelNoisyClusterRemover* processor.
For monitoring the clustering operation, hit maps of clusters for each sensor plane as well as the associated cluster sizes are plotted. In Figure 8.13a, the number of clusters built for each plane as function of the cluster size is displayed. The minimum number of pixels in a cluster is equal to one and the majority of clusters have a size of one or two, which depends on the chosen noise threshold for the MIMOSA26 sensors. The corresponding cluster hit map for one selected plane is shown in Figure 8.13b with a uniform density of cluster hits over the full active detection area exposed to the particle beam.

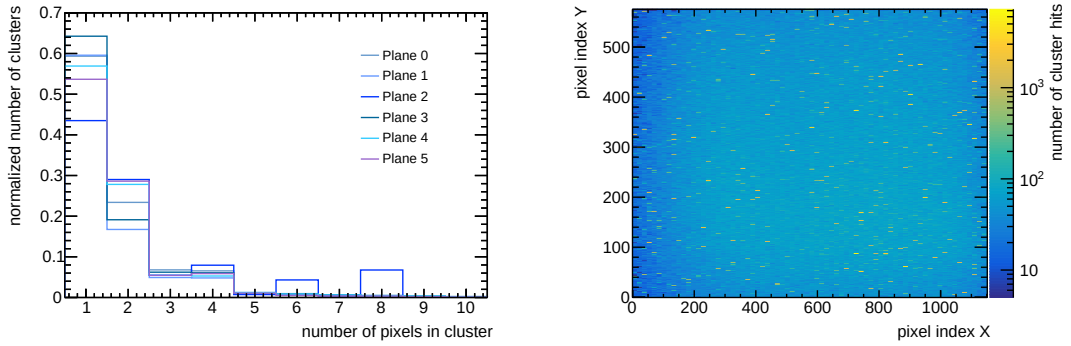

(a) Cluster size distribution. **(b)** Cluster hit map.

Figure 8.13: Monitoring plots for the clustering. Shown are the cluster size distribution for all planes (a) and the cluster hit map for one selected plane (b).

Hit derivation and pre-alignment

In the next step, the hit positions in the local frame of reference, meaning the sensor plane itself, are derived from the clusters by the *EUTelHitMaker* processor. The hit position is calculated as the charge-weighted center of gravity[55] of the pixel hits contained in that cluster and subsequently stored in a LCIO collection.
For the transformation from the local to the global frame, meaning the telescope coordinate system starting with the origin in the first telescope plane and the beam direction defining the z-axis, the geometry from the GEAR file is used in the *EUTelHitCoordinateTransformer* processor. Here, planes are rotated with Euler angles around the global ZXY axes and shifted linearly as provided by the alignment values in the GEAR file.

[54] The metric used for the distance between two pixels i,j is defined as $d_{ij} = (x_i - x_j)^2 + (y_i - y_j)^2$.
[55] The charge-weighted center of gravity as $\bar{x} = \frac{1}{Q}\Sigma_{i=0}^{N} x_i q_i$, with x_i as pixel index and q_i as charge of the i-th pixel in the cluster and $Q = \Sigma_i q_i$ as total charge, calculated for both spatial indices separately.

On the one hand, the transformed global hits are used for producing correlation plots for data quality management with the *EUTelCorrelator* processor. On the other hand, the *EUTelPreAligner* processor produces a pre-alignment with shifts of the sensors in the x- and y-direction, which is propagated to an updated GEAR file. The pre-alignment constants are determined in the following way: the spatial hit positions on the first sensor plane are extrapolated to all other detector planes assuming no beam divergence; then the difference between the extrapolated and the measured hit position per plane is calculated with a configurable cut parameter on the residual value to reduce permutation background; from the resulting residual distributions, the pre-alignment shifts can be determined as the highest bin content.
The ROOT monitoring plots in this step are two-dimensional hit correlations between detector planes before the pre-alignment from the *EUTelCorrelator* processor and the hit correlation distribution along the spatial directions from the *EUTelPreAligner* processor. In Figure 8.14a, the hit correlation between the first and second sensor plane along x is illustrated, showing a good alignment of the planes as indicated by the straight diagonal line. To evaluate the linear shifts in the pre-alignment, the hit correlation distributions from the first to all other planes is used, as it is shown for the x direction in Figure 8.14b.

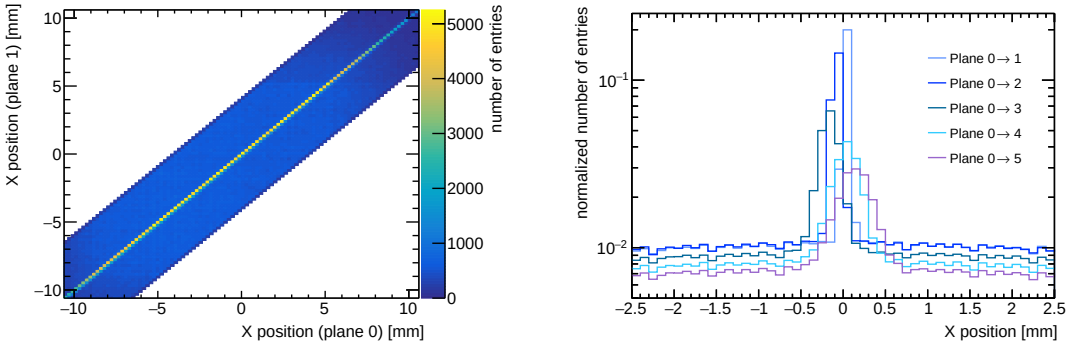

(a) Hit correlation in x.

(b) Pre-alignment shifts in x.

Figure 8.14: Monitoring plots for the pre-alignment. Shown are the hit correlation in x direction between plane 0 and plane 1 (a) and the hit correlations for all planes with respect to plane 0 used for applying linear shifts (b).

Alignment

After the pre-alignment, another alignment step for fine tuning the alignment parameters is executed, using the MillepedeII framework. For even better results, this step can be repeated in order to iteratively converge towards a final set of alignment constants.
Firstly, the stored local hits are transformed to global hits with the *EUTelHitCoordinate-Transformer* processor and using the alignment constants from the pre-aligned GEAR file. The next task is track finding and fitting and here EUTelescope offers different possibilities, but for this thesis the GBL algorithm, as explained in detail in Section 8.4.4, is used. The *EUTelGBL* processor generates a binary file with the needed parameters for an alignment with MillepedeII, containing local and global derivatives, residuals between a straight-line seed and the hits, and measurement uncertainties. These parameters depend on the chosen alignment mode, as in principle, arbitrary rotations around and shifts along the X, Y and Z axis are allowed. But in the case of the EUDET-type beam telescope, rotations around X and Y axis can be fixed due to the stable mounting of sensor planes and the z-positions as a weak mode in the alignment are measured directly from the telescope setup.

Moreover, estimates for the spatial resolution of the detector planes as well as cut values for the track finding as well as fitting procedure are given by the user. After execution of MillepedeII, the results are propagated back by the *EUTelPedeGEAR* processor and an updated GEAR file is created. Finally, for a higher precision of the alignment, this routine can be iterated, while each time loading the previously updated alignment constants from the GEAR file. A new implemented functionality in the *TripletGBLUtility* processor allows to suggest suitable track quality criteria for the next alignment iteration in order to improve the final result[56].
With the monitoring plots of the *EUTelGBL* processor, the residual distributions along the spatial coordinates for each detector plane can be compared between different iterations of the alignment. The residuals in x for all sensor planes and for three GBL alignment iterations are displayed in Figure 8.15. After the first alignment, the residual distributions for some planes exhibit sizable shifts from zero and feature a broad profile, which are indications for the necessity of further iterations. With the next iterations, the residuals of all planes are centered around zero and have similar widths, indicating a convergence of alignment parameters and reaching a well aligned telescope.

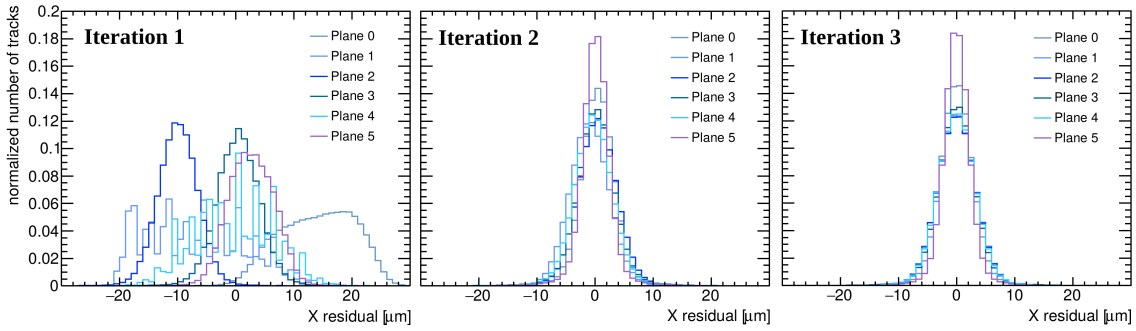

Figure 8.15: Monitoring plots for the GBL alignment steps. Shown are the residuals along the x-direction for all planes and three GBL alignment iterations.

Track fitting and analysis

The last reconstruction step performs the final track fit. For this, the final alignment constants are loaded again from the latest GEAR file by the *EUTelHitCoordinateTransformer* processor to get the global telescope hits. The fitting of the hits for the final telescope tracks can be executed by different algorithms, so for this work the *EUTelGBL* processor is used again, with the alignment mode turned off in this case. Finally, the reconstructed tracks can be exported for use in an external analysis framework, as the *EUTelGBLOutput* processors writes the tracks in the format of a ROOT n-tuple to a file. Moreover, additional information such as the stored pixel hit collections can be exported.
For monitoring the final track fitting performance, histograms showing the numbers of found upstream and downstream triplets as well as the matched tracks per event are created, as shown in Figure 8.16a. Here, on average six to eight triplets per event are reconstructed for the upstream and downstream telescope arm resulting on average in approximately five matched tracks per event. Furthermore, Figure 8.16b shows the goodness-of-fit distribution calculated as the χ^2 of the GBL track fit divided by the number of degree of freedoms in the fit model. Here, the peak of the distribution at approximately 1.0 and a mean value of 1.6 indicate a good quality in the majority of the fitted GBL tracks.

[56] Based on a Gaussian approximation of the residual distributions, cut values for track quality parameters are suggested as $\mu \pm 4\sigma$ with μ as mean and σ as width of the fitted Gaussian function.

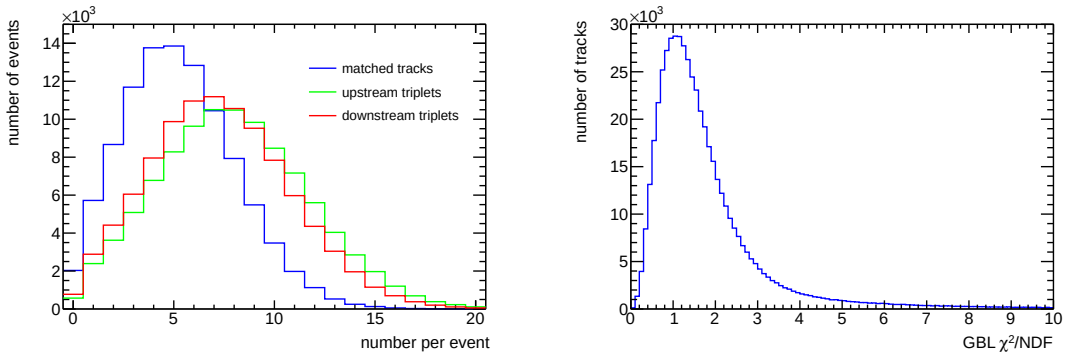

(a) Number of triplets and tracks.

(b) Goodness-of-fit.

Figure 8.16: Monitoring plots for the final GBL track fit. Shown are the numbers of found upstream and downstream triplets as well as matched tracks per event (a) and the goodness-of-fit as the χ^2/NDF of the GBL fit (b).

8.4.4 Track reconstruction with GBL

For the reconstruction of the particle trajectory from a set of measured hits in the detector, a variety of track reconstruction algorithms exists. The main task of a track reconstruction algorithm is to identify the most likely combination of hits to form a track stemming from a traversing particle through the detector planes. This is needed, e.g. in case of the EUDET-type beam telescopes, as usually a higher track multiplicity per event as well as the existence of noise hits can lead to the reconstruction of false tracks. Moreover, the used track model can differ in terms of physics processes included in the description of the particle's trajectory. In the case of test beam measurements at the DESY II Test Beam Facility with moderate beam momenta of up to 6 GeV/c, the effect of multiple scattering in the detector planes plays a crucial role to take into account for the track reconstruction.

Currently, two track reconstruction algorithms are available in the EUTelescope framework: the Deterministic Annealing Filter as an implementation of a Kálmán filter [247, 248] and the **G**eneral **B**roken **L**ines (GBL) track fitting method, which will be the focus in this thesis. Moreover, the track reconstruction with GBL is a two-step process: firstly, a track finding algorithm selects track candidates consisting of a measured hit in each sensor plane; in the second step, the identified track candidates are the input for the track fitting algorithm. The principle of track reconstruction with GBL used for a typical beam telescope setup with six sensor planes and additional users' DUT is explained in the following.

Track finding

The triplet method is used as the track finding algorithm for the GBL implementation in EUTelescope. In this process, track candidates are constructed from an upstream and a downstream triplet, consisting of particle hits in the sensor planes from the up- and downstream arm of the telescope, respectively. As seed of a triplet, the hits on the first and last plane of the telescope arm are used and straight lines between them are constructed, called doublets. For reducing the combinatorial background on the doublets, a user-defined cut on the slope of the straight line with respect to the nominal beam direction can be set. In the next step, the distance between the particle hits on the central plane and the incident position of the doublet on it is calculated. Triplets are selected if the residuals in x and y are smaller than a user-defined cut value.

The up- and downstream triplets are then extrapolated to a virtual plane at a configurable z-position in the telescope center. If the distance between the extrapolations is within a user-defined matching cut, the six hits of the two triplets are grouped to form a track. Moreover, an isolation requirement is set by discarding all triplets with extrapolation distances to other triplets of the same telescope arm smaller than the isolation distance, defined as the doubled triplet matching cut. The inserted DUT plane is not part of the six planes forming the telescope and therefore needs special handling: on the one hand, the trajectory will be impacted by the DUT's material and the matching distance needs to be scaled appropriately; on the other hand, the matching of DUT hits to a track is done by extrapolating the triplets onto the DUT plane and applying dedicated matching cuts.
In total, five independent track quality parameters (plus the dependent triplet isolation) are defined for the triplet method as follows and visualized in Figure 8.17: the slope of the straight line between first and last plane, called *UpstreamTripletSlopeCut* and *DownstreamTripletSlopeCut*; the residual of extrapolated doublets on the central plane, called *UpstreamTripletResidualCut* and *DownstreamTripletResidualCut*; the distance of matching between the up- and downstream triplet, called *TripletMatchingCut*.

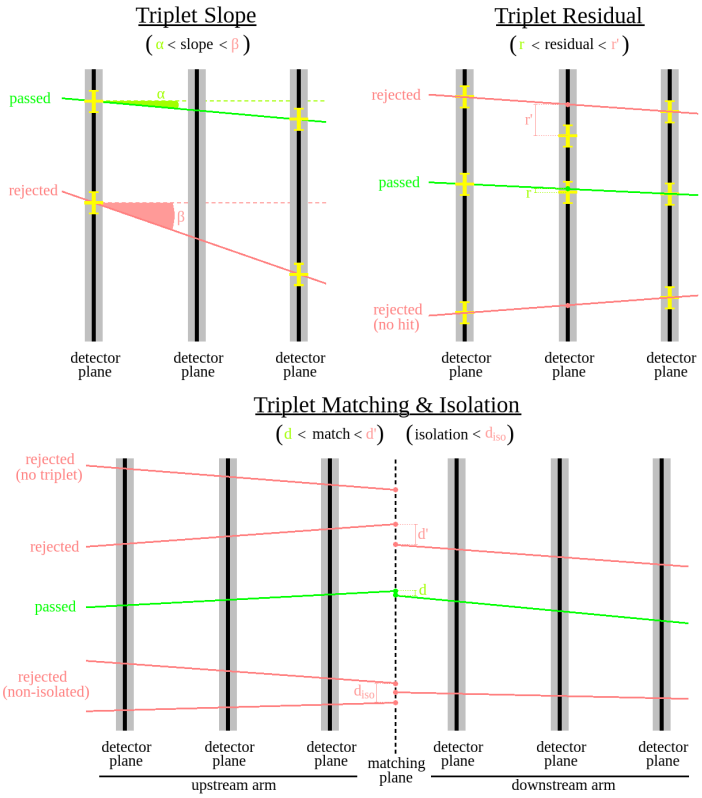

Figure 8.17: The triplet method with its associated track quality parameters, namely cut criteria on the triplet slope, the triplet residual, the triplet matching and the triplet isolation. Shown are examples of passed (green) and rejected (red) track candidates for the different steps of the triplet method.

Track fitting

The track candidates taken as output of the track finding algorithm form already a track with a possible kink in the center of the telescope. Therefore, the track fitting performed within the GBL framework provides actually a track refit of the preliminary track as input. Here, a more realistic track model is used, allowing for kinks in the trajectory along the beam axis described by the multiple scattering of the particle in the detector planes, in any additional material or in the air volume between planes.
A GBL trajectory is constructed from a series of GBL points along the beam axis and the propagation from the previous to the next point is performed by the propagation Jacobian.

A GBL point is characterized by a set of attributes as following:

- one or more position measurements and their uncertainties in an active sensor plane,
- an amount of multiple scattering in the thin-scatterer approximation for a plane,
- local and global derivatives used for detector alignment by describing the impact of alignment constants on the residuals.

In the GBL implementation in EUTelescope, every active and passive plane specified in the GEAR geometry file will be added as a point in the GBL trajectory. A sensor plane has a measurement including an uncertainty as well as an amount of multiple scattering calculated according to the Highland formula [88] and depending on the beam momentum, the radiation length of the material and its thickness. A passive material plane (e.g. shielding and isolation material) is described as a scattering point without a position measurement. In the same way, the scattering effect of the particle passage through air between two sensor planes can be modelled by two GBL points introduced after the first and before the second plane. An illustration of the construction of a GBL trajectory for a typical beam telescope setup is shown in Figure 8.18.

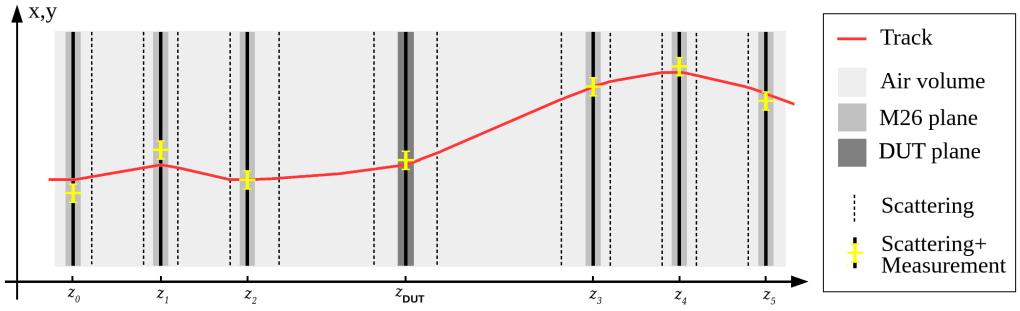

Figure 8.18: Construction of the GBL trajectory for a typical beam telescope setup. The six sensor planes (M26) and the DUT provide a hit measurement with uncertainty and also act as scattering plane. Each air volume in between detector planes is taken into account by constructing two scattering planes.

The following step is to create a seed trajectory as a straight line from the first to the last measurement point described in the GBL geometry. By this, the residuals in both directions of the hit relative to the seed trajectory as well as the hit resolution is added to the GBL point on the respective detector plane. In the final track fit based on all GBL points, a χ^2 minimization is performed to obtain the optimal track trajectory matching the given particle hits in the sensor planes. As a result, the EUTelescope framework gives the residuals for x and y for every particle hit on the sensor planes as the difference between measured hit position and the hit position from the obtained track as well as the kink angles at every defined scattering plane. The probability of the track model to describe the data correctly is calculated from the minimized χ^2, and the user can select reconstructed tracks by a cut criterion on the goodness-of-fit.
Moreover, it is possible to exclude a plane from the GBL fit. In case of an active plane, its hit information and global parameters are not added to its GBL point, e.g. for a DUT the track reconstruction should not be biased by its hit information. In case of the investigation on the material budget of a passive plane, no information on the expected multiple scattering is added to the GBL point, which is discussed further in Chapter 9.
The GBL track fit can be used either for the alignment of the telescope setup with MillepedeII by optimizing the positions and rotations of detector planes to obtain a better track description, or the obtained tracks are the final output of the reconstruction.

8.5 Characteristics of Test Beam Experiments

When conducting a test beam experiment at the DESY II Test Beam Facility with the EUDET-type beam telescopes, the user has the opportunity to change the measurement conditions by selecting various parameters.
These influencing parameters on the measurement are discussed for the particle beam characteristics in Section 8.5.1 and for the beam telescope characteristics in Section 8.5.2. Moreover, the additional instrumentation of the telescope setup with a lead-glass counter as calorimeter and its calibration are introduced in Section 8.5.3.

8.5.1 Testbeam parameters

The particle beam of the DESY II Test Beam Facility can be operated by the user in a customized manner. It is of interest in a test beam experiment to know the beam timing structure, the beam rate, the beam momentum and its spread as well as the beam shape. Moreover, due to the instrumentation of the beam lines, some of the parameters can be controlled by the user. This is shortly discussed in the following, but a detailed beam characterization can be found in [208].

Beam timing

The particles at the test beam lines are delivered with a timing structure dependent on the beam generation principle. On the one hand, every time the beam is fed into the PETRA III storage ring the test beam is interrupted for short times. On the other hand, the cycling frequency of the DESY II accelerator is the reason that only test beam particles with a chosen momentum are available in times when the energy in the accelerator is high enough. Due to this cycle-dependent limit, particles are supplied in time periods being shorter for a higher selected momentum. Both influences, as depicted in Figure 8.19, are not controllable by the user, but have to be taken into account for the measurement planning.

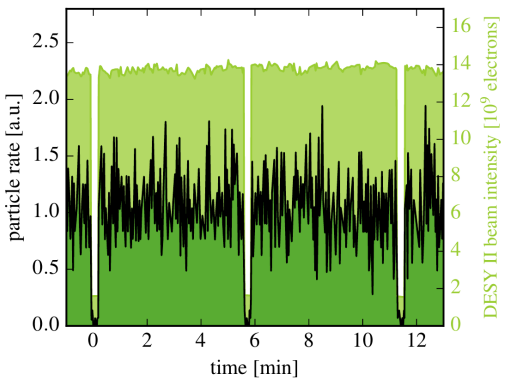

(a) The PETRA III top-up filling interrupts the stable DESY II intensity (right axis) and such the test beam particle rate (left axis) drops to zero for few tens of seconds.

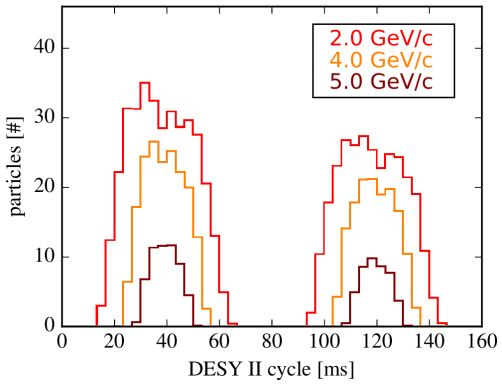

(b) The time structure of test beam particles within a DESY II cycle of 160 ms and its dependence on the selected beam momentum for 2, 4 and 5 GeV/c.

Figure 8.19: Test beam characteristics for the beam timing structure at the DESY II Test Beam Facility. Modified from [208].

Beam rate

The particle rate of the test beam depends on the following parameters along the process of the beam generation:

- the *position of the carbon fiber* with respect to the beam orbit in the DESY II ring can be optimized to allow for a maximal generation of bremsstrahlung photons;
- by the choice of the *secondary target* in terms of material and thickness the pair production rate and therefore also the final beam particle rate can be controlled;
- the *primary collimator* shapes the spatial beam profile behind the dipole magnet for momentum selection and a wider opening results in a higher particle rate;
- most importantly, the choice of the *beam momentum* influences the particle rate due to its dependence on the particle spectrum[57].

Measurements characterizing these effects on the particle rate for the beam line TB22 are summarized in Figure 8.20.

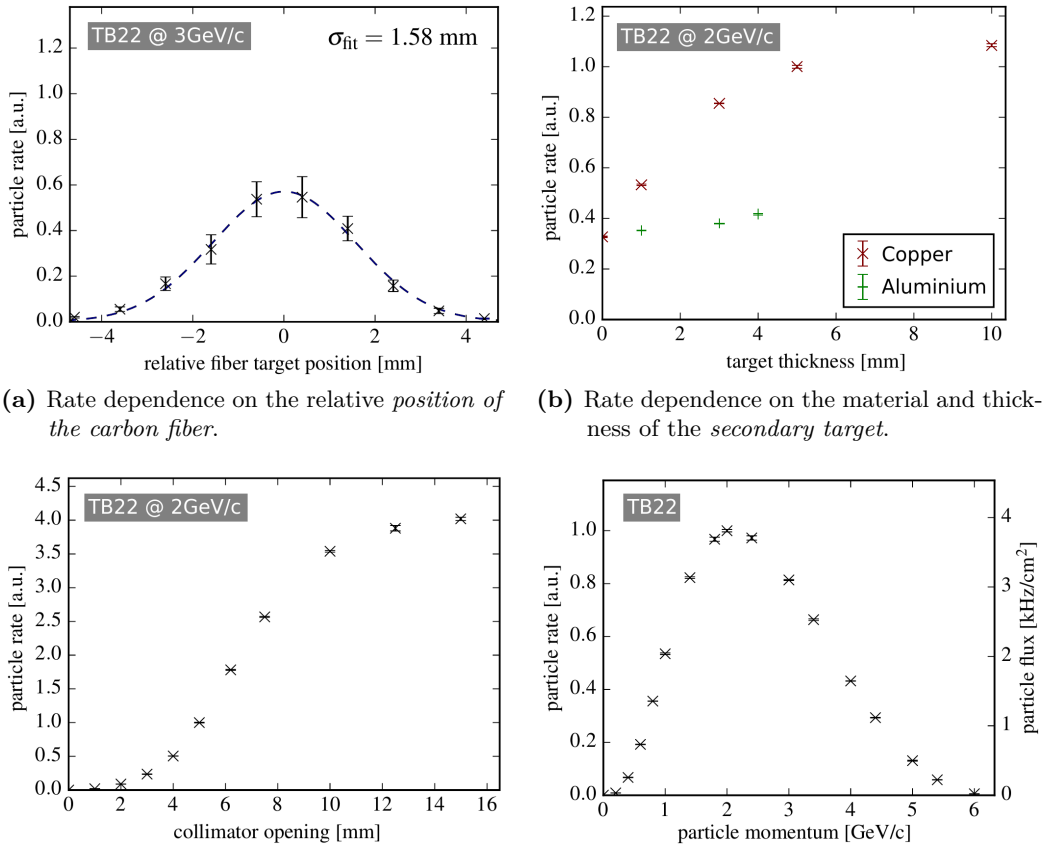

(a) Rate dependence on the relative *position of the carbon fiber*.

(b) Rate dependence on the material and thickness of the *secondary target*.

(c) Rate dependence on the opening of the *primary collimator*.

(d) Rate dependence on the selected *beam momentum*.

Figure 8.20: Test beam characteristics for the beam rate at the DESY II Test Beam Facility. Modified from [208].

[57] The particle spectrum is a convolution of the energy spectrum and the photon spectrum, as a convolution of the bremsstrahlung spectrum with the time-dependent energy profile of DESY II.

Beam momentum

The momentum of beam particles is set by the user via the dipole magnet current, but a detailed knowledge on the momentum and its spread is necessary for the test beam analysis. The calibration of the beam momentum was measured for beam line TB21 using the magnetic field of the additional BRM in a dedicated test setup with the DATURA beam telescope (details can be found in [208]).

As shown in Figure 8.21a, the measured beam momenta as function of the selected momentum fits well the nominal expected values. The absolute momentum spread was determined to be constant at $(158 \pm 6)\,\mathrm{MeV/c}$ over the measured momentum range, implying a decrease of the relative momentum spread for higher beam momenta, as shown on the other axis.

Moreover, due to the momentum selection process inside the dipole magnet, a dependence on the horizontal position inside the particle beam is expected and was determined by a spatially resolved measurement of the momentum spread. The results for two measurements with different openings of the secondary collimator (denoted as $d_{\mathrm{x,coll}}$) at different currents of the BRM (denoted as I_{BRM}) are depicted in Figure 8.21b. A clear increase of the measured mean momentum from the left to the right side in the horizontal plane (roughly $150\,\mathrm{MeV/c}$ for a range of $5\,\mathrm{mm}$) can be observed, showing the importance of this effect to take into account for measurements strongly dependent on the particle momentum.

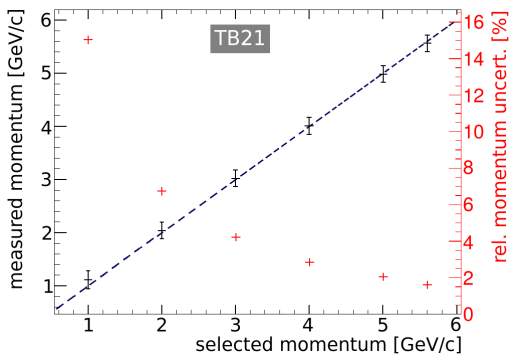

(a) *Momentum calibration*: Measured beam momentum as function of the selected momentum matches well the nominal values (dashed line) and the relative uncertainty (red) decreases with higher momenta.

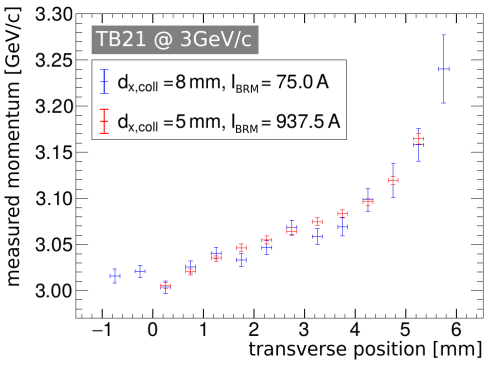

(b) *Horizontal momentum dependence*: The mean momentum shows a dependence on the transverse particle position at the secondary collimator, measured for two configurations of $d_{\mathrm{x,coll}}$ and I_{BRM}.

Figure 8.21: Test beam characteristics for the beam momentum at the DESY II Test Beam Facility. Modified from [208].

Beam size

In general, with the two-step collimation process, the movable primary collimator after the test beam dipole magnet for momentum selection and the exchangeable secondary collimator in the experimental areas, the beam shape can be controlled in such a way that the active sensor area of the beam telescope is completely irradiated by particles.
At the same time, inherently the properties of particle rate and momentum spread are influenced, as discussed before.

8.5.2 Telescope parameters

The EUDET-type beam telescopes allow the operator to adjust its performance by different settings. In the following, the performance of the telescope depending on the choice of its threshold on the MIMOSA26 sensors and its setup in terms of plane spacing for different use cases is discussed. A detailed characterization of the EUDET-type beam telescopes with measurements of the DATURA telescope can be found in [214].

MIMOSA26 sensor threshold

The MIMOSA26 sensor threshold, ξ_n, applied to each telescope sensor plane is a critical parameter for the telescope performance. A higher threshold implies a reduction of the amount of firing sensor pixels, resulting in smaller and fewer hit clusters found on average per plane and respectively limiting the number of reconstructible tracks or the efficiency. This is shown in Figure 8.22a for the triplet efficiency[58] of the telescope as a function of its sensor threshold for two different plane spacings and various beam momenta.

Apart from this, the intrinsic resolution of the telescope plane is affected as well: on the one hand, for an increased threshold a hit is constructed from smaller clusters, resulting in a deterioration of the position estimate; on the other hand, for a decreased threshold the number of noise induced hits is increased, resulting as well in a deterioration of spatial reconstruction. In Figure 8.22b, the intrinsic sensor resolution of the MIMOSA26 sensor is measured as function of the threshold for two different plane spacings and beam momenta.

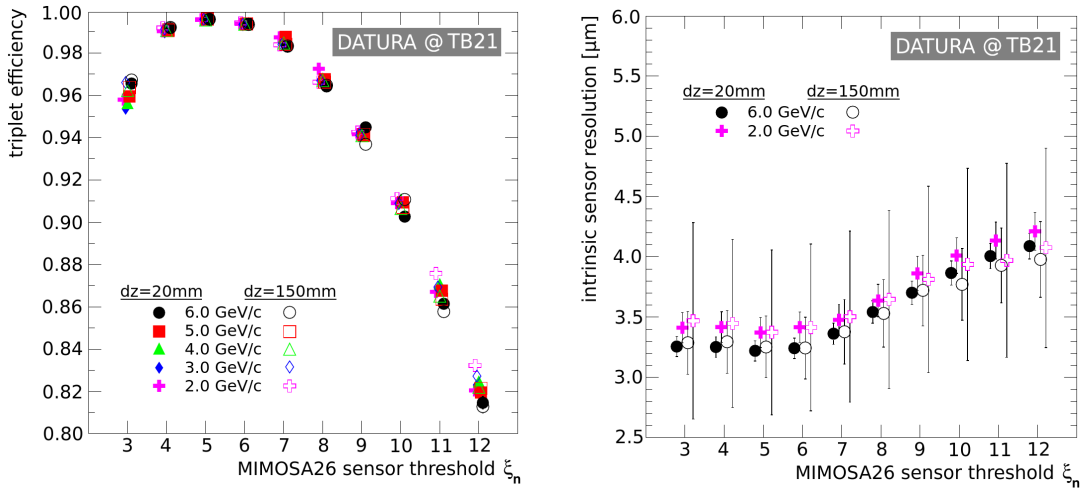

(a) Triplet efficiency as function of threshold for different beam momenta and sensor spacings.

(b) Intrinsic resolution as function of threshold for different beam momenta and sensor spacings.

Figure 8.22: Telescope performance depending on the choice of the MIMOSA26 sensor threshold ξ_n. Modified from [214].

In both cases, threshold values of $\xi_n = 5-6$ yield the best performance in terms of efficiency as well as intrinsic resolution.

[58] The triplet efficiency is defined as the ratio of isolated, upstream triplets with a matching hit on plane 3 in an acceptance range d around the extrapolation to the overall number of isolated, upstream triplets.

Telescope setup

The setup of the beam telescope in terms of plane positions and spacings of the telescope sensors as well as the integrated DUT strongly influences the telescope performance. To allow an optimization of the setup, predictions of the track resolution can be derived with the intrinsic sensor resolution and a description of the material budget. The GBL Track Resolution Calculator [219] performs such a priori calculations by using the GBL formalism to retrieve the track resolution at points of interest along the particle trajectory.

For the characterization of a DUT, the pointing resolution of the telescope is the interesting quantity to optimize. In Figure 8.23a, the track resolution at the position of the DUT with four different material budgets, ϵ_{DUT}, is plotted versus the spacing between DUT and the neighboring telescope planes, dz_{DUT}, for two telescope configurations with equidistant spacings, dz. An optimal track resolution can be achieved by a minimal distance between DUT and neighboring planes, whereas the optimal plane spacing depends on the material budget of the DUT. This can be also observed in Figure 8.23b, showing the achievable track resolution as function of the DUT's material budget for two different telescope configurations and various spacings to the DUT.

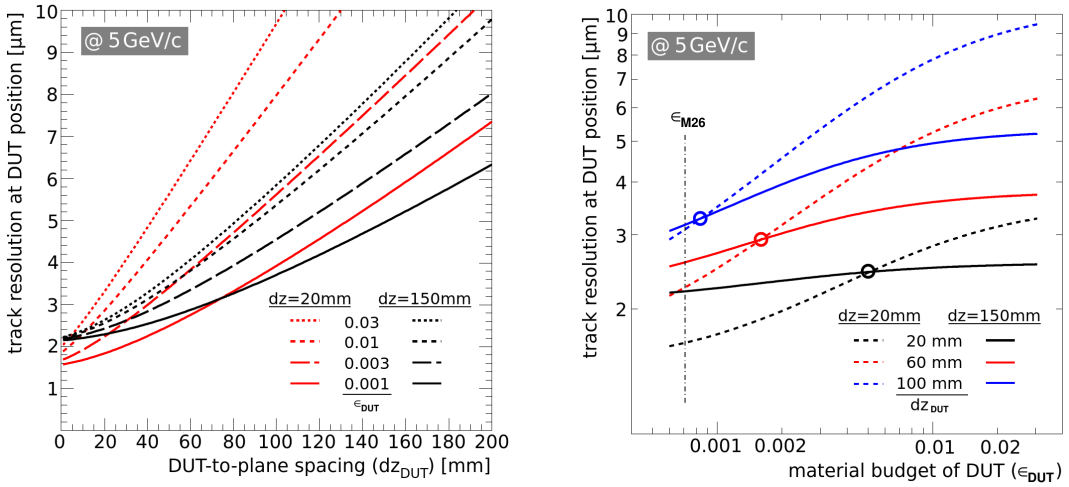

(a) Track resolution as function of spacing between DUT and neighboring telescope planes for various material budgets and two different telescope plane spacings.

(b) Track resolution as function of DUT's material budget for various DUT spacings and two different telescope plane spacings.

Figure 8.23: Telescope performance depending on the choice of the telescope setup. Modified from [214].

In the case of the characterization of a SUT, not only a high pointing resolution of the tracks but also the achievable resolution of the angle measurement is of interest. Therefore, the requirements and calculations with the GBL Track Resolution Calculator for an optimal telescope setup in the case of a precise measurement of a SUT will be discussed in Chapter 9.

8.5.3 Calibration of lead-glass counter

For the test beam measurements in this thesis, additional equipment with a lead-glass counter was used to measure the fractional energy loss of particles after the passage through the telescope and the scattering material inside. The integration of the calorimetric device in the test beam experiment was conducted as part of a summer student project at the DESY II Test Beam Facility to deploy a photon-tagged beam line.
Further information about this project can be found in [249].

Setup

A lead-glass counter, originally used in the HERAb detector at the HERA accelerator at DESY, with an acceptance area of $12 \times 12\,\mathrm{cm}^2$ was mounted on a remotely steerable stage and placed behind the DATURA telescope, as shown in Figure 8.24a.
The calorimeter is powered with high voltage by a CAEN 40-channel high voltage system and the output signal is read out by an oscilloscope, as displayed in Figure 8.24b. As both are installed in the test beam hut, the power and data is transmitted via the patch panel system of the test beam facility.

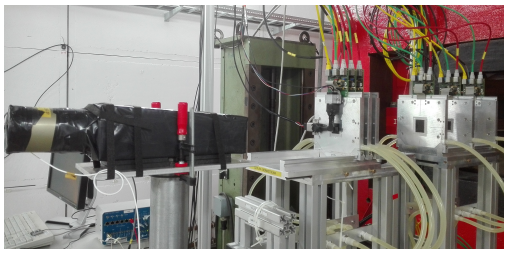

(a) *Calorimeter setup:*
The lead-glass counter is mounted on a movable stage behind the DATURA telescope. Readout and high voltage supply is provided remotely over the patch panel.

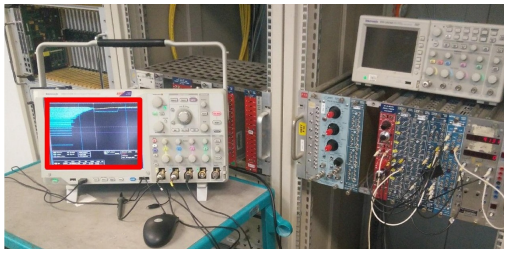

(b) *Calorimeter readout:*
The lead-glass counter signal as well as the trigger signal from the telescope scintillators is recorded by an oscilloscope in the test beam hut.

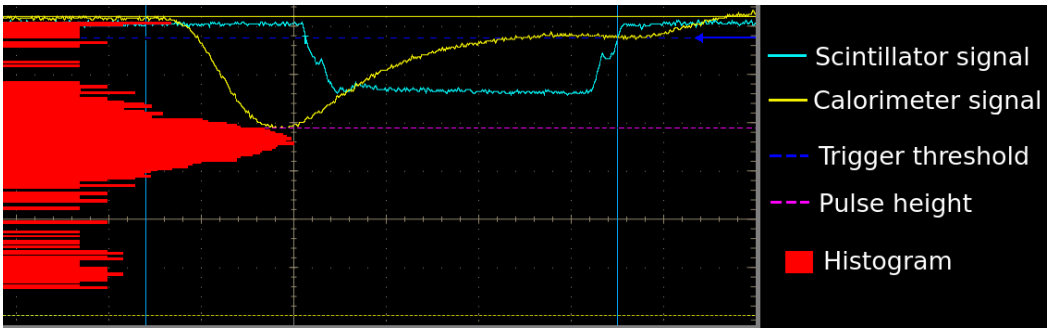

(c) *Calorimeter data:*
The scintillator pulse is used as trigger for the calorimeter pulse and the absolute pulse height of the calorimeter signal is histogrammed internally to record a pulse height spectrum.

Figure 8.24: Setup and readout of the lead-glass counter at the test beam experiment.

To allow triggering on particle hits in the telescope, the scintillator system of the telescope is used and its signal is recorded as well with the oscilloscope. The readout, as depicted in Figure 8.24c, is done via the connected oscilloscope using the scintillator signal as trigger (threshold on negative pulse) and recording the corresponding calorimeter pulse.

The absolute pulse height of the signal pulse is internally histogrammed and stored as pulse spectrum for the offline analysis. Data taking is started and stopped manually on a run basis as given by the EUDAQ readout of the telescope. By this, the data from the lead-glass counter can be directly linked to the tracking data of the beam telescope.

Operation voltage

In the first step, the optimal operating voltage was determined by measuring the count rate of the lead-glass counter, measured by a discriminator and counting unit, as function of the applied bias voltage at a particle momentum of 4 GeV/c. From Figure 8.25, the plateau region for the detector can be determined to be between −1 700 V and −2 000 V.

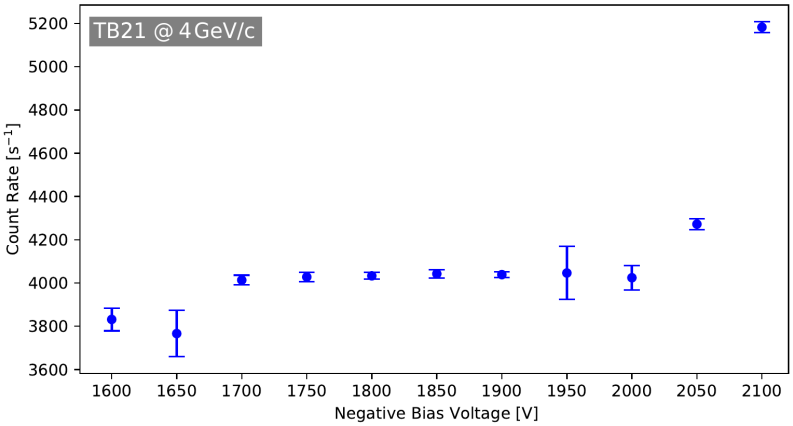

Figure 8.25: Measurement of the count rate in the lead-glass counter as function of applied bias voltage at a particle momentum of 4 GeV/c.

Energy calibration

In the next step, the pulse height as detector response of the calorimeter was calibrated by performing measurements of pulse spectra without a scatterer inside the telescope. Of course, the telescope planes and its supports itself act as scatterers for the beam particles, but as the telescope will be in the beam for all consecutive measurements anyway, this represents a null measurement usable for calibration. Moreover, the calibration is not absolute as the input of the selected beam energy will be used as the nominal energy.

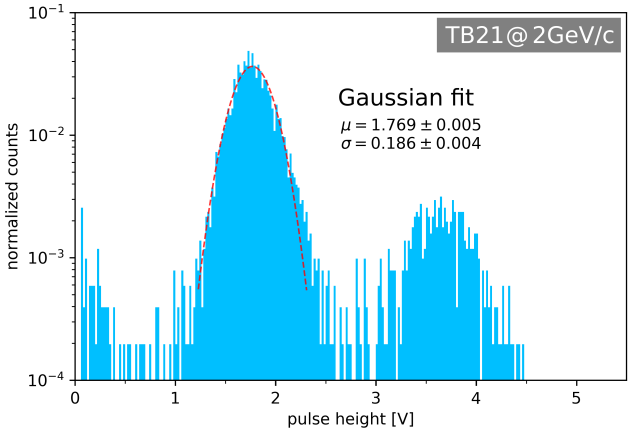

Figure 8.26: Pulse spectrum of the lead-glass counter for a selected beam momentum of 2 GeV/c. The major peak is fitted with a Gaussian distribution, whereas the second peak represents a two-particle recording with a doubled pulse height signal.

The recorded pulse spectrum for a selected beam energy of 2 GeV is shown in Figure 8.26. The intrinsic pulse spectrum is a single line which is smeared by a Gaussian distribution due to the detector resolution as well as the momentum spread of the beam particles.

Moreover, per trigger signal it is possible to record more than one particle, which can be observed as a second peak with a doubled pulse height. For the calibration, the first peak is fitted with a Gaussian distribution with the mean value representing the conversion factor and the standard deviation being a measure for the folded resolution effects.

For the calibration, beam momenta between 1 GeV/c and 5 GeV/c were used. An overlay of pulse spectra at different selected beam energies is depicted in Figure 8.27a and the data is used for the calibration curve in Figure 8.27b with a linear fit of the data points.

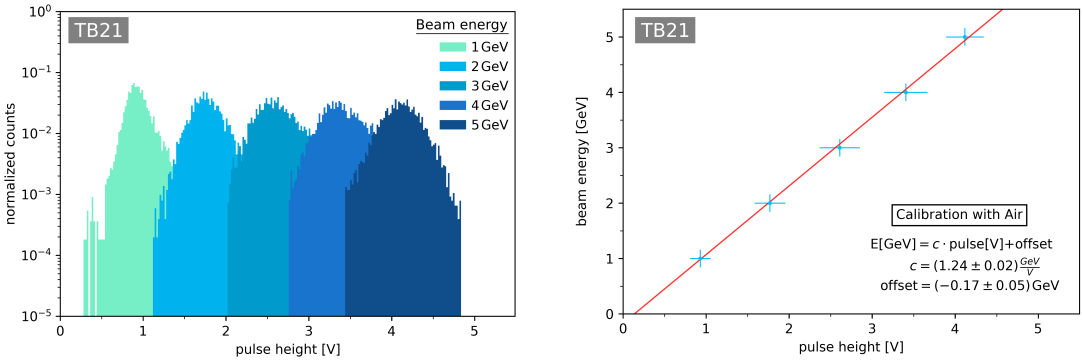

(a) Overlay of calibration pulses at different particle energies, shown is only the dominant peak.

(b) Calibration curve with a linear fit resulting in a factor of (1.24 ± 0.02) GeV/V.

Figure 8.27: Energy calibration of the lead-glass counter.

This calibration procedure is repeated for each individual test beam campaign to eliminate changing operation conditions. In the following, the derived energy calibration functions are already applied to the recorded pulse spectra, such that results for different test beam measurements will be shown as energy spectra.

Chapter 9

Material Budget Imaging

When a charged particle traverses any material layer, it interacts with the atoms inside of the material and looses either a part of its energy or it is deflected from its original direction of traveling. The latter effect is caused by multiple Coulomb scattering of the particle in the material. For the application of a tracking detector, the design is often guided by the criterion to use as little material as possible inside the tracking volume, to decrease these influencing factors. As such, the multiple Coulomb scattering inside any traversed material leads to a deflection of the particle, which in turn deteriorates the resolution for the track reconstruction and therefore the actual measurement of the particle's trajectory in the tracking detector.

But at the same time, the effect of multiple scattering can be used to retrieve information about the traversed material and to measure quantities specific to this effect. For this purpose, the deflection angle for the particle trajectory at the position of the material must be reconstructed, which is possible when accurately measure the angles of the particle track before and after the material. For measuring a multitude of particles, the individual measured deflection angles leads to a distribution of kink angles, which shape depends on the amount of material traversed. This allows therefore to estimate the material budget as a measure for the amount of traversed material relative to the material's specific radiation length. By using also the incident positions of the individual particles on the sample under test, the material budget can be measured in a position-resolved way, which is especially interesting for samples with an inhomogeneous distribution of material. This measurement technique is therefore referred to as **M**aterial **B**udget **I**maging (MBI).

This novel imaging technique was studied within this work by performing measurements of the material budget for a large variety of samples using the DESY II Test Beam Facility, as introduced before. Here, the offered electron beam with momenta between 1 and 6 GeV/c as well as the provided high-resolution EUDET-type beam telescopes are perfectly suited to perform this type of measurement.
In general, the MBI technique is actively investigated by several research groups in terms of the possibilities and limitations of this imaging technique [250, 251, 252, 253]. A rather wide range of possible applications of the MBI technique is covered. In the context of high-energy physics experiments, it is possible to directly measure the material budget of newly developed detector systems, such as for the currently planned upgrades of the particle physics experiments at the LHC. The extracted values of radiation lengths for the individual types of materials can then also be used as an input for simulations modelling the expected detector performance. But the MBI technique is also investigated for general material studies as well as imaging applications in the medical area.

In Section 9.1, the material's specific radiation length as well as its corresponding material budget are defined and values for a number of materials are given. Moreover, the underlying theory of multiple Coulomb scattering is briefly described, showing especially appropriate models used for the MBI technique, which basics are introduced as well.

An overview of the performed test beam measurements within this work is provided in Section 9.2, explaining the choice of parameters for the test beam and the telescopes. This is followed by a description of the tested samples in the measurements, ranging from homogeneous material samples up to specific materials as well as complex structures used in the design of the ATLAS ITk detector.

In Section 9.3, an introduction to the reconstruction of kink angles is given. Here, an unbiased measurement of the kink angle is performed using the General Broken Lines algorithm and for the overall track reconstruction the EUTelescope framework is used.

The analysis of the reconstructed kink angle distributions is discussed in Section 9.4, showing the dependencies of the distribution's shape and evaluating appropriate estimators for the width of the distribution, as needed for the material budget calculation. Moreover, several characteristics of the scattering distributions are described ranging from studies on the correlation, over acceptance effects up to investigations on the beam energy variation.

The investigation on the calibration procedure for the MBI technique is presented in Section 9.5, showing the performed calibration with a number of different material samples. Furthermore, a calibration with water samples is conducted for a possible medical application as well as the material budget extraction for multi-layered material structures is studied.

In Section 9.6, the measurement results for the studied samples as used for the ATLAS ITk detector are presented. Here, on the one hand estimates for the radiation length of different materials foreseen in the local support structures of the detector are given. On the other hand, the imaging capabilities of the technique is used to evaluate the internal structure of several test samples of the detector system.

The effect of large material budgets, as reached for high Z materials or simply large sample thicknesses, on the estimated material budget with this technique is studied in Section 9.7. Here, a special focus lies on the energy loss inside the material and the investigation to correct for the resulting effect in the MBI analysis.

At the end of this chapter, a conclusion of the performed investigations on the MBI technique is given in Section 9.8, providing also an outlook for the further characterization and the future applications of this imaging technique.

9.1 Radiation Length & Multiple Scattering

In the traversal of a charged particle through a material layer with defined material properties, the particle interacts in various ways with the atoms of the material.
On the one hand, the charged particle experiences an energy loss by the interaction with the nuclei or atomic shell electrons of the material, as it was introduced in Section 2.1.1.
On the other hand, the charged particle experiences also an effective deflection in the material due to the effect of *multiple Coulomb scattering* occurring by the interaction with the electric fields of the material's nuclei, which was discussed in Section 2.1.2.

As the amount and strength of the multiple scattering interaction is linked to the *radiation length* X_0 of the traversed material, this material property is defined in Section 9.1.1 in detail and its relevance for the development of particle detectors is highlighted.
The theoretical description of multiple Coulomb scattering in the material as well as appropriate models to describe the resulting deflection angle for the traversing particle are briefly introduced in Section 9.1.2.
In Section 9.1.3, the calculation of the radiation lengths for pure elements is shown and compared to the tabulated X_0 values by the **P**article **D**ata **G**roup (PDG) [14] for various raw materials of interest in this work. Furthermore, the theoretical calculation of the radiation length for multi-layered structures of different raw materials or the determination of the effective radiation length of composite materials such as adhesives is explained.
Finally, the idea of the MBI technique to measure the material budget of samples directly is summarized in Section 9.1.4.

9.1.1 Radiation length and material budget

When a highly energetic, charged particle, such as an electron in the following, traverses a material layer, a number of single scattering interactions with the electric fields of the nuclei occur. The individual interactions along the way through the material result in random deflections in the lateral directions, which are summed up to an effective deflection described by the theory of multiple Coulomb scattering (cf. Sec. 9.1.2).
The probability for the occurrence of larger deflections depends on the one hand on the amount of traversed material, which scales effectively with the number of single scattering interactions; and on the other hand, higher deflection angles for the traversing particle are observed if the material is denser, which scales therefore effectively with the strength of the individual interactions.
These dependencies are combined by defining the *material budget* as $\epsilon = x/X_0$ (cf. Eq. 2.8) with the thickness of the material layer x and the material's radiation length X_0. Here, the radiation length is a material property and the relevant values as well as a way to theoretically calculate the radiation length of materials are given in Section 9.1.3.

The material budget ϵ is a key quantity for the development of particle detectors, e.g. for high-energy physics experiments, which is especially the case for the design of tracking detectors. Here, the tracks of the created particles in the collision event should be reconstructed with high accuracy to measure the particle's momentum. But by the effect of multiple scattering occurring in the various material layers of the detector, such as the passive support structures, the particle track resolution and correspondingly the accuracy of the momentum measurement is deteriorated.

One of the design goals of the ATLAS ITk detector is to decrease the material budget of the tracking detector considerably compared to the currently employed ATLAS Inner Detector. With the herein introduced MBI method, selected materials for the petal design, which represents the planned local support structure for the ITk strip end-cap detector, are investigated in terms of their radiation length in Section 9.6.

9.1.2 Theory of multiple Coulomb scattering

The *Coulomb scattering*, or also referred to as Rutherford scattering [2], describes the elastic scattering process of a relativistic charged particle with the electric field of a nuclei via the Coulomb interaction.

The differential cross section $\frac{d\sigma}{d\Omega}$ for this *single scattering* process follows then the Rutherford scattering formula[59] as

$$\frac{d\sigma}{d\Omega} = \left(\frac{1}{4\pi\epsilon_0}\frac{Z_1 Z_2 e^2}{4E_0}\right)^2 \frac{1}{\sin^4(\theta/2)}, \tag{9.1}$$

with the scattering angle θ of the scattered particle with charge number Z_1 and an initial energy E_0 on the nucleus with charge number Z_2. With the occurrence of only small scattering angles, the relationship for single scattering events can be approximated with

$$\frac{d\sigma}{d\Omega} \sim \frac{1}{\theta^4}, \tag{9.2}$$

showing a broad distribution of scattering angles centered around the mean value of zero.

When a highly energetic particle, such as an electron, traverses a material, multiple of single scattering interactions occur on the individual atomic nuclei. The mean number of scatterings N_{scat} inside a material with thickness x is then expressed as

$$N_{\text{scat}} = \sigma \frac{N_A}{A} x\rho, \tag{9.3}$$

depending on the Rutherford cross section σ, the material's density ρ and its mass number A. Even for thin material layers of thicknesses $\mathcal{O}(100\,\mu\text{m})$, several hundred single scattering interactions occur, such that the overall effect is then called *multiple scattering*.

The distribution of the scattering angle θ in the case of multiple scattering is deduced in the following way: on the one hand, the large number of individual single scattering events leads to a Gaussian scattering angle distribution according to the central limit theorem, featuring a symmetric distribution with a mean value centered around zero; on the other hand, single scattering events with a large scattering angle occurring on a rare basis are causing tails in the distribution to higher deflections. Overall, the multiple scattering distribution consists of a Gaussian core with non-Gaussian tails proportional to θ^{-4}.

A complete theoretical description for the modelling of multiple Coulomb scattering is provided by Molière [86] with a fully analytical model describing both the core and the tails of the scattering distribution, as shown in [87].
On the contrary, the multiple scattering model introduced by Highland [88] describes only the core of the scattering distribution. Here, the width σ_θ of a Gaussian function fitted to the inner 98% quantile of the scattering distribution is used. In the parametrization according to [89], the Highland formula - as it was shown in Eq. 2.7 - with

$$\theta_0 = \frac{13.6\,\text{MeV}}{\beta cp} z\sqrt{\epsilon}\left(1 + 0.038\ln(\epsilon)\right), \tag{9.4}$$

correlates the scattering angle width θ_0 to the material budget ϵ of the traversed material and the momentum p of the scattered particle with charge number z. It is stated that the Highland model is valid with uncertainties below 11% for all values of Z and agrees with the Molière predictions within 2% [89].

In the course of a summer student project [254], first investigations of the Molière model to describe the experimental data were conducted, but for this thesis, the Highland formula is exclusively used in the following.

[59] The Rutherford formula has a pole at zero, but the cross section is finite here due to the screening effect of shell electrons requiring a minimum scattering angle Θ_{min}. Moreover, an upper boundary Θ_{max} on the scattering angle can be defined.

9.1.3 Radiation length of materials

The radiation length X_0 as a material property is used for the description of the multiple scattering interactions in a material by a traversing particle. But this quantity is also used for the description of the energy loss of a charged particle via bremsstrahlung, which is expressed in Equations 2.2 and 2.5. Here, the radiation length of a material is defined as the mean path after which the energy of a charged particle has decreased by the factor $1/e$.

The calculation of X_0 for the general case as given in Equation 2.4 depending on the mass m and the charge number z of the incident particle is simplified in the following by assuming an electron as the incident particle. Furthermore, different analytical formulas exist to calculate approximate X_0 values for a given material depending on the assumed bremsstrahlung interaction model.
The radiation length, parametrized here according to Y. Tsai [255], is then expressed as

$$\frac{1}{X_0} = 4\alpha r_e^2 \frac{N_A}{A} \left(Z^2 (L_{\text{rad}} - f(Z)) + Z L'_{\text{rad}} \right), \tag{9.5}$$

with the classical electron radius r_e and the specific functions L_{rad}, L'_{rad} and $f(Z)$ depending on the atomic number Z of the traversed material. Further details to the analytical formula and its inputs are given in Appendix C.1.
Moreover, tabulated values for experimentally measured radiation lengths for a number of materials, ranging from the chemical elements up to often used organic and inorganic material mixtures and compounds are provided by the PDG [256]. Here, the error between the analytically approximated values to the referenced measurement values are in the order of $\mathcal{O}(1\%)$, which is evaluated in Appendix C.1 as well.

In Table 9.1, the extracted radiation length values from the PDG database for a selection of raw materials as used in the later described MBI investigations in this work are shown. Here, the radiation length is conventionally given in units of g/cm^2, but can be expressed as a length dimension by dividing with the material's density ρ. The latter is also used for the calculation of the material budget ϵ and the preferred notation in this thesis.

Material	ρ [g/cm^3]	X_0 [g/cm^2]	X_0 [mm]
Tungsten (W)	19.3	6.76	3.504
Tin (Sn)	7.310	8.82	12.06
Copper (Cu)	8.960	12.86	14.36
Nickel (Ni)	8.90	12.68	14.24
Iron (Fe)	7.874	13.84	17.57
Titanium (Ti)	4.54	16.16	35.60
Aluminum (Al)	2.699	24.01	88.97
Silicon (Si)	2.329	21.82	93.70
Graphite (C)	2.210	42.70	193.2
Polyimide film (Kapton)	1.420	40.58	285.7
Polymethylmethacrylat (Acryl)	1.190	40.55	340.7
Water (liquid)	1.000	36.08	360.8
Air (dry, 1 atm)	$1.205 \cdot 10^{-3}$	36.62	$3.039 \cdot 10^5$

Table 9.1: Material properties of selected materials in terms of the specific density ρ and the radiation length X_0 given in units of [g/cm^2] and [mm], respectively. The values are taken from the PDG database [256].

The radiation length in a mixture or compound material can be determined by

$$\frac{1}{X_0} = \sum_i \frac{w_i}{X_{0,i}} \tag{9.6}$$

with the fractional weight w_i and the radiation length $X_{0,i}$ of the individual ith component in the mixture. With this formula, it is possible to calculate the effective radiation length of organic and inorganic compounds via the chemical composition, such as polymers like Kapton with the composition as $[C_{22}H_{10}N_2O_5]_n$.
For a composite structure consisting of two material layers with thickness d_1 and d_2, density ρ_1 and ρ_2 and the individual radiation lengths $X_{0,1}$ and $X_{0,2}$, the radiation length X_0 of the composite with thickness $d_0 = d_1 + d_2$ is simply determined with

$$X_0 = \frac{d_0\rho_0}{\frac{d_1\rho_1}{X_{0,1}} + \frac{d_2\rho_2}{X_{0,2}}} \tag{9.7}$$

and $d_0\rho_0 = d_1\rho_1 + d_2\rho_2$ [257].

For the theoretical calculation of the material budget of mixtures and multi-layered structures, a detailed knowledge of the individual elements of the composite is required. On the one hand, the exact chemical composition, e.g. for adhesives, is often not known due to proprietary reasons. On the other hand, structures like electrical PCBs have a complex geometry with different materials such that an easy extraction of the material budget by calculation is not possible. Therefore, the direct measurement of the material budget of unknown materials as well as the spatially-resolved imaging of the material budget distribution for complex structures is the advantage of the MBI technique presented in this chapter. Moreover, the determined X_0 values can serve as an input for the GEANT4 detector simulations, e.g. for the performance simulation of the ATLAS ITk detector.

9.1.4 Basics of material budget imaging

The **M**aterial **B**udget **I**maging (MBI) technique is a standalone imaging technique which allows to investigate experimentally the material budget ϵ of samples, ranging from homogeneous blocks of a defined material up to structured objects with complex material budget distributions. Here, the technique allows, apart from a qualitative investigation of the material budget and its distribution in the sample, to perform a quantitative analysis by extracting the material properties of the sample in terms of its radiation length.
In principle, the MBI technique can be divided in a two-dimensional and a three-dimensional imaging technique. The focus of this work is on the two-dimensional imaging of samples, whereas the developed tools serve also as a direct input for the tomographic reconstruction in the three-dimensional imaging. Further information about the status and development of the 3D-MBI technique can be found in [253, 258].

The idea of the MBI technique is to exploit the multiple Coulomb scattering of particles inside the material under test, called in the following **S**catterer **U**nder **T**est (SUT). For this purpose, highly energetic, charged particles have to traverse the SUT and the resulting deflection angles after the sample are measured. Moreover, to allow for a position-resolved investigation of the SUT in two dimensions, the incident position of the traversing particles on the SUT should be known precisely. In the final step, an estimate of the material budget of the traversed SUT is retrieved from the reconstructed kink angle distributions using appropriate models for the underlying scattering process, such as the Highland formula.

For the studies of the MBI technique in this work, multi-GeV electrons produced at the beam lines TB21 and TB22 of the DESY II Test Beam Facility (cf. Sec. 8.1) are used in several conducted testbeam campaigns. Moreover, the high-resolution EUDET-type beam telescopes (cf. Sec. 8.2) are utilized for the reconstruction of the particle tracks, meaning the precise measurement of the spatial position and the deflection angles of the scattered electrons in the SUT. The reconstruction and analysis of the kink angle distributions as well as the evaluation of the corresponding material budget values are the topic of the following sections.

9.2 Test Beam Campaigns: Setups & Samples

Several test beam campaigns at the DESY II Test Beam Facility were conducted for this thesis and the recorded data sets are used for the following MBI analyses. Starting with a first test beam week dedicated to MBI measurements in February 2017, two further weeks of test beams were taken in December 2017 and March 2019. Here, in each case the opportunity to use the beam lines TB21 and TB22 in parallel was used, allowing to measure a large variety of samples and to perform tests of different measurement conditions. Additionally, two summer student projects were devoted to MBI measurements in 2018 [254] and 2019 [259], increasing the available scattering data set.

In the following, the relevant parameters selected for the test beam measurements are discussed. Starting in Section 9.2.1 with the test beam parameters, the choice of the optimal beam momentum for multiple scattering investigations is discussed. This is followed by the parameter settings for the EUDET-type beam telescopes and the influence of the telescope setup in terms of the spacing between the MIMOSA26 sensor planes on the achievable spatial and angular track resolution is described. Finally, Section 9.2.3 shows the selected measurement routine for the MBI investigations, providing also an overview of the measured samples, ranging from homogeneous and pure material samples for the purpose of calibration up to unknown material samples and complex structures relevant for the planned ATLAS ITk detector.

9.2.1 Test beam parameters

The DESY II Test Beam Facility offers electron beams with beam momenta between 1 and 6 GeV/c, which allows to traverse most of the inserted samples by the particles. Nonetheless, the choice of the optimal beam momentum for MBI measurements depends on the following factors.
Firstly, the beam momentum should be selected to allow for sufficient scattering angles, which can be recorded by the high-resolution EUDET-type beam telescopes and depends therefore on the investigated SUT. Here, it is expected that the scattering angles are increasing for lower beam momenta according to the multiple scattering theory (cf. Eq. 9.4). This means that for a low material budget sample, the selection of a lower beam momentum can be beneficial, as otherwise the kink angles could be rather small. But for a high-Z or rather thick SUT, the contrary is the case as a higher beam momentum results in a higher penetration depth and an accordingly higher probability that electrons traverse the full thickness of the sample. For the reconstruction of the tracks with larger deflection angles, the geometrical acceptance of the beam telescopes must be taken into account.
Secondly, the particle rate at the beam lines varies strongly with the selected beam momentum, as it was shown in Figure 8.20. For a good MBI result, especially for the case of a high contrast of the two-dimensional image, a high number of particle tracks is required.

With a maximal particle rate at approximately 2.4 GeV/c, a higher measurement time is necessary for higher or lower momenta to record the same amount of tracks.
Last but not least, the provided electron beam is not mono-energetically at the selected nominal beam momentum but comes with a momentum spread (cf. Fig. 8.21). For higher beam momenta the relative momentum spread is lower which is due to the direct dependence of the scattering on the particle momentum beneficial for MBI measurements.
Therefore, a trade-off between these factors must be made, which requires to choose the parameters in the best way according to the foreseen MBI measurement.

For this work, a large variety of beam energies was tested to investigate the influence of the beam energy on the individual measurements. For some measurements of the test beam campaigns, the beam momentum was systematically varied between 1 and 5 GeV/c in steps of 1 GeV/c. Furthermore, beam momenta of 2.4 and 3.4 GeV/c were used to test samples with the highest available particle rate.
With conducted measurements in TB21 and TB22, a comparison of the influence of the chosen beam line is also possible, whereas here the largest impact is expected from the available beam telescope and not directly the characteristics of the beam.
Finally, the choice of the primary and secondary collimator influences the test beam measurement. For a larger opening of the primary collimator, the particle rate is increased but also the momentum variation is larger, therefore also here a trade-off must be made. The secondary collimator should be selected according to the investigated size of the SUT. This is in the most cases, especially for imaging, the total detection area of the sensors in the telescope with roughly $(2 \times 1)\,\mathrm{cm}^2$.

9.2.2 Telescope setup & parameters

For the MBI measurements at the DESY II Test Beam Facility, the EUDET-type beam telescopes DATURA and DURANTA in TB21 and TB22, respectively, were used. With the telescopes, it is possible to not only reconstruct the incident positions in the x- and y-direction of the particle on the SUT with a precision down to 2 µm, but also to precisely reconstruct the track angles with respect to a defined longitudinal axis for the particle before and after the inserted sample. As it was described in Section 8.5.2, a number of user-controllable parameters exist for the telescopes influencing the measurement result.

First of all, the telescope setup is important as it directly affects the track resolution. For the MBI analysis, apart from a high pointing resolution to reconstruct the spatial positions, a high angular resolution of the track is demanded to measure the deflection angles caused by the SUT. The GBL Track Resolution Calculator [219] allows to perform a detailed modelling of the achievable spatial and angular track resolutions for a given telescope setup and beam momentum. Here, the contributions of the scattering in the telescope planes as well as the air volume is taken into account due to the used GBL algorithm.
The telescope setup for the performed test beam measurements can be described by a number of longitudinal distances dz between the telescope planes and the inserted SUT:

- the MIMOSA26 sensor planes are spaced equally with a distance of dz_{up} in the upstream and dz_{down} in the downstream arm of the telescope;
- the distance between both telescope arms is $dz_{\mathrm{total}}^{\mathrm{SUT}}$ corresponding also to the allowed space to insert the SUT into the telescope;
- the relative position of the SUT in between the telescope is described by the distance $dz_{\mathrm{up}}^{\mathrm{SUT}}$ to the upstream arm and the thickness d of the sample.

In Figure 9.1, the spatial and angular resolutions are simulated as function of the varying plane spacings dz_{up} and dz_{down} to find the optimal telescope setup for MBI investigations. Here, the intrinsic resolution of $\sigma_{\text{x,y}} = 3.24\,\mu\text{m}$ [214] for the MIMOSA26 sensor planes is used, the SUT is placed in the middle of the telescope with a spacing $dz_{\text{total}}^{\text{SUT}} = 70\,\text{mm}$ and a beam momentum of 2 GeV/c is assumed.

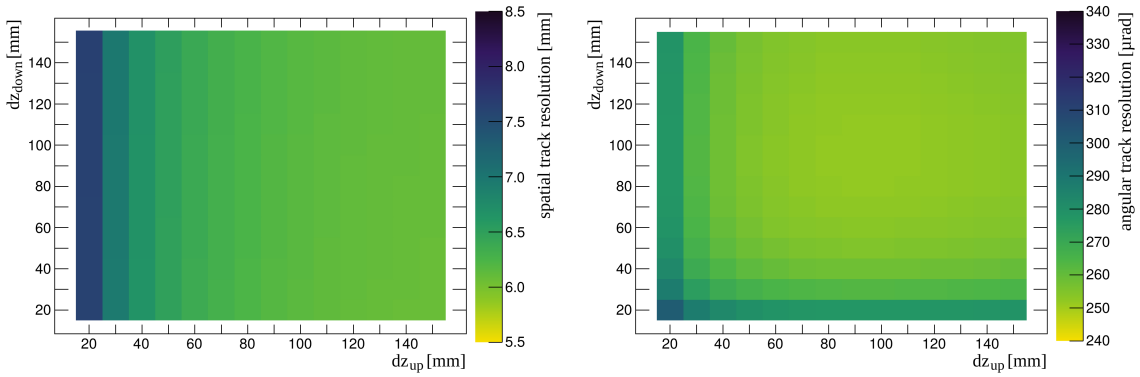

Figure 9.1: Simulation of the spatial (left) and angular (right) track resolution as function of the plane spacing in the upstream (dz_{up}) and downstream (dz_{down}) telescope arm with the GBL Track Resolution Calculator [219]. The distance between the telescope arms is $dz_{\text{total}}^{\text{SUT}} = 70\,\text{mm}$ with the SUT placed in the middle and the beam momentum is 2 GeV/c.

The spatial track resolution is only influenced by the plane spacing in the upstream telescope arm and is improving for larger values dz_{up}. For the angular resolution, also a larger plane spacing in the downstream arm results in a better angular measurement, whereas the spacing dz_{up} shows only a minor influence on the track resolution for large enough values of dz_{down}. In this case, the SUT position is fixed to the middle of the telescope, but also the distance $dz_{\text{up}}^{\text{SUT}}$ has a direct influence on the pointing resolution of the track. Here, the extrapolation length of the upstream triplet to the SUT is shorter for a smaller distance and also the contribution of air scattering is correspondingly less.
Overall, a good spatial and angular resolution is expected for a wide telescope setup with larger plane spacings dz_{up} and dz_{down}. For a good image resolution, the distance $dz_{\text{up}}^{\text{SUT}}$ should be minimized as well. But in the case of larger material budgets, a wide spacing of the downstream telescope arm can cause acceptance effects as larger deflection angles are not reconstructed, which will be investigated later.

For the MBI measurements, several telescope setups were used as shown in Table 9.2.

Name	dz_{up} [mm]	dz_{down} [mm]	$dz_{\text{total}}^{\text{SUT}}$ [mm]
S1	30	50	50
S2	30	50	70
S3	30	80	60
S4	50	50	70
S5	100	100	70
S6	150	30	100
S7	150	30	450

Table 9.2: Overview of telescope setups in terms of the spacings dz_{up}, dz_{down} and $dz_{\text{total}}^{\text{SUT}}$ for the MBI investigations.

The setup geometry was in most cases selected according to the required space for the SUT between the telescope arms, e.g. telescope setup S7 allows to insert large samples. But also direct comparisons of the results for different setups, e.g. between S4 and S5, can be used to investigate the resolution effect on the reconstructed kink angle distribution. Moreover, different distances $dz_{\text{up}}^{\text{SUT}}$ are used for the individual samples, influenced e.g. by the thickness of the samples.

For the other telescope parameters, no larger dependence for the scattering results are expected. Therefore, the default parameters are used, e.g. a MIMOSA26 sensor threshold of $\xi_n = 6$ was chosen for all measurements to get the best performance in terms of efficiency as well as intrinsic resolution of the pixel sensor (cf. Fig. 8.22).

9.2.3 Measurement routine & samples

The measurement routine for the MBI investigations can be summarized as following:

- preparation of the telescope setup by measuring the longitudinal distances dz;
- choice of beam parameters, e.g. selecting the beam momentum for the run sequence;
- performing of an empty telescope run, corresponding to only scattering in the air volume (used for telescope alignment in the track reconstruction);
- placing sample as SUT in between the telescope arms using the x-y-positioning stage;
- performing runs of scattering measurements.

Here, each measurement run collects one million of events and per sample at least one run is performed. Depending on the sample type, e.g. homogeneous material or complex structure, several runs are performed to acquire a higher data statistics in terms of the amount of recorded particle tracks.
In terms of investigated samples, two categories can be differentiated: On the one hand, homogeneous samples of a defined material type are used to measure the individual kink angle distributions for various sample thicknesses and to extract accordingly the material budget. The results of these *known samples* can be used then to calibrate the material budget estimate and compare it also to appropriate model predictions, e.g. the Highland formula. On the other hand, *unknown samples* are investigated focusing in this work on materials and structures planned to use for the construction of the ATLAS ITk detector. Here, unknown refers to the exact material composition of the sample, like an adhesive, or to the complex distribution of materials inside a multi-layered structure. An overview of the tested known and unknown samples is given in the following.

Homogeneous material samples

In the performed measurements, homogeneous plates of different raw materials and of different thicknesses were used to extract the material budget of the samples. Due to the varying radiation lengths of the materials, a broad range of material budgets can be covered in the measurement, allowing also to compare the estimated material budgets for samples with a comparable ϵ. The investigated materials (in alphabetical order) are aluminum, copper, graphite, nickel, stainless steel, tin, titanium and tungsten, with their radiation lengths X_0 as provided in Table 9.1. The thickness of the individual samples depending on its type ranges between 0.05 and 10.0 mm and covers therefore known material budgets between $\epsilon = 3.5 \cdot 10^{-4}$ and $\epsilon = 1.42$.

To allow for an efficient testing of a large amount of material samples, the automatic movement of the x-y-positioning stage (cf. Sec. 8.3.3) was exploited to scan various SUTs in consecutive runs. Figure 9.2 shows several photographs of the setup with different material samples placed between the upstream and downstream telescope arm.

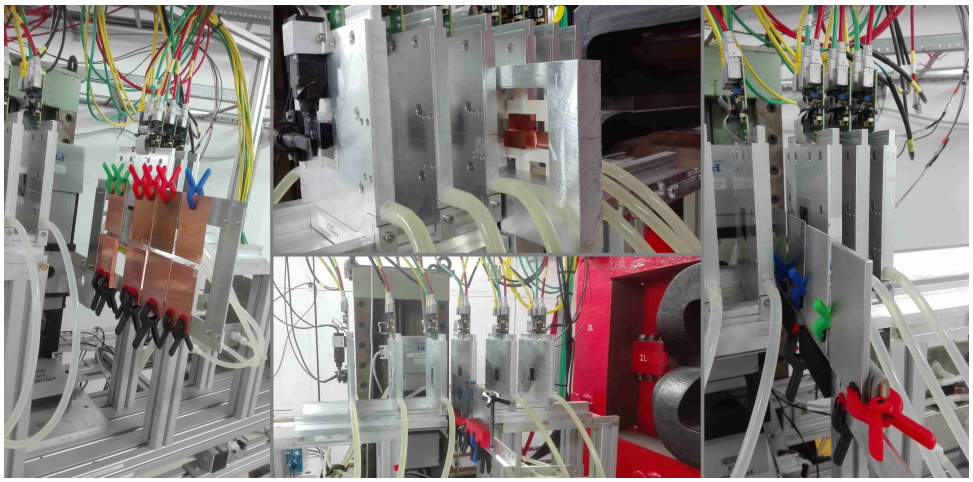

Figure 9.2: Collection of photographs showing different setups with known material samples placed on the x-y-positioning stage for automated movements. The pictures were taken before the final alignment of the SUT with the beam.

For a possible application of the MBI technique in medical imaging, the material budget determination of water is of interest, as the human body consists to a large fraction of water. Therefore, samples containing distilled water with thicknesses between 5 and 400 mm were prepared and measured [259]. Due to the length of the water samples, as shown in Figure 9.3, a large distance between the upstream and downstream arm of the telescope is required, which resulted in using the telescope setup S7.

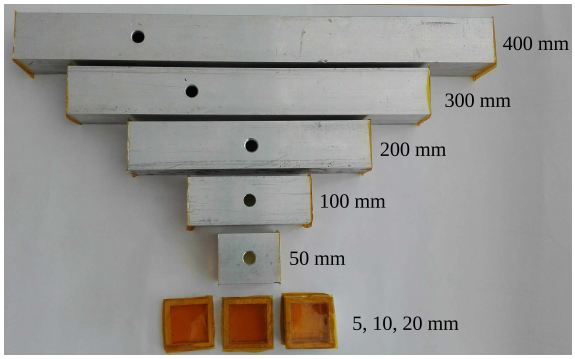

Figure 9.3: Prepared water samples with thicknesses between 5 and 400 mm. Aluminum boxes of the specified length are sealed by thin Kapton foils (adding as little additional material as possible) and filled with distilled water.

Moreover, the scattering inside composite structures is investigated by measuring the scattering inside dual-layered material probes modelling a simple composite material. It is then possible to study the dependence on the orientation of the two layers on the estimated material budget. For this purpose, two material samples with different characteristic radiation lengths $X_{0,i}$ and thicknesses d_i, but comparable material budgets ϵ_i, are added to a respective material budget $\epsilon_{\text{composite}}$, which has approximately the doubled value.

In Table 9.3, the modelled composites as acryl+aluminum, tin+nickel and copper+tungsten are shown with their characteristic material values and the radiation length of the composite is calculated with Equation 9.7.

Material	ρ [g/cm^3]	X_0 [mm]	d [mm]	ϵ [%]
Acryl (PMMA)	1.190	340.7	15.0	4.32
Aluminum (Al)	2.699	88.97	4.0	4.50
Composite	1.508	213.5	19.0	8.90
Tin (Sn)	7.310	12.06	1.25	10.36
Nickel (Ni)	8.900	14.24	1.50	10.53
Composite	8.180	13.17	2.75	20.88
Copper (Cu)	8.960	14.36	4.1	28.55
Tungsten (W)	19.300	3.504	1.0	28.54
Composite	10.987	8.930	5.1	57.11

Table 9.3: Material properties for the modelled dual-layered composites as acryl+aluminum, tin+nickel and copper+tungsten. Given are the values of specific density ρ, radiation length X_0, thickness d and resulting material budget ϵ.

ATLAS ITk materials & structures

The MBI measurements performed with unknown samples focus on materials and structures foreseen for the planned ATLAS ITk strip end-cap detector (cf. Sec. 5.3). The goal here is firstly to measure the material budget and extract the radiation length values for several raw materials used in the design of the petal core as the local support structure. Secondly, larger components and assemblies for the detector, such as electronic boards, the silicon sensor modules or the fully assembled support structure, will be investigated in terms of their material budget distribution, resolving the internal structures with high resolution.

For the investigation of raw materials, homogeneous samples with different thicknesses similar to the known material samples used for the calibration are prepared for the scattering measurements. Figure 9.4 shows an overview of the selected ITk materials studied in this work, for which the different material types are briefly presented in the following.

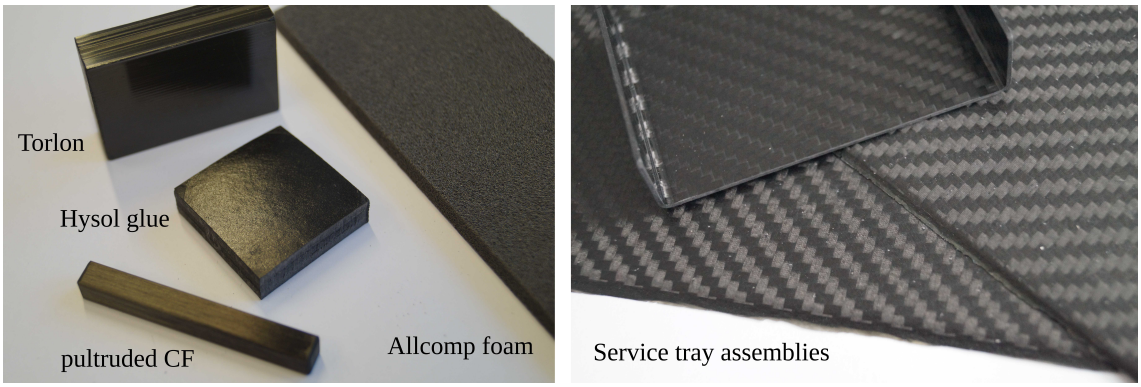

Figure 9.4: Overview of investigated ATLAS ITk raw materials for material budget measurements. Shown is a selection of prepared samples with a block of carbon-based foam (Allcomp), a bar of pultruded carbon fibers, a block of the thermoplastic Torlon, a cured token of the Hysol glue and three different samples of the service tray assembly.

- **Carbon-based foam (Allcomp)**:
  The carbon-based foam (Allcomp K9, $\rho_{\text{Allcomp}} = 0.23\,\text{g/cm}^3$) provides a high thermal conductivity between the embedded titanium cooling pipe and the core surface.
  The expected radiation length for the Allcomp foam can be calculated from the radiation length of graphite ($X_{0,\text{C}} = 193.2\,\text{mm}$, $\rho_{\text{C}} = 2.21\,\text{g/cm}^3$) by scaling with the material's density as

$$X_{0,\text{Allcomp}} = X_{0,\text{C}} \frac{\rho_{\text{C}}}{\rho_{\text{Allcomp}}} = 1\,856\,\text{mm}. \tag{9.8}$$

  Several blocks of the foam with thicknesses between 5.5 and 31.5 mm are prepared for the MBI measurements to experimentally determine the foam's radiation length.

- **Pultruded carbon fiber**:
  The pultruded carbon fiber material is made of carbon fibers which are converted into a fiber-reinforced plastic material using the technique of pultrusion with an adhesive matrix. It is foreseen for the lateral closeouts of the core featuring C/V-channels. Two types of pultruded CF bars are investigated with carbon fibers of type T300 and either using an epoxy-based adhesive or a vinyl-based adhesive. Due to the unknown resin content of the pultruded material as well as the exact properties of the selected adhesive, the radiation length cannot be calculated and is therefore directly measured with the MBI technique.

- **Thermoplastic (Torlon)**:
  The thermoplastic material Torlon 4301 is the chosen material for the top and bottom closeouts of the core, including also the high-precision manufactured petal locators. The material is based on a polyamide-imide (PAI) resin, but the exact composition of the polymer structure is proprietary. The radiation length of Torlon is therefore determined experimentally using two blocks of the material with different thicknesses of 3 and 10.2 mm in the scattering measurements.

- **Glue (Hysol)**:
  For the assembly of the core structure, the epoxy-based adhesive Hysol EA9396 is the selected choice. To enhance the thermal and electrical conductivity of the glue, Hysol is mixed with carbon powder with 30% mass fraction. Again, the radiation length of the adhesive cannot be calculated as the exact composition is proprietary knowledge, requiring therefore the direct extraction of the X_0 value from scattering measurements. Different sample tokens of the cured glue, either pure or carbon-loaded, are prepared with thicknesses ranging between 4.9 and 10.2 mm.

- **Service tray assemblies**:
  The service trays are foreseen for the global support structure of the end-cap detector, containing the services for the detector in terms of power and data cables as well as the cooling lines. The design of the service tray consists of six layers of woven 0-90 prepreg cocured in the autoclave and forming a U-shape structure.
  Also here, the exact composition in terms of the resin content of the cocured assembly cannot be used for a calculation of the radiation length. With scattering measurements on three different samples, a cut-out of a U-shaped service tray as well as two cocured rectangular test structures, the radiation length value for the service tray assembly is studied experimentally.

A collection of photographs for the telescope setups with the different prepared samples placed between the upstream and downstream telescope arm is shown in Figure 9.5.

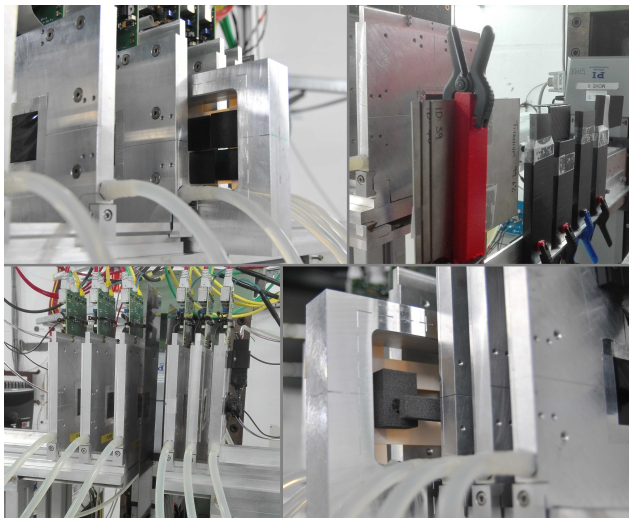

Figure 9.5: Collection of photographs showing different setups with the investigated ATLAS ITk materials placed on the x-y-positioning stage. Some of the pictures were taken before the final alignment of the SUT with the beam.

With the possibility of the MBI technique to resolve the two-dimensional material budget distribution of samples with a high resolution, several assembled structures for the ITk detector are investigated in this work, which are briefly introduced in the following.

- **Electrical break assembly**:
  The electrical break assembly, integrated at the in- and outlet of the petal's cooling loop, will ensure the electrical insulation between the local and global support structure to provide a noise-free ground potential to the electrical components on the petal. It is a vacuum brazed assembly of an alumina ceramic part for the insulation with a titanium weld sleeve to be connected to the titanium cooling loop on the one side and a copper tube for the connection to the cooling lines of the global end-cap structure on the other side. The selected section of the electrical break in the MBI measurements as well as geometrical information about the assembly are shown in Figure 9.6a.

- **End of Substructure board**:
  The **E**nd **o**f **S**ubstructure (EoS) is the gateway between the on-detector electronics on the petal and the off-detector system and is responsible for powering, data transmission, control and triggering. It consists of a complex, multi-layered PCB with several soldered electronic components (e.g. resisistors, coils and ASICs) providing the power and data links. An early version of the EoS board, as shown in Figure 9.6b, is imaged with the MBI technique by scanning along the x-direction in five consecutive measurements.

- **Cocured bus tape**:
  The cocured bus tape is the top and bottom surface of the petal core and is an assembly of the carbon fiber face-sheets with three layers of prepreg material cocured to the polyamide-based bus tape with embedded copper lines. It provides the electrical services (low/high voltage and data) for the modules mounted on the petal core. The internal structure of the 185 µm thin bus tape has a complex geometry with copper lines arranged in two layers embedded in polyamide and adhesive layers with openings on the top and bottom for electrical contacting. For the MBI measurements, a test structure of the 335 µm thin cocured bus tape with several individual copper lines as well as larger copper areas is scanned along the x-direction in seven consecutive measurements, as depicted in Figure 9.6c.



(a) Electrical break assembly with its technical drawing.

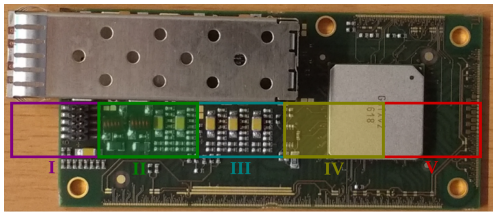

(b) End of Substructure board prototype.

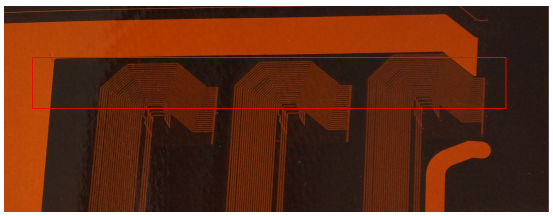

(c) Cocured bus tape structure.

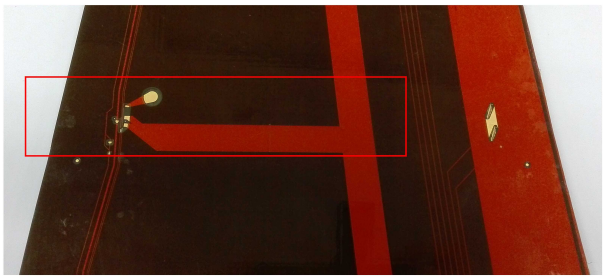

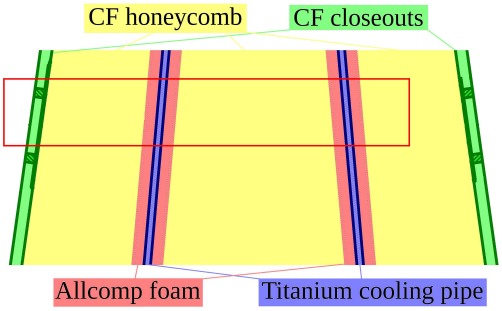

(d) Petal core prototype with its inner structure.

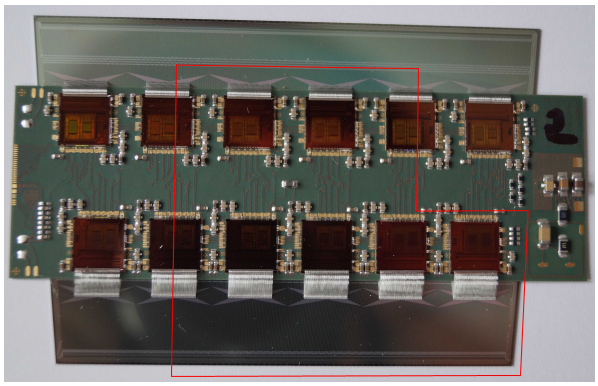

(e) Silicon sensor module prototype.

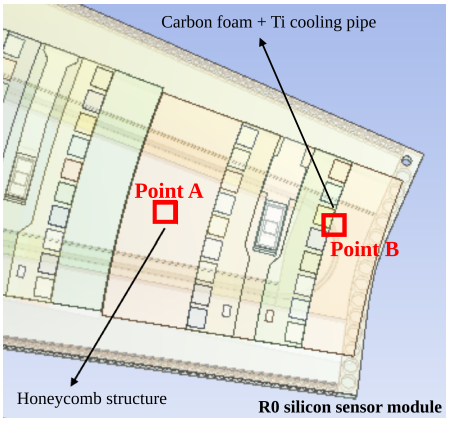

(f) Thermo-mechanical petal prototype.

Figure 9.6: Overview of investigated ATLAS ITk structures for two-dimensional material budget measurements. The red boxes mark in each case the covered area for the imaging, exploiting also the automatic scanning functionality of the x-y positioning stage to study larger areas than the detection area of the telescope sensors with $(2 \times 1)\,\mathrm{cm}^2$.

- **Petal core**:
  The petal core (cf. Sec. 5.3.2) is the local support structure for the ITk strip endcap detector and consists of a sandwich structure to provide mechanical support, electrical connections and cooling for the glued on sensor modules. The material budget distribution for a petal core prototype is imaged in a two-dimensional scan over the core's surface with nineteen consecutive measurements, as shown in Figure 9.6d. Here, different sections of the core with the top and bottom surface covered by a cocured bus tape are traversed: the lateral CF closeouts, the CF honeycomb and the titanium cooling pipe embedded in the carbon-based foam.

- **Silicon sensor module**:
  The silicon sensor module (cf. Sec. 5.3.1) is the main sensing element of the ITk detector consisting of a silicon strip sensor with the readout, power and control electronics attached on top. Figure 9.6e shows an early prototype of a silicon module with a trapezoidal-shaped microstrip sensor and a glued on PCB for readout. Here, twelve readout ASICs are connected to the individual strips via wire bonds with additional electronic components soldered on the PCB.
  The silicon module is imaged with the MBI technique by performing a two-dimensional scan in the x- and y-direction with fifteen consecutive measurements covering a large fraction of module's surface.

- **Thermo-mechanical petal**:
  The thermo-mechanical petal prototype (cf. Sec. 6.3.2) is a petal core structure fully loaded with dummy silicon strip modules, allowing to mimic the expected heat load of the electronics and to study the corresponding response on the thermo-mechanical characteristics of the petal. The material budget distribution of the TM petal is studied at two different points on the surface, as depicted in Figure 9.6f: in point A, the beam traverses a section on the R0 module covered with the blank silicon crystal and with the honeycomb structure inside the petal core; for point B, one of the hybrid PCBs of the R0 module is traversed and the internal structure of the core features the titanium cooling pipe embedded in the carbon-based foam.

The various used setups to insert the ATLAS ITk structures between the upstream and downstream telescope arm, using in most cases the x-y-positioning stage to perform the scans over the sample's surface in an automated way, are shown in Figure 9.7.



Figure 9.7: Collection of photographs showing different setups with the investigated ATLAS ITk structures, placed in some cases on the x-y-positioning stage for automated movements. The pictures were taken before the final alignment of the SUT with the beam.

9.3 Reconstruction of Kink Angles

For the evaluation of the SUT's material budget, the distribution of the kink angles of the scattered electrons in the material are required. Moreover, the knowledge of the spatial position of incident on the SUT allows to extract a position-resolved image of the tested sample. Therefore, the trajectory for each individual beam particle traversing the sample is necessary to infer the x- and y-position and the two independent deflection angles in the horizontal and vertical direction. For this purpose, a track reconstruction for each particle is performed with the high resolution measurement of the spatial positions in the six MIMOSA26 sensor planes of the EUDET-type beam telescopes as input.

To perform an unbiased measurement of the deflection angles at the position of the SUT, the **G**eneral **B**roken **L**ines (GBL) track fitting algorithm (cf. Sec. 8.4.4) is modified for the case of an unknown scattering inside the SUT plane. The procedure for this unbiased kink measurement is introduced in Section 9.3.1.
Overall, the track reconstruction for the scattering data recorded in the various test beam campaigns is performed within the EUTelescope framework (cf. Sec. 8.4). Section 9.3.2 describes the reconstruction flow with the consecutive steps of raw data processing, noisy pixel determination, cluster and hit building, telescope alignment and final track fitting, in the special case of analysing scattering data of a passive SUT.
Finally, the optimal choice of the track quality parameters as used in the track finding algorithm with the triplet method are investigated in Section 9.3.3. Here, the dependencies on the beam momentum, the telescope setup and the material budget of the measured SUT are studied.

After the track reconstruction with the EUTelescope framework, the reconstructed data consists of a flat ntuple with the spatial coordinates in the x- and y-direction as well as the unbiased measurement of the kink angles in the horizontal and vertical plane for each reconstructed track, which is used then in the consecutive material budget analysis.

9.3.1 Kink angle reconstruction with GBL

The GBL track model allows for kinks in the particle trajectory along the beam axis according to the multiple scattering effect occurring in any defined plane (active detector, passive material or the air volume). This is formally achieved by defining scattering planes and providing a specification of the material budget of that plane. For the SUT as an unknown scatterer without a-priori knowledge on ϵ, this implementation of the GBL track model would result in the suppression of larger deflection angles at the SUT position during the track optimization. Accordingly, the estimated kink angle at the SUT is biased.

Instead, an unbiased estimator of the kink angle inside the SUT representing a passive scatterer without a specified material budget estimate must be implemented in the GBL algorithm. This is realized by adding local derivatives in the x- and y-direction to the track model, as it is possible with a local derivative to allow for an independent change in the slope of the particle trajectory along the x- and y-axis. As the local derivative is implemented totally unconstrained and is also not part of the performed χ^2 optimization of the track, an unbiased kink angle inside the SUT can be represented.
In the multiple scattering interaction, the particle does not only change its slope, but also an additional offset of a few micrometers in the lateral direction depending on the material budget is introduced in the particle trajectory.

Therefore, for the full description of the trajectory in an unbiased way and covering all possible combinations of kink angles and offsets, two local derivatives are required. The SUT plane in the GBL trajectory is consequently modelled by two local derivatives[60] placed in distance of $\pm d/\sqrt{12}$ from the SUT's middle position between the telescope arms, where d is the measured or estimated thickness of the sample.
The effective, estimated kink angle θ_{eff} for the SUT independently in the x- and y-plane is then the sum of the two defined kinks θ_i for the local derivatives and provides a fully unbiased measurement of the unknown scattering inside the SUT. The modified GBL track model of the telescope for the measurement of a SUT, compared to the case of a DUT analysis as displayed in Figure 8.18, is shown in Figure 9.8.

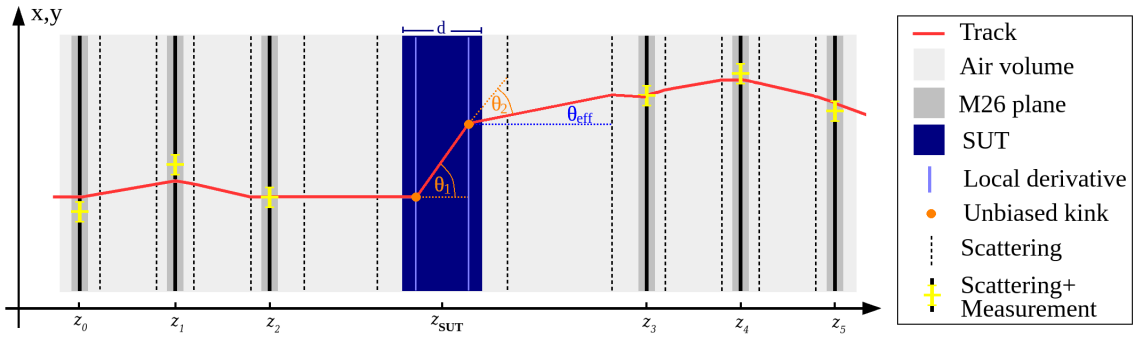

Figure 9.8: Construction of the modified GBL track model for the unbiased measurement of the kink angle inside the SUT, as a plane of unknown scattering material. Two local derivatives are added with a distance of $\pm d/\sqrt{12}$ at the position of the SUT to allow for an angle and a displacement in the trajectory. The effective kink angle is the sum of the individual deflections determined for the local derivatives as $\theta_{\text{eff}} = \theta_1 + \theta_2$.

9.3.2 Track reconstruction in EUTelescope

The track reconstruction within the EUTelescope framework performed for the scattering data of SUTs can be separated into two parts. Firstly, the test beam data with an empty telescope setup, representing the scattering in the air volume only, is used for a full reconstruction including the determination of the noisy pixels in the MIMOSA26 sensor planes and the alignment procedure for the telescope. Secondly, for the reconstruction of test beam data with various inserted SUTs between the telescope arms, the beforehand acquired information from the empty telescope reconstruction in terms of the noisy pixel database as well as the GEAR file after the alignment procedure is used as an input for the SUT reconstruction. On the one hand, the performance of the alignment process is expected to be better in this case, as no deterioration of an additional scatterer apart from the air volume exists. On the other hand, the reconstruction speed is increased as the alignment procedure requires a large fraction of the processing time and a better comparability between the samples over one sequence of runs is reached. Of course, this approach is only possible if the telescope setup is not altered during the insertion of a new sample between the telescope arms and also all other settings in terms of beam and telescope parameters remain the same over the sequence of runs.
The overall reconstruction work flow for the track reconstruction of MBI data is briefly explained for the air and SUT runs in the following.

[60] The local derivatives are added to the measurement on each of the downstream telescope planes and scaled according to the distance of the scatterer.

Reconstruction of air runs

For the telescope runs without passive scatterer, each of the individual reconstruction steps for the test beam data is performed as described in Section 8.4.3. After converting the raw data into the LCIO format used in the EUTelescope framework, the noisy pixel determination for the MIMOSA26 sensor planes is performed with the default value of 0.1% for the noise cut. The clustering of adjacent pixel hits is conducted, while removing all clusters containing pixels marked as noisy. Consecutively, hits are derived from the clustered pixel data and a pre-alignment is performed by extrapolating the hits of the first sensor plane to the other planes and applying shifts along the x- and y-axis. For the further alignment of the telescope planes, the GBL algorithm is used and a number of alignment iterations are performed with MillepedeII allowing shifts in the x- and y-plane as well as rotations around the z-axis. For each iteration, the track quality parameters for the track finding with the triplet method are optimized according to the provided suggestions of EUTelescope. Typically after three to four iterations, stable alignment parameters with a maximum of reconstructed tracks are achieved and the GEAR geometry file containing the six telescope planes with their optimized alignment constants is stored.
For the final track fitting in the reconstruction of air runs, a SUT plane is introduced to the aligned GEAR file, where the z-position matches with the position of the later inserted material samples. The track fitting is performed in a two-step approach: in the first iteration, the latest set of track quality cuts of the alignment are used as input, whereas the suggested cuts of the first run are used for a final iteration. In the end, a ROOT file is provided, containing the reconstructed tracks of the air run with an estimate of the kink angle caused by the scattering in the empty telescope setup.

Reconstruction of SUT runs

For the reconstruction with a passive scatterer in the central position between the telescope arms, an optimized process for the EUTelescope analysis is used. The SUT plane is defined in the already aligned GEAR geometry file from the corresponding air measurement with the same setup and settings, using the correct thickness and z-position of the sample. Moreover, the noisy pixel determination is excluded and the information from the created database in the air analysis is used instead. Therefore, the steps of clustering, hit derivation and a first iteration of the track fit can be merged into one reconstruction step. Here, the track quality cuts for the first track fit are also taken from the air measurement, but will certainly not be the optimal set of cuts due to the higher material budget of the sample compared to air. Therefore, optimized cuts as suggested by the EUTelescope processor are used for the final iteration of the track fit. As the output of the reconstruction of SUT runs, again a ROOT file is provided containing information about the reconstructed tracks in terms of the spatial coordinates as well as the unbiased measurement of the kink angles at the position of the SUT plane.

9.3.3 Dependence of track quality parameters

In the presented reconstruction of particle tracks with the EUTelescope framework, track candidates are found by using the triplet method. For the efficient selection of particle tracks consisting of six hits on the individual MIMOSA26 sensor planes, five independent track quality parameters are defined with the triplet residual and triplet slope cut for both the upstream and downstream triplet as well as the triplet matching cut (cf. Fig. 8.17). The optimal set of cuts depends on a number of factors such as the beam momentum, the telescope setup and also the material budget of the SUT.

A systematic study comparing the optimized track quality cuts for the SUT analysis of aluminum samples with thicknesses between 0.5 and 10.0 mm as well as the corresponding measurement for the empty telescope is shown in Figure 9.9. Here, the results for the reconstruction with beam momenta of 2 and 4 GeV/c and the telescope setups S4 and S5 at beam line TB21 are compared.

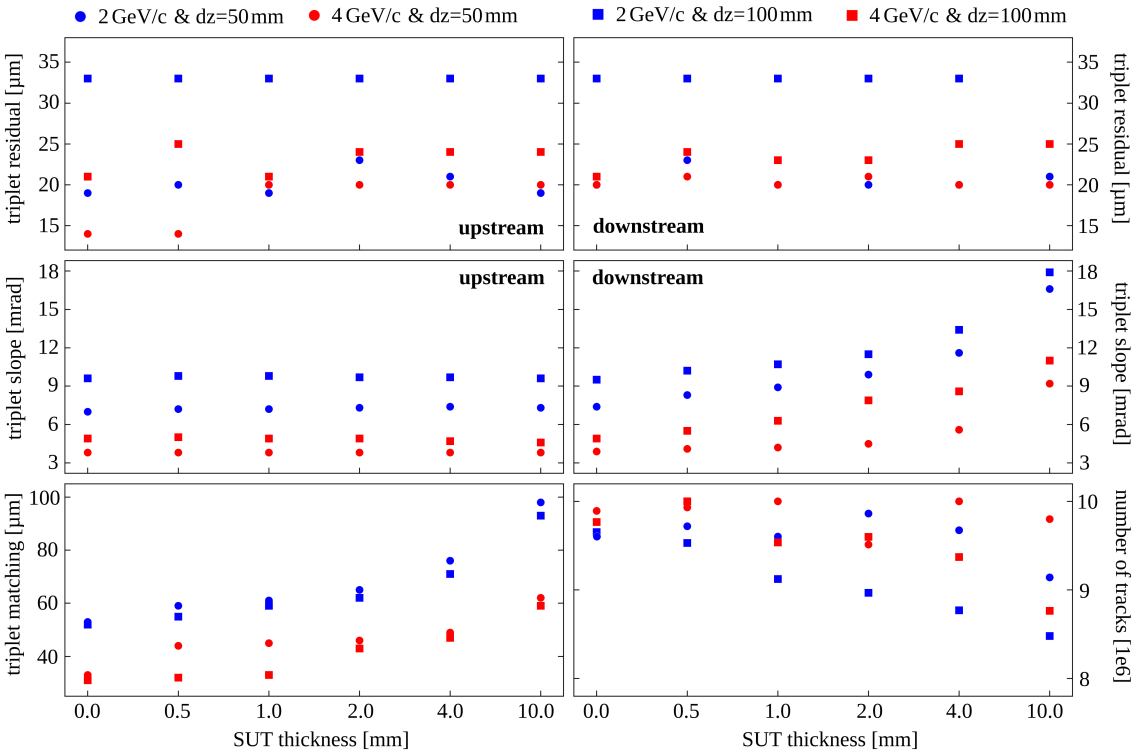

Figure 9.9: Dependence of the track quality parameters in the triplet method on the beam momentum, the telescope setup and the material budget of the SUT. Shown are the optimized values for the triplet residual and slope cut for the up- and downstream arm as well as the triplet matching cut and the total number of reconstructed tracks. Evaluated are the results for aluminum samples of thicknesses between 0.5 and 10.0 mm measured at beam momenta of 2 and 4 GeV/c and with telescope setups S4 and S5 at beam line TB21.

For the triplet residual cuts of the upstream and downstream arm of the telescope, the cuts are rather constant for the different SUT thicknesses, which is at least for the upstream triplet expected, as the influence of the SUT impacts only the downstream part of the telescope. Moreover, three of the four configurations in terms of beam momentum and telescope setup show comparable result, here only the cut values for the measurement with a lower beam momentum and a larger telescope spacing are considerably higher, indicating a worse spatial track resolution.
The determined upstream triplet slope cuts are again constant for the different SUT thicknesses, which is again expected. But also a certain structure for the four different configurations is observed. Here, the smallest values are observed for the configuration with a beam momentum of 4 GeV/c and a small plane spacing of $dz = 50$ mm, whereas the highest values are observed for the low momentum case in the wider opened telescope setup. This is caused by the scattering in the air volume between the telescope planes, as for the case of effectively more air for a wider setup or a lower beam momentum the respective scattering angles are increasing, which has therefore a direct impact on the triplet slopes.

For the downstream slope cuts, equal values as in the upstream triplet are observed for the measurement with no SUT, but otherwise increasing cut values are determined for an increasing SUT thickness. This is clearly caused by the multiple scattering of the beam particles inside the SUT material with an impact increasing for higher traversed material budgets. Moreover, the same ordering for the four configuration as before are observed, as the deflection angles are increasing for a lower beam momentum and for a wider telescope setup the lever arm for the slopes is larger.
A similar behaviour is also observed for the triplet matching, as for higher material budgets the matching criterion should be relaxed due to the lateral offsets in the sample caused by the multiple scattering interaction.
Finally, the number of reconstructed track candidates is changing as well, showing less reconstructed tracks for thicker aluminum samples. Moreover, the decrease in the track count is larger for the wider telescope setup as well as for lower beam momenta. This observation can be traced back to particles being scattered outside of the acceptance region of the telescope, meaning no detection in the downstream telescope arm. The effect due the loss of particle tracks by the acceptance is larger for higher deflection angles caused by lower momenta as well as a larger plane spacing.

The performed analysis on the track quality parameters shows that one can already infer the effects of multiple scattering, either in the air volume or the SUT material, during the reconstruction. Moreover, the choice of the measurement configuration in terms of the telescope geometry and the beam momentum has a large impact on the recorded tracks.

9.4 Analysis of Kink Angle Distributions

For the investigation of the material budget of tested SUTs, the measured distributions of reconstructed kink angles are of interest. Here, the output of the reconstruction with the EUTelescope framework using the GBL algorithm, as explained before, provides the reconstructed tracks with the spatial coordinates on the SUT plane in the x- and y-direction as well as the unbiased measurement of the deflection angles for each measured particle track. Two independent measurements of the kink angle according to the deflection in the horizontal and vertical plane, k_x and k_y, are determined.
The measured kink angle distribution results from the single scattering processes of a multitude of particle traversals through the SUT, exhibiting individual kinks inside the material according to the multiple Coulomb scattering. Due to the dependence of the observable kink angle on the material properties in terms of the material budget ϵ, the distribution of kink angles can be probed in terms of this dependence to infer the material budget from the kink angle measurement.

The reconstructed kink angle distributions from the measurement with different SUT thicknesses as well as different beam momenta are investigated in Section 9.4.1. This allows to study the major dependencies of the kink angle on the corresponding material budget of the SUT as well as on the beam momentum of the scattered electrons.
The mean of the scattering distribution is centered around zero due to the central limit theorem of the individual scattering processes and only the width of the distribution depends on the properties of the traversed material, as it was discussed in Section 9.1.2.
To evaluate the width of the kink angle distribution, an appropriate estimator $E(k_{x,y})$ for the kink angle width $\theta_0^{x,y}$ has to be found. Section 9.4.2 evaluates different estimators for the scattering width using statistical and fitting methods and compares the resulting kink estimates for the application of MBI.

Furthermore, the correlations between the two independent kink angles k_x and k_y as well as the according width estimators for the horizontal and vertical plane of the SUT are experimentally studied and evaluated in Section 9.4.3.
For scatterers of high-Z materials and an accordingly higher material budget, the measurement of the kink angle distributions is constrained due to the acceptance area of the telescope, dependent intrinsically on the active sensor area of the MIMOSA26 planes as well as the spacing of the individual planes and the SUT. The resulting acceptance effects observed in the kink angle measurement for k_x and k_y are briefly discussed in Section 9.4.4.
The beam momentum of the electrons at the DESY II Test Beam Facility is selected by a dipole magnet and collimator system, which results in a respective momentum spread in the horizontal direction, as it was described in Section 8.5.1. The corresponding influence of the energy variation along the lateral direction on the MBI technique is therefore investigated in Section 9.4.5.

9.4.1 Dependence of kink angle distributions

Several dependencies are observed for the reconstructed kink angle distributions of the individual kink angles k_x and k_y in the horizontal and vertical plane, respectively.
In principle, the deflection angles for the traversing electrons of the beam over the complete active area of the MIMOSA26 sensors, ranging from $\pm 10.6\,\text{mm}$ in the x-direction and $\pm 5.3\,\text{mm}$ in the y-direction, are reconstructed and could be used for the kink angle analysis.

But instead a *fiducial area* in the x-y-plane at the position of the SUT is chosen, such that tracks outside of the fiducial region are discarded in the analysis. Here, the size and position of the fiducial area are chosen to exclude unwanted or biasing effects on the kink angle distributions. On the one hand, it is possible that particles traversing the upstream arm of the telescope with a position close to the sensor edges and then deflected strongly on the inserted SUT to the outside will miss one of the downstream sensor planes. In this case, the particle traversal yields no reconstructed track, whereas a particle at the same position but deflected to the center of the sensor planes will most likely be reconstructed. Therefore, the resulting scattering distribution for positions at the sensor edges are biased. These edge effects as well as their zone of influence depend on the chosen telescope setup. On the other hand, the fiducial area can be chosen such that the scattering inside other materials than the to-be-measured SUT is excluded. Examples are the cut-out of the MIMOSA26 sensor frame, which is observed in the measurement of only scattering in the air volume between the telescope arms, or the influence of the SUT holder, when inside the active detection region.

In general, the fiducial area should be selected as large as possible to not loose too many tracks and reducing thereby the available data statistics, while of course excluding any unwanted effects biasing the resulting kink angle distributions. For the following analyses, the fiducial areas are chosen according to these guidelines and further details to the determination of the fiducial area are given in Appendix C.2.

First of all, the scattering distribution depends on the type and thickness of the SUT sample, which is exemplary shown in Figure 9.10 for a measurement with a selected beam momentum of $2\,\text{GeV/c}$ and telescope setup S2. The kink angle distributions for the deflection in the horizontal plane are compared for the case of only scattering in air, meaning no inserted SUT sample, and several homogeneous aluminum plates with varying thicknesses of 0.5, 1.0, 2.0, 4.0 and 10.0 mm.

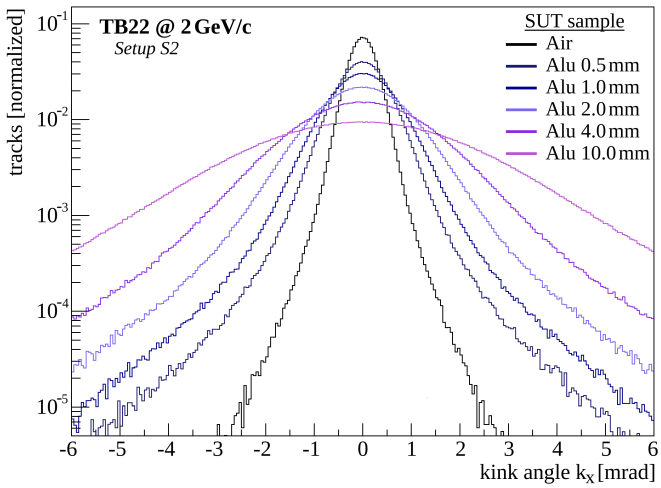

Figure 9.10: Dependence of the scattering distribution on the SUT sample for the horizontal kink angle k_x. Compared are the normalized distributions for the scattering without a SUT (only the air volume) and for several aluminum plates of varying thicknesses between 0.5 and 10.0 mm. The measurement was performed at TB22 with the telescope configuration S2 and a selected beam momentum of 2 GeV/c.

Here, a broader kink angle distribution is observed for an increasing SUT thickness, while the mean of the distribution is centered in all cases around zero. This can be explained by the fact that for a thicker SUT sample the mean number of scattering processes for the traversing beam particle inside the material is increasing. On average over the multitude of particle tracks, the mean of the individual deflection angles is zero following the central limit theorem, whereas the width of the distribution is increasing.
Moreover, it is expected that the width of the kink angle distribution does not depend individually on the type and thickness of the scattering material but only on its material budget ϵ. This dependence can be tested by selecting different material types and SUT thicknesses with similar material budgets, as it is done for the calibration of the MBI technique in Section 9.5.

Secondly, the dependence of the measured kink angle distribution on the beam momentum for the scattered particles is investigated in Figure 9.11 for the measurement of a nickel plate with a thickness of 1.0 mm. Again, the scattering distributions for the horizontal kink angle k_x are compared for varying beam momenta between 1 and 5 GeV/c.

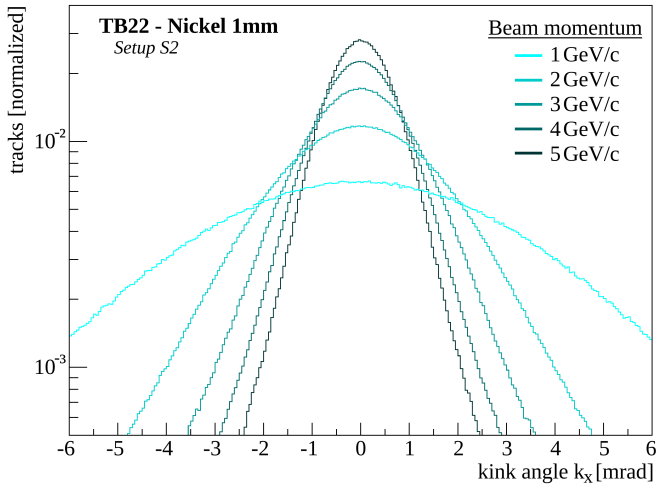

Figure 9.11: Dependence of the scattering distribution on the beam momentum for the horizontal kink angle k_x. Compared are the normalized distributions for electrons with varying momenta of 1, 2, 3, 4 and 5 GeV/c. The measurement was performed at TB22 with the telescope configuration S2 and a 1 mm thick nickel plate as SUT.

Here, the scattering distributions show a broader shape for a decreasing momentum of the scattered electrons in the SUT. This aspect is described in the Highland formula by the proportionality of the kink angle width θ_0 to the inverse of the particle momentum p due to the underlying physics of multiple Coulomb scattering.

Further possible dependencies on the choice of the beam parameters, e.g. comparing the beam lines TB21 and TB22, or the telescope setup, e.g. in terms of the spacing between the sensor planes, on the measured kink angle distributions are discussed as well in the context of the calibration procedure in Section 9.5.

9.4.2 Estimators for the scattering width

For the evaluation of the SUT's material budget, the measured scattering angle distributions of the kink angles k_x and k_y are used. Here, the scattering distribution results from the single scattering processes of a multitude of particle traversals through the SUT and exhibiting individual kinks inside the material. Whereas the mean of the distribution is centered around zero and does not contain information about the scattering material, the width of the distribution depends on the traversed material budget. Due to the features of the distribution with a Gaussian-like core and considerable tails proportional to the fourth power of the kink angle, as described by the multiple scattering theory (cf. Sec. 9.1.2), an appropriate estimator $E(k_{x,y})$ for the kink angle width $\theta_0^{x,y}$ must be found.

In the case of the Highland model, the scattering width is retrieved as the width of a Gaussian distribution fitted to the inner 98% quantile of the kink angle distribution. Nevertheless, the influence of the choice of the estimator is studied in the following for two different methods[61], which allows to optimize the width estimator according to the requirements of the measured data set, e.g. for the handling of low data statistics.

On the one hand, a *statistical approach* is used by calculating the mean and width of the kink angle distribution as the statistical mean $\bar{k}$ and the **R**oot-**M**ean-**S**quare (RMS) with

$$\bar{k}^{x,y} = \frac{1}{N}\sum_{j=0}^{N} k_j^{x,y} \quad \text{and} \quad \text{RMS} = \sqrt{\frac{1}{N}\sum_{j=0}^{N}\left(k_j^{x,y} - \bar{k}^{x,y}\right)^2}. \tag{9.9}$$

On the other hand, a *fitting approach* is tested by retrieving the mean and the width of the kink angle distribution as the fitted parameters μ and σ of a Gaussian distribution with

$$f(k^{x,y}) = a \cdot \exp\left(-\frac{1}{2}\left(\frac{k^{x,y}-\mu}{\sigma}\right)^2\right). \tag{9.10}$$

To accommodate for the influence of the tails of the scattering distribution, the estimated width for the full data set meaning 100% is compared to the results from the estimators applied to inner quantiles of the distribution using 98%, 95% and 90% of the data, denoted in the following as RMS_i and Gauss_i with $i = 100, 98, 95, 90$ for the corresponding quantiles. This approach is chosen to not bias the estimated kink angle width by applying any a-priori cuts on the measured data, but reducing nonetheless the influence of the tails.

For the comparison of the different estimator methods, a data set from a measurement with aluminum as SUT over a range of thicknesses between 0.5 mm and 10 mm is exemplary used in the following. The data were collected with the DURANTA telescope in TB22 with a selected beam momentum of 2 GeV/c and using the telescope setup S2.

[61] A detailed study on the influence of even more estimators on the retrieved kink angle width, also in terms of the contrast-to-noise ratio (CNR), was conducted in [253]. Here, the average absolute deviation with $\text{AAD} = \frac{1}{N}\sum_{j=0}^{N}|k_j^{x,y} - \bar{k}^{x,y}|$ for the inner 90% quantile as a robust statistical estimator was evaluated with the highest CNR value.

In the *inclusive analysis*, the kink angle widths for the different sample thicknesses are extracted by applying the estimators on the kink angle distributions from all events inside the selected fiducial area. In Figure 9.12, the results for the estimators evaluated for the inner quantiles of 100%, 98%, 95% and 90% of the data are shown, using the measured scattering distribution for the kink angle k_x with the 2 mm aluminum sample.

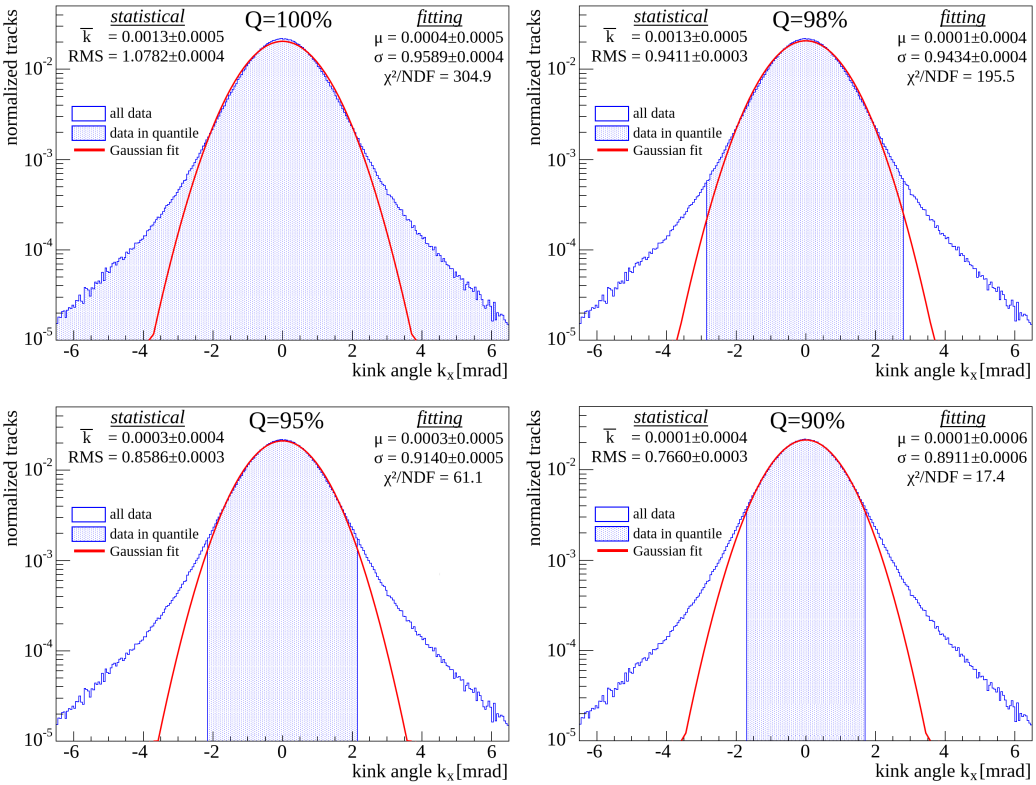

Figure 9.12: Comparison of the statistical and the fitting approach in the inclusive analysis to estimate the mean and the width of the kink angle distribution using the inner quantiles of 100%, 98%, 95% and 90% of the data. Shown is the resulting kink angle distribution for the horizontal kink angle k_x extracted from all reconstructed tracks inside the fiducial area for a measurement with the 2 mm aluminum sample at a beam momentum of 2 GeV/c.

By selecting different ranges in terms of inner quantiles of the reconstructed track data, the estimated values for the mean and the width of the kink angle distribution is changing. Whereas the estimated mean value is in all cases and methods very compatible with zero, which is shown in Appendix C.3, the estimated kink width is decreasing when constraining the distribution to smaller quantile intervals. This is due to the fact that the non-Gaussian tails of the distribution are omitted for smaller quantiles, resulting in a better estimate of the Gaussian-like core of the distribution with the statistical and fitting method. When comparing the estimated kink angle widths from the RMS and the fitted standard deviation of the Gaussian fit, one observes very comparable values for the 98% quantile, whereas for smaller quantiles the RMS value is decreasing faster than the width of the Gaussian fit.

For the *binned analysis*, the reconstructed track positions in the x- and y-direction are used to construct a spatially-resolved kink angle map for the individual kinks k_x and k_y. Here, the virtual reconstruction plane at the position of the SUT is divided in the following standardly into image cells of 100 µm × 100 µm.

The resulting scattering distribution for each cell originates from particle tracks with a reconstructed x- and y-position inside the defined cell. In the two-dimensional kink angle map, the width of the scattering distribution of each cell using an appropriate estimator is then displayed, allowing to study the position-resolved kink angle width.
Figure 9.13 shows the resulting kink angle maps for the 4 mm aluminum sample, when using as the estimator for the kink angle width either the RMS or the Gaussian fit on the inner 98% quantile of the image cell's distribution.

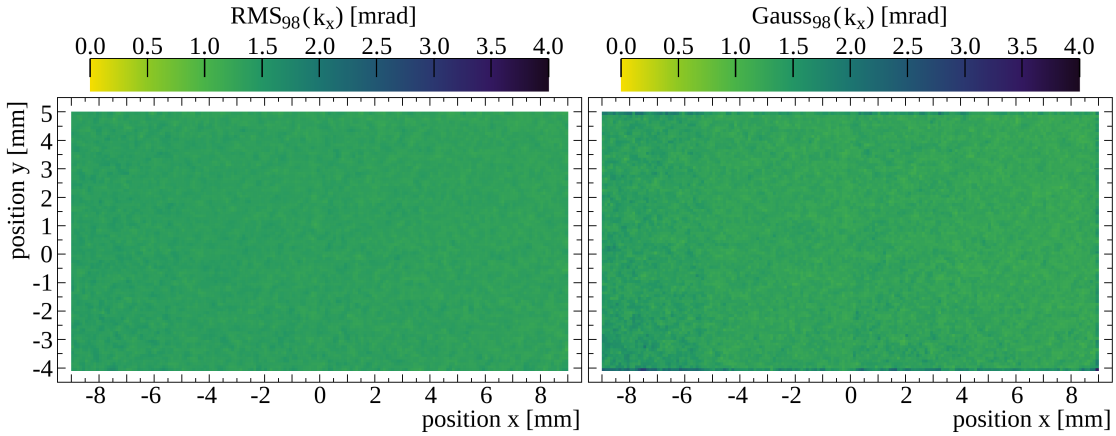

Figure 9.13: Comparison of the two-dimensional kink angle maps using the RMS_{98} (left) and the Gauss_{98} (right) estimator in the binned analysis. Shown are the position-resolved kink angle widths for the horizontal kink angle k_x inside the fiducial area for a measurement with the 4 mm aluminum sample at a beam momentum of 2 GeV/c.

The resulting kink angle maps from the RMS_{98} and the Gauss_{98} estimator are very comparable, with the only difference that the map for the fitted approach appears to have a higher contrast with the possibility to finer resolve structures in the sample.
In general, smaller variations along the x- and y-direction are observed for the kink angle maps, even though that the investigated SUT is a homogeneous sample of constant thickness and material composition. These variations of measured kink angles along the lateral directions are investigated in detail in Section 9.4.5.

Figure 9.14 compares the estimated kink angle widths using the statistical and the fitting approach evaluated on the different quantiles for the inclusive and binned analysis. In the case of the inclusive analysis, the extracted values for the kink angle width from the distributions as the RMS or the width of the Gaussian fit and their respective uncertainty are used directly. For the binned analysis, the mean value and its standard deviation are calculated from the individual estimated kink angle widths in each image cell. Moreover, the kink angle widths calculated with the Highland formula (cf. Eq. 9.4) for the corresponding material budgets of the aluminum samples are shown for reference.

In general, it is again observed that the estimated values for the kink angles are decreasing with smaller quantile sizes for the statistical as well as the fitting approach.
For the statistical approach, the RMS values for the case of 100% of data are overshooting the predicted value by the Highland formula significantly, whereas the RMS values for smaller quantiles are underestimating the kink angle for increasing material budgets of the SUT. Therefore, the RMS_{98} estimator shows the most consistent results over the measurement range with values always slightly above the prediction.

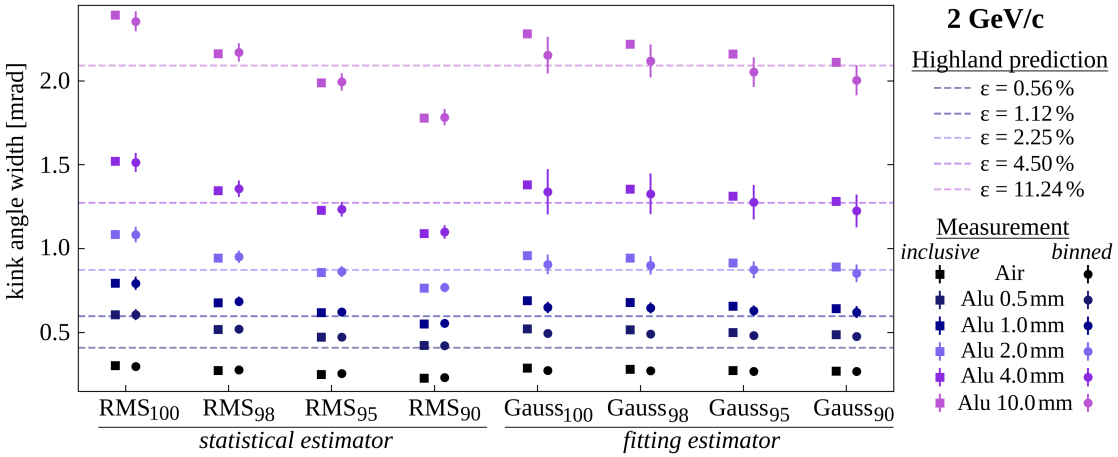

Figure 9.14: Evaluation of the width estimators for the kink angle using the statistical approach with the RMS and the fitting approach with the Gaussian fit. A measurement of aluminum samples with thicknesses of 0.5, 1.0, 2.0, 4,0 and 10.0 mm for momentum of 2 GeV/c is used. Shown are the estimated widths for the two methods evaluated for the different selected inner quantiles of 100%, 98%, 95% and 90% in the inclusive and binned analysis. Moreover, the kink angle widths calculated with the Highland formula are displayed.

For the fitting approach, the inclusive analysis provides always higher estimates for the kink angle than the average value of the binned analysis and depending on the selected quantile the one or the other is more compatible with the predicted value. Here, the Gauss_{98} estimator is overall a good estimator and also used formally in the Highland formula. Comparing the results from the inclusive and binned analysis, the observed variations in the two-dimensional kink angle maps are visible as the higher uncertainty in terms of the standard deviation of the individual estimated kink widths from the image cells. The binned approach will be also used in the following, as it provides a more robust result with an appropriate level of measurement uncertainty on the estimated kink angle width.

The decision on the appropriate estimator, either following a statistical or a fitting approach, depends on several aspects of the measurement. In general, fitting methods are expected to be less sensitive to the influence of tails in the distribution than statistical methods, providing therefore in principle a better estimate for SUTs with larger material budgets and corresponding kink angle distributions. Moreover, a higher contrast in the shown kink angle map for the fitting approach compared to statistical approach is observed, favoring the Gauss_{98} over the RMS_{98} estimator. On the contrary, fitting methods are less robust than statistical methods when facing a lower number of data points. In the case of the shown kink angle maps with a cell size of 100 µm × 100 µm on average (852 ± 184) tracks are contained in each cell providing therefore a solid basis for a fit of the distribution. But the fitting approach could fail for smaller image cells, if the same total amount of measured tracks for the SUT are provided. Furthermore, the fit result can strongly depend on the choice of boundary conditions and initial parameters of the fitting algorithm.

In the course of this work, studies were performed with both estimators, RMS_{98} and Gauss_{98}. But since some artifacts for the fitting approach, especially for SUTs with higher material budgets, were observed and are at the time of writing under investigation, the RMS_{98} estimator in the binned analysis is the selected choice in the following.

9.4.3 Correlation of horizontal and vertical kinks

The unbiased measurement of the kink angle in the track reconstruction with the GBL algorithm (cf. Sec. 9.3.1) yields two independent measurements for the deflection angle in the horizontal and vertical plane. The values k_x and k_y are expected to be fully uncorrelated as the deflection is described individually for the orthogonal x- and y-axis and due to the underlying multiple scattering interaction as a quantum mechanical process.
For the experimental test of the correlation, the scattering data of aluminum samples with different SUT thicknesses and taken with a beam momentum of 2 GeV/c is used. Figure 9.15 shows the measured correlation between the reconstructed kink angles k_x and k_y for the 2.0 mm thick aluminum plate.

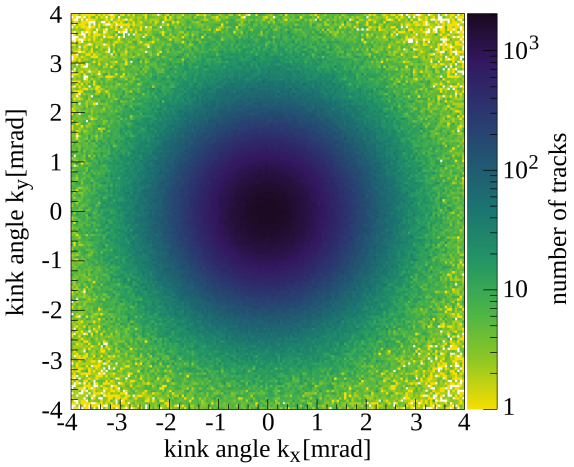

Figure 9.15: Measurement of the correlation between the kink angles k_x and k_y. Shown are the results for a measurement with the 2.0 mm thick aluminum sample performed at TB22 with the telescope setup S2 and a selected beam momentum of 2 GeV/c.

With a calculated Pearson correlation coefficient of $\rho_{k_x,k_y} = -0.0009$ for this data set and comparable values for the other sample thicknesses, no correlation between the kink angles k_x and k_y is observed.

In the next step, the correlation between the estimators of the kink angle width in the x- and y-direction is investigated to prove that both independent measurements follow the same scattering distribution. In Figure 9.16, the correlation for the estimator RMS_{98} applied on the individual kink angle distributions in the horizontal and vertical plane is shown. The kink angle widths are extracted per image cell, using the standard cell size of 100 µm × 100 µm. Moreover, the aluminum data for SUT thicknesses of 0.5, 1.0, 2.0 and 4.0 mm are combined to evaluate the trend of the correlation over different kink angles.

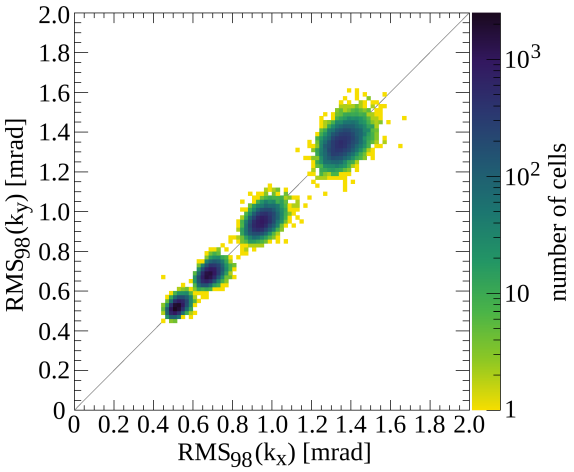

Figure 9.16: Measurement of the correlation for the estimator RMS_{98} of the kink angle width between the x- and y-direction. Shown are the combined results for the 0.5, 1.0, 2.0 and 4.0 mm aluminum samples for the individual measurements at TB22 with the telescope setup S2 and a selected beam momentum of 2 GeV/c.

A strong correlation for the width estimators in the x- and y-plane using the RMS_{98} method is observed for the different data sets. In this case, the calculated correlation coefficients $\rho_{E(k_x),E(k_y)}$ for the estimator $E(k)$ and various evaluated SUT samples show values larger than 0.97. Only for measured SUTs with a larger material budget, a higher deviation from the central line is observed, showing larger deflection angles in the horizontal than in the vertical plane. This observation is explained by the asymmetric active sensor area in the x- and y-direction leading for higher ϵ to acceptance effects, as discussed in the next section.

Overall, the performed tests show that the measurements of the kink angles in the horizontal and vertical plane are usable as independent estimators of the scattering inside the SUT. Therefore, the two measurements can be combined for the evaluation of kink angle distributions: the values of k_x and k_y are filled in the same histogram denoted with k_{x+y}, which provides then two data points per reconstructed track.
By this approach, the available amount of kink angle data is effectively doubled and leads to a decreasing statistical uncertainty on the resulting material budget estimate.

9.4.4 Acceptance effects for kink angle distributions

For the investigation of SUT samples with a larger material budget ϵ, another effect is observed for the edge regions of the spatially-resolved kink angle maps. The reason is the limited *acceptance* of the active area covered by the sensor planes of the telescope, which is important when particles traversing through the edge regions are deflected strongly to the outside and leaving therefore the detection area. This causes a biasing of the measured kink angle distribution to angles pointing to the center of the telescope.

Figure 9.17 shows the kink angle maps for the measurement of the 5 mm thick tungsten sample performed at beam line TB21 with 2 GeV/c and using telescope setup S4. The two-dimensional distributions of the estimated kink angle widths $\mathrm{RMS}_{98}(k_x)$ and $\mathrm{RMS}_{98}(k_y)$ are plotted individually and the standard cell size of $(100\,\mu\mathrm{m})^2$ is used.

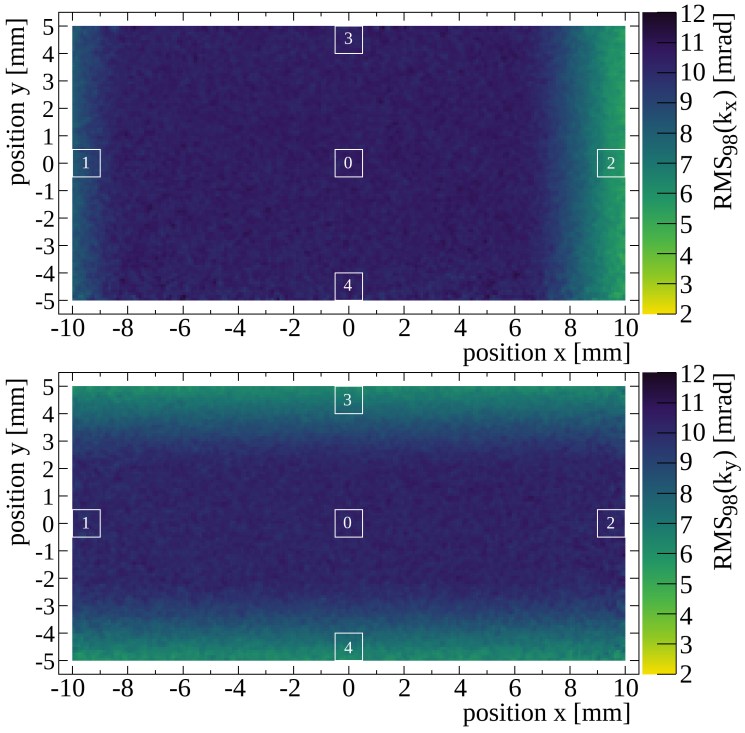

Figure 9.17:
Position-resolved kink angle maps for the horizontal and vertical plane with the estimated kink angle widths $\mathrm{RMS}_{98}(k_x)$ (top) and $\mathrm{RMS}_{98}(k_y)$ (bottom), respectively. Shown are the results for a measurement with the 5 mm thick tungsten sample performed at TB21 with a beam momentum of 2 GeV/c and telescope setup S4. Regions of 1 mm^2 are marked in the center (0) and at the left (1), right (2), top (3) and bottom (4) edge for the following analysis.

For the kink angle map in the x-direction, smaller estimated values of $\mathrm{RMS}_{98}(k_x)$ are observed for the left and right edges, whereas the effect on the right edge is much more pronounced. A similar behaviour is observed for the kink angles in the y-direction with smaller values of $\mathrm{RMS}_{98}(k_y)$ at the top and bottom edge.
To further investigate the acceptance effect, the kink angle distributions for k_x and k_y are evaluated in selected regions at the left, right, top and bottom edge and compared with a region in the center. Here, selected subsets of the kink angle data in areas of $1\,\mathrm{mm}^2$ are used as marked in Figure 9.17. The normalized scattering distributions are compared separately for the horizontal and vertical plane in Figure 9.18.

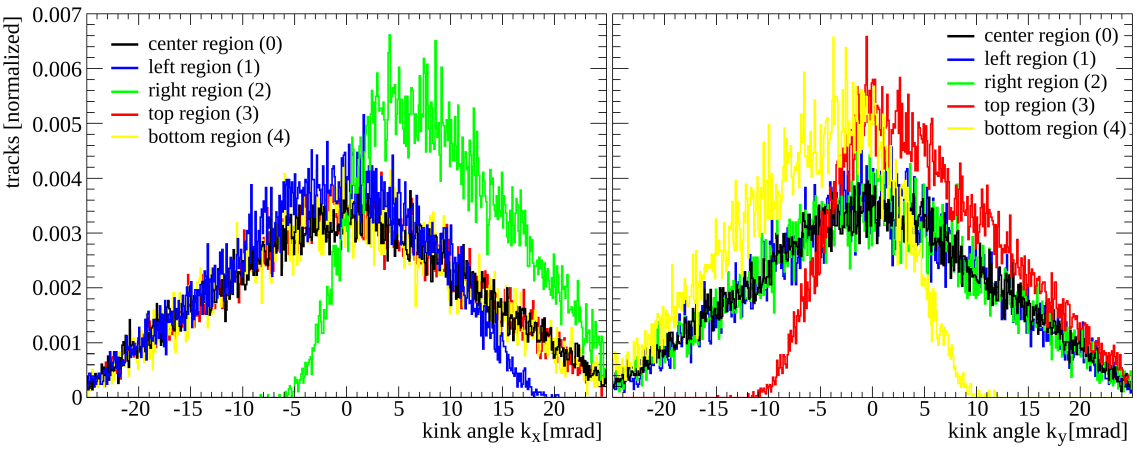

Figure 9.18: Comparison of the normalized scattering distributions for the kink angle k_x (left) and k_y (right) for selected regions in the x-y-plane. The regions at the center as well as at the left, right, top and bottom edge of the detection area are defined as marked in Fig. 9.17.

In the kink angle distributions, it is observed that for the kink angle k_x the distributions for the top and bottom region overlay well with the center region, and the same is the case for the distribution of the left and right region for the kink angle k_y. On the contrary, the kink angle distribution in k_x for the left region is slightly skewed to negative deflection angles, whereas the distribution for the right region is strongly skewed to positive angles. Similarly, the kink angle distributions in k_y are skewed to positive angles for the top region and to negative values in the bottom region, with the tails of the distribution limited to values of $\pm 10\,\mathrm{mrad}$ in the respective direction.
This measurement clearly indicates the effect of a limited acceptance area of the telescope, which can be explained e.g. for the case of traversing particles at the right edge of the active sensor area as following: for positive deflection angles, the particle is deflected to the inside of the telescope acceptance and its trajectory is most likely reconstructed, whereas the traversing particle is leaving the acceptance area for negative deflection angles and the corresponding track is not reconstructed. Therefore, the kink angle distribution is biased to the respective direction yielding considerably smaller kink angle widths. This is shown quantitatively in Table 9.4, evaluating the estimated kink angle widths as RMS_{98} of k_x, k_y and the combination k_{x+y} (cf. Sec. 9.4.3) in the defined regions.

The kink angle map for the combination k_{x+y} of the independent measurements k_x and k_y is shown in Figure 9.19 for the case of the 5 mm thick tungsten sample. Here, the acceptance effect is clearly visible at all edges as a superposition of the observed effects in the two independent planes x and y.

Region	$\text{RMS}_{98}(k_x)$ [mrad]	$\text{RMS}_{98}(k_y)$ [mrad]	$\text{RMS}_{98}(k_{x+y})$ [mrad]
Center (0)	10.57 ± 0.19	10.34 ± 0.17	10.45 ± 0.13
Left (1)	8.90 ± 0.45	10.06 ± 0.25	9.49 ± 0.24
Right (2)	6.20 ± 0.40	10.22 ± 0.23	9.59 ± 0.28
Top (3)	10.43 ± 0.18	7.11 ± 0.52	9.20 ± 0.15
Bottom (4)	10.43 ± 0.28	6.98 ± 0.53	9.30 ± 0.17

Table 9.4: Estimation of the kink angle width as RMS_{98} of k_x, k_y and k_{x+y} for the defined regions (center, left, right, top, bottom). The value is determined as the mean value and its standard deviation of the kink angle widths extracted from each image cell inside the $1\,\text{mm}^2$ areas.

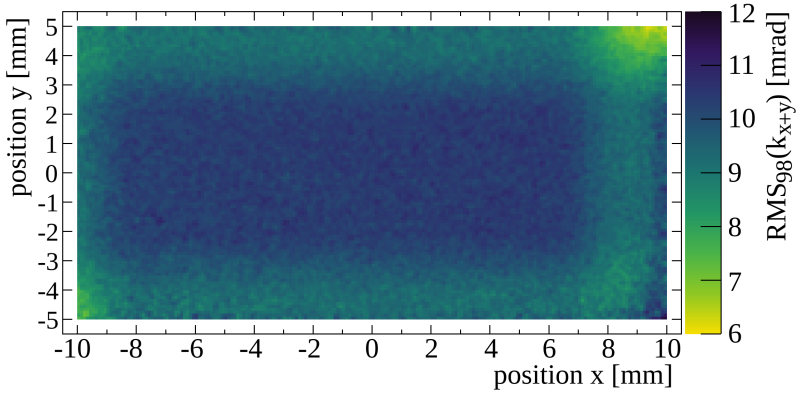

Figure 9.19: Position-resolved kink angle map for the combination k_{x+y} with the RMS_{98} estimator applied on the same measurement of the 5 mm thick tungsten sample at 2 GeV/c.

In this case, only the measured kinks in the central region, here between $-8\,\text{mm}$ and $7\,\text{mm}$ in the x-direction and $\pm 3\,\text{mm}$ in the y-direction, yields an unbiased measurement of the kink angle width. Therefore, the fiducial area in the analysis of SUTs with higher material budgets[62], resulting in the observed acceptance effects at the edges of the active sensor area, should be selected accordingly for the extraction of the kink angle width serving as input for the material budget evaluation.

In general, the acceptance effect in the y-direction is more pronounced than in the x-direction, as it is more likely that a scattered particle leaves the acceptance area of the telescope along the y-axis. This is simply caused by the rectangular shape of the MIMOSA26 sensor planes with a larger active area along the x- than the y-axis.
Moreover, the telescope setup has a direct influence on the acceptance effect as for a smaller distance $dz_{\text{down}}^{\text{SUT}}$ between the SUT and the first sensor plane of the downstream telescope arm as well as for smaller plane distances dz_{down} in the downstream arm, the limiting acceptance angle for the measurement is increased. But as at the same time the angular resolution of the telescope decreases, the telescope setup in the measurement should be always optimized for the expected material budget of the SUT.

9.4.5 Influence of the horizontal beam momentum variation

In a further study, the observed variation of the estimated kink angle widths for the position-resolved kink angle maps is analysed in detail. Figure 9.20 shows in this context the measured kink angle map for the 1.0 mm thick nickel sample at a selected beam momentum of 2 GeV/c and telescope setup S2 at beam line TB22.

[62] The acceptance effect can also occur for moderate material budgets, but low particle energies due the antiproportionality of the kink angle width with the particle momentum.

To distinguish the variation for the estimated kink angle widths $\mathrm{RMS}_{98}(k_{x+y})$ along the x- and y-axis, a higher contrast scale is chosen. Moreover, the two-dimensional map is projected along the horizontal and vertical direction and a linear fit of the data points is performed to evaluate possible systematic variation effects along the respective axis.

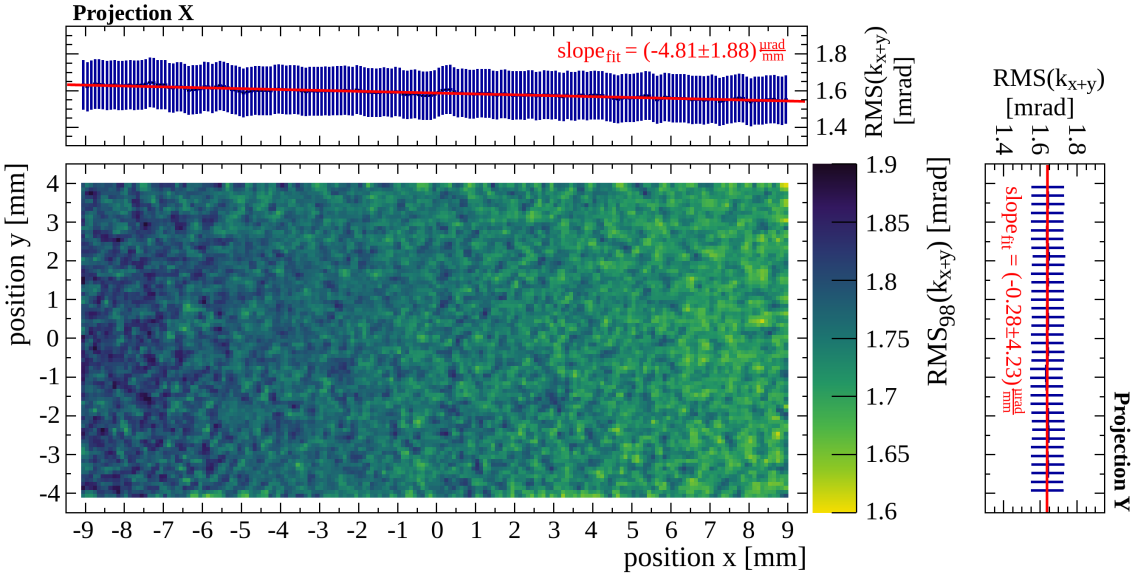

Figure 9.20: Position-resolved kink angle map for the estimated widths $\mathrm{RMS}_{98}(k_{x+y})$ of the 1.0 mm thick nickel SUT. The projections along the x- and y-axis are shown as well and a linear fit to determine the slope of the projected data points is performed. The measurement was performed at a selected beam momentum of 2 GeV/c and with telescope setup S2 at beam line TB22.

From the displayed kink angle map, one can deduce a negative trend for the kink angle widths along the horizontal axis, whereas no systematic variation along the vertical axis is observed. This observation is also proven by the fitted slopes of the projection along the x- and y-axis: the slope for the horizontal direction is determined with $(-4.81 \pm 1.88)\frac{\mu\mathrm{rad}}{\mathrm{mm}}$ indicating clearly a negative trend for the kink angle widths along this direction, whereas the slope for the y-direction with $(-0.28 \pm 4.23)\frac{\mu\mathrm{rad}}{\mathrm{mm}}$ is consistent with no systematic variation along the vertical axis. To study the systematic variation of the kink angle widths quantitatively, the fitted slopes for the projected data points along the x-direction as well as the kink angle widths $\mathrm{RMS}_{98}(k_{x+y})$ determined from all image cells are shown in Table 9.5. Here, the measurement results of nickel samples with a thickness of 0.25 and 1.0 mm at varying beam momenta between 1 and 5 GeV/c are compared.

Beam	Nickel 0.25 mm		Nickel 1.0 mm	
momentum	$\mathrm{RMS}_{98}(k_{x+y})$ [mrad]	slope_x $[\frac{\mu\mathrm{rad}}{\mathrm{mm}}]$	$\mathrm{RMS}_{98}(k_{x+y})$ [mrad]	slope_x $[\frac{\mu\mathrm{rad}}{\mathrm{mm}}]$
1 GeV/c	1.477 ± 0.035	-2.94 ± 1.73	3.018 ± 0.085	-5.20 ± 2.48
2 GeV/c	0.851 ± 0.018	-2.46 ± 1.31	1.750 ± 0.044	-4.81 ± 1.88
3 GeV/c	0.592 ± 0.019	-1.66 ± 1.10	1.212 ± 0.039	-3.10 ± 1.57
4 GeV/c	0.452 ± 0.012	-1.16 ± 0.96	0.911 ± 0.022	-2.14 ± 1.36
5 GeV/c	0.379 ± 0.019	-0.88 ± 0.88	0.739 ± 0.035	-1.47 ± 1.22

Table 9.5: Estimated kink angle widths $\mathrm{RMS}_{98}(k_{x+y})$ and slope of projected values along the x-axis for the measurement of 0.25 and 1.0 mm thick nickel samples performed at varying beam momenta between 1 and 5 GeV/c.

When calculating the relative variations in the kink angle using the determined overall value of $\mathrm{RMS}_{98}(k_{x+y})$ for the different tested beam momenta, the 0.25 mm nickel sample yields a value of $(-0.25 \pm 0.04)\,\frac{\%}{\mathrm{mm}}$ and $(-0.23 \pm 0.04)\,\frac{\%}{\mathrm{mm}}$ for the 1.0 mm thick SUT. Therefore, the relative variation seems to be constant within the uncertainties for the different beam momenta and the SUT thicknesses corresponding to different material budgets of the sample.

This observed systematic variation of kink angle widths along the horizontal direction is explained by the generation of the beam at the DESY II Test Beam Facility. Here, the beam momentum of particles is selected in the final step of the beam generation by a dipole magnet and a beam collimator, as described in Section 8.1.1. Only particles with a matching momentum corresponding to the selected current through the dipole magnet are passing the collimator. Nonetheless, the beam momentum is not constant at the nominal selected value, but a constant momentum spread of $(158 \pm 6)\,\mathrm{MeV/c}$ for different beam momenta was measured (cf. Sec. 8.5.1). The momentum of the beam particles varies with the horizontal position over the opening of the beam collimator and the determined increase of approximately 150 MeV/c over a transverse range of 5 mm matches well with the observed overall momentum spread.

The variation of the beam momentum is therefore the reason for the variation of the kink angle widths along the horizontal axis, as the kink angle width directly depends on the energy of the scattering particles inside the SUT. For the binned analysis of the kink angle widths for homogeneous SUTs, the observed variation simply yields a source of additional uncertainty for the material budget measurement, when assuming a constant beam momentum. But in the case of inhomogenous SUTs with a complex and changing structure along the lateral directions, the individual image cells for the material budget imaging are influenced depending on their horizontal position due to the respective beam momentum at that position. Therefore, appropriate methods to correct the influence of the horizontal beam momentum variation on the scattering data are under investigation.

9.5 Calibration for Material Budget Imaging

For the evaluation of the material budget from the measured kink angle distributions, the estimated kink angle width is used to calculate the corresponding value for ϵ.
On the one hand, this is possible by applying appropriate models for the description of the multiple scattering inside the traversed material, such as the Highland formula relating the kink angle width to the material budget (cf. Eq. 9.4). Here, the estimated width of the scattering distribution as input to the model is not necessarily expected to be fully compatible to the Highland approximation, as in this work the RMS_{98} estimator is used instead of the Gaussian fit approach formally described in the Highland model. Moreover, the measurement of the kink angle distributions with the beam telescopes can lead to systematic deviations from the theoretically calculated values using the Highland model.
On the other hand, it is possible to use the measured samples with known material budgets to extract the functional dependence between the estimated kink angle width and ϵ in a model-independent way. In both cases, an appropriate calibration procedure is required to reconstruct the most precise values for the material budget of the inserted SUT samples in the performed measurements. After evaluating a well-performing calibration method using the measurements of the known material samples, the calibration can be applied to the measurement results for the kink angle widths of unknown material samples as well as the position-resolved two-dimensional kink angle maps.

In the first step of the calibration procedure, described in Section 9.5.1, the SUT measurements are corrected for the intrinsic influence of the scattering inside the air volume, accounting also for systematic effects in the measurement with the telescope.
This is followed by the evaluation of the material budget from calibration measurements in Section 9.5.2, comparing the measured kink angle widths to the prediction of the Highland model. Furthermore, a model-dependent and a model-independent calibration method is evaluated for the further use of the material budget extraction of unknown SUT samples. In Section 9.5.3, the dependence of the material budget calibration on the selected beam momentum as well as the choice of the test beam and telescope parameters is investigated. For the purpose of a possible application of the MBI technique in the area of medical imaging, a dedicated calibration with water samples is presented in Section 9.5.4.
Finally, the material budget evaluation for modelled composites using dual-layered material structures is studied in Section 9.5.5, testing also the influence of the orientation of the dual-layered sample relative to the traversing beam.

9.5.1 Correction of air scattering

In all performed measurements of the scattering caused by the inserted SUT, the scattering in the air volume is added to the effective scattering of the SUT. Moreover, systematic effects of the measurement are folded in the resulting kink angle width of the air measurement as well as the SUT measurement. Therefore, the estimated kink angle width from each SUT measurement is corrected by quadratic subtraction of the contribution of the scattering in air, which is retrieved from the corresponding empty telescope run without any SUT present. Here, the mean value and its standard deviation for the individual estimated kink angle widths in the binned analysis for the SUT and air measurement are used in the correction. This approach is favored over a bin-by-bin subtraction of the air contribution as a more stable output without artifacts in the image is expected. Furthermore, no large variations in the kink angle maps of the scattering in air are observed such that no position-resolved correction by image cells seems to be necessary.

Figure 9.21 shows the distributions for the combined kink angle k_{x+y} and varying beam momenta between 1 and 5 GeV/c measured with telescope setup S2 at beam line TB22. The estimated kink angle widths with $\mathrm{RMS}_{98}(k_{x+y})$ for the binned analysis evaluated with an image cell size of $(100\,\mu\mathrm{m})^2$ are displayed as well, showing the contribution of scattering in air folded with systematic measurement effects.

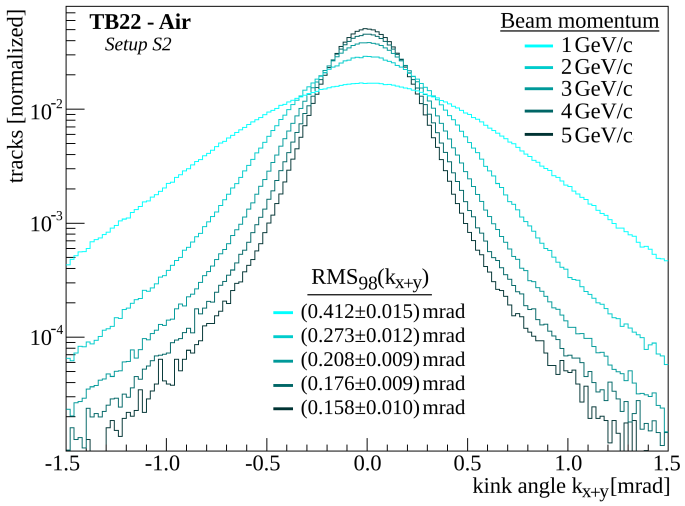

Figure 9.21: Scattering distributions for the combined kink angle k_{x+y} for air measurements with beam momenta between 1 and 5 GeV/c. The estimated kink angle widths with $\mathrm{RMS}_{98}(k_{x+y})$ for the binned analysis are shown as well. The measurement was performed at beam line TB22 with the telescope configuration S2.

9.5.2 Calibration of material budget evaluation

For the calibration of the MBI technique to correctly extract the material budget from the recorded scattering distributions, the measurement of known material samples are used. With various sample thicknesses and different material types (e.g. aluminum, nickel, tin, tungsten and copper) corresponding to different radiation lengths of the samples, a wide range of material budget values is covered for the calibration.

Figure 9.22 shows an example of a calibration curve using various material samples of different thicknesses for a measurement at a beam momentum of 2 GeV/c performed at beam line TB22 and using telescope setup S2. Here, the measured kink angle widths, θ_0^{meas}, which are estimated with the RMS_{98} estimator and corrected by the influence of the air scattering, are compared to the predicted values from the Highland formula, θ_0^{HL}. Moreover, the relative deviation between measurement and prediction is calculated.

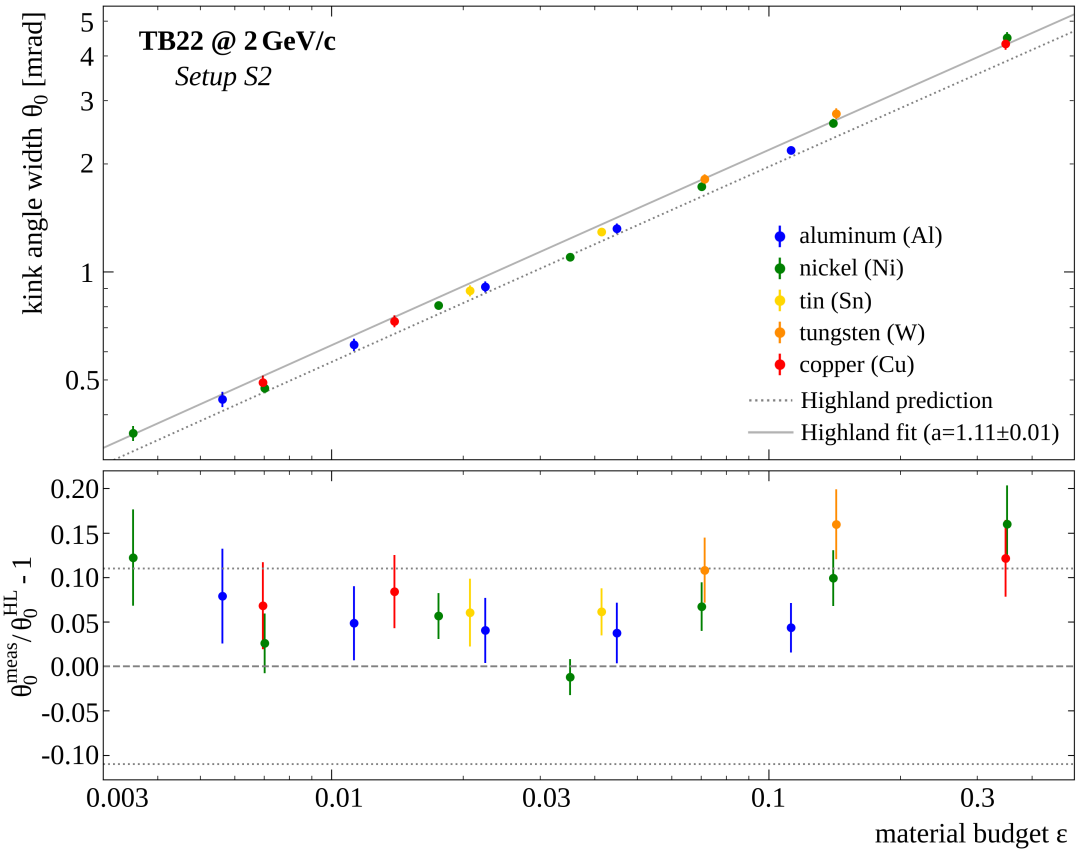

Figure 9.22: Calibration curve for various material samples (Al, Ni, Sn, W, Cu) of different thicknesses at a beam momentum of 2 GeV/c, measured at beam line TB22 with telescope setup S2. The prediction from the Highland model and the deviation to the measurement is shown as well as a model-dependent fit using the Highland formula with a calibration factor a (cf. Eq. 9.11).

Firstly, one can observe that the measured kink angle widths of different material types but with a comparable material budget overlap within the measurement uncertainties in the calibration curve, which is the case for nickel and copper samples as well as nickel and tungsten samples in this measurement. This proves that the extracted kink angle width depends only on the material budget ϵ of the SUT, but not on the material type, as it is described e.g. in the Highland model.

Secondly, the measured kink angle widths show always higher values than the predicted ones from the Highland model. Here, the deviation between measurement and prediction ranges up to 15% for the covered material budget region between $\epsilon = 3.5 \cdot 10^{-4}$ and $\epsilon = 0.35$ in this measurement. But one can also observe an increasing deviation for the known material samples with a larger material budget, which will be covered in detail in Section 9.7 for the evaluation of SUTs with larger material budgets up to $\epsilon = 1.42$.
The reasons for the observed deviation are on the one hand, that the Highland approximation claims to be correct only within ±11%, which is actually the case for most of the tested samples (dotted line in Fig. 9.22). On the other hand, systematic effects of the measurement as well as from the analysis of the scattering distribution, e.g. the choice of the width estimator, have an influence, which can be accommodated by performing a calibration fit of the measured data. Two different approaches for the calibration are selected, tested and evaluated in the following.

First of all, a *model-dependent calibration* is performed using the Highland formula with a to be determined global calibration factor a as

$$\theta_0 = f(\epsilon) = a \cdot \frac{13.6\,\mathrm{MeV}}{p}\sqrt{\epsilon}\,(1 + 0.038\ln(\epsilon))\,. \tag{9.11}$$

The result of this *Highland fit* is also shown in Figure 9.22, yielding a calibration factor of $a = 1.11 \pm 0.01$, which effectively represents the observed deviation between the measurement and the Highland prediction. Nonetheless, not all measurement points of the calibration curve are described well by the calibration fit, when evaluating the fit on the log-log-scale indicating further discrepancies between measurement and model prediction.

Furthermore, a *model-independent calibration* is performed with an arbitrary function selected to describe the measured data. The idea is to use the calibration function directly to extract the material budget from the measured values of kink angle widths without the requirement of inverting the function, which allows e.g. an easier implementation for the two-dimensional imaging. In the case of the Highland formula, a numerical approximation for the material budget must be used as the functional dependence cannot be inverted to an analytical expression for ϵ due to the logarithmic correction.
Therefore, the calibration curve is inverted to perform the calibration fit, meaning that the truth material budget ϵ is plotted as function of the squared kink angle width θ_0^2 in this case. After investigating several functional dependencies for the fit, the following calibration function, consisting of a polynomial function convoluted by a correction term with the power of the kink angle width, was found empirically as

$$\epsilon = f\left(\theta_0^2\right) = \left[p_0 + p_1 \cdot \theta_0^2\right] \cdot \left[1 + \left(\theta_0^2\right)^c\right], \tag{9.12}$$

with the polynomial coefficients p_0, p_1 and the exponent c as free fit parameters.

The result of the model-independent calibration is shown in Figure 9.23 for the same measurement as before. Here, the calibration fit yields the fit parameters as following:

$$p_0 = (-1.1 \pm 1.6) \cdot 10^{-3}, \qquad p_1 = (1.5 \pm 0.2) \cdot 10^{-2}, \qquad c = (-5.0 \pm 2.7) \cdot 10^{-1}.$$

Even though that the uncertainty on the fit parameters is quite large, the overall agreement between the calibration fit and the measurement points is quite good, excluding here the tested samples with very low material budgets, for which a larger discrepancy between measurement and fit is observed in this calibration measurement.

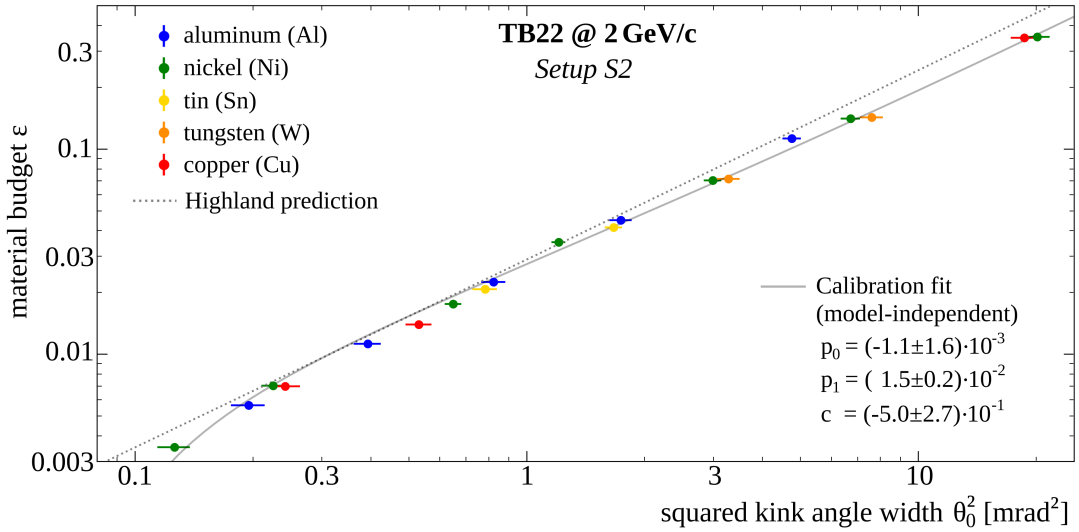

Figure 9.23: Model-independent calibration of various material samples (Al, Ni, Sn, W, Cu) of different thicknesses at a beam momentum of 2 GeV/c. Shown is the material budget (ϵ) of the known samples as function of the measured kink angle widths squared (θ_0^2). The result of the model-independent fit (cf. Eq. 9.12) as well as the prediction from the Highland model are displayed.

For the evaluation of the material budget for unknown samples, both calibrations, model-dependent and model-independent, can be used in the following, comparing the resulting material budget estimates. In the case of the position-resolved imaging of the material budget of complex structures, the model-independent calibration allows an easier and direct implementation of the calibration function to get the material budget of the image cell from the respectively measured squared kink angle width compared to the required numerical inversion of the Highland fit.

9.5.3 Dependencies of the calibration

The measured scattering distributions in the MBI measurements depend on a number of influencing factors, such as the beam momentum or the achieved resolution in the track reconstruction. In the following, the influence of these factors on the calibration is evaluated to study possible dependencies of the calibration function.

Dependence on the beam momentum

The momentum of the scattered electron inside the SUT has a strong dependence on the resulting kink angle distribution and therefore the estimated kink angle width. This is described in the Highland model with an inverted proportionality of the scattering width θ_0 to the beam momentum p (cf. Eq. 9.4).

Figure 9.24 shows the calibration curves for beam momenta between 2 and 5 GeV/c for measurements of the same known material samples as before, covering material budgets between $\epsilon = 3.5 \cdot 10^{-4}$ and $\epsilon = 0.35$. Moreover, the Highland predictions with the $1/p$ dependence are plotted for comparison to the measurement.
Here, the measured kink angle widths are decreasing expectedly for higher beam momenta and the individual measurements at different beam momenta show also a comparable trend to higher kink angle widths for higher material budgets of the sample.

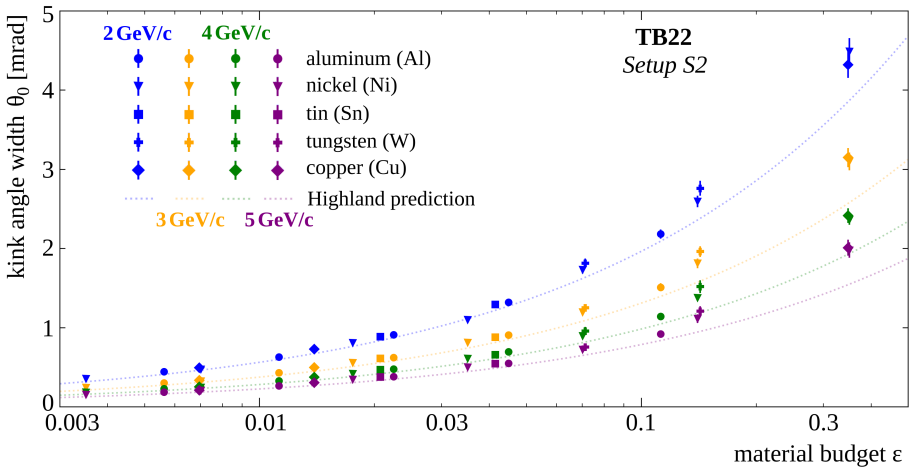

Figure 9.24: Calibration curves for beam momenta between 2 and 5 GeV/c and predictions from the Highland model. The measurement was performed with various material samples (Al, Ni, Sn, W, Cu) of different thicknesses at beam line TB22 with telescope setup S2.

To further evaluate the possible dependence of the calibration on the beam momentum, the relative deviation between the measurement and the Highland prediction is calculated in Figure 9.25 for each setting of the beam momentum.

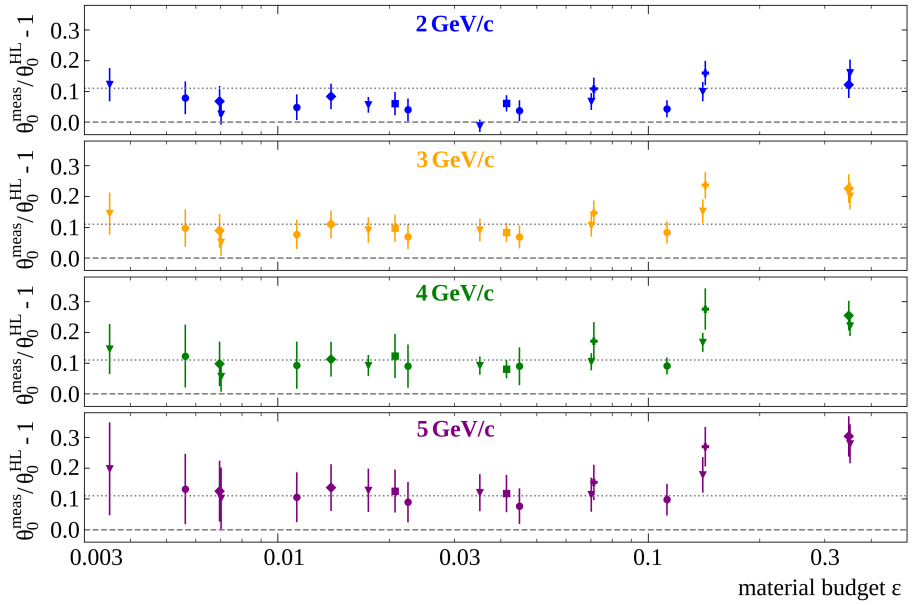

Figure 9.25: Deviation between the measured kink angle widths (θ_0^{meas}) and the Highland prediction (θ_0^{HL}) for beam momenta between 2 and 5 GeV/c.

Here, the deviation of the measurement to the Highland prediction is increasing for higher beam momenta: whereas the maximal deviation for the case of 2 GeV/c is 16%, a maximal deviation of 30% is observed for a beam momentum of 5 GeV/c. Therefore, new calibration functions should be determined for the individual measurements at different beam momenta. This approach is favored over an extrapolation from one calibration at a given beam momentum to other beam momenta, as systematic effects of the measurement are folded in the data and no attempt of an unfolding of these detector effects is done.

The results for the performed calibrations of the measurement with different beam momenta is shown in Figure 9.26 for the model-dependent Highland fit and the model-independent calibration fit, respectively.

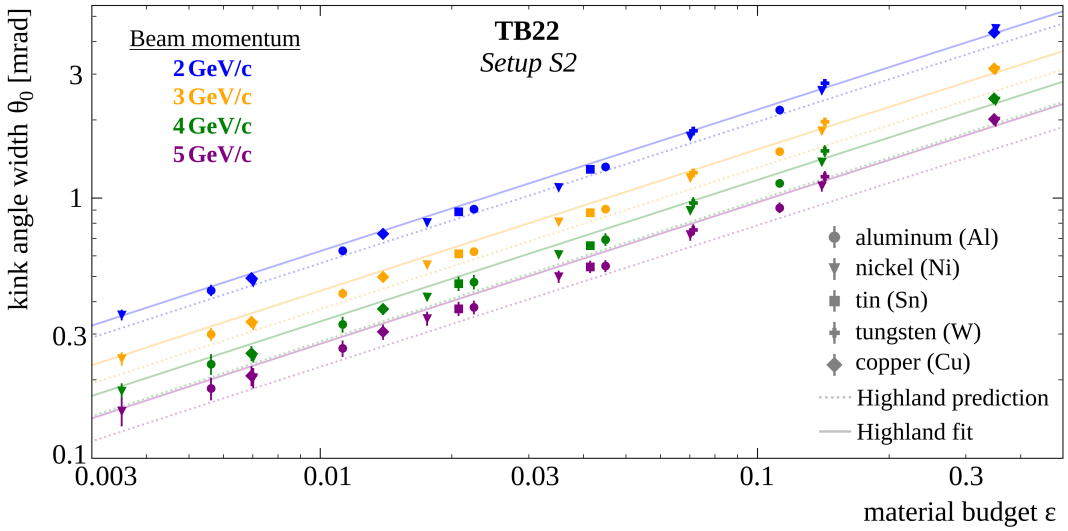

(a) Model-dependent calibration fit.

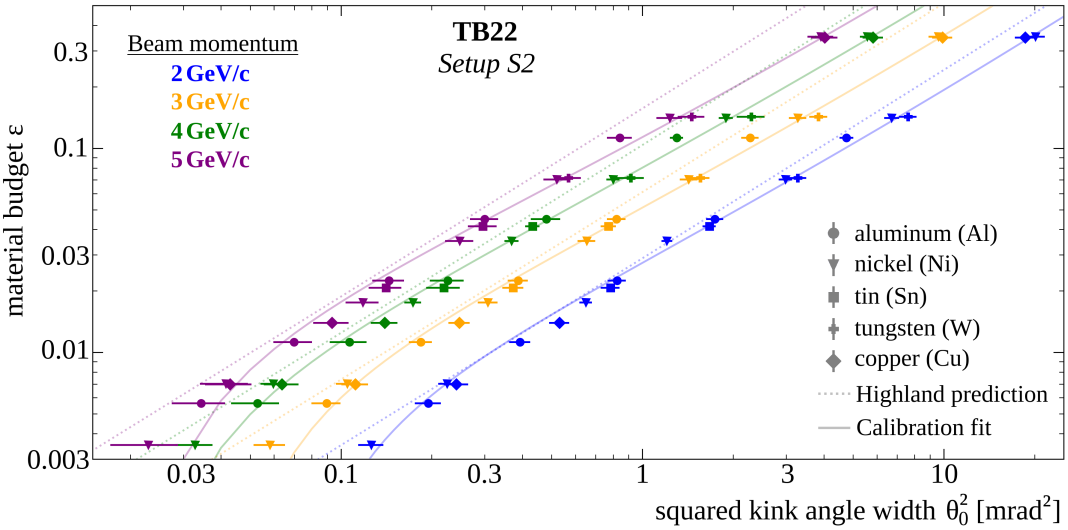

(b) Model-independent calibration fit.

Figure 9.26: Model-dependent and model-independent calibration fit for the calibration curves with beam momenta between 2 and 5 GeV/c.

For the Highland fit (cf. Eq. 9.11), the global calibration factor is determined to be 1.11 ± 0.01, 1.17 ± 0.01, 1.20 ± 0.02 and 1.23 ± 0.02 for the beam momentum setting of 2, 3, 4 and 5 GeV/c, respectively. The relative deviation of the fit to the data points is on average between -3% and -6%, worsening slightly for higher beam momenta, indicating an underlying effect dependent on the selected beam momentum.
For the model-independent calibration, a good description of the data points by the fit is reached with deviations on average between -1% and -2%, excluding again the samples with very low material budgets in the measurement.
The determined fit parameters and the evaluated deviations between the measurement and the calibration fits are provided in Appendix C.4.

Dependence on the telescope setup

For the investigation of a possible dependence of the telescope setup on the calibration for the MBI measurement, the scattering distributions for aluminum samples with thicknesses of 0.5, 1.0, 2.0, 4.0 and 10.0 mm are measured at beam line TB21 with beam momenta of 2 and 4 GeV/c. Here, the influence of the chosen telescope setup is studied by performing the individual measurements with the telescope setups S4 and S5 (cf. Tab. 9.2) and comparing the resulting kink angle distributions for the setup with the longitudinal distances $dz = 50$ mm and $dz = 100$ mm in the up- and downstream arm, respectively.
Figure 9.27 shows the overlayed scattering distributions for the measurement with a 1 mm thick aluminum sample using both telescope setups and beam momenta.

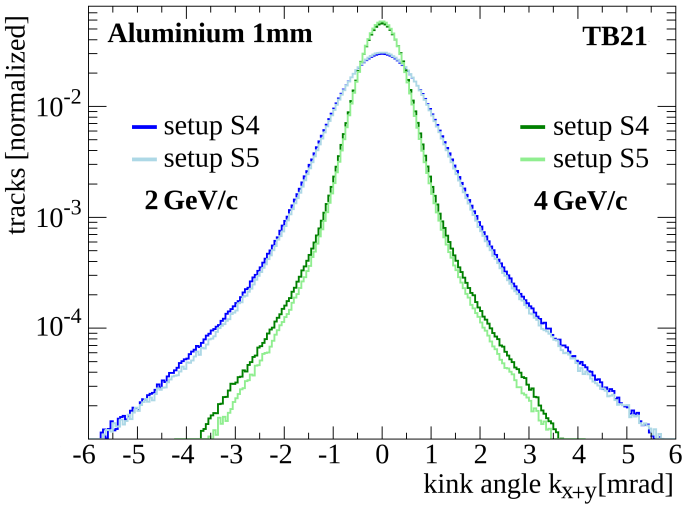

Figure 9.27: Scattering distributions for the combined kink angle k_{x+y} for a 1 mm thick aluminum sample, comparing the telescope setups S4 and S5 for beam momenta of 2 and 4 GeV/c.

The kink angle distributions show a good agreement between the measurement with the two different telescope setups, but smaller differences in the tails of the distribution are nonetheless observed. Here, the telescope setup S5 results in a slightly smaller shape of the distribution than the telescope setup S4, consistently for both tested beam momenta. For the detailed analysis, the kink angle widths of the individual scattering distributions of the aluminum samples are estimated with the RMS_{98} estimator and the influence of the air scattering is corrected. The resulting calibration curves for both telescope setups and both beam momenta are shown in Figure 9.28. Moreover, the Highland prediction for both beam momenta is displayed and the relative deviations between the measurement and the prediction is evaluated for each case.

Overall, the typical calibration curve is observed independent of the selected telescope setup with only minor differences between the individual measurement points. For the relative deviations between the measurement and the Highland prediction, in all cases positive deviations from the prediction are observed with maximal values of up to +9% for the measurement at a beam momentum of 2 GeV/c and +14% at 4 GeV/c. These observations are matching well with the previous calibration measurements.
But the relative deviations for the measurement with telescope setup S5 are smaller than with telescope setup S4, indicating an influence of the choice of the plane spacing for the telescope. For setup S5, a wider plane spacing with $dz = 100$ mm in the up- and downstream arm results in an improved spatial as well as angular track resolution compared to the setup S4 with $dz = 50$ mm. The corresponding resolutions for the used telescope configurations can be calculated with the GBL Track Resolution Calculator (cf. Sec. 9.2.2), which is evaluated in Table 9.6.

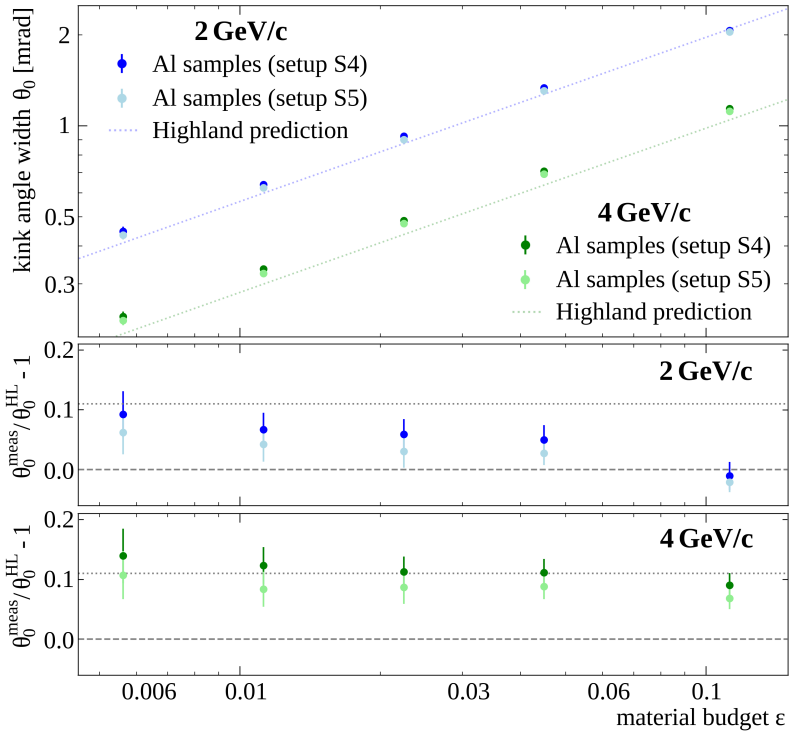

Figure 9.28: Comparison of calibration curves measured with the telescope setups S4 and S5 at beam line TB21 for beam momenta of 2 and 4 GeV/c. The measured kink angle widths are compared to the Highland prediction and the relative deviation for both telescope setups and beam momenta is evaluated. For the calibration, a measurement of aluminum samples with thicknesses of 0.5, 1.0, 2.0, 4.0 and 10.0 mm is used.

Telescope setup	Track resolution	Beam momentum 2 GeV/c	Beam momentum 4 GeV/c
S4	spatial	4.73 µm	3.95 µm
	angular	258.5 µrad	144.8 µrad
S5	spatial	4.53 µm	3.79 µm
	angular	251.9 µrad	133.9 µrad

Table 9.6: Spatial and angular track resolution for the setups S4 and S5 at beam momenta of 2 and 4 GeV/c calculated with the GBL Track Resolution Calculator [219].

With the slightly improved angular track resolution, the scattering distributions are measured with a higher accuracy with telescope setup S5, showing therefore also a better agreement with the Highland prediction before applying an appropriate calibration.

Even though that the choice of the telescope setup has only a minor effect on the MBI analysis, it is recommended to perform for each selected telescope setup an appropriate calibration to reach the best possible results for the extraction of the sample's material budget. For the MBI measurements in this work, dedicated calibration runs with various material samples with known material budgets were performed for each measurement configuration in terms of the selected beam momentum and the chosen telescope setup. The respective calibration functions are then used for the following evaluation of material budgets of measurements with unknown samples.

9.5.4 Water calibration for medical applications

The MBI technique is also investigated for a possible application in medical imaging to resolve structures in the human body by multiple Coulomb scattering of particles. Due to the high fraction of water contained in the human body, a calibration of the MBI technique with water was conducted in the course of a summer student project in 2019 [259].

The prepared water samples (cf. Fig. 9.3) were measured for moderate beam momenta of 1 and 2 GeV/c at beam line TB21 using the wide telescope setup S7. Figure 9.29 shows the reconstructed scattering distributions for the combined kink angle k_{x+y} and sample thicknesses between 5 and 400 mm.

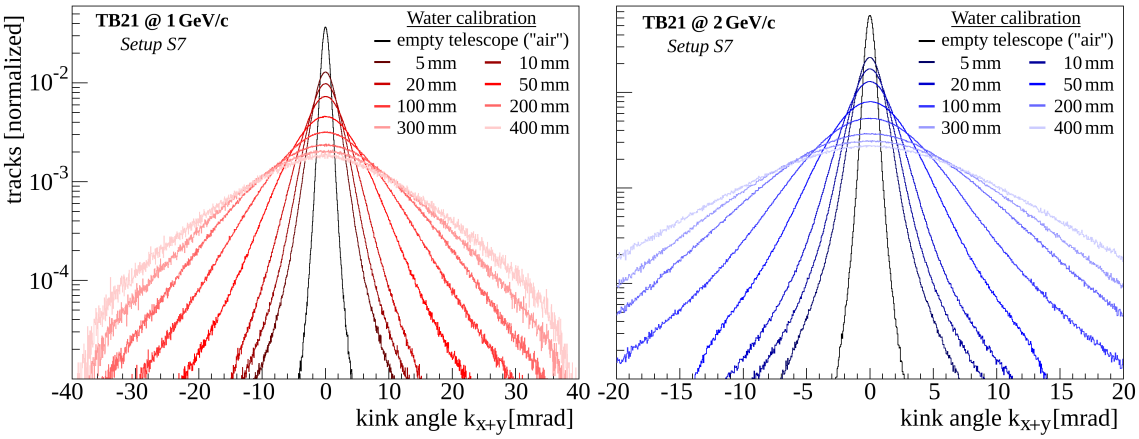

Figure 9.29: Scattering distributions for the combined kink angle k_{x+y} for the calibration with water at a beam momentum of 1 GeV/c (left) and 2 GeV/c (right). Shown are the normalized distributions for the scattering in various thicknesses of distilled water between 5 and 400 mm measured at beam line TB21 with the telescope setup S7.

The kink angle widths θ_0^{meas} from the individual scattering distributions are estimated with the RMS_{98} estimator from the measurement and corrected by the scattering in the air. In Figure 9.30, the kink angle width is plotted as function of the sample thickness d for both measured beam momenta. The predicted kink angle widths from the Highland model θ_0^{HL} are shown as well and the relative deviation between measurement and prediction is evaluated. Furthermore, a fit using the Highland model with a global calibration factor a is performed for the calibration of the MBI data.

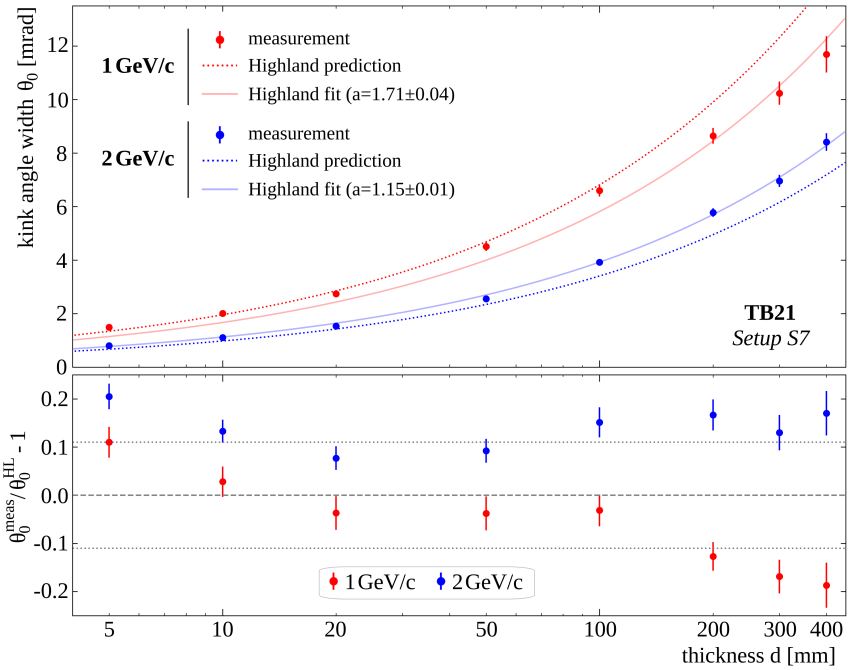

Figure 9.30: Calibration curves for distilled water with thicknesses between 5 and 400 mm for a beam momentum of 1 GeV/c and 2 GeV/c. Moreover, the prediction from the Highland model and the Highland fit with the calibration factor a are shown for both beam momenta.

For a beam momentum of 2 GeV/c, a similar behaviour as before is observed: the measured kink angle widths are larger than the prediction of the Highland formula, with deviations between 8 to 20%; this is also confirmed by the calibration fit using the Highland model with a global calibration factor, which is determined to be $a = 1.15 \pm 0.01$ in this case.
On the contrary, the measurement with a beam momentum of 1 GeV/c shows smaller values than the prediction for larger sample thicknesses, which is also observed in the calibration curve as a smaller slope for larger thicknesses. The Highland fit provides in this case a rather large calibration factor of $a = 1.71 \pm 0.04$ and describes the data points inadequately. A possible explanation is that due to the rather low beam momentum and an increasing sample thickness, the deflection angles become quite large (cf. Fig. 9.29). At the same time, a relatively wide telescope setup was chosen to allow to insert the long water samples in between the telescope arms, but which has also a negative influence on the acceptance area in the measurement. In the analysis, the fiducial area is already adapted to accommodate the increasing influence of the acceptance effect, but at least for the largest water samples, the measured scattering distributions are biased.

Therefore, the water calibration for 1 GeV/c should be repeated with an optimized telescope setup to acquire a good calibration also for this beam energy. In general, for the purpose of medical imaging, the beam energy should be reduced even further, as the radiation dose received by the biological sample or the human patient is an important parameter for the success of the MBI technique in the medical sector.

9.5.5 Material budget of composite structures

In this study, the scattering inside simple composite samples modelled as dual-layered structures of two types of raw materials is investigated. The scattering measurements are conducted for the individual material samples as well as the modelled composite, where for the latter case both orientations of the dual-layered structure relative to the traversing particles are tested. The relevant questions for this study are if the effective material budget of the composite can be extracted correctly from the individual measurements and if the scattering measurement depends on the order of the materials in the composite as traversed by the electrons.

In Figure 9.31, the measured distributions for the combined kink angle k_{x+y} for the three investigated composite samples, namely acryl+aluminum, tin+nickel and copper+tungsten (cf. Tab. 9.3), are shown for a measurement at beam line TB21 with a beam momentum of 2 GeV/c and using telescope setup S6.
When comparing the scattering distributions for the single material samples, e.g. 4 mm of aluminum and 15 mm of acryl, one observes smaller differences in the shape of the distributions. This is expected as, even though that the thicknesses of the samples were selected to result in a comparable material budget, the exact values are slightly different, e.g. the material budget of the aluminum plate is 4% higher than the respective acryl plate, showing therefore a slightly broader kink angle distribution.
On the contrary, for the composite structure as the combination of two materials each, the effective material budget should be fixed. But in each of the three performed measurements, differences in the scattering distributions are observed when comparing the two orientations for the beam traversal. Here, as shown in Figure 9.31 for the relative fraction between both distributions from the composites, the central part of the distribution agrees well, but larger differences are observed in the tails of the distribution, meaning effectively the occurrence of larger kink angles due to single scattering interactions.

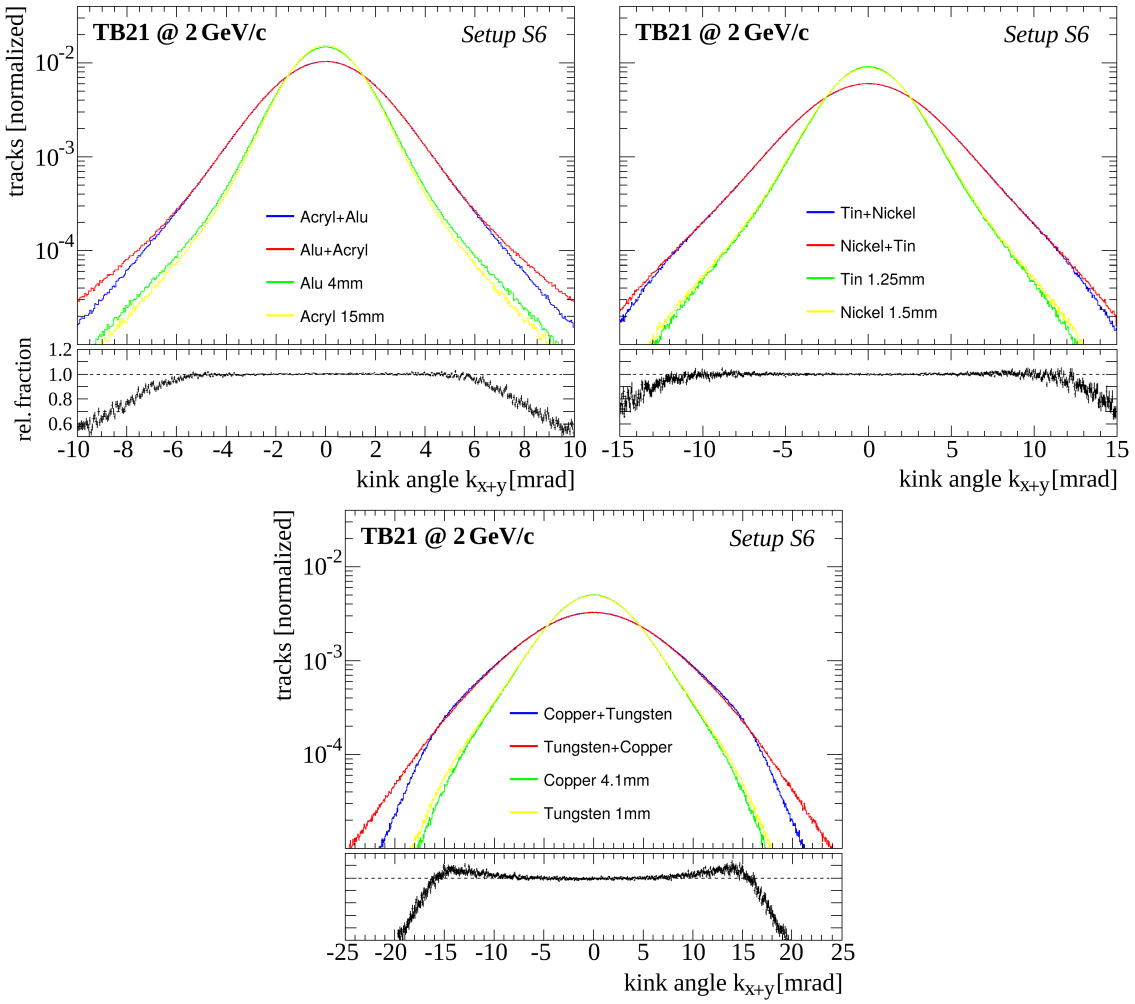

Figure 9.31: Scattering distributions for the combined kink angle k_{x+y} for measurements with modelled composites, namely acryl+aluminum, tin+nickel and copper+tungsten. Compared are the normalized distributions for the scattering in the individual material layers as well as the dual-layered samples for both orientations, showing also the relative fractions between the distributions of the composites in both orientations. The measurement was performed at TB21 with the telescope setup S6 and a beam momentum of 2 GeV/c.

In this case, the tested composite orientation with the material featuring a larger radiation length as the first traversed layer shows also the broader distribution. This observation could be explained by a higher probability for the occurrence of larger deflection angles, when the higher X_0 material is traversed first, resulting in the observed differences of the the scattering distribution's tails.

For a quantitative comparison, the determined kink angle widths (θ_0^{meas}) estimated with $\text{RMS}_{98}(k_{x+y})$ are shown in Table 9.7. The measured kink angle widths are evaluated as the mean and its standard deviation of the individual image cells of $(100\,\mu\text{m})^2$ in the binned analysis and corrected by quadratic subtraction of the contribution of scattering in air. Moreover, the measurement is compared to the expected kink angles using the Highland model (θ_0^{HL}), evaluating also the relative difference.

Material	ϵ [%]	θ_0^{meas} [mrad]	θ_0^{HL} [mrad]	rel. difference [%]
Acryl 15 mm	4.32	1.30 ± 0.02	1.25	4.0%
Aluminum 4 mm	4.50	1.35 ± 0.02	1.27	6.1%
Acryl+Aluminum	8.90	1.93 ± 0.03	1.84	4.7%
Aluminum+Acryl		1.95 ± 0.03		5.9%
Tin 1.25 mm	10.36	2.22 ± 0.04	2.00	10.8%
Nickel 1.25 mm	10.53	2.26 ± 0.04	2.02	12.2%
Tin+Nickel	20.88	3.37 ± 0.05	2.92	15.3%
Nickel+Tin		3.38 ± 0.05		15.6%
Copper 4.1 mm	28.55	4.04 ± 0.07	3.46	16.7%
Tungsten 1.0 mm	28.54	4.11 ± 0.08	3.46	18.9%
Copper+Tungsten	57.11	6.00 ± 0.13	5.03	19.3%
Tungsten+Copper		6.05 ± 0.15		20.3%

Table 9.7: Comparison of estimated kink angles widths $\theta_0^{\text{meas}} = \text{RMS}_{98}(k_{x+y})$ of modelled composites with the Highland prediction (θ_0^{HL}). Compared are the values for the individual material layers as well as the dual-layered samples for both orientations. The relative difference for the kink angle width between the measurement and the Highland prediction is also given.

Here, the estimated kink angle widths for the composites in both orientations are also slightly different, meaning that the width estimation is influenced by the observed differences in the tails of the two measured scattering distributions. When comparing the measured and predicted kink angles, the measurement shows larger kink angle values than the prediction with the Highland formula, as it was already observed in the calibration. The relative difference between the measurement and the prediction is increasing with larger material budgets of the investigated SUTs, ranging from 4% up to 20%.

Overall, the effective material budget of the modelled composites can be reconstructed correctly, if an appropriate calibration is applied to the estimated kink angle widths. Furthermore, the scattering inside the dual-layered structure shows a small dependence on the orientation of the sample when traversed by the beam, which is not expected from the theoretical calculation of the effective material budget in the case of composites.

9.6 Investigation of ATLAS ITk Materials & Structures

After the evaluation of the calibration procedure for MBI measurements by using scattering measurements of known material samples as SUT, raw material samples with an a-priori unknown material budget are investigated. Moreover, the advantage of the MBI technique to create position-resolved maps of the material budget is used to investigate complex structures assembled out of different materials.

In the course of this work, the focus is on the investigation of the material budget of materials and structures foreseen for the ATLAS ITk detector. In Section 9.6.1, the material budgets for several raw materials in the detector assembly are extracted from the conducted scattering measurements. By measuring also the thickness of the various material samples, an estimate of the characteristic radiation length X_0 of the material is retrieved as well, which can be used to model the detector correctly in simulations.

The imaging of the material budget distribution for a measured SUT is used in Section 9.6.2 for several assembled structures of the ITk detector, showing the achievable image resolution with the MBI technique and providing a detailed insight to the distributed material budget of the structure.

9.6.1 Material budget calculation for ATLAS ITk materials

The step-by-step determination of the material budget of unknown material samples using the measured scattering distributions of the samples is summarized as following:

1. Extraction of the width of the kink angle distribution from the sample using an appropriate estimator. Here, the RMS_{98} estimator for the combined kink angle k_{x+y} is used and the binned analysis with an image cell size of $(100\,\mu\mathrm{m})^2$ provides then the mean value and its standard deviation for the kink angle over the selected fiducial area (cf. Sec. 9.4.2).

2. Correction of the measured kink angle width from the sample by quadratic subtraction of the air scattering contribution (cf. Sec. 9.5.1)

3. Determination of the material budget ϵ^{meas} from the corrected kink angle width θ_0^{meas}, by applying the evaluated calibration function.

4. Calculation of the material's radiation length X_0^{meas} by dividing the sample thickness d with the measured material budget.

For the following calculation of the material budgets of the ATLAS ITk material samples, the model-dependent calibration with the Highland fit is the selected choice for the calibration procedure, using a numerical inversion of the calibration function to retrieve the material budget value for a given kink angle width. But also the model-independent calibration function was studied and could be used as well for the extraction of the material budget. The calculation of the uncertainty on the material budget estimate is performed by varying systematically the kink angle width as input to the numerical calibration function around the mean value with the determined standard deviation, resulting in asymmetric uncertainties. For the determination of the material's radiation length using the estimated material budget and the measured thickness of the sample, the respective uncertainty on the value is calculated using error propagation with the uncertainty on ϵ as well as the assumed measurement uncertainty for the sample thickness.
The presented results for the individual tested materials (cf. Sec. 9.2.3) are based on the test beam campaigns conducted in February 2017 and March 2019. Here, the scattering measurements were performed at both beam lines, TB21 and TB22, and using three different telescope setups, namely the setups S1, S2, and S3 (cf. Tab. 9.2). Due to the repetition of some of the measurements with the same SUTs, a cross-check over different test beam configurations is possible.

Carbon-based foam (Allcomp)

The carbon-based Allcomp foam was investigated in several test beam measurements for a beam momentum of 2.4 GeV/c and changing test beam configurations in terms of the beam line and the telescope setup. Two kind of samples were measured, one with a homogeneous thickness of $(5.5 \pm 0.1)\,\mathrm{mm}$ and the other as a test assembly with regions of different thicknesses between 10 and 31.5 mm. The results for the measured and corrected kink angle width (θ_0^{meas}), the calibrated material budget (ϵ^{meas}) and the calculated radiation length (X_0^{meas}) evaluated for the individual measurements are shown in Table 9.8.

Configuration	d [mm]	θ_0^{meas} [mrad]	ϵ^{meas} [%]	X_0^{meas} [mm]
2017, TB22, S3	10.0 ± 0.1	0.431 ± 0.038	$0.742^{+0.123}_{-0.115}$	1348^{+224}_{-209}
	13.7 ± 0.1	0.432 ± 0.041	$0.745^{+0.133}_{-0.123}$	1839^{+329}_{-304}
	17.8 ± 0.1	0.560 ± 0.038	$1.197^{+0.152}_{-0.143}$	1487^{+189}_{-178}
	23.7 ± 0.1	0.597 ± 0.033	$1.344^{+0.141}_{-0.135}$	1763^{+185}_{-177}
	31.5 ± 0.1	0.701 ± 0.039	$1.805^{+0.190}_{-0.181}$	1745^{+184}_{-175}
2019, TB21, S2	5.5 ± 0.1	0.273 ± 0.017	$0.331^{+0.037}_{-0.039}$	1662^{+198}_{-188}
2019, TB22, S1	5.5 ± 0.1	0.266 ± 0.019	$0.368^{+0.049}_{-0.046}$	1495^{+201}_{-189}

Table 9.8: Results of the MBI measurements of the carbon-based foam material measured with three different configurations at a beam momentum of 2.4 GeV/c.

Between the individual measurements, some deviations are observed, even for the case of investigating the same sample in a different configuration. This can be explained by the fact, that for each measurement campaign a new calibration based also on different known material samples is determined as well as that some differences in the individual measurement configurations can occur. Nonetheless, within the calculated uncertainties, an overall agreement of the determined radiation length values is found. For the measurement of the sample with regions of different thickness inside the same SUT, a larger uncertainty on the extracted material budget values is observed for the individual regions, which is caused by the effectively lower measurement area available to evaluate the kink angle widths for each region of the sample.
Overall, the radiation length of the carbon-based foam is determined by the performed measurements to be 1620^{+584}_{-549} mm. This experimentally determined X_0 value can be compared to the calculated one with 1 856 mm (cf. Eq. 9.8), showing that the extracted mean value from the measurement underestimates the radiation length, but agrees nonetheless within the measurement's uncertainty.

Pultruded carbon fiber

The pultruded carbon fiber material was investigated in two test beam measurements with different configurations. In one of the test beam campaigns, the measurement was repeated for varying beam momenta of 2.4, 3.4 and 5.0 GeV/c, whereas otherwise a fixed beam momentum of 2.4 GeV/c was selected. Moreover, two different kinds of samples are investigated: one carbon fiber bar with an epoxy-based adhesive and one bar with a vinyl-based adhesive with thicknesses of (6.0 ± 0.1) mm and (8.0 ± 0.1) mm, respectively. The results of the material budget analysis for the pultruded carbon fiber materials are summarized in Table 9.9.

For the repeated measurement at different beam momenta, but otherwise with the same configuration, a slight variation to smaller extracted radiation lengths is observed. This can be explained by the observed dependence of the calibration on the selected beam momentum (cf. Sec. 9.5.3) and the correspondingly performed calibration per beam momentum selection. Overall, the radiation length for pultruded carbon fiber with epoxy-based adhesive is determined to be 271^{+35}_{-34} mm, whereas the X_0 value for the CF sample with vinyl-based adhesive is estimated with 245^{+12}_{-12} mm. This indicates a slight difference of the radiation length depending on the chosen adhesive for the pultruded carbon fiber bars, with a lower value for the vinyl-based than the epoxy-based adhesive.

Configuration	Sample	θ_0^{meas} [mrad]	ϵ^{meas} [%]	X_0^{meas} [mm]
2017, TB21, S2, 2.4 GeV/c	CF + epoxy	0.740 ± 0.020	$2.110^{+0.105}_{-0.102}$	284^{+15}_{-15}
2017, TB21, S2, 3.4 GeV/c		0.549 ± 0.015	$2.159^{+0.112}_{-0.109}$	278^{+15}_{-15}
2017, TB21, S2, 5.0 GeV/c		0.394 ± 0.017	$2.208^{+0.173}_{-0.167}$	272^{+22}_{-21}
2019, TB22, S1, 2.4 GeV/c	CF + epoxy	0.739 ± 0.025	$2.399^{+0.151}_{-0.147}$	250^{+16}_{-16}
2019, TB22, S1, 2.4 GeV/c	CF + vinyl	0.875 ± 0.023	$3.266^{+0.158}_{-0.154}$	245^{+12}_{-12}

Table 9.9: Results of the MBI measurements of the pultruded carbon fiber samples for a (6.0 ± 0.1) mm thick bar with epoxy-based and a (8.0 ± 0.1) mm bar with vinyl-based adhesive.

Thermoplastic (Torlon)

The material budget of the thermoplastic Torlon was studied in three different test beam measurements. One sample with a thickness of (10.2 ± 0.1) mm was measured at a beam momentum of 2.4 GeV/c, whereas the other sample with a thickness of (3.0 ± 0.1) mm was tested at varying beam momenta of 2.4, 3.4 and 5.0 GeV/c. The results for the individual measurements are compared in Table 9.10.

Configuration	d [mm]	θ_0^{meas} [mrad]	ϵ^{meas} [%]	X_0^{meas} [mm]
2017, TB21, S2, 2.4 GeV/c	3.0 ± 0.1	0.516 ± 0.017	$1.088^{+0.066}_{-0.064}$	276^{+19}_{-19}
2017, TB21, S2, 3.4 GeV/c		0.379 ± 0.013	$1.094^{+0.072}_{-0.069}$	274^{+20}_{-20}
2017, TB21, S2, 5.0 GeV/c		0.271 ± 0.014	$1.112^{+0.104}_{-0.100}$	270^{+27}_{-26}
2019, TB21, S2, 2.4 GeV/c	10.2 ± 0.1	0.978 ± 0.015	$3.422^{+0.096}_{-0.095}$	298^{+9}_{-9}
2019, TB22, S1, 2.4 GeV/c	10.2 ± 0.1	0.961 ± 0.022	$3.266^{+0.162}_{-0.159}$	263^{+11}_{-11}

Table 9.10: Results of the MBI measurements of the thermoplastic Torlon samples for different thicknesses measured with different test beam configurations.

Again, a slight variation of the extracted radiation lengths for the measurements at different beam momenta is observed, but otherwise consistent results for both samples are measured. Overall, the estimated radiation length for the thermoplastic Torlon from the performed measurements is determined to be 276^{+41}_{-40} mm.

Glue (Hysol)

Samples of the Hysol glue for the petal core assembly were investigated in two different test beam campaigns at a fixed beam momentum of 2.4 GeV/c. On the one hand, the material budget of the glue itself is measured for two cured samples with thicknesses of (4.9 ± 0.3) mm and (10.2 ± 0.3) mm. On the other hand, a mixture of Hysol and carbon powder is prepared and three samples are cured with thicknesses of (4.9 ± 0.3) mm, (8.1 ± 0.2) mm and (10.2 ± 0.3) mm. The uncertainty on the thickness of the sample is higher for the glue samples, as a homogeneous thickness was difficult to achieve in the process of curing. The measurement results for the pure and the loaded Hysol glue are presented in Table 9.11.

Configuration	Sample	d [mm]	θ_0^{meas} [mrad]	ϵ^{meas} [%]	X_0^{meas} [mm]
2017, TB22, S3	pure	4.9 ± 0.3	0.614 ± 0.041	$1.418^{+0.178}_{-0.168}$	346^{+48}_{-46}
		10.2 ± 0.3	0.930 ± 0.039	$3.038^{+0.239}_{-0.231}$	339^{+28}_{-27}
2017, TB22, S3	loaded	4.9 ± 0.3	0.603 ± 0.029	$1.369^{+0.124}_{-0.119}$	358^{+39}_{-38}
		10.2 ± 0.3	0.922 ± 0.052	$2.990^{+0.318}_{-0.303}$	341^{+38}_{-36}
2019, TB21, S2	loaded	8.1 ± 0.2	0.790 ± 0.015	$2.312^{+0.079}_{-0.078}$	350^{+15}_{-15}

Table 9.11: Results of the MBI measurements of the pure and loaded Hysol glue samples measured at a beam momentum of 2.4 GeV/c.

For the samples with different thicknesses, consistent results in terms of the material budget are observed, resulting overall in an extracted radiation length of 341^{+38}_{-37} mm for the pure Hysol glue and 350^{+56}_{-54} mm for the carbon-loaded Hysol glue. The mixture with carbon powder increases correspondingly the radiation length of the glue, but is nonetheless added for the assembly of the petal core to improve the thermal and electrical conductivity of the local support structure.

Service tray assemblies

Three different service tray assemblies were investigated in the 2019 test beam campaign at beam line TB21 and TB22 using the telescope configuration S2. The three samples are a cut-out of a fully prepared service tray with a thickness of (1.3 ± 0.1) mm as well as two cocured test pieces comparing different procedures in the cocuring with thicknesses of (1.4 ± 0.1) mm and (1.3 ± 0.1) mm. The measured results for these samples in terms of their material budget as well as the estimated radiation lengths are given in Table 9.12.

Configuration	Sample	d [mm]	θ_0^{meas} [mrad]	ϵ^{meas} [%]	X_0^{meas} [mm]
TB21, S2	Cut-out	1.3 ± 0.1	0.324 ± 0.013	$0.452^{+0.032}_{-0.031}$	288^{+48}_{-46}
TB22, S2	Test A	1.4 ± 0.1	0.342 ± 0.016	$0.512^{+0.044}_{-0.043}$	273^{+48}_{-46}
	Test B	1.3 ± 0.1	0.325 ± 0.017	$0.467^{+0.045}_{-0.043}$	278^{+48}_{-46}

Table 9.12: Results of the MBI measurements of three different samples of the service tray assembly measured at a beam momentum of 2.4 GeV/c in 2019.

The service tray consists of six layers of woven 0-90 prepreg cocured in the autoclave to provide the required stability for the services in the end-cap structure. The measured cut-out of a completed service tray is an example of the aimed for design of the structure with a specified thickness of 1.3 mm. In the process of finding the correct cocuring procedure, various test samples such as the investigated test sample A and B were made. Here, test sample A shows a higher thickness as well as a larger material budget, but the radiation length is effectively smaller than for test sample B. This can be explained by the amount of epoxy remaining in the cocured assembly compared to the raw prepreg layup. The weight of the carbon fiber layups before cocuring are rather comparable with 63.8 g and 65.2 g for test sample A and B, respectively. But the weights after cocuring with 60.47 g and 55.80 g shows a larger discrepancy between both test pieces, as a higher fraction of epoxy remained in piece A.

This results in a higher thickness and material budget of the assembly, but the effective radiation length for the thicker samples is smaller, as the additional glue has no large impact on the radiation length of the composite dominated by the X_0 of the carbon fibers.

9.6.2 Material budget imaging of ATLAS ITk structures

With the MBI technique it is also possible to perform a measurement of the two-dimensional material budget distribution of a SUT by evaluating the measured kink angle distributions in a position-resolved way. Here, the high spatial resolution for the reconstruction of tracks with the EUDET-type beam telescopes allows to finely resolve structures of the SUT with a high image resolution. But at the same time, a sufficient contrast must be achieved in the image to allow to differentiate the individual features of the sample.

The theoretical resolution limit for the MBI technique is determined on the one hand by the spatial track resolution of the beam telescope depending on its setup and defining the accuracy to reconstruct the incident position of the traversing electrons. On the other hand, the multiple Coulomb scattering results not only in a deflection of the particle, but also a lateral displacement after the traversal depending directly on the material budget of the sample. Overall, resolutions down to 10 µm are feasible with this imaging technique, as it is demonstrated in the following.

In the MBI analysis, the size of the image cells in the two-dimensional kink angle maps must be reduced to enhance the image resolution. But at the same time, a smaller cell size results in a smaller number of reconstructed tracks per image cell, which can result in a deterioration of the estimated kink angle width and leads to a reduced contrast of the image. Therefore, for a image with a high contrast as well as a high resolution, a large number of reconstructed tracks is required to reduce the cell size accordingly. The influence of different cell sizes on the two-dimensional kink angle maps is shown in detail for an exemplary structure in Appendix C.5.
For the measured material budget images in this work, the image cell size was individually selected for each sample depending on the amount of recorded data and to resolve the internal structures with a high resolution and contrast.

The procedure to extract the two-dimensional image of the sample's material budget distribution is described step-by-step as following:

1. Extraction of the width of the kink angle distribution for each image cell of the chosen size using the RMS_{98} estimator for the combined kink angle k_{x+y}.

2. Correction of the measured kink angle widths for each cell by quadratic subtraction of the air scattering contribution determined as the mean value over the fiducial area.

3. Determination of the material budget per image cell from the corrected kink angle width by applying the evaluated calibration function.

4. Creating position-resolved maps of the material budget distribution with an image resolution depending on the selected cell size.

For the material budget extraction, both calibration procedures, the model-dependent and the model-independent approach, were implemented and used, providing comparable results of the images, as shown for both approaches in the following.

The presented images of the individual studied structures, focusing on assembled structures for the ATLAS ITk detector (cf. Sec. 9.2.3), are also based on the test beam campaigns conducted in February 2017 and March 2019, using both beam lines, TB21 and TB22, and the telescope setups S2, S3 and S4. In most cases, a beam momentum of 2.4 GeV/c was selected to measure with the highest available particle rate, but some measurements were also performed at beam momenta of 2 and 4 GeV/c. Moreover, to acquire a large amount of scattering data to reduce the image cell sizes sufficiently, long measurement runs were performed, using also the automatic movement of the SUT with the x-y-positioning stage to scan larger areas of the structure. In the final analysis, the individual images with a size in the x- and y-direction according to the chosen fiducial area can be stitched together.

Electrical break assembly

A scattering measurement with the electrical break assembly (cf. Fig. 9.6a) was conducted at beam line TB22 with a beam momentum of 4 GeV/c and telescope setup S2. In total, 20×10^6 triggered events were recorded with roughly 31.7×10^6 reconstructed tracks. Due to the high number of tracks, an image cell size of $(10\,\mu\text{m})^2$ could be selected resulting in 123 ± 25 tracks per image cell for the MBI analysis and providing still a high image contrast. Figure 9.32 shows the two-dimensional maps of the corrected scattering angle θ_0 and the resulting material budget estimate ϵ, using the model-independent calibration.

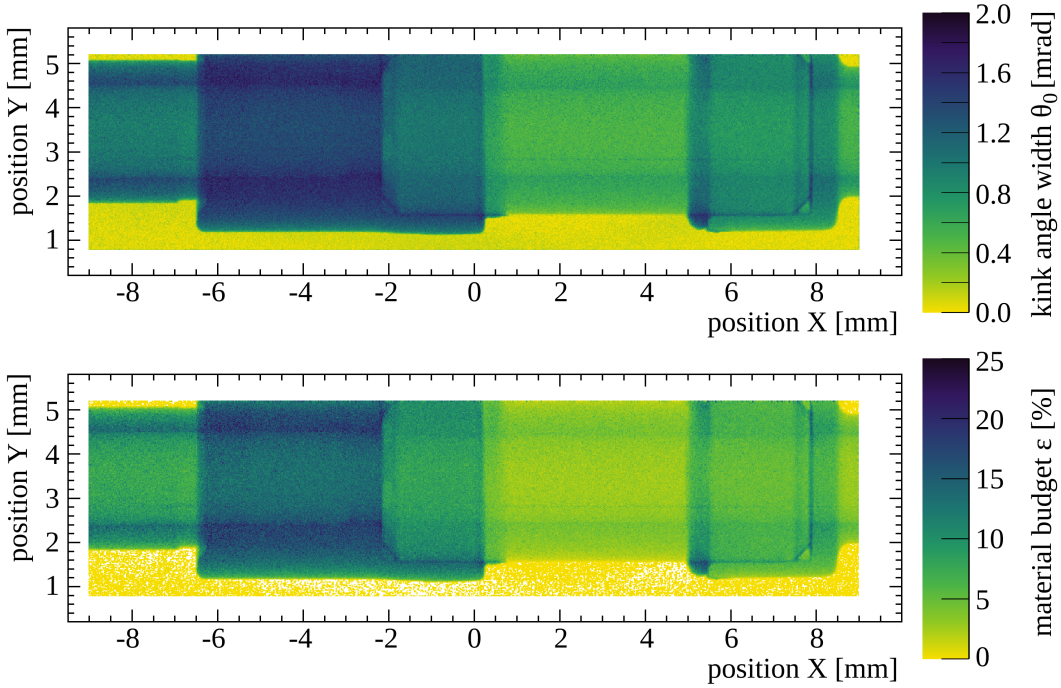

Figure 9.32: Two-dimensional maps of the corrected scattering angle θ_0 (top) and the material budget ϵ (bottom) of the electrical break assembly. An image cell size of $(10\,\mu\text{m})^2$ is used and the measurement was conducted at beam line TB22 with a beam momentum of 4 GeV/c and telescope setup S2.

The resulting image shows the details of internal structure of the electrical break assembly: on the left side of the image, the copper pipe with an inner diameter of 2 mm and an outer diameter of 3.2 mm is visible; this is followed by the connection sleeve made out of a copper-nickel alloy which is vacuum brazed to the copper pipe with an outer diameter of 4.5 mm and features the highest material budget of up to $\epsilon = 20\%$ in the image;

the insulating part, made out of an alumina ceramic, is inserted on the right side of the sleeve and is connected to the assembly by vacuum brazing as well; the shape of the ceramic with a length of 10 mm is clearly resolved in the image with the correct inner (2.05 mm) and outer diameter (3.8 mm) and shows the lowest material budget value; the assembly is finished on the right side with a titanium weld sleeve again vacuum brazed to the ceramic.

The example of the electrical break assembly shows the possibility to finely resolve the internal structure of the investigated sample with the MBI technique, providing also a correct geometrical representation of the individual parts in the assembly. Therefore, it is possible to analyse such welded assemblies with the MBI technique and detect possible defects, while reaching similar image results as for an X-ray scan or a CT measurement. But for the MBI measurements, the effort in terms of measurement time and cost of the test beam operation are much higher compared to the conventional measurement techniques.

Prototype of the End of Substructure board

A prototype version of the **E**nd **o**f **S**ubstructure (EoS) board (cf. Fig. 9.6b) was studied in scattering measurements at beam line TB21 with a beam momentum of 2.4 GeV/c and telescope setup S2. The electrical PCB with several attached components, e.g. resisistors, coils and an ASIC, was scanned by five consecutive measurement runs. Each time, the detection area of $(2 \times 1)\,\mathrm{cm}^2$ is imaged, but a small overlap between each image is introduced to account for the fiducial selection during the MBI analysis. This allows to manually stitch the individual images together to gain a larger image area.
With 48×10^6 triggered events per image and correspondingly 121 to 179×10^6 tracks after reconstruction, the selected image cell size of $(10\,\mu\mathrm{m})^2$ provides a very good contrast in the resulting images[63]. This is demonstrated in Figure 9.33, showing the two-dimensional material budget distribution of the EoS board of the second measurement (section II).

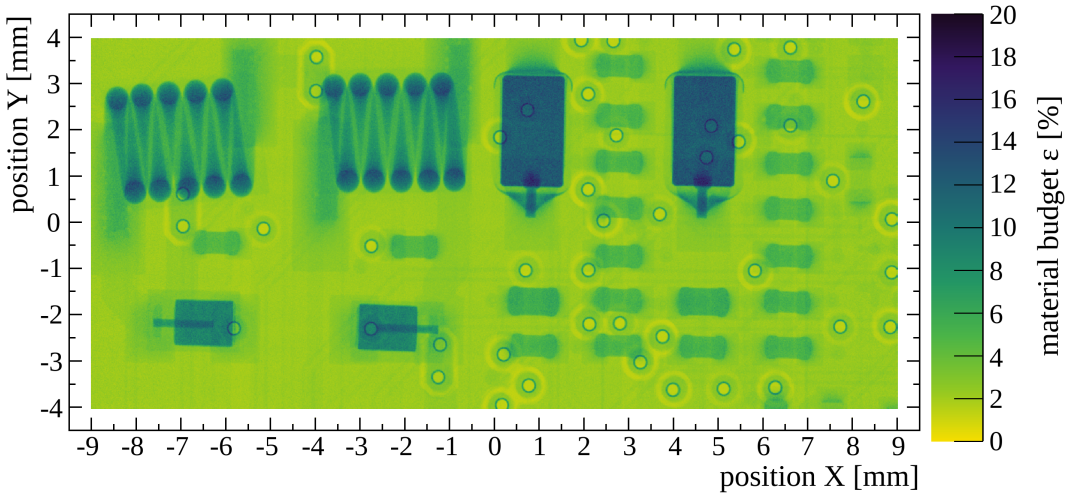

Figure 9.33: Two-dimensional material budget distribution of the EoS board in section II (cf. Fig. 9.6b). An image cell size of $(10\,\mu\mathrm{m})^2$ is used and the measurement was conducted at beam line TB21 with a beam momentum of 2.4 GeV/c and telescope setup S2.

[63] The average number of reconstructed tracks per image cell is in this case around 800 ± 140, which allows in principle to even resolve the material budget distribution with a lower cell size. This was studied with a cell size of $(5\,\mu\mathrm{m})^2$, but here several artifacts were observed in the reconstructed images as the resolution limit defined by the spatial resolution of the telescope setup is reached.

The material budget image allows to clearly resolve the individual electrical components soldered on top of the PCB: two coils with their individual windings as well as two conductivities placed on the soldering pads are visible in the upper part of the PCB, featuring rather large material budgets around 15% due to the contained metal in the components; also several resisistors soldered onto the electrical pads on the PCB can be resolved with a higher material budget around 5% than the multi-layered PCB in the background with $\epsilon \approx 3\%$. Apart from the components visible also in the photograph of the EoS board (cf. Fig. 9.6b), the material budget image shows also hidden features of the PCB: the electrical *vias*, being cylindrical holes with a metalized inner surface to connect different copper layers in the PCB, can be identified in the image as perfect empty circles of higher material budgets with a diameter of around 500 µm and surrounded by another ring showing the integrated passivation region around the vias. Here, it is even possible to resolve the vias below the mounted electrical components, such as the conductivities. Moreover, the complex layout of the multi-layered PCB with areas of copper surrounded by passivation layers can be faintly resolved in the image, but shows in the 2D case a superposition of all layers of the PCB at a given spatial position.

In Figure 9.34, the stitched image of the EoS board covering then a total area of $(75 \times 8)\,\mathrm{mm}^2$ is shown. The five individual measurements recorded in a scan along the x-direction with an overlap of 2 mm are used and the individual material budget images of the scan before stitching are presented in Appendix C.6.

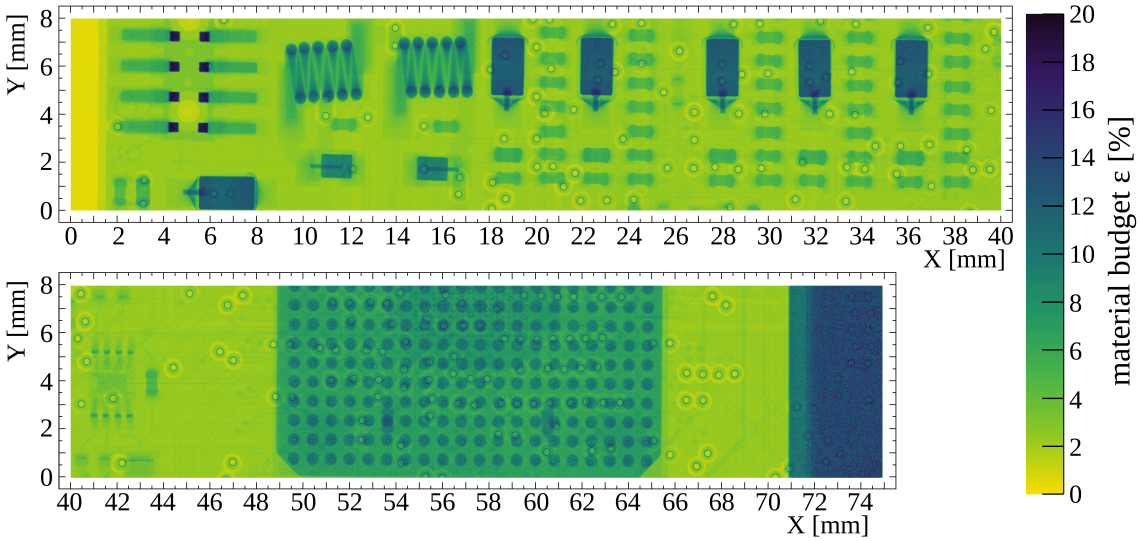

Figure 9.34: Two-dimensional map of the material budget after stitching of a scan over the EoS board along the x-direction, covering a total area of $(75 \times 8)\,\mathrm{mm}^2$ with five individual measurements. An image cell size of $(10\,\mu\mathrm{m})^2$ is used and the measurements were conducted at beam line TB21 with a beam momentum of 2.4 GeV/c and telescope setup S2.

Similar as before, the electrical components on the surface as well as the internal features of the PCB can be resolved over the full area of the stitched material budget image. The transition between the individual measured images is in this case very smooth and difficult to detect after the stitching, indicating a good comparability of the images in the overlap region. Apart from the already discussed features of the PCB, the attached ASIC on the EoS board ($49\,\mathrm{mm} < X < 65\,\mathrm{mm}$) is imaged as well. Here, it is possible to resolve the internal structure of the ASIC below its metallic cover.

On the one hand, a regular pattern of dots is visible, showing the soldering pads to connect the multi-channel ASIC to the PCB. On the other hand, the main chip in the central part of the ASIC can be identified in the image, faintly showing also the internal connections made by *bump bonds*, being small solder balls between two metalization layers.

The example of the EoS board proves again the high resolution of the MBI technique to accurately resolve internal structures of the investigated sample, in this case a complex, multi-layered PCB with soldered on electronic components showing material budgets up to 20% and internal structures with a size of $\mathcal{O}(100\,\mu\text{m})$. Furthermore, the stitching of individual scattering measurements to study the material budget distribution over a larger area than the detection area was successfully demonstrated with the EoS board.

Cocured bus tape structure

The material budget distribution of a cocured bus tape structure (cf. Fig. 9.6c) was investigated in several scattering measurements at beam line TB22 with a beam momentum of 2.4 GeV/c and using telescope setup S2. A very low material budget is expected for the polyimide-based structure, which was scanned along the x-direction in seven consecutive measurement runs with a overlap of 1 mm between each image to allow for a stitching of a larger image area. In total, 6×10^6 triggered events per image were recorded, which resulted on average in 15×10^6 tracks after reconstruction. An image cell size of $(20\,\mu\text{m})^2$ for the bus tape structure was chosen, providing on average 245 ± 49 tracks per image cell, and the model-independent calibration function is used for the following analysis. In Figure 9.35, the resulting material budget image for the last position of the scan is shown.

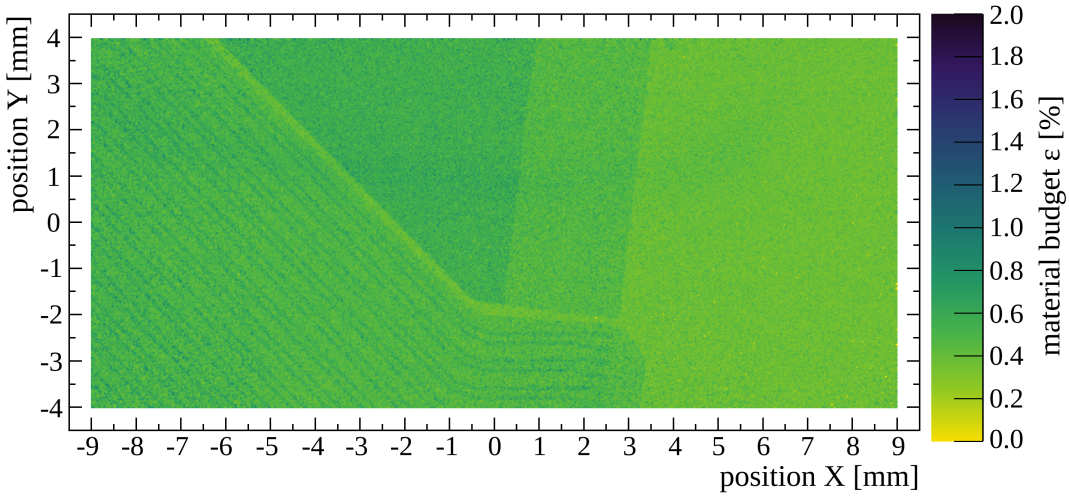

Figure 9.35: Two-dimensional material budget distribution of a section of the cocured bus tape. An image cell size of $(20\,\mu\text{m})^2$ is used and the measurement was conducted at beam line TB22 with a beam momentum of 2.4 GeV/c and using telescope setup S2.

Due to the low material budget of the structure, mostly in the order of $\epsilon = 0.3\%$, and its rather homogeneous distribution, the contrast in the image is not comparable to the previously analysed structures. Nonetheless, the changing layup inside the bus tape can be clearly resolved as regions with a higher material budget and the geometrical shape of the internal substructure is correctly reconstructed. It is also possible to resolve the individual copper lines embedded between the polyimide layers, whereas the resolution and contrast is limited in this case requiring a higher number of tracks for a better differentiation.

After stitching the seven individual measurements recorded in an automated scan along the x-direction with a step size of $\Delta x = 18\,\text{mm}$, the two-dimensional distribution of the material budget for the bus tape structure over an area of $(126 \times 8)\,\text{mm}^2$ is shown in Figure 9.36. The corresponding images for the individual measurement positions before stitching, providing a minimal lateral overlap of 1 mm, are shown in Appendix C.6.

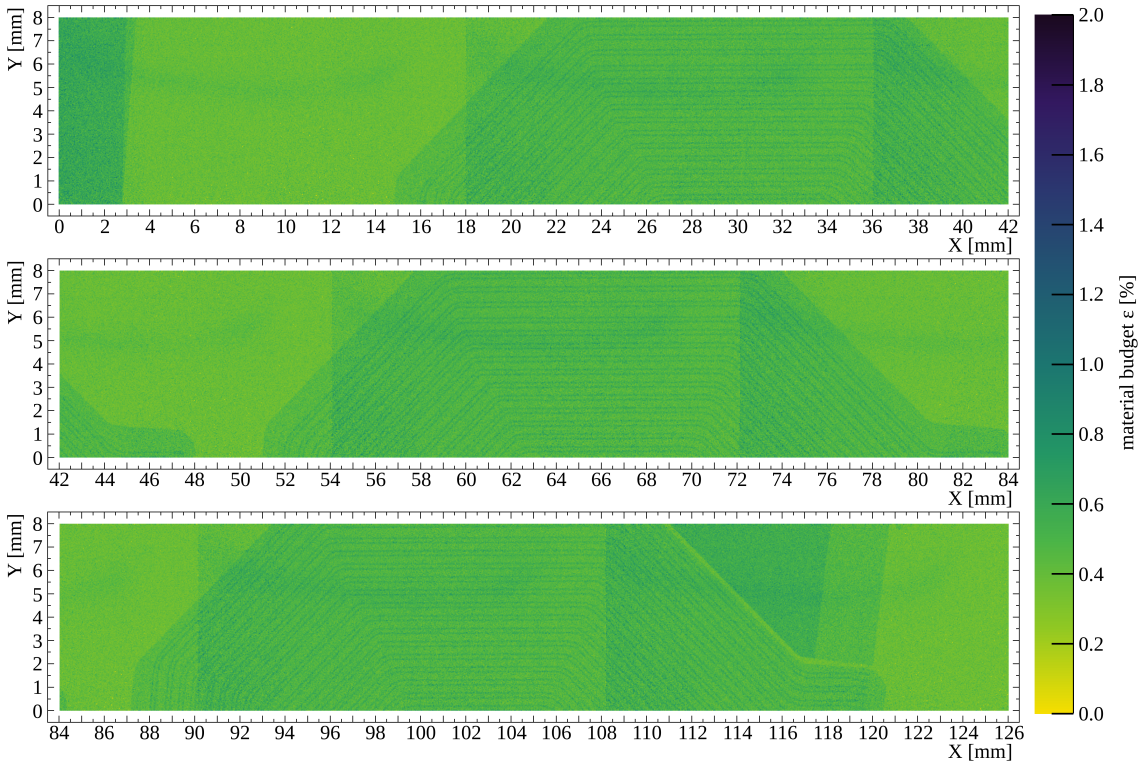

Figure 9.36: Two-dimensional map of the material budget after stitching of a scan over the cocured bus tape along the x-direction, covering a total area of $(126 \times 8)\,\text{mm}^2$ with seven individual measurements. An image cell size of $(20\,\mu\text{m})^2$ is used and the measurements were conducted at beam line TB22 with a beam momentum of 2.4 GeV/c and telescope setup S2.

For the stitched image, the internal substructure of the bus tape can be resolved over a larger area as well, resulting in regions of different material budget values, but also two further observations can be made. On the one hand, the transition between the individual recorded images is clearly visible for the imaged bus tape structure, as slightly larger material budget values are observed on the left side of the individual images than for the right side, which results in sharp transitions for the stitched images. This can be most probably interpreted as an effect of the beam momentum variation along the horizontal direction, as it was discussed in Section 9.4.5. For the bus tape structure, with an overall low material budget, this variation is effectively quite pronounced and motivates the planned investigations on an according correction procedure. On the other hand, in each image a feature of a slightly higher material budget region is observed between $4.5\,\text{mm} < Y < 6\,\text{mm}$, which was also observed for the corresponding scattering measurements without an SUT as well as with the calibration materials with lower material budgets in the according test beam campaign at beam line TB22. The reason for this variation could be either some additional material in the setup, e.g. a wrinkle in the Kapton foil covers of one of the MIMOSA26 sensors of the DURANTA telescope, or an artifact of the reconstruction.

Overall, the feasibility of the MBI technique to resolve also the material budget distribution with low material budget values could be demonstrated with the measurement of the cocured bus tape structure, even though that the amount of recorded data and correspondingly reconstructed tracks is rather on the low side for this low material budget measurement. Moreover, the stitching technique for individual measured images was successfully applied for the scan of the bus tape structure over a larger area, whereas in this case the transition between individual images is visible due to the horizontal dependence of the beam momentum resulting in a variation of the material budget from the left to the right side of the individual images.

Petal core

The internal structure of a petal core prototype with a cocured bus tape surface (cf. Fig. 9.6d) was studied in a large number of individual scattering measurements at beam line TB22 with a beam momentum of 4 GeV/c and telescope setup S2. A two-dimensional scan over the petal core's surface in the x- and y-direction, consisting of nineteen measurement runs, was performed to allow for an investigation of a larger image area using the procedure of image stitching. For this investigation, measurement runs with 10×10^6 triggered events per image were taken, resulting on average in 16.5×10^6 reconstructed tracks[64]. The selected image cell size of $(20\,\mu\text{m})^2$ provides in this case on average 263 ± 50 tracks per image cell and for the calibration of the material budget estimate the Highland fit is used for the following analysis. Figure 9.37 shows the two-dimensional material budget distribution analysed from one of the performed measurements of the petal core structure.

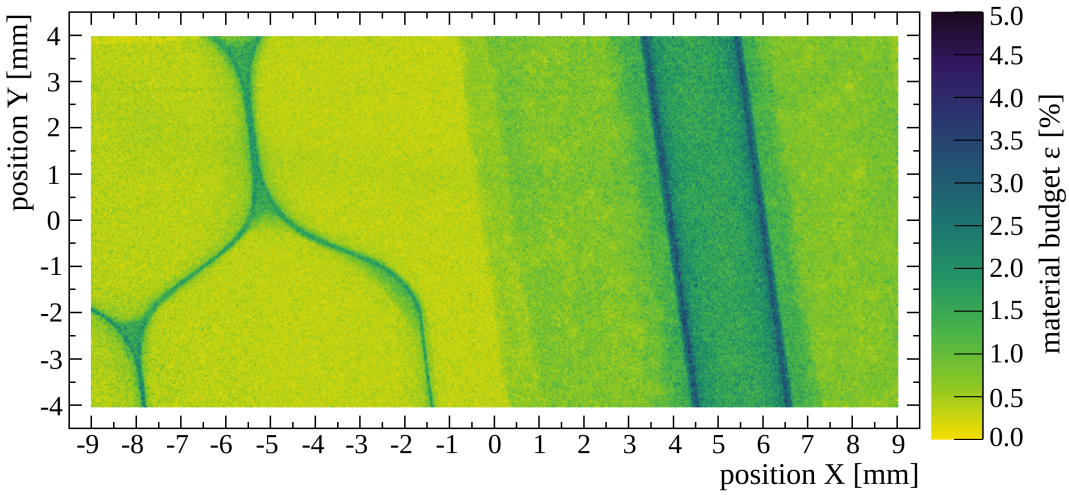

Figure 9.37: Two-dimensional material budget distribution of a section of the petal core. An image cell size of $(20\,\mu\text{m})^2$ is used and the measurement was conducted at beam line TB22 with a beam momentum of 4 GeV/c and setup S2.

The resulting material budget image resolves clearly the internal structure of the petal core with its individual components in the assembly: on the left side of the image, the CF honeycomb structure with a cell size of 6.25 mm and a wall thickness of only 100 µm for the individual elements is observed; the material budget of the CF walls is around 2% compared to the image background of $\epsilon \approx 0.5\%$ as the superposition of the scattering in the top and bottom cocured bus tape and the enclosed air volume within the cells;

[64] For some of the measurements, only 8×10^6 triggered events per image were recorded with on average 12.5×10^6 tracks after reconstruction and 200 ± 39 tracks per image cell with a size of $(20\,\mu\text{m})^2$.

at the the edges between the honeycomb elements, larger regions than the CF wall thickness with a higher material budget are identified, which can be explained by the applied glue between the honeycomb structure and the carbon fiber face-sheets accumulating at the wider sections of the honeycomb structure; on the right side of the image, the titanium cooling pipe can be identified with the largest material budget in the image up to 3.5%, when the particle traverses the round shaped pipe wall; the geometry of the straight pipe section with an inner pipe diameter of 1.955 mm as well as a wall thickness of 160 µm are correctly reconstructed in the image; the cooling pipe is surrounded by the carbon-based Allcomp foam which is glued to the pipe with carbon-loaded Hysol glue, also observable as an irregular shaped region of slightly higher material budget around the pipe; also in this case, the evaluated material budgets account for the total thickness of the sandwich-structure with the cocured bus tapes at the top and bottom surface of the core.

Figure 9.38 shows the stitched image consisting of the nineteen individual measurements of the scan along the x- and y-direction with defined overlaps at the edges for images of neighboring positions, covering a total area of $(148 \times 16)\,\mathrm{mm}^2$. The individual material budget images before the stitching are shown in Appendix C.6.

It is possible to stitch the images to the quite large image area of the petal core structure without any observable transition between the individual measurements. But in some images with regions of lower material budgets inside the honeycomb regions, the previously observed artifact in the image for the bus tape investigation can be observed here as well. Also for the measured material budget distribution over the full area of the scan, the individual elements of the sandwich-structured core assembly can be identified: starting on the left side, the lateral closeouts manufactured as 4 mm wide C-channels made out of pultruded CF with inserted pins to allow for clamping of the core are visible; this is followed by a region with CF honeycomb with a width of five and a half cells showing the regular honeycomb pattern; here, also the structures inside the bus tapes as the surfaces of the core can be identified due to the embedded copper layers increasing the effective material budget along these structures; larger regions of copper for the purpose as shielding layers are formed, but also individual electrical lines with pad openings at the top and bottom for electrical contacting can be resolved in the image; the honeycomb region is intersected by the titanium cooling pipe embedded and glued to the carbon-based foam; the middle section of the internal petal core structure is made out of ten cells of the CF honeycomb, before intersected by the returning titanium cooling loop surrounded again by the foam; afterwards, the honeycomb structure is continued up to the lateral closeout on the other side of the petal core, which is outside of the selected image area.

Overall, with the measured material budget distribution of the petal core, the feasibility to resolve the internal structure of a middle-ranged material budget object was demonstrated. The geometrical features of the structure with object sizes down to 100 µm are reconstructed correctly and also smaller features such as the copper layers inside the bus tapes can be resolved over the background of the petal core structure. Moreover, the successful application of the stitching technique allowed to investigate the petal core structure over a comparable large image area of $(148 \times 16)\,\mathrm{mm}^2$.
With the known geometry of the petal core and the experimentally determined radiation length values for the individual materials of the core assembly, a detailed and position-resolved calculation of the expected material budget distribution of the petal core could be made and compared to the presented measurement results, which is a planned follow-up for the study of the petal core's material budget distribution.

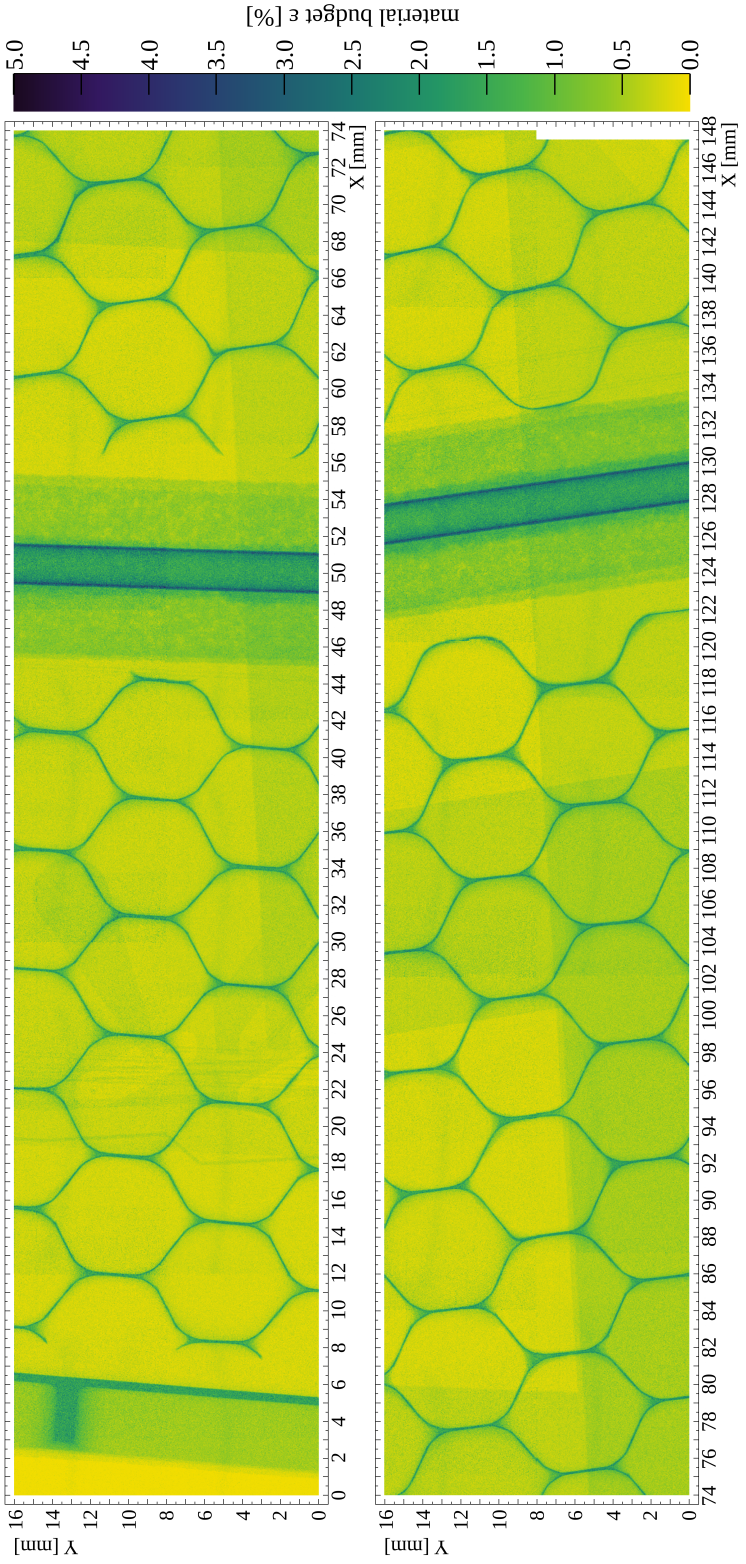

Figure 9.38: Two-dimensional map of the material budget after stitching of a scan over the petal core in the x- and y-direction, covering a total area of $(148 \times 16)\,\mathrm{mm}^2$ with nineteen individual measurements. An image cell size of $(20\,\mu\mathrm{m})^2$ is used and the measurement was conducted at beam line TB22 with a beam momentum of $4\,\mathrm{GeV/c}$ and telescope setup S2.

Prototype of a silicon strip module

The material budget distribution of the silicon strip module (cf. Fig. 9.6e) was investigated in several scattering measurements at beam line TB21 with a beam momentum of 2 GeV/c and using telescope setup S4. An automated scan in the x- and y-direction was performed with fifteen measurement runs, which allows to perform again a stitching with an overlap of 2 mm at the left and right edges and an overlap of 1 mm for the top and bottom edges of the individual images.
In total, 20×10^6 triggered events per image were recorded with the number of reconstructed tracks ranging between 183 and 198×10^6. Due to the rather high data statistics, an image cell size of $(10\,\mu\text{m})^2$ was chosen, providing a good contrast in the image with on average 249 ± 50 tracks per image cell. For the MBI analysis of the module prototype, the model-independent calibration function is used. The resulting material budget image, analysed at one of the measurement positions for the scan over the silicon sensor module's surface, is depicted in Figure 9.39.

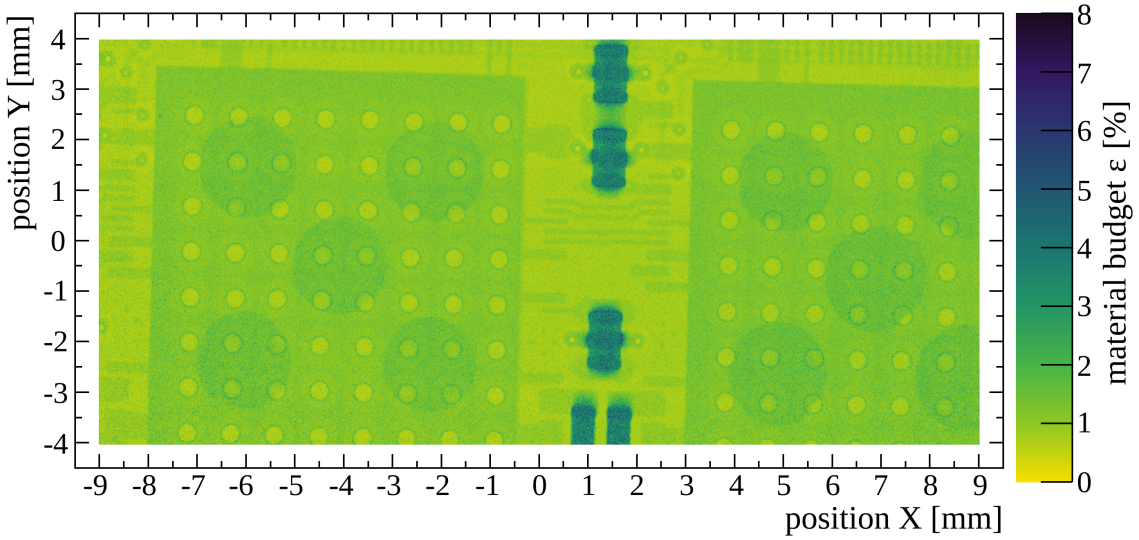

Figure 9.39: Two-dimensional material budget distribution of a section of the silicon strip module prototype. An image cell size of $(10\,\mu\text{m})^2$ is used and the measurement was conducted at beam line TB21 with a beam momentum of 2 GeV/c and telescope setup S4.

The image shows the material budget distribution for a section of the silicon strip module on top of the hybrid PCB, where the particles traverse two of the attached readout ASICs as well as the multi-layered PCB with soldered on electronic components.
Similar as for the EoS board, the conductivities soldered on the corresponding pads of the PCB show the largest material budget values of the image with $\epsilon \approx 5\%$ due to their high fraction of contained metals with rather large radiation length values. Moreover, apart from the visible components attached on top of the PCB, the internal structure of the PCB with the individual copper lines for the electrical connections as well as the electrical vias for contacting the individual layers inside the PCB can be resolved.
For the ASICs, their quadratic contour with a length of 7.5 mm is clearly visible with material budget values around 1.5%, compared to the material budget of the PCB itself with values below 1%. Below the chips, a regular pattern of 8×8 circular openings with a diameter below 500 µm can be identified. These openings are a special kind of vias integrated in the PCB and dedicated for the thermal management of the attached ASICs.

Moreover, a characteristic pattern of five dots with diameters of approximately 2 mm is visible, featuring larger material budget values than the chip itself. This is the pattern of glue dots applied on the hybrid PCB before attaching the readout ASICs from the top. A feature visible on the photograph of the silicon sensor module, but not visible in the material budget image is the electrical contacting of the ASIC to the pads on the PCB via *wire bonds*. Wire bonds are tiny aluminum strings with a typical diameter of 25 µm attached to a surface contact by ultrasonic pressure with a wire bonding machine. Due to the low material budget value of the wire bond added on top of the material budget of the PCB as well as its small geometrical dimensions close to the size of the image cells, the wire bonds cannot be resolved in the measured material budget image.

After performing the image stitching of the individual measurements for the two-dimensional scanning of the sample, the two-dimensional distribution of the material budget for the silicon sensor module over an area of $(50 \times 48)\,\mathrm{mm}^2$ is shown in Figure 9.40. The corresponding images at each scanning position with $\Delta x = 16\,\mathrm{mm}$ and $\Delta y = 8\,\mathrm{mm}$ before applying the stitching are presented in Appendix C.6.

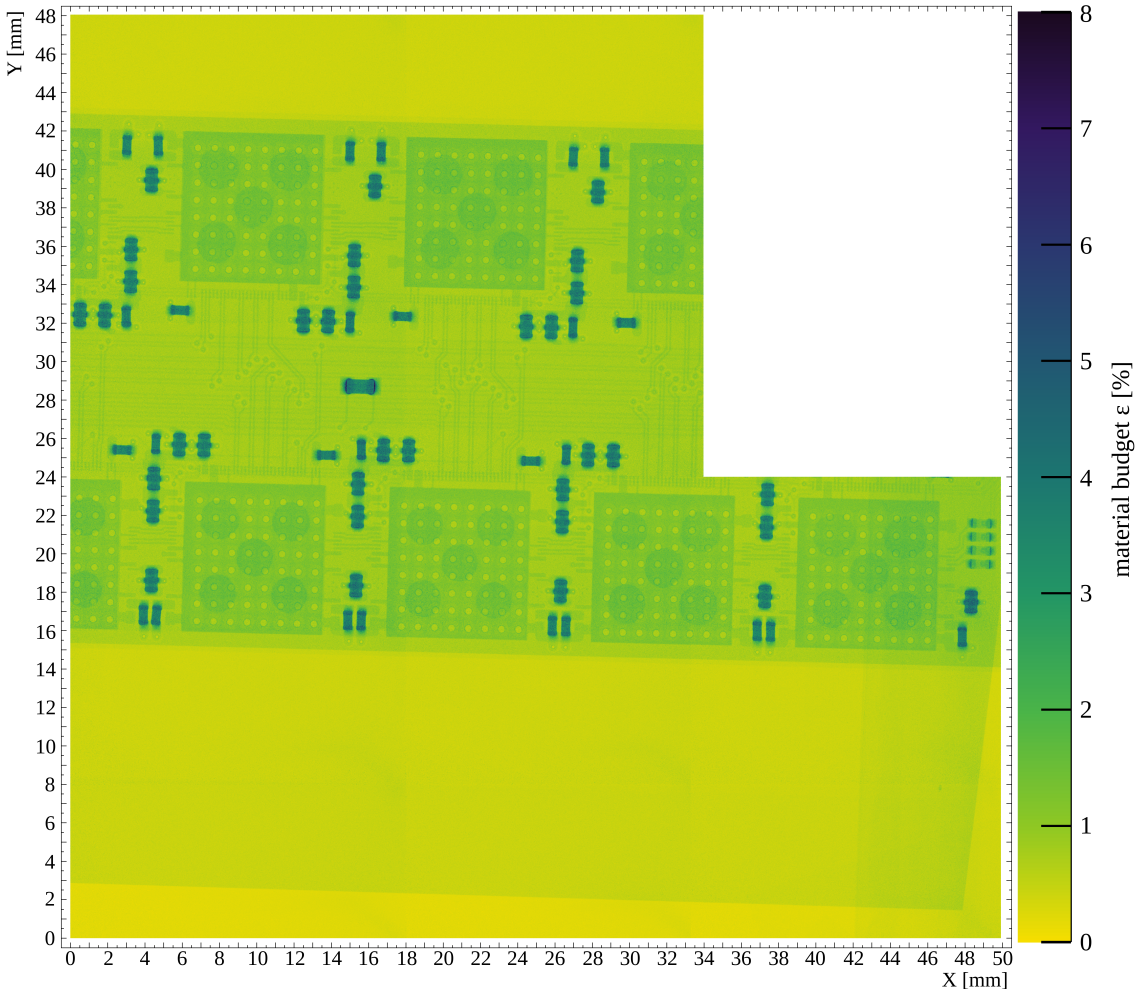

Figure 9.40: Two-dimensional map of the material budget after stitching of a scan over the silicon strip module in the x- and y-direction, covering a total area of $(50 \times 48)\,\mathrm{mm}^2$ with fifteen individual measurements. An image cell size of $(10\,\mu\mathrm{m})^2$ is used and the measurements were conducted at beam line TB21 with a beam momentum of 2 GeV/c and telescope setup S4.

For the stitched image, three different regions can be identified: at the bottom of the image, the beam particles do not hit the silicon sensor module, showing therefore the reconstructed material budget of $\epsilon \approx 0.2\%$ corresponding to the scattering in the air volume between the telescope arms; a slightly larger material budget of $\epsilon \approx 0.4\%$ is contributed to the scattering in the silicon sensor, for which its characteristic, trapezoidal contour can be clearly identified in the image; with a total thickness of 350 µm for the silicon sensor with an aluminum metalization layer at the backside of 25 µm, the expected radiation length in this region is around 0.375%, discarding here the contribution of the individual strip implants, and matches well with the measurement; the final region is the hybrid PCB with the readout ASICs directly glued on the silicon sensor showing a material budget value of $\epsilon \approx 0.8\%$. Moreover, on the right side of the image, the additional contribution of the adhesive tape on the material budget for the three regions is observed, where the tape is used for the fixation of the prototype module on the SUT holder.
In the hybrid region, the same features in terms of the soldered on electronic components, the ASIC chips with the glue dots and the internal structure of the PCB with copper lines and electrical vias can be identified as in the case of analysing the material budget image in Figure 9.39. The wire bonds, connecting also the input channels of the readout ASICs with the individual strip implants of the silicon sensor, cannot be discriminated from the background of the silicon sensor's material budget due to the feature size and the amount of additional material ($\epsilon_{\text{wirebond}} < 0.028\%$) from the wire bonds.

Overall, the MBI investigation of the silicon sensor module proves again the feasibility of the imaging technique to analyse the two-dimensional distribution of the sample's material budget and to resolve the internal structure of the object with a high resolution and contrast. Here, the wire bonds, made out of 25 µm thin aluminum strings, must be excluded as they could not be resolved in front of the material budget contribution of the silicon sensor module itself. With the stitching technique, it was possible to investigate the structure over an image area of $(50 \times 48)\,\text{mm}^2$. Here, transitions between the individual measured images can be detected for regions on the silicon sensor with a lower material budget, but not for the regions of the hybrid PCB. This indicates again an effect of the horizontal beam momentum variation on the stitching procedure, whereas the relative influence depends on the overall material budget in the stitched areas of the image.

Thermo-mechanical petal prototype

In the final study, the material budget distribution for the thermo-mechanical petal prototype (cf. Fig. 9.6f) was investigated in two dedicated scattering measurements at beam line TB22 with a beam momentum of 2.4 GeV/c and using telescope setup S3. Here, the thermo-mechanical petal represents in principle the combination of the material budget investigations with the bare petal core structure and the silicon sensor module, as shown before. Due to the sensitivity of the object, no automated scan over a larger surface area was conducted for the TM petal, but instead the MBI measurements were performed at two, manually adjusted positions, namely point A and point B, featuring different characteristics of the traversed object.
In total, 30×10^6 triggered events were recorded for each measurement position and the number of reconstructed tracks is 29.1 and 25.1×10^6 for point A and B, respectively. The selected image cell size for the TM petal investigation is $(10\,\mu\text{m})^2$, providing 133 ± 48 and 118 ± 44 reconstructed tracks per image cell, and for the calibration the Highland fit is chosen. The evaluated material budget image for point A is depicted in Figure 9.41.

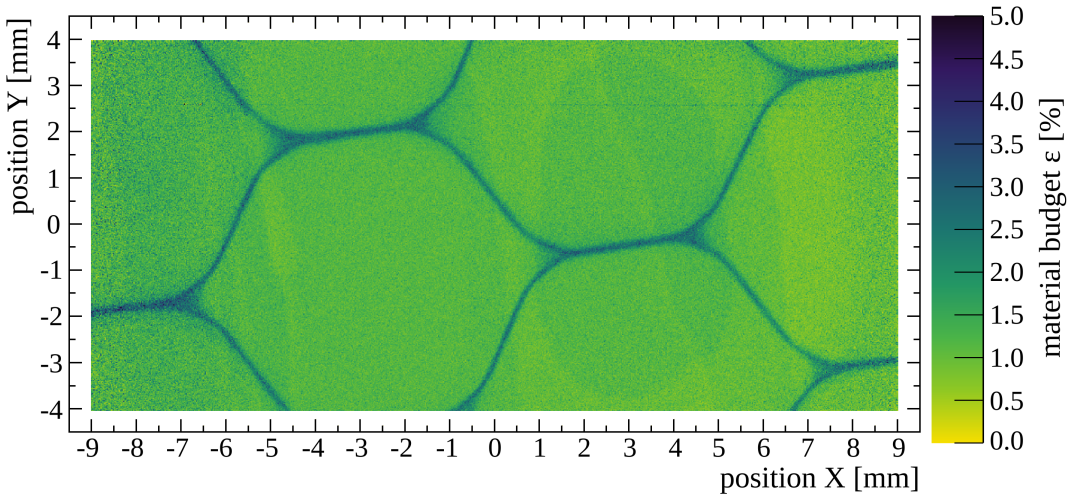

Figure 9.41: Two-dimensional material budget distribution of the TM petal at point A, traversing a section with honeycomb structure. An image cell size of $(10\,\mu m)^2$ is used and the measurement was conducted at beam line TB22 with a beam momentum of 2.4 GeV/c and telescope setup S3.

For the point A, the particles traverse the TM petal in a section of the R0 module with the blank silicon crystal at the top and bottom and the middle section of the core structure with honeycomb cells. Similar as for the investigation of the petal core structure, the in this case paper-based honeycomb cells with a cell size of 6.25 mm can be clearly resolved in the image showing the comparable largest material budget values. In the right part of the image, a region in an oval shape with a slightly larger material budget is observed, which could be accounted for a dot of the glue between the core surface and the module, but otherwise no distinct features can be identified in the measured material budget image.

For the second measurement of the TM petal at point B, the resulting two-dimensional material budget distribution is shown in Figure 9.42.

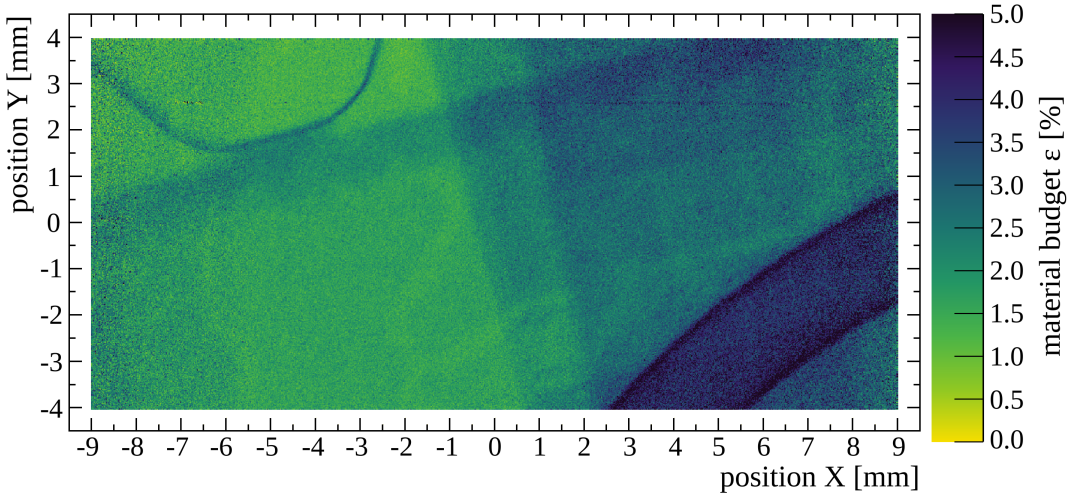

Figure 9.42: Two-dimensional material budget distribution of the TM petal at point B, traversing a section with the titanium cooling pipe. An image cell size of $(10\,\mu m)^2$ is used and the measurement was conducted at beam line TB22 with a beam momentum of 2.4 GeV/c and telescope setup S3.

For the point B, the beam traverses the TM petal in a section of the R0 module on top of the hybrid PCB with the titanium cooling loop embedded in the carbon-based Allcomp foam below in the core structure. The curved titanium cooling loop, located in the lower right corner of the image, features the highest material budget and the contours of the in this case larger foam section is visible in the upper left part of the image, showing also a fraction of a honeycomb cell. The two intersecting regions in the right half of the image, showing also higher material budget values, can be identified as the hybrid PCBs of the top and bottom R0 module, slightly misaligned between each other. Also the individual pattern heaters, mimicking the quadratically shaped readout ASICs and attached on top of the hybrid PCBs, can be faintly differentiated.

Overall, the two performed measurements with the TM petal showed similar features as observed for the individually investigated petal core structure and the silicon sensor module. Also for this study, an automated scan over a larger area of the TM petal's surface would have allowed to gain a better insight in the internal structure of the thermo-mechanical prototype and to differentiate the individual contributions of the support structure and the mounted on modules. But at the time of the test beam campaign, the risk for damaging the valuable object during movements between the telescope arms was too high.

9.7 Investigation on Energy Loss Effects

In the calibration of the material budget estimate from the kink angle widths (cf. Sec. 9.5), known material samples with material budgets between 0.35% and 35% were used. This is completely sufficient for the application of the calibration on the analysis of the unknown material samples for the ATLAS ITk detector (cf. Sec. 9.6): on the one hand, material budget values between 0.3% and 3.5% were measured for the raw material samples, ranging from thin Allcomp foam blocks up to the pultruded CF bars; on the other hand, the overall material budget values in the the two-dimensional imaging of structures were between 0.5% for the cocured bus tape and 20% for the electrical break assembly. Therefore, the range of material budgets values is covered perfectly well in the calibration procedure.
But the potential of the MBI technique should be also evaluated for samples consisting of higher Z materials and featuring correspondingly higher material budget values. In this case, the calibration procedure should be performed also with known material samples of comparable material budgets as the investigated high-Z samples. Moreover, it was observed in the presented calibration in this work that the relative deviation between the measured kink angle width and the predicted value from the Highland formula is increasing for samples with higher material budgets as well as for a higher beam momentum.
A possible explanation for this discrepancy could be that the beam particles are not only deflected by the multiple Coulomb scattering inside the sample, but have also lost a part of its energy after the traversal. Here, the effect of the energy loss is expected to be higher for samples with a larger material budget and depends on the nominal beam momentum. But in the description of the multiple scattering with the Highland model, a constant beam momentum p is assumed in the relationship of the scattering angle width θ_0 and the material budget ϵ of the sample (cf. Eq. 9.4). Therefore, the energy loss effect and its influence on the measured kink angle widths for high-Z material samples is investigated in this section.

For the purpose of studying the scattering inside high-Z materials, measurements with tungsten samples featuring material budgets in the range of $\epsilon = 2.85\%$ and $\epsilon = 142.7\%$ are performed. The results in terms of the measured kink angle widths as well as the comparison to the Highland prediction are discussed in Section 9.7.1.

For the evaluation of the energy loss of the particles after traversing the tungsten samples, the particles' energy is measured with a lead-glass counter (cf. Sec. 8.5.3) behind the beam telescope. The measured energy spectra for varying nominal beam momenta and the different material budgets of the tungsten samples are presented in Section 9.7.2.
Finally, first investigations and ideas on a possible correction of the Highland model to account for the energy loss effect of the scattered particles are described in Section 9.7.3.

9.7.1 Measurement of kink angle widths for high-Z material samples

A scattering measurement of tungsten samples ($X_{0,\mathrm{W}} = 3.50\,\mathrm{mm}$) with thicknesses of 0.1, 0.2, 1.0, 2.0 and 5.0 mm was performed at beam line TB21 with varying beam momenta of 2, 4 and 5 GeV/c and using telescope setup S4. The measured kink angle widths (θ_0^{meas}), estimated with the RMS_{98} estimator and corrected by the influence of the air scattering, are shown in Figure 9.43 for the different samples thicknesses and beam momenta. Here, for the thicker tungsten samples, the fiducial region for the evaluation of the kink angle width in the binned analysis is adjusted to mitigate the influence of the acceptance effect with larger material budgets and correspondingly larger deflection angles (cf. Sec. 9.4.4). Moreover, the predicted values from the Highland formula (θ_0^{HL}) are plotted and the relative deviation between measurement and prediction is calculated.

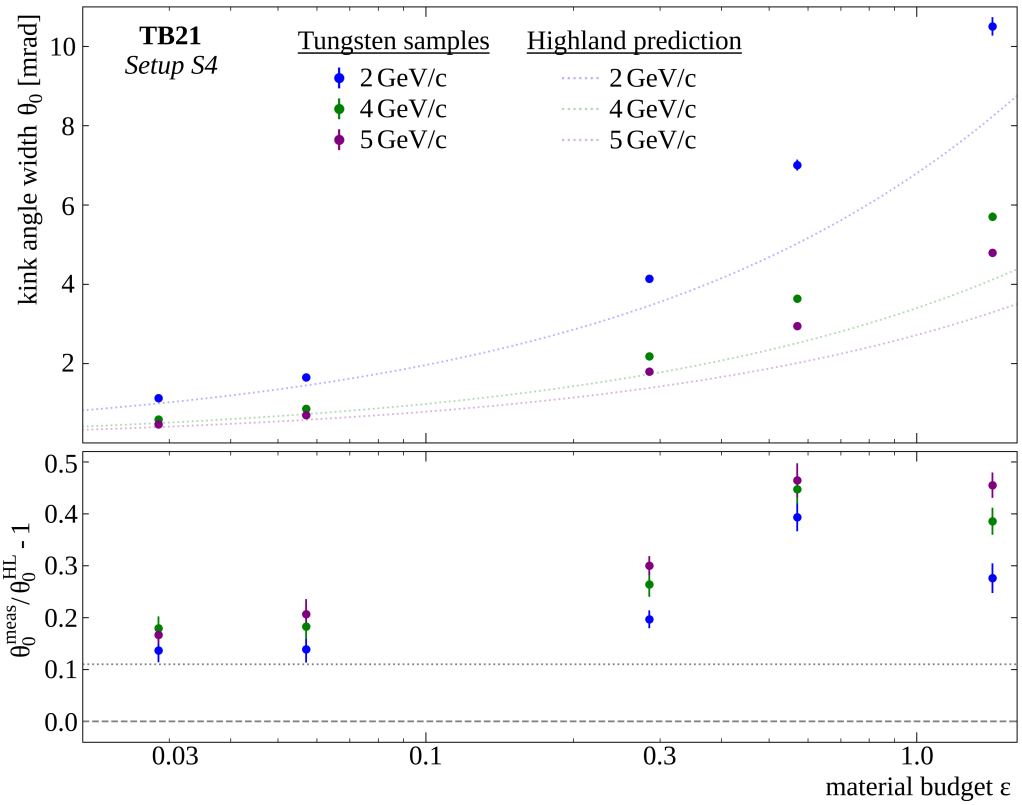

Figure 9.43: Kink angle widths for the scattering in tungsten samples with thicknesses between 0.1 and 5.0 mm and measured with varying beam momenta of 2, 4 and 5 GeV/c at beam line TB21 using telescope setup S4. The kink angle width is extracted from the distributions of the combined kink angle k_{x+y} with the RMS_{98} estimator and corrected by the contribution of the air scattering. The prediction from the Highland model as well as the relative deviation to the measurement is shown.

The measured kink angle widths are in all cases above the prediction of the Highland formula, as it was observed before, but for an increasing material budget of the sample, the discrepancy between measurement and prediction increases as well. Whereas the relative deviation for the thinner tungsten samples is around 15%, the deviation for the thicker samples increases to values around 45%. Here, the measurement for the thickest tungsten sample with $\epsilon = 1.42$ must be excluded, as the relative deviation is lower than expected from the other thicknesses. Reasons for this are that the fiducial area was adjusted to a rather small area to account for the increasing acceptance effect and that the width of the scattering distribution is not anymore adequately represented by the RMS_{98} estimator and correspondingly underestimated due to the contribution of the non-Gaussian tails.
Moreover, a dependence on the selected beam momentum is observed, as the relative deviations for a beam momentum of 5 GeV/c are in all cases higher than for the performed measurement with a beam momentum of 2 GeV/c.
A calibration with the Highland fit using a global calibration factor is therefore not sufficient to describe the data points adequately, as the deviation depends on the material budget of the individual SUTs as well as the chosen beam momentum. Instead, one can suspect another influencing effect depending on the SUT's material budget and the beam momentum: the effect of the *energy loss* for the scattered particles after the traversal of the sample.

The energy loss for charged particles in matter was described in Section 2.1.1 and for electrons in the multi-GeV range, the dominant effect for the energy loss comes from the emission of bremsstrahlung photons (cf. Fig. 2.3). With the mean energy loss for bremsstrahlung described according to Eq. 2.5, the electron's energy E' after the traversal of a material with material budget ϵ and an initial energy E_0 can be calculated with

$$E' = E_0 \cdot e^{-\epsilon}. \tag{9.13}$$

In the Highland formula (cf. Eq. 9.4), a constant particle's momentum p for the traversal of the sample is assumed, which seems to be inadequate for material budgets $\epsilon > 10\%$ due to the additional energy loss of the particle in the traversal depending on the material budget. Therefore, the influence of the energy loss due to bremsstrahlung on the multiple scattering is investigated in the following.

9.7.2 Calorimeter measurement of the energy loss

Apart from the reconstruction of the deflection angles for the scattered electrons in the SUT using the EUDET-type beam telescopes, the measurement setup for the investigation of the energy loss effect is extended by the installation of a lead-glass counter behind the telescope to perform also a measurement of the electron's energy. The setup as well as the performed energy calibration for the calorimeter was described in Section 8.5.3.
Figure 9.44 shows the measured energy spectra for electrons after the traversal of tungsten samples with a thickness of 0.1, 1.0 and 5.0 mm and a selected beam momentum of 5 GeV/c. In each case, the peak of the spectrum is fitted with a Gaussian distribution to extract the mean energy value and its spread as the corresponding standard deviation.

For higher material budgets of the traversed sample, the mean energy value[65] is shifted to lower values and a broader shape with an asymmetry to lower energy values is observed, indicating the energy loss of the particles by bremsstrahlung effects.

[65] The observed offset of the energy compared to the nominal beam momentum also for the low material budget sample can be explained by measurement inaccuracies of the lead-glass counter as well as a not perfect energy calibration.

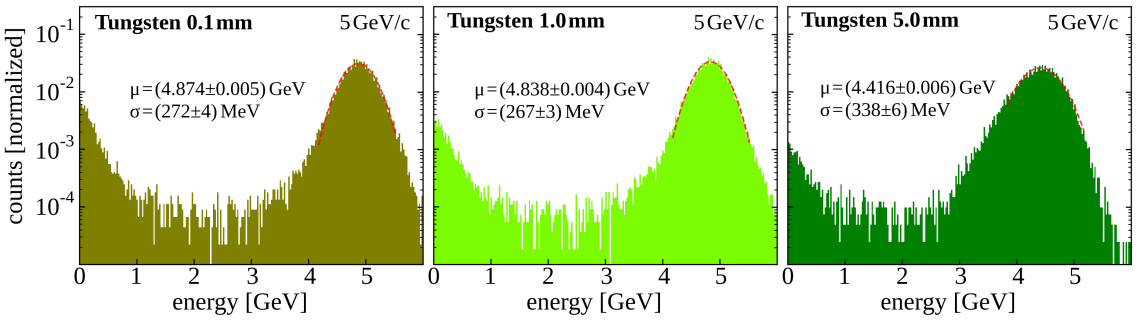

Figure 9.44: Energy spectra for electrons after the traversal of tungsten samples with thicknesses of 0.1, 1.0 and 5.0 mm and a selected beam momentum of 5 GeV/c. The peak is fitted with a Gaussian distribution and the measurement was performed at beam line TB21 with a lead-glass calorimeter.

To quantify the energy loss for the different tungsten samples, the fitted mean values and their standard deviations are plotted as function of the corresponding material budget. This is shown in Figure 9.45 for the performed calorimeter measurements at nominal beam momenta of 2 and 5 GeV/c and the various used tungsten samples. Moreover, an exponential fit with $E = a \cdot \exp(-\epsilon/b)$ is performed to describe the measured dependence of the energy on the amount of traversed material.

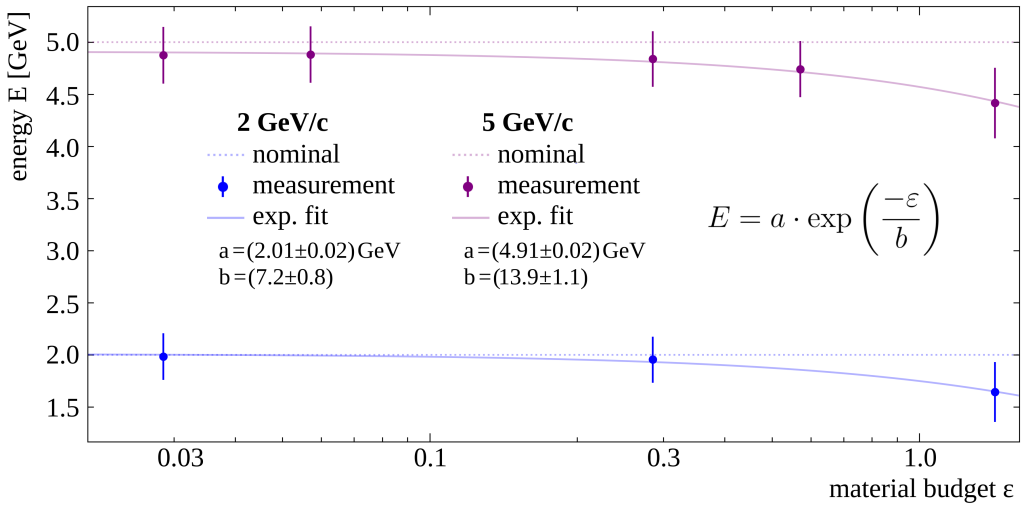

Figure 9.45: Measured electron energy E as function of the material budget ϵ of the traversed tungsten samples for nominal beam momenta of 2 and 5 GeV/c. The extracted mean value and its standard deviation from the calorimeter measurement is used and the data points are fitted by an exponential fit of the form $E = a \cdot \exp(-\epsilon/b)$.

For both tested nominal beam momenta, the electron energy measured in the lead-glass counter after the traversal of tungsten samples is decreasing for higher material budgets of the sample and can be well described by the exponential dependence.
This result proves that the assumption of a constant particle momentum in the Highland formula is inadequate for larger material budgets and the energy loss in the material sample due to the emission of bremsstrahlung photons should be taken into account for the description of the multiple Coulomb scattering interaction.

9.7.3 Energy loss correction for the Highland model

First investigations on a possible correction for the Highland model to consider the energy loss of the scattered particles in the sample were conducted in the course of this thesis. Two different approaches are tested on the measured scattering data of tungsten samples at different beam momenta and evaluated in terms of the relative deviation between the measurement and the corrected Highland model prediction.

The first approach, the *calorimeter-based correction*, uses a correction of the particle's momentum p in the Highland formula according to the found dependence of the electron energy E on the material budget in the calorimeter measurement. The relationship between the kink angle width θ_0 and the material budget ϵ can be expressed then as

$$\theta_0[\text{mrad}] = \frac{13.6}{E(\epsilon)[\text{GeV}]}\sqrt{\epsilon}\,(1 + 0.038\ln(\epsilon)) \quad \text{with} \quad E(\epsilon) = a \cdot \exp(-\epsilon/b). \tag{9.14}$$

Here, the fit parameters a and b are taken from the corresponding calorimeter measurement at the nominal beam momentum p of the scattering measurement.
The second approach, the *energy-weighted correction*, replaces the nominal and constant momentum p in the Highland formula with a weighted momentum $\bar{p}$ calculated as the mean value of the particle's energy before and after the traversed sample with material budget ϵ. Using the expected energy loss described by Eq. 9.13 with the nominal beam momentum p, the energy-corrected formula for the kink angle width θ_0 as function of the material budget ϵ can be expressed then as

$$\theta_0[\text{mrad}] = \frac{13.6}{\bar{p}(\epsilon)[\text{GeV/c}]}\sqrt{\epsilon}\,(1 + 0.038\ln(\epsilon)) \quad \text{with} \quad \bar{p}(\epsilon) = \frac{p}{2}\cdot(1 + e^{-\epsilon}). \tag{9.15}$$

Figure 9.46 shows the measured kink angle widths for the scattering measurements with tungsten samples at the tested beam momenta with the applied *calorimeter-based correction* on the Highland model prediction. For the evaluation of the correction's influence to reach a better description of the measured data, the relative deviation is calculated.

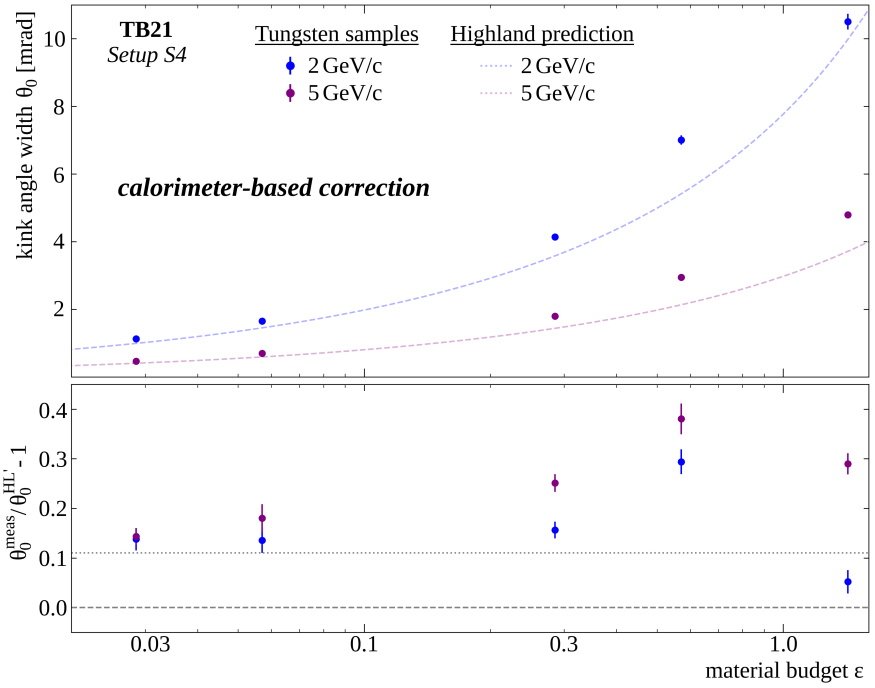

Figure 9.46: Measured kink angle widths for the scattering in various tungsten samples at varying beam momenta and comparison to the predicted values from the *calorimeter-based correction* of the Highland model.

The calorimeter-based correction results in a slight improvement by reducing the relative deviation between the measured kink angle width and the prediction from the corrected Highland formula. But the deviation increases still with the material budget of the sample, indicating that the underlying energy loss effect is not entirely corrected with this approach.

The evaluation of the *energy-weighted correction* of the Highland model on the measurement data is shown in Figure 9.47.

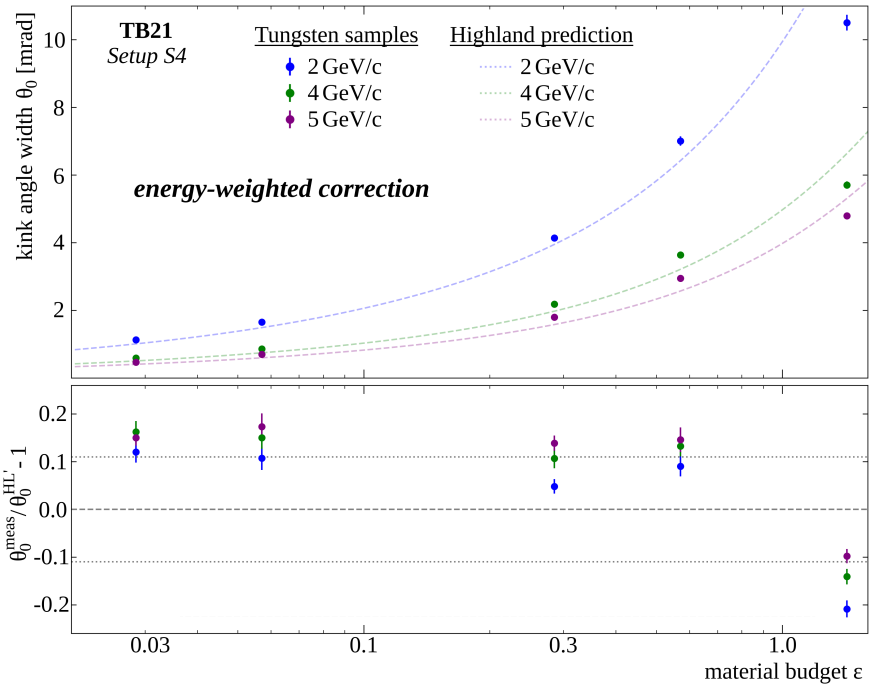

Figure 9.47: Measured kink angle widths for the scattering in various tungsten samples at varying beam momenta and comparison to the predicted values from the *energy-weighted correction* of the Highland model.

Here, the relative deviation between measurement and the corrected prediction shows rather constant values of around 5 to 15% over the range of tested material budget values, when the thickest tungsten sample is excluded[66]. This means that the dependence of an increasing deviation with the SUT's material budget could be removed by the energy-weighted correction, whereas the relative deviation for each individual sample is still increasing with a higher nominal beam momentum. After the applied correction, it is now possible to perform a calibration, either model-dependent or model-independent (cf. Sec. 9.5.2), for the extraction of the material budget from the measured kink angle widths.

Overall, it was shown that with a correction of the beam momentum in the Highland formula, taking into account the energy loss via bremsstrahlung, a better description of the measured kink angle widths for samples of high-Z materials is achieved. Here, first investigations with the energy-weighted correction provide already promising results. Nonetheless, further studies are foreseen for the influence of the energy loss on the multiple Coulomb scattering, using also a larger data set of scattering measurements as well as developing other, more sophisticated correction schemes.

[66] Due to the previously discussed reasons, the kink angle width for this sample is underestimated in the measurement, resulting therefore in the case of the relative deviation to the energy-corrected Highland prediction to negative values. Further investigations for this observation are planned.

9.8 Conclusion

The **M**aterial **B**udget **I**maging (MBI) as a novel imaging technique to directly measure the material budget of samples and to resolve the two-dimensional material's distribution inside the sample was extensively studied in the course of this thesis. For the extraction of the material budget ϵ, depending on the sample's thickness x and its characteristic radiation length X_0, the effect of multiple Coulomb scattering of relativistic particles in the traversed sample is exploited. By measuring the angles for the individual particle tracks before and after the traversal, the effective deflection angle of the particle caused by the interaction with the sample is reconstructed. When the spatial coordinates of the incident position of the particle on the sample is measured as well, a position-resolved measurement of the deflection angle is possible. The width of the resulting scattering distributions is then used to extract the corresponding material budget using the Highland model, which describes the multiple scattering interaction by a relationship between the kink angle width θ_0 and the material budget ϵ with a dependence on the momentum p of the particles.

The MBI measurements presented in this work were conducted with multi-GeV electron beams offered by the DESY II Test Beam Facility and using the high-resolution EUDET-type beam telescopes for the track reconstruction. Here, all relevant steps from the choice of the measurement configuration, the reconstruction of the particle tracks, the evaluation of the kink angle distributions to estimate the kink angle width and the application of an appropriate calibration procedure to extract the actual material budget value from the measurement were described and discussed in this chapter. Moreover, the results for dedicated measurements of the material budget for unknown material samples stemming from the design of the ATLAS ITk detector as well as the two-dimensional imaging of the material budget distribution for assembled ITk detector structures were presented.

For the scattering measurements, the choice of the test beam and beam telescope parameters plays a crucial role on the accuracy of the kink angle measurement. Here, the beam momentum has a major influence on the resulting kink angles as for higher beam momenta the resulting kink angles are decreasing for a given sample. Therefore, the beam momentum should be selected according to the expected material budget of the sample such that the resulting kink angles can be reconstructed with the telescope. For the beam lines at the DESY II Test Beam Facility, the selected beam momentum determines on the one hand the achievable particle rate in the measurement and on the other hand the spread of the beam momentum around its nominal value is increasing for lower beam momenta. This requires to find a compromise for the selection of the beam momentum best suited for the sample with a given material budget. For the telescope, the major influence comes from the chosen telescope setup in terms of the longitudinal plane spacing between the MIMOSA26 sensor planes. Here, it was shown that for larger distances the spatial and angular track resolution can be improved, but at the same time the integration of the **S**catterer **U**nder **T**est (SUT) in between the up- and downstream arm must be possible.

The reconstruction of the particle tracks in the scattering measurements was performed with the EUTelescope framework, starting with the raw pixel hit information over the telescope alignment using the measurement without a passive SUT up to the final track fitting. For the measurement of the effective deflection angle caused by the multiple scattering interaction, the General Broken Lines algorithm for the track fitting was adjusted to allow for an unbiased measurement of the scattering inside the sample without a-priori knowledge of its material budget. This was feasible by describing the SUT with two local derivatives.

Moreover, it was shown that the optimal selection of the track quality parameters used for the track finding in the reconstruction with the triplet method already contains information on the material budget of the inserted SUT.

The reconstructed kink angles for the individual particle tracks result in a scattering distribution, which shape depends on the one hand on the amount of traversed material and on the other hand on the momentum of the scattered electrons. The scattering distribution with a Gaussian-like core and non-Gaussian tails to higher kink angles is centered around zero due to the central limit theorem and only the width of the distribution contains information on the traversed material. Different width estimators with the RMS as a statistical method and the standard deviation of a Gaussian distribution as a fitting method were evaluated using subsets of the kink angle data by inner quantiles. For the inclusive analysis, the width estimators are applied on the overall kink angle distribution stemming from all events inside a defined fiducial area, whereas for the binned analysis, the mean value and its standard deviation of the individually estimated kink angle widths from distributions of reconstructed tracks inside image cells with a size of $(100\,\mu\text{m})^2$ in the x- and y-direction are calculated. After the comparison of the different width estimators, the RMS_{98} estimator was selected for the following analysis in this work using the binned approach for the extraction. Nonetheless, further investigations on appropriate width estimators, such as the also well-performing Gauss_{98} estimator, should be performed.
Furthermore, it was shown that the reconstructed kink angle in the horizontal and vertical direction, k_x and k_y, are uncorrelated, whereas the estimated widths for both scattering distributions are correlated. Therefore, it is possible to merge the information of the kink angles k_x and k_y and using instead the combined kink angle k_{x+y}, which results in an effectively doubled data statistics enhancing the quality of the material budget distribution.
For samples with larger material budgets, it was found that the acceptance effect must be taken into account for the evaluation of the material budget from the two-dimensional kink angle maps. Here, the scattering distributions for track positions at the edges of the active detection area become biased to kink angles pointing to the center of the telescope, as particles scattered to the outside will miss the downstream telescope arm and are correspondingly not reconstructed. To use an unbiased kink angle width estimate for the material budget calculation, the fiducial region for these samples with higher material budgets should be adjusted to exclude the occurring acceptance effects.
Finally, the influence of the horizontal beam momentum variation, caused by the procedure of the beam generation at the DESY II Test Beam Facility, on the two-dimensional distributions of kink angle widths was studied. Here, a clear tendency for a decreasing kink angle width with the horizontal position of the reconstructed tracks was observed and the relative variation could be determined to be around $-0.25\,\frac{\%}{\text{mm}}$ for different tested SUTs and beam momenta. As the next step, the variation of the kink angle width along the horizontal direction should be corrected, which is especially important for the evaluation of the two-dimensional material budget images of investigated structures.

With the evaluated kink angle width from the scattering distribution, the material budget of the sample can be extracted either by applying an appropriate model for the multiple scattering interaction, such as the Highland formula, or by finding a model-independent functional dependence between the material budget of the sample and the measured kink angle width. In both cases, a calibration function must be evaluated accounting also for the systematic effects folded in the estimated kink angle widths.
In the first calibration step, the effect of the scattering inside the air volume between the telescope arms, inherently also present for all SUT measurements, was corrected.

Here, the determined kink angle width from the measurement without a passive SUT is quadratically subtracted from the determined kink angle width of the SUT measurement. In the next step, scattering measurements with homogeneous material samples and a known material budget were used to perform a fit of the calibration curve. Here, a model-dependent calibration with the Highland fit using a global calibration factor was evaluated on the one hand and compared to a model-independent calibration with an empirically found functional dependence of the squared kink angle width and the material budget on the other hand. Both calibration methods were evaluated and used for the extraction of the material budget of unknown material samples and structures, but also further in-depth investigations on the calibration procedure are planned.
Furthermore, it was shown that the calibration depends on the selected beam momentum as well as the chosen telescope setup, observable as a changing relative deviation between measurement and the Highland prediction with these factors. Therefore, for each measurement configuration dedicated measurement runs with known material samples for the calibration should be conducted, as it was the case for the presented measurements.
Two further studies in the context of the calibration of the MBI technique were performed. On the one hand, a dedicated calibration with water samples and varying thicknesses was performed for moderate beam momenta of 1 and 2 GeV/c as an input for the investigation of possible medical applications of this novel imaging technique.
On the other hand, the material budget of simple composite materials modelled as dual-layered structures of two types of materials was systematically investigated. Here, it was shown that the measured kink angle width of the dual-layered structure slightly depends on the orientation of the sample when traversed by the beam, whereas with the same material budget such an effect is theoretically not expected.

After the performed calibration, the MBI technique was used to investigate samples in the context of the planned ATLAS ITk detector, focusing here on the measurement of the radiation length of materials foreseen for the petal core as the detector's local support structure as well as the position-resolved material budget imaging of assembled structures. For the extraction of the radiation length of various material samples, scattering measurements with different sample geometries and measurement configurations in terms of the beam momentum and the telescope setup were conducted to determine the kink angle width estimates. The material budget was then estimated by applying the corresponding calibration, in this case the Highland fit, and used to calculate the X_0 value of the material with the sample thickness as another input. The corresponding results for the tested materials, namely the carbon-based Allcomp foam, pultruded carbon fiber bars, the thermoplastic Torlon, the Hysol glue and the service tray assembly, are summarized in Table 9.13, showing also the currently used estimates [260] in the detector simulation and the material budget calculations for the full detector system.
For the comparison of measured X_0 values and their currently used estimates in simulations and calculations of the ITk detector, a good agreement for most of the materials is observed. The uncertainty on the measurement ranges between 5 and 35% depending on the material as well as the number of used individual measurements. It was shown that with the MBI technique the radiation length of material samples with a not specified X_0 value can be extracted from scattering measurements, allowing therefore to investigate also materials with an unknown material composition such as adhesives and cocured CF composites. With a further refined and standardized measurement routine and analysis procedure, the future goal is to provide an independent material database with measured radiation lengths extracted from MBI measurements. Such a database would be valuable for the development of future detector systems for high-energy physics experiments and beyond.

Material type	X_0^{meas} [mm]	X_0^{sim} [mm]
Carbon-based foam (Allcomp K9)	1620^{+584}_{-549}	1860
Pultruded carbon fiber (T300 CF+adhesive)	271^{+35}_{-34} (epoxy-based) 245^{+12}_{-12} (vinyl-based)	292
Thermoplastic (Torlon 4301)	276^{+41}_{-40}	320
Hysol EA 9396	341^{+38}_{-37} (pure) 350^{+56}_{-54} (carbon-loaded)	300
Service tray (cocured CF layup)	288^{+48}_{-46}	290

Table 9.13: Comparison of the measured radiation lengths (X_0^{meas}) and the currently used estimates in calculations and simulations (X_0^{sim}) for the investigated material samples in the context of the ATLAS ITk detector.

The two-dimensional material budget distributions for several complex structures and assemblies in the context of the ATLAS ITk detector were investigated, ranging from low material budget objects such as a cocured bus tape or a silicon sensor module up to objects like electrical PCBs, welded pipe assemblies or the petal core structure itself.
It was demonstrated that it is feasible to resolve the internal structure of these objects with a high resolution up to 10 µm, while providing still a sufficient contrast in the image to differentiate the individual features in the structure. In this case, the material budget is evaluated for smaller image cell sizes down to $(10\,\mu\text{m})^2$, requiring a sufficient amount of reconstructed tracks per image cell. For the imaging, a high number of recorded events is therefore essential to create material budget distributions with a high resolution and contrast, requiring correspondingly long measurement times.
With the analysed structures, it was shown that the geometrical dimensions of the imaged structures are correctly reconstructed and that structures posing a different material budget can be resolved over the material budget of the background. As such, it was possible to resolve e.g. electrical vias in the electrical PCBs, the glue dots below the readout ASICs of the silicon sensor module or the copper lines in the bus tape structure. A limit of the technique was reached by trying to resolve wire bond connections on the silicon sensor, as here the dimension of the tiny aluminum strings as well as their small amount of additional material are below the achievable resolution and contrast.
Moreover, it was demonstrated that individual measurements of a performed scan in the x- and y-direction over the object's surface can be manually stitched together to acquire a larger image area. Here, in most cases no transitions between the individual images are detectable, but for low material budget objects, such as the cocured bus tape, sharper transitions are caused by the horizontal beam momentum variation, which was for this study not corrected.
For the next investigations, the expected material budget could be calculated with the knowledge of the geometry of the structures and their exact material composition and compared to the experimental result to validate the detector model used in simulations. Also the limitations of the MBI technique in terms of the achievable resolution and contrast in the two-dimensional material budget images should be further explored. The stitching technique to resolve the internal structures of samples over a larger image area should be further refined and possibly automatized instead of the current manual procedure.

In the final study, the behaviour of the multiple Coulomb scattering with high-Z materials was analysed in detail. It was found that the deviation between the measured kink angle widths and the prediction of the Highland formula is increasing with the material budget of the tested sample. The reason for this observation is that the single particles are not only deflected in the material, but lose also fractions of their energy in interactions with the material's atoms, which is for multi-GeV electrons dominantly the emission of bremsstrahlung photons. The energy loss for the beam particles in the MBI measurements was measured by extending the beam telescope setup with an additional lead-glass counter to measure also the particle's energy after the traversal of the sample. Moreover, first investigations on a possible correction of the Highland model, assuming in its original form a constant particle's momentum for the traversal of the sample, were conducted. Here, two different approaches to consider the energy loss for the prediction of the kink angle widths of the multiple scattering interaction were studied. With the energy-weighted correction method, the dependence of the relative deviation between measured and predicted kink angle widths on the sample's material budget could be removed. Nonetheless, further investigations of the influence of the energy loss on the description of the multiple Coulomb scattering are foreseen.

Overall, the investigated concept of the two-dimensional material budget imaging is an interesting measurement technique for the application in the detector development for high-energy physics experiments, but potentially also for applications in medical imaging or industrial applications of non-destructive testing of complex material assemblies.
Currently, the two-dimensional imaging technique (and also its application in 3D tomographic imaging) is only studied for research purposes [250, 251, 252, 253] as it has several disadvantages compared to the conventional imaging techniques like X-ray or CT measurements: a particle accelerator reaching several GeV is required and poses a high cost factor, if not be used in a parasitic mode such as for a test beam facility; for a high-resolution 2D material budget image, a long measurement time of several hours is needed to record a sufficient amount of scattering events; finally, also the required computational power to reconstruct each single particle track is another cost factor for the MBI technique.
Nonetheless, the promising potential of this novel imaging technique, providing artifact-free images of generic samples, should be further investigated. A possible improvement for the feasibility of a wider range of applications is on the one hand to decrease the required measurement time and on the other hand to increase the sensitive area of the telescope. The first aspect could be reached by a higher particle rate, currently constrained to several kHz at the DESY II Test Beam Facility, with the possibility to be improved in a future upgrade of the facility [210]. For the second aspect, the next generation of beam telescopes, after the currently well-suited EUDET-type beam telescopes, needs to be developed offering larger active sensor areas and lower readout and integration times to cope with a higher particle rate [261].

Conclusion and Outlook

The particle detector is, apart from the accelerator, the most important tool for modern particle physics experiments at the high-energy frontier. The results of the various physics analyses of the LHC experiments, e.g. the Higgs boson observation by the ATLAS and CMS experiment, rely completely on the recorded data. Therefore, the outcome of the data analysis is only as good as the performance of the detector. This means, how well the particles, which were created in the highly energetic proton-proton collisions, were measured in the detector. And how well the detector signals are used to reconstruct and identify the physical particles. The employed particle detector consists out of several specialized sub-detector systems, optimized for the detection and measurement of specific types or families of particles. Correspondingly, specialized algorithms for the reconstruction and identification of particle types are developed.

In the case of detecting photons, the electromagnetic calorimeter is the most important subdetector system which allows to reconstruct photons. Here, the deposited energy inside the finely granular calorimeter cells is measured when the photon is electromagnetically showering in the material. At that moment, the photon is not the high-level physics object used in the data analysis, but rather a collection of electric signals recorded in the calorimeter. As the next step, advanced algorithms to reconstruct the physical photon from the measured detector signals must be employed, which allow then to infer properties of the reconstructed photon such as its energy. After detecting, measuring and reconstructing the photon candidate, an identification algorithm is used to distinguish different types of reconstructed photons. Here, the candidate can be a prompt photon originating directly from the hard scattering interaction, but also a decay product of a hadronic jet or something else faking only the signature of a photon in the detector. For the physics analysis, it is important to know with a high efficiency as well as accuracy, if it is a prompt photon or not as typically a very specific event topology is searched for, e.g. two prompt photons from the decaying Higgs boson.

In the case of detecting electrons, the tracking detector is used to reconstruct the trajectories of the electrons, which allows then to measure their momenta due to the applied magnetic field. A key parameter for the tracker is therefore the achieved spatial resolution for the positions of the traversing electrons. Here, silicon detectors are one of the best suited detector technologies for the application in a tracking detector, offering a high detection efficiency and resolution. But the silicon sensors require a number of supports to be used in the detector: they must have a mechanical support to maintain their positions inside the detector volume; they require electrical connections for powering and data readout; and they need to be cooled to reach the highest measurement accuracy and to better cope with the effects of radiation damages in the silicon due to high particle fluences. Therefore, not only a good design of the sensing elements in a detector is important, but equally important is the development of suitable and advanced support structures and services.

But when the particle traverses the material of the support structure or other required services in the detector, interactions with the atoms of the material can occur. Here, the particle can loose a part of its energy before reaching the calorimeter or the particle is deflected by multiple Coulomb scattering which results in a deterioration of the reconstructed track. For these type of effects, the material budget is the interesting quantity and in the case of the tracking detector, the overall amount should be minimized. But with the just described multiple scattering effect of electrons inside the material layer, it is possible to measure the respective material budget when reconstructing the according deflection angles of the electrons, exploiting again the high resolution measurement capabilities of silicon detectors in test beam experiments.

These aspects motivated the work of this thesis to highlight the importance for the best possible exploitation of particle detectors to detect and identify particles, namely electrons and photons, as well as to measure their properties with the highest precision and accuracy. Firstly, the *optimization of the photon identification* in the ATLAS experiment was studied to reach a high efficiency to discriminate prompt photons from background photons, e.g. originating from hadronic jet decays.
Secondly, the work was focused on the *thermo-mechanical characterization of petals* for the new ATLAS Inner Tracker to cope with the challenging conditions expected for the high-luminosity phase of the LHC. Moreover, detailed investigations for the *dual-phase CO_2 cooling* of the petals were performed.
And finally, the direct measurement of the material budgets of samples using the multi-GeV electron beam and the EUDET-type beam telescopes at the DESY II Test Beam Facility was investigated by using the technique of *material budget imaging*.

Optimization of the Photon Identification

The optimization of the photon identification describes the selection of well-performing selection criteria on the discriminating shower shape variables to maximize the efficiency in identifying prompt photons from the hard scattering interaction while rejecting photons originating from hadronic jet decays or detector signals simply faking the characteristic photon signature. Different classification approaches can be used for this task, ranging from the application of rectangular cuts up to more sophisticated multivariate techniques like **B**oosted **D**ecision **T**rees (BDTs) or **N**eural **N**etworks (NNs).

For a systematic investigation of the photon identification optimization, the *PhotonIDOptimizer* framework was developed in the course of this work allowing to test in principle all different kinds of classifiers and evaluate their corresponding performance in terms of the identification efficiency for signal and background samples as function of the photon energy E_{T} or the pile-up μ. Here, the framework was successfully validated by a comparison to the output of the currently employed cut-based optimization tool in the ATLAS experiment.

The developed framework was used to perform dedicated studies with the cut-based approach and supporting thereby the reoptimization of the tight photon identification conducted for the physics data analysis in Run 2. Here, a systematic study on the optimal parameters for the cut-based optimization was presented. An investigation of the cut value on the f_{side} variable showed also that the proposed cut value was too strong when applied on a data sample from radiative Z decays due to the known data-MC differences. Therefore, for the final reoptimized tight ID menu as used for physics analyses with 2015 and 2016 data, the cut values were accordingly adjusted.

Furthermore, studies on a MVA-based photon identification were performed using a BDT approach as chosen optimization method. After evaluating also for this approach the optimal parameter settings and performing an N-1 classification test to study the discrimination power of the individual shower shape variables in the BDT, the performance of the BDT in the tight photon identification was compared to the cut-based ID performance, resulting in very comparable performances.
But the implementation of a MVA-based photon identification has several implications on the data-driven photon efficiency measurements. For the matrix method as one of the three currently employed methods, the tight photon ID should be least correlated to the photon isolation to acquire an inclusive photon sample. To reach this with the BDT approach, a new strategy was tested in this thesis: two separate BDTs are trained on two sets of shower shape variables, one of them least correlated to the photon isolation; the resulting two independent classifier outputs can be used firstly to derive the tight photon ID by applying rectangular cuts and secondly for the definition of the inclusive photon sample in the matrix method. In terms of the performance, comparable photon identification efficiencies were measured for the two-BDT approach.
In a final study, the impact of a p_{T}-dependent training for a BDT, similar to the proposed p_{T}-dependent training for the next reoptimization of the cut-based ID, was investigated. A gain in performance was observed, when training in bins of p_{T}, but at the same time a large influence of the isolation on the ID performance was seen.

The goal in this work was to path the way for a MVA-based photon identification in the ATLAS experiment by conducting dedicated studies to explore the potential of MVA techniques to increase the efficiency for the tight photon identification. Due to the promising results reached with a BDT-approach, the investigation on a MVA-based photon ID should be pursued further. In parallel to this work, several studies were performed in the ATLAS collaboration using the full spectrum of machine learning tools, e.g. training high-level NNs for the photon identification.
As so far the performance of the BDT-based photon ID was only evaluated with samples from MC simulations, the developed photon ID should be applied to data samples in the next step. Moreover, the encouraging strategy of the two-BDT approach have to be tested in the matrix method to evaluate the performance also in the data-driven efficiency measurements and to check the application strategy.

Thermo-Mechanical Studies on Petals

For the success of the planned ATLAS ITk strip end-cap detector, the thermo-mechanical performance of the petals as well as a high reliability for this central component in the challenging environment of the HL-LHC and for the different operation scenarios in terms of cooling temperature and thermal load are key factors. Therefore, an intensive test programme in terms of **Q**uality **A**ssurance (QA) and **Q**uality **C**ontrol (QC) test procedures will be established for the production phase. Several of these tests to evaluate the mechanical, thermal and thermo-mechanical characteristics of the petal were developed in the course of this work and measurements with various prototypes ranging from petal cores of different design stages up to the thermo-mechanical petal from the R&D phase were conducted. Also a multitude of measurement techniques and equipment was used for the thermo-mechanical characterization: an optical microscope for the geometrical metrology, a high-resolution IR camera for infrared thermography, an evaporative CO_2 cooling system for the petal cooling as well as different software tools to simulate the thermo-mechanical response of the petal.

The emissivity of the object's surface has a large impact on the correct measurement of the object's temperature for the application of IR thermography. Therefore, dedicated studies to the various dependencies of the emissivity were conducted in the context of testing the thermal performance of petal cores and the TM petal. The blank silicon crystals on the TM petal pose a challenge for IR thermography due to the observed rather low emissivity values. Moreover, a non-negligible transmissivity effect was measured for the silicon, requiring the application of appropriate correction methods. To extract the correct surface temperatures on the TM petal, a black paint spray was applied, for which the emissivity was measured in an auxiliary measurement to be 0.977 ± 0.004. On the contrary, for the petal cores rather high surface emissivities were observed, but here an emissivity variation along the geometrical shapes embedded in the surface, e.g. copper lines in the case of the bus tape surface, was seen. Instead of a direct correction of this effect, the idea is to use a "golden image" approach to compare the thermal performance of petal cores.

For the thermal performance assessment of the petal, a dedicated test setup with an IR camera and the TRACI cooling system for evaporative CO_2 cooling was developed for this work, which will be also used for the regular thermal QC procedure in the coming years. The thermal performance of various petal core prototypes with different surfaces (commercial CF, cocured CF facesheet or bus tapes) was measured and found to be very consistent for all cores at the different tested CO_2 pressure set points. Moreover, it was shown that defects in the assembled core structures, e.g. delaminations, can be detected with the thermal QC measurement as for a broken thermal interface a higher temperature is measured in the defect region. This is important in the production phase to detect any failure in the assembly as early as possible in the construction chain.
Results for the thermal performance of the TM petal under various operation conditions were presented as well. It was found that the temperature on the silicon area of the R5S1 sensor is considerably higher than the other silicon sensor areas, which resulted in an optimized routing of the cooling loop for the next design iteration of the core. The difference between the unpowered and powered state of the TM petal was studied, showing the expected increase of the silicon surface temperature for the full heat load of 54 W, while reaching also in this case a thermally stable state proving that the cooling concept of the petal design works. The influence of a higher CO_2 mass flow on the resulting temperature distributions on the silicon is only marginal, indicating that the nominal CO_2 mass flow of 1.3 g/s is sufficient for the dual-phase cooling of the petal under the full heat load. Finally, the experimental results were compared to the outcome of the thermal FEA simulation showing a very good agreement within the measurement uncertainties as well as the model assumptions, which led to the successful validation of the petal FEA model.

For the evaluation of the thermo-mechanical properties of the petal core design, the mechanical deformations caused by the expected temperature changes over the operation were measured in a dedicated setup. Here, the thermal deformations were measured for warm temperatures with distilled water up to $\Delta T = +60\,\mathrm{K}$ relative to the room temperature and for cold temperatures with evaporative CO_2 down to $\Delta T = -40\,\mathrm{K}$. It was proven that the magnitude of the surface deformation depends only on the absolute temperature difference, whereas the relative sign determines the direction of the deformation.
Overall, deformations in the order of $\mathcal{O}(\pm 100\,\mu\mathrm{m})$ for the measured temperature differences were observed and it was shown that the local flatness specification for the core over operational temperature gradients will be fulfilled. In terms of the expansion and contraction of the petal core, moderate shifts over the operational temperature gradients in the order of $\mathcal{O}(25\,\mu\mathrm{m})$ were measured.

Whereas an explanation for the observed shifts in the x-direction was not conclusively found, the linear CTE of the core in the y-direction was estimated to be around $\sim 0.31\,\mu m/K$. Moreover, the results of the thermal cycling of a core, performed in a climate chamber for 100 iterations between $-40\,^{\circ}C$ and $+40\,^{\circ}C$, were presented. Here, no degradation of the mechanical and thermal performance was observed after thermal cycling.
Finally, the resistance of the petal core design for extreme low temperatures was evaluated by performing a thermal shock test in a dry ice bath. Comparing again the mechanical and thermal performance of the core before and after the test, no indication of a performance degradation was found.

The thermo-mechanical characterization conducted on several petal core prototypes as well as the TM petal showed a valid and appropriate design of the local support structure for the ATLAS ITk strip end-cap detector. It was proven by dedicated performance measurements that most of the defined specifications in terms of the mechanical, thermal and thermo-mechanical properties of the petal design are fulfilled. This is also expressed by the successful evaluation of the design in the internal ATLAS reviews.
In the thermal performance tests presented in this work, the lowest reached CO_2 coolant temperature with the TRACI system was approximately $-24\,^{\circ}C$, whereas the specified design temperature is considerably lower with $-38\,^{\circ}C$. Therefore, it will be important to validate the thermal performance of petals with another CO_2 system offering a higher cooling capacity and to conduct the regular thermal QC procedure also down to the specified coolant temperatures.
The developed setup for thermal testing employing infrared thermography is foreseen for the regular QC testing of petal cores during production and the presented measurements are a good starting point for this. But in the conducted measurements, the influence of slightly different conditions in terms of the cooling performance of the TRACI system or the ambient conditions in the setup, especially the ambient temperature, on the measured temperature distribution for the petal cores was clearly observed. Therefore, the test routine for the final QC procedure during production should be further refined to allow for direct comparisons between the different tested petal core objects in the thermal analysis under well-controlled measurement conditions.
For the thermal performance evaluation of fully loaded petals with silicon sensor modules using infrared thermography, the low emissivity of silicon must be taken into account. Here, a non-destructive testing method is required, which excludes therefore the application of a correction method, such as the application of paint in the case of the TM petal. Instead, the emissivity value for the silicon surface must be determined by dedicated characterization measurements, e.g. using the presented emissivity test setup in this thesis.

Investigations on Dual-Phase CO_2 Cooling

The cooling of the petal in the ATLAS ITk detector using dual-phase CO_2 cooling is a key factor for the successful operation of the detector in the challenging environment of the HL-LHC. Therefore, investigations on the dual-phase CO_2 cooling for the petal were conducted by experimental measurements of the CO_2 properties in the course of this thesis.

It was shown in a first study, that the CO_2 flow orientation, comparing the normal, horizontal orientation with the two most extreme situations occurring in the end-cap with the vertical $+90^{\circ}$ and the vertical -90° orientation, has no severe influence on the cooling performance of the petal. Only for measurements with the TM petal, hints for a possible effect of gravity on the CO_2 in sections of the cooling loop featuring turns were observed.

Moreover, measurements of the pressure drop over the petal's cooling loop were presented in this thesis. The pressure drop is an important quantity for the design of the cooling system and determines the actual saturation temperature of the CO_2 coolant at the inlet of the petal due to the corresponding temperature drop. For the various performed thermal measurements with petal cores as well as the TM petal, the pressure and temperature drop was calculated for a number of different CO_2 conditions. Here, it was observed that the pressure and temperature drop increases for lower CO_2 pressures, but is otherwise comparable for the different core prototypes. For the TM petal, it was shown that the pressure drop in the powered state is higher than in the unpowered state due to the influence of the applied heat load on the CO_2 coolant. Furthermore, a higher CO_2 mass flow results in a higher pressure and temperature drop, whereas no difference was measured for the different tested flow orientations.

Finally, investigations on the CO_2 state inside the petal's cooling loop were conducted. The expected operation cycle for the I-2PACL system in terms of CO_2 state points in the log(p)-h diagram could be reconstructed from the recorded pressure and temperature sensors. Moreover, the vapour quality of the dual-phase coolant was estimated by the visual inspection of sightglasses at the cooling loop's in- and outlet. A subcooling of the CO_2 fluid at the inlet was detected for the highest tested CO_2 pressure set points, matching well with the measured temperature and pressure data. On the contrary, large differences between the estimated and the theoretically calculated state points of the dual-phase CO_2 coolant were observed. This is most probably caused by a wrongly estimated vapour quality from the sightglasses, indicating that the fill levels in the sightglasses are not sufficient to determine the vapour quality of the CO_2 fluid correctly.

Overall, the investigations on the dual-phase CO_2 cooling allowed a deeper insight into the thermodynamical processes of the cooling for the petal.
Nonetheless, the influence of the CO_2 flow orientation on the properties of the coolant should be investigated further to reach a more conclusive statement on a possible influence of gravity on the CO_2, which is currently planned for one cooling disk of the end-cap.
The measured values for the pressure drop over the petal's cooling loop in the various scenarios are well within the specification of the cooling system, but were not evaluated at the design coolant temperature of $-38\,^{\circ}\mathrm{C}$ due to the constrained cooling capacity of the TRACI system. Therefore, this type of measurement should be repeated with another cooling machine in the future.
Finally, the vapour quality is a very important quantity for a dual-phase cooling system. But with the herein used estimation of the vapour quality by the visual inspection of sightglasses and analysing fill levels, no satisfying results were reached. Therefore, trying other measurement methods to estimate the vapour quality, e.g. exploting the observed turbulent flow pattern at the outlet of the cooling loop, will be interesting.

Material Budget Imaging

The material budget distribution of an object can be measured by exploiting the occurring multiple Coulomb scattering interaction in the traversal of a charged particle through the corresponding object. Here, the distribution of deflection angles from a multitude of scattered particles contains information on the amount of traversed material expressed as its material budget, which is calculated as its thickness divided by the characteristic material's radiation length. Several theoretical models exist to describe the relationship of the resulting kink angle and the material budget, such as the Highland model.

With the novel technique of **M**aterial **B**udget **I**maging (MBI), the deflection angles for multi-GeV electrons produced at test beam facilities and traversing a material sample, called **S**catterer **U**nder **T**est (SUT), are measured by reconstructing the particle trajectories with high-resolution beam telescopes. Due to the possibility to reconstruct also the spatial coordinates of the incident positions on the sample, the two-dimensional material budget distribution of the object can be inferred. The potentials and limitations of the MBI technique were thoroughly studied in this thesis by conducting measurements at the DESY II Test Beam Facility and using the EUDET-type beam telescopes.

Firstly, the optimal measurement configuration for scattering measurements with a SUT was studied in terms of the selectable beam momentum as well as the telescope setup. As the size of the scattering angles depends inversely on the particle's momentum, the beam momentum must be chosen to allow for a reconstruction of the kink angles with the telescope, where the spatial and angular track resolution directly depends on the spacing between the MIMOSA26 sensor planes. But as also a high event statistics is required for the creation of high resolution material budget images and the delivered particle rate at the DESY II Test Beam Facility depends on the beam momentum, a compromise for these parameters must be found. Therefore, an optimal measurement configuration depends in general on the type of the SUT, e.g. its material budget or in the case of two-dimensional imaging on the required resolution to resolve its internal structures.

For the reconstruction of the individual particle tracks, the EUTelescope framework was used in this work and a dedicated reconstruction flow for the analysis of scattering measurements was developed. Starting here with the raw pixel data, the track-based alignment procedure for the telescope is performed and concluded with the final track fit. To allow for an unbiased measurement of the kink angle in the scatterer without a-priori knowledge of its material budget, the General Broken Lines track fit was adjusted to allow for an unconstrained kink via two local derivatives in the GBL trajectory. The reconstruction output is then the incident positions of the tracks on the SUT in the x- and y-direction as well as the reconstructed kink angles k_x and k_y in the horizontal and vertical plane.

Several investigations were conducted on the reconstructed kink angle distributions.
It was shown that the shape of the scattering distribution depends on the thickness and correspondingly the material budget of the traversed sample as well as the momentum of the scattered particles, as expected from the Highland model. For the analysis of the kink angle distributions, an appropriate estimator for the kink angle width was found in a systematic study of different estimators using statistical and fitting methods. The selected choice for the further evaluation of kink angles was the determination of the RMS value based on the inner 98% quantile of the distribution.
Moreover, the combined kink angle k_{x+y} can be used for the material budget extraction, as it was demonstrated that the horizontal and vertical kink angle are uncorrelated, whereas both follow the same distribution with a Gaussian core and non-Gaussian tails due to the rare single scattering interactions.
Two further influencing effects on the kink angle distributions were investigated with the acceptance effect and the variation of the beam momentum in the horizontal direction.
In the first case, for larger material budget samples the scattering angles can be larger than the acceptance area of the telescope, such that particles scattered to the outside are not reconstructed, whereas a scattering to the inside results in a reconstructed track. But if this happens, the resulting kink angle distribution is biased and the acceptance effect must be considered therefore for the material budget extraction.

In the second case, the beam momentum for the DESY II Test Beam Facility is not mono-energetic at the selected momentum value, but a variation along the horizontal direction is introduced due to the mechanism of the beam generation. Here, the same level of variation was also observed in the position-resolved kink angle maps, as the kink angle width directly depends on the beam momentum.

For the extraction of the material budget estimate from the measured width of the kink angle distribution, an appropriate calibration procedure must be developed and applied. First of all, the systematic influence of the scattering in the air volume in between the telescope arms, inherently also contributing to the SUT measurements, was corrected.
In the next step, the measurement of material samples with known material budgets were used for the calibration of the material budget extraction. Here, a model-dependent calibration fit based on the Highland formula with a global calibration factor as well as a model-independent functional dependence between the material budget and the kink angle width were evaluated and tested. It was shown that both calibrations can be used for the following extraction of the material budget of unknown material samples.
Two further studies in this context were done: firstly, a dedicated calibration measurement with water samples and moderate beam momenta was performed for the possible application of the MBI technique in the medical sector; secondly, dual-layered material structures were investigated in terms of their material budget and it was found that the measured kink angle width depends on the orientation of the sample to the traversing beam.

After performing all necessary preparation steps, the MBI technique was used to extract the material budget of materials and structures from the planned ATLAS ITk detector. It was possible to determine the radiation length of several materials used in the design of the petal ranging from the carbon-based foam over carbon fiber composites (pultruded CF and cocured layups) and plastics (Torlon) to the foreseen glue (Hysol). The measured X_0 values were compared to the current estimates used for calculations and detector simulations and provide a valuable input for a better description of the detector design.
Moreover, the two-dimensional material budget distributions of assembled detector structures with complex geometries and made out of several materials were measured and analysed. Here, objects with low material budgets such as a cocured bus tape structure were investigated as well as structures with higher material budgets like an electrical PCB or welded assemblies. It was also demonstrated that it is possible to manually stitch the individual reconstructed images measured by a scan over the object's surface and individually limited in size by the active detection area to larger images. This allows to investigate the internal structure of the object, e.g. the petal core, over quite remarkable surface areas. Overall, it was shown that a high contrast to differentiate the individual features in the imaged object as well as a high resolution of 10 to 20 µm is feasible with the MBI technique, if the amount of recorded events and correspondingly reconstructed tracks is sufficiently high with the drawback of long measurement times.

In a final study, the scattering in high-Z material samples was investigated, showing larger discrepancy between the measured kink angle widths and the predicted values from the Highland model for larger material budgets. It was demonstrated that this effect is caused by the energy loss of the particles in the traversed material, which was also directly measured with a calorimeter in the setup. As the energy loss of the particle is not considered in the Highland formula assuming there a constant momentum, first investigations on a possible correction for the Highland formula were conducted. Here, it was shown that the energy-weighted correction of the prediction allows to remove this dependency.

The MBI technique was extensively studied in the course of this work with several performed studies on the different ingredients of the MBI technique, ranging from the optimal choice of the measurement configuration, over the track reconstruction with an unbiased measurement of the deflection angle and the evaluation of the kink angle distribution and their influencing factors to the calibration procedure for the material budget extraction and its application on dedicated test samples in terms of materials and structures for the ATLAS ITk detector. Nonetheless, the novel imaging technique should be explored even further to define its limitations as well as to evaluate its potential also for applications beyond the detector development in high-energy physics experiments such as for biological and medical imaging or non-destructive testing of complex assemblies for industry needs.
Based on the results presented in this thesis, the choice of the estimator for the kink angle width can be further studied and influencing effects, such as the horizontal beam momentum variation, should be corrected for an optimal measurement result. It is also possible to further refine the calibration procedure to allow a high repeatability and validity for the measured material budgets and the extract radiation lengths for unknown material samples. Here, the possibility to provide a material database with measured radiation length values for a multitude of materials interesting for the detector development and beyond should be evaluated. For the two-dimensional imaging, the limitations in terms of the achievable resolution and image contrast must be studied systematically, which can be used also to determine the required measurement time for the imaging to resolve the internal structure of an object with a defined level of detail. Moreover, for the scanning of larger areas the presented stitching technique can be further studied and automatized.

Outlook

With several presented examples in this thesis, it was shown how important a good understanding of the developed particle detector is to detect particles with the highest possible accuracy and also to develop sophisticated procedures to identify the characteristics of the particle from the raw detector signals.
With the planned data taking of Run 3 and Run 4 for the LHC, the amount of recorded collision data by the high-energy physics experiments will increase even further allowing to study the SM and its limitations with precision measurements to unprecedented levels. At the same time, the need for optimized and very efficient reconstruction and identification algorithms will increase, requiring new ideas and tools, while most probably exploiting the full potential of machine learning applications in the field of high-energy physics.
Moreover, the planned start of production for the ATLAS ITk detector to be delivered by 2026 for the operation at the HL-LHC is approaching fast. Therefore, the so far developed QA and QC procedures for the different detector components such as the petal with its silicon strip modules and the core structure must be refined and fully evaluated to be prepared for the (pre-)production phase. But in parallel with the currently running high-energy physics experiments it is the time to develop already now the ideas and concepts for the next generation of particle detector systems, involving future sensor technologies as well as new materials and concepts for the support structures and services in the detector. Finally, test beam experiments play a crucial role for the development of particle detectors, but provide at the same time a unique playground to develop also new measurement techniques and concepts with applications reaching even beyond particle physics. Here, it is interesting to follow the further development of the material budget imaging as well as other emerging concepts developed in the beginning for particle physics applications but evolving then also to other areas.

List of Acronyms

ABCStar	**A**TLAS **B**inary **C**hip
ALICE	**A** **L**arge **I**on **C**ollider **E**xperiment
AMAC	**A**utonomous **M**onitor & **C**ontrol **C**hip
ASIC	**A**pplication **S**pecific **I**ntegrated **C**ircuit
ATLAS	**A** **T**oroidal **L**HC **A**pparatu**S**
AUC	**A**rea **U**nder **C**urve
BDT	**B**oosted **D**ecision **T**ree
BSM	**B**eyond **S**tandard **M**odel
CCE	**C**harge **C**ollection **E**fficiency
CERN	European Organization for Nuclear Research
CF	**C**arbon **F**iber
CMS	**C**ompact **M**uon **S**olenoid
CoBra	**Co**$_2$ **Bra**nch Calculator
CTE	**C**oefficient of **T**hermal **E**xpansion
DAQ	**D**ata **A**c**Q**uisition
DCS	**D**etector **C**ontrol **S**ystem
DUT	**D**etector **U**nder **T**est
EM	**E**lectro**M**agnetic
EoS	**E**nd **o**f **S**ubstructure
EWSB	**E**lectro**W**eak **S**ymmetry **B**reaking
FDR	**F**inal **D**esign **R**eview
FEA	**F**inite **E**lement **A**nalysis
FOV	**F**ield **O**f **V**iew
GA	**G**enetic **A**lgorithm
GBL	**G**eneral **B**roken **L**ines

GUT **G**rand **U**nifying **T**heory

HCCStar **H**ybrid **C**ontroller **C**hip

HEP **H**igh **E**nergy **P**hysics

HL-LHC **H**igh-**L**uminosity **LHC**

HLT **H**igh-**L**evel **T**rigger

HTC **H**eat **T**ransfer **C**oefficient

I-2PACL **I**ntegrated **2**-**P**hase **A**ccumulator **C**ontrolled **L**oop

IBL **I**nsertable **B**-**L**ayer

ID **I**nner **D**etector

IP **I**nteraction **P**oint

IR **I**nfra**R**ed

ISR **I**nitial **S**tate **R**adiation

ITk **I**nner **T**rac**k**er

L1 **L**evel-**1** trigger

LAr **L**iquid **Ar**gon

LHC **L**arge **H**adron **C**ollider

LHCb **L**arge **H**adron **C**ollider **b**eauty

MAPS **M**onolithic **A**ctive **P**ixel **S**ensors

MBI **M**aterial **B**udget **I**maging

MC **M**onte **C**arlo

MIP **M**inimum **I**onizing **P**article

ML **M**achine **L**earning

MLP **M**ulti **L**ayer **P**erceptron

MSSM **M**inimal **S**upersymmetric **S**tandard **M**odel

MVA **M**ulti **V**ariate **A**nalysis

NIEL **N**on-**I**onizing **E**nergy **L**oss

NN **N**eural **N**etwork

PCB **P**rinted **C**ircuit **B**oard

PD **P**roduction **D**atabase

PDF **P**arton **D**istribution **F**unction

PDG **P**article **D**ata **G**roup

PDR **P**reliminary **D**esign **R**eview

Pixel **Pixel** Detector

PL **P**etal **L**ocator

PMT **P**hoto **M**ultiplier **T**ube

PTM **P**etal **T**hermal **M**easurement chamber

QA **Q**uality **A**ssurance

QC **Q**uality **C**ontrol

QCD **Q**uantum **C**hromo **D**ynamics

QED **Q**uantum **E**lectro **D**ynamics

RH **R**elative **H**umidity

RMS **R**oot-**M**ean-**S**quare

ROC **R**eceiver **O**perating **C**haracteristic

ROI **R**egion **O**f **I**nterest

SCT **S**emi**C**onductor **T**racker

SEU **S**ingle **E**vent **U**pset

SF **S**cale **F**actor

SM **S**tandard **M**odel

SUT **S**catterer **U**nder **T**est

TDAQ **T**rigger and **D**ata **A**c**Q**uisition

TDR **T**echnical **D**esign **R**eport

TLU **T**rigger **L**ogic **U**nit

TMVA **T**oolkit for **M**ulti **V**ariate **A**nalysis

TRACI **T**ransportable **R**efrigeration **A**pparatus for **C**O_2 **I**nvestigation

TRT **T**ransition **R**adiation **T**racker

TTC **T**rigger, **C**lock and **C**ontrol

VBF **V**ector **B**oson **F**usion

X_0 radiation length

List of Figures

1.1 Illustration of the Standard Model of particle physics. 8
1.2 Representation of the Higgs potential. 11
1.3 Layout of the accelerators and the LHC at CERN. 12
1.4 Cross section of pp-collision with factorization theorem. 14
1.5 Full event topology of a typical pp collision. 14
1.6 Schedule for LHC and HL-LHC. 15
1.7 Luminosity for the ATLAS experiment in LHC Run 1 and Run 2. 16
1.8 Pile-up conditions for the ATLAS experiment in LHC Run 2. 16
1.9 W boson mass: Transverse momentum and transverse mass. 18
1.10 W boson mass: Results per decay channel and comparison. 18
1.11 Higgs boson: production and decay modes. 19
1.12 Higgs boson: mass in the $H \to 4l$ channel for Run 1 and Run 2. 19
1.13 Higgs boson: mass in $H \to \gamma\gamma$ channel for Run 1 and Run 2. 20
1.14 Higgs boson: couplings to fermion and bosons from ATLAS Run-2 results. . 21
1.15 Light-by-light scattering: ATLAS event display. 22
1.16 Light-by-light scattering: Acoplanarity and invariant mass spectrum. 22
1.17 Hierarchy problem of the Higgs boson mass. 23
1.18 Running coupling constants and GUT. 24

2.1 Trend graph for silicon detector systems. 27
2.2 Mean energy loss of charged particles as function of $\beta\gamma$. 29
2.3 Energy loss for electrons and positrons in lead. 29
2.4 Straggling functions for the energy loss in silicon. 30
2.5 Multiple Coulomb scattering and the scattering angle distribution. 32
2.6 Total cross section of photons in lead. 33
2.7 Electromagnetic showers and their characteristics. 34
2.8 Energy band model for insulators, semiconductors and conductors. 36
2.9 Energy bands and atomic lattices of pure, n- and p-type silicon. 37
2.10 The pn-junction and depletion region. 37
2.11 Design of a p-in-n silicon sensor. 39
2.12 Bulk damage in silicon crystal lattice by radiation. 41
2.13 Fluence dependence of the leakage current and depletion voltage. 43
2.14 Annealing behaviour for the leakage current and depletion voltage. 44
2.15 Cut-away view of the ATLAS detector. 45
2.16 Cut-away view of the ATLAS Inner Detector. 46
2.17 Cross-sectional view through the ATLAS Inner Detector. 47
2.18 Cut-away view of the ATLAS calorimeter system. 48
2.19 The lateral and longitudinal segmentation of the ATLAS EM calorimeter. . 48
2.20 Cut-away view of the ATLAS Muon Spectrometer. 49
2.21 Overview of the ATLAS TDAQ system. 50

3.1 Calorimeter signatures of prompt photons and background photons. 55
3.2 Feynman graphs of processes used for photon identification. 56
3.3 Shower shape variables for photon identification. 58
3.4 Shower shape dependence: conversion state. 58
3.5 ATLAS detector geometry with pseudorapidity regions. 59
3.6 Shower shape dependence: pseudorapidity η. 59
3.7 Shower shape dependence: transverse energy E_{T}. 60
3.8 Shower shape dependence: pile-up μ. 60
3.9 Linear correlation matrix of shower shape variables. 61
3.10 Correction of data-MC differences for shower shape variables. 61
3.11 Discrimination power of shower shape variables. 62
3.12 Strategy of cut-based optimization for photon identification. 63
3.13 Tight photon identification efficiency versus E_{T}. 64
3.14 Tight photon identification efficiency versus μ. 64
3.15 Overview about data-driven photon efficiency measurements. 65
3.16 Selection of radiative decays in $Z \to ee\gamma$ events. 66
3.17 Electron extrapolation method for shower shape variable R_{ϕ}. 67
3.18 Track isolation efficiency and signal purity in the matrix method. 68
3.19 Combination of photon identification efficiency. 68
3.20 Scale factors for the photon identification efficiency. 69
3.21 Pile-up dependence of the combined photon identification efficiency. 69

4.1 Rectangular cut on shower shape variable R_{ϕ}. 72
4.2 Visualization of a boosted decision tree. 73
4.3 Visualization of a neural network. 74
4.4 *PhotonIDOptimizer* framework: ROC and significance curves. 77
4.5 Validation of *PhotonIDOptimizer* framework: ROC curves. 78
4.6 Validation of *PhotonIDOptimizer* framework: identification efficiency. . . . 78
4.7 Rectangular cuts: sweep of optimization parameters. 80
4.8 Rectangular cuts: dependence of cut values. 81
4.9 Rectangular cuts: data-MC differences for f_{side}. 82
4.10 BDT: sweep of optimization parameters. 84
4.11 BDT: significance curve and classifier distribution. 85
4.12 BDT: signal and background efficiency versus E_{T}. 86
4.13 BDT: signal and background efficiency versus μ. 86
4.14 N-1 study for BDT: ROC curves. 87
4.15 N-1 study for BDT: signal and background efficiency versus E_{T}. 88
4.16 Two-BDT approach: linear correlation matrix to photon isolation. 89
4.17 Two-BDT approach: ROC curves. 89
4.18 Two-BDT approach: linear correlation matrix of classifiers. 90
4.19 Two-BDT approach: Classifier distributions for signal and background MC. 90
4.20 Two-BDT approach: signal and background efficiency versus E_{T}. 91
4.21 p_{T}-dependent BDT: ROC curves. 92

5.1 ATLAS Phase-2 upgrade programme for the HL-LHC phase. 95
5.2 HL-LHC projection of expected uncertainties for Higgs couplings. 97
5.3 Track occupancy for pile-up conditions of $\langle\mu\rangle = 60$ and $\langle\mu\rangle = 200$. 98
5.4 Simulated radiation environment for the ATLAS ITk detector. 99
5.5 Material budget along η for ATLAS ID versus ATLAS ITk. 100
5.6 Layout of the ATLAS ITk detector. 100

5.7 Anatomy of the ITk strip end-cap petal. 102
5.8 Naming scheme for the ITk strip end-cap modules. 102
5.9 Design of the ITk strip end-cap module. 103
5.10 Design of the ITk microstrip silicon sensor. 103
5.11 Design of the ITk strip end-cap petal core. 105
5.12 Mass and material budget of the petal core. 105
5.13 Petal core assembly process. 106
5.14 DAQ and powering scheme for the ITk strip end-cap detector. 106
5.15 Global support structure of the ITk strip end-cap detector. 107
5.16 Production flow for the ITk strip end-cap detector. 107
5.17 ITk production database with petal core implementation. 108

6.1 Technical drawing of the petal core. 112
6.2 Geometrical metrology with the SmartScope. 115
6.3 IR thermography: emissivity, transmissivity, reflexivity. 116
6.4 CO_2 cooling: log(p)-h diagram. 118
6.5 CO_2 cooling: flow pattern for different vapour qualities. 119
6.6 CO_2 cooling: operation cycle for I-2PACL concept. 120
6.7 CO_2 cooling: layout of TRACI. 120
6.8 CO_2 cooling: pressure and temperature probe. 121
6.9 CO_2 cooling: heating element and sightglasses. 122
6.10 FEA simulation of petal core and petal. 123
6.11 CoBra GUI with CO_2 simulation of petal core. 124
6.12 Petal core prototypes at DESY. 126
6.13 Overview of the thermo-mechanical petal prototype. 127
6.14 Observation of the Narcissus effect. 129
6.15 Transmission spectrum of air. 130
6.16 Application of emissivity correction methods. 131
6.17 Measurement of the angular emissivity dependence. 132
6.18 Investigation on the emissivity of the petal core surfaces. 133
6.19 Transmissivity spectrum of silicon. 134
6.20 Measurement of the transmissivity of silicon. 134
6.21 Peltier setup for the paint emissivity study. 135
6.22 Measurement cycle with Peltier setup. 136
6.23 Determination of black paint emissivity. 136
6.24 Emissivity correction for petal cores. 137
6.25 Emissivity correction for the TM petal. 138
6.26 TM petal with black caps and Pt100 sensor. 138
6.27 Design and impressions of the PTM for thermal testing. 139
6.28 Overview of complete thermal test setup. 140
6.29 Typical measurement cycle for thermal analysis of petal cores. 142
6.30 Thermograms of front and back side of core 02 at 20 bar. 143
6.31 Definition of line markers along cooling loop for the back side of core 02. . . 143
6.32 Comparison of temperature along the cooling loop at 20 bar. 144
6.33 Temperature distributions along the cooling loop at different set points. . . 145
6.34 Minimum temperature along the cooling loop at different set points. 145
6.35 Difference between surface and coolant temperature for core 02. 146
6.36 Measurement of the thermal performance of core 04. 146
6.37 Temperature along the cooling loop at different set points. 147
6.38 Investigation on the detected delamination for the back side of core 04. . . . 148

6.39 Measurement of the thermal performance of core 07. 149
6.40 Definition of IR markers for cores with cocured bus tapes. 149
6.41 Comparison of temperatures after two temperature cycles at 20 bar. 150
6.42 Detection of delamination in EoS region for the back side of core 08. 150
6.43 Comparison of temperature along cooling loop for core 07 and 08. 151
6.44 Comparison of temperature on module areas for core 07 and 08. 152
6.45 Simulated surface temperature on the semielectrical petal core. 152
6.46 Measurement cycle for the TM petal under nominal conditions. 153
6.47 IR thermograms of the TM petal in the unpowered and powered state. . . . 154
6.48 Definition of area markers on the silicon areas for the TM petal. 155
6.49 Temperature distributions on marker areas for the unpowered TM petal. . . 155
6.50 Comparison of the unpowered versus powered state of the TM petal. 156
6.51 Temperature distributions for different CO_2 mass flows at 26 bar. 157
6.52 Temperature stability of the powered TM petal at the lowest set point. . . . 158
6.53 IR thermograms for different powering scenarios of the TM petal. 159
6.54 Investigation of the TM petal for different powering scenarios. 160
6.55 Surface temperature comparison between IR data and FEA simulation. . . 161
6.56 Silicon temperature distributions for IR data and FEA simulation. 162
6.57 Core mounting on the SmartScope via locking points. 163
6.58 Specialities of warm and cold deformation test setup. 164
6.59 Measurement of the height profile map. 165
6.60 Measurement of the fiducial pad positions on the bus tape. 165
6.61 Deformation map for $\Delta T = +60\,\mathrm{K}$. 166
6.62 Deformation maps for warm and cold test. 167
6.63 Linearity of thermal deformations for positive and negative ΔT. 167
6.64 Local flatness definition according to ISO standard. 168
6.65 Module area definition for local flatness calculation. 168
6.66 Local flatness measurement over measured temperature range. 169
6.67 Shifts Δx and Δy of fiducial pad positions for different ΔT. 170
6.68 Linear fit of the fiducial shifts Δy. 170
6.69 Setup for thermal cycling with climate chamber. 171
6.70 Measurement of a typical, programmed temperature cycle. 172
6.71 Average temperature for 100 temperature cycles of core 08. 172
6.72 Nominal distance shifts of fiducial pads before and after thermal cycling. . . 173
6.73 Comparison of thermal performance before and after thermal cycling. . . . 174
6.74 Thermal shock test with petal core 08. 175
6.75 Logged temperatures for the thermal shock test of 08. 175
6.76 Thermal shock test with the TM petal. 176
6.77 Visual and IR inspection of TM petal after thermal shock. 176

7.1 Design of the ATLAS ITk CO_2 cooling system. 182
7.2 CO_2 state and temperature for the ATLAS ITk CO_2 cooling system. 183
7.3 Test setup for petal orientation studies using the rotated PTM. 185
7.4 Temperature distributions for different core orientations. 185
7.5 Thermograms of the powered TM petal in three orientations. 186
7.6 Temperature distributions for different TM petal orientations. 186
7.7 Pressure and temperature drop for the measurement cycle of core 07. 188
7.8 Comparison of Δp and ΔT for various petal core prototypes. 189
7.9 Comparison of Δp and ΔT for the unpowered and powered TM petal. . . 190
7.10 Pressure and temperature drop for the unpowered and powered TM petal. . 190

7.11 Dependence of Δp and ΔT in the TM petal on the mass flow. 191
7.12 Dependence of Δp and ΔT in the TM petal on the orientation. 192
7.13 Convective heat flow on the petal's surface. 192
7.14 Evaluation of pressure and temperature drop for petal cores. 193
7.15 Evaluation of pressure and temperature drop for the TM petal. 193
7.16 CO_2 state over the full cooling cycle in the log(p)-h diagram. 195
7.17 Visual inspection of sightglasses for different CO_2 pressure set points. . . . 196
7.18 Calculation of the volumetric and mass fraction for dual-phase CO_2. 197
7.19 Subcooling at the in- and outlet of the petal's cooling loop. 198
7.20 Transferred heat load and enthalpy from convection and active powering. . 199
7.21 Estimation of CO_2 state inside the petal's cooling loop. 200
7.22 CoBra simulation of vapour quality, flow pattern and HTC. 201
7.23 Simulated vapour quality for different set points of the TM petal. 201

8.1 Illustration of the DESY II operation cycle. 206
8.2 Overview about the beam generation at the DESY II Test Beam Facility. . 207
8.3 Components of the DESY II test beam generation. 208
8.4 Photograph of the DURANTA beam telescope. 210
8.5 Photograph of the MIMOSA26 monolithic active pixel sensor. 211
8.6 Sketch of the standard setup of the EUDET-type beam telescope. 211
8.7 Overview of the EUDAQ framework. 213
8.8 Operation of EUDAQ framework with graphical user interfaces. 215
8.9 Integration scheme of the EUTelescope framework into ILCSoft. 218
8.10 Operational principle of a single EUTelescope processor. 219
8.11 Reconstruction flow in EUTelescope. 220
8.12 EUTelescope: Noisy pixel identification. 220
8.13 EUTelescope: Clustering. 221
8.14 EUTelescope: Pre-alignment. 222
8.15 EUTelescope: GBL alignment 223
8.16 EUTelescope: GBL track fit. 224
8.17 Triplet method with associated track quality parameters. 225
8.18 Construction of GBL trajectory. 226
8.19 Testbeam characteristics: beam timing structure. 227
8.20 Testbeam characteristics: beam rate. 228
8.21 Testbeam characteristics: beam momentum and momentum spread. 229
8.22 Telescope performance: MIMOSA26 sensor threshold. 230
8.23 Telescope performance: telescope setup. 231
8.24 Setup of lead-glass counter. 232
8.25 Lead-glass counter: bias voltage. 233
8.26 Lead-glass counter: pulse spectrum. 233
8.27 Lead-glass counter: energy calibration. 234

9.1 Simulated spatial and angular track resolution versus telescope spacing. . . 243
9.2 Photographs of setups with known material samples as SUT. 245
9.3 Water samples with different thicknesses. 245
9.4 Overview of investigated ATLAS ITk materials in MBI measurements. . . . 246
9.5 Photographs of setups for the measurement of ATLAS ITk materials. . . . 248
9.6 Overview of investigated ATLAS ITk structures in MBI measurements. . . 249
9.7 Photographs of setups for the imaging of ATLAS ITk structures. 250
9.8 Modified GBL track model for an unknown scattering plane. 252

9.9 Dependence of the track quality parameter in the triplet method. 254
9.10 Kink angle dependence on the SUT thickness. 257
9.11 Kink angle dependence on the beam momentum. 257
9.12 Estimators for the kink angle width using an inclusive measurement. 259
9.13 Estimators for the kink angle width using a binned measurement. 260
9.14 Evaluation of statistical and fitting estimators for the kink angle width. . . 261
9.15 Correlation between the kink angles k_x and k_y. 262
9.16 Correlation for the kink angle width estimator RMS_{98}. 262
9.17 Kink angle maps of $\mathrm{RMS}_{98}(k_x)$ and $\mathrm{RMS}_{98}(k_y)$ for 5 mm tungsten. 263
9.18 Kink angle distributions for selected edge regions. 264
9.19 Kink angle map of $\mathrm{RMS}_{98}(k_{x+y})$ for 5 mm tungsten. 265
9.20 Variation of kink angle widths along the horizontal and vertical direction. . 266
9.21 Kink angle distributions for scattering in air. 268
9.22 Calibration curve for various material samples at 2 GeV/c. 269
9.23 Model-independent calibration for various material samples at 2 GeV/c. . . 271
9.24 Calibration curves for different beam momenta. 272
9.25 Deviation to the Highland prediction for different beam momenta. 272
9.26 Calibration fit for different beam momenta. 273
9.27 Scattering distributions for different telescope setups. 274
9.28 Calibration curves for different telescope setups. 275
9.29 Kink angle distributions for the calibration with water. 276
9.30 Calibration curves for water at 1 and 2 GeV/c. 276
9.31 Kink angle distributions for the investigation of modelled composites. . . . 278
9.32 2D maps of θ_0 and ϵ for the electrical break assembly. 285
9.33 2D material budget image of section II of the EoS board. 286
9.34 Stitched material budget image of a scan of the EoS board. 287
9.35 2D material budget image of a section of the cocured bus tape. 288
9.36 Stitched material budget image of a scan of the cocured bus tape. 289
9.37 2D material budget image of a section of the petal core. 290
9.38 Stitched material budget image of a scan of the petal core. 292
9.39 2D material budget image of a section of the silicon strip module. 293
9.40 Stitched material budget image of a scan of the silicon strip module. 294
9.41 2D material budget image of the TM petal (point A). 296
9.42 2D material budget image of the TM petal (point B). 296
9.43 Measurement of kink angle widths for high-Z material samples. 298
9.44 Calorimeter measurement of electron energy after tungsten samples. 300
9.45 Measured electron energy versus the material budget. 300
9.46 Evaluation of the Highland model with the calorimeter-based correction. . . 301
9.47 Evaluation of the Highland model with the energy-weighted correction. . . . 302

A.1 Temperature comparison along the cooling loop for core 02. i
A.2 Temperature distributions along the cooling loop for core 02. ii
A.3 Minimum temperature along the cooling loop for core 02. iii
A.4 Temperature distributions along the cooling loop for core 04. iv
A.5 Minimum temperature along the cooling loop for core 04. iv
A.6 Thermal performance comparison in the module areas for core 07 and 08. . v
A.7 Thermal performance comparison along the cooling loop for core 07 and 08. vi
A.8 Temperature distributions for the marker areas for the TM petal. vii
A.9 Temperature comparison of the unpowered versus powered TM petal. . . . viii
A.10 Temperature distributions for different CO_2 mass flows. ix

B.1 Temperature comparison for the TM petal in three different orientations. . xi
B.2 Thermograms of the TM petal in three different orientations. xii
B.3 Dependence of Δp and ΔT on the mass flow. xiii
B.4 Dependence of Δp and ΔT on the orientation. xiii
B.5 Geometry of the sightglass to calculate the fill level. xvi
B.6 CO_2 density in the liquid and gaseous phase for different set points. xvii
B.7 Calculation of $\dot{Q}$ and h for convection on the TM petal. xviii

C.1 Fiducial area selection: influence of edge effects. xx
C.2 Fiducial area selection: influence of SUT holder. xx
C.3 Evaluation of statistical and fitting estimators for the kink angle mean. . . xxi
C.4 Deviations for the model-dependent calibration fit. xxii
C.5 Deviations for the model-independent calibration fit. xxiii
C.6 Material budget image with cell sizes of $(100\,\mu m)^2$ and $(50\,\mu m)^2$. xxiv
C.7 Material budget image with cell sizes of $(25\,\mu m)^2$, $(20\,\mu m)^2$ and $(10\,\mu m)^2$. . xxv
C.8 Material budget images of the EoS board before stitching. xxvi
C.9 Material budget images of the cocured bus tape before stitching. xxvii
C.10 Material budget images of the petal core before stitching. xxviii
C.11 Material budget images of the silicon strip module before stitching. xxix

List of Tables

3.1 Overview of photon isolation working points. 55
3.2 Shower shape variables for photon identification. 57

4.1 Advantages and disadvantages of classification methods for photon ID. . . . 75
4.2 Rectangular cuts: AUC performance for parameter sweep. 81
4.3 Rectangular cuts: tight ID efficiencies for f_{side} study. 83
4.4 BDT: AUC performance for parameter sweep.. 85
4.5 N-1 study for BDT: AUC performance. 87
4.6 p_{T}-dependent BDT: performance gain for f_{S} and f_{R}. 92

6.1 Overview of petal core prototypes. 125
6.2 Measured power consumption of TM petal. 127
6.3 Thermal deformation results as mean, minimum and maximum value. . . . 166
6.4 Metrology measurements of PL accuracy before and after thermal cycling. . 173

8.1 Overview of EUDET-type beam telescopes. 209

9.1 Radiation length of selected materials from PDG. 239
9.2 Overview of telescope setups for MBI investigations. 243
9.3 Material properties for modelling of simple, dual-layered composites. 246
9.4 Estimated kink angle widths (k_x, k_y and k_{x+y}) for the acceptance effect. . . 265
9.5 Slope of projected kink angle widths along the horizontal direction. 266
9.6 Spatial and angular track resolution for telescope setup S4 and S5. 275
9.7 Comparison of estimated kink angles widths of modelled composites. 279
9.8 Results of the MBI measurements for the carbon-based Allcomp foam. . . . 281
9.9 Results of the MBI measurements for the pultruded carbon fiber. 282
9.10 Results of the MBI measurements for the thermoplastic Torlon. 282
9.11 Results of the MBI measurements for the pure and loaded Hysol glue. . . . 283
9.12 Results of the MBI measurements for the service tray assemblies. 283
9.13 Comparison between measurement and simulation estimates. 306

C.1 Analytical radiation length values versus experimental data. xix
C.2 Fit parameter for calibrations with different beam momenta. xxii
C.3 Relative deviations for the calibration with different beam momenta. xxiii

Bibliography

[1] J. J. Thomson, "Cathode rays," *Phil. Mag. Ser. 5*, vol. 44, pp. 293–316, 1897.

[2] E. Rutherford, "The scattering of alpha and beta particles by matter and the structure of the atom," *Phil. Mag. Ser. 6*, vol. 21, pp. 669–688, 1911.

[3] W. Heisenberg, "Über den anschaulichen Inhalt der quantentheoretischen Kinematik und Mechanik," *Zeitschrift für Physik*, vol. 43, pp. 172–198, 1927.

[4] E. Schrödinger, "Quantisierung als Eigenwertproblem," *Annalen Phys.*, vol. 384, no. 4, pp. 361–376, 1926.

[5] P. Dirac, *The Principles of Quantum Mechanics*. Clarendon Press, 1930.

[6] C. Anderson, "The Apparent Existence of Easily Deflectable Positives," *Science*, vol. 76, pp. 238–239, 1932.

[7] C. Anderson and S. Neddermeyer, "Cloud Chamber Observations of Cosmic Rays at 4300 Meters Elevation and Near Sea-Level," *Phys. Rev.*, vol. 50, pp. 263–271, 1936.

[8] C. L. Cowan *et al.*, "Detection of the free neutrino: A Confirmation," *Science*, vol. 124, pp. 103–104, 1956.

[9] R. Feynman, *QED: The Strange Theory of Light and Matter*. Princeton Univ. Press, 1986.

[10] W. Greiner, S. Schramm, and E. Stein, *Quantum Chromodynamics*. Springer-Verlag Berlin Heidelberg, 2007.

[11] D. Griffiths, *Introduction to Elementary Particles*. Wiley, 2008.

[12] R. Mann, *An Introduction to Particle Physics and the Standard Model*. CRC Press, 2011.

[13] R. Oerter, *The theory of almost everything : the Standard Model, the unsung triumph of modern physics*. Plume, 2006.

[14] M. Tanabashi *et al.*, "Review of Particle Physics," *Phys. Rev. D*, vol. 98, no. 3, p. 030001, 2018.

[15] D. Galbraith, "Standard Model of the Standard Model." `davidgalbraith.org/portfolio/ux-staandard-model-of-the-standard-model/`. Accessed: 20.06.2020.

[16] K. Wilson, "Confinement of Quarks," *Phys. Rev.*, vol. D10, pp. 2445–2459, 1974.

[17] E. Noether, "Invariant Variation Problems," *Gott. Nachr.*, pp. 235–257, 1918. [Transp. Theory Statist. Phys.1,186(1971)].

[18] H. Georgi, *Weak Interactions and Modern Particle Theory.* Dover Publications, 2009.

[19] S. Glashow, "Partial symmetries of weak interactions," *Nucl. Phys.*, vol. 22, pp. 579–588, 1961.

[20] S. Glashow, J. Iliopoulos, and L. Maiani, "Weak interactions with lepton-hadron symmetry," *Phys. Rev.*, vol. D2, pp. 1285–1292, 1970.

[21] A. Salam and J. Ward, "Electromagnetic and weak interactions," *Phys. Lett.*, vol. 13, pp. 168–171, 1964.

[22] S. Weinberg, "A model of leptons," *Phys. Rev. Lett.*, vol. 19, pp. 1264–1266, 1967.

[23] M. Gell-Mann, "The interpretation of the new particles as displaced charge multiplets," *Nuovo Cim.*, vol. 4, no. 2, pp. 848–866, 1956.

[24] UA1 Collaboration, "Experimental observation of isolated large transverse energy electrons with associated missing energy at $\sqrt{s} = 540\,\mathrm{GeV}$," *Phys. Lett. B*, vol. 122, pp. 103–116, 1983.

[25] UA2 Collaboration, "Observation of single isolated electrons of high transverse momentum in events with missing transverse energy at the CERN $\bar{p}p$ collider," *Phys. Lett. B*, vol. 122, pp. 476–485, 1983.

[26] UA1 Collaboration, "Experimental observation of lepton pairs of invariant mass around $95\,\mathrm{GeV/c^2}$ at the CERN SPS Collider," *Phys. Lett. B*, vol. 126, pp. 398–410, 1983.

[27] UA2 Collaboration, "Evidence for $Z_0 \to e^+e^-$ at the CERN $\bar{p}p$ Collider," *Phys. Lett. B*, vol. 129, pp. 130–140, 1983.

[28] D. Gross and F. Wilczek, "Ultraviolet Behavior of Non-Abelian Gauge Theories," *Phys. Rev. Lett.*, vol. 30, pp. 1343–1346, 1973.

[29] D. Politzer, "Reliable Perturbative Results for Strong Interactions?," *Phys. Rev. Lett.*, vol. 30, pp. 1346–1349, 1973.

[30] F. Englert and R. Brout, "Broken Symmetry and the Mass of Gauge Vector Mesons," *Phys. Rev. Lett.*, vol. 13, pp. 321–323, 1964.

[31] P. Higgs, "Broken Symmetries and the Masses of Gauge Bosons," *Phys. Rev. Lett.*, vol. 13, pp. 508–509, 1964.

[32] CERN Press Release, "CERN experiments observe particle consistent with long-sought Higgs boson." `https://home.cern/news/press-release/cern/cern-experiments-observe-particle-consistent-long-sought-higgs-boson`. Accessed: 20.06.2020.

[33] J. Ellis, "Higgs Physics," *CERN-PH-TH-2013-315*, pp. 117–168, 2013.

[34] L. Evans and P. Bryant, "LHC Machine," *JINST*, vol. 3, p. S08001, 2008.

[35] ATLAS Collaboration, "The ATLAS Experiment at the CERN Large Hadron Collider," *JINST*, vol. 3, p. S08003, 2008.

[36] CMS Collaboration, "The CMS Experiment at the CERN LHC," *JINST*, vol. 3, p. S08004, 2008.

[37] ALICE Collaboration, "The ALICE experiment at the CERN LHC," *JINST*, vol. 3, p. S08002, 2008.

[38] LHCb Collaboration, "The LHCb Detector at the LHC," *JINST*, vol. 3, p. S08005, 2008.

[39] E. Mobs, "The CERN accelerator complex." https://cds.cern.ch/record/2636343, 2018.

[40] A. Einstein, "Ist die Trägheit eines Körpers von seinem Energieinhalt abhängig?," *Annalen der Physik*, vol. 323, no. 13, pp. 639–641, 1905.

[41] J. Collins, D. Soper, and G. Sterman, "Factorization of Hard Processes in QCD," *Adv. Ser. Direct. High Energy Phys.*, vol. 5, pp. 1–91, 1989.

[42] A. Martin, W. Stirling, R. Thorne, *et al.*, "Parton distributions for the LHC," *Eur. Phys. J. C*, vol. 63, p. 189–285, 2009.

[43] R. Teuscher, "Understanding the proton in collision." `https://steve.cooleysekula.net/goingupalleys/wp-content/uploads/2011/09/Proton-Collision-Event.jpg`, 2011. Accessed: 20.06.2020.

[44] CERN, "LHC/HL-LHC Plan." `https://project-hl-lhc-industry.web.cern.ch/content/project-schedule`. Accessed: 20.06.2020.

[45] ATLAS Collaboration, "Luminosity Public Results Run-2." `https://twiki.cern.ch/twiki/bin/view/AtlasPublic/LuminosityPublicResultsRun2`. Accessed: 20.06.2020.

[46] T. Schörner-Sadenius *et al.*, *The Large Hadron Collider*. Springer Verlag (Berlin), 2015.

[47] M. Awramik, M. Czakon, A. Freitas, and G. Weiglein, "Precise prediction for the W boson mass in the Standard Model," *Phys. Rev. D*, vol. 69, p. 053006, 2004.

[48] ATLAS Collaboration, "Measurement of the W-boson mass in pp collisions at $\sqrt{s} = 7$ TeV with the ATLAS detector," *Eur. Phys. J. C*, vol. 78, p. 110, 2018.

[49] ATLAS Collaboration, "Observation of a new particle in the search for the Standard Model Higgs boson with the ATLAS detector at the LHC," *Phys. Lett. B*, vol. 716, p. 1, 2012.

[50] D. de Florian *et al.*, "Handbook of LHC Higgs Cross Sections: 4. Deciphering the Nature of the Higgs Sector." arXiv:1610.07922, 2016.

[51] ATLAS Collaboration, "Measurements of the Higgs boson inclusive, differential and production cross sections in the 4ℓ decay channel at $\sqrt{s} = 13$ TeV with the ATLAS detector." ATLAS-CONF-2019-025, 2019.

[52] ATLAS Collaboration, "Measurements and interpretations of Higgs-boson fiducial cross sections in the diphoton decay channel using 139 fb^{-1} of pp collision data at $\sqrt{s} = 13$ TeV with the ATLAS detector." ATLAS-CONF-2019-029, 2019.

[53] ATLAS Collaboration, "Combined measurements of Higgs boson production and decay using up to 80 fb^{-1} of proton–proton collision data at $\sqrt{s} = 13$ TeV collected with the ATLAS experiment." ATLAS-CONF-2019-005, 2019.

[54] ATLAS Collaboration, "Observation of light-by-light scattering in ultraperipheral Pb+Pb collisions with the ATLAS detector." ATLAS-CONF-2019-002, 2019.

[55] ATLAS Collaboration, "ATLAS Event Display: Light Scattering Off Light." https://cds.cern.ch/record/2667216, 2019.

[56] A. Vieira, B. Hiller, M. Nemes, and M. Sampaio, "Naturalness and Theoretical Constraints on the Higgs Boson Mass," *Int. J. Theor. Phys.*, vol. 52, pp. 3494–3503, 2013.

[57] H. Georgi and S. Glashow, "Unity of All Elementary Particle Forces," *Phys. Rev. Lett.*, vol. 32, pp. 438–441, 1974.

[58] SNO Collaboration, "Measurement of the rate of $\nu_e + d \rightarrow p + p + e^-$ interactions produced by ^8B solar neutrinos at the Sudbury Neutrino Observatory," *Phys. Rev. Lett.*, vol. 87, p. 071301, 2001.

[59] Super-Kamiokande Collaboration, "Evidence for oscillation of atmospheric neutrinos," *Phys. Rev. Lett.*, vol. 81, pp. 1562–1567, 1998.

[60] E. Majorana, "Teoria simmetrica dell'elettrone e del positrone," *Nuovo Cim.*, vol. 14, pp. 171–184, 1937.

[61] N. Cabibbo, "Unitary Symmetry and Leptonic Decays," *Phys. Rev. Lett.*, vol. 10, pp. 531–533, 1963.

[62] M. Kobayashi and T. Maskawa, "CP-Violation in the Renormalizable Theory of Weak Interaction," *Progress of Theoretical Physics*, vol. 49, no. 2, pp. 652–657, 1973.

[63] Z. Maki, M. Nakagawa, and S. Sakata, "Remarks on the Unified Model of Elementary Particles," *Progress of Theoretical Physics*, vol. 28, no. 5, pp. 870–880, 1962.

[64] B. Pontecorvo, "Inverse beta processes and nonconservation of lepton charge," *Sov. Phys. JETP*, vol. 7, pp. 172–173, 1958.

[65] R. Mohapatra, "CP-Violation: Weak and Strong," in *Unification and Supersymmetry. Frontiers of Quark-Lepton Physics.*, pp. 65–91, 1986.

[66] R. Peccei and H. Quinn, "CP Conservation in the Presence of Pseudoparticles," *Phys. Rev. Lett.*, vol. 38, pp. 1440–1443, 1977.

[67] A. Sakharov, "Violation of CP Invariance, C asymmetry, and baryon asymmetry of the universe," *Pisma Zh. Eksp. Teor. Fiz.*, vol. 5, pp. 32–35, 1967.

[68] F. Zwicky, "Die Rotverschiebung von extragalaktischen Nebeln," *Helv. Phys. Acta*, vol. 6, pp. 110–127, 1933.

[69] F. Zwicky, "On the Masses of Nebulae and of Clusters of Nebulae," *Astrophys. J.*, vol. 86, pp. 217–246, 1937.

[70] A. Riess *et al.*, "Observational evidence from supernovae for an accelerating universe and a cosmological constant," *Astron. J.*, vol. 116, pp. 1009–1038, 1998.

[71] S. Perlmutter *et al.*, "Measurements of Ω and Λ from 42 high redshift supernovae," *Astrophys. J.*, vol. 517, pp. 565–586, 1999.

[72] G. Giesen, J. Lesgourgues, B. Audren, and Y. Ali-Haimoud, "CMB photons shedding light on dark matter," *JCAP*, vol. 1212, p. 008, 2012.

[73] S. Martin, "A Supersymmetry primer." arXiv:hep-ph/9709356, 1997.

[74] C. Csáki and P. Tanedo, "Beyond the Standard Model." arXiv:1602.04228, 2015.

[75] V. Schomerus, *A primer on string theory.* Cambridge University Press, 2017.

[76] J. Kemmer *et al.*, "Development of 10-micrometer resolution silicon counters for charm signature observation with the ACCMOR spectrometer," in *Proceedings: Silicon Detectors For High-Energy Physics.*, pp. 195–217, 1981.

[77] E. Belau *et al.*, "Silicon detectors with 5-micrometer spatial resolution for high-energy particles," *Nucl. Instrum. Meth.*, vol. 217, pp. 224–228, 1983.

[78] F. Hartmann, *Evolution of Silicon Sensor Technology in Particle Physics.* Springer, 2017.

[79] J. Lindhard, M. Scharff, and H. Schiøtt, "Range concepts and heavy ion ranges," *Kgl. Danske Videnskab Selskab*, vol. 33, no. 14, 1963.

[80] H. Andersen and J. Ziegler, "Hydrogen. stopping powers and ranges in all elements," *Pergamon Press (United States)*, 1977.

[81] W. Barkas, W. Birnbaum, and F. Smith, "Mass-Ratio Method Applied to the Measurement of L-Meson Masses and the Energy Balance in Pion Decay," *Phys. Rev.*, vol. 101, pp. 778–795, 1956.

[82] H. Bethe, "Zur Theorie des Durchgangs schneller Korpuskularstrahlen durch Materie," *Annalen Phys.*, vol. 5, pp. 325–400, 1930.

[83] L. Landau, "On the energy loss of fast particles by ionization," *J. Phys.*, vol. 8, pp. 201–205, 1944.

[84] P. Vavilov, "Ionization losses of high-energy heavy particles," *Sov. Phys. JETP*, vol. 5, pp. 749–751, 1957.

[85] H. Bichsel, "Straggling in Thin Silicon Detectors," *Rev. Mod. Phys.*, vol. 60, pp. 663–699, 1988.

[86] G. Moliere, "Theorie der Streuung schneller geladener Teilchen II - Mehrfach- und Vielfachstreuung," *Z. Naturforsch. Teil A*, vol. 3, pp. 78–97, 1948.

[87] H. Bethe, "Moliere's theory of multiple scattering," *Phys. Rev.*, vol. 89, pp. 1256–1266, 1953.

[88] V. Highland, "Some Practical Remarks on Multiple Scattering," *Nucl. Instrum. Meth.*, vol. 129, p. 497, 1975.

[89] G. Lynch and O. Dahl, "Approximations to multiple Coulomb scattering," *Nucl. Instrum. Meth. B*, vol. 58, pp. 6–10, 1991.

[90] O. Klein and Y. Nishina, "Über die Streuung von Strahlung durch freie Elektronen nach der neuen relativistischen Quantendynamik von Dirac," *Z. Physik*, vol. 52, pp. 853–868, 1929.

[91] H. Bethe and W. Heitler, "On the Stopping of fast particles and on the creation of positive electrons," *Proceedings of the Royal Society of London*, vol. A, no. 146, pp. 83–112, 1934.

[92] Oxford Physics, "Big European Bubble Chamber (BEBC)." `http://www.physics.ox.ac.uk/dwb/BEBC.pdf`. Accessed: 20.06.2020.

[93] R. Wigmans, "Calorimetry: Energy measurement in particle physics," *Int. Ser. Monogr. Phys.*, vol. 107, pp. 1–726, 2000.

[94] S. Sze, *Semiconductor Devices: Physics and Technology*. John Wiley & Sons, 2012.

[95] H. Kolanoski and N. Wermes, *Teilchendetektoren - Grundlagen und Anwendungen*. Springer, 2016.

[96] E. Fermi, "Zur Quantelung des idealen einatomigen Gases," *Zeitschrift für Physik*, no. 36, pp. 902–912, 1926.

[97] P. Dirac and R. Fowler, "On the theory of quantum mechanics," *Proceedings of the Royal Society of London*, vol. A, no. 112, pp. 661–677, 1926.

[98] W. Shockley, "Currents to Conductors Induced by a Moving Point Charge," *J. Appl. Phys.*, vol. 9, no. 10, pp. 635–636, 1938.

[99] S. Ramo, "Currents induced by electron motion," *Proc. Ire.*, vol. 27, pp. 584–585, 1939.

[100] A. Einstein, *Investigations on the Theory of the Brownian Movement*. Dover Publications, 1956.

[101] G. Mueller, N. Wilsey, and M. Rosen, "The Structure of Displacement Cascades in Silicon," *IEEE Transactions on Nuclear Science*, vol. 29, no. 6, pp. 1493–1497, 1982.

[102] A. Vasilescu, "The NIEL scaling hypothesis applied to neutron spectra of irradiation facilities and in the ATLAS and CMS SCT," *ROSE Technical Note*, 1997.

[103] T. Luera *et al.*, "Neutron damage equivalence for silicon, silicon dioxide, and gallium arsenide," *IEEE Transactions on Nuclear Science*, vol. 34, no. 6, pp. 1557–1563, 1987.

[104] R. Wunstorf *et al.*, "Damage-induced surface effects in silicon detectors," *Nucl. Instrum. Meth. A*, vol. 377, no. 2, pp. 290 – 297, 1996.

[105] M. Moll, *Radiation damage in silicon particle detectors: Microscopic defects and macroscopic properties*. PhD thesis, Universität Hamburg, 1999.

[106] ATLAS Collaboration, "ATLAS inner detector: Technical Design Report, 1." CERN-LHCC-97-016, 1997.

[107] ATLAS Collaboration, "ATLAS inner detector: Technical Design Report, 2." CERN-LHCC-97-017, 1997.

[108] ATLAS Collaboration, "ATLAS pixel detector: Technical Design Report." CERN-LHCC-98-013, 1998.

[109] ATLAS Collaboration, "ATLAS Insertable B-Layer Technical Design Report." CERN-LHCC-2010-013, 2010.

[110] ATLAS Collaboration, "ATLAS liquid-argon calorimeter: Technical Design Report." CERN-LHCC-96-041, 1996.

[111] ATLAS Collaboration, "ATLAS tile calorimeter: Technical Design Report." CERN-LHCC-96-042, 1996.

[112] ATLAS Collaboration, "ATLAS muon spectrometer: Technical Design Report." CERN-LHCC-97-022, 1997.

[113] ATLAS Collaboration, "Performance of the ATLAS trigger system in 2015," *Eur. Phys. J. C*, vol. 77, p. 317, 2017.

[114] ATLAS Collaboration, "ATLAS Computing: Technical Design Report." CERN-LHCC-2005-022, 2005.

[115] ATLAS Collaboration, "Measurement of the inclusive isolated prompt photons cross section in pp collisions at $\sqrt{s} = 7\,\text{TeV}$ with the ATLAS detector using $4.6\,\text{fb}^{-1}$," *Phys. Rev. D*, vol. 89, p. 052004, 2014.

[116] ATLAS Collaboration, "Measurement of the inclusive isolated prompt photon cross section in pp collisions at $\sqrt{s} = 8\,\text{TeV}$ with the ATLAS detector," *JHEP*, vol. 08, p. 005, 2016.

[117] ATLAS Collaboration, "Measurement of the cross section for inclusive isolated-photon production in pp collisions at $\sqrt{s} = 13\,\text{TeV}$ using the ATLAS detector," *Phys. Lett. B*, vol. 770, p. 473, 2017.

[118] D. d'Enterria and J. Rojo, "Quantitative constraints on the gluon distribution function in the proton from collider isolated-photon data," *Nucl. Phys. B*, vol. 860, pp. 311–338, 2012.

[119] ATLAS Collaboration, "Measurement of Higgs boson production in the diphoton decay channel in pp collisions at center-of-mass energies of 7 and 8 TeV with the ATLAS detector," *Phys. Rev. D*, vol. 90, p. 112015, 2014.

[120] ATLAS Collaboration, "Measurements of Higgs boson properties in the diphoton decay channel with $36\,\text{fb}^{-1}$ of pp collision data at $\sqrt{s} = 13\,\text{TeV}$ with the ATLAS detector," *Phys. Rev. D*, vol. 98, p. 052005, 2018.

[121] ATLAS Collaboration, "Search for high-mass diphoton resonances in pp collisions at $\sqrt{s} = 8\,\text{TeV}$ with the ATLAS detector," *Phys. Rev. D*, vol. 92, p. 032004, 2015.

[122] ATLAS Collaboration, "Search for new phenomena in high-mass diphoton final states using $37\,\text{fb}^{-1}$ of proton–proton collisions collected at $\sqrt{s} = 13\,\text{TeV}$ with the ATLAS detector," *Phys. Lett. B*, vol. 775, p. 105, 2017.

[123] ATLAS Collaboration, "Search for photonic signatures of gauge-mediated supersymmetry in 13 TeV pp collisions with the ATLAS detector," *Phys. Rev. D*, vol. 97, p. 092006, 2018.

[124] ATLAS Collaboration, "Search for supersymmetry in a final state containing two photons and missing transverse momentum in $\sqrt{s} = 13\,\text{TeV}$ pp collisions at the LHC using the ATLAS detector," *Eur. Phys. J. C*, vol. 76, p. 517, 2016.

[125] ATLAS Collaboration, "Search for new phenomena in photon+jet events collected in proton–proton collisions at $\sqrt{s} = 8\,\text{TeV}$ with the ATLAS detector," *Phys. Lett. B*, vol. 728, p. 562, 2014.

[126] ATLAS Collaboration, "Search for new phenomena with photon+jet events in proton–proton collisions at $\sqrt{s} = 13\,\text{TeV}$ with the ATLAS detector," *JHEP*, vol. 03, p. 041, 2016.

[127] ATLAS Collaboration, "Electron efficiency measurements with the ATLAS detector using the 2015 LHC proton–proton collision data." ATLAS-CONF-2016-024, 2016.

[128] ATLAS Collaboration, "Measurement of the photon identification efficiencies with the ATLAS detector using LHC Run 2 data collected in 2015 and 2016," *Eur. Phys. J. C*, vol. 79, p. 205, 2019.

[129] ATLAS Collaboration, "Measurement of the photon identification efficiencies with the ATLAS detector using LHC Run-1 data," *Eur. Phys. J. C*, vol. 76, p. 666, 2016.

[130] W. Lampl *et al.*, "Calorimeter Clustering Algorithms: Description and Performance." ATL-LARG-PUB-2008-002, 2008.

[131] S. Agostinelli *et al.*, "Geant4 - a simulation toolkit," *Nucl. Instrum. Meth. A*, vol. 506, no. 3, pp. 250–303, 2003.

[132] T. Sjostrand, S. Mrenna, and P. Skands, "A Brief Introduction to PYTHIA 8.1," *Comput. Phys. Commun.*, vol. 178, pp. 852–867, 2008.

[133] ATLAS Collaboration, "The ATLAS Simulation Infrastructure," *Eur. Phys. J. C*, vol. 70, p. 823, 2010.

[134] A. Hoecker *et al.*, "TMVA - Toolkit for Multivariate Data Analysis." arXiv:physics/0703039, 2007.

[135] L. Devroye, *Non-Uniform Random Variate Generation*. Springer-Verlag (New York), 1986.

[136] L. Lyons, D. Gibaut, and P. Clifford, "How to Combine Correlated Estimates of a Single Physical Quantity," *Nucl. Instrum. Meth. A*, vol. 270, p. 110, 1988.

[137] ATLAS Collaboration, "ATLAS b-jet identification performance and efficiency measurement with $t\bar{t}$ events in pp collisions at $\sqrt{s} = 13\,\text{TeV}$." arXiv:1907.05120, 2019.

[138] ATLAS Collaboration, "Training and validation of the ATLAS pixel clustering neural networks." ATL-PHYS-PUB-2018-002, 2018.

[139] J. Saxon, *Discovery of the Higgs Boson, Measurements of its Production, and a Search for Higgs Boson Pair Production*. PhD thesis, Pennsylvania U., 2014.

[140] J.-H. Arling, "*PhotonIDOptimizer* framework." `https://gitlab.cern.ch/ATLAS-EGamma/Software/PhotonID/PhotonIDOptimizer`. Accessed: 20.06.2020.

[141] DESY IT, "BIRD - Batch Infrastruktur Resource at DESY." `https://confluence.desy.de/display/IS/BIRD`. Accessed: 20.06.2020.

[142] T. Gleisberg, S. Hoeche, F. Krauss, M. Schonherr, S. Schumann, F. Siegert, and J. Winter, "Event generation with SHERPA 1.1," *JHEP*, vol. 02, p. 007, 2009.

[143] G. Apollinari, I. Béjar Alonso, O. Brüning, P. Fessia, M. Lamont, L. Rossi, and L. Tavian, "High-Luminosity Large Hadron Collider (HL-LHC)," *CERN Yellow Rep. Monogr.*, vol. 4, pp. 1–516, 2017.

[144] A. Dainese, M. Mangano, A. Meyer, A. Nisati, G. Salam, and M. Vesterinen, "Report on the Physics at the HL-LHC, and Perspectives for the HE-LHC," *CERN Yellow Rep. Monogr.*, vol. 7, 2019.

[145] ATLAS Collaboration, "Radiation Simulation Public Results: Phase II ITk Inclined Duals." `https://twiki.cern.ch/twiki/bin/view/AtlasPublic/RadiationSimulationPublicResults`, 2018. Accessed: 20.06.2020.

[146] ATLAS Collaboration, "Technical Design Report for the ATLAS Inner Tracker Strip Detector." CERN-LHCC-2017-005, 2017.

[147] ATLAS Collaboration, "Expected Tracking Performance of the ATLAS Inner Tracker at the HL-LHC." ATL-PHYS-PUB-2019-014, 2019.

[148] ATLAS Collaboration, "Technical Design Report for the ATLAS Inner Tracker Pixel Detector." CERN-LHCC-2017-021, 2017.

[149] Y. Unno *et al.*, "Development of n^+-in-p large-area silicon microstrip sensors for very high radiation environments – ATLAS12 design and initial results," *Nucl. Instrum. Meth. A*, vol. 765, pp. 80–90, 2014.

[150] K. Mahboubi *et al.*, "The front-end hybrid for the ATLAS HL-LHC silicon strip tracker," *JINST*, vol. 9, p. C02027, 2014.

[151] A. Affolder *et al.*, "DC-DC converters with reduced mass for trackers at the HL-LHC," *JINST*, vol. 6, p. C11035, 2011.

[152] S. Diez, "Silicon strip staves and petals for the ATLAS Upgrade tracker of the HL-LHC," *Nucl. Instrum. Meth. A*, vol. 699, pp. 93–96, 2013.

[153] ATLAS ITk Collaboration, "Petal core specifications." `https://edms.cern.ch/document/2027757/4`, AT2-IS-ES-0011 v.4, 2020. Accessed: 20.06.2020.

[154] ATLAS ITk Collaboration, "Petal 3D CAD file and engineering drawings." `https://edms.cern.ch/document/2061432/6`, AT2-IS-EP-0035 v.6, 2020. Accessed: 20.06.2020.

[155] ATLAS ITk Collaboration, "QC/QA procedures for cores." `https://edms.cern.ch/document/2028814/2`, AT2-IS-GP-0002 v.2, 2020. Accessed: 20.06.2020.

[156] OGP (Optical Gaging Products), "SmartScope CNC 670." `www.ogpnet.com/products/systems/smartscope-video-multisensor-systems/smartscope-flash-systems/smartscope-cnc-670`. Accessed: 20.06.2020.

[157] M. Vollmer and K.-P. Möllmann, *Infrared Thermal Imaging*. Wiley-VCH (Berlin), 2013.

[158] InfraTec GmbH, "VarioCAM® HD research 900." `www.infratec.eu/thermography/infrared-camera/variocam-hd-research-900`. Accessed: 20.06.2020.

[159] J. Collier and J. Thome, *Convective Boiling and Condensation*. Clarendon Press (Oxford), 2001.

[160] CERN EP-DT, "TRACI II Webpage." www.ep-dep-dt.web.cern.ch/co2-cooling-plants/traci-geneva. Accessed: 20.06.2020.

[161] National Instruments Corporation, "NI cDAQ-9174 - datasheet." www.ni.com/de-de/support/model.cdaq-9174.html. Accessed: 20.06.2020.

[162] Baker Hughes Company, "UNIK 5000 - datasheet." https://www.bakerhughesds.com/download/druck-unik-5000-datasheet. Accessed: 20.06.2020.

[163] T. Seebeck, *Magnetische Polarisation der Metalle und Erze durch Temperaturdifferenz*. Hansebooks, 2017.

[164] TC Mess- und Regeltechnik GmbH, "Thermocouple - datasheet." www.tcgmbh.de/downloads/Mantel-Thermoelemente-Typ-12.pdf. Accessed: 20.06.2020.

[165] Tektronix Inc., "Keithley 2700 Multimeter/Data Acquisition/Switch Systems." www.tek.com/keithley-switching-and-data-acquisition-systems/keithley-2700-multimeter-data-acquisition-switch-sys. Accessed: 20.06.2020.

[166] Freek GmbH, "Cartridge heater - datasheet." www.freek-heaters.com/products/cartridge-heaters/high-density-cartridge-heaters. Accessed: 20.06.2020.

[167] Castel S.r.l., "Sightglass - datasheet." www.castel.it/en/product/moisture-liquid-indicators-for-r744/. Accessed: 20.06.2020.

[168] Sensirion AG, "SHT21 sensor - datasheet." www.sensirion.com/fileadmin/user_upload/customers/sensirion/Dokumente/2_Humidity_Sensors/Datasheets/Sensirion_Humidity_Sensors_SHT21_Datasheet.pdf. Accessed: 20.06.2020.

[169] Raspberry Pi Foundation, "Raspberry Pi webpage." www.raspberrypi.org. Accessed: 20.06.2020.

[170] M. Caspar, "Thermal imaging of silicon detector components," *DESY Summer Student Report*, 2017.

[171] D. Logan, *A first course in the finite element method*. Cengage Learning, 2011.

[172] H.-C. Huang and A. Usmani, *Finite Element Analysis for Heat Transfer*. Springer (London), 1994.

[173] ANSYS Inc., "ANSYS Academic Research Mechanical, Release 2020 R1." www.ansys.com, 2020.

[174] G. Beck, K. Brendlinger, Y.-H. Chen, and G. Viehhauser, "Thermo-electrical modelling of the ATLAS ITk Strip Detector." arXiv:2003.00055, 2020.

[175] Y.-H. Chen *et al.*, "Finite Elements Thermo-Mechanical Analysis on Strip Petals for the ATLAS Phase-II Upgrades." ATL-COM-ITK-2017-058, 2017.

[176] L. Cheng, G. Ribatski, J. Moreno Quibén, and J. Thome, "New prediction methods for CO_2 evaporation inside tubes: Part I - A two-phase flow pattern map and a flow pattern based phenomenological model for two-phase flow frictional pressure drops," *International Journal of Heat and Mass Transfer*, vol. 51, no. 1, pp. 111–124, 2008.

[177] L. Cheng, G. Ribatski, and J. Thome, "New prediction methods for CO_2 evaporation inside tubes: Part II - An updated general flow boiling heat transfer model based on flow patterns," *International Journal of Heat and Mass Transfer*, vol. 51, no. 1, pp. 125–135, 2008.

[178] Verlaat, B. and Zhang, Z., "CoBra GUI." version 1, 2014.

[179] N. Jeong, S. Ahrens, *et al.*, "Mechanical Properties of Petal Cores for the ATLAS Phase-II Upgrade of the Inner Tracker." ATL-COM-UPGRADE-2018-004, 2018.

[180] Precision Micro-Optics Inc., "Optical properties of silicon." `http://www.pmoptics.com/silicon.html`. Accessed: 20.06.2020.

[181] A. Beck, "Thermal Performance of the Petal Prototype," *DESY Summer Student Report*, 2018.

[182] J. Peltier, "Nouvelles expériences sur la caloricité des courants électrique," *Annales de Chimie et de Physique*, vol. 56, pp. 371–386, 1834.

[183] International Organization for Standardization (ISO), "ISO 12781-1." `www.iso.org/obp/ui/#iso:std:iso:12781:-1:ed-1:v1:en`. Accessed: 20.06.2020.

[184] M. Teresa Restivo *et al.*, "Flatness Fundamentals." `remotelab.fe.up.pt/planesa/assets/Flatness_fundamentals.pdf`. Accessed: 20.06.2020.

[185] CTS GmbH, "Temperature Test Chambers, Series T." `www.cts-umweltsimulation.de/en/products/temperature-t.html`. Accessed: 20.06.2020.

[186] GHM Messtechnik GmbH, "Immersion probe Greisinger GTF 1200." `www.greisinger.de/p/handmessgeraete-und-sensoren/temperatur/fuehler-thermoelemente/gtf-1200-300/600507`. Accessed: 20.06.2020.

[187] ATLAS ITk Collaboration, "ITk Strips Local Support Cores and Module Loading Preliminary Design Review." `https://indico.cern.ch/event/734211/`, 2018. Accessed: 20.06.2020.

[188] M. Capeans *et al.*, "Report of the Preliminary Design Review of the ATLAS Strips Local Supports Cores and Module Loading." `https://edms.cern.ch/document/2029823/1`, 2018. Accessed: 20.06.2020.

[189] ATLAS ITk Collaboration, "ITk Strip Local Support and Module Loading Final Design Review." `https://indico.cern.ch/event/872236/`, 2020. Accessed: 20.06.2020.

[190] ATLAS ITk Collaboration, "Specification Review for the ATLAS ITk CO_2 cooling system." `https://indico.cern.ch/event/759197/`. Accessed: 20.06.2020.

[191] CERN EP-DT, "ATLAS ITk detector requirements for the CO_2 cooling system." `https://edms.cern.ch/document/2044760/1`. Accessed: 20.06.2020.

[192] Verein deutscher Ingenieure, *VDI-Wärmeatlas*. Springer, 11 ed., 2013.

[193] National Institute of Standards and Technology (NIST), "REFPROP documentation." `https://refprop-docs.readthedocs.io/`. Accessed: 20.06.2020.

[194] E. W. Lemmon, , I. H. Bell, M. L. Huber, and M. O. McLinden, "NIST Standard Reference Database 23: Reference Fluid Thermodynamic and Transport Properties-REFPROP, Version 10.0, National Institute of Standards and Technology," 2018.

[195] CoolProp developers, "CoolProp documentation." `http://www.coolprop.org/`. Accessed: 20.06.2020.

[196] I. Bell, J. Wronski, S. Quoilin, and V. Lemort, "Pure and pseudo-pure fluid thermophysical property evaluation and the open-source thermophysical property library coolprop," *Industrial & Engineering Chemistry Research*, vol. 53, no. 6, pp. 2498–2508, 2014.

[197] J.-H. Arling, "Video sequence of sightglass investigation." 10.5281/zenodo.3900052, 2020.

[198] Deutsches Elektronen-Synchrotron DESY, "DESY Summer Student Programme." `http://summerstudents.desy.de`. Accessed: 20.06.2020.

[199] Deutsches Elektronen-Synchrotron DESY, "Forschungsaufenthalt bei DESY in Hamburg - Schwerpunkt Teilchenphysik." `http://www.desy.de/infos_services/schule/lehrerfortbildung/forschungsaufenthalt/schwerpunkt_teilchenphysik`. Accessed: 20.06.2020.

[200] CERN, "Beamline for Schools (BL4S)." `https://beamline-for-schools.web.cern.ch`. Accessed: 20.06.2020.

[201] SPS Coordinators, "CERN SPS Test Beam Facility." `http://sba.web.cern.ch/sba`. Accessed: 20.06.2020.

[202] FTBF Coordinators, "Fermilab Test Beam Facility." `https://ftbf.fnal.gov`. Accessed: 20.06.2020.

[203] C. Has, "ESTB Test Beam Facility." `http://estb.slac.stanford.edu`. Accessed: 20.06.2020.

[204] ELSA Coordinators, "ELSA Test Beam Facility." `https://www-elsa.physik.uni-bonn.de`. Accessed: 20.06.2020.

[205] H. Augustin *et al.*, "The MuPix Telescope: A Thin, high Rate Tracking Telescope," *JINST*, vol. 12, no. 01, p. C01087, 2017.

[206] K. Akiba *et al.*, "The Timepix Telescope for High Performance Particle Tracking," *Nucl. Instrum. Meth. A*, vol. 723, p. 47, 2013.

[207] M. Benoit *et al.*, "The FE-I4 Telescope for particle tracking in testbeam experiments," *JINST*, vol. 11, no. 07, p. P07003, 2016.

[208] R. Diener *et al.*, "The DESY II Test Beam Facility," *Nucl. Instrum. Meth. A*, vol. 922, pp. 265–286, 2019.

[209] DESY II Testbeam Coordinators, "DESY II Testbeam Website." `http://testbeam.desy.de`. Accessed: 20.06.2020.

[210] J.-H. Arling *et al.*, "Summary and Conclusions of the First DESY Test Beam User Workshop." arXiv:physics/1802.00412, 2018.

[211] N. Potylitsina-Kube, C. de la Taille, K. Desch, R. Diener, I. M. Gregor, L. Jonsson, J. Mnich, F. Sefkow, and J. Timmermans, "EUDET project." `http://www.eudet.org`. Accessed: 20.06.2020.

[212] CERN, "AIDA/AIDA2020 project." `http://aida2020.web.cern.ch`. Accessed: 20.06.2020.

[213] Beam Telescope Coordinators, "EUDET-type Beam Telescopes." `https://telescopes.desy.de`. Accessed: 20.06.2020.

[214] H. Jansen *et al.*, "Performance of the EUDET-type beam telescopes," *EPJ Tech. Instrum.*, vol. 3, no. 1, p. 7, 2016.

[215] C. Hu-Guo *et al.*, "First reticule size MAPS with digital output and integrated zero suppression for the EUDET-JRA1 beam telescope," *Nucl. Instrum. Meth. A*, vol. 623, pp. 480–482, 2010.

[216] J. Baudot *et al.*, "First test results of MIMOSA-26, a fast CMOS sensor with integrated zero suppression and digitized output," in *IEEE NSS Conference Record*, pp. 1169–1173, 2009.

[217] D. Cussans, "Description of the JRA1 Trigger Logic Unit (TLU), v0.2c," *EUDET-Memo-2009-04*, 2009.

[218] D. Cussans, "A Trigger/Timing Logic Unit for ILC Test-beams," in *1st topical workshop on electronics for particle physics (TWEPP), Prague*, 2007.

[219] S. Spannagel and H. Jansen, "GBL Track Resolution Calculator." https://github.com/simonspa/resolution-simulator. Accessed: 20.06.2020.

[220] EUDAQ Software Developers, "EUDAQ Website." `http://eudaq.github.io`. Accessed: 20.06.2020.

[221] P. Ahlburg *et al.*, "EUDAQ – A Data Acquisition Software Framework for Common Beam Telescopes," *JINST*, vol. 15, no. 01, p. P01038, 2020.

[222] Y. Liu *et al.*, "EUDAQ2 - A flexible data acquisition software framework for common test beams," *JINST*, vol. 14, no. 10, p. P10033, 2019.

[223] P. Baesso, D. Cussans, and J. Goldstein, "The AIDA-2020 TLU: a flexible trigger logic unit for test beam facilities," *JINST*, vol. 14, no. 09, p. P09019, 2019.

[224] T. Bisanz, J.-H. Arling, *et al.*, "EUTelescope: A modular reconstruction framework for beam telescope data," *JINST*, vol. 15, no. 09, pp. P09020–P09020, 2020.

[225] EUTelescope Software Developers, "EUTelescope Website." `http://eutelescope.desy.de`. Accessed: 20.06.2020.

[226] G. McGoldrick *et al.*, "Judith - Pixel particle detector testbeam analysis." `https://github.com/gmcgoldr/judith`. Accessed: 20.06.2020.

[227] M. Kiehn *et al.*, "Proteus beam telescope reconstruction." `https://gitlab.cern.ch/unige-fei4tel/proteus`,`https://doi.org/10.5281/zenodo.2586736`. Accessed: 20.06.2020.

[228] B. Schwenker, "Test Beam Software Framework." `https://bitbucket.org/BenjaminSchwenker/tbsw.git`. Accessed: 20.06.2020.

[229] D. Hynds, S. Spannagel, *et al.*, "Corryvreckan - The Maelstrom for Your Test Beam Data." https://gitlab.cern.ch/corryvreckan/corryvreckan. Accessed: 20.06.2020.

[230] ILCSoft Community, "ILCSoft - common software packages developed for the International Linear Collider ILC." http://ilcsoft.desy.de. Accessed: 20.06.2020.

[231] ILCSoft Community, "Marlin - Modular Analysis & Reconstruction for the LINear Collider." http://ilcsoft.desy.de/portal/software_packages/marlin. Accessed: 20.06.2020.

[232] ILCSoft Community, "LCIO - Linear Collider Input/Output." http://lcio.desy.de/, http://ilcsoft.desy.de/portal/software_packages/lcio. Accessed: 20.06.2020.

[233] F. Gaede, T. Behnke, N. Graf, and T. Johnson, "LCIO - a persistency framework for linear collider simulation studies." arXiv:physics/0306114, 2003.

[234] ILCSoft Community, "GEAR - GEometry API for Reconstruction." http://ilcsoft.desy.de/portal/software_packages/gear. Accessed: 20.06.2020.

[235] ILCSoft Community, "ilcinstall - Installation script for ILCSoft packages." http://ilcsoft.desy.de/portal/software_packages/ilcinstall. Accessed: 20.06.2020.

[236] EUTelescope Software Developers, "ilcinstall for EUTelescope installation." https://github.com/eutelescope/iLCInstall. Accessed: 20.06.2020.

[237] DESY IT, "NAF - National Analysis Facility." https://confluence.desy.de/display/IS/NAF+-+National+Analysis+Facility. Accessed: 20.06.2020.

[238] CERN, "LXPLUS Service - Computing cluster at CERN." http://information-technology.web.cern.ch/services/lxplus-service. Accessed: 20.06.2020.

[239] EUTelescope Software Developers, "EUTelescope on DockerHub." https://hub.docker.com/orgs/eutelescope. Accessed: 20.06.2020.

[240] Eigen3 Software Developers, "Eigen3." http://eigen.tuxfamily.org. Accessed: 20.06.2020.

[241] R. Brun and F. Rademakers, "ROOT - an object oriented data analysis framework," *Nucl. Instr. Meth. A*, vol. 389, no. 1-2, pp. 81–86, 1997.

[242] C. Kleinwort, "Millepede II Wiki." https://www.terascale.de/wiki/millepede_ii. Accessed: 20.06.2020.

[243] V. Blobel, "Software alignment for tracking detectors," *Nucl. Instrum. Meth. A*, vol. 566, pp. 5–13, 2006.

[244] C. Kleinwort, "General broken lines as advanced track fitting method," *Nucl. Instr. Meth. A*, vol. 673, pp. 107–110, 2012.

[245] V. Blobel, C. Kleinwort, and F. Meier, "Fast alignment of a complex tracking detector using advanced track models," *Comput. Phys. Commun.*, vol. 182, pp. 1760–1763, 2011.

[246] C. Kleinwort, "General Broken Lines - Wiki." `https://www.terascale.de/wiki/generalbrokenlines`. Accessed: 20.06.2020.

[247] Frühwirth, R., "Application of Kalman filtering to track and vertex fitting," *Nucl. Instrum. Meth. A*, vol. 262, pp. 444–450, 1987.

[248] Strandlie, A. and Frühwirth, R., "Track and vertex reconstruction: From classical to adaptive methods," *Rev. Mod. Phys.*, vol. 82, pp. 1419–1458, 2010.

[249] K. Dunne, "Photon Tagged Beamline at the DESY II Test Beam Facility," *DESY Summer Student Report*, 2018.

[250] U. Stolzenberg, A. Frey, B. Schwenker, P. Wieduwilt, C. Marinas, and F. Lütticke, "Radiation length imaging with high-resolution telescopes," *Nucl. Instrum. Meth. A*, vol. 845, pp. 173 – 176, 2017.

[251] H. Jansen, J. Dreyling-Eschweiler, P. Schütze, and S. Spannagel, "Scattering Studies with the DATURA Beam Telescope," *Springer Proc. Phys.*, vol. 212, pp. 243–250, 2018.

[252] P. Schütze and H. Jansen, "Simulation of material budget measurements with beam telescopes," in *Proceedings on The 26th International Workshop on Vertex Detectors 2017*, p. 049, 12 2018.

[253] P. Schütze, *Silicon Pixel Detectors - Performance after Irradiation and Application in Three-dimensional Imaging*. PhD thesis, Universität Hamburg, 2019.

[254] S. Zakharov, "Studies of X_0 measurements at the DESY II test beam facility," *DESY Summer Student Report*, 2018.

[255] Y. Tsai, "Summary and Conclusions of the First DESY Test Beam User Workshop," *Rev. Mod. Phys.*, vol. 46, pp. 815–851, 1974.

[256] Particle Data Group, "Atomic and Nuclear Properties of Materials." `http://pdg.lbl.gov/2019/AtomicNuclearProperties/`. Accessed: 20.06.2020.

[257] M. Gupta, "Calculation of radiation length in materials." PH-EP-Tech-Note-2010-013, 2010.

[258] H. Jansen and P. Schütze, "Feasibility of track-based multiple scattering tomography," *Appl. Phys. Lett.*, vol. 112, no. 14, p. 144101, 2018.

[259] T. Povar, "Calibration with water for track-based multiple scattering tomography at the DESY II Test Beam Facility," *DESY Summer Student Report*, 2019.

[260] S. Diez Cornell, "Radiation length values for the ATLAS ITk strip detector." Personal communication.

[261] J. Dreyling-Eschweiler *et al.*, "Summary and Conclusions of the 'JRA Beam Telescope 2025'-Forum at the 6th Beam Telescopes and Test Beams Workshop." arXiv:1805.09572, 2018.

Acknowledgements

Without the support I have received from so many people over the last, nearly four years of working on my PhD, the completion and submission of this thesis would not have been successful. I am very grateful about this support and happy about the people who have guided my way in the last years, so that I would like to say thank you here.

First of all, I would like to thank the supervisors of this thesis, Kevin Kröninger and Ingrid Gregor, for giving me the chance to conduct my PhD work in cooperation between the TU Dortmund and the DESY in Hamburg and for their support and advice along this way. They provided me with the interesting topics I have conducted my research on and always motivated me to continue further in my studies.

A special thanks goes to Ingrid Gregor as she offered my a PhD position in Hamburg right away and was always encouraging in pursuing my studies up to the final end, independent on the required time and paper for writing this thesis. Moreover, she allowed me to participate in many conferences worldwide such that I was able to start building up my personal network in science and to collect many memories and great moments.

I would like to thank Claire David, Sergio Diez Cornell and Kurt Brendlinger as my direct supervisors in the daily work. Kurt succedded in pushing me through the ATLAS analysis jungle in my qualification task and provided me always advice with a good portion of humour. Sergio helped me to find my way and position in the ATLAS ITk collaboration and I always felt his trust when giving me a new challenging task. Claire was my mentor and direct contact for all my research topics. We worked uncountable hours together on fighting with TRACI to cool down the petal or performing night shifts at the DESY test beam or having just fun. Without her enthusiastic support and her push bringing me always to top performances, my PhD times would have been certainly very different and less entertaining and enjoyable.

Many thanks goes to the petal mechanics crew with Frauke, Lisa, Dario, Sören, Volker, Carina and Nico, supporting me in all questions about the petal design and for urgently required pieces in the workshop. Thank you Frauke for teaching me thermodynamics and the mysteries of CO_2 cooling, without your help I would have failed in many occasions. And thank you Dario that your door is always open for questions and that you always provide solutions even in cases when you are super busy.

I would like to thank the DESY test beam and telescope support crew. It was always a pleasure to work with you and discuss new ideas across the borders of groups and to learn what it means to have test beam time, here a special thanks to Jan Dreyling-Eschweiler for teaching me a lot.

Furthermore, I would like to thank my two working groups, the E4 group at Dortmund and the DESY ATLAS group in Hamburg. I was feeling very comfortable in both groups and enjoyed the great working atmosphere with my colleagues and friends. There was always the possibility to ask someone a question or to just have a chat with him/her about topics also outside of work. And it is also needless to say that the DESY ATLAS group is celebrating the best parties and have the best barbecues - happy to be a part of it!

Many thanks for the people helping me with writing this thesis by providing comments, suggestions and corrections: Frauke, Ingrid, Marta, Sergio, Kurt, Simon, Dario, Sören. Your invested time was greatly appreciated.

Last but not least I would like to thank my friends and family and will switch therefore to German. Ein großes Dankeschön gilt meinen Eltern, Angelika und Dietmar Arling, für die Unterstützung über mein ganzes Physikstudium hinweg, ohne euch wäre ich nicht da, wo ich jetzt bin. Ich möchte auch meiner ganzen Familie, meiner Schwiegerfamile, den Vossels, und allen Freunden und Weggefährten danken, dass sie immer an mich geglaubt haben und mich auch in den schwierigen Zeiten weiter motiviert haben. Aber den größten Dank möchte ich meiner großen Liebe Claudia aussprechen, die ich während meiner Doktorandenzeit auch heiraten durfte. Sie hat immer zu mir gestanden und mir auch die Freiheit gegeben, mal wieder auf Dienstreise zum CERN oder sonst wo auf der Welt gehen zu können.

Danke! Thanks! Merci!

Appendix

A Thermo-Mechanical Studies on Petals

A.1 Thermal performance of petal cores

Cores with commercial CF facesheet

The comparison between the front and back side of core 02 evaluated for the temperature distribution along the cooling loop is also performed for all tested CO_2 pressure set points between 56 and 20 bar, as it is shown in Figure A.1.

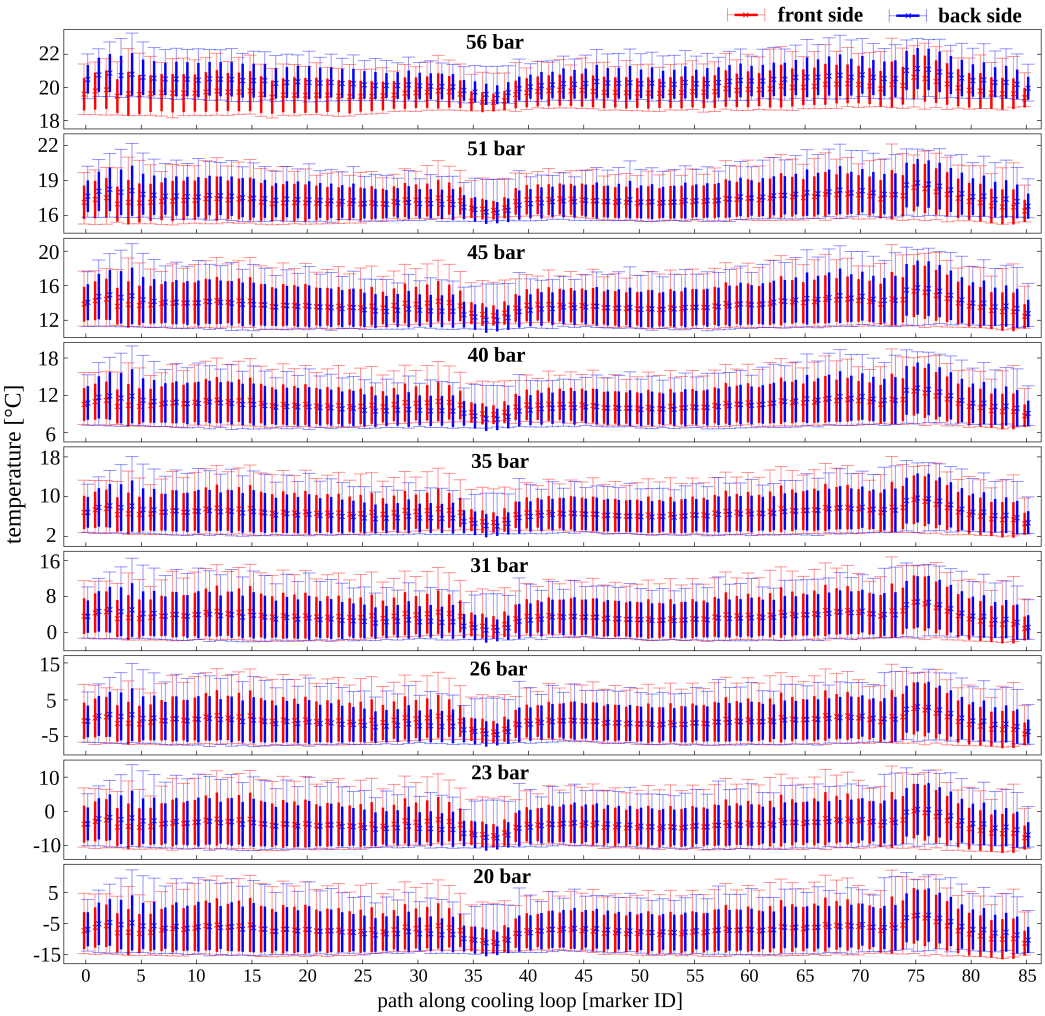

Figure A.1: Comparison of measured temperatures along the cooling loop of the front and back side of core 02 for CO_2 pressure set points between 56 and 20 bar.

Moreover, the measured IR temperatures along the cooling loop for both sides of core 02 are shown separately in Figure A.2.

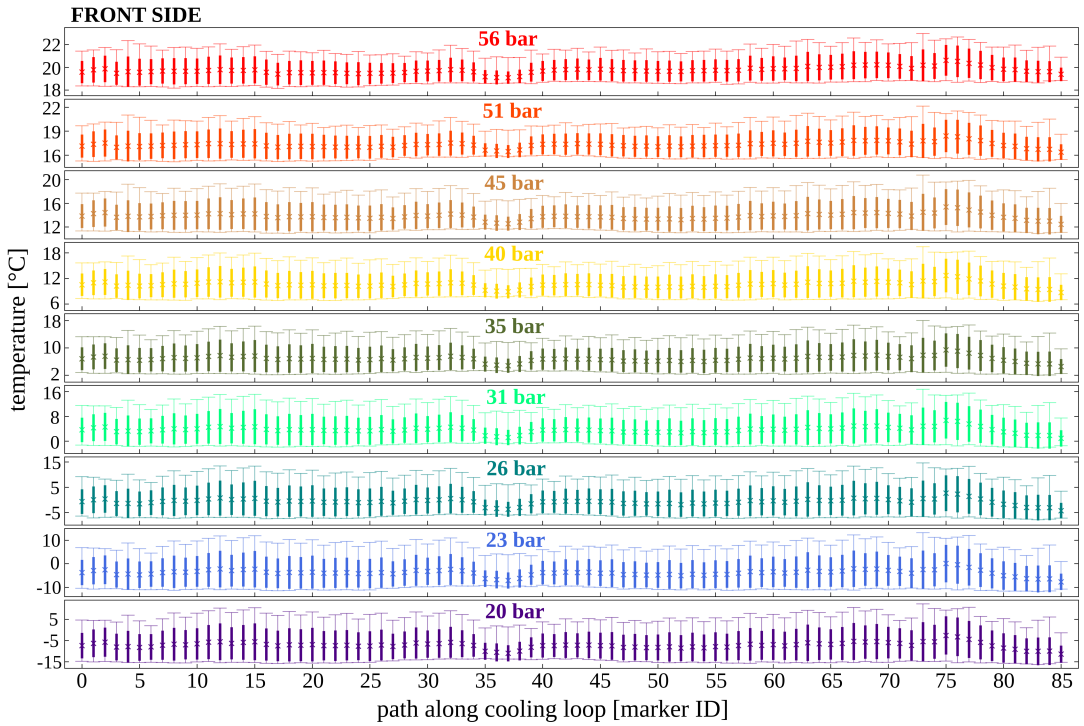

(a) IR temperatures along the cooling loop for the front side of core 02.

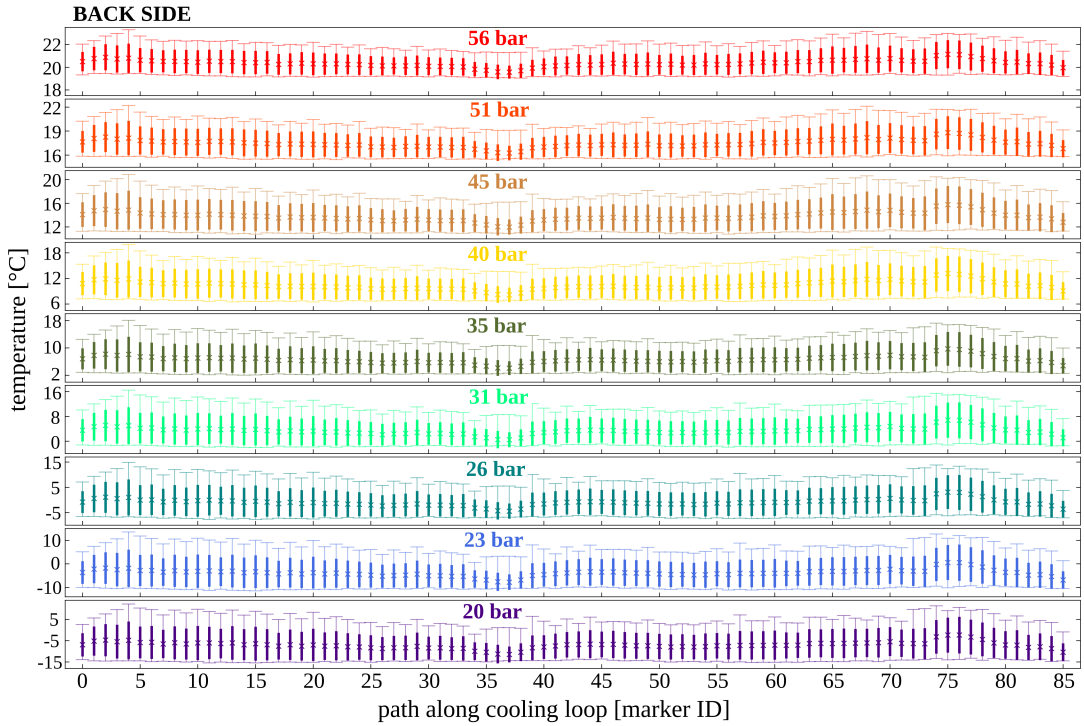

(b) IR temperatures along the cooling loop for the back side of core 02.

Figure A.2: Measured IR temperature distributions along the cooling loop for core 02 evaluated between CO_2 pressure set points of 56 to 20 bar.

Finally, the minimal surface temperatures along the cooling loop and the absolute difference to the CO_2 coolant temperature are analysed in Figure A.3a and Figure A.3b for the front and back side of core 02, respectively.

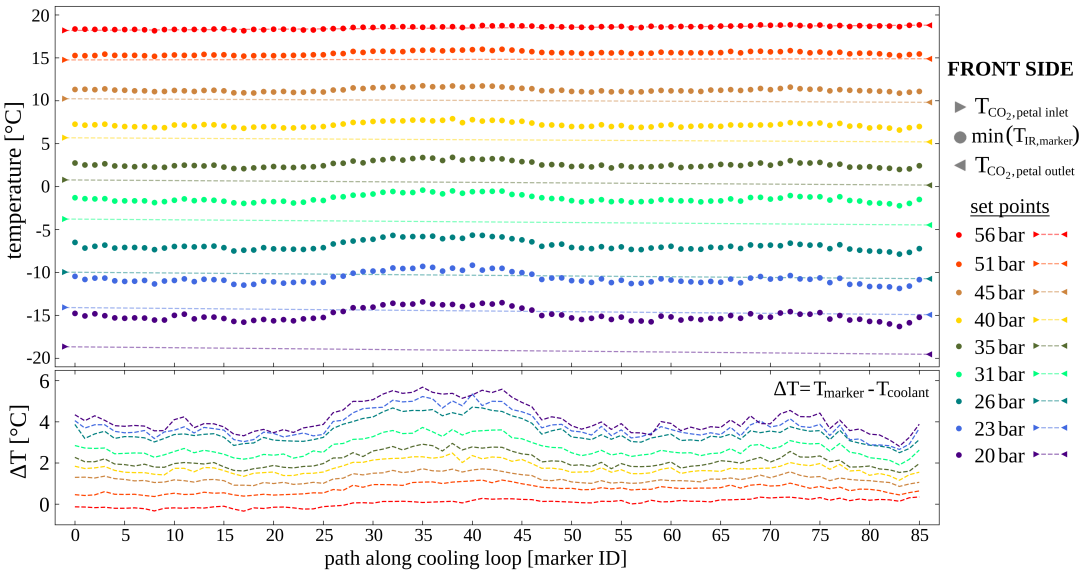

(a) Minimum IR temperatures and absolute difference ΔT for the front side of core 02.

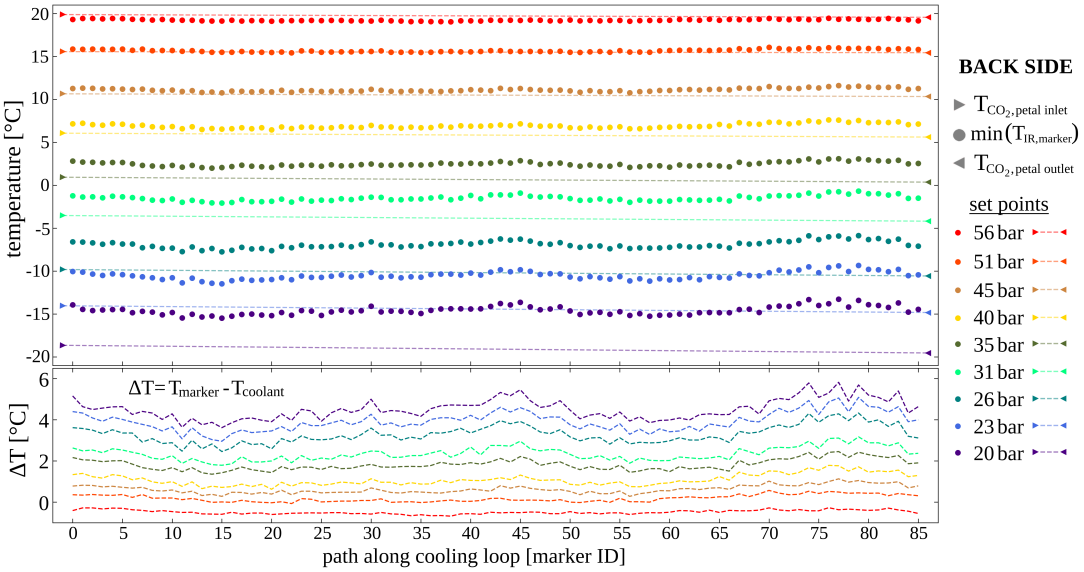

(b) Minimum IR temperatures and absolute difference ΔT for the back side of core 02.

Figure A.3: Comparison of the minimum temperatures measured along the cooling loop and the measured CO_2 coolant temperature at the core's in- and outlet for core 02 at different CO_2 pressure set points. Shown is also the absolute difference ΔT between the IR marker temperature and the averaged CO_2 coolant temperature.

Cores with cocured CF facesheet

For the measurement of core 04 as a petal core prototype with a cocured CF facesheet, the measured IR temperatures evaluated with the defined markers along the cooling loop are shown in Figure A.4 for the tested CO_2 pressure set points between 57 and 18.2 bar.

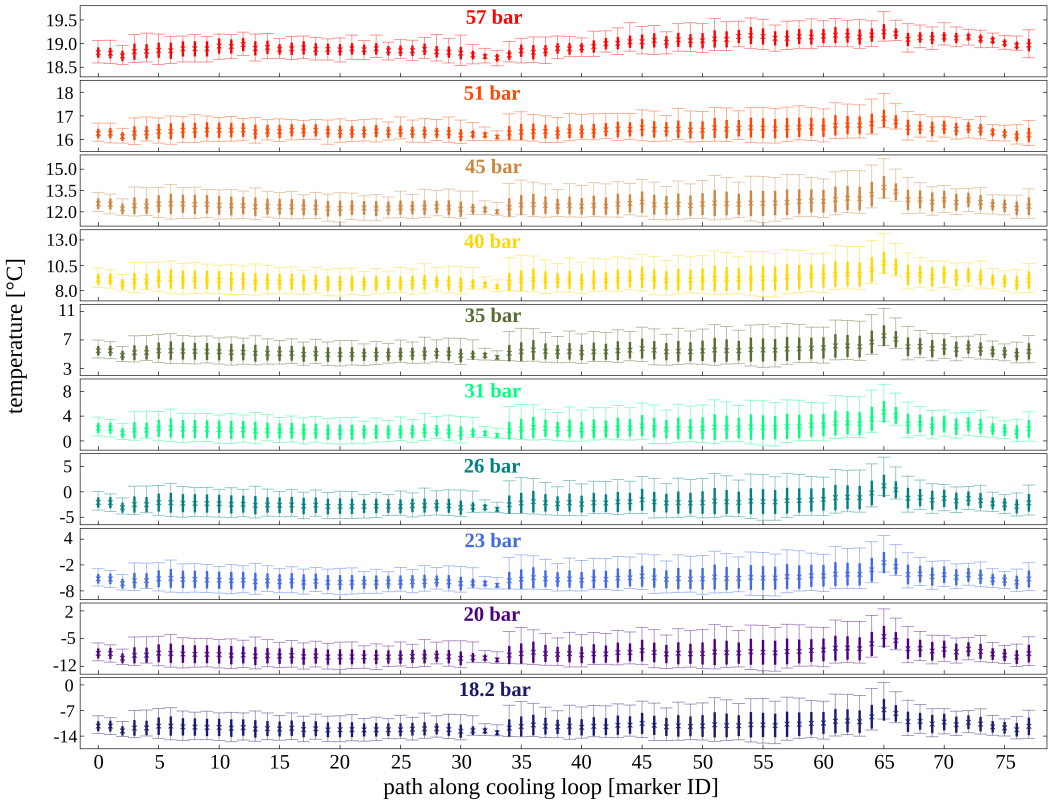

Figure A.4: Measured IR temperature distributions along the cooling loop for the back side of core 04 evaluated between CO_2 pressure set points of 57 to 20 bar.

Moreover, the analysis of the minimum temperature along the cooling loop and the difference to the measured CO_2 coolant temperatures at the core's in- and outlet are shown in Figure A.5 for the different tested set points with the back side of core 04.

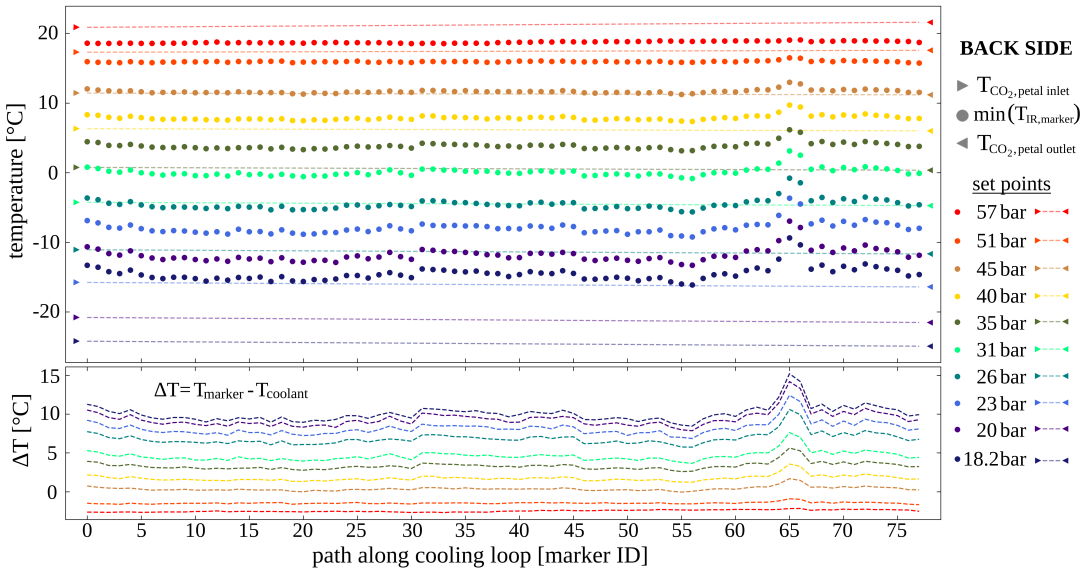

Figure A.5: Comparison of the minimum temperatures measured along the cooling loop and the measured CO_2 coolant temperature at the core's in- and outlet for the back side of core 04 at different CO_2 pressure set points. The absolute difference as $\Delta T = T_{\text{marker}} - T_{\text{coolant}}$ is shown as well.

The detected delamination in the region of marker IDs between 60 and 70 is clearly visible with higher minimal temperature values for these markers as well as a larger ΔT to the CO_2 coolant temperature. In general, larger temperature differences between the measured IR temperatures on the petal surface to the coolant temperature are observed, compared to e.g. core 02, most probably caused by the different petal core surface.

Cores with cocured bus tapes

The thermal performance of the petal core prototypes 07 and 08 with cocured bus tapes is evaluated by measuring the IR temperatures for line markers along the cooling loop and for area markers of the module areas.

The temperature distributions in the module areas is compared between core 07 and 08 for the front and back sides in Figure A.6.

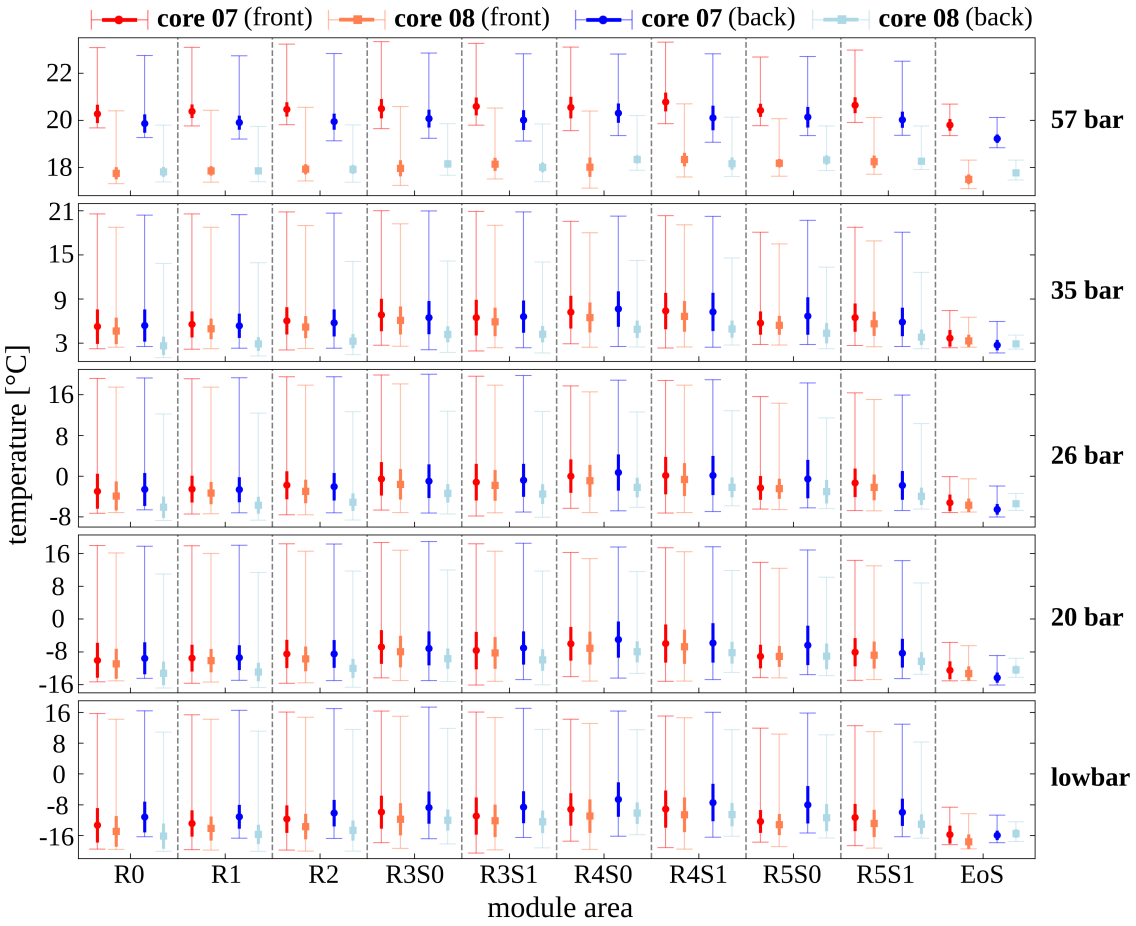

Figure A.6: Comparison of the temperature distribution on the module areas for the front and back side of core 07 and 08. Evaluated are all tested CO_2 pressure set points of 57, 35, 26, 20 bar and the lowest reached set point.

Here, in most cases a similar thermal performances for the front sides are observed, whereas larger differences are observed for the back sides due the previously discussed inverted measurement cycle for core 08, resulting in constantly lower temperatures. Moreover, the delamination defect in the EoS region for the back side of core 08 can be identified by the comparing the temperature distributions.

In the same way, the thermal performances evaluated for the temperature distributions along the cooling loop for both cores and for all tested CO_2 pressure set points are analysed in Figure A.7a and Figure A.7b for the front and back sides, respectively.

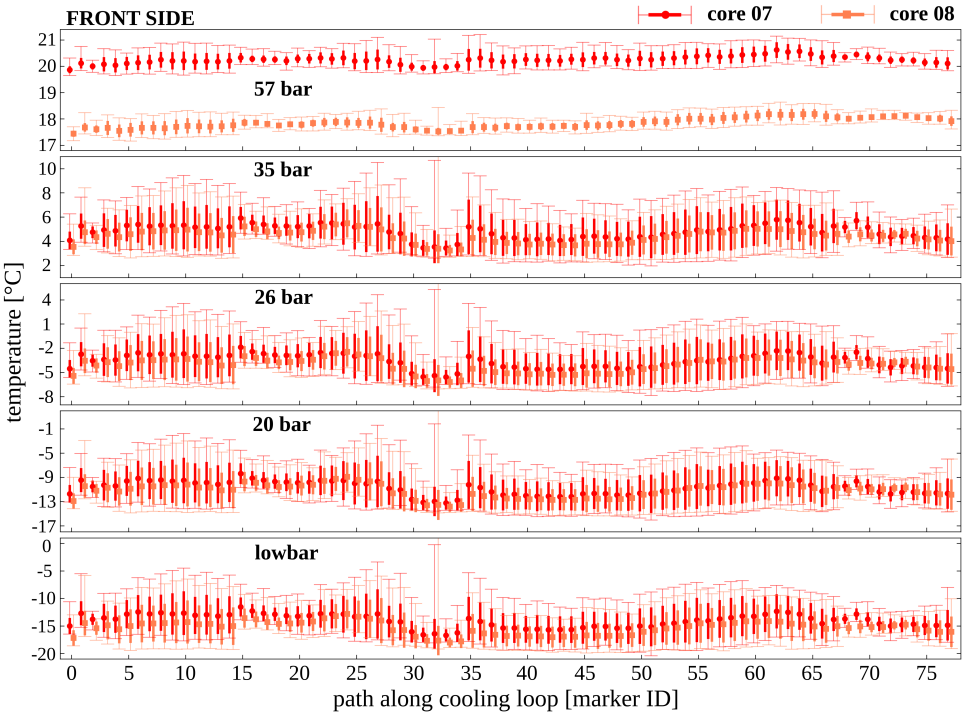

(a) Comparison of the temperature distribution along the cooling loop for the front side.

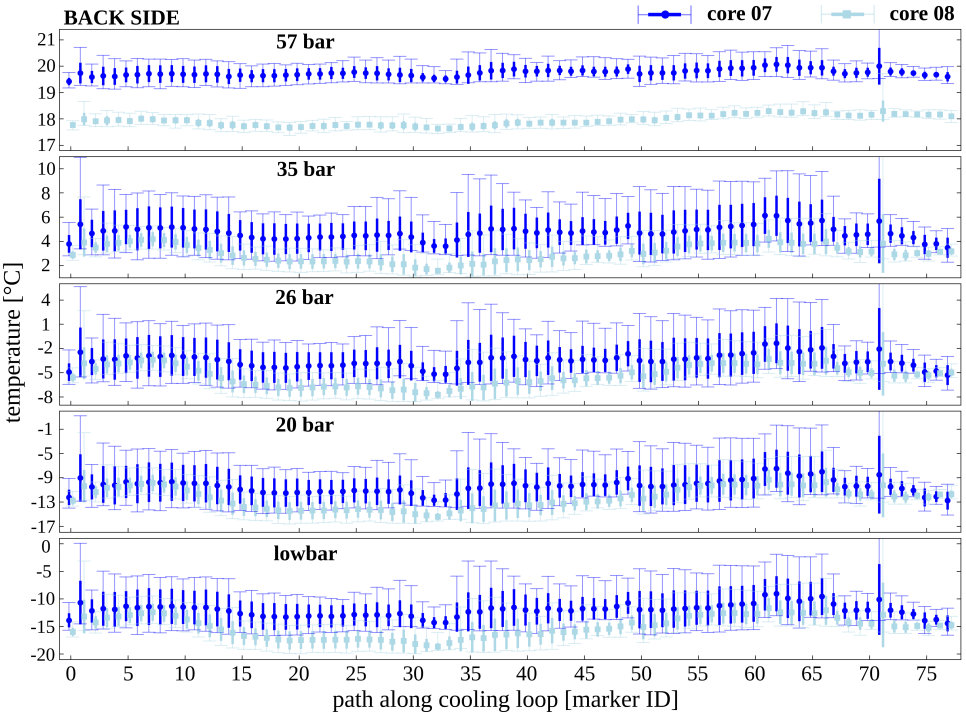

(b) Comparison of the temperature distribution along the cooling loop for the front side.

Figure A.7: Comparison of the temperature distribution along the cooling loop for the front and back side of core 07 and 08. Evaluated are all tested CO_2 pressure set points of 57, 35, 26, 20 bar and the lowest reached set point.

A.2 Thermal performance of the TM petal

The measured IR temperatures of the TM petal under nominal cooling conditions are shown in Figure A.8 for the defined marker areas of the individual silicon sensor pieces.

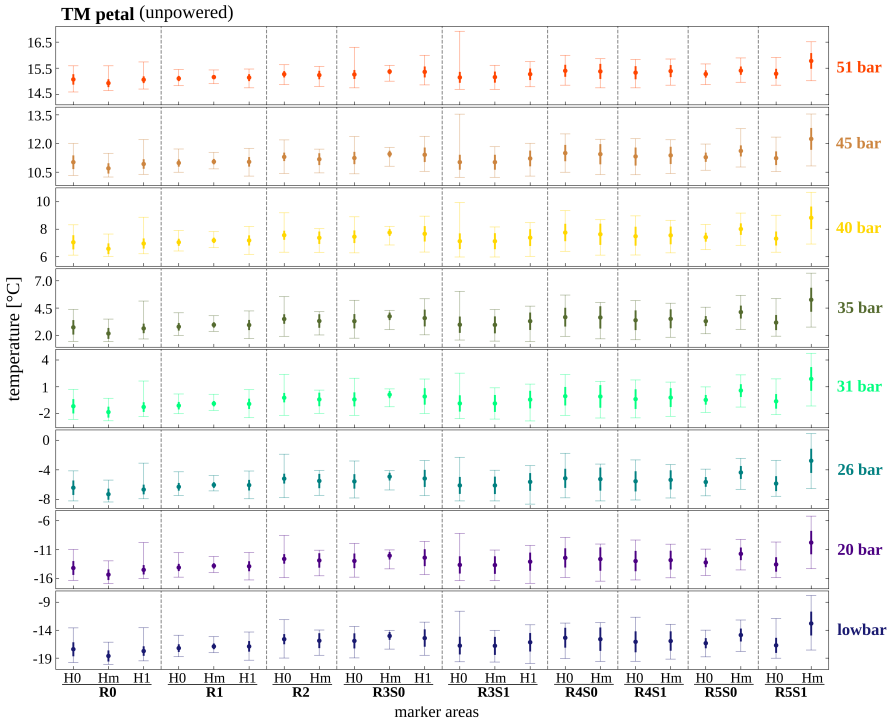

(a) Temperature distribution in the marker areas for the unpowered TM petal.

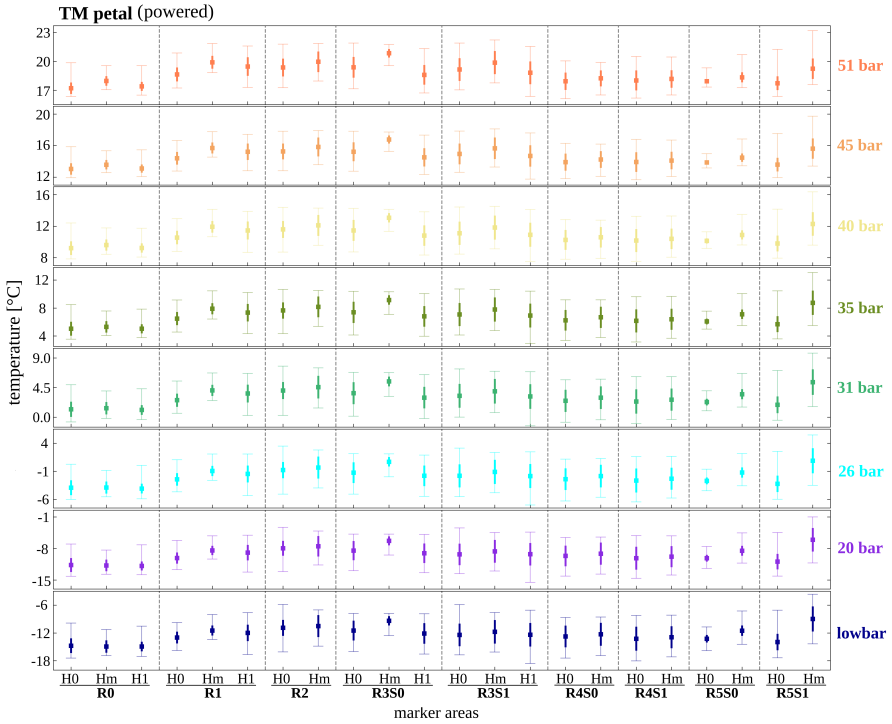

(b) Temperature distribution in the marker areas for the fully powered TM petal.

Figure A.8: Temperature distributions for the individual marker areas on the TM petal, evaluated for all tested CO_2 pressure set points between 51 and 18.1 bar.

Here, the different tested CO_2 pressure set points between 51 and 18.1 bar are evaluated for the case of the unpowered and powered TM petal. The measured temperature of the area marker for R5S1Hm shows in nearly all investigated cases the highest values compared to the other silicon areas, indicating the need for an improved routing of the cooling loop to allow a better thermal contact in this region of the petal.

The direct comparison of the temperatures between the unpowered and powered state of the TM petal is depicted in Figure A.9. Here, the temperature distributions in the merged silicon sensor areas are evaluated for all CO_2 pressure set points.

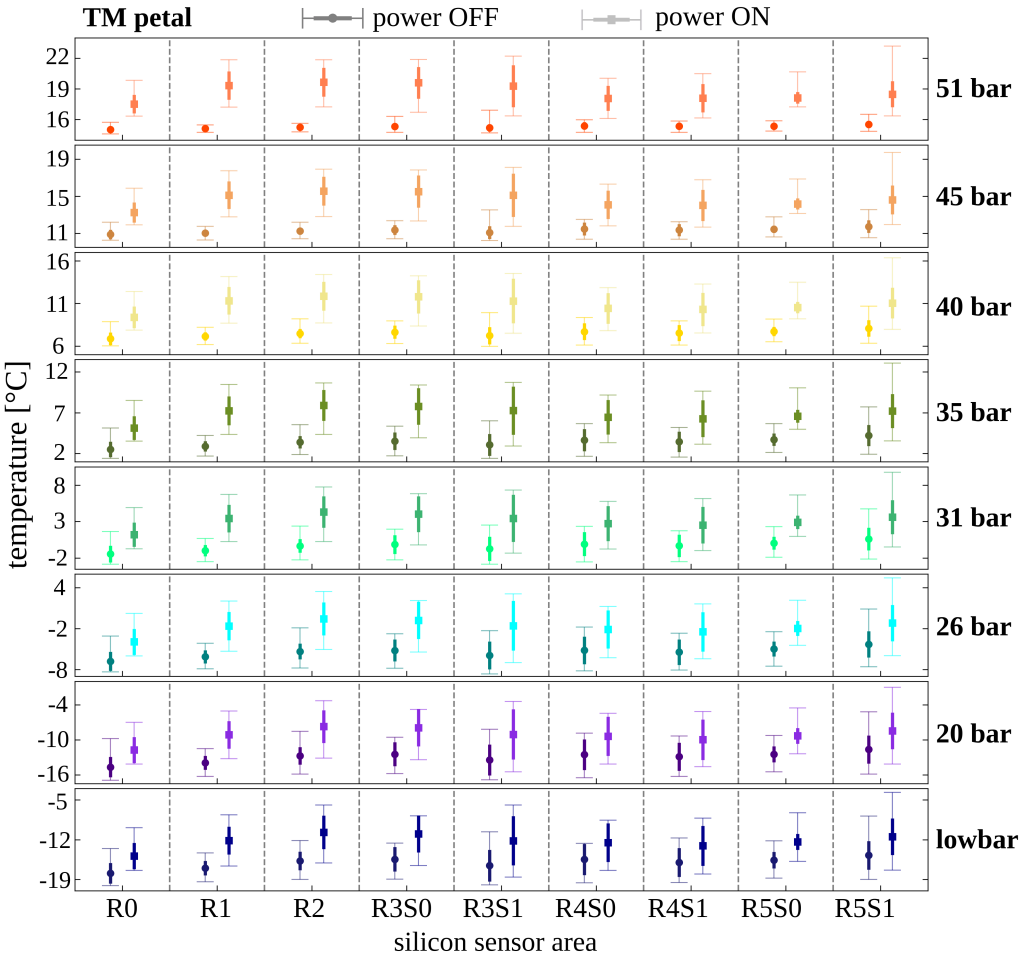

Figure A.9: Comparison of the silicon temperature on the sensor areas for the unpowered and powered state of the TM petal. Evaluated are all tested CO_2 pressure set points between 51 and 18.1 bar.

For all CO_2 pressure set points, a relatively equal increase in temperature for all silicon sensor areas is observed when powering the active electronics on the corresponding dummy silicon modules. The presented data here served as the input for the detailed analysis of the individual temperatures on the the silicon sensor areas for the different tested set points, as it was shown in Figure 6.50b.

Finally, the comparison of the thermal performance for different CO_2 mass flows of 1.3 and 2.5 g/s is shown in Figure A.10. Evaluated are again all tested CO_2 pressure set points for the unpowered and powered state of the TM petal.

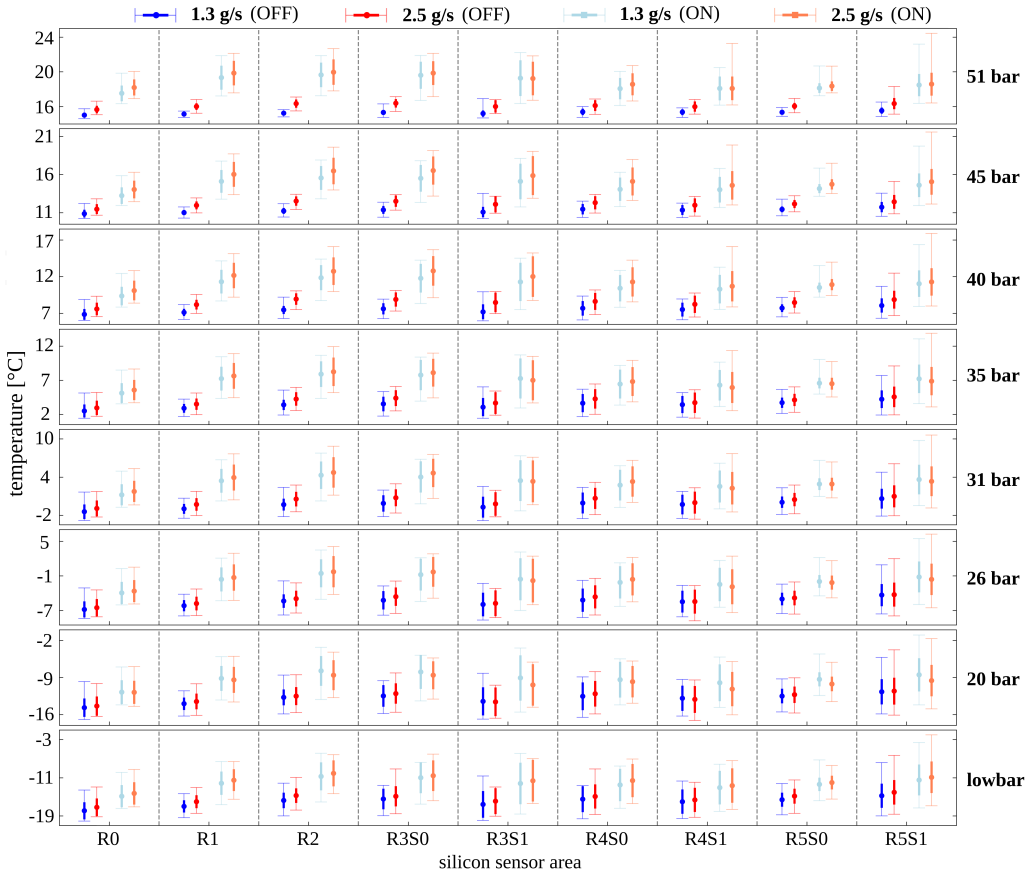

Figure A.10: Temperature distributions on the silicon sensor areas comparing the effect of two different CO_2 mass flows of 1.3 and 2.5 g/s. Shown are the results for the unpowered and powered state of the TM petal at all tested CO_2 pressure set points between 51 and 18.1 bar.

Here, in almost all cases a very good agreement between the temperature distributions for the two tested mass flows is observed, also independent of the powering state of the TM petal. This indicates, as discussed before, that the nominal CO_2 mass flow of 1.3 g/s seems to be sufficient for the cooling of the fully powered petal.

A.3 Calculation of the local flatness

For the calculation of the local flatness according to ISO/TS 12781-1 [183], the method of the least squares reference plane (LSPL) is used to assess the flatness deviation of the petal core's surface. The step-by-step procedure [184] can be described as following:

1. **Definition of measurement points**
   The points on the test object's surface are measured relative to a given measurement reference with coordinates X_i, Y_i, Z_i and the z-axis is defined perpendicular to the plane to be measured.

2. **Definition of new origin**
   A new point of origin $O = (\bar{X}, \bar{Y}, \bar{Z})$ for a new reference system is defined with

$$\bar{X} = \frac{1}{n}\sum_i X_i, \qquad \bar{Y} = \frac{1}{n}\sum_i Y_i, \qquad \bar{Z} = \frac{1}{n}\sum_i Z_i. \tag{A.1}$$

3. **Measurement points in new reference system**
   The coordinates of the individual measuring points are determined for the new reference coordinate system with the previously defined origin O with

$$x_i = X_i - \bar{X}, \qquad y_i = Y_i - \bar{Y}, \qquad z_i = Z_i - \bar{Z}. \tag{A.2}$$

4. **Definition of the LSPL**
   The least squares reference plane is passing through the new point of origin and is defined by the equation $z = a \cdot x + b \cdot y$. Assuming the deviations measurement to be performed in the z direction, the parameters a and b can be estimated from the measurement points with

$$\hat{a} = \frac{\sum y_i^2 \cdot \sum z_i x_i - \sum x_i y_i \cdot \sum z_i y_i}{\sum x_i^2 \cdot \sum y_i^2 - \left(\sum x_i y_i\right)^2}, \quad \hat{b} = \frac{\sum x_i^2 \cdot \sum z_i y_i - \sum x_i y_i \cdot \sum z_i x_i}{\sum x_i^2 \cdot \sum y_i^2 - \left(\sum x_i y_i\right)^2}. \tag{A.3}$$

5. **Deviations to the LSPL**
   The individual deviations e_i between the measured points on the surface and the constructed least squares reference plane are calculated as

$$e_i = \frac{z_i - \hat{a} \cdot x_i - \hat{b} \cdot y_i}{\sqrt{\hat{a}^2 + \hat{b}^2 + 1}}. \tag{A.4}$$

6. **Local flatness deviation**
   The local flatness deviation of the surface relative to the LSPL can be defined as peak-to-valley flatness deviation, FLT_t, with

$$FLT_t = FLT_P - FLT_V = |e^+_{\max}| + |e^-_{\max}|. \tag{A.5}$$

   with maximum value of the positive local flatness deviation, FLT_P, and the maximum absolute value of the negative local flatness deviation, FLT_V.

B Investigations on Dual-Phase CO_2 Cooling

B.1 CO_2 orientation study

The evaluation of the CO_2 orientation study with the TM petal for all the tested CO_2 pressure set points between 51 and 20 bar is shown in Figure B.1.

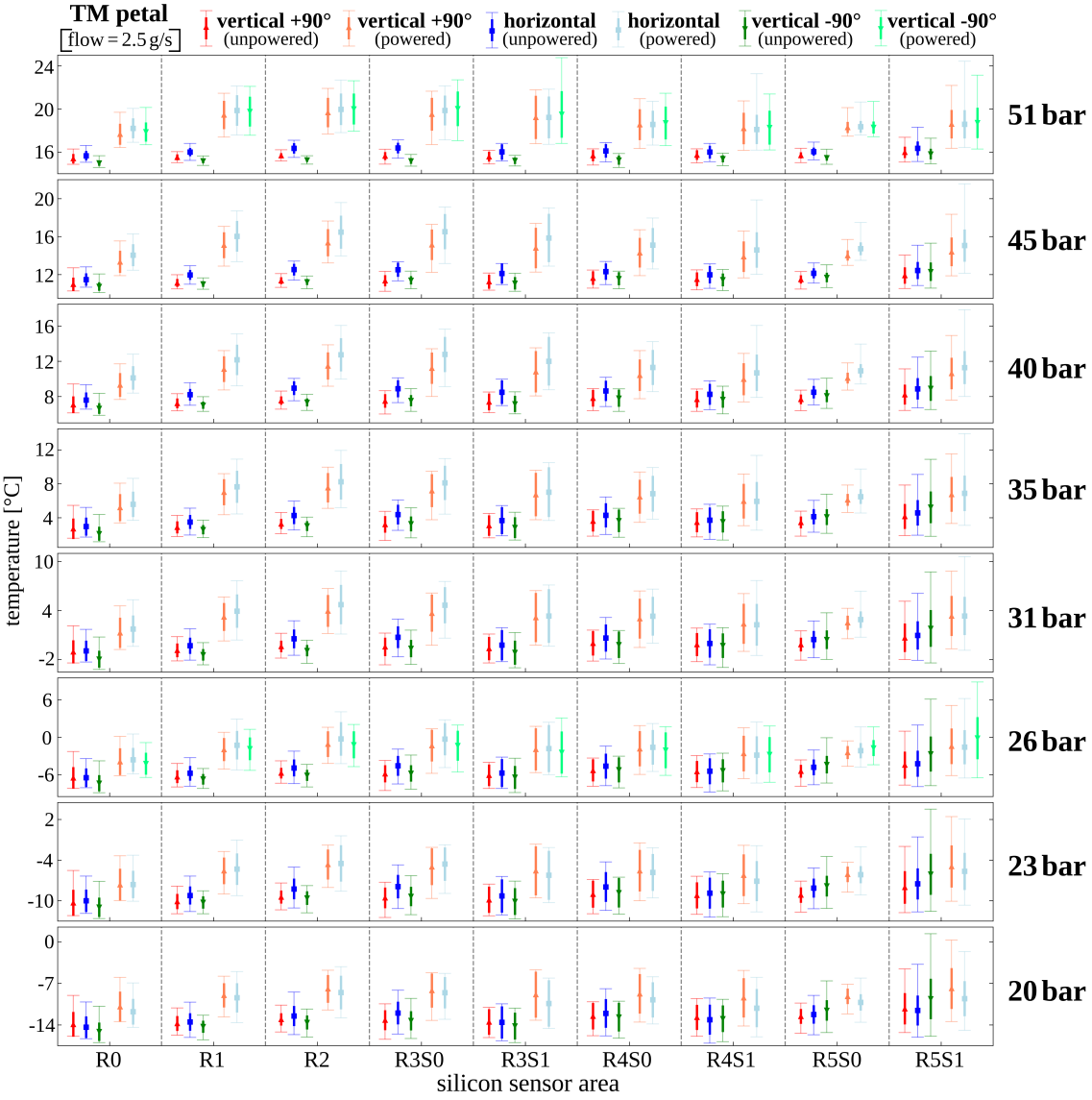

Figure B.1: Comparison of the temperature distribution on the silicon sensor areas for the unpowered and powered TM petal in three different orientations. Evaluated are all tested CO_2 pressure set points of 57, 45, 40, 35, 31, 26, 23 and 20 bar.

For the interpretation of the comparison at the individual set points, the logged CO_2 data in terms of the measured values of pressure, temperature and mass flow have to be taken into account. But overall, the previous interpretation is valid also for the other tested CO_2 pressure set points, indicating no major difference for the different tested orientations.

In Figure B.2, the corresponding thermograms for the TM petal in the *vertical +90°*, *horizontal* and *vertical -90°* orientation are shown for the individually reached lowest CO_2 pressure set points, comparing the unpowered and powered state.

Also here, no significant differences, e.g. occuring hot spots, are observed in a qualitative comparison of the different tested orientations.

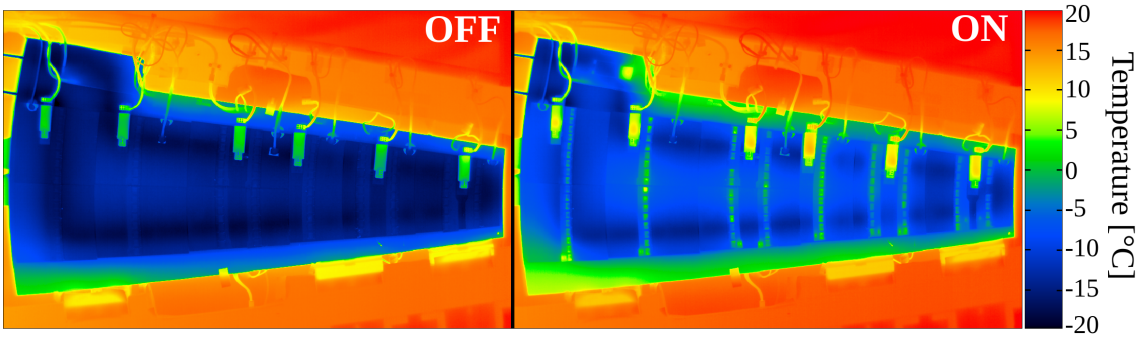

(a) Vertical +90° orientation.

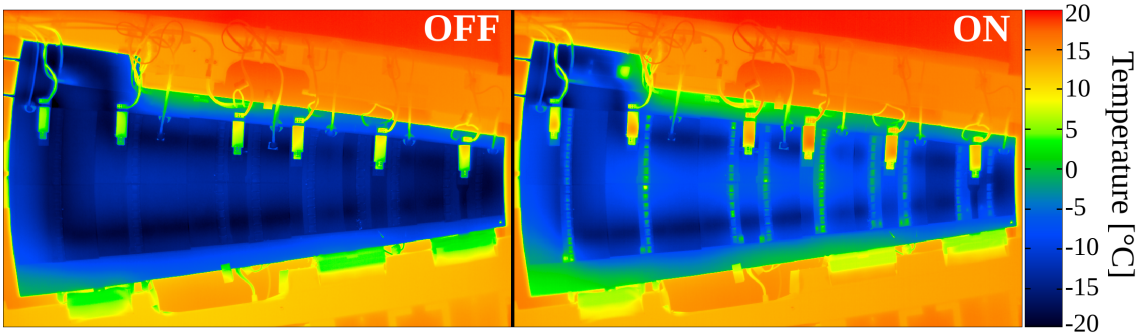

(b) Horizontal orientation.

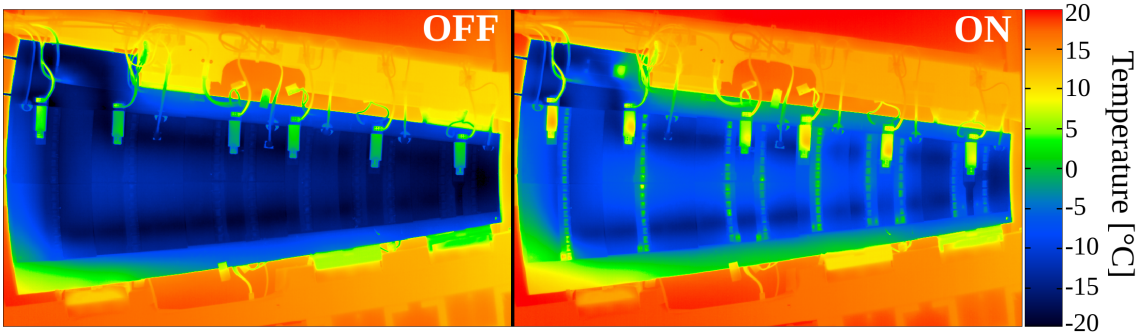

(c) Vertical -90° orientation.

Figure B.2: Thermograms of the TM petal in the three different tested orientations for the unpowered and powered state. Evaluated is the individually reached lowest CO_2 pressure set point around 18.6 bar.

B.2 CO_2 pressure drop study

The dependence of the pressure drop over the petal's cooling loop was also investigated for the powered state of the TM petal.
Figure B.3 shows the measured pressure drop for two different CO_2 mass flows with 1.3 and 2.5 g/s, analogous to Figure 7.11 of the unpowered case.

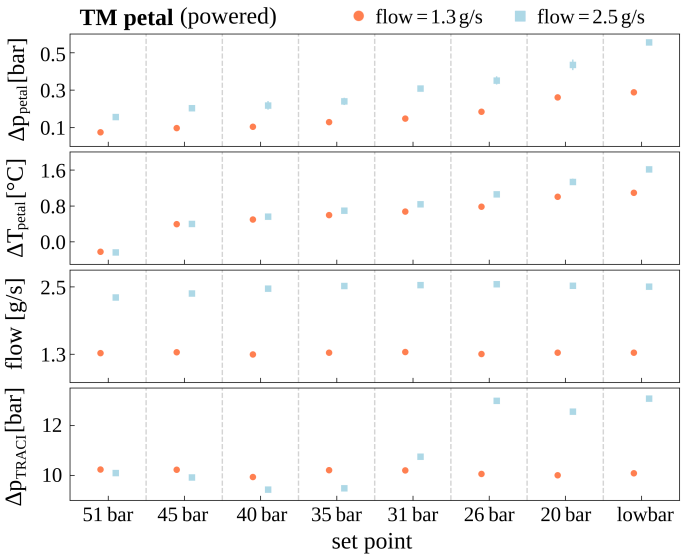

Figure B.3: Analysis of the dependence of the pressure and temperature drop on the CO_2 mass flow. Compared are the results for mass flows of 1.3 and 2.5 g/s evaluated at the different tested CO_2 pressure set points for the TM petal in the powered state.

The possible dependence on the flow orientation using the measurement of the powered TM petal in three different orientations, *vertical +90°*, *horizontal* and *vertical -90°*, is analysed in Figure B.4, which can be compared to the result of the unpowered TM petal as shown in Figure 7.12.

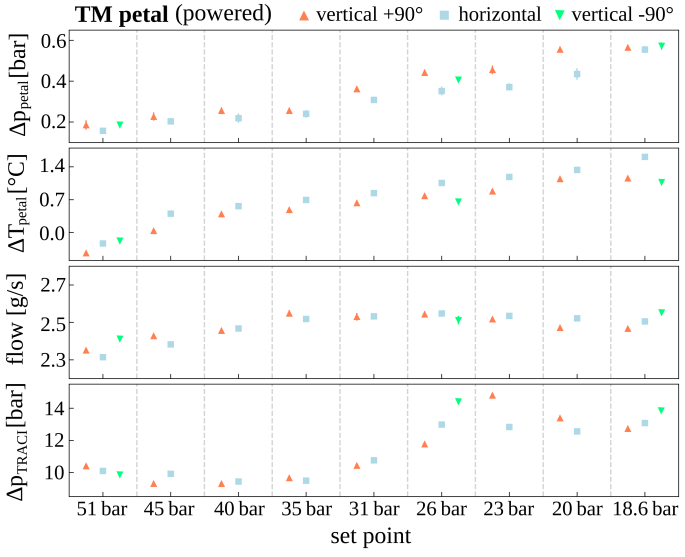

Figure B.4: Analysis of the dependence of the pressure and temperature drop on the flow orientation. Compared are the results for the *vertical +90°*, *horizontal* and *vertical -90°* orientation evaluated at the different tested CO_2 pressure set points for the TM petal in the powered state with a mass flow of 2.5 g/s.

The interpretation is the same as for the previously investigated case of the unpowered TM petal: a higher CO_2 mass flow results in a higher pressure drop over the cooling loop, whereas no significant difference in the measured pressure drops for the three different orientation is observed.

B.3 Heat transfer by free convection

The convective heat flow on the petal originating from the ambient air in the thermal test setup is calculated by the model of free convection on a vertical wall, according to [192]. Free convection is caused by a temperature difference ΔT in the flowing medium, in this case the temperature difference between the ambient air volume in the PTM, T_{ambient} and the surface temperature on the petal, T_{petal} with

$$\Delta \mathrm{T} = |T_{\text{petal}} - T_{\text{ambient}}|. \tag{B.1}$$

The total heat flow $\dot{Q}$ between the air volume and the petal is a function of the temperature difference and is calculated for a homogeneous surface temperature distribution as

$$\dot{Q} = \alpha \cdot A \cdot \Delta \mathrm{T}, \tag{B.2}$$

with α as the heat transfer coefficient and A as the surface area of the object.
In the case of free convection, the heat transfer coefficient depends on a number of thermodynamical key parameters of the considered flowing medium.
Under the assumption of a stationary flow and using the Boussinesq approximation[67], the heat transfer coefficient has the following functional dependence:

$$\alpha = \alpha \left(\rho, \nu, \kappa, \beta, \lambda, L, \Delta \mathrm{T}, g\right). \tag{B.3}$$

Here, the parameters are the density ρ, the kinematic viscosity ν, the thermal diffusivity κ, the isobaric coefficient of thermal expansion β, the thermal conductivity λ, the characteristic length L, the temperature difference ΔT and the gravitational acceleration g. For the calculation, the parameters of the flowing medium are evaluated at a reference temperature

$$T_* = \frac{1}{2}\left(T_{\text{petal}} + T_{\text{ambient}}\right). \tag{B.4}$$

In the next step, the dimensionless key numbers used in fluid dynamics with the *Grashof number* Gr, the *Prandtl number* Pr and the *Rayleigh number* Ra are calculated as

$$Gr = \frac{g \cdot L^3 \cdot \beta(T_{\text{ambient}}) \cdot \Delta \mathrm{T}}{\nu(T_*)^2}, \quad Pr = \frac{\nu(T_*)}{\kappa(T_*)}, \quad Ra = Gr \cdot Pr. \tag{B.5}$$

The *Nusselt number* Nu describes the dimensionless heat transfer coefficient and for the case of a vertical wall with the height as the characteristic length L and laminar or turbulent flows, the following relation holds:

$$Nu = \left(0.825 + 0.387 \cdot \left[Ra \cdot f_1(Pr)\right]^{\frac{1}{6}}\right)^2. \tag{B.6}$$

Here, the function $f_1(Pr)$ considers the influence of the Prandtl number over the range of $0.001 < Pr < \infty$ with

$$f_1(Pr) = \left[1 + \left(\frac{0.492}{Pr}\right)^{\frac{9}{16}}\right]^{\frac{-16}{9}}. \tag{B.7}$$

In the last step, the heat transfer coefficient α is determined as

$$\alpha = \frac{Nu \cdot \lambda(T_*)}{L} \tag{B.8}$$

and can be inserted in Eq. B.2 to calculate the convective heat flow.

[67] In the Boussinesq approximation, valid for small temperature differences between the medium and the object relative to a reference temperature, the temperature dependencies of the thermodynamical parameters of the medium are ignored in the Navier-Stokes equation.

When performing thermal tests inside the PTM, the input parameters for the calculation of the convective heat transfer on the petal are as following:

- the characteristic length is $L_{\text{petal}} = 0.2\,\text{m}$;
- the surface area is $A_{\text{petal}} = 0.236\,\text{m}^2$;
- the surface temperature on the petal is extracted as the average temperature from the IR measurement with $T_{\text{petal}} = \frac{1}{n}\sum_i T_{\text{IR}}^i$;
- the ambient temperature is the average air temperature inside the PTM logged by the SHT21 sensors with $T_{\text{ambient}} = T_{\text{air}}$.

As an example, the calculation steps for a measured surface temperature of $T_{\text{petal}} = -20\,^\circ\text{C}$ and an ambient temperature of $T_{\text{ambient}} = 20\,^\circ\text{C}$ is shown in the following:

1. Calculate temperature difference and reference temperature:

$$\Delta\text{T} = |-20\,^\circ\text{C} - 20\,^\circ\text{C}| = 40\,^\circ\text{C} = 314\,\text{K}$$
$$T_* = \frac{1}{2}\left(-20\,^\circ\text{C} + 20\,^\circ\text{C}\right) = 0\,^\circ\text{C} = 273\,\text{K}$$

2. Determine thermodynamical key parameters for dry air at the relevant temperature:

$$\lambda_{\text{air}}(273\,\text{K}) = 0.0244\,\frac{\text{W}}{\text{m}\cdot\text{K}}$$
$$\beta_{\text{air}}(314\,\text{K}) = 0.0034\,\text{K}^{-1}$$
$$\nu_{\text{air}}(273\,\text{K}) = \frac{\nu^{\text{dyn}}}{\rho} = \frac{1.72\cdot 10^{-5}\,\text{Pa}\cdot\text{s}}{1.72\,\frac{\text{kg}}{\text{m}^3}} = 1.33\cdot 10^{-5}\,\frac{\text{m}^2}{\text{s}}$$

3. Calculate the dimensionless key numbers of Gr, Pr and Ra:

$$Gr = \frac{9.81\,\frac{\text{m}}{\text{s}^2}\cdot(0.2\,\text{m})^3\cdot 0.0034\,\text{K}^{-1}\cdot 314\,\text{K}}{\left(1.33\cdot 10^{-5}\,\frac{\text{m}^2}{\text{s}}\right)^2} = 0.61\cdot 10^8$$
$$Pr = 0.711$$
$$Ra = 0.61\cdot 10^8\cdot 0.711 = 0.43\cdot 10^8$$

4. Determine Nu for the scenario of a heat transfer on a vertical wall:

$$f_1(0.711) = \left[1 + \left(\frac{0.492}{0.711}\right)^{\frac{9}{16}}\right]^{\frac{-16}{9}} = 0.35$$
$$Nu = \left(0.825 + 0.387\cdot\left[0.43\cdot 10^8\cdot 0.35\right]^{\frac{1}{6}}\right)^2 = 47.6$$

5. Calculate the heat transfer coefficient α:

$$\alpha = \frac{47.6\cdot 0.0244\,\frac{\text{W}}{\text{m}\cdot\text{K}}}{0.2\,\text{m}} = 5.80\,\frac{\text{W}}{\text{m}^2\cdot\text{K}}$$

6. Determine the convective heat flow on the petal:

$$\dot{Q} = 5.80\,\frac{\text{W}}{\text{m}^2\cdot\text{K}}\cdot 0.236\,\text{m}^2\cdot 314\,\text{K} = 54.7\,\text{W}$$

B.4 Estimation of the vapour quality by sightglass analysis

For the visual inspection of the sightglasses, the fill levels of liquid CO_2 in the sightglasses at the in- and outlet of the petal's cooling loop are observed for the corresponding measurement points and manually recorded as percentage values.

In the first step of the calculation, the fill level x_{level} in percentage is translated into the fraction x_{vol} between vapour and liquid relative to the volume. Here, the geometry of the vapour filled part of the sightglass with diameter D is estimated in one dimension as an arc segment with the shown geometry in Figure B.5.

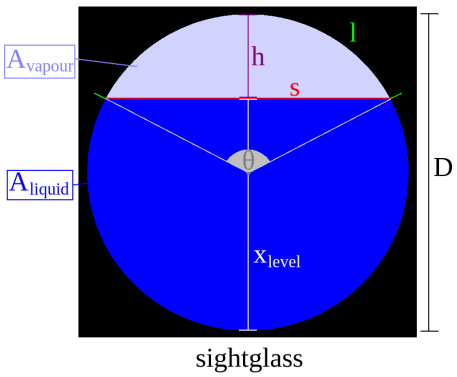

Figure B.5: Geometry of the sightglass with diameter D filled with liquid and gaseous CO_2 with an observed fill level of x_{level}. For the volumetric fraction of vapour and liquid, the area filled with vapour, A_{vapour}, is calculated relative to the total area of the sightglass. Here, the corresponding arc segment is characterized by the height h, the central angle θ, the chord length s and the arc length l.

The height h of the arc segment filled with vapour is calculated from the given fill level of the liquid phase, x_{level}, with

$$h = D \cdot (1 - x_{\text{level}}). \tag{B.9}$$

The surface area filled with vapour, A_{vapour}, is given by

$$A_{\text{vapour}} = \frac{r \cdot l}{2} - \frac{s \cdot (r - h)}{2}, \tag{B.10}$$

using the following relations for an arc segment with radius $r = D/2$:

$$\theta = 2 \cdot \arccos\left(1 - \frac{h}{r}\right)$$
$$l = r \cdot \theta$$
$$s = 2 \cdot \sqrt{2 \cdot r \cdot h - h^2}.$$

The volumetric fraction between vapour and liquid is finally calculated as the vapour filled part of the sightglass relative to the full surface area of the sightglass with

$$x_{\text{vol}} = \frac{A_{\text{vapour}}}{A_{\text{sightglass}}}, \tag{B.11}$$

where $A_{\text{sightglass}} = \pi \cdot r^2$.

In the second step, the fraction x_{mass} between vapour and liquid is evaluated relative to the mass, corresponding by convention to the CO_2 vapour quality x. With the previously calculated values of x_{vol}, the values relative to the mass are calculated as

$$x_{\text{mass}} = \frac{x_{\text{vol}} \cdot \rho_{\text{vapour}}}{x_{\text{vol}} \cdot \rho_{\text{vapour}} + (1 - x_{\text{vol}}) \cdot \rho_{\text{liquid}}}, \tag{B.12}$$

with the densities ρ_{vapour} and ρ_{liquid} of the CO_2 in the gaseous and liquid phase, respectively.

As the CO_2 density is changing with the pressure, the density values corresponding to the tested CO_2 pressure set points for the sightglass analysis are shown in Figure B.6.

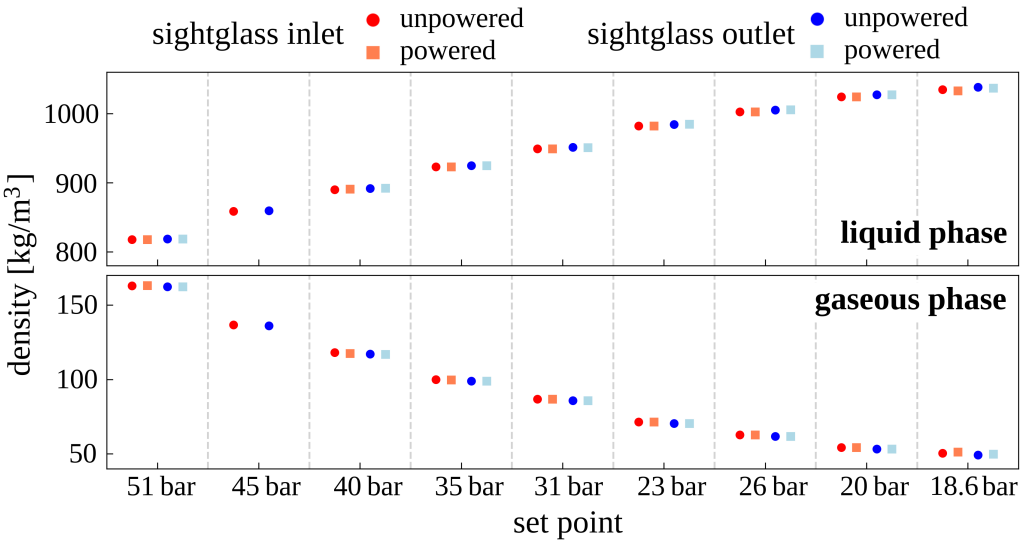

Figure B.6: Density of CO_2 for the liquid (top) and gaseous (bottom) phase corresponding to the different tested CO_2 pressure set points in the sightglass analysis.

B.5 Calculations for the CO_2 state analysis of the TM petal

For the analysis of the CO_2 state inside the cooling loop of the TM petal, the heat load corresponding to each tested set point has to be calculated.
On the one hand, the heat transfer $\dot{Q}_{\text{conv}}$ by convection with the ambient air in the test setup is taken into account, using the calculation described in Appendix B.3. The input for the calculation of $\dot{Q}_{\text{conv}}$ is the ambient temperature as the averaged air temperature, T_{ambient}, logged with the SHT sensors in the PTM and the surface temperature on the petal as the mean value of the extracted IR temperature values on the silicon areas, T_{petal}. The uncertainty on the heat transfer is determined by systematic variation of the input parameters and their uncertainties.
Moreover, the corresponding enthalpy h_{conv} for the convective heat transfer is calculated as

$$h_{\text{conv}} = \frac{\dot{Q}_{\text{conv}}}{\dot{m}} \tag{B.13}$$

with the CO_2 mass flow rate $\dot{m}$.

Figure B.7 shows the determined values of $\dot{Q}_{\text{conv}}$ and h_{conv} together with the relevant input parameters (temperature of the ambient air and on the petal as well as the CO_2 mass flow) for the individually tested CO_2 pressure set points of the unpowered and powered TM petal measurement used in the CO_2 state analysis.

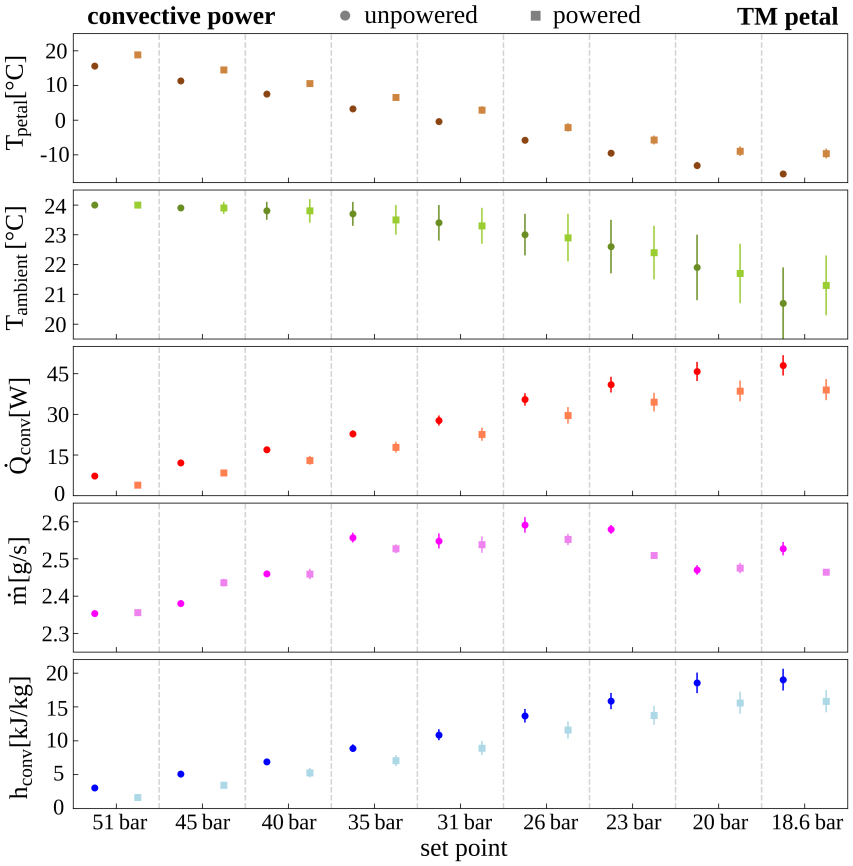

Figure B.7: Calculation of the convective heat transfer $\dot{Q}_{\text{conv}}$ and the corresponding enthalpy h_{conv} using the measured input parameters of ambient air temperature, T_{ambient}, the petal surface temperature, T_{petal}, and the CO_2 mass flow rate, $\dot{m}$. Evaluated are the different tested CO_2 pressure set points for the TM petal measurement in the unpowered and powered state.

On the other hand, the heat load of the TM petal in the powered state with a constant power of $Q_{\text{load}} = 54\,\text{W}$ by the dummy silicon modules is considered and the corresponding enthalpy h_{load} is determined similar to Eq. B.13.

C Material Budget Imaging

C.1 Analytical calculation of radiation length

For the analytical calculation of the radiation length X_0 of an element with charge number Z and mass number A, the parametrization according to Y. Tsai [255], as it was shown in Eq. 9.5, can be used:

$$\frac{1}{X_0} = 4\alpha r_e^2 \frac{N_A}{A} \left(Z^2 (L_{\text{rad}} - f(Z)) + Z L'_{\text{rad}} \right). \tag{C.1}$$

Here, r_e is the classical electron radius and N_A is Avogadro's number. The functions L_{rad} and L'_{rad} depends on the type of the investigated element and can be parametrized for $Z > 4$ as

$$L_{\text{rad}} = \ln\left(184.15 \cdot Z^{-1/3}\right) \quad \text{and} \quad L'_{\text{rad}} = \ln\left(1194 \cdot Z^{-2/3}\right). \tag{C.2}$$

Finally, the function $f(Z)$ is an infinite sum, which can be approximated for elements up to $Z = 92$ and using the substitution $a = \alpha Z$ as

$$f(Z) = a^2 \left[(1 + a^2)^{-1} + 0.20206 - 0.0369 \cdot a^2 + 0.0083 \cdot a^4 - 0.002 \cdot a^6 \right]. \tag{C.3}$$

In the following, a often used and more handy parametrization of the analytical expression [257] is used as

$$X_0 = \frac{716.4\,\text{g/cm}^2 \cdot A[\text{g/mol}]}{Z(Z+1)\ln\frac{287}{\sqrt{Z}}}. \tag{C.4}$$

In Table C.1, the analytical radiation length values are calculated for a number of elements and compared to the tabulated values from the PDG [256], based on experimental data.

element	Z	A [g/mol]	$X_0^{\text{analytical}}$ [g/cm^2]	$X_0^{\text{experimental}}$ [g/cm^2]	rel. error [%]
Al	13	26.9815385	24.27	24.01	1.1
Si	14	28.0855	22.08	21.82	1.2
Ti	22	47.867	16.47	16.16	1.9
Fe	26	55.845	14.14	13.84	2.2
Ni	28	58.6934	12.97	12.68	2.3
Cu	29	63.546	13.16	12.86	2.3
Sn	50	118.710	9.01	8.82	2.1
W	74	183.84	6.77	6.76	0.1

Table C.1: Comparison of analytical radiation length values versus experimental data tabulated by the PDG [256] for a selection of elements. Shown is also the relative difference between the calculated and tabulated value.

The relative difference between the analytical calculated radiation length and the experimental determined X_0 value is up to 2%. For the analysis in this work, the experimental data is taken as the reference values in the investigations.

C.2 Determination of the fiducial area

The fiducial area for the MBI analysis is selected to exclude effects reconstructed at the edge of detection area. These are on the one hand caused by an acceptance effect for the tracks close to the edges, which results in a biased scattering distribution. On the other hand, the scattering on the aluminum cut-out of the MIMOSA26 sensors is observed, as it is shown in Figure C.1 for a run with an empty telescope (only air scattering) at a beam momentum of 4 GeV/c and evaluated for the combined kink angle k_{x+y}.

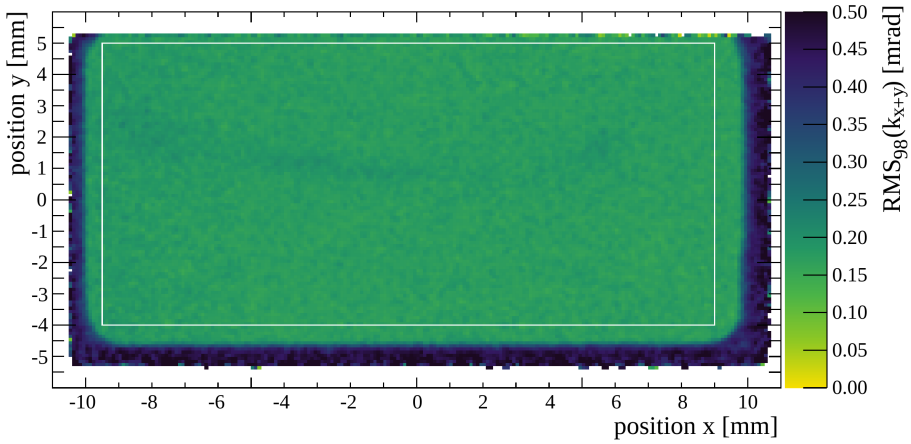

Figure C.1: Two-dimensional kink angle map for $\mathrm{RMS}_{98}(k_{x+y})$ resulting from an empty telescope measurement at a beam momentum of 4 GeV/c. The selected fiducial area is shown as a white rectangle.

In this case, the fiducial area was selected to be between $-9.5\,\mathrm{mm} < x < 9\,\mathrm{mm}$ and $-4\,\mathrm{mm} < y < 5\,\mathrm{mm}$ to exclude the edge effects clearly visible with larger kink angle widths.

The exact alignment of the probes between the telescope arms and matching with the active detection area of the MIMOSA26 sensors of roughly 2 cm × 1 cm is difficult and done manually. Therefore, it can happen that the holder for the sample is also in the active area, as it is shown in Figure C.2 for the homogeneous nickel sample of 0.1 mm thickness.

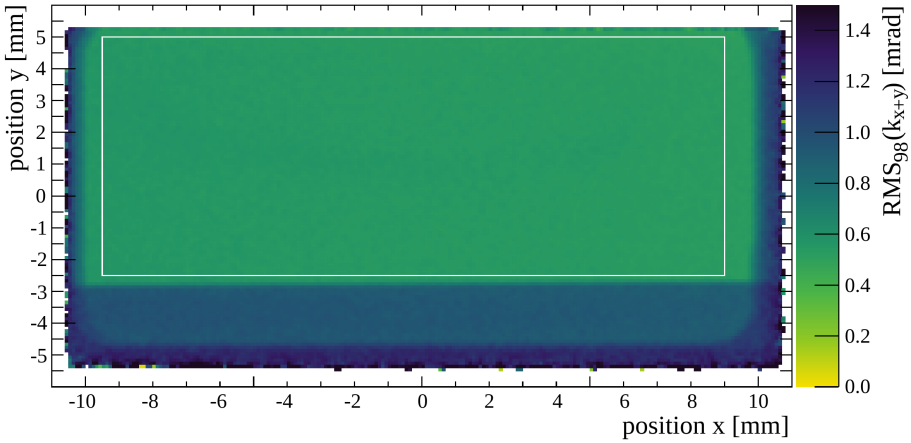

Figure C.2: Two-dimensional kink angle map of a 0.1 mm thick nickel samples at a beam momentum of 2 GeV/c. The kink angle width is shown as $\mathrm{RMS}_{98}(k_{x+y})$ and the selected fiducial area for this measurement is shown as a white rectangle.

In this case, the fiducial area was selected to be between $-9.5\,\text{mm} < x < 9\,\text{mm}$ and $-2.5\,\text{mm} < y < 5\,\text{mm}$ to exclude the influence of the holder, visible as an additional scattering effect at the lower edge.

Overall, the fiducial area was determined for the individual performed measurements within different test beam campaigns to allow for a maximum of detection area while excluding any biasing effects on the kink angles for the SUT.

C.3 Estimator of the kink angle mean value

The estimated mean values of the kink angle distribution using the statistical and fitting approach are compared in Figure C.3, separately for the inclusive and binned analysis. Here, the results for the scattering in aluminum samples with thicknesses of 0.5, 1.0, 2.0, 4,0 and 10.0 mm and a beam momentum of 2 GeV/c are shown.

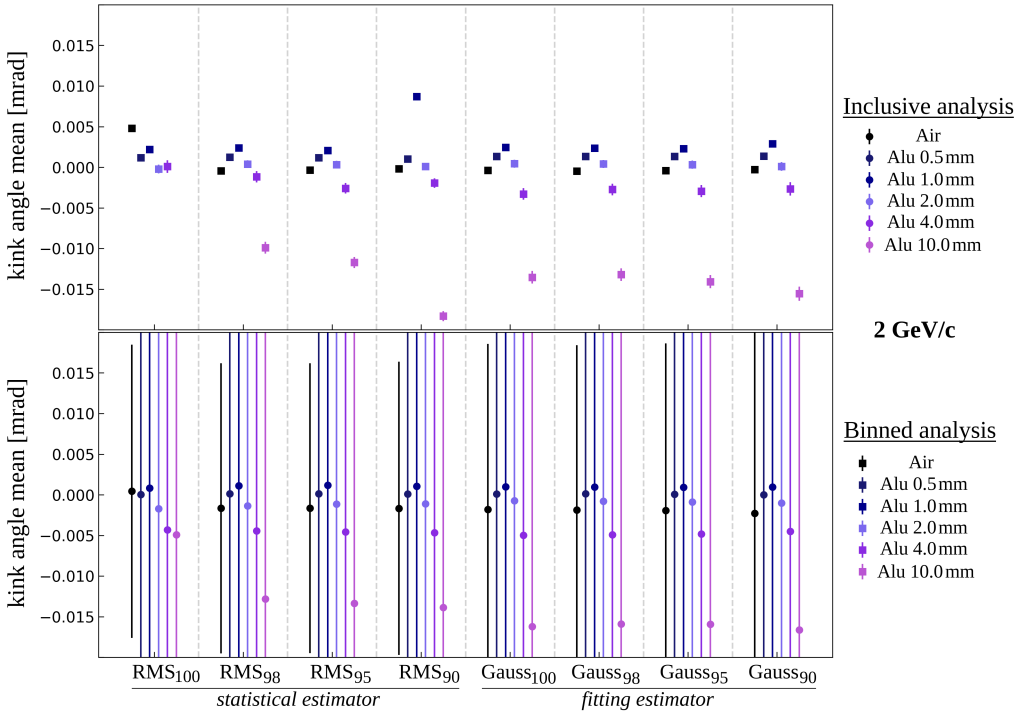

Figure C.3: Evaluation of the mean estimators for the kink angle using the statistical mean value and the fitted Gaussian mean value on different selected inner quantiles of 100%, 98%, 95% and 90% in the inclusive (top) and binned (bottom) analysis. A measurement of aluminum samples with thicknesses of 0.5, 1.0, 2.0, 4,0 and 10.0 mm for a beam momentum of 2 GeV/c is used.

The estimated mean values are all consistent with zero for the individual estimators and the inclusive and binned analysis. Only for the case of the 10.0 mm thick sample, a systematic offset is observed indicating already the non-Gaussian from of the distribution with the amount of scattering.

C.4 Energy dependence of MBI calibration

The determined fit parameters for the performed calibration fit using the model-dependent and the model-independent approach for the calibration curves measured at different beam momenta between 2 and 5 GeV/c are given in Table C.2.

Fit parameter	Beam momentum			
	2 GeV/c	3 GeV/c	4 GeV/c	5 GeV/c
a	1.11 ± 0.01	1.17 ± 0.01	1.20 ± 0.02	1.23 ± 0.02
p_0 $[10^{-3}]$	-1.10 ± 1.57	-1.14 ± 0.82	-0.92 ± 0.85	-1.24 ± 0.51
p_1 $[10^{-2}]$	1.48 ± 0.23	2.67 ± 0.15	4.10 ± 0.17	5.79 ± 0.12
c $[10^{-1}]$	-5.02 ± 2.72	-4.65 ± 0.93	-4.06 ± 0.73	-4.59 ± 0.44

Table C.2: Determined fit parameters for the model-dependent (cf. Eq. 9.11) and model-independent (cf. Eq. 9.12) calibration with fit parameters a and p_0, p_1, c, respectively. Evaluated are measurements at different beam momenta between 2 and 5 GeV/c.

For the model-dependent calibration, as shown in Figure 9.26a, the corresponding relative deviations between the individual measurement points of the kink angle widths and the determined calibration function are calculated and plotted for the different beam momenta in Figure C.4.

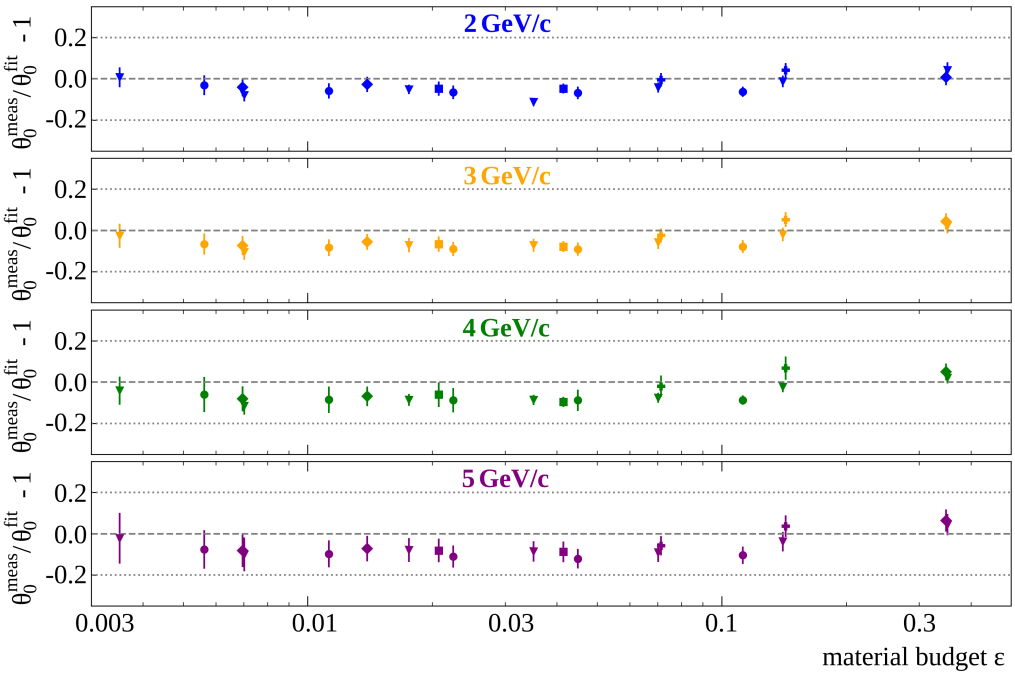

Figure C.4: Relative deviation between the measurement points and the model-dependent calibration fit for the calibration curves with beam momenta between 2 and 5 GeV/c.

For the model-independent calibration, as shown in Figure 9.26b, the relative deviations between the truth material budget and the determined value from the calibration fit are shown in Figure C.5 for the different beam momenta.

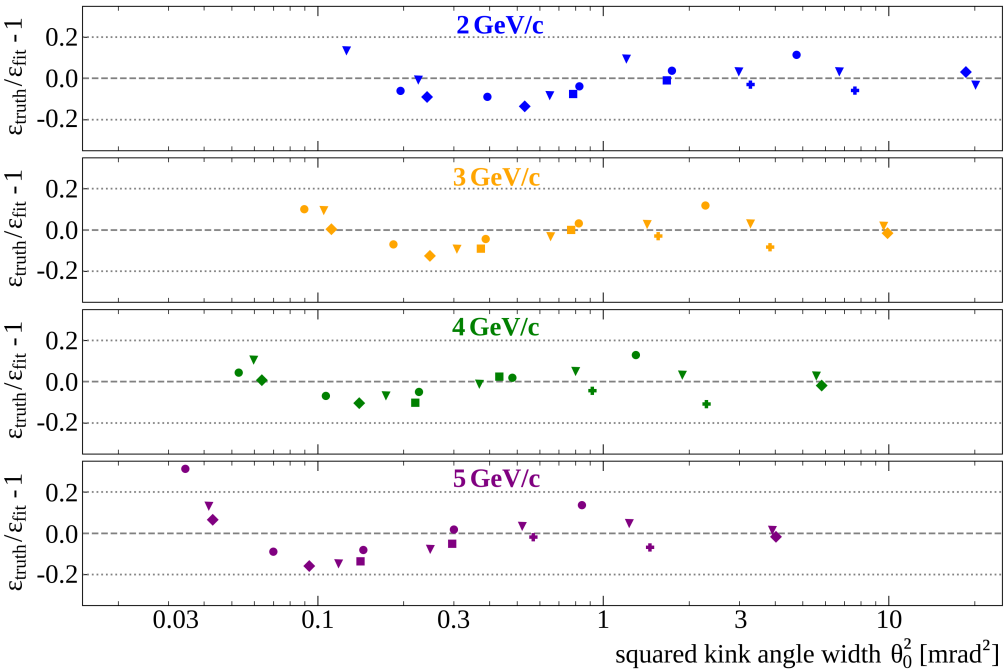

Figure C.5: Relative deviation between the measurement points and the model-independent calibration fit for the calibration curves with beam momenta between 2 and 5 GeV/c.

In Table C.3, the mean value and its standard deviation as well as the minimum and maximum of the relative deviations for both calibration approaches are given, evaluated for the different beam momentum settings. In the case of the model-independent calibration, the two samples with the lowest material budget, namely 0.05 mm nickel and 0.1 mm aluminum, are excluded here due to the large discrepancy for these measurement points.

	Beam momentum	Relative deviation		
		mean ± std	minimum	maximum
Model-dependent	2 GeV/c	-3.4 ± 3.9	-11.3	4.2
	3 GeV/c	-5.0 ± 4.5	-10.5	5.2
	4 GeV/c	-5.4 ± 5.0	-11.6	6.7
	5 GeV/c	-6.1 ± 5.3	-12.1	6.4
Model-independent	2 GeV/c	-1.8 ± 6.7	-13.6	11.5
	3 GeV/c	-1.4 ± 6.5	-12.5	12.0
	4 GeV/c	-1.0 ± 6.8	-10.9	12.9
	5 GeV/c	-2.3 ± 8.7	-15.8	13.7

Table C.3: Relative deviation between measurement points and the evaluated calibration fit using the model-dependent as well as the model-independent approach. Shown are the calculated mean value and its standard deviation as well as the minimum and maximum value of the relative deviations for the measurements at different beam momenta between 2 and 5 GeV/c.

For the model-dependent calibration, the relative deviation shows systematically negative values apart from the highest material budget samples and is quite constant over the covered material budget range. On the contrary, the model-independent calibration shows a larger fluctuation of the relative deviation in both directions.

C.5 Resolution and contrast for material budget image

To study the dependence of the image resolution and contrast for the two-dimensional kink angle maps on the selected image cell size and correspondingly the number of reconstructed tracks per image cell, the cell size in the MBI analysis of a measurement with the petal core prototype (cf. Sec. 9.2.3) is systematically varied. The measurement was conducted at beam line TB22 with a beam momentum of 4 GeV/c and telescope setup S2. In total, 10×10^6 triggered events were recorded with roughly 16.5×10^6 tracks after reconstruction.

In Figures C.6 and C.7, the two-dimensional distributions of the corrected kink angle widths θ_0 (meaning an estimation of the width with the RMS_{98} estimator on the combined kink angle k_{x+y} and the quadratic subtraction of the air scattering contribution) for cell sizes of $(100\,\mu\mathrm{m})^2$, $(50\,\mu\mathrm{m})^2$, $(25\,\mu\mathrm{m})^2$, $(20\,\mu\mathrm{m})^2$ and $(10\,\mu\mathrm{m})^2$ are shown. The numbers of reconstructed tracks per image cell are on average 6446 ± 1244, 1627 ± 295, 409 ± 75, 262 ± 50 and 67 ± 16 for the respective cell sizes.

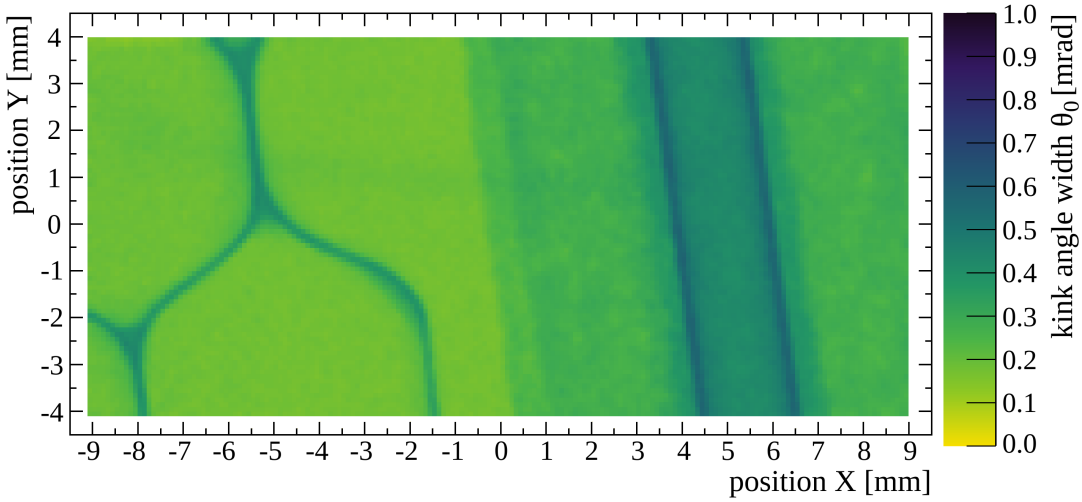

(a) $(100\,\mu\mathrm{m})^2$ cell size.

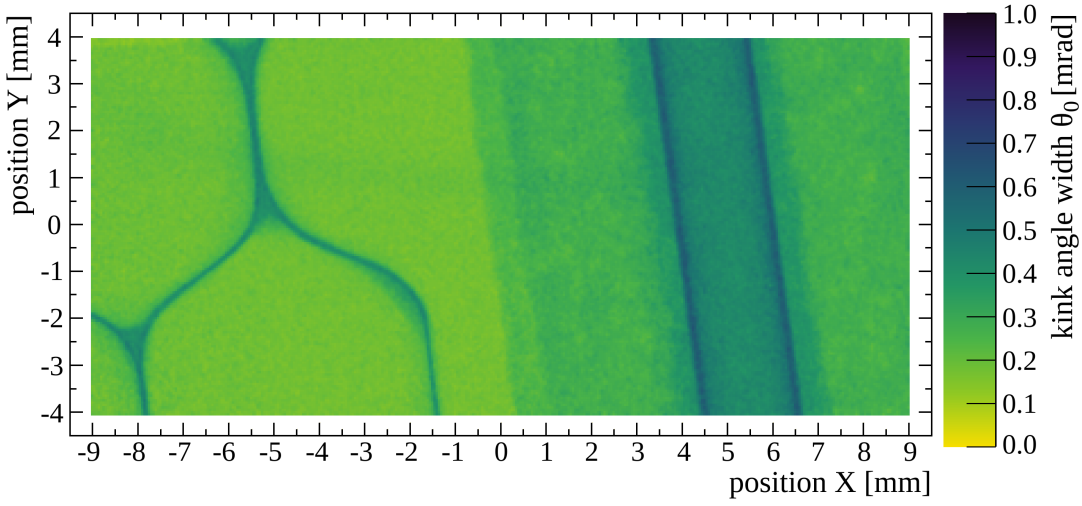

(b) $(50\,\mu\mathrm{m})^2$ cell size.

Figure C.6: Material budget image of a part of the petal core structure with cell sizes of $(100\,\mu\mathrm{m})^2$ and $(50\,\mu\mathrm{m})^2$.

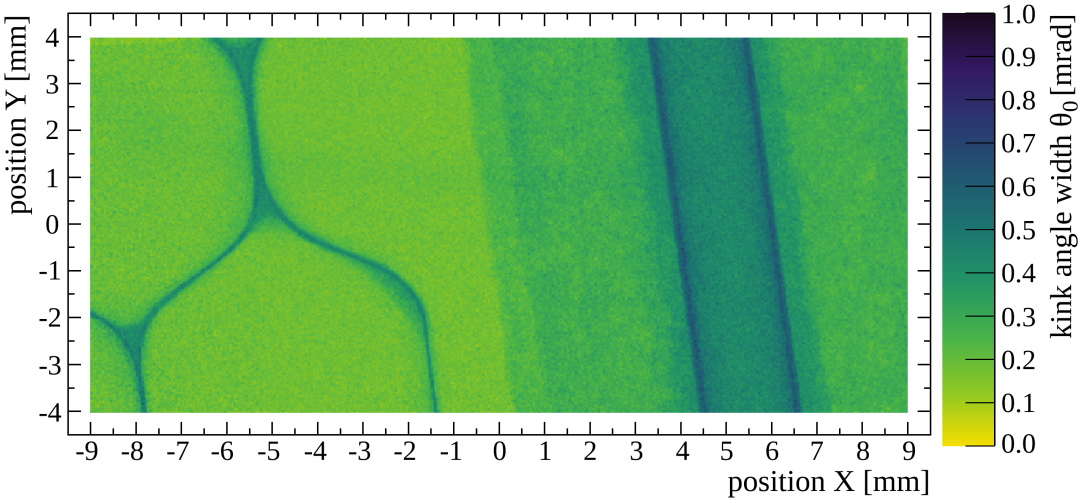

(a) $(25\,\mu\text{m})^2$ cell size.

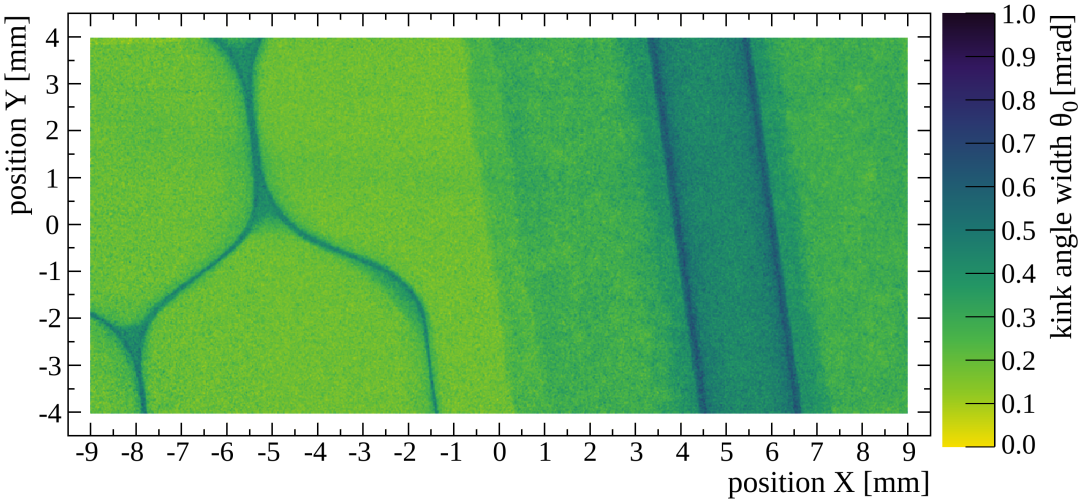

(b) $(20\,\mu\text{m})^2$ cell size.

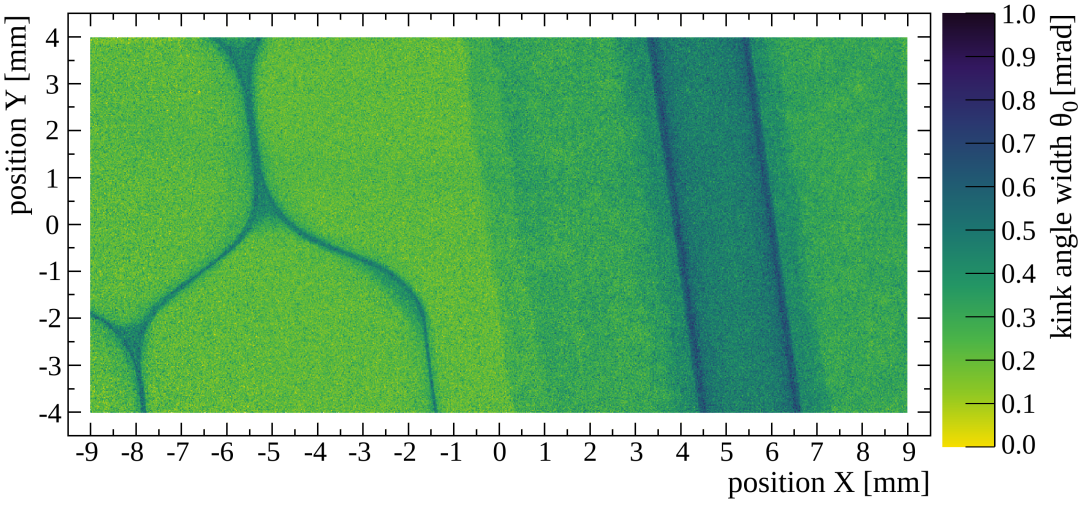

(c) $(10\,\mu\text{m})^2$ cell size.

Figure C.7: Material budget image of a part of the petal core structure with cell sizes of $(25\,\mu\text{m})^2$, $(20\,\mu\text{m})^2$ and $(10\,\mu\text{m})^2$.

The image resolution is improving with a smaller cell size allowing to finer resolve the features of the structure, such as the titanium cooling pipe embedded in the carbon-based foam or the walls of the CF honeycomb. But for a too small cell size, such as $(10\,\mu\text{m})^2$, and with a corresponding low number of reconstructed tracks per image cell, here only 67 ± 16 tracks on average, the estimated width of the kink angle distribution becomes biased and provides no stable output anymore, resulting in artifacts in the two-dimensional kink angle maps. In the performed investigations, it was found that at least 100 tracks per image cell should be required, defining therefore also the cell size to be selected in the MBI analysis. For the analysis of the measurement with the petal core structure, an image cell size of $(20\,\mu\text{m})^2$ was accordingly selected, providing a high resolution and contrast in the image.

C.6 Two-dimensional stitching of material budget images

For the investigation of the two-dimensional material budget distribution of samples, several scattering measurements are performed in terms of a scan along the x- and y-direction with the automated x-y-positioning stage. This allows to image also larger areas of the sample than the detection area of $(2 \times 1)\,\text{cm}^2$ by stitching the individual material budget images to a larger image. To account for the fiducial region cut introduced in the MBI analysis, a respective overlap between images of neighboring scanning positions is used.

For the imaging of the **EoS board**, five measurements along the x-direction were performed with a step size of $\Delta x = 16\,\text{mm}$, corresponding to an overlap of 2 mm on both sides. The two-dimensional maps of the material budget before stitching are shown in Figure C.8.

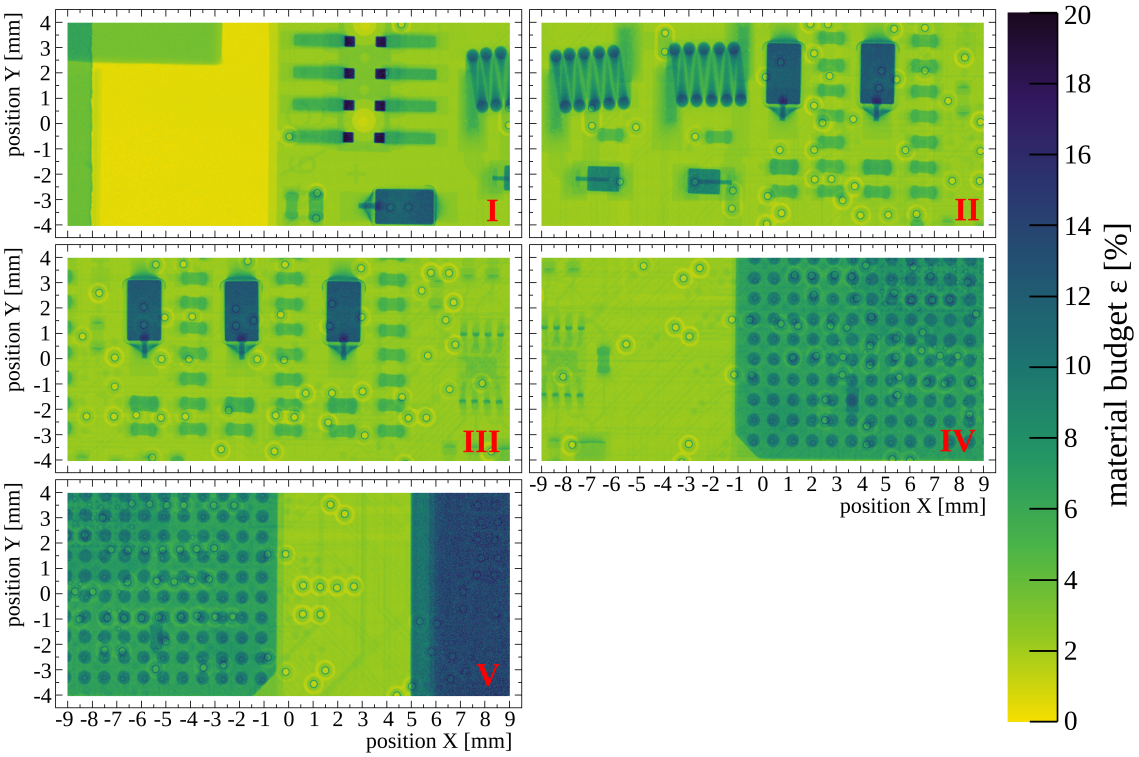

Figure C.8: Two-dimensional maps of the material budget before stitching of a scan over the EoS board along the x-direction, covering a total area of $(75 \times 8)\,\text{mm}^2$ with five individual measurements. The images with a cell size of $(10\,\mu\text{m})^2$ are labeled according to the imaged section between I and V (cf. Fig. 9.6b) with the defined step size of $\Delta x = 16\,\text{mm}$.

The material budget distribution of the **cocured bus tape** was investigated in seven consecutive measurements along the x-direction, covering a total area of $(126 \times 8)\,\mathrm{mm}^2$. Here, a step size of $\Delta x = 18\,\mathrm{mm}$ was chosen, resulting in a minimal overlap of 1 mm per side taking into account the smaller fiducial region for the MBI analysis. The material budget images of the structure before the manual stitching are depicted in Figure C.8, labeled according to their respective x-position.

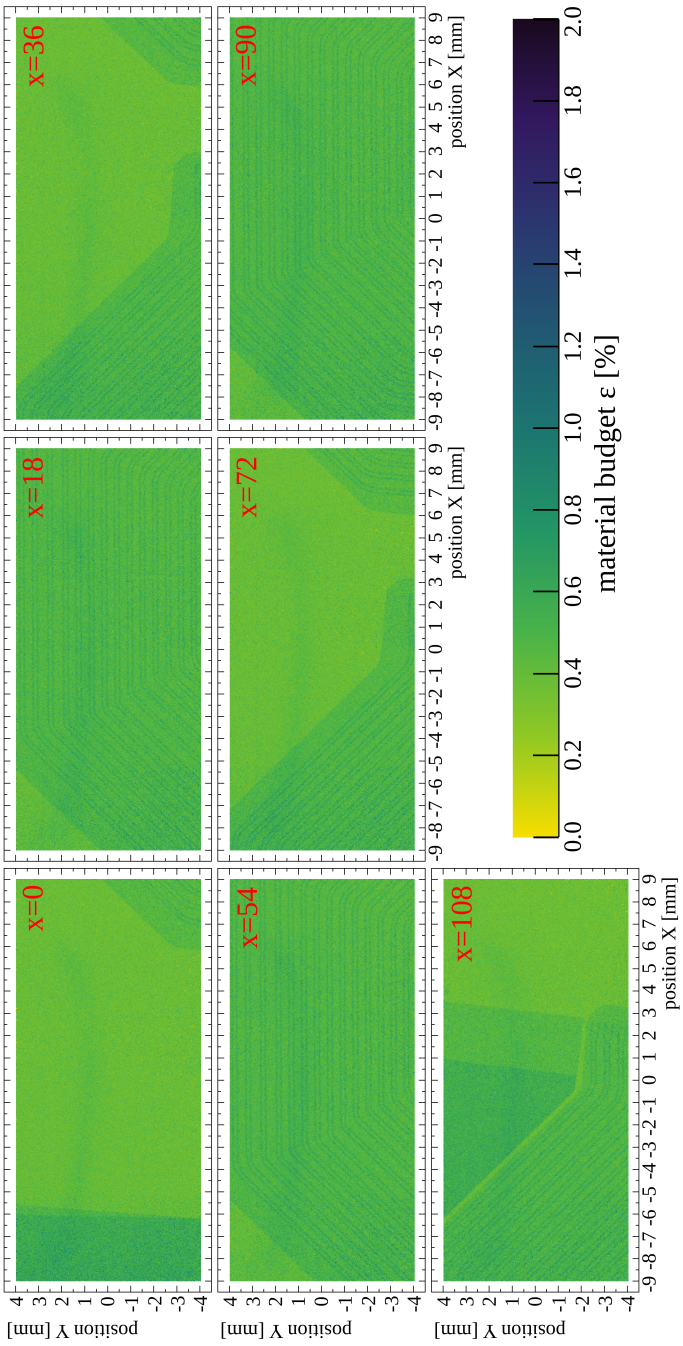

Figure C.9: Two-dimensional maps of the material budget before stitching of a scan over the cocured bus tape along the x-direction, covering a total area of $(126 \times 8)\,\mathrm{mm}^2$ with seven individual measurements. The images with a cell size of $(20\,\mu\mathrm{m})^2$ are labeled with the position of the x-y-positioning stage with the defined step size of $\Delta x = 18\,\mathrm{mm}$.

For the imaging of the **petal core**, a scan in the x- and y-direction with nineteen individual measurements was performed, covering a total image area of $(148 \times 16)\,\mathrm{mm}^2$. Measurements were performed at $y = 0$ and $y = 8$, resulting in an overlap of 1 mm at the top and bottom of the images. The step size in the x-direction was varied between $\Delta x = 15\,\mathrm{mm}$ and $\Delta x = 18\,\mathrm{mm}$, depending on the corresponding y-position and resulting in overlaps of 2.5 and 1 mm per lateral side, respectively. The two-dimensional maps of the material budget at the respective x- and y-positions before stitching are shown in Figure C.10.

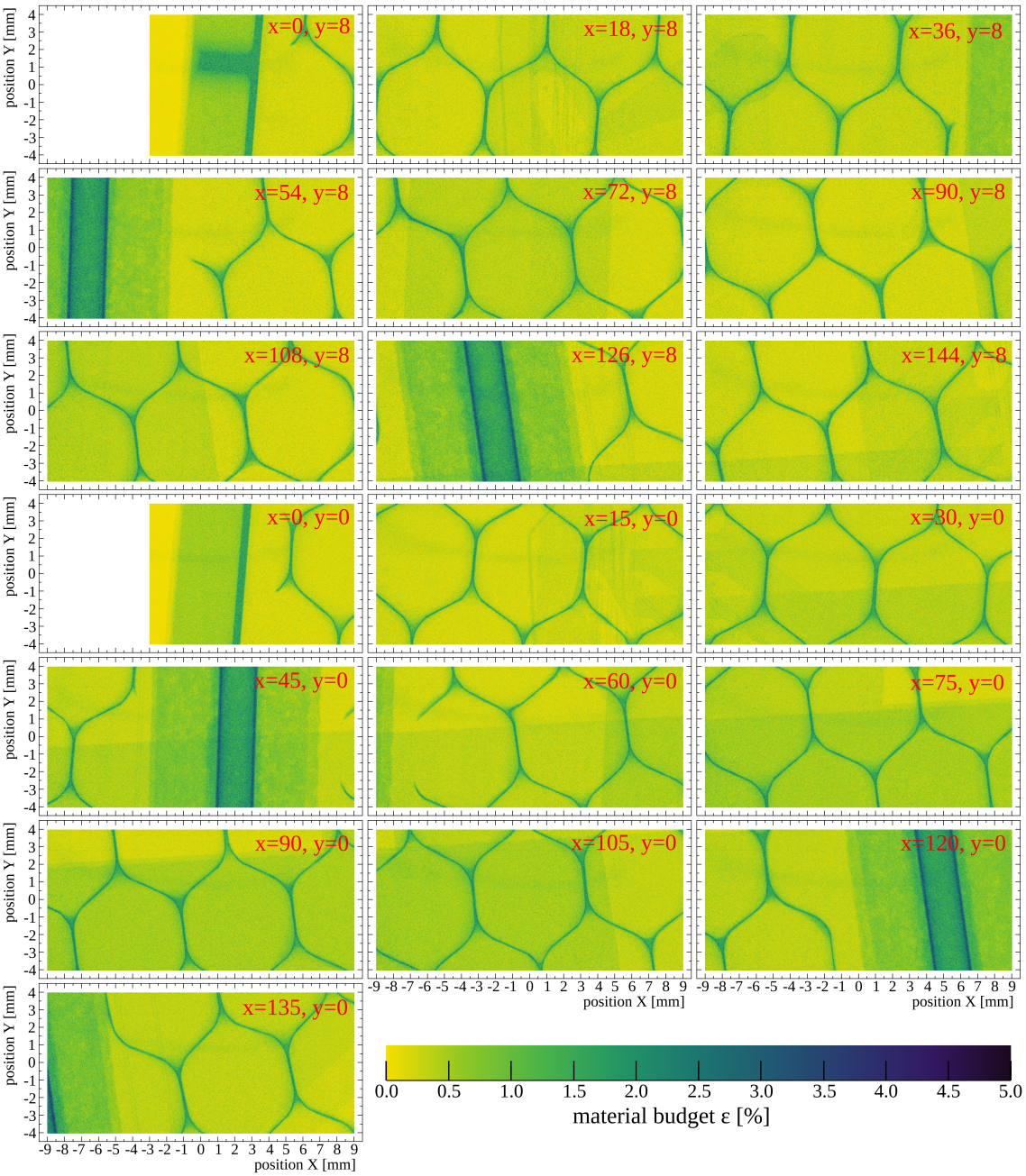

Figure C.10: Two-dimensional maps of the material budget before stitching of a scan over the petal core in the x- and y-direction, covering a total area of $(148 \times 16)\,\mathrm{mm}^2$ with nineteen individual measurements. The images with a cell size of $(20\,\mu\mathrm{m})^2$ are labeled with the position of the x-y-positioning stage with the defined step sizes Δx and Δy between neighboring positions.

Finally, the material budget distribution of the **silicon sensor module** was investigated in a x-y-scan with fifteen individual measurements, covering a rectangular area of $(50 \times 48)\,\mathrm{mm}^2$. Here, a step size of $\Delta x = 16\,\mathrm{mm}$ was chosen in the x-direction, resulting in an overlap of 2 mm per side, whereas the step size in the y-direction with $\Delta x = 8\,\mathrm{mm}$ results in an overlap of 1 mm at the top and bottom of the images. The material budget images of the structure before the manual stitching are depicted in Figure C.11, labeled according to the respective positions of the x-y-positioning stage.

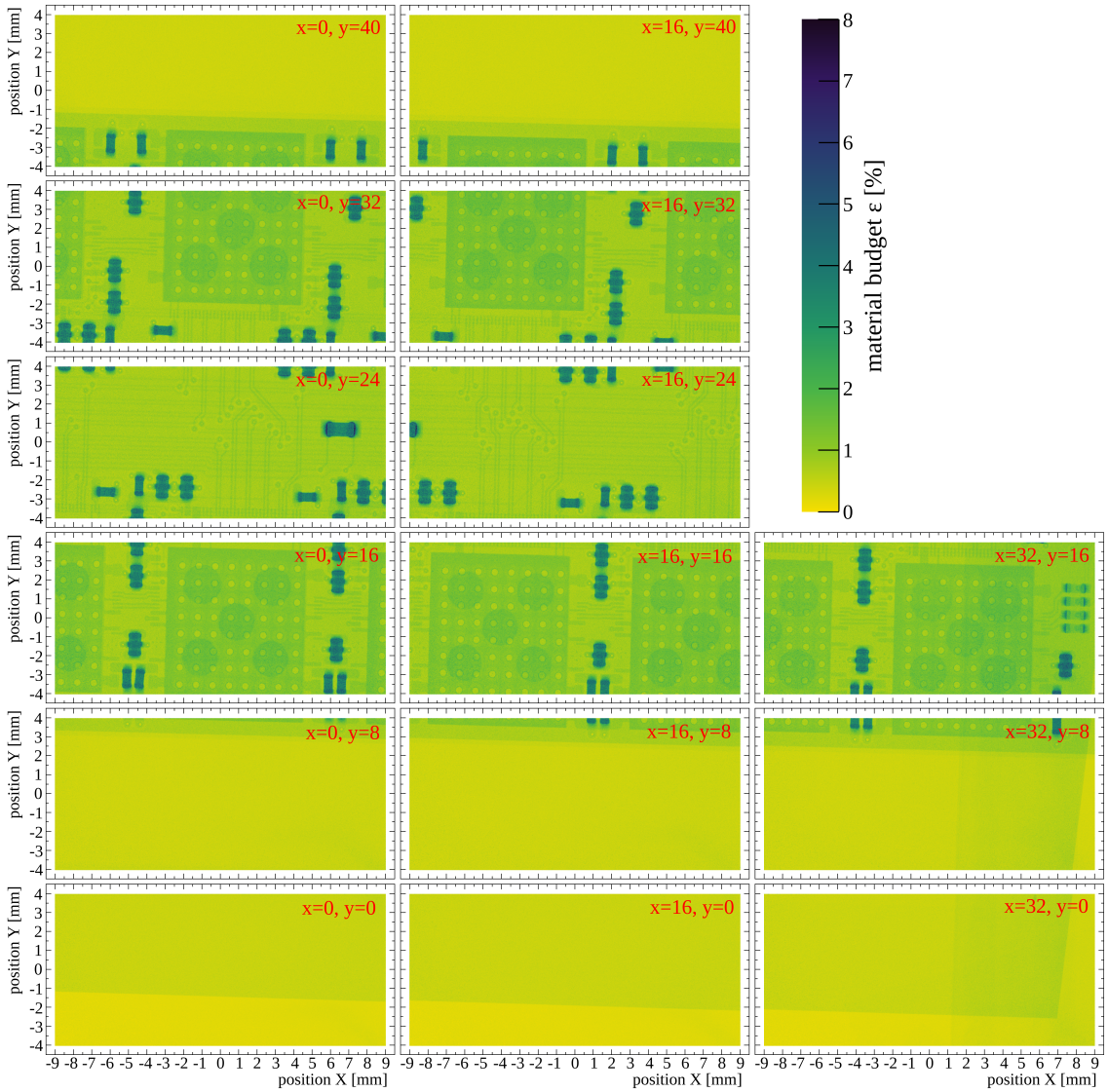

Figure C.11: Two-dimensional maps of the material budget before stitching of a scan over the silicon strip module in the x- and y-direction, covering a total area of $(50 \times 48)\,\mathrm{mm}^2$ with fifteen individual measurements. The images with a cell size of $(10\,\mu\mathrm{m})^2$ are labeled with the position of the x-y-positioning stage with the defined step sizes Δx and Δy between neighboring positions.